THE SEISMIC WAVEFIELD IN NENANA BASIN AND COOK INLET BASIN OF ALASKA

By

Kyle Smith, M.S.

A Dissertation Submitted in Partial Fulfillment of the Requirements

for the Degree of

Doctor of Philosophy

in

Geophysics

University of Alaska Fairbanks

May 2020

APPROVED:

Dr. Carl Tape, Committee Chair
Dr. Michael West, Committee Member
Dr. Jeffrey Freymueller, Committee Member
Dr. Richard Koehler, Committee Member
Dr. Marwan Wartes, Committee Member
Dr. Paul McCarthy, Chair
Department of Geosciences
Dr. Kinchel Doerner, Dean
College of Natural Science and Mathematics
Dr. Michael Castellini, *Dean of the Graduate School*

Abstract

Sedimentary basins amplify ground motion from earthquakes which can have severe consequences for major cities on basins like Tokyo and Los Angeles. Ground motion on sedimentary basins is complex and it depends on the geometry and elastic properties. We study the seismic wavefield from ambient noise and earthquake sources in Nenana Basin and Cook Inlet Basin with seismic stations from the Fault Locations and Alaska Tectonics from Seismicity (FLATS) and Southern Alaska Lithosphere and Mantle Observation Network (SALMON) projects. The FLATS project consists of 13 seismic stations placed over the Nenana Basin region in Central Alaska from 2014 to 2019. In South-Central Alaska, 28 seismic stations were placed around the Cook Inlet Region from 2015-2017 for the SALMON project. In this thesis, we have established two valuable data sets of events that can be used to better understand the complex influence of sedimentary basins on the seismic wavefield. Our analyses help quantify the frequency-dependent amount of amplification that occurs within these sedimentary basins.

A greater understanding of ambient noise can improve site selection as well as understanding other forces of nature. Many FLATS stations are near trees and a river, so we quantify the influence of river, wind and basin on ambient noise. We analyze ambient noise in the frequency domain with power spectral densities on annual, daily and hourly time scales. Rivers affect ground motion from shearing and turbulent forces. For FLATS stations within several meters of the Tanana River, we found consistent seasonal perturbations around 10 Hz. A comparison of the 10 Hz signal with river stage height, measured 14 km upriver, shows strong correlations exist during the summer and ambient noise increases by 40 dB. In the town of Nenana, a weather station shows wind occurs less during the winter than summer. Wind can directly interact with the ground through shearing forces or indirectly with the transfer of energy through trees. In this study, we found that wind can affect the ground motion by at least 10 dB for < 0.05 Hz. Basins amplify ground motion because it is easier to shear the materials. When we analyzed basin amplification from ambient noise we found that we had to correct for other noise sources like wind and river conditions. We also found that there were three classes of basin influence: Basin stations, marginal basin stations, and non-basin stations.

Cook Inlet Basin is a large forearc basin that overlies the subduction zone where the Pacific plate meets the North American plate. We study basin amplification from 34 regional earthquakes and ambient noise in two frequency bands (0.1–0.5 Hz and 0.5–4.0 Hz) with 48 seismic stations. We compared earthquake spectra of basin stations to non-basin reference stations and found an amplification of 6–14 dB on the vertical component low-frequency band. The results correspond closely to amplification of ambient noise at 9–15 dB. For a third technique, we computed earthquakes metrics such as radiated energy to basin depth and found stronger correlations on the horizontal component than the vertical. The results have implications for assessing seismic hazard for earthquakes such as the November 30, 2018 M_w 7.1 Anchorage event.

Nenana Basin overlies the Minto Flats Fault Zone which can produce earthquakes with $M_w \geq 6$. We study the Nenana Basin with 16 seismic stations and 48 earthquakes. Similar techniques from Cook Inlet Basin are used but distance corrections are applied to earthquake spectral ratios and teleseismic earthquakes are analyzed. The Nenana Basin amplifies ambient noise by 8–14 dB and earthquakes by 11–14 dB on the vertical component at 0.1–0.5 Hz. Results from teleseismic P waves are perplexing since amplification is not as strong as S waves. Other results show that radiated energy correlates more with basin depth as the magnitude of earthquake sources increase.

Overall, Nenana Basin has higher amplification levels than Cook Inlet Basin for earthquake spectral ratios on 0.1–0.5 Hz for all components. Noise spectral ratios prove to be a useful tool for studying amplification when earthquake data is sparse. Amplification is highly variable and future work in 3D simulations will address the complexities.

Table of Contents

Page

Page

Page

List of Figures

Page

Page

Page

Page

Page

Page

List of Tables

Page

List of Appendices

Page

Acknowledgements

First, I'd like to recognize my advisor Carl Tape who deserves a great big thanks. He sets a good example for others to follow and is a dedicated mentor, collaborator, and scientist. Thanks goes to my committee members who have been helpful for giving feedback and support: Michael West, Jeff Freymueller, Marwan Wartes, and Rich Koehler. Special thanks goes to Vipul Silwal for having my back and being a great friend and of course my family for their support and encouragement. I'd like to recognize Victor Tsai for giving detailed feedback and collaborating with us on the final project. More thanks goes to my other collaborators who provided some tools, data, feedback, and a helping hand in the field: Morgan Moschetti, Michael West, Christopher Bruton, Heather Best, Kasey Aderhold, and Cole Richards. Additionally, I am grateful for the basin map provided by Doyon Limited. I am also thankful for the financial support from Alaska Division of Geological and Geophysical Surveys, UAF Department Geoscience, Alaska Earthquake Center, UAF Geophysical Institute, and NSF (EAR-1352688). This work would not have been possible without their support.

Chapter 1

Introduction

In the past 15 years, seismic noise has become a cornerstone of seismology (Shapiro et al., 2005; Nakata et al., 2019). Advances in theory and computational resources have enabled the proliferation of seismic noise studies. Seismic noise is useful for characterizing data quality and monitoring other forces of nature. In some cases, seismic noise is used for obtaining subsurface structure such as sedimentary basins. Many sedimentary basins contain reservoirs of lucrative hydrocarbons that match the world's energy needs. Basins are also the foundation to the homes of millions of people worldwide in cities like Los Angeles, Tokyo, and Mexico City. Sedimentary basins present a hazard to many of these places because their elastic properties amplify ground motion from earthquakes.

As part of this thesis, we installed two networks of seismic stations in two sedimentary basins in Alaska—Nenana and Cook Inlet—to study seismic noise and basin amplification. In central Alaska we had a set of 13 broadband seismometers covering the Nenana basin region from September 2014 to September 2019 in a project called Fault Locations and Alaska Tectonics from Seismicity (FLATS) (Chapter 2). In south-central Alaska, 28 broadband stations covered the Cook Inlet basin region from May 2015 to July 2017 in a project called Southern Alaska Lithosphere and Observation Network (SALMON) (Tape et al., 2017). From 2014 to 2019 a large network of seismic stations from the Transportable Array (TA) (Williams et al., 2010) was transported to Alaska at 70 km spacing. Prior to 2014, most of the seismic data came from the Alaska Network, managed by the Alaska Earthquake Center. This has yielded the richest seismic dataset of all time in the most tectonically active region in the US.

The Nenana and Cook Inlet basins lie in active complex tectonic environments. Nenana basin (Figure 2.1) overlies the Minto Flats fault zone (MFFZ) which produced a M_w 6.0 earthquake in 1995, a M_w 5.8 in 2000, and a M_w 5.0 in 2014. The MFFZ consists of two large NE trending left-lateral faults that accommodate transtensional deformation (Tape et al., 2015; Dixit et al., 2017). The MFFZ lies *en echelon* with the Fairbanks seismic zone and Salcha seismic zone, and these three left-lateral strike-slip zones have been interpreted within the context of a block rotation model (Page et al., 1995). The Nenana basin consists of major formations from Nenana gravel and the Usibelli group (Wartes et al., 2013; Van Kooten et al., 2012). Nenana gravel consists of deposits

from the Alaska Range and Yukon-Tanana Terrane from the Pliocene and the Usibelli group which were both deposited during the Miocene (Ridgway et al., 2007). Estimates of the basin depth (Doyon Limited, 2012; Dixit et al., 2017; PRA, 2017) are ever changing due to new techniques and data but we will use the latest estimate from PRA (2017) which gives a maximum depth of 6.7 km.

Cook Inlet forearc basin is situated within a subduction zone where the Pacific plate converges with the North American Plate in south-central Alaska (See Figure 3.1). The subduction zone is the cause of major earthquakes such as the 1964 M_w 9.2 Great Alaska earthquake and the 2018 M_w 7.1 Anchorage event. South-central Alaska is further complicated with the tectonic influence of the subducting Yakutat microplate and Castle Mountain fault. Many of the earthquakes since 1964 did not occur from thrust faulting on the plate boundary as we would expect, but occurred within the slab (Li et al., 2013). Within the Cook Inlet region there have also been a lack of crustal events since 1964 (Silwal et al., 2018). The Cook Inlet basin consists of multiple formations where a large influx of sedimentation occurred 180–140 Ma (Fisher & Magoon, 1978; Saltus et al., 2007; LePain et al., 2014). The Cook Inlet basin was mapped out from (Shellenbaum et al., 2010) using marine seismic reflection data and oil and gas wells which indicates a maximum depth of 7.6 km.

1.1 Environmental Monitoring

Seismic noise is popularly exploited to obtain images of subsurface structure (Shapiro et al., 2005) but it can also be used as a tool to monitor the activity of the local environment (Schmandt et al., 2013; De Angelis & Bodin, 2012). In general, low-frequency signals identify with distal sources and high-frequency signals identify with nearby sources because of the attenuation of high frequency signals. Environmental seismology brings new opportunities to monitor natural hazards and improve existing scientific studies.

In Green et al. (2017) an array of seismometers were deployed across the city of London to study anthropogenic noise. They found that the noise wavefield was largely influenced by transportation sources, except at 0.167–0.5 Hz. However, exceptions exist for stations closest to large transportation sources. The noise in urban environments is useful because engineers can account for it in site effects when they plan future projects (e.g., Panou et al., 2005). Seismic noise has also been used to study the effects of wind speed and burial conditions. Withers et al. (1996) quantified the effects of wind on seismic noise with respect to burial depth and found a greater influence from

short frequencies (<20 Hz) but the study was limited to short-period sensors. They were fortunate enough to subtract the effects of cultural noise and test their study in a windy environment in a remote location in the deserts of western New Mexico. Lott et al. (2017) established a linear regression model for wind speed and power of ground velocity for three frequency bands (0.01–0.1 Hz, 0.1–1 Hz, 1–100 Hz). The relationship is not perfect because it does not account for the variability of the terrain and burial conditions. An important conclusion from Chapter 2 highlights the importance of accounting for wind in seismic noise to study site effects.

The effects of seismic noise from rivers was first documented by Burtin et al. (2008). The various signals from rivers, which include sediment transport, river turbulence and shearing, and river–air interactions can be monitored respectively at 15–45 Hz, 0.5–2 Hz, 2–15 Hz (Schmandt et al., 2013). In Chapter 2, our results suggest river influence at 10 Hz. Our study also suggests the potential for using seismometers to monitor river ice at the onset of breakup, an event that can cause devastating flooding in communities along the river (e.g., Kontar et al., 2015).

Seismometers have also been used to monitor the effects of cyclones on ground motion. Chi et al. (2010) used the vertical component of ocean bottom seismometers and on-land seismometers to closely monitor the direct impacts of Typhoon Shanshan (Category 4). They found maximum amplification of ground motion hours after the eye had passed and stronger ground motion for stations closest to the ocean than those further inland. Tanimoto & Lamontagne (2014) made some key observations with the TA network for a smaller cyclone, Hurricane Isaac (Category 1), that made landfall. They found a strong relationship of amplitude variations and distance to the eye at 0.01–0.02 Hz.

1.2 Spectral Ratio Methods

Two popular methods exist for evaluating site effects. The methods rely on spectra, which are an expression of a time series signal at various frequencies. Spectra are obtained from the Fourier transform of a signal, which breaks down a signal into a combination of harmonic waves at different frequencies and amplitudes. The first method is called standard spectral ratio (SSR). It was developed by Kagami et al. (1982) and Kagami et al. (1986). It compares a station's signal spectra to a reference station's spectra. This has been applied to compare the response of basin stations to non-basin stations. It assumes similar paths for both stations and the availability of a reliable

reference station. The other method is the horizontal-to-vertical spectral ratio (HVSR) developed by Nakamura (1989). It compares the spectra of horizontal components to vertical components for the same station. The method assumes the basement has the same amplitude for vertical and horizontal components and that the vertical-to-horizontal comparison at the surface is related to the fundamental mode of Rayleigh waves. It has the advantage of not relying on a reference station but it can have disadvantages for interpretation at higher frequencies. Nakamura's method has gained significant popularity and it has been used to evaluate tilting from the atmosphere and obtain resonant frequencies for landslides (Pilz et al., 2014).

1.3 Basin Effects

Amplification from sedimentary basins are explored with direct observations and computer simulations at low frequencies. In Cook Inlet basin, Moschetti et al. (2019) studied amplification using regression models called ground motion prediction equations (GMPEs) to predict strong motion from several earthquake clusters at intermediate depths. They were able to find stronger correlations of amplification and basin depth for shorter frequencies (< 2 Hz). The highest amplifications occurred for signals at 1 Hz. A study from Bindi et al. (2009) used the SSR to show that the Gubbio basin in central Italy amplified ground motions by a factor of 5 with the highest amplifications occurring close to 1 Hz. Bindi et al. (2009) also found that shaking lasted 2 times longer inside the basin than outside with the highest amplitudes at 1 Hz. A study from Pratt et al. (2003) showed the basin response < 1 Hz from incoming S Waves in Seattle basin from the M_w 7.6 Chi-Chi earthquake and response at > 1 Hz from local earthquake and blast sources using the SSR method. The S waves showed a maximum amplification at 12 for 0.5–0.8 Hz and a general decrease in amplification for increasing frequencies above 1 Hz for local events.

Seismic data from large earthquakes are limited in many regions, and therefore some scientists focus on studying scenario earthquakes using computer simulations. Short-frequency simulations are easiest to perform but it can have issues if the geometry is not well known or if shallow structures are poorly mapped (e.g. Wald & Graves (1998)). Simulations of the Los Angeles basin by Vidale & Helmberger (1988) showed amplification in LA basin from surface waves by a factor of 3 for 0.1–0.5 Hz. Further investigation of simulated surface waves from Toshinawa & Ohmachi (1992) indicated that Love waves are highly influenced from higher dimensional models (e.g. 3D

and 2D) than lower ones (e.g. 2D and 1D). However, engineers prefer simplistic and consistent 1D models, so efforts are underway to improve prediction of surface waves (Bowden & Tsai, 2017). Another important issue with surface waves is accounting for nonlinear effects which occur for places close to the large earthquakes (Joyner, 2000).

Earthquakes across the world have unique shapes and sizes which makes amplification patterns unique. The approaches to modelling the basin can have significant impacts on ground motion prediction. For engineers, most are concerned with basin depth. In the basin of Santiago de Chile, the basin has a very irregular shape with islands of bedrock that emerge because of the shallow structure. Results from Pilz et al. (2011) display a scenario earthquake with complex amplification patterns that emerge from the influence of basin shape and local topography. Additionally, they were able to see a correlation with basin depth and significantly smaller amplifications on the bedrock islands. The Taipei basin is less irregular and Sokolov et al. (2000) noted that the surrounding topography can have an influence on ground motion.

Higher dimensional models are generally more realistic and accurate but require significantly more effort and data. In many cases lower dimensional models are sufficient but it is beneficial to know the differences between low-dimensional models and high-dimensional models. Bard & Bouchon (1985) found significant differences of 2D model amplification and resonance with 1D models. They were able to conclude that shape ratios play a large role in resonance frequency. Smerzini et al. (2011) performed 1D, 2D and 3D simulations in the Gubbio basin in central Italy and was able to see more amplification in 3D models than 2D models.

Depth seems to play a large role in basin amplification as it is considered for predicting ground motions. Several observational and numerical studies show some evidence for an impact of depth on amplification. It is incorporated in GMPEs because there is a correlation with depth and amplification (Lee & Anderson, 2000). Specifically, Field (2000) noted that amplification in the center of LA basin was 2 times larger than near the edge. Numerical simulations carried out by Day et al. (2008) found a significant relationship between amplification and depth to be used in other empirical models. Depth is just one way to characterize basin geometry and the definition of basement can easily have significant impacts on basin shape.

Large material heterogeneities exist within basins that should be accounted for whenever modelling occurs. Many engineers classify basins by the limits at which wave travel speeds are less

than some threshold value such as 1 km/s or 2.5 km/s. If such data does not exist then basins can be estimated from its contrast to the density of basement with gravititational surveys. Whatever the definition of a basin, there exists inherent heterogeneous materials that generally get stronger and denser with depth. Many unconformities exist and the geological units have variable thicknesses and lateral discontinuities which alter wave propagation. High frequency waves generally correspond to shorter wavelengths which makes them more sensitive to smaller heterogeneities. Using 3D simulations Qin et al. (2012) found a wider area of enhanced peak ground velocity (PGV) values for a basin with a vertical velocity gradient than the homogeneous basin on the vertical component. For a realistic scenario Chavez-Garcia & Bard (1994) were able to provide evidence for amplification from a clay layer on top of the Mexico City basin from the great 1985 Michoacan earthquake. With new tomographic studies, the relationship with heterogeneities and basin amplification can be further explored and understood.

Additional basin amplification also depends on source variation, focusing, and trapping. Earthquake sources can be modelled with a point or rupturing plane called a finite source. With point sources it is imperative to consider the depth, magnitude, location, and focal mechanism because they can each play a role in basin amplification. In particular, shallow earthquakes produce greater amplifications due to their efficiency to produce surface waves at the basin edges (Wirth et al., 2019). Whenever finite sources are considered, Frankel (1993) showed that there can be a strong interaction with basin edges when the rupture is nearby. Rupture direction can also have a large impact on amplitudes. Basin edges present a hazard because they produce strong ground motion from large impedance contrasts and they facilitate the production of surface waves. One of the most well-known cases was for the 1995 Hyogo-ken Nambu earthquake in Kobe, Japan which created a path of destruction along the basin edge (Kawase, 1996). From the 1992 Landers aftershock sequence, Field (1996) used SSR to conclude that basin edges only have an effect for < 4 Hz, and an amplification factor of 18 can occur.

Sometimes sedimentary basins can act like a lens and amplify ground motion at certain parts of the basin. In this case, a 1D model will not be able to account for such effects. For an earthquake in Caracas, Venezuela, Rial (1984) found evidence of focusing from the pattern of destruction. Further investigation from Shani-Kadmiel et al. (2014) explored focusing using an analytical method in which impedance contrasts can modify the locations of amplification. Like with any object,

a basin carries a natural frequency and the waves that get trapped from reflections will prolong the duration of shaking and that can have consequences for ground motion (Rial et al., 1992). Since each basin is unique, the response from source variation, focusing, and trapping will also be unique as well.

1.4 Chapter overview and other collaborations

This thesis contains work for three main projects which correspond to seismic noise in Nenana basin in central Alaska (Chapter 2), amplification of seismic waves in Cook Inlet basin in south-central Alaska (Chapter 3), and amplification of seismic waves in Nenana basin in central Alaska (Chapter 4). Chapter 2 will discuss the influence of rivers, wind, people and basin on seismic noise and monitoring these effects with other available data from river gauges, weather stations, basin maps, and *in situ* measurements. Appendix 1 provides further details about the analysis and a new paper about the effects of river ice on seismic noise. Chapter 3, discusses basin amplification using three different methods from seismic noise and earthquake sources. The methods explore the frequency-dependence of amplification and ground motion metrics like duration, radiated energy, peak ground displacement, etc and its relation to basin depth. The second and third method uses the SSR method for earthquake sources and seismic noise. In our SSR method we account for signal-to-noise ratio and varying geologic units from regional earthquakes. Appendix 2 provides more detail about the methodology and aggregate results from other components (radial and transverse). Further details for our analysis are in Smith (2019), which gives a detailed account of our other results in terms of all channels and variation of spectral ratios, signal-to-noise ratio, and metrics for event characteristics like distance-to-basin, depth, and magnitude. Chapter 4 refines techniques from Chapter 3 with distance corrections and environmental corrections of noise-based amplification. From Chapter 3, we have a better idea of source effects from focal mechanism and response from teleseismic waves and amplification from other reference stations. Appendix 3 is the supplementary material and provides more detail about our earthquake characteristics, aggregate results of SSRs, and the effect of magnitude on correlations with radiated energy and basin depth.

1.5 References

Bard, P.-Y. & Bouchon, M., 1985. The two-dimensional resonance of sediment-filled valleys, *Bull. Seismol. Soc. Am.*, **75**(2), 519–541.

Bindi, D., Parolai, S., Cara, D., Di Giulio, G., Ferretti, G., Luzi, L., Monachesi, G., Pacor, F., & Rovelli, A., 2009. Site amplifications observed in the Gubbio basin, central Italy: Hints for lateral propagation effects, *Bull. Seismol. Soc. Am.*, **99**(2A), 741–760, doi: 10.1785/0120080238.

Bowden, D. C. & Tsai, V. C., 2017. Earthquake ground motion amplification for surface waves, *Geophys. Res. Lett.*, **44**, 121–127, doi: 10.1002/2016GL071885.

Burtin, A., Bollinger, L., Vergne, J., Cattin, R., & Nábělek, J. L., 2008. Spectral analysis of seismic noise induced by rivers: A new tool to monitor spatiotemporal changes in stream hydrodynamics, *J. Geophys. Res.*, **113**, B05301, doi: 10.1029/2007JB005034.

Chavez-Garcia, F. J. & Bard, P.-Y., 1994. Site effects in Mexico City eight years after the September 1985 Michoacan earthquakes, *Soil Dynamics and Earthquake Engineering*, **13**, 229–247.

Chi, W.-C., Chen, W.-J., Kuo, B.-Y., & Dolenc, D., 2010. Seismic monitoring of western Pacific typhoons, *Marine Geophysical Researches*, **31**, 239–251, doi: 10.1007/s11001-010-9105-x.

Day, S. M., Graves, R., Bielak, J., Dreger, D., Larsen, S., Olsen, K. B., Pitarka, A., & Ramirez-Guzman, L., 2008. Model for basin effects on long-period response spectra in southern California, *Earthquake Spectra*, **24**(1), 257–277.

De Angelis, S. & Bodin, P., 2012. Watching the wind: seismic data contamination at long periods due to atmospheric pressure-field-induced tilting, *Bull. Seismol. Soc. Am.*, **102**(3), 10.1785/0120110186.

Dixit, N., Hanks, C., Rizzo, A., McCarthy, P., & Coakley, B., 2017. Cenozoic tectonic and thermal history of the Nenana basin, central interior Alaska: new constraints from seismic reflection data, fracture history, and apatite fission-track analyses, *Can. J. Earth Sci.*, **54**, 766–784, doi: 10.1139/cjes-2016-0197.

Doyon Limited, 2012. Nenana Basin Depth Map, Available as an interactive website at http://doyonoil.com/HiResImage/NenDepthMap-ForWeb, last accessed 2015-04-12, depth data and contours from Gary Thompson.

Field, E. H., 1996. Spectral amplification in a sediment-filled valley exhibiting clear basin-edge-induced waves, *Bull. Seismol. Soc. Am.*, **86**(4), 991–1005.

Field, E. H., 2000. A modified ground-motion attenuation relationship for southern California that accounts for detailed site classification and a basin-depth effect, *Bull. Seismol. Soc. Am.*, **90**(6B), S209–S221.

Fisher, M. A. & Magoon, L. B., 1978. Geologic framework of lower Cook Inlet, *Am. Assoc. Petroleum Geol. Bull.*, **62**(3), 373–402.

Frankel, A., 1993. Three-dimensional simulations of ground motions in the San Bernadino Valley, California, for hypothetical earthquakes on the San Andreas fault, *Bull. Seismol. Soc. Am.*, **83**(4), 1020–1041.

Green, D. N., Bastow, I. D., Dashwood, B., & Nippress, S. E., 2017. Characterizing broadband seismic noise in Central London, *Seismol. Res. Lett.*, **88**(1), 113–124, doi: 10.1785/0220160128.

Joyner, W., 2000. Strong motion from surface waves in deep sedimentary basins, *Bull. Seismol. Soc. Am.*, **90**(6B), S95–S112.

Kagami, H., Duke, C. M., Liang, G. C., & Ohta, Y., 1982. Observation of 1-to 5-second microtremors and their application to earthquake engineering. Part II. Evaluation of site effect upon seismic wave amplification due to extremely deep soil deposits, *Bull. Seismol. Soc. Am.*, **72**(3), 987–998.

Kagami, H., Okada, S., Shiono, K., Oner, M., Dravinski, M., & Mal, A. K., 1986. Observation of 1- to 5-second microtremors and their application to earthquake engineering. Part III. A two-dimensional study of site effects in the San Fernando Valley, *Bull. Seismol. Soc. Am.*, **76**(6), 1801–1812.

Kawase, H., 1996. The cause of the damage belt in Kobe: "The basin-edge effect," constructive interference of the direct S-wave with the basin-induced diffracted/Rayleigh waves, *Seismol. Res. Lett.*, **67**(5), 25–34.

Kontar, Y. Y., Bhatt, U. S., lindsey, S. D., Plumb, E. W., & Thoman, R. L., 2015. Interdisciplinary approach to hydrological hazard mitigation and disaster response and effects of climate change on the occurrence of flood severity in central Alaska, *Proceedings of the International Association of Hydrological Sciences*, **369**, 13–17, doi: 10.5194/piahs-369-13-2015.

Lee, Y. & Anderson, J. G., 2000. Potential for improving ground-motion relations in southern California by incorporating various site parameters, *Bull. Seismol. Soc. Am.*, **90**(6B), S170–S186.

LePain, D. L., Stanley, R. G., Helmold, K. P., & Shellenbaum, D. P., 2014. Geologic framework and petroleum systems of Cook Inlet basin, south-central Alaska, in *Oil and Gas Fields of the Cook Inlet Basin, Alaska*, vol. 104 of **AAPG Memoir**, pp. 37–116, eds Stone, D. M. & Hite, D. M., American Association of Petroleum Geologists.

Li, J., Abers, G. A., Kim, Y., & Christensen, D., 2013. Alaska megathrust 1: Seismicity 43 years after the great 1964 Alaska megathrust earthquake, *J. Geophys. Res.*, **118**, 4861–4871, doi: 10.1002/jgrb.50358.

Lott, F. F., Ritter, J. R. R., Al-Qaryouti, M., & Corsmeier, U., 2017. On the analysis of wind-induced noise in seismological recordings, *Pure App. Geophys.*, **174**, 1453–1470, doi: 10.1007/s00024-017-1477-2.

Moschetti, M. P., Thompson, E. M., Rekoske, J., Hearne, M. G., Powers, P. M., McNamara, D., & Tape, C., 2019. Ground-motion amplification in Cook Inlet Region, Alaska from intermediate-depth earthquakes, including the 2018 M_w 7.1 Anchorage earthquake, *Seismol. Res. Lett.*, **91**(1), 142–152, doi: 10.1785/0220190179.

Nakamura, Y., 1989. A method for dynamic characteristics estimation of subsurface using microtremor on the ground surface, *Quarterly Report of the Railway Technical Research Institute*, **30**(1), 25–33.

eds Nakata, N., Gualtieri, L., & Fichtner, A., 2019. *Seismic Ambient Noise*, Cambridge, UK, Cambridge U. Press, 1st edn.

Page, R. A., Plafker, G., & Pulpan, H., 1995. Block rotation in east-central Alaska: A framework for evaluating earthquake potential?, *Geology*, **23**(7), 629–632.

Panou, A., Theodulidis, N., Hatzidimitriou, P., Stylianidis, K., & Papazachos, C., 2005. Ambient noise horizontal-to-vertical spectral ratio in site effects estimation and correlation with seismic damage distribution in urban environment: the case of the city of Thessaloniki (Northern Greece), *Soil Dynamics and Earthquake Engineering*, **25**, 261–274, doi: 10.1016/j.soildyn.2005.02.004.

Pilz, M., Parolai, S., Stupazzini, M., Paolucci, R., & Zschau, J., 2011. Modelling basin effects on earthquake ground motion in the Santiago de Chile basin by a spectral element code, *Geophys. J. Int.*, **187**(2), 929–945, doi: 10.1111/j.1365-246X.2011.05183.x.

Pilz, M., Parolai, S., Bindi, D., Saponaro, A., & Abdybachaev, U., 2014. Combining seismic noise techniques for landslide characterization, *Pure App. Geophys.*, **171**, 1729–1745, doi: 10.1007/s00024-013-0733-3.

PRA, 2017. Depth to Basement Map of Nenana Basin, Alaska, Proprietary map provided by Petrotechnical Resources of Alaska, April 2017.

Pratt, T. L., Brocher, T. M., Weaver, C. S., Creager, K. C., Snelson, C. M., Crosson, R. S., Miller, K. C., & Trehu, A. M., 2003. Amplification of seismic waves by the Seattle basin, Washington state, *Bull. Seismol. Soc. Am.*, **93**(2), 533–545.

Qin, Y., Wang, Y., Takenaka, H., & Zhang, X., 2012. Seismic ground motion amplification in a 3d sedimentary basin: the effect of the vertical velocity gradient, *J. Geophysics and Engineering*, **9**(6), 761–772, doi: 10.1088/1742-2132/9/6/761.

Rial, J., 1984. Caustics and focusing produced by sedimentary basins: applications of catastrophe theory to earthquake seismology, *Geophys. J. Int.*, **79**, 923–938.

Rial, J. A., Saltzman, N. G., & Ling, H., 1992. Earthquake-induced resonance in sedimentary basins, *American Scientist*, **80**, 566–578.

Ridgway, K. D., Thoms, E. E., Layer, P. W., Lesh, M. E., White, J. M., & Smith, S. V., 2007. Neogene transpressional foreland basin development on the north side of the central Alaska Range, Usibelli Group and Nenana Gravel, Tanana basin, in *Tectonic Growth of a Collisional Continental Margin: Crustal Evolution of Southern Alaska*, pp. 507–547, eds Ridgway, K. D., Trop, J. M., Glen, J. M. G., & O'Neill, J. M., Geol. Soc. Am., Boulder, Colo., USA, Special Paper 431.

Saltus, R. W., Hudson, T. L., & Wilson, F. H., 2007. The geophysical character of southern Alaska—Implications for crustal evolution, in *Tectonic Growth of a Collisional Continental Margin: Crustal Evolution of Southern Alaska*, pp. 1–20, eds Ridgway, K. D., Trop, J. M., Glen, J. M. G., & O'Neill, J. M., Geol. Soc. Am., Boulder, Colo., USA, Special Paper 431.

Schmandt, B., Aster, R. C., Scherler, D., Tsai, V. C., & Karlstrom, K., 2013. Multiple fluvial processes detected by riverside seismic and infrasound monitoring of a controlled flood in the Grand Canyon, *Geophys. Res. Lett.*, **40**, 4858–4863, doi: 10.1002/grl.50953.

Shani-Kadmiel, S., Tsesar sky, M., Louie, J. N., & Gvirtzman, Z., 2014. Geometrical focusing as a mechanism for significant amplification of ground motion in sedimentary basins: analytical and numerical study, *Bull. Earthquake Engineering*, **12**(2), 607–625, doi: 10.1007/s10518-013-9526-4.

Shapiro, N. M., Campillo, M., Stehly, L., & Ritzwoller, M. H., 2005. High-resolution surface-wave tomography from ambient seismic noise, *Science*, **307**, 1615–1618.

Shellenbaum, D. P., Gregersen, L. S., & Delaney, P. R., 2010. Top Mesozoic unconformity depth map of the Cook Inlet Basin, Alaska, Alaska Div. Geol. Geophys. Surv. Report of Investigation 2010-2, 1 sheet, scale 1:500,000, available at http://www.dggs.alaska.gov/pubs/id/21961 (last accessed 2016-10-30).

Silwal, V., Tape, C., & Lomax, A., 2018. Crustal earthquakes in the Cook Inlet and Susitna region of southern Alaska, *Tectonophysics*, **745**, 245–263, doi: 10.1016/j.tecto.2018.08.013.

Smerzini, C., Paolucci, R., & Stupazzini, M., 2011. Comparison of 3D, 2D, and 1D numerical approaches to predict long period earthquake ground motion in the Gubbio plain, Central Italy, *Bull. Earthquake Engineering*, **9**, 2007–2029, doi: 10.1007/s10518-011-9289-8.

Smith, K., 2019. Supplement to "Seismic response of Cook Inlet sedimentary basin, southern Alaska", ScholarWorks@UA at http://hdl.handle.net/11122/10568 (last accessed July 2019): descriptor file, figures of seismic noise spectra, ground motion metrics, and spectral ratios.

Sokolov, V. Y., Loh, C.-H., & Wen, K.-L., 2000. Empirical study of sediment-filled basin response: The case of Taipei City, *Earthquake Spectra*, **16**(3), 681–707.

Tanimoto, T. & Lamontagne, A., 2014. Temporal and spatial evolution of an on-land hurricane observed by seismic data, *Geophys. Res. Lett.*, **41**, 7532–7538, doi: 10.1002/2014GL061934.

Tape, C., Silwal, V., Ji, C., Keyson, L., West, M. E., & Ruppert, N., 2015. Transtensional tectonics of the Minto Flats fault zone and Nenana basin, central Alaska, *Bull. Seismol. Soc. Am.*, **105**(4), 2081–2100, doi: 10.1785/0120150055.

Tape, C., Christensen, D., Moore-Driskell, M. M., Sweet, J., & Smith, K., 2017. Southern Alaska Lithosphere and Mantle Observation Network (SALMON): a seismic experiment covering the active arc by road, boat, plane, and helicopter, *Seismol. Res. Lett.*, **88**(4), 1185–1202, doi: 10.1785/0220160229.

Toshinawa, T. & Ohmachi, T., 1992. Love-wave propagation in a three-dimensional sedimentary basin, *Bull. Seismol. Soc. Am.*, **82**(4), 1661–1677.

Van Kooten, G. K., Richter, M., & Zippi, P. A., 2012. Alaska's Interior rift basins: a new frontier for discovery, *Oil & Gas J.*, **110**(1a), 48–57.

Vidale, J. E. & Helmberger, D. V., 1988. Elastic finite-difference modeling of the 1971 San Fernando, California earthquake, *Bull. Seismol. Soc. Am.*, **78**(1), 122–141.

Wald, D. J. & Graves, R. W., 1998. The seismic response of the Los Angeles basin, California, *Bull. Seismol. Soc. Am.*, **88**(2), 337–356.

Wartes, M. W., Gillis, R. J., Herriott, T. M., Stanley, R. G., Helmold, K. P., Peterson, C. S., & Benowitz, J. A., 2013. Summary of 2012 reconnaissance field studies related to the petroleum geology of the Nenana basin, Interior Alaska, Alaska Div. Geol. Geophys. Surv. Preliminary Interpretive Report 2013–2, 13 p.

Williams, M., Fischer, K., Freymueller, J., Tikoff, B., Tréhu, A., et al., 2010. Unlocking the secrets of the North American continent: an EarthScope science plan for 2010–2020, *EarthScope*.

Wirth, E. A., Vidale, J. E., Frankel, A. D., Pratt, T. L., Marafi, N. A., Thompson, M., & Stephenson, W. J., 2019. Source-dependent amplification of earthquake ground motions in deep sedimentary basins, *Geophys. Res. Lett.*, **46**, 6443–6450, doi: 10.1029/2019GL082474.

Withers, M. M., Aster, R. C., Young, C. J., & Chael, E. P., 1996. High-frequency analysis of seismic background noise as a function of wind speed and shallow depth, *Bull. Seismol. Soc. Am.*, **86**(5), 1507–1515.

Chapter 2

Seismic noise in central Alaska and influences from rivers, wind, and sedimentary basins[1]

2.1 Abstract

Ambient noise is useful for characterizing frequency-dependent noise levels and for assessing data quality for seismic stations. We use three years of ambient noise spectra from 16 stations in central Alaska to examine environmental and structural influences on seismic stations. The region contains a major river (Tanana river) that is ice-covered for half the year and is underlain by a sedimentary basin (Nenana basin) that strongly influences the seismic wavefield. Nenana basin amplifies ambient seismic noise by 12–16 dB at 0.1–0.7 Hz and 17–30 dB at 0.7–3 Hz. A meteorological station and river gauge at Nenana provide environmental data for comparison with seismic stations. During the summer, the Tanana river produces noise levels elevated by 30–40 dB at frequencies near 10 Hz, as recorded by all stations within 100 m of the main river channel. The Tanana river lacks any sediment larger than sand in this region; therefore we attribute the 10 Hz river signal to turbulence within the water and to unsteady shearing on the river bottom. The influence of wind is apparent on seismic noise at low (<0.05 Hz) frequencies, due to atmospheric-induced tilting, and at high (>2.0 Hz) frequencies, due to unsteady shearing and turbulence near the ground. Our empirical findings motivate future studies, such as how flow from air or water couples to the ground and how deep sedimentary basins influence the ambient noise wavefield. Our results have implications for seismic site selection, environmental monitoring, and detection and characterization of earthquakes.

[1]Published as: **Smith, K.**, and C. Tape (2019), Seismic noise in central Alaska and influences from rivers, wind, and sedimentary basins, *J. Geophys. Res. Solid Earth*, doi:10.1029/2019JB017695.

2.2 Introduction

"As soon as fairly sensitive seismographs were available, it was found that the ground is never at rest." This was the opening of Gutenberg (1951), who provided the first comprehensive classification of the different types of waves that are continuously recorded by seismometers. These waves, known as microseisms or ambient noise, were characterized by their period range, their kind of movement, their hypothetical causes, and the relative distance of the causes (Table A.1). The problem facing Gutenberg—to interpret a source of origin from a set of recorded oscillating waves—remains a formidable challenge today, even with the advantages of modern data quality, coverage, and resolution (whether seismic, meteorological, or oceanographic).

In Gutenberg's seminal 1958 review of microseisms, he does not explicitly state his motivation for pursuing the topic. Nevertheless, some of the motivations are clear or implied from the content, and we list them here. The primary pursuit of understanding seismic noise is one of basic scientific curiosity: What source regions and processes are responsible for constantly recorded ground motions, and how does each type of source couple to the solid earth? This pursuit began as early as Hecker (1906) and continues today (Anthony et al., 2015). The second benefit is the potential for using a seismometer to monitor the environment, such as changing atmospheric or oceanographic conditions (Aster et al., 2008). There are better instruments than seismometers for certain environmental monitoring, but in places without instruments, an already-deployed seismometer could provide useful information at no extra cost. A third benefit is to use seismic noise to better understand the performance of a seismometer. By understanding how noise levels are influenced by the environment, we may be able to inform how sites are selected, how stations are designed, and how seismometers are designed (Aki & Richards, 2002, Ch. 12). A fourth benefit arises from the fact that ambient noise often obscures signals—like earthquakes—for which a station has been deployed. Changing noise levels will impact operational monitoring and scientific studies, such as the ability to pick arrival times needed for earthquake location, the selection of waveforms to use for estimating source mechanisms for earthquakes, or the analysis of normal mode spectral peaks (Zürn et al., 2015). Finally, it has become clear in the past 15 years that seismic waves (body waves, Rayleigh waves, Love waves) comprise major portions of ambient noise, and these waves can be used to estimate seismic velocity structure (Shapiro et al., 2005; Tanimoto

et al., 2013; Lin et al., 2013). The literature review of Bonnefoy-Claudet et al. (2006) demonstrates the increasing importance of using noise for characterizing seismic structure.

Our goal is to understand the sources of noise in the Minto Flats region of central Alaska (Figure 2.1a). Our approach is an empirical one, based on an extensive analysis of the time-, frequency-, and spatial-dependence of variations in noise amplitudes. As with similar studies, we benefit from using non-seismic data—in our case, wind speeds and river gauge heights—to help understand the variations in seismic noise. The global ambient seismic wavefield between 0.003 Hz and 1 Hz is generated by oceanic waves that couple to the seafloor (Webb, 1998; Tanimoto, 2005; Kedar et al., 2008; Gimbert & Tsai, 2015). These ocean-generated seismic waves can be strongly influenced by local structure and can be masked out by local, more dominant noise sources, such as from wind.

Wind effects on ground motion have been documented at low and high frequencies. Haubrich & MacKenzie (1965) discovered that for frequencies <0.1 Hz the seismic displacement was "partially coherent" with pressure and attributed the effect "to elastic deformation of the ground by the atmosphere" (p. 1432). The degree of ground tilting caused by the atmosphere was shown to depend on the elastic properties near the surface (Sorrells, 1971; Sorrells et al., 1971; Sorrells & Goforth, 1973; Ziolkowski, 1973; Dybing et al., 2019). Nearly all stations on Earth, including within the Global Seismographic Network, record elevated levels of horizontal component noise relative to vertical component noise (H/Z ratio), which is suggestive of ground tilting. Wind can also directly couple to the ground and generate high frequencies (>1 Hz) of ground motion (Young et al., 1994; Withers et al., 1996; Naderyan et al., 2016; Lott et al., 2017; Dybing et al., 2019). The effects of wind at low and high frequencies are reduced by installing seismometers deeper (Hutt et al., 2017).

A major influence in seismic wave propagation—whether from earthquakes or ambient noise—are sedimentary basins, which are filled with low-velocity sedimentary strata that amplify seismic waves (Bard & Bouchon, 1980, 1985; Rial et al., 1992; Field & Jacob, 1993; Wald & Graves, 1998; Olsen, 2000). The margins of basins also have a strong influence on the seismic wavefield (Graves et al., 1998; Frankel et al., 2009). Basins are not a source of noise themselves, but they are structures that distort seismic waves and also influence how external noise sources (e.g., wind) couple to the solid earth.

Seismic stations in the Minto Flats region provide a natural laboratory for investigating several variables affecting seismic noise: anthropogenic sources, rivers, wind (on ground, trees, and towers), and a km-scale sedimentary basin (Nenana basin). Cultural noise influence is expectedly low (<6 dB at 10 Hz) at most stations in this remote region. As will be shown, we discovered that the Tanana river produces noise levels at 10 Hz that are up to 40 dB higher in summer than in the winter, when the river surface is covered in meter-thick ice. The river noise signal is strongest for stations within 100 m of the main channel; it is also characterized by uniform H/Z ratios during peak river flow and negative decibels of H/Z ratios starting near freezeup (generally October). The effects of wind on the ground are documented across all frequencies except for the highest-amplitude ocean microseism range of 0.1–0.5 Hz. Nenana basin (described next) has a strong influence on seismic noise, amplifying 0.1–0.7 Hz by 12–16 dB and 0.7–3 Hz by 17–30 dB. We hope that the empirical results presented here will help inform theoretical (Sorrells & Goforth, 1973; Tsai et al., 2012; Gimbert et al., 2014; Naderyan et al., 2016) and experimental (Mucciarelli et al., 2005; Hutt et al., 2017; Anthony et al., 2018; Dybing et al., 2019) efforts to investigate the effects of earth structure and environmental conditions on seismic noise.

2.2.1 Study region and data

The Minto Flats region is a low-lying area in central Alaska between the town of Minto and Nenana and containing the Tanana river (Figure 2.1). The Tanana river flows north from Nenana and then west, to Manley and then the village of Tanana, where it flows into the Yukon river (Collins, 1990). The region is underlain by Nenana sedimentary basin, which was identified from anomalously low gravity measurements (Barnes, 1961) and active-source seismic images (Van Kooten et al., 2012). On the sides of Nenana basin are two faults identified from seismicity (Tape et al., 2013) and having no geological expression at the surface (Koehler et al., 2015). Earthquakes on the two faults exhibit left-lateral faulting, leading to the interpretation of a transtensional setting for the Minto Flats fault zone and Nenana basin (Tape et al., 2015).

From 2014 to 2019 a set of 13 seismometers was deployed in the Minto Flats region. The main goal of the FLATS (Fault Locations and Active Tectonics from Seismicity) experiment was to characterize the structural and kinematic relationships between deep sub-basin crustal faulting and

active basin formation and deformation. The deployment was partially motivated by a nucleation signal that preceded a triggered earthquake (Tape et al., 2013); additional unusual events, including very-low-frequency earthquakes, occurred during the FLATS deployment (Tape et al., 2018). Prior to the FLATS project, no seismometer had ever been deployed in the low-lying region.

The FLATS deployment, along with nearby stations, provides a opportunity to examine a unique setting that contains minimal cultural noise (the roadless region is unpopulated), a major river that is undammed and is covered in meter-thick ice during winter, and a major sedimentary basin overlying an active fault zone. Three stations surrounding the region (AK.NEA2, TA.I23K, AK.MLY) are high-quality seismic installations in bedrock and provide valuable comparisons for FLATS stations. All 16 stations are directly buried posthole sensors; therefore effects related to cavities or vaults should be absent (Kroner et al., 2005; Aderhold et al., 2015), though tilting effects should still be present, as the case for almost all stations in the world, including deep boreholes. Furthermore, as its name suggests, Minto Flats lacks topography; topographic variations can influence tilt observations on seismometers (Harrison, 1976; Gebauer et al., 2009). (Extremely local topography, such as a river adjacent to the seismometer, could be relevant.) Finally, the range of temperatures in the high-latitude setting are extreme, in part due to the distance (>500 km) from oceans and also protection by the Alaska Range to the south. The hourly temperature recorded at Nenana between 2014-09-01 and 2019-09-01 averaged -0.3°C with a minimum of -47.8°C and a maximum of 33.3°C.

2.3 Data

2.3.1 Seismic data

Our study is based on seismic data recorded at all 13 FLATS stations and at three bedrock stations. All 13 FLATS stations have Nanometrics Trillium 120 posthole (T120PH; corner period 120 s) broadband sensors installed at a depth of approximately 1.0–1.2 m. The material adjacent to the sensors—either damp sand or compacted loess soil—is excellent for coupling the sensor to the ground. An example station site is shown in Figure A.1.

Each of the bedrock stations is installed in a cased borehole at a depth of approximately 2.5 m: AK.NEA2 (T120PH), TA.I23K (STS-5A), and AK.MLY (T120PH). Construction logs from

the bedrock stations include the following notes on the rock adjacent to the sensors: (AK.MLY) "Solid rock, granitic, medium-hard drilling," (TA.I23K) "Tan-grayish rock, with quartz? medium-hard drilling," (AK.NEA2) "Schist, harder drilling, light buff color." These installations result in low noise levels at low frequencies (<0.1 Hz), especially on the horizontal components, relative to stations in the regional networks (Busby, 2016). At high frequencies (>1 Hz), anthropogenic sources can cause higher noise levels. TA.I23K is next to an outer road in the village of Minto. AK.NEA2 is in the woods and adjacent to a state microwave site with a 38-m tower and a small building containing telecom hardware and a constantly running HVAC system. AK.MLY is in a remote location, on top a dome of treeless bedrock.

In low-lying areas (see station elevations in Table 2.1), the water table is expected to be shallow; the base of the holes at three FLATS stations (FAPT, FPAP, F2TN) were damp or contained water-saturated mud. Such a shallow water table is likely to freeze, especially considering the extreme cold and relatively low snow levels (therefore less insulation) in central Alaska. For much of the year, the shallowly buried FLATS sensors are within a frozen layer that thaws by mid to late summer. Only one hole—the 2018-reinstalled F2TN—had frozen ground at 1 m depth in July, at the time of installation. Most installations were performed in September in order to avoid frozen ground at 1.2 m depth.

All 16 sensors in this study send three-component, telemetered data to the Alaska Earthquake Center, where they are sent to the IRIS Data Management Center for archival. The recorded samples per second varies from 40 (TA.I23K) to 200 (XV.F3TN) (Table 2.1); the maximum allowable frequencies (i.e., Nyquist) in the power spectra range from 20 Hz to 100 Hz. The use of telemetry allows the data to be used in real-time operations (for earthquake locations) and also allows us to identify station outages and prepare for site repairs. The use of telemetry produces a small number of data gaps that would otherwise be absent if data were recorded on site and collected later.

2.3.2 River gauge data

The Tanana river is a glacially fed river and includes the Delta, Nenana, and Kantishna rivers as tributaries; it is the largest tributary of the Yukon river. The USGS operates a river gauge (site

number 15515500) on the Tanana river in the town of Nenana, just east of the Parks Highway bridge (Figure 2.1b). The river gauge height data are provided with 15-minute intervals. Over the time period of our study, the most notable data gap occurred between February and April, 2017.

2.3.3 Meteorological data

As far as we know, the only meteorological station in our region with readily available data is in the town of Nenana. The National Weather Service operates a meteorological station (station code PANN) south of the airport runway in Nenana, 513 m from seismic station XV.FAPT. At 51 minutes past each hour, PANN records data every five seconds for a period of two minutes, and then lists the average value of wind speed, mean sea level pressure, wind gust speed, relative humidity, percent relative humidity, air temperature, and dew point temperature. (Therefore the hourly measurements do not constitute an hourly average.) We average the 24 hourly measurements within each UTC day to provide a daily value.

There are no meteorological stations collocated with seismic stations at Minto (TA.I23K), Manley (AK.MLY), or Nenana (AK.NEA2). Outside our study region, dozens of EarthScope (TA) stations in Alaska contain collocated meteorological sensors. These stations would be ideal for investigating the influences of environmental effects on time-dependent seismic noise.

Characteristics of the hourly wind speeds at Nenana are shown in Figure A.2. The winter months of December, January, and February contain higher wind speeds and no diurnal variability, whereas the summer months of June, July, and August exhibit lower wind speeds and diurnal variability (Figure A.2a), with stronger wind speeds during the daytime.

Wind arises from spatial differences in pressure, and pressure can influence deformation of the ground surrounding a sensor or vault (Zürn & Widmer, 1995; Zürn et al., 2007). We examined the relationship between pressure and seismic noise power but did not find relationships that were suggestive of a causal relationship between local weather conditions and seismic noise.

2.4 Methods

2.4.1 Power spectra of seismic noise

Three-component (north, east, and up) seismic data are sent via radio or cell modem telemetry to the Alaska Earthquake Center (AEC) at University of Alaska's Geophysical Institute. These data are transferred to the IRIS Data Management Center, which archives the waveforms and also performs a data quality assessment using a program called MUSTANG (Casey et al., 2018). MUSTANG produces probability spectral densities using methods of McNamara & Buland (2004). These spectra form the basis of our analysis.

We used two data products from MUSTANG: daily probability density functions (PDF) and hourly power spectral densities (PSD). The daily PDF is an aggregate of 47 hourly spectra, each representing 60 minutes of ground motion and overlapping with the next hourly spectrum by 30 minutes. We obtain a daily spectrum from the daily PDF by extracting the most frequent (mode) noise level for each frequency. The hourly spectra were necessary for examining sub-daily variations, such as anthropogenic influences due to night-day differences, and for isolating the influence of wind on seismic noise.

We downloaded hourly noise spectra at all 16 stations from 2015-09-01 through 2019-09-01. For five stations (F3TN, FPAP, NEA2, I23K, MLY), we examined their data from 2014-09-01 to 2019-09-01. For some analyses we examined data from all stations within 100 km of Nenana; this included a few more stations than those listed in Table 2.1 (AK.BWN, AK.CCB, IU.COLA, AK.MCK, AK.MDM, TA.TCOL, & AK.WRH).

Using a set of daily noise spectra, we display a spectrogram (Figure 2.2), which shows the time-dependence of noise at one station. Each spectrogram conveys a large amount of information on a long time series (Tsai & McNamara, 2011). For example, a three-year-long, single-component time series of ground motion at F3TN (200 samples per second) has 1.9×10^{10} values. The spectrogram is discretized with 1096 daily values spanning three years and 114 frequency values ranging from 0.0053 Hz to 94 Hz. Our spectrograms are constructed using the pre-calculated daily (or hourly) spectra from MUSTANG; alternatively, one could construct them directly from the time series, by specifying the window width and time increment for the sliding window.

To examine the time-independent noise characteristics at each station, we calculate an annual spectrum from multi-year long set of daily noise spectra. We used a median operation to diminish the effects of occasional spurious spectra. A comparison between the effects of using a median or mean operation is shown in Figure A.3.

The time-dependence of noise is better displayed by subtracting the station-specific, time-independent spectrum from the original spectrogram (e.g., Ringler et al., 2010; Schmandt et al., 2013), as shown in Figure 2.2. The resulting "residual spectrogram" (Figure 2.2d) reveals the time-dependent variations in noise, with the 0 dB value representing the median noise level for that station and for a particular frequency. For example, the residual spectrogram in Figure 2.2d reveals clear seasonal variation of −10 dB (summer) to +10 dB (winter) for frequencies 0.1–0.5 Hz. It also shows elevated high-frequency (2–10 Hz) noise during the winters.

The units for the acceleration power spectra, prior to logarithmic scaling, can be written as $(\mathrm{m/s^2})^2/\mathrm{Hz}$ or $\mathrm{m^2/s^4/Hz}$ or $\mathrm{m^2/s^3}$. The conversion to decibels (dB) is achieved by $p = \log_{10}(x/x_0)^{10}$, where x is a power spectrum value and $x_0 = 1\ (\mathrm{m/s^2})^2/\mathrm{Hz}$ is a normalization factor that removes units. (For example, if $x = 100\ (\mathrm{m/s^2})^2/\mathrm{Hz}$, then $p = 20$ dB.) For brevity in our plots, we use the label "Accel. PSD, dB." instead of "PSD, dB relative to 1 $(\mathrm{m/s^2})^2/\mathrm{Hz}$." The dB label is a reminder that quantities have been log-scaled. When we take a ratio of power spectra, x_b/x_a, this will lead to a "differential spectrum" $p_b - p_a = 10\log_{10}(x_b/x_a)$. Throughout our results, we compare sets of spectra, such as a station's spectrum vs a bedrock station, a station's spectrum during high-wind conditions vs low-wind conditions, and a station's horizontal component vs its vertical component. Subtracting these log-scaled spectra $(p_b - p_a)$ is equivalent to representing ratios of power spectra (x_b/x_a).

Using daily spectra (PDFs) from MUSTANG, spectrograms are calculated for Z, E, and N components. The spectrograms for the E and N components are averaged to give a spectrogram for the horizontal (H) component. The difference between the H spectrogram and the Z spectrogram provides the (log-scaled) H/Z ratio (e.g., Anthony et al., 2015, fig. 3c), which is used in several analyses.

2.4.2 Identification of suspected noise sources

We document characteristics of each station that could influence the recorded seismic noise levels. Measurements of these characteristics are shown in Table 2.1 and are based on site conditions and not on seismic noise data.

We use the characteristics to classify each station according to each noise source. (Here we refer to the basin as a noise source, though it would be more accurate to describe it as a structure that *influences* seismic noise.) For each station, a noise source is labeled **red** if the source is present: **blue** if it is somewhat present, and **green** if it is not present. The river classification is based on a station's distance from the main river channel: **red** if less than 100 m, **blue** if between 100 m and 2000 m, and **green** if greater than 2000 m. The basin classification is based on a station's depth-to-basement (Figure 2.1): **red** if greater than 2000 m, **blue** if between 10 m and 2000 m, and **green** if less than 10 m. The expected presence of anthropogenic noise is qualitatively labeled **red**, **blue**, or **green**. At the outset, we did not know which of these factors will manifest within the seismic data. We recognized that there could be cases where multiple noise sources are present at a site, yet there would be only one noise source that was dominantly visible in the seismic data.

Our primary goal is to determine whether these noise sources are identifiable within the seismic data. If they are identifiable, then we seek to characterize the frequency range and time period of influence. River gauge and wind speed data in Nenana are used to investigate the influence of the river and wind on seismic noise.

2.5 Results

We examine annual noise spectra in order to convey differences among stations, either due to structure or to local environmental influences. We then quantify the influence of anthropogenic noise sources, which allows us later to interpret environmental noise sources. A basic calculation we perform is to correlate the time-dependent seismic noise, for one station and for one frequency, with the time-dependent data from an environmental sensor, such as river height or wind speed.

Two stations near the Tanana river, F2TN and F4TN, were reinstalled during the project, due to rapid lateral erosion of the riverbank. Although the new shallow boreholes were within 30 m of the previous hole, the change has a strong impact on the noise signals that are due to the river.

Additional caution is needed when interpreting F2TN (reinstalled in 2016, 2017 and 2018) and F4TN (reinstalled in 2016).

The Supporting Information contains a large set of figures, mainly because we have include figures for all 16 stations. The figures are categorized by anthropogenic noise (Figures A.8–A.12), river noise (Figures A.13–A.32), wind noise (Figures A.33–A.73), and basin noise (Figures A.74–A.78).

2.5.1 Reference noise spectra

Figure 2.3 provides an overview of the annual noise at all FLATS stations. Each subplot shows the 3-year spectra for vertical and horizontal components. Although the stations are all within the same region (Figure 2.1), their noise spectra exhibit dramatic variability.

To examine spatial variations in seismic noise, we need to establish a reference noise spectrum that characterizes the background regional noise level. We have five bedrock (or non-basin) stations in the region to choose from: AK.NEA2, AK.MLY, XV.F8KN, XV.FTGH, and TA.I23K (Figure A.4). The shallow borehole station AK.NEA2 is the logical choice for a reference, as it is the highest-quality installation that is close to the FLATS stations. However, its higher frequency noise levels are elevated due to a nearby lattice tower, as we will discuss later (Section 2.5.4.1), and its low-frequency noise levels are only slightly better than at F8KN ($\sim$5 dB on horizontal, 0 dB on vertical). AK.MLY has the lowest noise levels, but it is 96 km from Nenana and therefore not as representative of the region. We choose F8KN as a reference station; this has the advantage that the sensor and type of installation (shallow, direct burial) is the same as the other 12 FLATS stations.

Figure 2.3 compares each station with F8KN. FTGH, installed on a ridge in proximity to bedrock, has comparable low-frequency vertical-component noise to F8KN and elevated (10 dB) horizontal noise. The other 11 FLATS stations are in or near Nenana basin and exhibit elevated noise levels across all frequencies, relative to bedrock station F8KN.

We also use a station's own multi-year spectrum as a reference for showing time-dependent changes. Figure 2.4 shows the seasonal variations in horizontal-component noise for each station. The origin of some of these variations will become apparent in Section 2.5.3.

2.5.2 Influence of anthropogenic sources

Cultural noise from anthropogenic sources—either humans, their structures, or their machines—is generally recorded at high frequencies (>10 Hz). Transient cultural activity can assist our understanding of seismic noise recorded during those events. For example, station FNN1 is in the middle of a large clearing made for a geophysical exploratory well (Van Kooten et al., 2012). Typically in the fall, moose hunters set up their camps in the clearing, within 50 m of the sensor, in preparation for the opening of the season on September 1st. The activities of the hunters are clearly visible in the 10 Hz time series at FNN1 in 2016, 2017, and 2018 (Figure A.8). The signature of the activity is that the 10 Hz noise is elevated by 20 dB during the day and falls down toward the background noise level at night. This pattern starts near September 1st and lasts a couple weeks. Other examples of 10 Hz cultural noise include a week-long camp held at Old Minto (F5MN) in July 2017 (Figure A.9) and a 3D active source seismic survey in Minto Flats in April 2017 (Figure A.10). All three of these examples are marked by diurnal variations in the 10 Hz noise.

We classified seven stations in Table 2.1 as having anthropogenic noise sources present (FAPT, FPAP, I23K) or somewhat present (F5MN, F7TV, FTGH, NEA2). The spectra for six of these stations (NEA2 excluded) all have elevated noise at >10 Hz, relative to F8KN (Figure 2.3). They also have elevated noise levels during summer and fall, seasons when locals and visitors to the region are more active (Figure 2.4).

Human activity is elevated during the day and diminished during the night. This effect can be examined by comparing noise levels during daytime with those from nighttime (Wilson et al., 2002). Using three years of hourly spectra, we plot the difference between day spectra (08:00–20:00 AKST) and night spectra. In Figure 2.5 we plot six spectra, colored by the expected presence of cultural noise (Table 2.1). As expected, we see elevated daytime noise levels at FPAP and FAPT, in Nenana, and at I23K, in Minto. This gives us some confidence in quantifying cultural noise influences of up to 4–6 dB for frequencies 10–20 Hz.

The day-vs-night assessment has some shortcomings for representing anthropogenic sources. First, it assumes that the anthropogenic source varies with night and day, which is not always the case. For example, there is a constantly-running HVAC in the building near AK.NEA2, and therefore it would not be visible in Figure 2.5. Second, there are other day-vs-night differences that

could very well be non-anthropogenic. For example, wind speeds during summer are stronger during the day (Figure A.2a). It is also possible that thermal effects could cause higher daytime noise levels, such as at sites that are not expected to have any anthropogenic influence (e.g., F6TP, FNN2: Figure A.12).

FTGH, which is 228 m from the Parks Highway, has high annual levels of >10 Hz noise (Figure 2.3), has slightly elevated summer noise levels (Figure 2.4), but it does not exhibit a diurnal difference (Figure 2.5). This indicates that the high-frequency noise levels arise from a source that is more uniform throughout the day.

2.5.3 Influence of Tanana river

Environmental influences on the annual spectra in Figure 2.3 start to become clear when we examine seasonal variations (Figure 2.4). The most conspicuous patterns occur for the two frequency ranges 0.1–1 Hz and 4–30 Hz. At 0.1–1 Hz, all 15 stations show the same pattern of +2 dB in fall (Sept/Oct/Nov), +5 dB in winter (Dec/Jan/Feb), −2 dB in spring (March/April/May), and −5 dB in summer (Jun/Jul/Aug). This reflects the annual regional cyclicity of ocean-generated ambient noise (Stutzmann et al., 2009), which is strongest in winter in mainland Alaska due to storms in the northern Pacific. These variations at 0.1–1 Hz are visible in the spectrograms in Figure 2.6 and in Figure 2.2c. At 4–30 Hz, a subset of stations in Figure 2.4 reveals noise levels of ≥10 dB in summer and diminished (5–10 dB) in fall. These turn out to be caused by the changing signal from the river, as discussed next.

The signature of the Tanana river on seismic noise is displayed in the residual spectrograms in Figure 2.6. To assist in interpretation, we plot vertical dashed lines for the date when the river ice breaks up on the Tanana river at the town of Nenana. This day and time is marked by the movement of a wooden tripod that is erected on top of the river ice each winter; Alaskans bet money on the breakup time. The event is known as the Nenana Ice Classic and provides a unique historical data set from 1917 to present (NSIDC, 2011). In Figure 2.6, we plot solid lines for the latest time in fall when any ice-free water is visible; this time is obtained from a time-lapse camera that we installed at station F3TN. (In fall 2018, the F3TN camera failed, so we use the freezeup date from F5MN instead.)

The four stations shown are all $\leq$100 m from the main river channel and all show elevated noise at 10 Hz that lasts from approximately river breakup to river freezeup. This pattern is emphasized in Figure 2.7, which shows multi-year 10 Hz time series for F3TN and three other stations near the river (F4TN, F5MN, F7TV). The H/Z ratio time series, plotted in Figure 2.7 for F3TN, shows that the noise levels on the Z and H components are nearly the same during summer, when the river influence is highest. Starting at freezeup, the 10 Hz noise levels drop, and the H component noise decreases below the Z component, reaching a H/Z minimum of about -15 dB in March, about 1 month before river ice breakup. Similar seasonal variations in H/Z ratio time series can be seen at other stations (Figures A.28–A.32).

Evidence for the link between the river and the 10 Hz seismic signal was provided in one unexpected case. As a preventative measure, on 2016-09-16 the sensor at F2TN was reinstalled 13 m further back from the river. The 10 Hz noise abruptly decreased by 20 dB (Figures A.7 and A.29).

Comparison between the time-dependence of the 10 Hz seismic noise at F3TN and the river height at Nenana reveals a complicated pattern when examining the entire four-year time period (Figure A.18a-b). The signals are correlated, but there is complexity in the scatter plot that suggests that the signals should be compared within shorter time periods. Figure 2.8 shows the data for five summers, and the pattern is clear with a correlation coefficient (cc) of 0.87: the 10 Hz seismic noise and river gauge are minimal in early June and late August and are maximal in mid-July.

Figure 2.9 provides a more complete view of the correlations between river gauge height and seismic noise at all frequencies and for different stations. Each point plotted represents a correlation coefficient between summertime daily values of horizontal-component seismic power at one frequency and summertime daily values of river gauge height. The example dot, plotted for F3TN at (10 Hz, cc 0.87) corresponds to the data shown in Figure 2.8. For four near-river stations (F3TN, F4TN, F5MN, F7TV), the correlations exceed 0.7 for frequencies 5–10 Hz. Station F1TN, which is farther from the main river channel (Table 2.1), exhibits a weaker correlation.

2.5.4 Influence of wind

To analyze the influence of wind on seismic noise, we compare winds speeds measured in Nenana (station PANN; Figure 2.1b) with seismic noise power at all frequencies and at several stations. We analyze correlations from data that are sampled hourly and daily. We focus on the winter time period (Dec/Jan/Feb), when river noise and cultural noise are at a minimum. The Tanana river is frozen at the surface, reducing the effects of water turbulence and wave action from wind. Also there is less industrial activity, fewer cars on the road, and fewer trains. Winter is also the time of year when wind in the region is strongest.

We find that at most stations wind enhances seismic noise at all frequencies. Two examples of our analysis are shown in Figures 2.10 and 2.11, and a large set of figures related to wind are included in the Supporting Information. Next we divide the seismic spectrum into three intervals to discuss the influences of wind.

2.5.4.1 Seismic noise $\geq$2.0 Hz

Figure 2.10a provides compelling evidence of wind influence on seismic noise. Each spectrum is a stack of hourly seismic noise at station F1TN during hourly time periods of winds speeds in Nenana (PANN) within a certain interval. The black spectrum is the median stack of seismic noise when wind speeds were 0 m/s. The magenta spectrum is for wind speeds $0 < v < 2$ m/s, and we see that it is higher than the lower-wind speed spectrum of seismic noise. As the wind increases, the seismic noise increases, by more than 25 dB on the vertical component for wind speeds 10–12 m/s.

A second way to examine the hourly data is shown in Figure 2.10b, which displays a scatter plot of hourly seismic power at 3 Hz versus hourly wind speed. The correlation between the two time series (0.54) is in agreement with the evidence in Figure 2.10a (see solid line at 3 Hz). Other examples like Figure 2.10b are shown in Figures A.58–A.72.

At many stations we identify an increase in seismic noise for frequencies $\geq$2.0 Hz. This pattern is most conspicuous—leading to a >10 dB increase for wind speeds 10–12 m/s—at F1TN, F6TP, F7TV, FNN1, FNN2, F8KN, NEA2, and MLY (Figures A.34–A.49). With the exception of F1TN, which we will discuss in Section 2.5.4.2, all these stations occur in places that are either high

elevation, in a clearing and away from trees, or both. We attribute the elevated high-frequency seismic noise to wind effects on the ground (e.g., Naderyan et al., 2016).

Stations FTGH, FPAP, and FAPT are influenced by wind, but our interpretations are complicated by the occurrence of already-high noise levels at high frequencies due to anthropogenic sources. Two anthropogenic sources, at NEA2 and FAPT, are nearby lattice towers that have resonant frequencies according to their height and design (Chiu & Taoka, 1973; Venkateswarlu et al., 1994). (Both stations also have sheds nearby.) At NEA2, unsmoothed seismic noise power spectra reveal a sharp spike at 2.5 Hz on the vertical and horizontal components. Due to a smoothing operation used within MUSTANG (see Section 2.6.1), this resonant peak appears as a mesa-shape spanning 2–3 Hz in Figure A.46. This feature is strongly enhanced by wind and is dominantly on the vertical component. Chiu & Taoka (1973) analyzed a 45 m microwave lattice tower having resonant frequencies of 1.9 Hz, 5.6 Hz, and 12.5 Hz for the first three translational modes. We interpret the 2.5 Hz resonant peak at NEA2 to be the fundamental mode of the microwave lattice tower, which is 38 m tall and 21.6 m from the sensor. At FAPT there is also a mesa-shape in the spectrum spanning 8–20 Hz and dominantly on the vertical component (Figure A.43d). We speculate that this is due to the lattice tower that is 18.1 m tall and 12.4 m from the sensor. For mesa-like signals at NEA2 and FAPT, the change in H/Z ratio with increasing wind speed indicates that the Z noise levels become more dominant (relative to H) at higher wind speeds (Figure A.51).

2.5.4.2 Seismic noise 0.5–2.0 Hz

Best practices for seismic installations advise not installing stations near tall trees or structures (Willmore, 1979; Trnkoczy et al., 2012), though we have not seen published evidence to support this guideline. The roots of trees swaying in the wind pull on the ground. The swaying frequency of a tree depends on the shape and the elastic properties of the tree. Gardiner (1992) measured resonant frequencies of 0.26–0.43 Hz (2.3–3.8 s) for ten Sitka spruce trees with heights 13–17 m. (With the branches removed, the measured resonant frequencies were 0.43–0.70 Hz, or 1.4–2.3 s.)

We examined the noise variations at 0.5–2.0 Hz with the hypothesis that swaying trees could be influential. The properties of nearby trees for our stations are listed in Table A.2. From the seismic spectra in Figures A.34–A.49, we identify the following stations exhibiting enhancement

of $\geq$10 dB seismic noise for 0.5–2.0 Hz for wind speeds $\geq$10 m/s: F1TN, F3TN, F4TN, F5MN, F7TV, F8KN, FNN1, FNN2, FPAP, FTGH, NEA2. F1TN is the closest station to a tree (1.8 m), and its seismic noise variations exhibit the strongest influence from wind, including a subtle peak at 1.5 Hz (Figure 2.10a and Figure A.34). We hypothesize that wind-induced movement of trees is responsible for the exceptional noise enhancement at F1TN.

Overall, the influence of wind on trees on seismic noise is unclear. Among the 11 stations exhibiting enhanced noise at 0.5–2.0 Hz, six are within 10 m of a tree (F1TN, F3TN, F4TN, F5MN, F7TV, NEA2), and four (FNN1, FNN2, FPAP, FTGH) are not (Table A.2). If the wind-elevated noise at these three sites is caused by trees, then it would require the swaying signal to not attenuate over distances of 10–100 m. Futher analysis and additional experiments are needed in order to understand the connection between swaying trees and seismic noise.

2.5.4.3 Seismic noise $\leq$0.05 Hz

Changing atmospheric conditions can push down on the ground, and these effects are recorded on horizontal and vertical components of seismic noise at low ($\leq$0.05 Hz) frequencies (Haubrich & MacKenzie, 1965; Sorrells, 1971). Figure 2.11a,b compares daily vertical-component seismic noise at a frequency of 0.03 Hz (period 30 s) with daily average wind speed. For the three-year time period, there is a correlation of 0.69 that appears to be strongest during the winter months, when daily wind speeds reach maximal and minimal values.

A more complete picture of the correlations between seismic noise and wind speed is shown in Figure 2.11c. There we display correlation coefficients as a function of seismic noise frequency, and we color the stations based on their distance from the weather station. It is clear that at low frequencies, the correlations are highest (and above 0.50) for the stations closest to the weather station. For seismic stations >50 km from the weather station, there is no significant correlation between low-frequency seismic noise and wind speed.

The ratio of the horizontal component spectrum to the vertical component spectrum—H/Z ratio—provides information on the susceptibility of a sensor to surface displacements caused by atmospheric changes. Very few seismic sensors on Earth escape these surface effects, and those

sensors tend to be deep (>100 m) and within bedrock. For seismometers installed within the same material, a greater depth will afford lower surface-induced noise levels (Hutt et al., 2017).

The H/Z ratios for all stations in Table 2.1 are shown in Figure 2.12. First, we note that all stations—even bedrock stations with 2.5 m cased boreholes (AK.NEA2, TA.I23K, AK.MLY)—exhibit positive decibels of H/Z ratios for frequencies <0.05 Hz. Second, the low-frequency H/Z ratios for basin stations are larger than those for bedrock stations, and the effect is more pronounced in winter than in summer (Figure 2.12). Examining the data from winter has the advantage that there is lower influence of the river, whose changing conditions during summer could possibly influence the low-frequency noise at stations near the river. During winter the marginal basin stations (Table 2.1: F6TP, F7TV, FAPT, FPAP) have H/Z values that are ≤30 dB, closer to the values for non-basin stations (Figure 2.12b).

2.5.5 Influence of Nenana basin

The influence of the basin is conspicuous for frequencies <0.7 Hz, as shown in the annual spectra in Figure 2.13. At low frequencies (≤0.1 Hz), the elevated noise levels are partly or mostly due to atmospheric effects, as discussed in the previous section. By comparing spectra from basin stations with a non-basin reference spectrum, we also find strong basin influence at 0.1–3 Hz. We examine results within two frequency intervals: 0.1–0.7 Hz and 0.7–3 Hz.

In order to better isolate the influence of Nenana basin, we focus on all basin stations but exclude FAPT and FPAP, whose spectra exhibit high noise levels at high frequencies, which we attribute to anthropogenic sources. We also examine summer and winter separately, with the expectation that river noise will be at a minimum in winter. Spectra from the subset of nine basin stations are shown in Figure 2.14.

2.5.5.1 Seismic noise 0.1–0.7 Hz

For frequencies 0.1–0.7 Hz the basin structure amplifies ocean-generated microseisms by 12–16 dB on the vertical component and by 15–20 dB on the horizontal component (Figure A.78). The influence of Nenana basin is more evident if we subtract a non-basin reference spectrum (F8KN) from each basin-station spectrum, as shown in Figure 2.14c-d. The absolute noise levels are clearly

higher in winter than in summer, but the 12–16 dB increase due to the basin is about the same year-round.

Two stations, F6TP and F7TV, do not exhibit the 12–16 dB increase between 0.1–0.7 Hz (Figure A.75). These are the two stations in the group that are on the edge of the basin and classified as intermediate-basin influence (Table 2.1, Figure 2.1a).

2.5.5.2 Seismic noise 0.7–3 Hz

In order to better isolate the influence of Nenana basin, we focus on winter hourly conditions when the wind speeds measured at Nenana are 0 m/s. This leads to a modified version of Figure 2.14d, shown in Figure 2.15. With the exception of FNN2, all stations exhibit a local peak in noise at 0.7–3 Hz relative to the noise levels at F8KN. The value of the peak ranges from 16 dB at F6TP to 27 dB at F4TN, with a median value of about 21 dB.

Examining the stations F5MN, F6TP, and F7TV provide insights into the origin of the 0.7–3 Hz elevated noise levels (Figure A.74). These stations, from east to west, transition from the deep basin (F5MN) to the margin of the basin (F6TP and F7TV) (Figure 2.1a). The frequency at which the noise levels rise (relative to F8KN) increases from 0.1 Hz (F5MN) to 0.4 Hz (F6TP) to 1.0 Hz (F7TV) in Figure A.75. We surmise that the geometry of the basin—tapering from east to west—leads to the change in frequency range of ambient seismic noise that is amplified.

2.6 Discussion

Our results show that seismic noise varies with time and is influenced by natural and anthropogenic sources. Structural influences may or may not vary with time. The elastic (and anelastic) properties at the scale of a deep sedimentary structure like Nenana basin will not vary with time. The elastic properties of the material adjacent to the direct-buried sensors ("site effects"), do vary with time, since the ground freezes during winter months. Anthropogenic sources may be diurnal, seasonal, constant, or transient.

Our deployment of 13 FLATS station was not designed as an experiment to understand the spatial and temporal variations in noise. Nevertheless, by examining a long time period (3–4 years) and by comparing time-dependent seismic noise with data from nearby environmental

sensors (river, wind), we are able to provide evidence for the influence of structure and of environmental conditions on seismic noise.

We presented our results in a deliberate order: anthropogenic sources, river, wind, basin. With multiple simultaneous sources of noise, it is necessary to examine subsets of time and subsets of stations in order to isolate different influences. For example, Figure 2.14 is a reminder that one cannot simply subtract a non-basin-station spectrum from a basin-station spectrum and attribute the differences to the effect of the basin. Figure 2.14 is annotated to indicate the influences that account for most of the variability among the nine spectra within designated frequency intervals: $<$0.1 Hz for wind+basin, 0.1–3 Hz for basin, 3–20 Hz for river.

2.6.1 Spectral smoothing

The power spectra used in this study are obtained from MUSTANG and are calculated using a smoothing operation that can be detrimental, at least in some cases. A very sharp peak will be smoothed out by the processing steps in MUSTANG. An example of this is the 2.5 Hz peak at AK.NEA2 that we interpret as the microwave lattice tower. This peak is sharp in an unsmoothed amplitude spectrum, but it appears as a mesa-shape in a MUSTANG-generated spectrum, with the mesa spanning from about 2 Hz to 3 Hz (Figure A.46). Similar caution is needed when interpreting the influence of trees, whereby we might expect a harmonic-like peak, yet the MUSTANG-generated spectrum will smooth such a peak. A future analysis of the seismic noise data would benefit from considering different levels of smoothing.

2.6.2 Local versus regional influence

For a time-dependent anomalous level of seismic noise at a station, our goal is to ascertain the type of noise source as well as its distance from the station. This is the basic spirit of Gutenberg (1958) (Table A.1), whose inferences were partly guided by an understanding of seismic wave attenuation: high-frequency waves attenuate over shorter distances than low-frequency waves. Therefore high-frequency noise is apt to arise from local sources, while low-frequency waves could arise from distant sources.

Consider the residual spectrogram in Figure 2.7a. Clearly the variations at 0.1–1 Hz are out of phase with the variations at 5–20 Hz. This is reinforced in Figure A.14, which shows noise time series for four stations at 10 Hz and 6 s. The $\sim$1 dB variance in the 6 s time series implies that the noise at this period is varying similarly in time throughout the region, suggesting a distant source: in this case, the ocean. The 10 Hz time series displays much larger variance that suggests small differences in the noise source: in this case, the interaction between the river and the solid ground adjacent to the river.

A future analysis with arrays of sensors could provide insights into the directions and distances of noise sources. Koper et al. (2010) provides an analysis of global seismic noise using seismic arrays.

2.6.3 10 Hz signal of the Tanana river

The 10 Hz signal of the Tanana river is a new discovery from this study, made possible by installing seismometers within 100 m of the main river channel (Table 2.1). Prior to discussing the results, we need to describe some of the river's characteristics (Collins, 1990). The river is undammed and is primarily fed by meltwater from glaciers in the Alaska Range. It carries glacial silt as well as larger sediment. Along the stretch of the Tanana river between Nenana (upstream of F1TN; see Figure 2.1) and the Tolovana river (near F7TV), we have seen no sedimentary particles larger than sand; however, large-scale organic debris, like trees, are widespread, especially piled up along the riverbanks. There are no rapids, though windy conditions can produce waves. The surface of the river freezes completely usually by early November, and the river ice breaks up in late April. In the summer there are few boats on the river; there is generally one barge per day transporting heavy goods to and from villages downriver that have no road access. The night-vs-day difference in high-frequency noise at river stations are 0–2 dB; therefore anthropogenic noise is assumed to be negligible. Next we summarize the key observations of the river signal, followed by a discussion of river characteristics that would be needed to model the observed river signal.

The seismic signal of the Tanana river spans from 4–30 Hz and is maximal near 10 Hz (Figure 2.6). It occurs on both horizontal and vertical components, and its peak-to-peak amplitude variations are larger on the horizontal component (Figure 2.6). The maximum occurs in mid-

July, likely associated with elevated flow arising from peak discharge from glaciers in the Alaska Range. The minimum occurs in March, associated with the lowest river levels. The peak-to-peak variability ranges between 30–40 dB for four stations near the river (Figure 2.7b). The signal is stronger at F3TN and F4TN, which are closer to an actively eroding riverbank (Table 2.1), than at F5MN and F7TV (Figure 2.7b). We assume the variability depends on the distance from the station to the main river channel and also on the geomorphic details of the main channel near each site. During peak flow in summer, the decibals of H/Z ratios are flat (Figure 2.7c) and are 0 dB for the two strongest river stations (F3TN, F4TN). Following freezeup, H/Z decreases due to decreasing H.

Using seismometers to study rivers is a relatively new field. (In part, this is because most seismic experiments are designed to measure earthquake signals and would therefore avoid noise-producing sources like from a river.) Examples of fluvial seismology include Burtin et al. (2008); Tsai et al. (2012); Schmandt et al. (2013), whose data sets and models are aimed at elastic energy produced by the collision of sedimentary particles, some as large as meter-scale boulders, in the case of Himalayan rivers (Burtin et al., 2008). Turbulence within the water has also been identified as a source of noise, in addition to noise from sediment particles interacting with each other or with the river bottom. Gimbert et al. (2014) provides a framework for modeling seismic noise arising from turbulence in rivers (Larose et al., 2015; Anthony et al., 2018).

In the case of the Tanana river, there is glacial-derived silt suspended in the water, and sand is transported and deposited. Therefore either turbulence within the water or unsteady shearing on the riverbank are the likely candidates for producing the 10 Hz signal. To benefit a future comparison with theoretical studies (e.g., Gimbert et al., 2014), we provide some relevant values for the Tanana river in Table 2.2, as well as Figure A.15, which shows how discharge and gauge height varied between 2014 and 2019. Sediment characteristics of the river near our sites can be approximated using data from just upstream of the town of Nenana, which was investigated as a possible site for hydropower (Toniolo et al., 2010; Toniolo, 2013; Johnson et al., 2013). (We note that a major tributary—the Nenana river—enters the Tanana river just downstream of Nenana.) Turbulence near the shoreline, closest to the seismometer, needs to be carefully considered. Turbulence at our sites is enhanced by curving riverbanks (notably at F3TN and F4TN; see also Lesh & Ridgway (2007)), highly irregular erosive riverbanks (meters per year at F4TN; see also Collins (1990)), and

large rafted or fallen trees along the riverbanks and in the water. Johnson et al. (2013) discussed the debris within the Tanana river. Anthony et al. (2018) discussed the role of larger materials on seismic noise. Based on measurements of a small mountain river in Colorado, they suggested that larger materials (such as boulders) were responsible for causing eddies and producing elevated noise levels on the horizontal component of nearby seismometers.

The Tanana river is the largest tributary of the Yukon river. We examined noise spectrograms for stations in villages on the Yukon river: AK.GCSA, TA.I21K, TA.H23K, AK.FYU, TA.I26K and US.EGAK. The closest station to the river is TA.I21K at 320 m. We did not detect any definitive signal arising from the river. Either the cultural noise levels are too high at these sites, or the stations are too far from the river, or the Yukon river at these sites does not produce a seasonal high-frequency signal.

2.6.4 The spatial reach of wind

Our results corroborate previous findings that the effects of wind are recorded by buried seismometers (Sorrells, 1971; Withers et al., 1996). The influence of the wind is visible within three different frequency bands (Section 2.5.4). At lower frequencies (<0.05 Hz), the seismometer likely records tilting ground motion arising from atmospheric-induced changes (e.g., De Angelis & Bodin, 2012). At moderate frequencies (0.5–2.0 Hz), the wind may interact with trees, which sway and oscillate the ground. At high frequencies (>2.0), the wind shears the ground and interacts with exposed irregularities.

Whether the seismometer is measuring ground tilt at long periods or wind shearing effects at high frequencies, this information can be used to study how correlated a single weather station is with seismic stations at a range of distances and settings. None of the seismic stations in Table 2.1 has a collocated meteorological station. The one meteorological station in the region is in Nenana (Figure 2.1b). As we might expect, if there is a correlation between wind speeds at Nenana and a seismic station, then—with all other factors being equal (which they are not)—we would expect such a correlation to decrease with increasing distance. This is what we see in Figure 2.11c, where daily seismic noise levels at stations closer to the wind station exhibit higher correlations with daily wind speeds, both at low frequencies and at high frequencies.

The winter hourly wind speeds at Nenana (PANN) are predictive of tilt-induced seismic noise and also >1 Hz noise at Manley (MLY), 96 km away (Figure A.48). In other words, high winter wind speeds in Nenana imply high wind speeds at some sites far from Nenana. The Manley station is at the top of a bedrock hill and is exposed to winds from the south. We hypothesize that the wind-amplified noise for >1 Hz arises from two sources: wind excitation of the ground and wind excitation of a 6 m tall tower that supports a pair of solar panels and is about 6 m from the borehole. At lower frequencies, the H/Z ratio increases with increasing wind speeds above 4 m/s, as recorded at Nenana (Figure A.51).

The spatial reach of wind depends on the details of a particular site: elevation, slope, coverage of trees, and also the subsurface site structure. FTGH, MLY and F8KN have relatively high elevations (286 m, 450 m, and 181 m) and exposed to wind; these stations exhibit increasing high-frequency (≥10 Hz) noise at higher wind speeds (Figures A.45, A.48, and A.49). The sensor at F1TN is within 4 m of two large spruce trees (17 m, 24 m tall), which are likely responsible for extremely elevated noise for ≥ 1 Hz (Figure 2.10a). Our results suggest a complex role of trees: they catch the wind and produce swaying frequencies, but they also shelter the ground from wind effects that we expect at higher frequencies.

It is possible that some elevated noise levels during highest wind conditions arise from distant effects rather than from local effects. During winter between 2015-09-01 and 2019-09-01, there were 24 hours that reached wind speeds of 10–12 m/s at Nenana. For each station we computed the median spectrum for these 24 hours and then subtracted a median spectrum computed during low wind (0–2 m/s) conditions. Figure A.57 shows the resultant set of differential spectra. Variations in the spectra at low (<0.1 Hz) and high (>0.5 Hz) frequencies are highly variable and depend on the details of each site (e.g., trees, tower, exposure to wind). These variations are in stark contrast with the spectra at 0.1–0.5 Hz, which shows 5–7 dB elevated seismic noise power at all stations. Either the influence of wind on local seismic noise at 0.1–0.5 Hz is nearly identical at all sites, or the background regional wavefield—which is generated in the ocean (Longuet-Higgins, 1950; Kedar et al., 2008)—is elevated during the time periods of extreme wind conditions at Nenana. (In other words, storm conditions in, say, the Gulf of Alaska may produce elevated regional seismic noise levels and also high wind speeds in adjacent continental regions.) Additional work is needed to explain the uniformly-elevated noise levels during time periods of highest wind speeds at Nenana.

2.6.5 Shallow structure vs deep structure

The role of local site structure and deep basin structure on low-frequency seismic noise levels is not entirely clear. The influence of site or basin requires some notion of length scale; for our purposes, we assume that the "site" encompasses structure in the uppermost 30 m, including the structure adjacent to the sensor (or vault), whereas the "basin" encompasses structure to the depth of the basin, which is up to 6 km (Figure 2.1a). We show that increasing wind speed increases the H/Z ratio at $\leq$0.05 Hz for most stations. Installing a seismometer deeper will mitigate this effect (Hutt et al., 2017). Low-velocity site structure, such as unconsolidated sediment, increases the H/Z ratio (Sorrells, 1971; Ziolkowski, 1973; Wilson et al., 2002; Wolin et al., 2015), even for stations overlying bedrock (Dybing et al., 2019). The role of deeper structure is more difficult to assess.

At zero-wind conditions, the H/Z ratios for basin stations are higher for deep basin stations (30–40 dB: FNN1, F3TN, F4TN, F5MN) than for stations in or near bedrock (15–30 dB: FTGH, NEA2, I23K, MLY, F8KN) (Figures A.50 and A.51). Marginal basin stations exhibit lower H/Z ratios than deep basin stations (F6TP 20 dB, F7TV 28 dB, FAPT 28 dB, FPAP 26 dB). There are not enough stations needed to control the possible variables that could influence the site conditions, such as the presence of trees, the permafrost characteristics, the variations in shallow water table, and the influence of the river (even at long periods). Nevertheless, our results suggest that deeper (km-scale) structure could influence ground tilting due to atmospheric conditions. Or perhaps the presence of deeper, slow structure implies the presence of shallower (10–100 m scale) slow structure, which is generally unknown but expected to influence the degree of ground tilting.

A second possible influence of the deep structure is that some of the observed H/Z ratios could be caused by seismic waves, rather than ground tilt. Sedimentary basins, including Nenana basin, distort Rayleigh wave particle motion toward ellipticity having $H/Z > 1$ (Lin et al., 2012; Tanimoto et al., 2013; Workman et al., 2017; Muir & Tsai, 2017; Berg et al., 2018). Large-scale variations in elastic structure will influence the ellipticity of Rayleigh waves as a function of the azimuth of the arriving seismic wave (Maupin, 2017; Bao & Shen, 2018; Ringler et al., 2019). Further study of ambient noise waveforms is needed in order to identify how much of the low-frequency noise is tilt versus seismic waves.

A third possibility is that the low-frequency elevated H/Z ratios are artifacts and neither ground tilt (from above) nor seismic waves (from below). An experiment with 16 sensors in a bedrock vault showed that tilt effects where not spatially coherent (Rohde et al., 2017). Another experiment with adjacent, buried sensors (ASL8 and ASL9) showed that coherence on the horizontal components between the two sensors decreased for low frequencies (<0.02 Hz) during a time period of low wind speeds (Dybing et al., 2019). These spatially incoherent horizontal recordings suggest that in these conditions the ground is not tilting under slow-moving atmospheric waves. The forcing effect from the atmosphere could be a much higher-frequency effect—like turbulence or wind tugging on the roots of shrubs or debris—that is manifested by a stochastic-direction tilt signal of the seismometer.

2.6.6 Implications for detecting earthquakes

Continuous ground motion recorded at FLATS stations were telemetered in real-time to the Alaska Earthquake Center. The data were used within operational tasks for earthquake location. Therefore we can examine how ambient noise variations with time could impact the detection of P waves from earthquakes and, in turn, the detection of earthquakes in the region.

Seismic noise is strongly seasonal, and the seasonality may arise from regional or local sources. Figure 2.4 shows seasonal variations in noise for each station in the Minto Flats region. At F3TN the horizontal-component summer noise levels at 10 Hz are 40 dB higher than in winter. The noise levels implies that the winter months of January–February offer the best time period for detecting P waves or analyzing high-frequency data at FLATS stations and especially those near the river. In other words, the magnitude of completeness is expected to decrease during the winter, when noise levels are lowest. We demonstrate this effect in Table A.3 and Figures A.79–A.83.

2.6.7 Unexplained features in the noise

Our analyses of seismic noise have revealed four features that warrant documenting and will require further analysis and additional data (or experiments):

2.6.7.1 20 Hz peak at basin stations (Figures 2.14 and 2.15)

At basin stations, the 20 Hz vertical-component noise is elevated by about 10 dB during summer and winter; see Figure 2.14c-d and also Figure 2.15. Noise levels on the vertical component at F1TN, F5MN, F6TP, F7TV, and FNN2 are 10 dB higher than at F8KN. Even during winter (and especially during summer) the river noise at F3TN and F4TN exceeds 10 dB, and therefore we cannot determine whether the 20 Hz peak is present. To give a rough estimate of the length scales involved, a 20 Hz wave traveling at 100 m/s would have a wavelength of 5 m. We interpret the 20 Hz signal as arising from structural amplification in the low-lying Minto Flats region. The structural feature is shallow and could be related to the water table or to permafrost, which is sporadic (10–50%) in the region (Jorgenson et al., 2008).

2.6.7.2 0.1 Hz H/Z peak at deep basin stations (Figure 2.12)

At 0.1 Hz there is a subtle peak of 10–20 dB in the H/Z ratio that is visible during winter and during low wind periods at basin stations F2TN, F3TN, F4TN, F5MN, and FNN2, yet absent at FNN1 (Figure 2.12a and A.50). The peak is not observed at marginal basin stations (F6TP, F7TV, FPAP, FAPT) or at non-basin stations. The 0.1 Hz peak is most conspicuous at non-river station FNN2, where it is visible year round and unaffected by wind. The visibility at FNN2 is likely due to its relatively low H/Z ratios at lower frequencies that do not cover the 0.1 Hz peak. If we assume that the 0.1 Hz peak is related to seismic wave propagation, then a rough estimate for wavelength of 10 km can be determined from the shear-velocity of 1000 m/s. This is similar to the width of Nenana basin and the distance between the seismically active left-lateral faults on either side of the basin (Figure 2.1a). We propose that the 0.1 Hz H/Z peak of 15 dB is due to the structure of Nenana basin distorting (and amplifying) ambient noise surface waves in Nenana basin.

2.6.7.3 Seasonality of a 10 Hz signal at basin stations

The 10 Hz horizontal component time series of all basin stations is seasonal, with high amplitudes in the summer and low amplitudes in the winter (Figures A.28–A.32). For stations close to the river, the seasonality is due to the river. For stations in the town of Nenana (FAPT, FPAP), the

seasonal noise is likely influenced by cultural noise. For stations 100–1000 m from the main river channel (F1TN, F6TP), the seasonal noise could influenced by the Tanana river. For remote stations far from the river (FNN1, FNN2), the seasonal noise is unlikely to be from the river. The seasonal variations at these stations suggest a seasonal dependence of the elastic structure at both sites. Such variations could arise from freezing and thawing within the upper few meters (James et al., 2019). It is possible that the seasonal structural variations are present at all basin stations but that their noise imprint is buried by the effects of cultural or river noise.

2.6.7.4 Spikes in daily noise at 10 Hz (Figure 2.7b)

During the winter, when river flow is lowest, there are spikes that occur in the 10 Hz time series, such as at F3TN (Figure 2.7b). These spikes often correlate in time with several other stations, so their source is not local to each site. We have demonstrated that high wind speed can increase high-frequency seismic noise at 10 Hz. However, at F3TN, the role of wind at 10 Hz is low: it may be lessened by the presence of trees, or it may be buried by the signal from the river. Our analysis of these spikes during winter, including at bedrock stations like NEA2, indicate that some spikes are due to extreme wind events. The simultaneous occurrence of spikes at river stations (e.g., F3TN, F7TN) and non-river stations (e.g., FNN2, NEA2) suggest that river ice is not the source. Further work is needed.

2.7 Summary

We present an empirical study of seismic noise variations in the Minto Flats region of central Alaska. Different structural and environmental factors are responsible for temporal and spatial noise variations in the region. Using river gauge and wind speed data from Nenana, we are able to quantify the frequency ranges and time periods of influence of rivers and wind on recorded ground motion. Our summary points are as follows:

1. We installed 13 stations in the region, and we compare noise results from these stations with three high-quality bedrock stations at Nenana, Minto, and Manley. All 16 stations were posthole seismometers, either directly buried in lightly damp soil or sand (13), or installed inside a cased borehole into bedrock (3). For directly buried sensors, coupling between the buried sensor and the adjacent ground (mostly damp sand) is very good.

2. In order to isolate a noise source (e.g., wind) for a particular time period, frequency range, and station, one must consider all possible influences on seismic noise. For example, high frequency (>5 Hz) ground motion may arise from wind, river, or anthropogenic sources. In our study region, we benefitted from a sequential analysis of noise from anthropogenic sources, rivers, wind (and trees), and basins.

3. Unlike rivers and wind, basins are not a source of noise. Seismic waves, either from earthquakes or from ambient noise, can be strongly affected by the elastic (and anelastic) properties of the basin. Basins may be best thought of as a transfer function (Field & Jacob, 1993), whereas rivers, wind, and anthropogenic sources like traffic are best thought of as noise sources.

4. In order to interpret anthropogenic noise, it is helpful to have photographs of sites and awareness of activities within the region. Without this information, there is danger of misinterpreting an anthropogenic source as an environmental source (such as river or wind). Although our study region is roadless and remote, there were activities during the time period such as 3D active-source seismic surveys and the construction and drilling of 3D exploratory wells.

5. Simultaneously recording environmental sensors are essential for examining environmental influences on seismic noise. We use the weather station and river gauge in Nenana (Figure 2.1b) to identify the range of frequencies and time periods where wind and river are influential on seismic noise.

6. Correlations between daily or hourly seismic power and environmental data need to be examined within seasons, as a single physical model may not always be applicable. For example, correlation of daily data over a full year shows no clear pattern between river gauge and 10 Hz seismic noise, but the pattern is clear during the summer period (Figure A.18). Similarly, the influence of wind is best examined during winter, when other noise sources (river, anthropogenic) are lowest.

7. The Tanana river produces a signal that is recorded by seismometers near the river. The signal is maximal at about 10 Hz and varies seasonally (Figure 2.4). Noise levels are as much

as 40 dB higher in summer, during peak flow, than during winter, when the river surface is covered in meter-thick ice. We hypothesize that the 10 Hz river signal arises from turbulence within the water and from unsteady shearing of the riverbank and river bottom.

8. We present evidence that wind can influence seismic noise at a range of frequencies. We propose interpretations for three frequency bands, based on plots like Figure 2.10a (see Electronic Supplement). At high frequencies ($\geq$2.0 Hz), the elevated noise is due to wind effects on the ground within meters of the station. A subtle peak at 0.5–2.0 Hz may be caused by nearby trees swaying. The station with the tree closest to the station (F1TN) exhibits the most extreme elevated noise due to wind: 27 dB higher when hourly wind speeds are 10–12 m/s. High winds are associated with changing atmospheric conditions, which push down on the ground and causing tilting of the seismometer, evidenced by elevated levels of low-frequency ($<$0.05 Hz) horizontal noise (Sorrells, 1971). Stronger wind enhances this effect, as evidenced from higher H/Z ratios for higher wind speeds; this effect is most pronounced for bedrock stations for which the H/Z low-wind reference value is lowest (Figure A.51).

9. High hourly-averaged wind speeds appear to be correlated at distances as great as 100 km. The wind speeds at Nenana (PANN) correlate with both low-frequency ($<$0.05 Hz) and high-frequency ($>$2.0) seismic noise at Manley (MLY), 96 km away.

10. The basin influence on seismic noise is best characterized in Figure 2.15. At basin stations, the vertical-component noise for 0.1–0.7 Hz is 12–16 dB higher than at bedrock station F8KN. At 0.7–3 Hz, noise levels are 17–30 dB higher. A similar pattern was identified for stations in Cook Inlet basin (Tape et al., 2017, fig. 6), a much larger and different-shaped basin than Nenana basin. It is possible that at high frequencies there is a different source of noise inside the basin (whether Cook Inlet or Nenana) than outside the basin.

    Numerical simulations using regional earthquakes and a realistic basin model (Figure 2.1a) should benefit our understanding of the basin amplification of noise.

11. We offer some strategies for pursuing noise studies in complex settings such as Minto Flats. First, there needs to be enough stations—as many as possible—to constrain the large number of known variables. At the same time, one must also keep open the possibility of unknown

effects (e.g., river ice, thermal changes in permafrost); Gutenberg (1958) urged to seek "wave types which had not been suspected" (p. 81). Finally, once the noise sources are isolated, they should be analyzed sequentially, using subsets of stations and subsets of time periods.

Our empirical findings would benefit from a future study that includes theoretical or numerical modeling. Flow and turbulence are likely important processes to understanding how wind and rivers couple to the solid earth (Gimbert et al., 2014). During winter, wind is interacting with the (snow-covered) ground or top of the river ice, while water is interacting with the bottom of the river ice and the base of the river. A key difference is that river flow is always "on"—even when it is covered in ice—whereas wind is not. A second area of study involves the role of structures (trees, towers, buildings) on wind-ground coupling.

Seismic noise provides insights into meter-scale site structure, km-scale local structure, and changing environmental conditions. In some cases, the environmental conditions may be a nuisance; in other cases, they may be the target. Understanding of the time-dependent variations in noise across all frequencies should help inform how to improve site selection, seismic installations, or the sensors themselves. Even equipped with an understanding of noise variations in a region, the choices can be challenging. For example, had we sacrificed telemetry and line-of-sight for FLATS stations, we could have put some stations further from the river, which would reduce the high-frequency noise but would have minimal impact on our lower-frequency ($\leq$1 Hz) range of interest for waveform modeling and moment tensor inversions (Tape et al., 2015). Or we could have installed F8KN slightly in the woods, where trees may have buffered effects of wind on high-frequency ground motion. In hindsight, we would have tried to install F1TN a few meters further from trees. Ultimately the high noise levels of the sedimentary basin corroborate our basic expectations for Nenana basin, though we could not have predicted the frequency range or amplification as shown in Figure 2.15. In spite of the noise levels from structure and from the environment, the FLATS stations were optimally positioned to record events—and exotic wave propagation effects—from the underlying active fault zone (Tape et al., 2018). Future seismic deployments in this region—or in other regions with basins, rivers, trees, or wind—may benefit from the findings from this study.

2.8 Tables

Table 2.1: Characteristics of 16 seismic stations. The entries are colored based on the presence of a possible noise source: red present, blue somewhat present, green not present. Basin depths are from PRA (2017); for stations outside the mapped region, we assign 1000 m depth for basin stations and 0 m for bedrock stations. Due to both erosion of the riverbank and to consequent reinstallations of sensors, the distance-to-river for F2TN and F4TN varies over the course of the project; minimum distances are 1 m for F4TN (2016-08-03) and 2 m for F2TN (2018-06-24). The elevation of the meteorological station PANN (see Figure 2.1) is 106 m. See Section 2.3 for details.

network	station	sample rate	anthro-pogenic	distance to river (m)	basin depth (m)	distance to PANN (km)	elevation (m)
XV	F1TN	100	0	820	4200	12.6	108
XV	F2TN	100	0	12.8	4700	18.2	104
XV	F3TN	200	0	14.0	3300	25.2	104
XV	F4TN	100	0	20.1	2500	32.2	102
XV	F5MN	100	1	18.3	3000	38.1	101
XV	F6TP	100	0	575	1000	42.8	115
XV	F7TV	100	1	62	1000	49.5	93
XV	FNN1	100	0	3960	4000	7.4	110
XV	FNN2	100	0	14860	3000	18.1	135
XV	FAPT	100	2	1200	1000	0.5	111
XV	FPAP	100	2	1114	1000	7.4	106
XV	FTGH	100	1	10100	0	19.9	285
AK	NEA2	50	1	2650	0	5.1	450
TA	I23K	40	2	25200	0	68.3	149
AK	MLY	50	0	6480	0	96.0	812
XV	F8KN	100	0	120	0	47.6	179

Table 2.2: Characeristics of the Tanana River near Nenana, Alaska. Flow measurements are taken from 244 m upstream from the USGS river gauge in Nenana (15515500) during a high-flow time period (2016-07-26).

property	value	reference
slope angle	$< 0.1^{\circ}$	FAPT to F7TV (Table 2.1)
width of main channel	233 m	USGS (2016-07-26)
depth of main channel	3–10 m	USGS (2016-07-26)
flow velocity	1.95 m/s	USGS (2016-07-26)
summer discharge	2670 m^3/s	USGS (2016-07-26)
average monthly discharge (May–October)	495.5–1704.7 m^3/s	Toniolo et al. (2010)
median sediment grain size	$\sim$0.25 mm	Toniolo (2013, fig. 4)

2.9 Figures

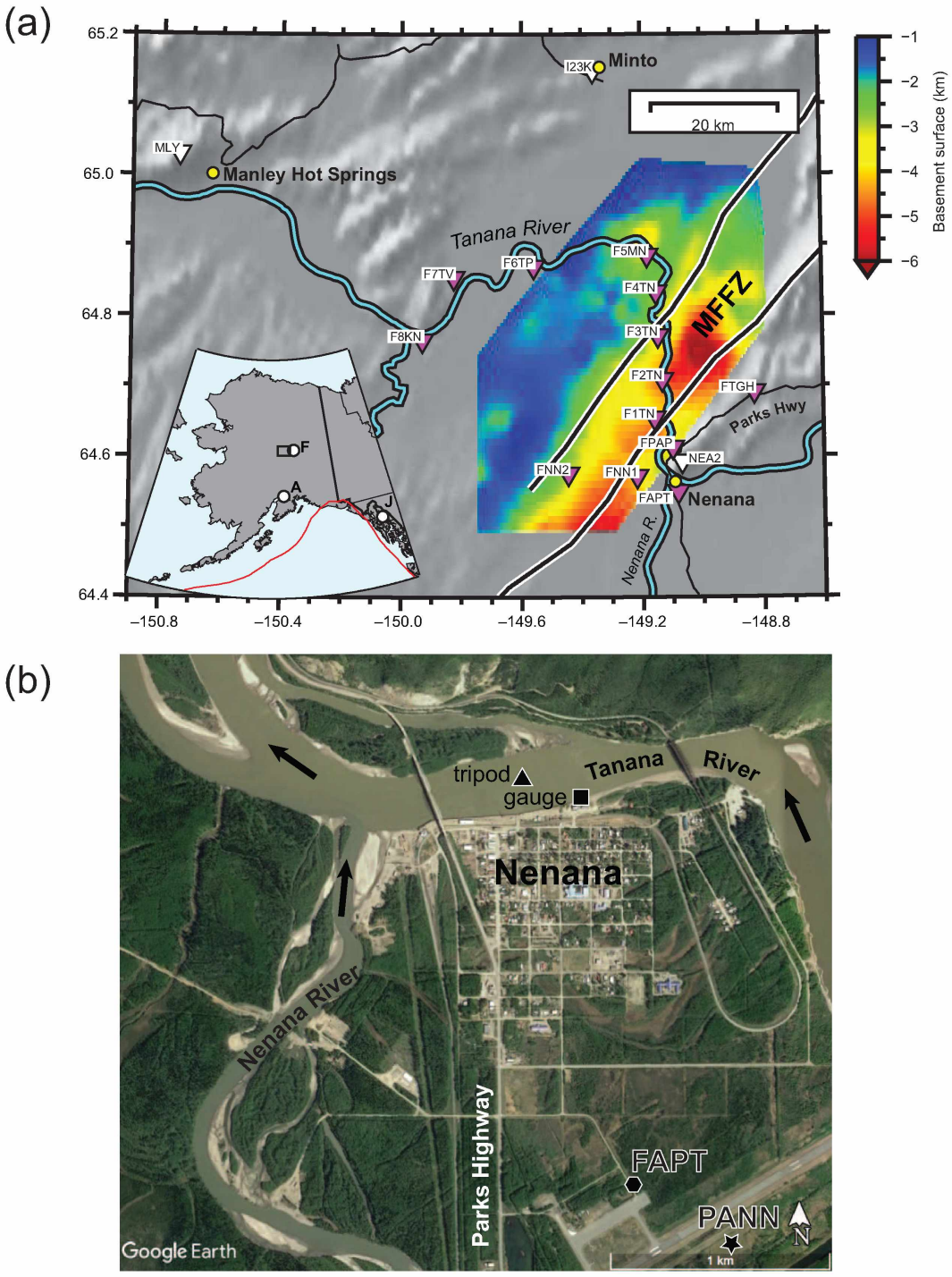

Figure 2.1: Study area of the Minto Flats region, central Alaska. (a) FLATS stations (magenta triangles), 2014–2019, and other seismic stations (white triangles). The coloring shows the depth to basement for the Nenana basin (PRA, 2017). The Minto Flats fault zone (MFFZ) contains two strike-slip faults inferred from seismicity and source mechanisms (Tape et al., 2015). (b) The town of Nenana, at the confluence of the Nenana and Tanana rivers. The seismic station FAPT and the weather station PANN are near the runway. Locations of the USGS river gauge and Nenana Ice Classic tripod are also shown.

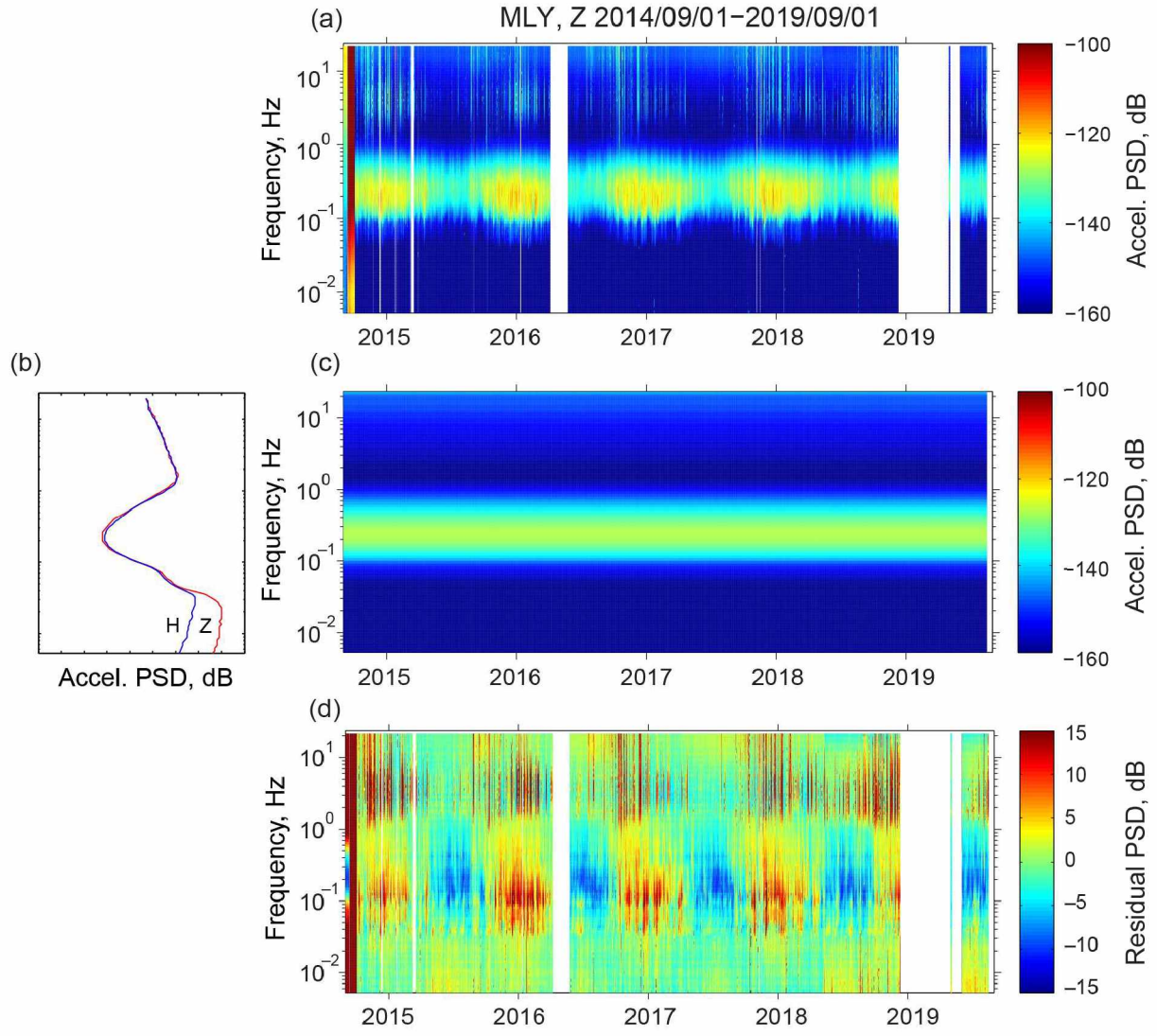

Figure 2.2: Procedure to obtain residual noise spectrogram (d), illustrated for station AK.MLY near Manley Hot Springs, Alaska. (a) Vertical component spectrogram for four years. The daily noise is represented as a vertical "strip" calculated from hourly empirical power density functions (PDFs) from MUSTANG (Casey et al., 2018). (b) Median of all daily spectra in (a) (blue); also shown is average of the median stacks of the two horizontal components (red). The plot is rotated for the sake of comparison with the spectrograms, which have frequency on the vertical axis. (c) Spectrogram of (b), depicting the reference ambient noise at this station. (d) Spectrogram of (a) minus (c), which enhances the time-dependent variations in noise.

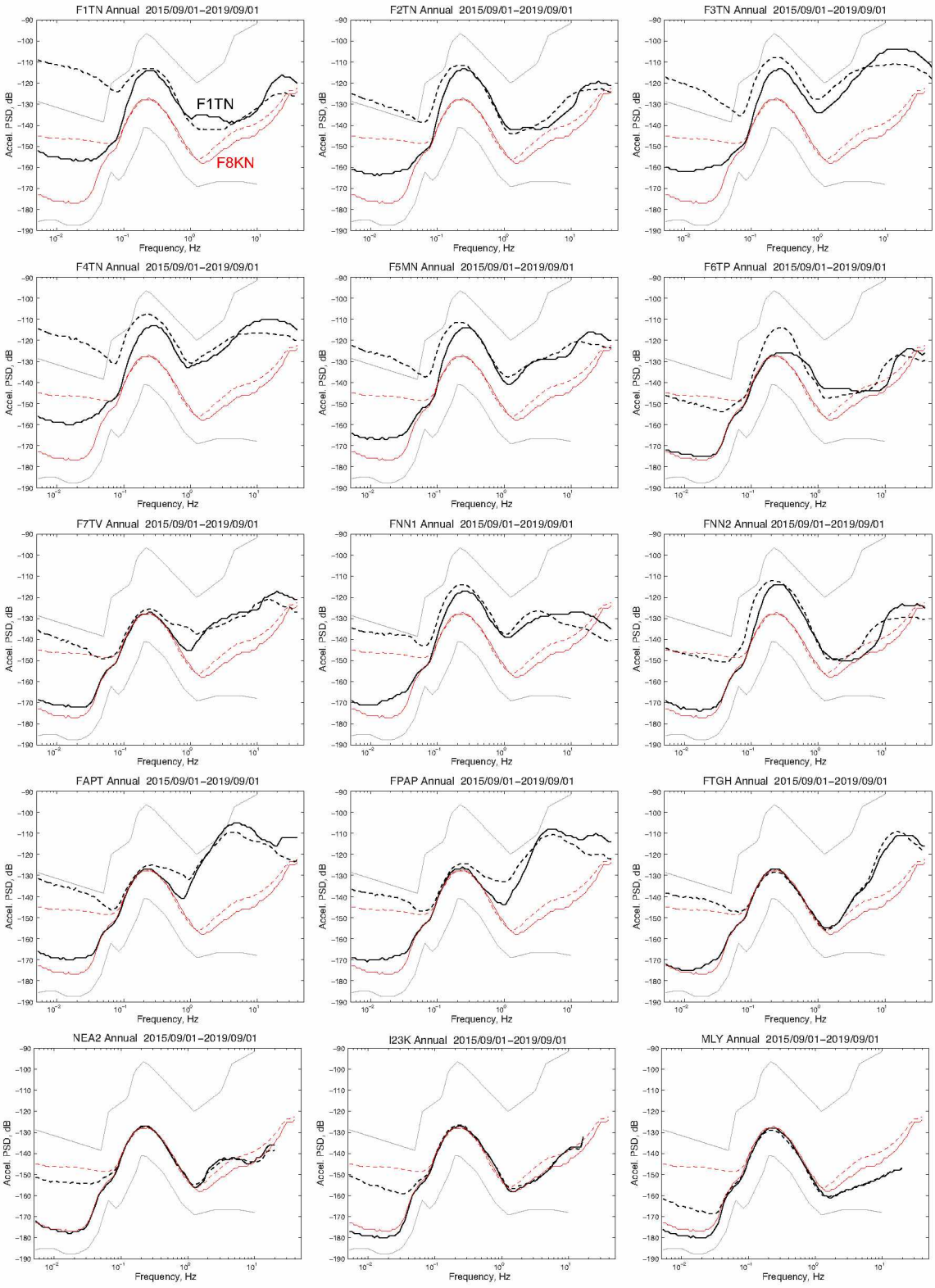

Figure 2.3: Annual ambient noise stack of 16 seismic stations in Minto Flats (Table 2.1), with the reference spectra for F8KN shown in red for each subplot. Solid and dashed black lines are vertical and horizontal components, respectively. The FLATS stations (F1TN–FTGH) exhibit higher noise levels than F8KN due to a combination of structural and environmental influences. The gray lines are the New High Noise Model (NHNM) and New Low Noise Model (NLNM) reference spectra (Peterson, 1993).

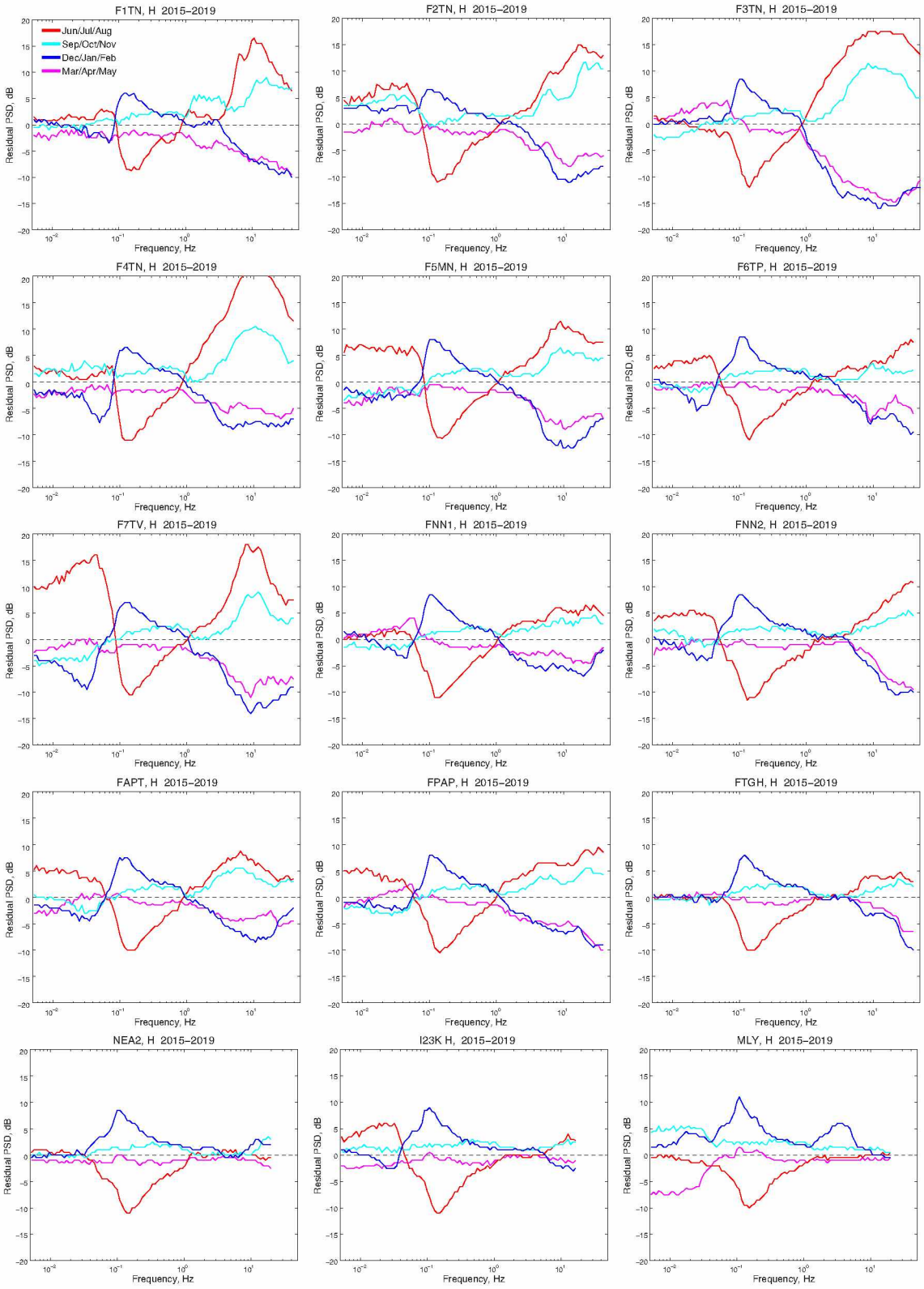

Figure 2.4: Seasonal variations of ambient seismic noise, horizontal component. Each subplot shows the deviation of each 3-month season from the corresponding annual spectrum in Figure 2.3. The seasons are colored as follows: June/July/August (red), September/October/November (cyan), December/January/February (blue), March/April/May (magenta). The seasonal variations for the vertical component (Figure A.5) are less than those for the horizontal component. Seasonal variations for F8KN are shown in Figure A.6.

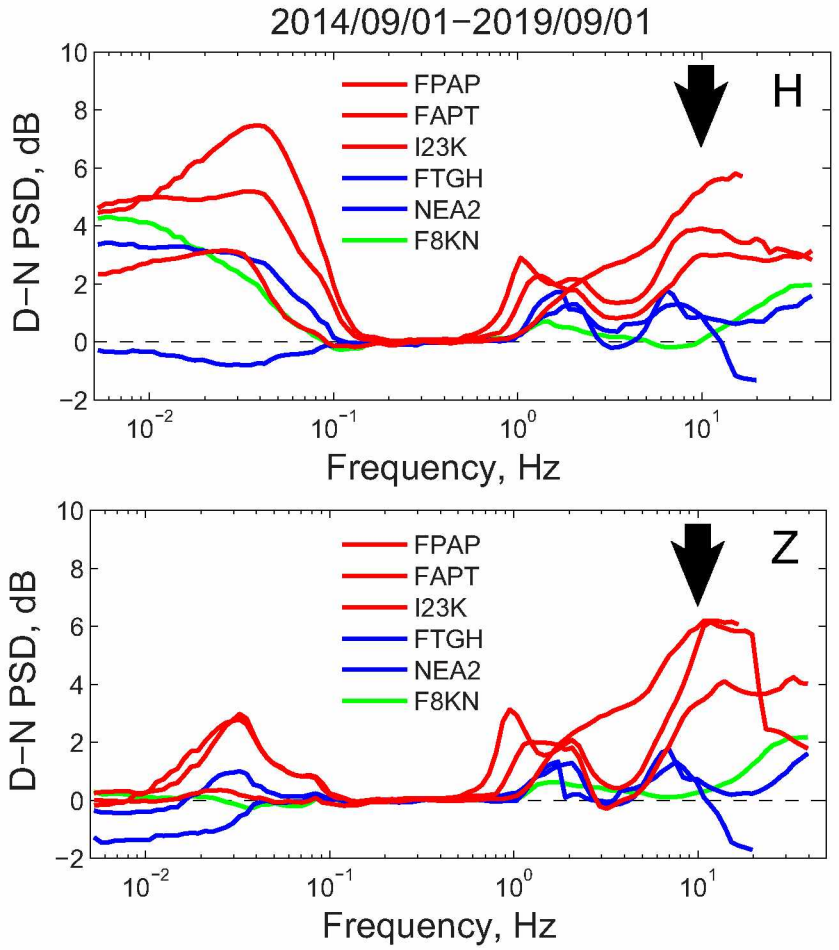

Figure 2.5: Differences between day and night (D-N) seismic noise spectra for six stations (XV.FPAP, XV.FAPT, TA.I23K, XV.FTGH, AK.NEA2, XV.F8KN). Differential spectra are colored according to expected influence of cultural noise sources (Table 2.1). Daytime (08:00–20:00 AKST) noise levels are 4–6 dB higher for the frequency range 10–20 Hz (denoted by arrows) for stations FPAP, FAPT, and I23K. See Figures A.11 and A.12 for other stations. Note that this analysis will not reveal constantly-running cultural noise sources such as a generator.

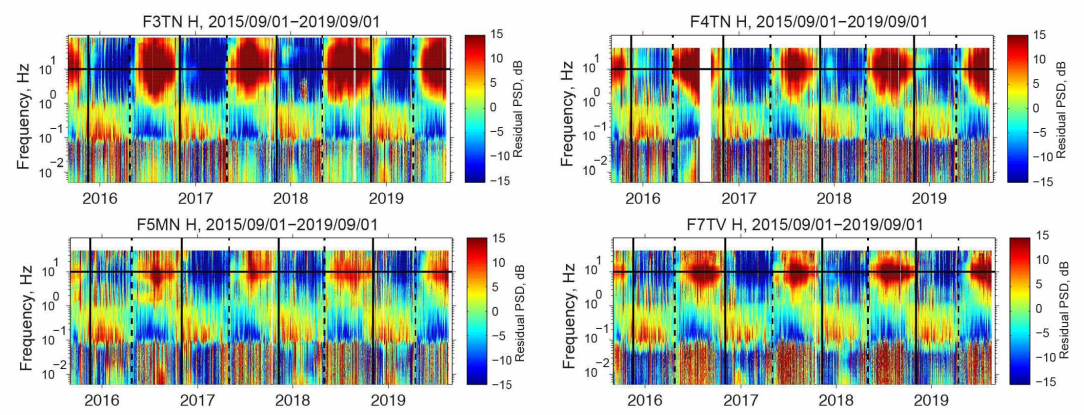

Figure 2.6: Residual spectrograms (horizontal component) for four of the five stations that are close to the main river channel (Table 2.1) for the time period from 2015-09-01 to 2019-09-01. The vertical dashed lines denote river ice breakup; the vertical solid lines denote river freezeup (Section 2.5.3). The horizontal line is selected at 10 Hz and is a representative frequency for the observed strong seasonal variability in the spectrograms. The 10 Hz signal is highest in summer and lowest in winter, when the surface of the river is ice-covered; see Figure 2.7b for corresponding time series. We attribute the signal to river flow. See Figure A.7 for spectrograms for all 16 stations for both components.

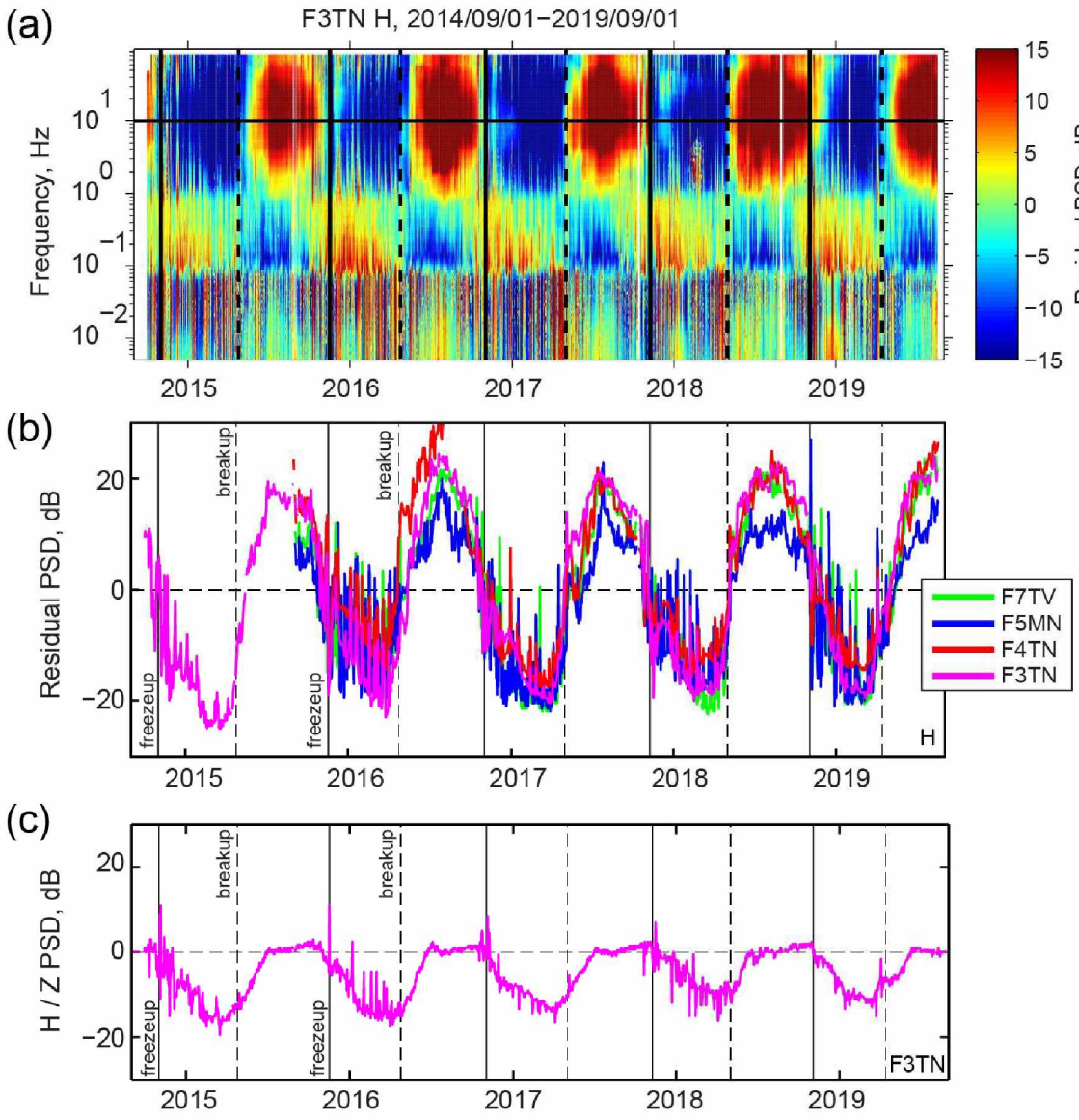

Figure 2.7: Annual variability of the 10 Hz noise signal at four FLATS stations installed within 100 m of the Tanana River. The vertical dashed lines denote river ice breakup; the vertical solid lines denote river freezeup (Section 2.5.3). (a) Residual spectrogram of the horizontal component at F3TN between 2014-09-01 and 2019-09-01. The horizontal black line at 10 Hz corresponds to the magenta time series in (b). (b) Time series of 10 Hz residual noise at four FLATS stations near the river channel (Table 2.1). See Figure A.13 for the vertical component. (c) Time series of H/Z for 10 Hz noise at F3TN (Figure A.28). During the winter, H/Z dB < 0, indicating that the noise on the horizontal component is less than on the vertical component.

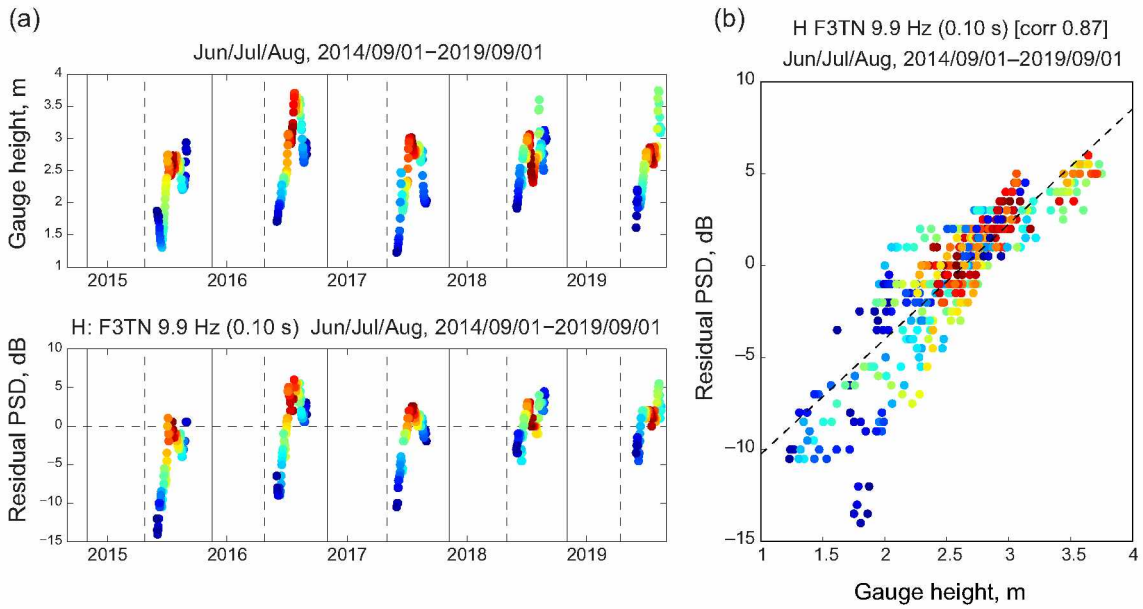

Figure 2.8: Comparison between Tanana river gauge height and the 10 Hz seismic noise at station F3TN, during summer (June/July/August). (a) Time series of the river gauge height (top) and the residual seismic noise power at 10 Hz (bottom). The data are colored red during the middle of summer (mid-July) and blue at the start (early June) and end (late August) of summer. (b) Scatter plot of seismic power versus river gauge height. Data spanning the entire time period are displayed in Figure A.18

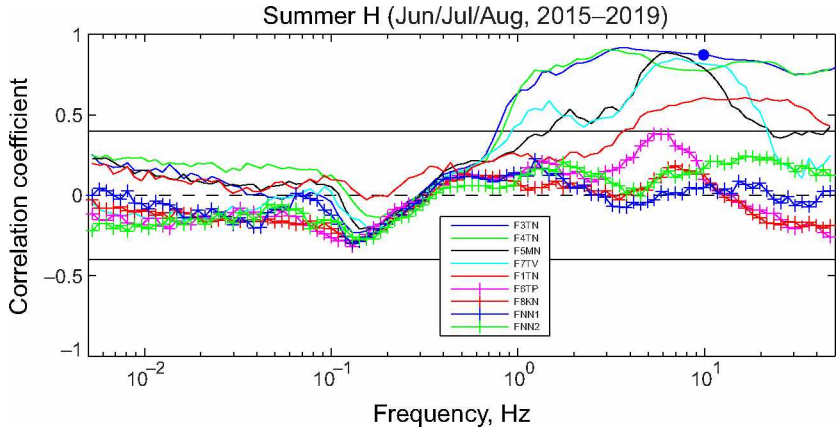

Figure 2.9: Correlations during summer months (June/July/August) between average daily river gauge height and horizontal-component seismic noise power across all frequencies. An example point is plotted at (10 Hz, cc 0.87) for F3TN and is based on the data shown in Figure 2.8. Curves are shown for 10 FLATS stations, four of which are close to the main river channel (smooth curves: F3TN, F4TN, F5MN, F7TV). The highest correlations (and above the $|cc| = 0.4$ reference lines) occur for the four river stations for the frequency range 1–10 Hz. See Figures A.25, A.26, and A.27 for other seasons and components. F2TN was reinstalled three times and is omitted from the plot.

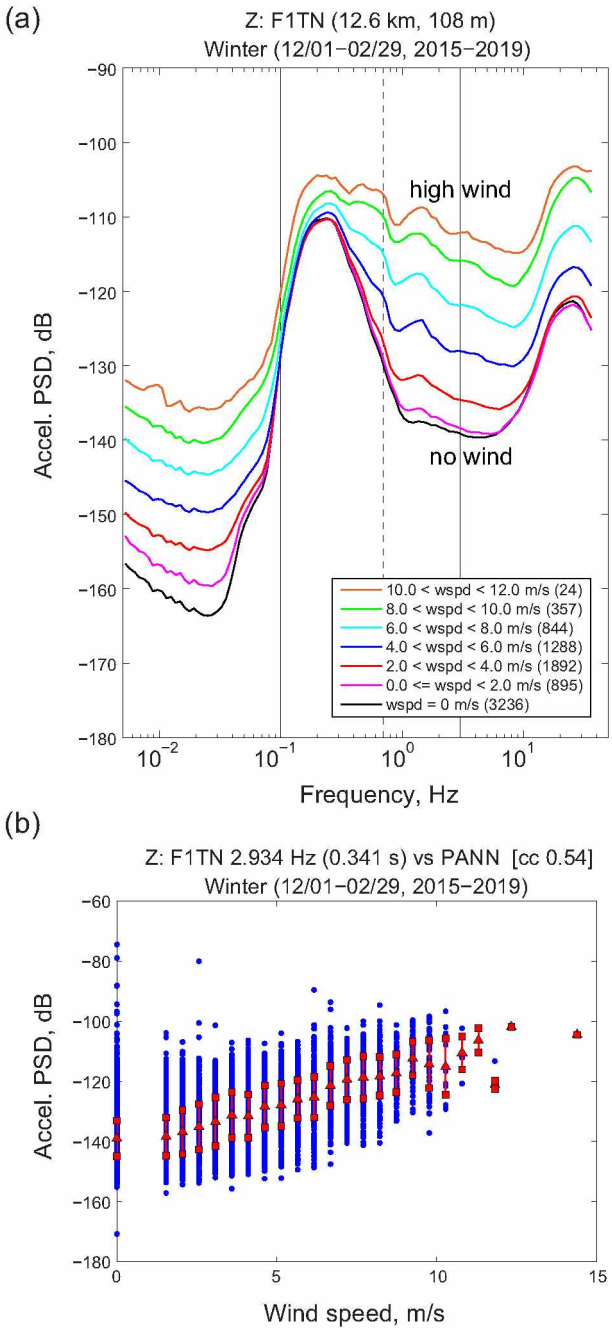

Figure 2.10: The influence of wind on seismic noise. (a) Ambient noise spectra at F1TN for winter (Dec/Jan/Feb) made from time periods of different wind speeds. The solid lines denote the frequency range of basin influence on seismic waves: 0.1–3 Hz (separated at 0.7 Hz). The number of hours used for each stack is listed in the legend. Other stations shown in Figures A.34–A.49. (b) Daily scatter plot of F1TN seismic power at 3 Hz versus PANN wind speed. The red triangles are the median seismic power for each wind speed and the squares are variation at 1 MAD. Other stations can be seen in Figures A.58–A.62.

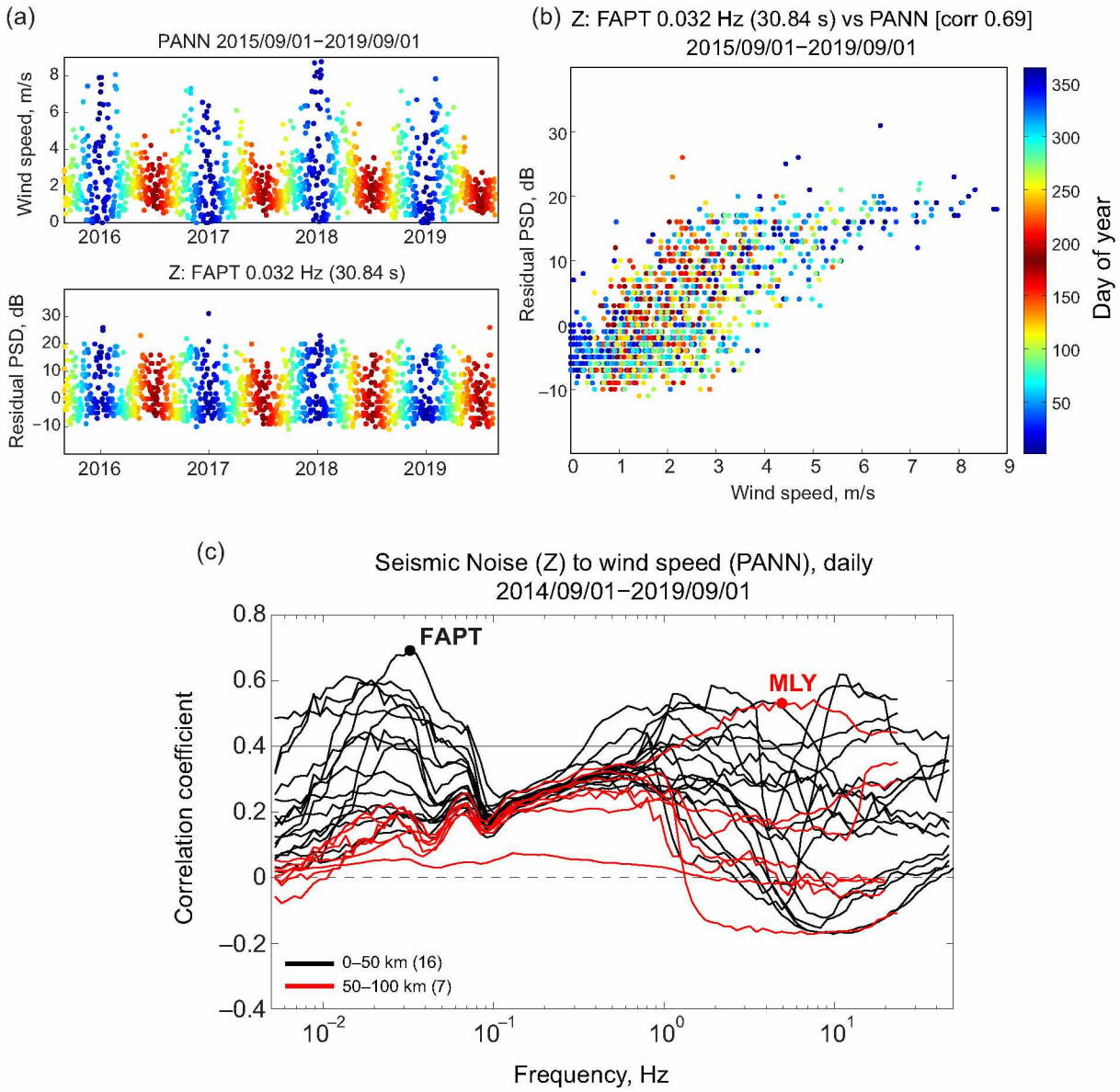

Figure 2.11: Comparison between daily wind speeds at PANN and daily seismic noise levels at different stations. (a) Time series of daily wind speed at PANN (top) and residual seismic noise (vertical component) at FAPT at a period of 30 s (0.032 Hz) (bottom). The seismic station (FAPT) and weather station (PANN) are near the Nenana runway and separated by 513 m (Figure 2.1b, Table 2.1). Daily data points are colored by time of year: cool colors are wintertime and warm colors are summertime. (b) Scatter plot comparing the two time series in (a). See Figure A.33 for results for the horizontal component of seismic noise. (c) Correlations of daily wind speed to residual seismic noise across all frequencies. Curves for 23 seismic stations are colored black (0–50 km) or red (50–100 km), according to the station's distance from weather station PANN, in Nenana. Higher correlations at frequencies $\leq$0.05 Hz are evident at stations closer to PANN, such as FAPT, which is shown in (b) and represented by the black dot at (0.032 Hz, 0.69). At high frequencies, the outlier high correlation is for MLY, a high-elevation, exposed bedrock site that is 96 km from PANN; the red dot is at (5 Hz, 0.53). The horizontal line is shown as a reference correlation of 0.4.

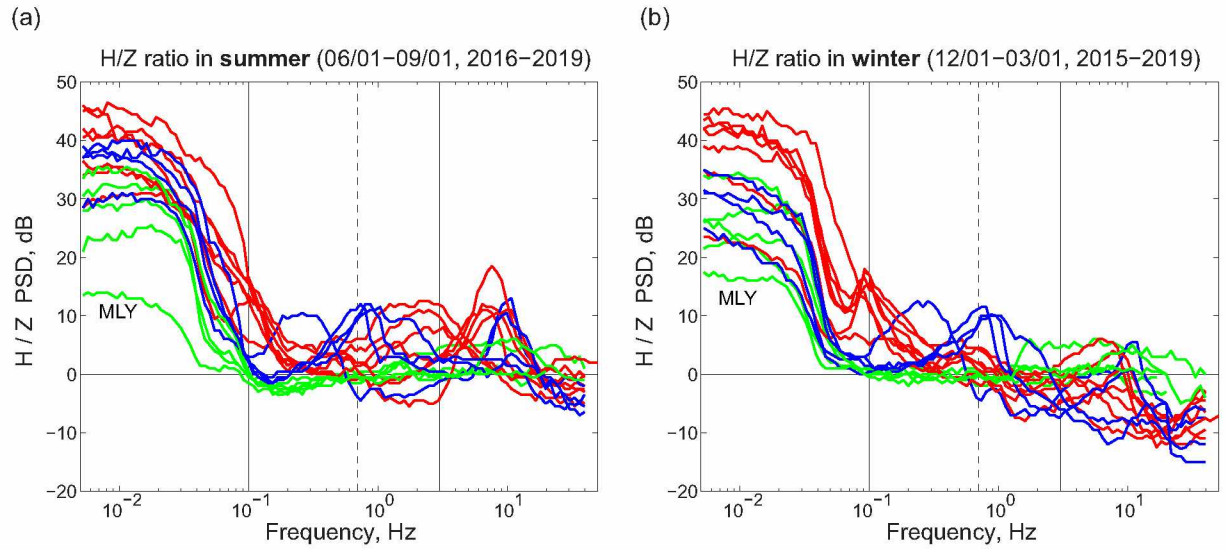

Figure 2.12: H/Z ratio spectra for all 16 stations in Table 2.1 during summer (a) and winter (b) and colored by expected influence of basin. The solid lines denote the frequency range of basin influence on seismic waves: 0.1–3 Hz (separated at 0.7 Hz). At low frequencies, the lowest H/Z ratio is 13 dB and occurs at the bedrock station MLY in summer. There is a subtle peak occurring in the winter at 0.1 Hz for F3TN, F4TN, F5MN, and FNN2; FNN2 exhibits the peak also in summer. For H/Z spectra during zero-wind conditions, see Figures A.50 and A.51.

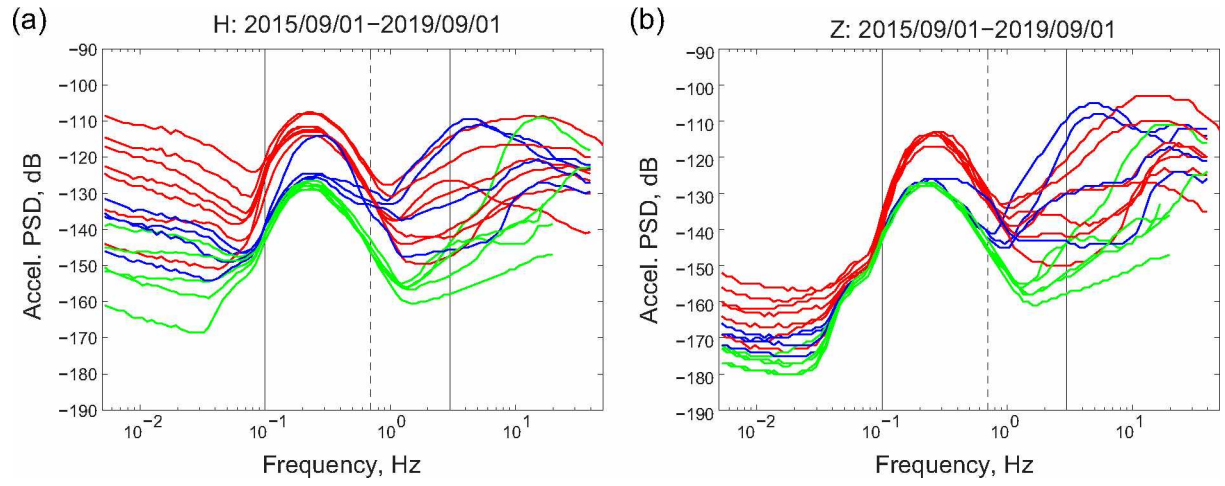

Figure 2.13: Seismic noise spectra, colored by the expected influence of Nenana basin: red is highest basin influence, green is lowest (Table 2.1). The lowest-noise spectrum is for AK.MLY (green). The solid lines denote the frequency range of basin influence on seismic waves: 0.1–3 Hz (separated at 0.7 Hz). See also Figure 2.14. (a) Horizontal component. (b) Vertical component.

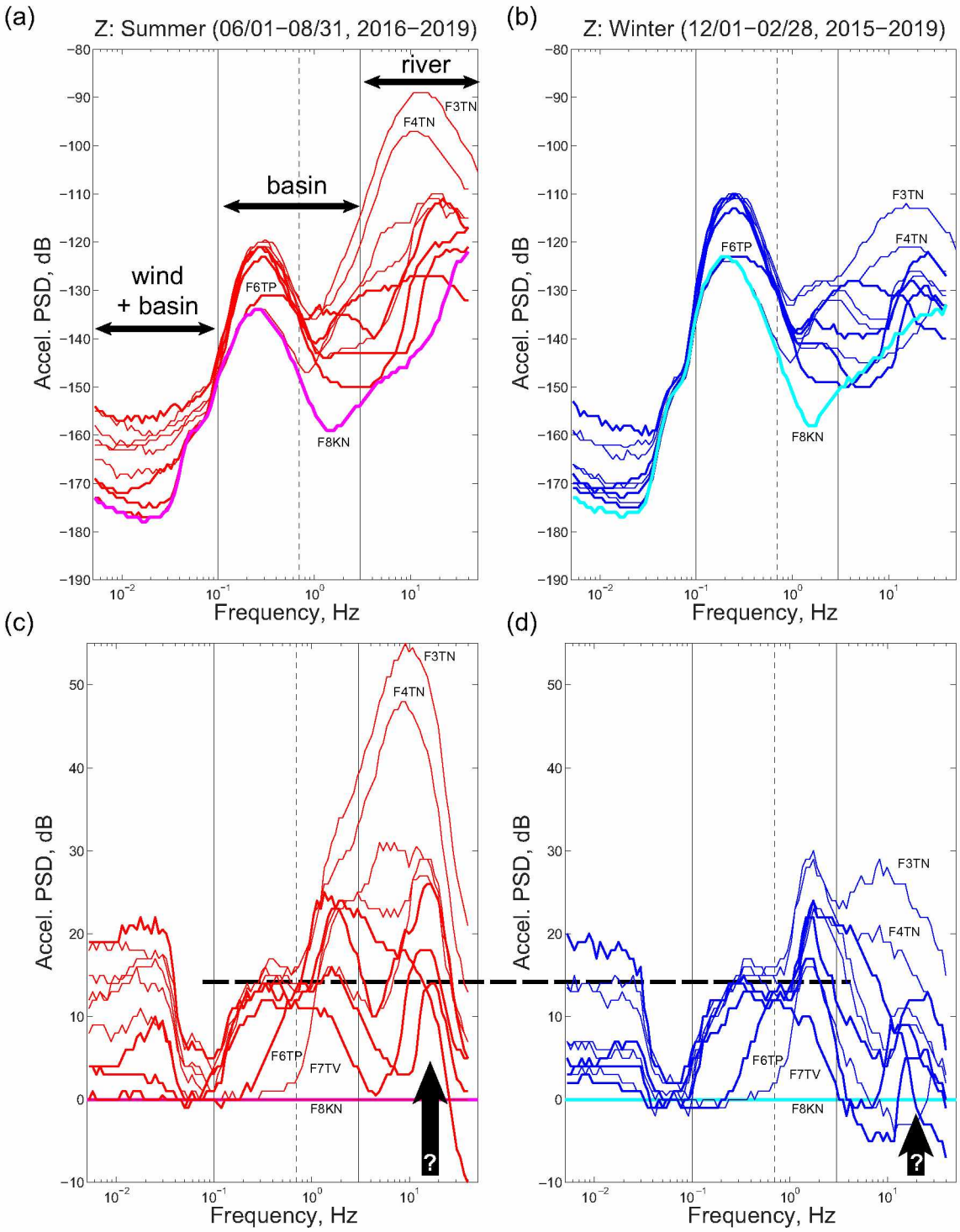

Figure 2.14: Seismic noise spectra and interpreted influences. (a) Vertical-component ambient noise during summer for nine stations in Nenana basin: F1–F7, FNN1, FNN2. Basin stations that are far from the river are bolded (F1TN, F6TP, FNN1, FNN2). The thick magenta line is the non-basin reference spectrum, which is F8KN. The solid lines denote the frequency range of basin influence on seismic waves: 0.1–3 Hz (separated at 0.7 Hz). (b) Same as (a), but for the winter time period. (c) Spectra in (a), minus the non-basin reference spectrum in (a). The dashed horizontal line shows the basin amplification at 0.1–0.7 Hz that is present during winter and summer. (d) Spectra in (b), minus the non-basin reference spectrum in (b); see also Figure 2.15. See Figure A.78 for the horizontal component.

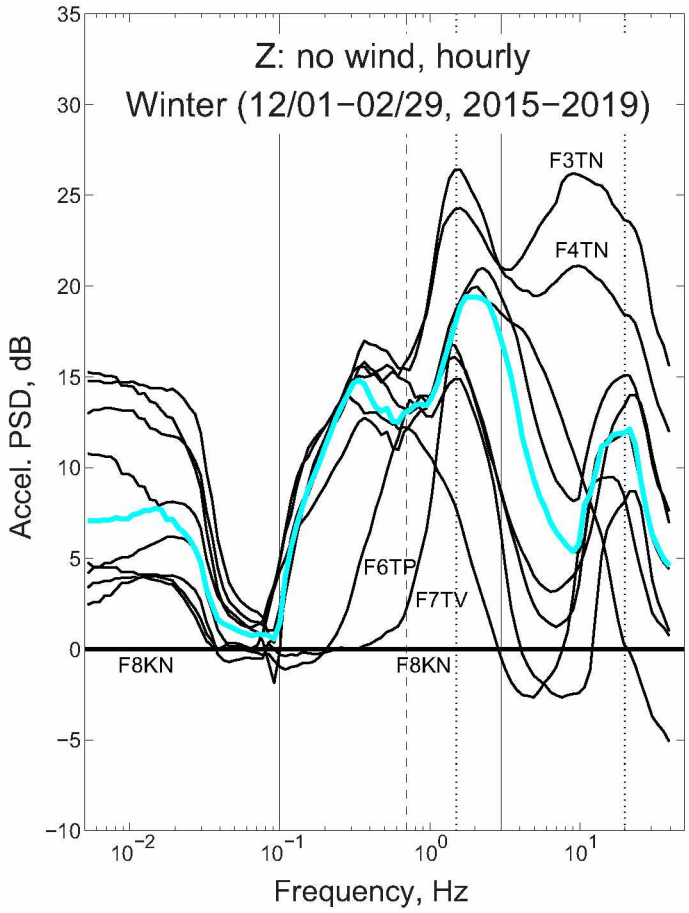

Figure 2.15: Ambient noise spectra for basin stations (F1–F7, FNN1, FNN2), minus the reference spectrum F8KN. Each spectrum is a stack of hourly seismic noise spectra during time periods of zero wind speed at PANN, in Nenana (Figure 2.1), during winter (Dec–Feb). The blue spectrum is the median stack. The solid lines denote the frequency range of basin influence on seismic waves: 0.1–3 Hz (separated at 0.7 Hz). The dotted lines denote peaks at 1.5 Hz and 20 Hz. See spectra for individual stations in Figures A.74–A.77.

2.10 References

Aderhold, K., Anderson, K. E., Reusch, A. M., Pfeifer, M. C., Aster, R. C., & Parker, T., 2015. Data quality of collocated portable broadband seismometers using direct burial and vault emplacement, *Bull. Seismol. Soc. Am.*, **105**(5), 2420–2432, doi: 10.1785/0120140352.

Aki, K. & Richards, P. G., 2002. *Quantitative Seismology*, University Science Books, San Francisco, Calif., USA, 2nd edn., 2009 corrected printing.

Anthony, R. E., Aster, R. C., Wiens, D., Nyblade, A., Anandakrishnan, S., Huerta, A., Winberry, J. P., Wilson, T., & Rowe, C., 2015. The seismic noise environment of Antarctica, *Seismol. Res. Lett.*, **86**(1), 89–100, doi: 10.1785/0220140109.

Anthony, R. E., Aster, R. C., Ryan, S., Rathburn, S., & Baker, M. G., 2018. Measuring mountain river discharge using seismographs emplaced within the hyporheic zone, *J. Geophys. Res. Earth Surface*, **123**, 210–228, doi: 10.1002/2017JF004295.

Aster, R. C., McNamara, D. E., & Bromirski, P. D., 2008. Multidecadal climate-induced variability in microseisms, *Seismol. Res. Lett.*, **79**(2), 194–202, doi: 10.1785/gssrl.79.2.194.

Bao, X. & Shen, Y., 2018. Full-waveform sensitivity kernels of component-differential traveltimes and ZH amplitude ratios for velocity and density tomography, *J. Geophys. Res.*, **123**, 4829–4840, doi: 10.1029/2017JB015421.

Bard, P.-Y. & Bouchon, M., 1980. The seismic response of sediment-filled valleys. Part 1. The case of incident *SH* waves, *Bull. Seismol. Soc. Am.*, **70**(4), 1263–1286.

Bard, P.-Y. & Bouchon, M., 1985. The two-dimensional resonance of sediment-filled valleys, *Bull. Seismol. Soc. Am.*, **75**(2), 519–541.

Barnes, D. F., 1961. Gravity low at Minto flats, in *Short Papers in the Geologic and Hydrologic Sciences, Articles 293–435: Geological Survey Research 1961*, pp. D254–D257, U.S. Geol. Survey, Washington, D.C., Professional Paper 424-D.

Berg, E. M., Lin, F.-C., Allam, A., Qiu, H., Shen, W., & Ben-Zion, W., 2018. Tomography of southern California via Bayesian joint inversion of Rayleigh wave ellipticity and phase velocity from ambient noise cross-correlations, *J. Geophys. Res. Solid Earth*, **123**, 9933–9949, doi: 10.1029/2018JB016269.

Bonnefoy-Claudet, S., Cotton, F., & Bard, P.-Y., 2006. The nature of noise wavefield and its applications for site effects studies: A literature review, *Earth-Sci. Rev.*, **79**, 205–227, doi: 10.1016/j.earscirev.2006.07.004.

Burtin, A., Bollinger, L., Vergne, J., Cattin, R., & Nábělek, J. L., 2008. Spectral analysis of seismic noise induced by rivers: A new tool to monitor spatiotemporal changes in stream hydrodynamics, *J. Geophys. Res.*, **113**, B05301, doi: 10.1029/2007JB005034.

Busby, R. W., 2016. Broadening the quality and Capabilities of the EarthScope Alaska Transportable Array, Abstract S14C-03 presented at 2016 Fall Meeting, AGU, San Francisco, Calif., 12-16 Dec.

Casey, R., Templeton, M. E., Sharer, G., Keyson, L., Weertman, B. R., & Ahern, T., 2018. Assuring the quality of IRIS data with MUSTANG, *Seismol. Res. Lett.*, **89**(2A), 630–639, doi: 10.1785/0220170191.

Chiu, A. N. L. & Taoka, G. T., 1973. Tower response to actual and simulated wind forces, *J. Structural Division*, **99**(ST9), 1911–1929.

Collins, C. M., 1990. Mophometric Analyses of Recent Channel Changes on the Tanana River in the Vicinity of Fairbanks, Alaska, U.S. Army Corps of Engineers, Cold Regions Research and Engineering & Laboratory Report 90-4, 48 p.

De Angelis, S. & Bodin, P., 2012. Watching the wind: seismic data contamination at long periods due to atmospheric pressure-field-induced tilting, *Bull. Seismol. Soc. Am.*, **102**(3), 10.1785/0120110186.

Dybing, S. N., Ringler, A. T., Wilson, D. C., & Anthony, R. E., 2019. Characteristics and spatial variability of wind noise on near-surface broadband seismometers, *Bull. Seismol. Soc. Am.*, **109**(3), 1082–1098, doi: 10.1785/0120180227.

Field, E. & Jacob, K., 1993. The theoretical response of sedimentary layers to ambient seismic noise, *Geophys. Res. Lett.*, **20**(24), 2925–2928.

Frankel, A., Stephenson, W., & Carver, D., 2009. Sedimentary basin effects in Seattle, Washington: Ground-motion observations and 3D simulations, *Bull. Seismol. Soc. Am.*, **99**(3), 1579–1611, doi: 10.1785/0120080203.

Gardiner, B. A., 1992. Mathematical modelling of the static and dynamic characteristics of plantation trees, in *Mathematical Modelling of Forest Ecosystems: Proceedings of a Workshop Organized by Forstliche Versuchsanstalt Rheinland–Pfalz and Zentrum Für Praktische Mathematik, Lambrecht/Pfalz, May 27-31, 1991*, pp. 40–61, eds Franke, J. & Roeder, A., J.D. Sauerländer's Verlag, Frankfurt am Main.

Gebauer, A., Kroner, C., & Jahr, T., 2009. The influence of topographic and lithologic features on horizontal deformations, *Geophys. J. Int.*, **177**, 586–602, doi: 10.1111/j.1365-246X.2009.04072.x.

Gimbert, F. & Tsai, V. C., 2015. Predicting short-period, wind-wave-generated seismic noise in coastal regions, *Earth Planet. Sci. Lett.*, **426**, 280–292, doi: 10.1016/j.epsl.2015.06.017.

Gimbert, F., Tsai, V. C., & Lamb, M. P., 2014. A physical model for seismic noise generation by turbulent flow in rivers, *J. Geophys. Res. Earth Surface*, **119**, 2209–2238, doi: 10.1002/2014JF003201.

Graves, R. W., Pitarka, A., & Somerville, P. G., 1998. Ground-motion amplification in Santa Monica area: Effects of shallow basin-edge structure, *Bull. Seismol. Soc. Am.*, **88**(5), 1224–1242.

Gutenberg, B., 1951. Observations and theory of microseisms, in *Compendium of Meterology*, pp. 1303–1311, ed. Malone, T. S., American Meteorological Society, Boston, Mass.

Gutenberg, B., 1958. Microseisms, *Advances in Geophysics*, **5**, 53–92.

Harrison, J. C., 1976. Cavity and topographic effects in tilt and strain measurement, *J. Geophys. Res.*, **81**(2), 319–328.

Haubrich, R. A. & MacKenzie, G. S., 1965. Earth noise, 5 to 50 millicycles per second 2. Reaction of the earth to oceans and atmosphere, *J. Geophys. Res.*, **70**(6), 1429–1440.

Hecker, O., 1906. Über die Uraschen der mikroseismischen Bewegung, in *Seismometrische Beobachtungen in Potsdam in der zeit vom 1. Januar bis 31. Dezember 1905*, vol. 29 of **Veröffentlichung des Königl. Preuszischen geodätischen institutes**, pp. 13–19, druck von P. Stankeiwicz' Buchdrkucerei, Berlin.

Hutt, C. R., Ringler, A. T., & Gee, L. S., 2017. Broadband seismic noise attenuation versus depth at the Albuquerque Seismological Laboratory, *Bull. Seismol. Soc. Am.*, **107**(3), 1402–1412, doi: 10.1785/0120160187.

James, S. R., Knox, H. A., Abbot, R. E., Panning, M. P., & Screaton, E. J., 2019. Insights into permafrost and seasonal active-layer dynamics from ambient seismic noise monitoring, *J. Geophys. Res. Earth Surface* (in press), doi: 10.1029/2019JF005051.

Johnson, J. B., Toniolo, H., Seitz, A. C., Schmid, J., & Duvoy, P., 2013. Characterization of the Tanana River at Nenana, Alaska, to Determine the Important Factors Affecting Site Selection, Deployment, and Operation of Hydrokinetic Devices to Generate Power, Alaska Center for Energy and Power, Alaska Hydrokinetic Energy Research Center, Fairbanks, Alaska, 130 p.

Jorgenson, T., Yoshikawa, K., Kanevskiy, M., Shur, Y., Romanovsky, V., Marchenko, S., Grosse, G., Brown, J., & Jones, B., 2008. Permafrost Characteristics of Alaska, Institute of Northern Engineering, University of Alaska Fairbanks.

Kedar, S., Longuet-Higgins, M., Webb, F., Graham, N., Clayton, R., & Jones, C., 2008. The origin of deep coean microseisms in the North Atlantic Ocean, *Proc. R. Soc.A*, **464**, 777–793, doi: 10.1098/rspa.2007.0277.

Koehler, R. D., Reger, R. D., Spangler, E. R., & Gould, A. I., 2015. Investigation of potentially active tectonic faults along the route of the proposed Alaska Stand Alone Pipeline, Livengood to Cook Inlet, Alaska, Alaska Div. Geol. Geophys. Surv., Report of Investigation 2015-4, 71 p.

Koper, K. D., Seats, K., & Benz, H., 2010. On the composition of Earth's short-period seismic noise field, *Bull. Seismol. Soc. Am.*, **100**(2), 606–617, doi: 10.1785/0120090120.

Kroner, C., Jahr, T., Kuhlmann, S., & Fischer, K. D., 2005. Pressure-induced noise on horizontal seismometer and strainmeter records evaluated by finite element modelling, *Geophys. J. Int.*, **161**, 167–178, doi: 10.1111/j.1365-246X.2005.02576.x.

Larose, R., Carriére, S., Voisin, C., Bottelin, P., Baillet, L., Guéguen, P., Walter, F., Jongmans, D., Guillier, B., Garambois, S., Gimbert, F., & Massey, C., 2015. Environmental seismology: What can we learn on earth surface processes with ambient noise?, *J. App. Geophys.*, **116**, 62–74, doi: 10.1016/j.jappgeo.2015.02.001.

Lesh, M. E. & Ridgway, K. D., 2007. Geomorphic evidence of active transpressional deformation in the Tanana foreland basin, south-central Alaska, in *Tectonic Growth of a Collisional Continental Margin: Crustal Evolution of Southern Alaska*, pp. 573–592, eds Ridgway, K. D., Trop, J. M., Glen, J. M. G., & O'Neill, J. M., Geol. Soc. Am., Boulder, Colo., USA, Special Paper 431.

Lin, F.-C., Schmandt, B., & Tsai, V. C., 2012. Joint inversion of Rayleigh wave phase velocity and ellipticity using USArray: Constraining velocity and density structure in the upper crust, *Geophys. Res. Lett.*, **39**, L12303, doi: 10.1029/2012GL052196.

Lin, F.-C., Li, D., Clayton, R. W., & Hollis, D., 2013. High-resolution 3D shallow crustal structure in Long Beach, California: Application of ambient noise tomography on a dense seismic array, *Geophysics*, **78**(4), Q45–Q56.

Longuet-Higgins, M. S., 1950. A theory of the origin of microseisms, *Phil. Trans. R. Soc. Lond.*, **243**, 1–35.

Lott, F. F., Ritter, J. R. R., Al-Qaryouti, M., & Corsmeier, U., 2017. On the analysis of wind-induced noise in seismological recordings, *Pure App. Geophys.*, **174**, 1453–1470, doi: 10.1007/s00024-017-1477-2.

Maupin, V., 2017. 3-D sensitivity kernels of the Rayleigh wave ellipticity, *Geophys. J. Int.*, **211**, 107–119, doi: 10.1093/gji/ggx294.

McNamara, D. E. & Buland, R. P., 2004. Ambient noise levels in the continental United States, *Bull. Seismol. Soc. Am.*, **94**(4), 1517–1527, doi: 10.1785/012003001.

Mucciarelli, M., Gallipoli, M. R., Di Giacomo, D., Di Nota, D., & Nino, E., 2005. The influence of wind on measurements of seismic noise, *Geophys. J. Int.*, **161**, 303–308, doi: 10.1111/j.1365-246X.2004.02561.x.

Muir, J. B. & Tsai, V. C., 2017. Rayleigh-wave H/V via noise cross correlation in southern California, *Bull. Seismol. Soc. Am.*, **107**(5), 2021–2027, doi: 10.1785/0120170051.

Naderyan, V., Hickey, C. J., & Raspet, R., 2016. Wind-induced ground motion, *J. Geophys. Res. Solid Earth*, **121**, 917–930, doi: 10.1002/2015JB012478.

NSIDC, 2011. Nenana Ice Classic: Tanana River Ice Annual Breakup Dates, Version 1, NSIDC Data Set ISIDC–0064, https://nsidc.org/data/NSIDC-0064, National Snow & Ice Data Center Data, Boulder, Colo.

Olsen, K. B., 2000. Site amplification in the Los Angeles basin from three-dimensional modelling of ground motion, *Bull. Seismol. Soc. Am.*, **60**(6B), S77–S94, doi: 10.1785/0120000506.

Peterson, J., 1993. Observations and Modeling of Seismic Background Noise, Open-File Report 93-322.

PRA, 2017. Depth to Basement Map of Nenana Basin, Alaska, Proprietary map provided by Petrotechnical Resources of Alaska, April 2017.

Rial, J. A., Saltzman, N. G., & Ling, H., 1992. Earthquake-induced resonance in sedimentary basins, *American Scientist*, **80**, 566–578.

Ringler, A. T., Gee, L. S., Hutt, C. R., & McNamara, D. E., 2010. Temporal variations in global seismic station ambient noise power levels, *Seismol. Res. Lett.*, **81**(4), 605–613, doi: 10.1785/gssrl.81.4.605.

Ringler, A. T., Wilson, D. C., Zürn, W., & Anthony, R. E., 2019. Rayleigh wave ellipticity measurement uncertainty across the IRIS/USGS and New China Digital Seismograph Networks, *Geophys. J. Int.*, **217**, 219–237, doi: 10.1093/gji/ggy527.

Rohde, M. D., Ringler, A. T., Hutt, C. R., Silson, D. C., Holland, A. A., Sandoval, L. D., & Storm, T., 2017. Characterizing local variability in long-period horizontal tilt noise, *Seismol. Res. Lett.*, **88**(3), 822–830, doi: 10.1785/0220160193.

Schmandt, B., Aster, R. C., Scherler, D., Tsai, V. C., & Karlstrom, K., 2013. Multiple fluvial processes detected by riverside seismic and infrasound monitoring of a controlled flood in the Grand Canyon, *Geophys. Res. Lett.*, **40**, 4858–4863, doi: 10.1002/grl.50953.

Shapiro, N. M., Campillo, M., Stehly, L., & Ritzwoller, M. H., 2005. High-resolution surface-wave tomography from ambient seismic noise, *Science*, **307**, 1615–1618.

Sorrells, G. G., 1971. A preliminary investigation into the relationship between long-period seismic noise and local fluctuations in the atmospheric pressure field, *Geophys. J. R. Astron. Soc.*, **26**, 71–82.

Sorrells, G. G. & Goforth, T. T., 1973. Low-frequency earth motion generated by slowly propagating partially organized pressure fields, *Bull. Seismol. Soc. Am.*, **63**(5), 1583–1601.

Sorrells, G. G., McDonald, J. A., Der, Z. A., & Herrin, E., 1971. Earth motion caused by local atmospheric pressure changes, *Geophys. J. R. Astron. Soc.*, **26**, 83–98.

Stutzmann, E., Schimmel, M., Patau, G., & Maggi, A., 2009. Global climate imprint on seismic noise, *Geochem. Geophy. Geosyst.*, **10**(11), Q11004, doi: 10.1029/2009GC002619.

Tanimoto, T., 2005. The oceanic excitation hypothesis for the continuous oscillations of the Earth, *Geophys. J. Int.*, **160**, 276–288, doi: 10.1111/j.1365-246X.2004.02484.x.

Tanimoto, T., Yano, T., & Hakamata, T., 2013. An approach to improve Rayleigh-wave ellipticity estimates from seismic noise: application to the Los Angeles Basin, *Geophys. J. Int.*, **193**, 407–420, doi: 10.1093/gji/ggs123.

Tape, C., West, M., Silwal, V., & Ruppert, N., 2013. Earthquake nucleation and triggering on an optimally oriented fault, *Earth Planet. Sci. Lett.*, **363**, 231–241, doi: 10.1016/j.epsl.2012.11.060.

Tape, C., Silwal, V., Ji, C., Keyson, L., West, M. E., & Ruppert, N., 2015. Transtensional tectonics of the Minto Flats fault zone and Nenana basin, central Alaska, *Bull. Seismol. Soc. Am.*, **105**(4), 2081–2100, doi: 10.1785/0120150055.

Tape, C., Christensen, D., Moore-Driskell, M. M., Sweet, J., & Smith, K., 2017. Southern Alaska Lithosphere and Mantle Observation Network (SALMON): a seismic experiment covering the active arc by road, boat, plane, and helicopter, *Seismol. Res. Lett.*, **88**(4), 1185–1202, doi: 10.1785/0220160229.

Tape, C., Holtkamp, S., Silwal, V., Hawthorne, J., Kaneko, Y., Ampuero, J. P., Ji, C., Ruppert, N., Smith, K., & West, M. E., 2018. Earthquake nucleation and fault slip complexity in the lower crust of central Alaska, *Nature Geoscience*, **11**, 536–541, doi: 10.1038/s41561-018-0144-2.

Toniolo, H., 2013. Bed forms and sediment characteristics along the thalweg on the Tanana river near Nenana, Alaska, USA, *Natural Resources*, **4**, 20–30, doi: 10.4236/nr.2013.41003.

Toniolo, H., Duvoy, P., Vanlesberg, S., & Johnson, J., 2010. Modelling and field measurements in support of the hydrokinetic resource assessment for the Tanana river at Nenana, Alaska, *Proc. IMechE. Part A: J. Power and Energy*, **224**, 1127–1139, doi: 10.1243/09576509JPE1017.

Trnkoczy, A., Bormann, P., Hanka, W., Holcomb, L. G., Nigbor, R. L., Shinohara, M., Shiobara, H., & Suyehiro, K., 2012. Site selection, preparation and installation of seismic stations, in *New Manual of Seismological Observatory Practice*, pp. 1–143, ed. Bormann, P., GFZ German Research Centre for Geosciences, Potsdam, Germany, http://nmsop.gfz-potsdam.de, doi:10.2312/GFZ.NMSOP-2_ch7.

Tsai, V. C. & McNamara, D. E., 2011. Quantifying the influence of sea ice on ocean microseism using observations from the Bering Sea, Alaska, *Geophys. Res. Lett.*, **38**, L22502, doi: 10.1029/2011GL049791.

Tsai, V. C., Minchew, B., Lamb, M. P., & Ampuero, J.-P., 2012. A physical model for seismic noise generation from sediment transport in rivers, *Geophys. Res. Lett.*, **39**.

Van Kooten, G. K., Richter, M., & Zippi, P. A., 2012. Alaska's Interior rift basins: a new frontier for discovery, *Oil & Gas J.*, **110**(1a), 48–57.

Venkateswarlu, B., Harikrishna, P., Rajan, S. S., & Kumar, M. S. R., 1994. Stochastic gust response of microwave lattice towers, *Computers & Structures*, **52**(5), 1031–1041.

Wald, D. J. & Graves, R. W., 1998. The seismic response of the Los Angeles basin, California, *Bull. Seismol. Soc. Am.*, **88**(2), 337–356.

Webb, S. C., 1998. Broadband seismology and noise under the ocean, *Rev. Geophys.*, **36**(1), 105–142.

Willmore, P. L., 1979. *Manual of Seismological Observatory Practice*, U.S. Dept. Commerce, National Oceanic and Atmospheric Administration, Environmental Data and Information Service, Boulder, Colo., USA, World Data Center A for Solid Earth Geophysics, Report SE-20.

Wilson, D., Leon, J., Aster, R., Ni, J., Schlue, J., Grand, S., Semken, S., Baldridge, S., & Gao, W., 2002. Broadband seismic background noise at temporary seismic stations observed on a regional scale in the southwestern United States, *Bull. Seismol. Soc. Am.*, **92**(8), 3335–3341, doi: 10.1785/0120010234.

Withers, M. M., Aster, R. C., Young, C. J., & Chael, E. P., 1996. High-frequency analysis of seismic background noise as a function of wind speed and shallow depth, *Bull. Seismol. Soc. Am.*, **86**(5), 1507–1515.

Wolin, E., van der Lee, S., Bollmann, T. A., Wiens, D. A., Revenaugh, J., Darbyshire, F. A., Frederiksen, A. W., Stein, S., & Wysession, M. E., 2015. Seasonal and diurnal variations in long-period noise at SPREE stations: the influence of soil characteristics on shallow stations' performance, *Bull. Seismol. Soc. Am.*, **105**(5), 2433–2452, doi: 10.1785/0120150046.

Workman, E., Lin, F.-C., & Koper, K. D., 2017. Determination of Rayleigh wave ellipticity across the Earthscope Transportable Array using single-station and array-based processing of ambient seismic noise, *Geophys. J. Int.*, **208**, 234–245, doi: 10.1093/gji/ggw381.

Young, C. J., Chael, E. P., Zagar, D. A., & Carter, J. A., 1994. Variations in noise and signal levels in a pair of deep boreholes near Amarillo, Texas, *Bull. Seismol. Soc. Am.*, **84**(5), 1593–1607.

Ziolkowski, A., 1973. Prediction and suppression of long-period nonpropagating seismic noise, *Bull. Seismol. Soc. Am.*, **63**(3), 937–958.

Zürn, W. & Widmer, R., 1995. On noise reduction in vertical seismic records below 2 mHz using local barometric pressure, *Geophys. Res. Lett.*, **22**(24), 3537–3540.

Zürn, W., Exß, J., Steffen, H., Kroner, C., Jahr, T., & Westerhaus, M., 2007. On reduction of long-period horizontal seismic noise using local barometric pressure, *Geophys. J. Int.*, **171**, 780–796, doi: 10.1111/j.1365-246X.2007.03553.x.

Zürn, W., Ferreira, A. M. G., Widmer-Schnidrig, R., Lentas, K., Rivera, L., & Clévédé, E., 2015. High-quality lowest-frequency normal mode strain observations at the Black Forest Observatory (SW-Germany) and comparison with horizontal broad-band seismometer data and synthetics, *Geophys. J. Int.*, **203**, 1787–1803, doi: 10.1093/gji/ggv381.

Chapter 3

Seismic response of Cook Inlet sedimentary basin, southern Alaska[1]

3.1 Abstract

Cook Inlet forearc basin in south-central Alaska is a large, deep (7.6 km) sedimentary basin that has the Anchorage metropolitan region on its margins. From 2015–2017 a set of 28 broadband seismic stations was deployed in the region as part of the SALMON (Southern Alaska Lithosphere and Mantle Observation Network) project. The SALMON stations, which also cover the remote western portion of Cook Inlet basin and the backarc region, form the basis for our observational study of the seismic response of Cook Inlet basin. We quantify the influence of Cook Inlet basin on the seismic wavefield using three data sets: (1) ambient noise amplitudes of 18 basin stations relative to a non-basin reference station, (2) earthquake ground motion metrics for 34 crustal and intraslab earthquakes, and (3) spectral ratios between basin stations and non-basin stations for the same earthquakes. For all analyses we examine how quantities vary with the frequency content of the seismic signal and with the basin depth at each station. Seismic waves from earthquakes and from ambient noise are amplified within Cook Inlet basin. At low frequencies (0.1–0.5 Hz), ambient noise ratios and earthquake spectral ratios are in general agreement, with power amplification of 6–14 dB, corresponding to amplitude amplification factors of 2.0–5.0. At high frequencies (0.5–4.0 Hz), the basin amplifies the earthquake wavefield by similar factors. Our results indicate stronger amplification for the deeper basin stations, such as near Nikiski on the Kenai peninsula, and weaker amplification near the margins of the basin. Future work devoted to three-dimensional wavefield simulations and to treatment of source and propagation effects should improve the characterization of the frequency-dependent response of Cook Inlet basin to recorded and scenario earthquakes in the region.

3.2 Introduction

Cook Inlet basin is a forearc sedimentary basin that is part of the Alaska subduction zone and borders the metropolitan region that includes Anchorage, Eagle River, Chugiak, Wasilla, and Palmer. The basin is 250 km long and 100 km wide (Figure 3.1a) and is one of the largest active forearc

[1]Published as: Smith, K., and C. Tape (2019), Seismic response of Cook Inlet sedimentary basin, southern Alaska, *Seismol. Res. Lett.*, doi:10.1785/0220190205.

basins in the world Clift & Vannucchi (2004). Cook Inlet has been a site of sedimentary deposition for most of the past 160 Ma, with a maximal Mesozoic thickness of 12 km and a maximal Tertiary thickness of 7.6 km Fisher & Magoon (1978); Shellenbaum et al. (2010). The lowermost Tertiary units were used by Shellenbaum et al. (2010) to define a detailed basement surface having a maximal depth of 7.6 km near Nikiski, on the western Kenai Peninsula (Figure 3.1a; ZE.NSKI in Figure 3.2), and overlying Mesozoic strata Gregersen & Shellenbaum (2016).

The Cook Inlet region is highly seismically active, with earthquakes $M_w > 7$ in both the subducting slab and within the crust. Notable intraslab earthquakes include 1954-10-03 M_w 6.4 under the Kenai Peninsula Doser & Brown (2001); Silwal et al. (2018), 2016-01-24 M_w 7.1 southwest of the basin Grapenthin et al. (2018), and 2018-11-30 M_w 7.1 beneath Anchorage Liu et al. (2019); West et al. (2019). Notable crustal earthquakes include the 1933-04-27 M_w 6.8 just below Cook Inlet basin (perhaps within the Mesozoic strata) and 1943-11-03 M_w 7.3 in the Susitna region north of Cook Inlet basin Silwal et al. (2018). The subduction megathrust is partially locked and last ruptured in the 1964-03-28 M_w 9.2 Prince William Sound earthquake Zweck et al. (2002). Few moderate ($M_w > 4$) earthquakes seem to occur on the interface Li et al. (2013) during the interseismic period between $M_w > 8$ ruptures and their aftershocks.

Our study focuses on a time period from May 2015 to July 2017 spanning the deployment of 28 broadband seismometers in the Cook Inlet region Tape et al. (2017). A primary scientific objective of the two-year deployment (Southern Alaska Lithosphere and Mantle Observation Network: SALMON) was to understand the influence of Cook Inlet basin on the seismic wavefield. The full set of stations considered for analysis is shown in the region of Figure 3.1b and tabulated in Figure 3.2.

The SALMON seismic stations provide an opportunity to investigate how Cook Inlet basin influences the seismic wavefield, both from earthquakes and from continuous ambient noise. A preliminary study based on the first year of SALMON data showed amplification of seismic noise in basin stations, as well as a correlation between basin depth and ground motion amplitudes filtered at 1.8–4 s, for one intraslab earthquake Tape et al. (2017). In this study we examine a total of 34 earthquakes recorded at 48 stations, including SALMON stations, EarthScope (TA) stations, and the permanent networks (AK, AV). Using earthquake recordings and ambient noise, we document basin amplification of 6–14 dB, corresponding to amplitude amplification factors of

2.0–5.0, for low frequencies (0.1–0.5 Hz). At high frequencies (0.5–4.0 Hz) the basin amplifies the earthquake wavefield by similar factors. Further work is needed to account for complexities of 3D structure (elastic and anelastic) and source mechanisms.

3.3 Previous studies of basin amplification

Sedimentary basins were acknowledged as a major factor in enhancing ground motions during the M_w 8.0 Mexico City earthquake Anderson et al. (1986); Bard et al. (1988); Lomnitz (1988). Some of these studies quoted the "bowl of jelly" metaphor commonly used to describe how sedimentary basins trap seismic waves and resonate (see also Carder (1963), p. 3). The observation that unconsolidated sediments amplify earthquake ground motions is well established. As pointed out in Borcherdt (1970), the 1908 report on the 1906 M_w 7.9 San Francisco earthquake concluded: "This investigation has clearly demonstrated that the amount of damage produced by the earthquake of April 18 in different parts of the city and county of San Francisco depended chiefly upon the geological character of the ground. Where the surface was of solid rock, the shock produced little damage; whereas upon made land great violence was manifested" (Lawson (1908), p. 241).

Improvements in theoretical models, numerical models, and improved instrumentation over the past century have led to a much improved understanding of how sedimentary basins effect seismic waves Gutenberg (1957); Borcherdt (1970); Bard & Bouchon (1980, 1985); Rial et al. (1992); Field & Jacob (1993); Wald & Graves (1998); Olsen (2000). The margins of basins can also have a strong influence on the seismic wavefield Frankel (1993); Hisada & Yamamoto (1996); Kawase (1996); Graves et al. (1998); Joyner (2000); Frankel et al. (2009); Wirth et al. (2019). Previous work has explored the amplification of basin structures from two end-member waves: shear waves entering from below basins and surface waves (Love, Rayleigh) entering from the side of basins Bard & Bouchon (1980). Efforts to model basin effects have assumed 1D, 2D, and 3D structural representations of basins Bard et al. (1988); Sánchez-Sesma & Luzón (1995); Bowden & Tsai (2017); Tsai et al. (2017); Feng & Ritzwoller (2017). Examples of data-based studies of specific basins include Pratt et al. (2003), Bindi et al. (2009), Yoshimoto & Takemura (2014), and Moschetti et al. (2017).

Numerical modeling and empirical observations have been used to better understand the relationship between basin depth and amplification of seismic waves, and to incorporate these effects

into ground motion prediction equations Choi et al. (2005); Fletcher & Wen (2005); Day et al. (2008); Cruz-Atienza et al. (2016). One example of this approach for the Cook Inlet region is Moschetti et al. (2019), which examines a suite of regional earthquakes recorded during the SALMON deployment and at other time periods.

3.4 Station selection

We analyze all broadband seismic stations within the region shown in Figure 3.1b that operated between 2015-01-01 and 2018-01-01. Stations from the AV network are intermediate-band and are excluded, with the exception of AV.RDWB on Redoubt Volcano. Our analysis of ambient seismic noise is based on an annual stack of daily spectra. Because ambient seismic noise amplitudes vary strongly with time, we need to stack over an integer number of years in order to minimize seasonal bias within the stack. Therefore we exclude any station that does not have an integer number of years (1, 2, or 3) within the time interval of interest. This criterion excludes three SALMON stations (HARR, HLC1, HOLG) that experienced outages due to bears Tape et al. (2019) and two TA stations (N18K, N20K) having outages due to power or telemetry issues. Station TA.M18K was not installed until May 2017. Six additional stations are excluded for reasons discussed later.

The 60 stations considered in our analysis (Figure 3.1b) are tabulated in Figure 3.2 and categorized based on their locations relative to the margin of Cook Inlet basin. A *basin station* is inside the outermost basin contour of Shellenbaum et al. (2010). A *marginal station* is outside the outermost basin contour of, but within 20 km of the contour. A *non-basin station* is at least 20 km outside the outermost basin contour. Our analysis includes 48 stations categorized as 18 basin stations, 12 marginal stations, and 18 non-basin stations (Figure 3.2). Among the 18 basin stations, 15 are from the SALMON experiment, and 3 are part of the permanent AK network (CAPN, HOM, FIRE).

We are interested in the amplitudes of ambient noise within Cook Inlet basin, relative to ambient noise outside the basin. There are several non-basin stations to consider for establishing a non-basin reference spectrum. We choose AK.SSN, which is a Streckeisen STS-5 sensor installed in bedrock at a depth of 2.71 m in a cased borehole on Susitna Mountain outside the northern margin of Cook Inlet basin (Figure 3.1a). The reference noise spectra for SSN are based on a single year of data (2016-07-01 to 2017-07-01) and are used for comparison with spectra from all other stations (e.g., Figures B.1 and B.2).

Ambient noise amplitudes are influenced by local structure, and therefore we might not expect the noise spectrum in the backarc bedrock region, such as at WFLW, to be the same as the noise in the forearc bedrock region, such as on the southern Kenai Peninsula. Figures B.3–B.5 show that the noise spectra for stations on the southern Kenai Peninsula (Figure 3.1a: AK.CNP, AK.BRLK, AK.BRSE, and AK.SWD; also ZE.HOLG though its data are limited) are similar to each other—suggestive of a regional noise reference—yet different from SSN. We attribute the differences in regional noise reference levels in the backarc and forearc to crustal-scale structural differences between these two non-basin settings. It is also possible that some differences between backarc and forearc spectra, especially for frequencies > 1 Hz, could be related to their different distances from regional, ocean-generated noise sources.

After examining the noise spectra (Figures B.3–B.8), we created a sub-classification for marginal stations for stations exhibiting basin-like spectra. Stations TA.O20K and TA.P19K are outside the Cook Inlet basin and are installed in bedrock, yet their spectra are consistent with those of basin stations overlying 1000s of meters of basin strata. However, the local site conditions at O20K and P19K are bedrock: both sensors are installed at 2.56 m depth in boreholes within "competent bedrock" according to the drill logs. We will revisit this topic in the Discussion.

Some marginal and non-basin stations are excluded due to anomalous noise levels at high frequencies (Figures B.7 and B.8). This includes three marginal stations north of Cook Inlet basin (ZE.JOES, ZE.JUDD, TA.M22K), one station on the Kenai Peninsula (TA.O22K), and two in the backarc region southwest of Cook Inlet (TA.P17K, TA.O19K). By excluding these stations, we are left with a set of stations that provide the most representative amplitudes of the regional ambient noise wavefield. Characteristics from the settings at these excluded stations are helpful in understanding the anomalous noise levels. Next we describe characteristics at two excluded stations, TA.O22K and ZE.JOES.

The sensor at TA.O22K is a Nanometrics Trillium 120PH sensor installed at a depth of 2.31 m in a "Competent layer of slate," as described in the drill log. The enhanced noise above 0.5 Hz (relative to SSN or SLK, which is closer) is likely due to a combination of structural, environmental, and anthropogenic influences. The structural influence could arise from the sedimentary deposits that the station is within. Environmental influences could arise from Kenai Lake (with or without ice), whose shoreline is 360 m to the southwest; the lake is the source of Kenai River. Anthro-

pogenic noise could arise from the Sterling Highway, which is 600 m to the northwest, from boats on Kenai Lake, or from activity on closer, smaller roads.

Station ZE.JOES is excluded because it may be influenced by the structure of Beluga basin Stanley et al. (2013); Saltus et al. (2016); Silwal et al. (2018), which is situated north of the Castle Mountain fault. JOES is near a remote summer camp on the edge of Beluga Lake, 18 km from the edge of Cook Inlet basin. Its spectra exhibit unusually large discrepancy between H and Z noise spectra for 0.2–1.0 Hz.

3.5 Earthquake selection

Earthquakes were selected between 2015-05-01 and 2017-08-01, aligned with the SALMON experiment (Figure 3.1b), in order to best examine the spatial variations of Cook Inlet basin effects. Since basin effects have been well documented for low frequencies (0.1–1.0 Hz), our focus was to examine the largest earthquakes recorded within the time period of SALMON. Smaller earthquakes ($M_w < 3$) do not generate sufficient signals at low frequencies. We exclude the largest earthquake, M_w 7.1 on 2016-01-24 Grapenthin et al. (2018), because it clipped most of the stations in Cook Inlet basin.

Our selection of earthquakes started with all events in the region of Figure 3.1b between 2015-05-01 and 2017-08-01 and having magnitudes between 3 and 7. With a desire of uniform spatial coverage without highly redundant events, we declustered the 372 events based on a volumetric grid of 8×8 cells, multiplied into depth sheets with boundaries at 30, 60, and 200 km. With the shallowest layer (0–30 km), we accept two earthquakes per cell having $M_l \geq 3.5$. Within the lower two layers we accept one earthquake per cell having $M_l \geq 4.0$. These criteria led to a set of 30 earthquakes. In order to examine excitation of the shallow basin structure, we added all earthquakes with M_l 3.0–3.5 with depths ≤ 30 km and with epicenters inside the basin boundary of Shellenbaum et al. (2010). These criteria resulted in four earthquakes, bringing our total to 34.

The 34 in our analysis are listed in Table 3.1 and plotted in Figure 3.1b. The cross section of stations and seismicity in Figure 3.1c highlights our source-station geometry and also our spatial declustering of events. Within the 100-km-wide corridor of seismicity there are 6 events in our analysis. The majority of the events, which are smaller crustal earthquakes, are within the northeast portion of our target region (Figure 3.1a).

3.6 Ambient noise

Our analysis of ambient noise in the Cook Inlet region is based on daily power spectral density plots computed and made available by IRIS MUSTANG Casey et al. (2018). These acceleration power spectra are log-scaled into units of dB. A table showing a comparison among dB values, power ratios, and amplification ratios is shown in Table B.1.

3.6.1 Methods

Ambient seismic noise amplitudes can be strongly time-dependent due to environmental or anthropogenic variations. Therefore in order to obtain a representative noise spectrum, one must use a time window that is an integer number of years. The time intervals used to calculate the annual station stacks are listed in Figure 3.2 for the 48 stations in our analysis.

Our goal is to quantify the frequency-dependent amplification of ambient noise at seismic stations. Our procedure is as follows:

1. For each of the 48 stations, calculate the station's annual spectra for the vertical and horizontal components. An example is shown in Figure 3.3a.

2. For each station, calculate a differential spectrum by subtracting the annual spectrum of SSN from the station's annual spectrum. An example is shown in Figure 3.3c.

3. For each differential spectrum, quantify the amplification within two frequency intervals: 0.1–0.5 Hz and 0.5–4.0 Hz. These intervals are chosen based on the characteristics of the differential spectra for 18 basin stations (Figure B.2). Within the first interval, the differential spectra tend to be flat (Figure 3.3c,d,g,h), and therefore we measure a median value of the entries between 0.1–0.5 Hz. The uncertainty is estimated by the median absolute deviation of values. Within the second interval, the differential spectra are often peaked (Figure 3.3c,d,g,h), and therefore we calculate the maximum value, which occurs at $0.5 < f_{\text{hf}} < 4.0$. The uncertainty is estimated by calculating the median absolute deviation of $\{A_k(f_{\text{hf}}), k = 1, \ldots, 365n\}$, where A_k is the kth day spectrum used in creating the annual spectrum, and n is the number of years used to make the annual spectrum.

3.6.2 Results

Our noise results are summarized in Figures 3.4 and 3.5. Figure 3.4 shows separation between basin spectra (red) and marginal basin spectra (blue) from the non-basin reference spectrum SSN (black). We will focus our discussion on the vertical component differential spectra shown in Figure 3.4d. Over the frequency range 0.1–0.5 Hz, the spectra of 18 basin stations are amplified by 9–15 dB relative to reference station SSN. (Table B.1 provides a comparison between power in dB and amplification factors.) Over the frequency range 0.5–4.0 Hz, the spectra of 18 basin stations are amplified by 15–50 dB relative to reference station SSN. Even at lowest frequencies (< 0.1 Hz), where ground tilting due to atmospheric effects occurs Sorrells et al. (1971), there is clear enhancement of noise at basin stations.

Distilling each differential spectrum to two numbers—one for 0.1–0.5 Hz and one for 0.5–4.0 Hz—we can examine the amplification in terms of basin depth at each station (Figure 3.5). The patterns visible in Figure 3.4 are also clear in Figure 3.5: ambient noise is amplified at basin stations. We color regions in Figure 3.5 for the sake of discussion: red for basin stations, blue for marginal stations and green for non-basin stations.

At low frequencies for both H and Z components, the overall pattern is that for stations with basin depths > 2 km, noise levels on the vertical component are 9–15 dB higher than non-basin station SSN (Figure 3.5b). The effect is stronger on the horizontal component (Figure 3.5a). There is a weak correlation between basin depth and noise amplitude: GOOS, with 1 km basin depth, has the lowest amplification, while NSKI and CAPN, with 7 km depth have the highest amplification. Also, the two basin-like marginal stations O20K and P19K exhibit similar amplification as GOOS.

The pattern at high frequencies is similar, though the basin amplification values are stronger (15–50 dB), and the variations among sets of stations is also larger. For example, even for non-basin stations (shaded green in Figure 3.5c-d) the noise levels on the vertical component are between -5 and 15 dB of SSN (Figure 3.5d), whereas for low frequencies the noise levels are within 3 dB of SSN (Figure 3.5b). For the vertical component the differences generally increase with distance from SSN (Figure 3.5d), implying that there are either systematic subsurface structural differences from west to east or there are different sources generating the 0.5–4.0 Hz noise. For example, noise near Redoubt volcano may be elevated (with respect to SSN) due to activity at the volcano,

at glaciers, or in Cook Inlet, or it could be due to structural differences that affect the same background wavefield at both sites. Marginal stations (shaded blue in Figure 3.5c-d) for the vertical component are mostly 8–16 dB higher than SSN. Note that O20K and P19K both exhibit elevated noise levels, as do PMR, at the northeastern tip of the basin (in Palmer).

3.7 Ground motion metrics measured from earthquakes

From a set of 34 earthquakes we examine three-component, filtered seismograms at 48 stations. From each filtered seismogram, we calculate five scalar ground motion metrics:

1. duration (dur)
2. radiated energy (E_R)
3. peak ground displacement (PGD)
4. peak ground velocity (PGV)
5. peak ground acceleration (PGA)

Using basin depths of Shellenbaum et al. (2010), we test the hypothesis that these quantities increase with basin depth at each station.

Our approach carries several assumptions. First, we do not know the exact relationship between basin depth and the five metrics. Therefore a correlation coefficient between depth versus a metric, for a set of stations for one event, may not be appropriate. Second, the ground motion metrics are based on amplitudes, which vary strongly at stations according to a station's azimuth relative to the earthquake source mechanism. Third, there are structural variations such as three-dimensional heterogeneity—elastic or anelastic structure—that will impact the recorded wavefield. Our assumption is that the depth of the basin is the only structural factor influencing the ground motion metrics.

3.7.1 Methods

Our methods for calculating and analyzing ground motion metrics are as follows:

1. Using ObsPy Beyreuther et al. (2010); Krischer et al. (2015), fetch seismograms from IRIS DMC, then remove instrument response. Using the source and station coordinates (and also the sensor angles), rotate to radial and transverse component. The result is a set of three-component velocity seismograms (units m/s).

2. Loop over a large set of bandpass filters. For each set of filtered seismograms:

   (a) Calculate signal-to-noise (SNR) as $\max(|v(t)|)$ over the first 400 s after the origin time, divided by the maximum over the 100 s prior to the origin time. Exclude stations with $SNR < 4$.

   (b) Proceed if there are ≥ 4 stations with basin depths > 1 km.

   (c) Apply a distance-based correction for geometric spreading. (Each correction will depend on the bandpass, via the filtered seismograms used.)

   (d) Calculate correlation coefficient between basin depth and a particular metric (e.g., PGV).

3. Generate a colored plot of correlation coefficients.

These methods are demonstrated in Figures 3.6–3.8. The example earthquake is northeast of Cook Inlet basin, depth 12 km, M_l 4.1, on 2016-11-06. A map in Figure B.9a shows the epicenter and the subset of 46 (out of 48) stations that recorded the earthquake. An unfiltered record section of transverse component is shown in Figure B.9b.

We choose frequency limits for bandpass filters by $\mathbf{f} = 10^{\text{linspace}(\log_{10} f_{\min}, \log_{10} f_{\max}, n)}$, where linspace($x$,$y$,$n$) returns a set of n linearly spaced values between x and y. With $f_{\min} = 0.10$ Hz, $f_{\max} = 4.00$, and $n = 8$, the frequencies are 0.10, 0.17, 0.29, 0.49, 0.82, 1.39, 2.36, 4.00 Hz. With n frequencies, we have a total set of $n(n-1)/2$ possible bandpass filters; therefore there are 28 filters used for each set of seismograms. One filtered record section (0.10–0.82 Hz) is shown in Figure B.9c. The record section excludes 2 stations (TA.O18K, TA.P19K) that does not meet the SNR threshold.

The next step is to correct the record section for geometrical spreading. We make the assumption that the seismograms are dominated by surface wave energy. In this case, the amplitudes of the seismograms have a term $1/\sqrt{\sin\Delta}$, where Δ is the arc-distance from source to station (Stein & Wysession, 2003, Sec. 4.3.4, Eq. 20). (The same equation has a frequency-dependent attenuation term, which we ignore.) We correct for geometrical spreading of surface waves by estimating a

single parameter,

$$K = \text{median}\left(\max(|v_i(t)|)\ \sqrt{\sin\Delta_i},\quad i = 1,\ldots,n\right) \tag{3.1}$$

where i is the station index and n is the number of non-basin stations with filtered seismograms passing the SNR threshold. The seismogram corrected for geometric spreading is then

$$v_i'(t) = \frac{\sqrt{\sin\Delta_i}}{K}\, v_i(t). \tag{3.2}$$

After normalizing by K, the seismogram is unitless. We estimate K for each record section of filtered waveforms and for each event. Figure 3.6 shows an example, where $K = 2.43 \times 10^{-6}$ m/s is calculated from a set of 26 non-basin stations. Basin stations are excluded from estimating K because amplitudes of seismograms at basin stations are strongly influenced by basin structure. As expected, the best-fitting curve $K/\sqrt{\sin\Delta}$ offers a reasonable fit to non-basin stations, and it does not explain the amplitude variations for the basin stations. The record section corrected for geometrical spreading is shown in Figure 3.6b.

From the filtered, distance-corrected seismograms in Figure 3.6b, we calculate five ground motion metrics. An example calculation of dur, PGV, and E_R is shown in Figure 3.7a for station KALN, transverse component filtered 0.10–0.82 Hz. In this case, dur = 208.0 s, PGV = 2.2 and E_R = 7.3. These calculations are performed for each station's seismogram, and then the values are plotted versus basin depth at each station, as shown in Figure 3.7b for E_R. In this case, the data for basin depth and E_R have a correlation coefficient of 0.90.

We use a matrix plot of colored correlation coefficients—which we will call 'matrix plots'—to represent the full set of different bandpass filters used. With n = 8 frequencies, there are 28 bandpass filters and therefore up to 28 colored boxes in matrix plots such as Figure 3.7c. The first bandpass considered is 0.10–0.17 Hz (5.90–10.00 s); for the event in Figure 3.6, there are not enough stations with sufficient SNR and therefore the uppermost left square of Figure 3.7c is left white. The next bandpass is 0.10–0.29 Hz (3.49–10.00 s), which happens to provide the highest correlation between basin depth and E_R, among all 28 bandpasses. This is represented by the dark red box in row 1, column 2 of Figure 3.7c, with the corresponding scatterplot in Figure 3.9. The example in Figure 3.7b, for bandpass 0.10–0.82 Hz, corresponds to row 1, col-

umn 4 of Figure 3.7c. The matrix plot boxes along the diagonal represent narrowband filters (0.10–0.17 Hz, 0.17–0.29 Hz, 0.29–0.49 Hz, etc), while the boxes at the far right represent broadband filters (0.10–4.00 Hz, 0.17–4.00 Hz, 0.29–4.00 Hz, etc). The matrix plot therefore provides a compact representation of which bandpass filters lead to ground motion metrics that are the best correlated with basin depths.

3.7.2 Results

The matrix plot in Figure 3.7c is one of 15 subplots in Figure 3.8. Each matrix plot is made from 28 possible scatterplots, and in Figure 3.9 we display the scatterplot having the highest correlation coefficient. A full set of plots such as Figures 3.8 and 3.9 is included in Smith (2019) for 34 earthquakes. Here we discuss the results for two earthquakes: a M_l 4.1 crustal event (12 km) on 2016-11-06 (Figures 3.8 and 3.9) and a M_l 5.2 intraslab event (126 km) on 2015-07-25 (Figures 3.10 and 3.11).

The ground motion metric E_R combines duration and amplitude, since it is an integration over time. Therefore if there are high correlations between peak amplitudes (*PGD*, *PGV*, *PGA*) and basin depth, we would expect to see correlations between E_R and basin depth. Similarly, if durations correlate with basin depth, we would expect to see correlations between E_R and basin depth.

For the crustal earthquake, there are $<$10 basin stations that exceed the SNR threshold for the lowest frequency bandpass (0.10–0.17 Hz, 5.90–10.00 s) for the vertical component. These stations produce correlation coefficients of 0.90–0.99, as indicated by the Z column of plots in Figure 3.9. Interestingly, for the same bandpass, the correlation between duration and basin depth is weak, indicated by the lack of red color in the upper left matrix plot in Figure 3.8. For the vertical and transverse components, duration correlates with basin depth at 0.49–1.39 Hz, yet there is large scatter even for non-basin stations (Figure 3.9, top row).

Like the crustal event, the intraslab event exhibits the highest (and most) correlations from E_R (Figure 3.10). Although this event is deeper from the crustal event, its magnitude is sufficiently greater (5.2 vs 4.1) such that its seismograms have overall higher SNR and more data points appear in the scatterplots (Figure 3.11). Correlations between duration and basin depth are highest

on the vertical component and for 0.29–0.82 Hz (cc 0.86). The biggest outliers in the (dur, Z) scatterplot in Figure 3.11 are the two basin-like stations O20K and P19K; they would not be outliers if they were assigned greater basin depths. For the other four metrics (E_R, PGD, PGV, PGA) there are much higher correlations with basin depth for horizontal components than for the vertical component (Figure 3.10). Correlations exceed 0.90 for the transverse component for the frequency range 0.17–0.49 Hz (2.06–5.90 s). Further work is needed to examine the influence of the source mechanism and the geometry of the basin on these results.

Based on the full set of bandpass filters for the full set of 34 earthquakes in Smith (2019), we provide some summary points regarding correlation coefficients between ground motion metrics and basin depth. (1) Among the five groundmotion metrics, E_R, which combines duration and amplitudes, has the highest correlations with basin depth. (2) PGD, PGV, and PGA have similar correlations with basin depth. This is not surprising, since a sinusoidal wave $d(t) = F \sin t$ would lead to PGD=F, PGV=F, and PGA=F. (3) For PGD, PGV, and PGA, correlations with basin depth are higher for R and T components than for Z.

3.8 Spectral ratios measured from earthquakes

3.8.1 Methods

Using the same set of 34 earthquakes and 48 stations, we calculate spectral ratios between each target station and a non-basin reference station. At this initial stage, we do not account for amplitude differences that would arise from either (1) different epicentral distances for the target station and the reference station, (2) different source-station azimuths that would result in different amplitudes with respect to the source mechanism, (3) different local structure at two stations (TA.O20K and TA.P19K) that would effect the recorded wavefield. We partially address (1) and (3) by grouping the stations into three subregions and assigning a different reference station for each subregion. West of Cook Inlet we use TA.N19K, north of Cook Inlet we use AK.SSN, and east of Cook Inlet we use AK.SLK (Figure 3.1a). The reference station for each target station is listed in Table B.2. The three primary reference stations are not used as target stations; therefore we have 45 (out of 48) target stations for the analysis.

Our goal is to calculate scalar quantities from the spectral ratio between a target station and a non-basin reference station. These scalar quantities are the median acceleration power over two frequency intervals: 0.1–0.5 Hz and 0.5–4.0 Hz. Our assumption is that basin effects are confined to 0.1–4.0 Hz. Our procedure is demonstrated in Figure 3.12 for target station NSKI and reference station SLK. For both stations, for the 'signal' we select a time window of 500 s following the origin time; for the 'noise' we select a time window of 500 s before the origin time. We calculate acceleration power spectra following the same procedures as in McNamara & Buland (2004). Four spectra—signal and noise for both stations—are shown in Figure 3.12a.

The signal and noise spectra are used to refine the two frequency intervals over which the spectral ratio measurements are made. For the earthquake in Figure 3.12, NSKI meets the SNR criterion at 0.97 Hz, while SLK meets the criterion at 0.52 Hz. Therefore, for the low-frequency interval (0.1–0.5 Hz) there is insufficient signal to calculate a spectral ratio. For the high-frequency interval (0.5–4.0 Hz), the lower limit of 0.5 Hz is increased to 0.97 Hz. Over this interval (0.97–4.0 Hz) the measurement is 12 dB, which corresponds to an amplification factor of about 4 (Table B.1). Note that the spectral ratio for noise is much larger (35 dB) than for earthquakes, something we find across most events and station pairs Smith (2019).

This procedure is repeated for all 34 earthquakes recorded by the target station, as shown in Figure 3.13. From this set of spectral ratio measurements, we calculate the median value and enter it into Table B.2. This process is performed for each station, for three components, and for two frequency intervals, in order to complete Table B.2.

3.8.2 Results

Our spectral ratio results are summarized in Table B.2 and in Figure 3.14a-b. We find that the median spectral ratios for 0.1–0.5 Hz for all 18 is positive and ranges from 6–14 dB. Furthermore the two basin-like marginal stations (TA.O20K, TA.P19K) have ratios of 5–7 dB (Figure 3.14a), further evidence that these stations should be characterized as basin stations. For 0.5–4.0 Hz spectral ratios (Figure 3.14b) there is a similar pattern of elevated values for basin stations, but the variability—even for non-basin stations—is large.

The scatter in the spectral ratio measurements is partially the result of geometric spreading not being included within our simplified approach. For any earthquake, the epicentral distances to the target station (Δ_{tar}) and reference station (Δ_{ref}) will be different. We calculate $\Delta D = \Delta_{ref} - \Delta_{tar}$ for all source–station pairs to identify the stations that would be most effected by ignoring the distance effect. Target stations whose mean value $\Delta D > 50$ km are generally further from earthquakes than is the reference station; this list includes basin station HOM as well as non-basin stations M19K, SAW, CNP, P18K, M20K, GHO, BRSE, BRLK, KNK, O18K, SVW2, and PMR. These stations are colored blue in Figure 3.14a and tend to have lower dB values than other stations with similar basin depths. Target stations whose mean value $\Delta D < 50$ km are generally closer to earthquakes than is the reference station; this list includes basin stations KALS and KALN as well as non-basin stations O20K, RDWB, HLC2, and HLC3. These stations are colored black in Figure 3.14a-b and tend to have higher dB values than other stations with similar basin depths. Careful treatment of the distance effect, as well as of source mechanisms, would allow for a better examination of any possible relationship between basin depth and amplification. This is particularly important for the high-frequency bandpass (0.5–4.0 Hz).

3.9 Discussion

The use of broadband seismometers allows us to examine how the seismic wavefield interacts with Cook Inlet sedimentary basin across a wide range of frequencies (0.01–40 Hz). Our three analyses examined frequency-dependent effects using ambient noise (no sources), ground motion metrics (1 source, all stations), and spectral ratios (1 station, all sources). Next we generalize our results and discuss some unresolved topics.

3.9.1 The seismic wavefield from earthquakes and ambient noise

Results from ground motion metrics and from spectral ratios indicate that the seismic wavefield from crustal and intraslab earthquakes is amplified by Cook Inlet basin. In the case of the ground motion metrics, the stations in the deeper basin exhibit higher amplitudes than stations at the margin or outside of the basin. Spectral ratios provide an opportunity to compare noise as well as signal for pairs of stations. An example for a single station is shown in Figure 3.13 for basin station NSKI. For the largest events, such as the five that have $M_l > 5$, the earthquake signal exceeds the

pre-earthquake noise level, even down to 0.1 Hz. The calculated spectral ratios for 0.1–0.5 Hz are all about 10 dB, corresponding to an amplification factor of about 3. The pre-earthquake noise spectral ratios have similar values. However for higher frequencies (0.5–4.0 Hz), the peak noise spectral ratios increase to 40–50 dB, similar to the values obtained when examining two years of continuously recorded ambient noise (Figure 3.5d).

The divergence above 0.5 Hz between earthquake spectral ratios and noise spectral ratios is highlighted between Figure 3.14c and d. It suggests that the same wavefield (earthquake or ambient noise) is not being measured at both the target basin station and the reference non-basin station. Rather than interpreting the 40 dB noise spectral ratio at 0.5–4.0 Hz (Figure 3.4d) as "basin amplification" of the same waves comprising ambient noise, we can interpret that there are two very different noise settings. With that interpretation, the waves comprising the ambient noise in the basin do not reach the non-basin reference station.

Analysis of seismic noise ratios—whether from 500 s of pre-earthquake noise or from two years of continuous data—suggests that surface waves at 0.1–0.5 Hz, either from earthquakes or within ambient noise, are amplified in Cook Inlet basin by 6–14 dB.

3.9.2 Improvements to the assumed basin model

Our modeling and interpretations are based on the detailed basement map of Shellenbaum et al. (2010), which is estimated from well logs and stacking velocities (mostly P waves) from industry data. Future seismic modeling with SALMON and other data may allow for improvements of the basement surface, the internal basin wavespeed structure, and the underlying structure. An optimal approach would be to perform tomographic inversion using the full seismic waveforms (earthquakes and ambient noise cross-correlations) and allowing for perturbations of the boundary surface in addition to the wavespeed structure Dahlen (2005); Tong et al. (2014).

Our analysis of low-frequency (0.1–0.5 Hz) noise provides some indication of corrections needed to the assumed basin geometry. The variations in the marginal basin differential spectra (blue) in Figure 3.4 are likely due to differences either in the basement surface or the subsurface wavespeed structure. Two marginal stations in our analysis, TA.O20K and TA.P19K, have low-frequency noise levels that fall between basin stations and marginal stations (Figure 3.4). The geological

unit at the surface at these two stations is mapped as the Upper Jurassic Naknek Formation and Kotsina Conglomerate, which are interpreted to underlie the Tertiary Cook Inlet basin Fisher & Magoon (1978). One interpretation is that the 0.1–0.5 Hz ambient noise wavefield at bedrock stations TA.O20K and TA.P19K is sensitive to basin structures that are up to 20 km east of the stations and within Cook Inlet basin. Alternatively, it is possible that the Naknek formation is anomalously slow and thick. This would imply that the Mesozoic strata—beneath the basement surface of Shellenbaum et al. (2010)—would be beneficial for modeling the seismic noise variations.

3.9.3 Intraslab bias from earthquake selection

Our results reveal basin influences down to 0.1 Hz. These frequencies are best excited by larger ($M_{\mathrm{l}} > 5$) earthquakes, which, in our study region, are all intraslab earthquakes. Two notable historical crustal earthquakes have occurred in this region: 1933-04-27 M_{w} 6.8 and 1943-11-03 M_{w} 7.3 Doser & Brown (2001); Silwal et al. (2018). Neither of these earthquakes is associated with an actively mapped fault Koehler et al. (2012). (The 1933 earthquake is within a region mapped as actively folding sub-basin structures Haeussler et al. (2000).)

With regard to basin excitation, it is important to acknowledge that our results are biased toward the intraslab earthquakes that were recorded during the SALMON deployment. Intraslab earthquakes of a given magnitude will not excite surface waves as strongly as a shallow crustal earthquake; furthermore the incident angle of the arriving wavefield will differ. Any future modeling of ground motions for the sake of seismic hazard estimates should take into account the possibility of crustal earthquakes from realistic (e.g., historical) source regions.

3.9.4 Attenuation and source radiation effects

Our treatment of modeling seismic amplitudes is overly simplified and should be revised in a future analysis of this data set. A distance correction for geometrical spreading was used in the analysis of ground motion metrics but not in the analysis of spectral ratios. Furthermore, our treatment of geometrical spreading assumes the dominance of surface waves, which may not be appropriate at higher frequencies, and does not account for the influence of source depth Wirth et al. (2019). Attenuation (anelasticity) was not considered. Attenuation of surface waves is en-

capsulated with the term $\exp[\tau \pi f / Q]$, where $\tau = a\Delta / U$ is the travel time, Δ is the arc-distance, a is the Earth radius, and U is the group velocity (Stein & Wysession, 2003, Sec. 4.3.4, Eq. 20). High values of Q correspond to a slow decay of amplitudes of seismic waves (low attenuation).

Source radiation has a strong influence on amplitudes of surface waves and body waves. The data coverage for all 34 earthquakes in this study should be sufficient to obtain reliable source mechanisms Silwal & Tape (2016); Silwal et al. (2018). Incorporating the amplitude variation expected at each station for each event would improve our estimates of the influence of basin depth on amplitudes.

3.10 Summary

Our main findings are as follows:

1. We analyze 34 earthquakes between 2015-05-01 and 2017-08-01 recorded by 48 stations. The time period spans the SALMON project Tape et al. (2017), which offers the best spatial coverage of Cook Inlet basin, including stations on the west side of Cook Inlet.

   Most of the larger earthquakes are intraslab events below 50 km depth. No large ($M_w > 5$) crustal events, which are known to occur in the region (e.g., 1933-04-27 M_w 6.8 in Cook Inlet, Doser & Brown (2001), and Silwal et al. (2018)), occurred during the SALMON deployment.

2. Earthquake spectral ratios between basin and non-basin stations imply basin amplification of 6–14 dB for 0.1–0.5 Hz.

3. Correlations between basin depth and ground motion metrics depend on the component of ground motion. Amplitude-based ground motion metrics (E_R, PGD, PGV, PGA) are generally higher for the horizontal component of ground motion than for the vertical component. For larger earthquakes, the correlations between basin depth and duration are higher for the vertical component than for the horizontal component.

4. Cook Inlet basin exhibits vertical-component ambient seismic noise that is amplified relative to a non-basin reference site by 9–15 dB at 0.1–0.5 Hz and 15–50 dB at 0.5–4.0 Hz. Similar amplification occurs for the horizontal component of noise.

5. The noise results at 0.1–0.5 Hz are in agreement with spectral ratios, suggesting that the low-frequency earthquake wavefield and ambient noise wavefield are similarly amplified by Cook Inlet basin.

6. The noise results at 0.5–4.0 Hz are not in agreement with the earthquake spectral ratios, even for crustal earthquakes, suggesting that the high-frequency noise wavefield is local to the basin.

Future efforts dedicated to understanding seismic wave propagation in Cook Inlet basin should be possible from analysis of 3D seismic wavefield simulations and from improved modeling of the recorded earthquake waveforms. As our 3D models of elastic and anelastic structure improve in this region Shellenbaum et al. (2010); Eberhart-Phillips et al. (2006); Ward & Lin (2018), we will be able to design realistic numerical experiments Day et al. (2008); Cruz-Atienza et al. (2016); Wirth et al. (2019) to investigate the influence of Cook Inlet basin on the seismic wavefield, by isolating the roles of source location, source depth, source radiation, 3D attenuation, and 3D structure.

3.11 Tables

Table 3.1: 34 earthquakes analyzed in this study.

origin time	longitude (°)	latitude (°)	depth (km)	magnitude (M_l)
2015-05-18 15:49:10.522	-150.4504	61.9398	22	4.3
2015-06-24 22:32:21.166	-151.9621	61.6644	114	5.8
2015-07-25 19:57:43.227	-152.0518	61.9493	126	5.2
2015-07-27 02:21:54.395	-150.9390	60.9827	16	3.4
2015-07-29 02:35:59.449	-153.1962	59.8935	119	6.4
2015-11-06 14:26:50.635	-149.8762	61.9965	46	4.4
2016-01-04 02:38:05.283	-148.9329	61.0382	21	3.6
2016-01-24 14:29:28.374	-153.1457	59.7312	107	4.7
2016-02-03 20:31:25.777	-153.5461	60.3334	189	4.5
2016-02-10 14:36:17.399	-152.9050	59.7693	19	3.4
2016-02-15 10:41:46.974	-150.0123	60.8957	48	4.2
2016-02-28 13:48:51.632	-150.6873	61.7805	62	4.3
2016-03-12 21:57:55.683	-152.3041	60.2609	100	4.7
2016-04-08 03:24:18.180	-149.9238	61.4564	40	4.0
2016-04-20 14:55:42.428	-148.1806	61.7490	15	4.0
2016-05-01 20:38:46.663	-152.9931	60.1136	129	4.7
2016-05-30 19:01:29.827	-153.7581	59.0778	103	4.1
2016-08-30 12:27:59.886	-149.1495	61.1186	38	4.0
2016-09-01 12:27:42.774	-152.1646	61.2991	132	4.5
2016-10-02 22:39:41.110	-149.5161	60.8787	24	4.0
2016-10-14 12:59:05.731	-151.7773	59.8029	63	4.0
2016-10-19 00:16:30.695	-148.9192	59.9489	11	3.5
2016-11-06 19:40:49.667	-148.2035	61.7493	12	4.1
2016-11-21 22:27:27.757	-150.1984	60.7706	50	4.0
2016-12-03 08:04:47.085	-150.4189	61.4436	14	3.3
2016-12-04 13:15:44.183	-150.9023	61.9700	9	4.2
2016-12-24 05:24:41.092	-148.3761	61.0454	13	3.5
2017-03-02 02:11:30.682	-152.6546	59.5785	78	5.6
2017-03-17 07:47:31.160	-149.2418	61.9406	3	3.6
2017-04-30 21:32:17.954	-150.7014	60.8369	26	3.3
2017-05-07 04:25:19.095	-151.6783	60.1828	67	5.3
2017-05-07 19:58:25.043	-151.2931	61.4974	17	3.5
2017-05-24 09:59:01.220	-151.4935	61.8085	10	3.5
2017-05-30 02:18:45.889	-151.8152	60.8341	81	5.2

3.12 Figures

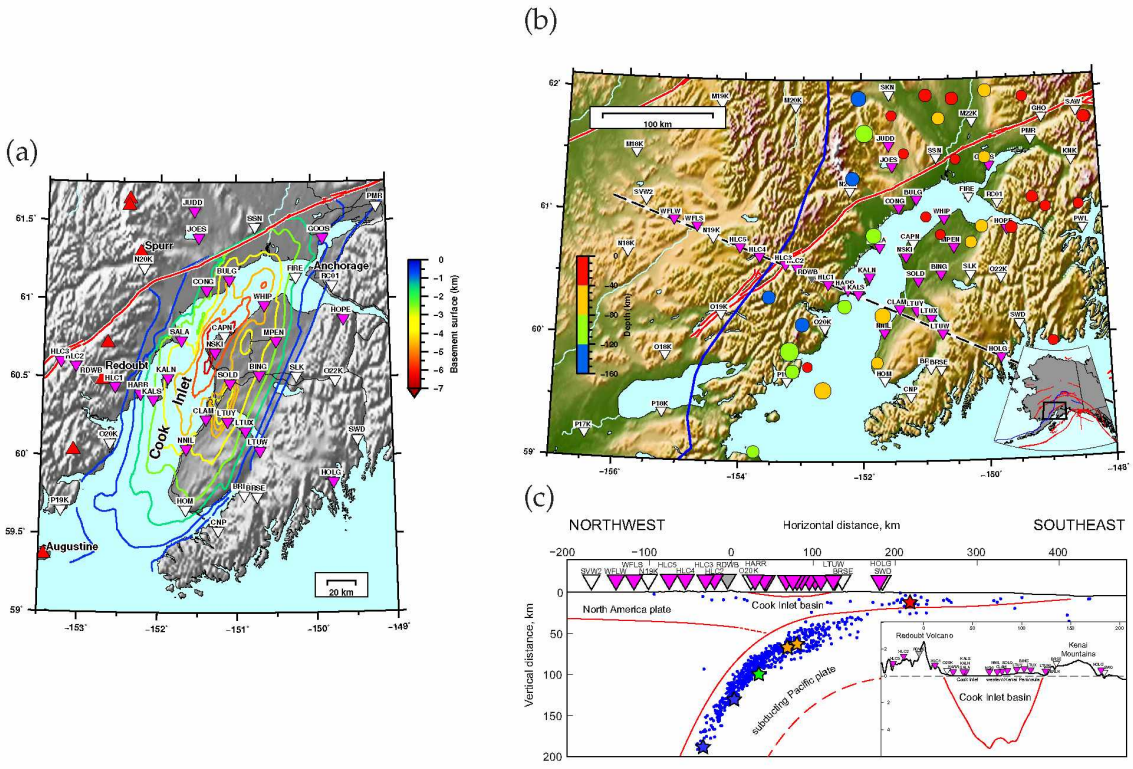

Figure 3.1: The Cook Inlet region, with seismic stations (2015–2017) and earthquakes used in this study. SALMON stations are plotted as magenta inverted triangles; other broadband stations are white. Active faults of Koehler et al. (2012) are plotted in red. (a) Cook Inlet basin: contours are for the base-Tertiary basement map of Shellenbaum et al. (2010). Red upright triangles are active volcanoes. (b) Earthquakes and stations within the full study region. The 34 earthquakes analyzed in this study (Table 3.1) are colored by depth and sized by magnitude. The Redoubt line of stations extends from AT.SVW2 in the west, through Redoubt volcano, and to ZE.HOLG on the eastern Kenai Peninsula. (c) Cross section of seismicity within 50 km of the Redoubt line and occurring between 2015-05-01 and 2017-08-01, $M_l \geq 2.0$. There are 6 events (out of 34 in our analysis) that are plotted as stars and within this corridor of seismicity. Also shown are stations within 50 km of the Redoubt line. Cook Inlet basin basement map from Shellenbaum et al. (2010), continental Moho from Wang & Tape (2014), subduction interface from Hayes et al. (2018).

	station	longitude (°)	latitude (°)	inoise	basin depth (km)	ibasin	distance to basin (km)	start date	end date
1	AK.CAPN	-151.15	60.77	1	7.3	3	0	2015-01-01	2018-01-01
2	ZE.NSKI	-151.28	60.66	1	7.0	3	0	2015-01-01	2018-01-01
3	ZE.LTUY	-151.12	60.22	1	5.2	3	0	2015-01-01	2018-01-01
4	ZE.SOLD	-151.08	60.46	1	5.2	3	0	2015-01-01	2018-01-01
5	ZE.WHIP	-150.63	60.97	1	5.2	3	0	2015-01-01	2018-01-01
6	ZE.BULG	-151.09	61.13	1	4.9	3	0	2016-01-01	2018-01-01
7	ZE.CLAM	-151.39	60.24	1	4.9	3	0	2015-01-01	2018-01-01
8	ZE.KALN	-151.89	60.50	1	4.3	3	0	2015-01-01	2018-01-01
9	ZE.BING	-150.70	60.52	1	3.7	3	0	2015-01-01	2018-01-01
10	ZE.NNIL	-151.65	60.05	1	3.7	3	0	2015-01-01	2018-01-01
11	ZE.SALA	-151.71	60.74	1	3.7	3	0	2015-01-01	2018-01-01
12	ZE.MPEN	-150.48	60.74	1	3.4	3	0	2016-05-21	2017-05-21
13	ZE.KALS	-152.07	60.36	1	3.0	3	0	2015-06-01	2016-06-01
14	ZE.CONG	-151.39	61.06	1	2.7	3	0	2015-01-01	2018-01-01
15	AK.HOM	-151.65	59.66	1	2.7	3	0	2015-01-01	2018-01-01
16	AK.FIRE	-150.22	61.14	1	2.4	3	0	2015-01-01	2018-01-01
17	ZE.LTUX	-150.88	60.16	1	2.4	3	0	2015-01-01	2018-01-01
18	ZE.GOOS	-149.85	61.39	1	0.9	3	0	2015-01-01	2018-01-01
19	TA.O20K	-152.62	60.08	1	0	2	5	2016-01-01	2018-01-01
20	TA.P19K	-153.23	59.65	1	0	2	11	2017-01-01	2018-01-01
21	AT.PMR	-149.13	61.59	1	0	1	2	2015-01-01	2018-01-01
22	AK.RC01	-149.74	61.09	1	0	1	3	2015-01-01	2018-01-01
23	ZE.LTUW	-150.70	60.03	1	0	1	4	2016-01-01	2018-01-01
24	AK.SLK	-150.22	60.51	1	0	1	6	2015-01-01	2018-01-01
25	AK.BRLK	-150.91	59.75	1	0	1	7	2015-01-01	2018-01-01
26	AK.GHO	-148.93	61.77	1	0	1	8	2015-01-01	2018-01-01
27	AK.SSN	-150.75	61.46	1	0	1	9	2016-07-01	2017-07-01
28	AK.CNP	-151.24	59.53	1	0	1	10	2015-01-01	2018-01-01
29	AK.BRSE	-150.74	59.74	1	0	1	15	2015-01-01	2018-01-01
30	ZE.HOPE	-149.60	60.87	1	0	1	19	2015-01-01	2018-01-01
31	AK.SAW	-148.33	61.81	1	0	0	21	2015-01-01	2018-01-01
32	AV.RDWB	-152.84	60.49	1	0	0	24	2015-08-01	2016-08-01
33	AK.KNK	-148.46	61.41	1	0	0	37	2015-01-01	2018-01-01
34	ZE.HLC2	-153.08	60.58	1	0	0	39	2016-01-01	2018-01-01
35	ZE.HLC3	-153.28	60.60	1	0	0	50	2015-01-01	2018-01-01
36	AK.SWD	-149.45	60.10	1	0	0	62	2017-01-01	2018-01-01
37	ZE.HLC4	-153.71	60.67	1	0	0	74	2016-01-01	2018-01-01
38	AK.SKN	-151.53	61.98	1	0	0	76	2016-06-01	2017-06-01
39	AK.PWL	-148.33	60.86	1	0	0	83	2017-01-01	2018-01-01
40	ZE.HLC5	-154.03	60.74	1	0	0	93	2015-01-01	2018-01-01
41	TA.M20K	-153.13	61.88	1	0	0	102	2017-01-01	2018-01-01
42	TA.N19K	-154.48	60.81	1	0	0	119	2016-01-01	2018-01-01
43	TA.P18K	-155.23	59.39	1	0	0	121	2016-01-01	2018-01-01
44	TA.O18K	-155.21	59.85	1	0	0	123	2016-01-01	2018-01-01
45	ZE.WFLS	-154.76	60.91	1	0	0	136	2015-01-01	2018-01-01
46	TA.M19K	-154.39	61.90	1	0	0	149	2016-01-01	2018-01-01
47	ZE.WFLW	-155.14	60.96	1	0	0	158	2015-01-01	2018-01-01
48	AT.SVW2	-155.62	61.11	1	0	0	185	2015-01-01	2018-01-01
49	ZE.HARR	-152.24	60.40	0	1.5	3	0	2015-01-01	2018-01-01
50	ZE.HLC1	-152.57	60.44	0	0	1	9	2015-01-01	2018-01-01
51	TA.N20K	-152.21	61.20	0	0	1	13	2017-01-01	2018-01-01
52	ZE.JOES	-151.49	61.40	0	0	1	18	2015-01-01	2018-01-01
53	TA.M22K	-150.12	61.75	0	0	1	20	2016-01-01	2018-01-01
54	TA.O22K	-149.72	60.48	0	0	0	31	2015-01-01	2018-01-01
55	ZE.JUDD	-151.55	61.57	0	0	0	37	2015-01-01	2018-01-01
56	ZE.HOLG	-149.77	59.84	0	0	0	59	2015-01-01	2018-01-01
57	TA.O19K	-154.32	60.20	0	0	0	85	2016-01-01	2018-01-01
58	TA.N18K	-155.89	60.68	0	0	0	187	2015-01-01	2018-01-01
59	TA.P17K	-156.44	59.20	0	0	0	190	2017-01-01	2018-01-01
60	TA.M18K	-155.82	61.49	0	0	0	200	2015-01-01	2018-01-01

Figure 3.2: Broadband seismic stations in the Cook Inlet region (Figure 3.1), sorted in decreasing order of basin depth. The first 48 stations (with inoise=1) are selected for analyses in this study; these are colored as 18 basin stations, 12 marginal basin stations, and 18 non-basin stations. The start and end dates denote the integer-year time period used in the noise analysis for 48 stations.

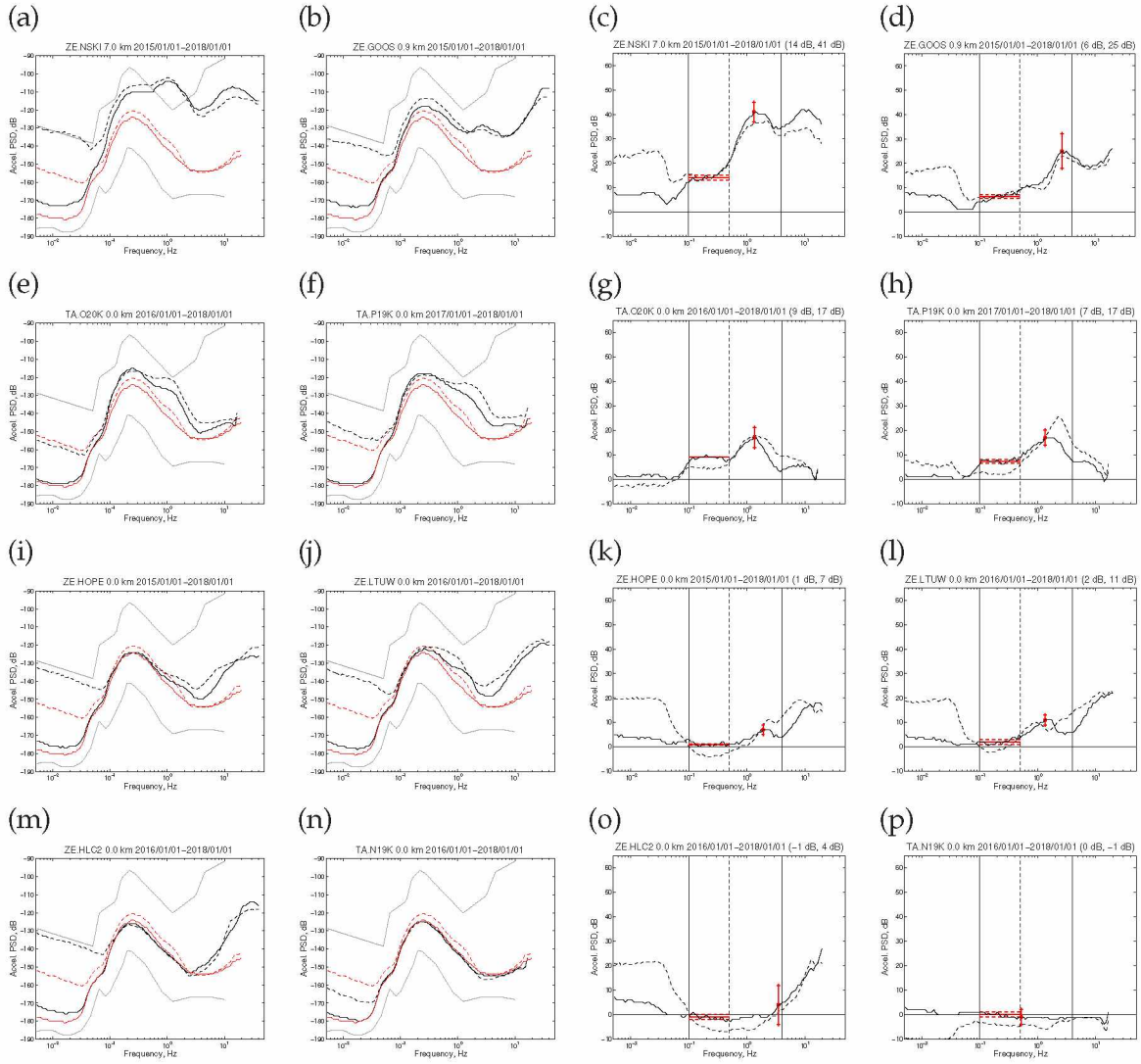

Figure 3.3: Annual ambient noise spectra for eight stations in the Cook Inlet region. The solid spectra are for the vertical component; the dashed spectra are for the average of the two horizontal components. In each subplot the red spectra are for the non-basin reference station SSN. The gray spectra denote the NHNM and NLNM reference spectra Peterson (1993). (a)-(b) Basin stations NSKI and GOOS. (c) Differential spectra for (a), which highlights the basin influence (and other differences). (d) Differential spectra for (b). (e)-(f) Basin-like marginal stations O20K and P19K. (g)-(h) Differential spectra for (e)-(f). (i)-(j) Marginal stations HOPE and LTUW. (k)-(l) Differential spectra for (i)-(j). (m)-(n) Non-basin stations HLC2 and N19K. (o)-(p) Differential spectra for (m)-(n).

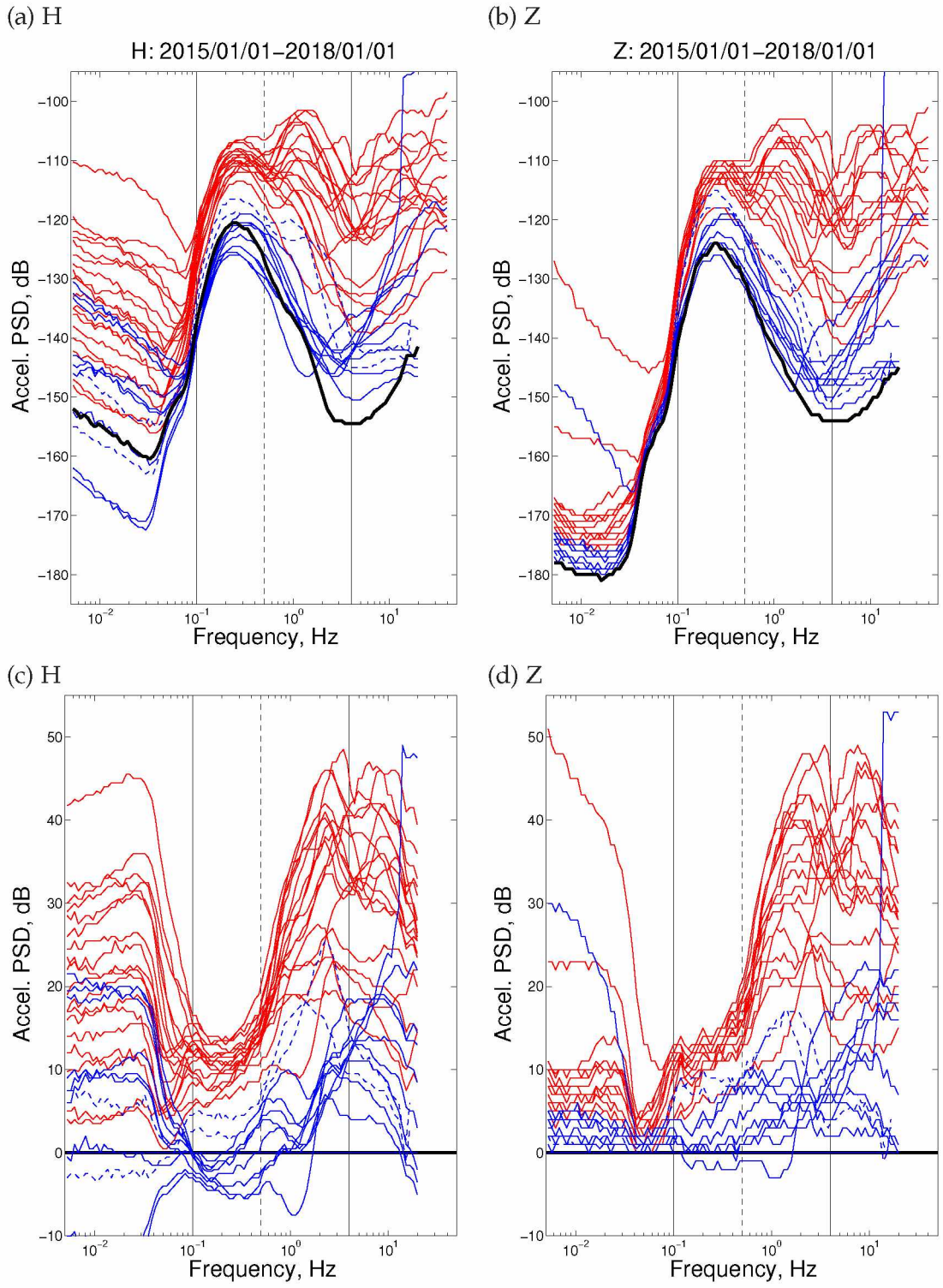

Figure 3.4: Seismic noise spectra and their differences from a non-basin reference station (SSN). (a) Horizontal-component annual ambient noise for 30 stations in the Cook Inlet region. Red spectra are for 18 basin stations. Dashed blue spectra are for marginal basin stations (P19K and O20K) that exhibit basin-like characteristics. Solid blue spectra are for 9 marginal basin stations that exhibit non-basin characteristics. The thick black line is the non-basin reference spectrum SSN. The solid lines denote the frequency range of basin influence on seismic waves: 0.1–4.0 Hz (separated at 0.5 Hz). (b) Same as (a), but for the vertical component. (c) Spectra in (a), minus the non-basin reference spectrum in (a). (d) Spectra in (b), minus the non-basin reference spectrum in (b).

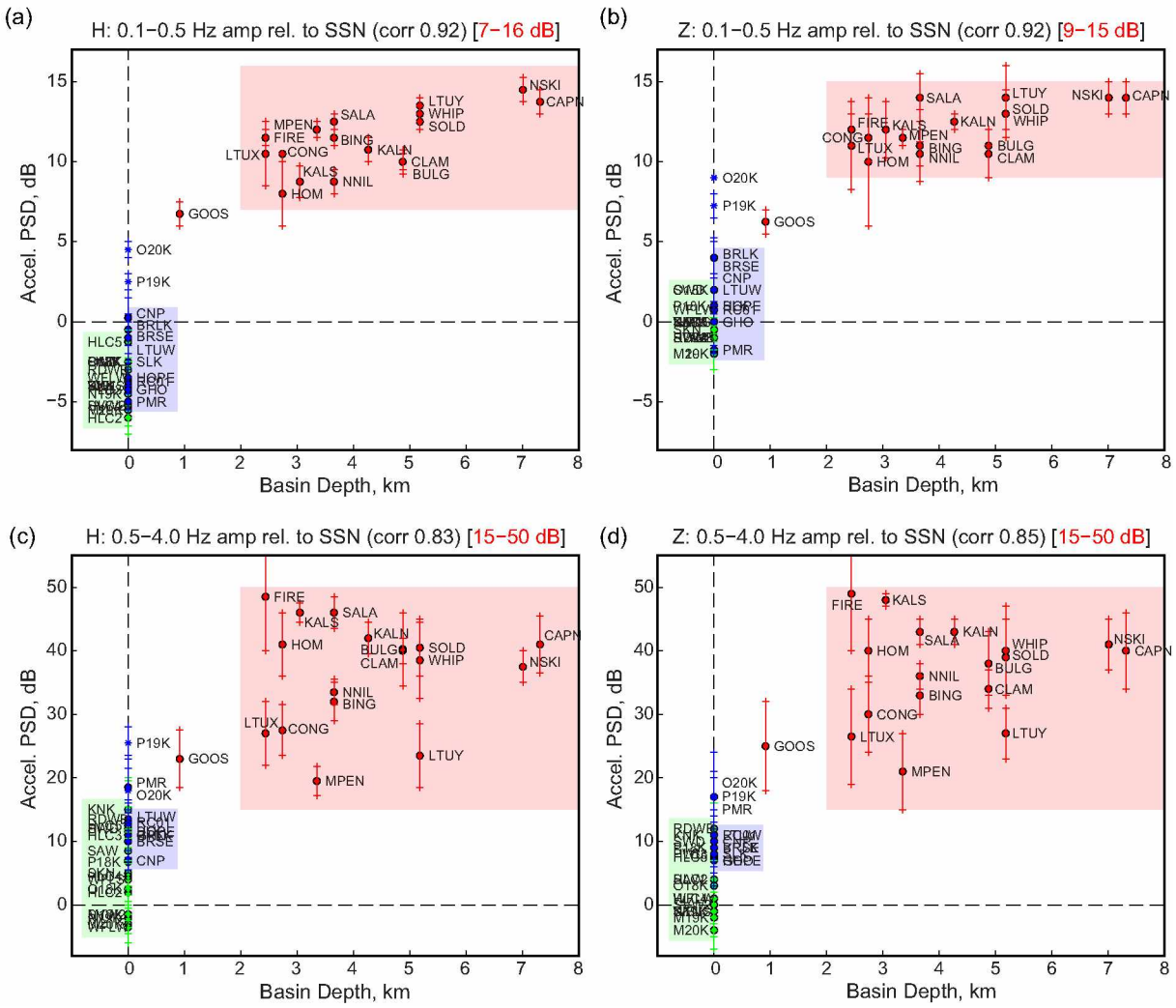

Figure 3.5: Seismic noise amplitudes compared with basin depth, shown for 48 stations in the Cook Inlet region. Red circles, highlighted by the red shaded region, denote 18 stations. Blue circles (and stars), highlighted by the blue shaded region, denote 12 marginal basin stations. (The stars are for P19K and O20K.) Green circles, highlighted by the green shaded region, are non-basin stations. See Figure B.2 for individual spectra. (a) Horizontal-component seismic noise amplitudes for the frequency range 0.1–0.5 Hz. Note the y-axis limits from $[-8, 17]$ dB. (b) Vertical component for 0.1–0.5 Hz. (c) Horizontal component for 0.5–4.0 Hz. Note the y-axis limits from $[-8, 55]$ dB. (d) Vertical component for 0.5–4.0 Hz.

(a)

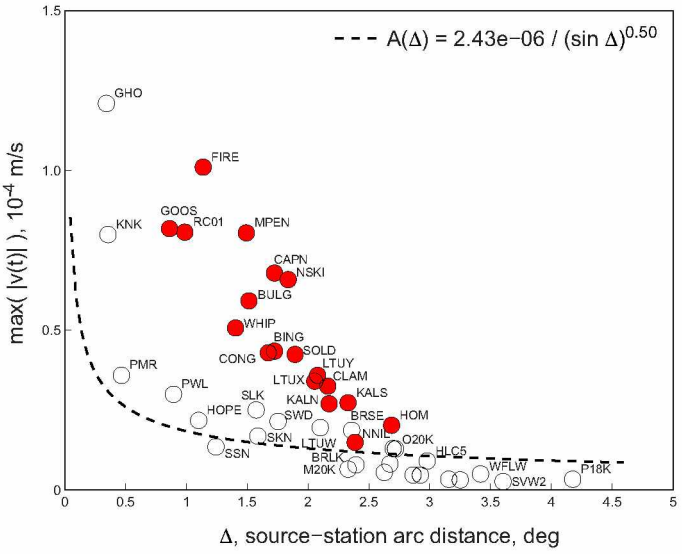

(b)

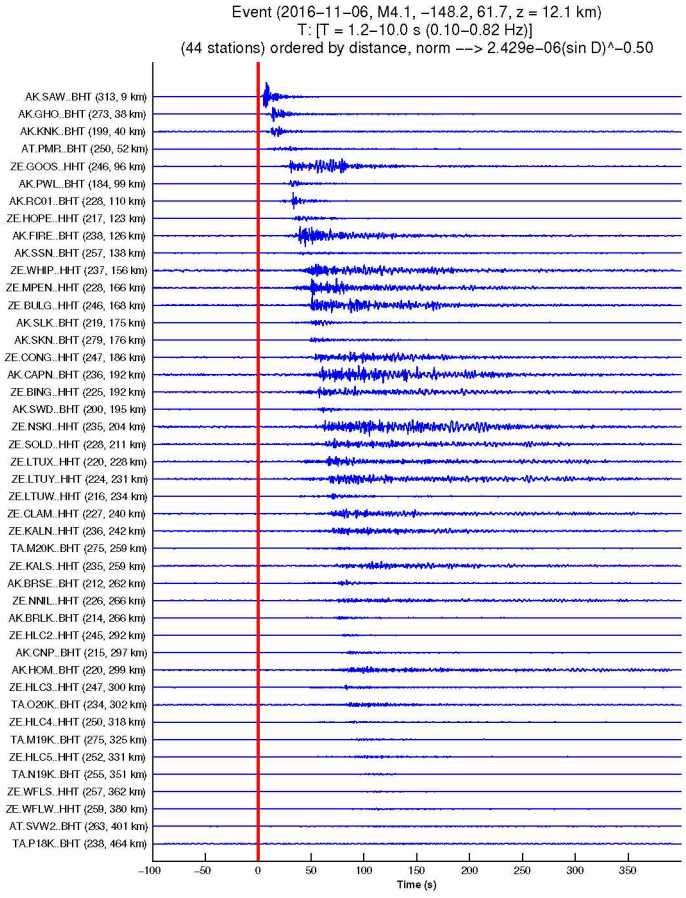

Figure 3.6: Distance-dependent correction for geometrical spreading. A full set of explanatory figures for earthquake metrics is shown in Figures 3.6–3.8. (a) Maximum absolute-value amplitudes of seismograms (in this case, transverse component) plotted as a function of epicentral distance Δ. The best-fitting curve is estimated using 26 non-basin and marginal basin stations whose seismograms exceed our signal-to-noise criteria. The closest station, AK.SAW, is not shown, as its value exceeds the plotting scale. (b) Record section filtered 0.10–0.82 Hz and corrected for geometrical spreading. Stations are sorted from top to bottom by increasing epicentral distance. The uncorrected record section is shown in Figure B.9.

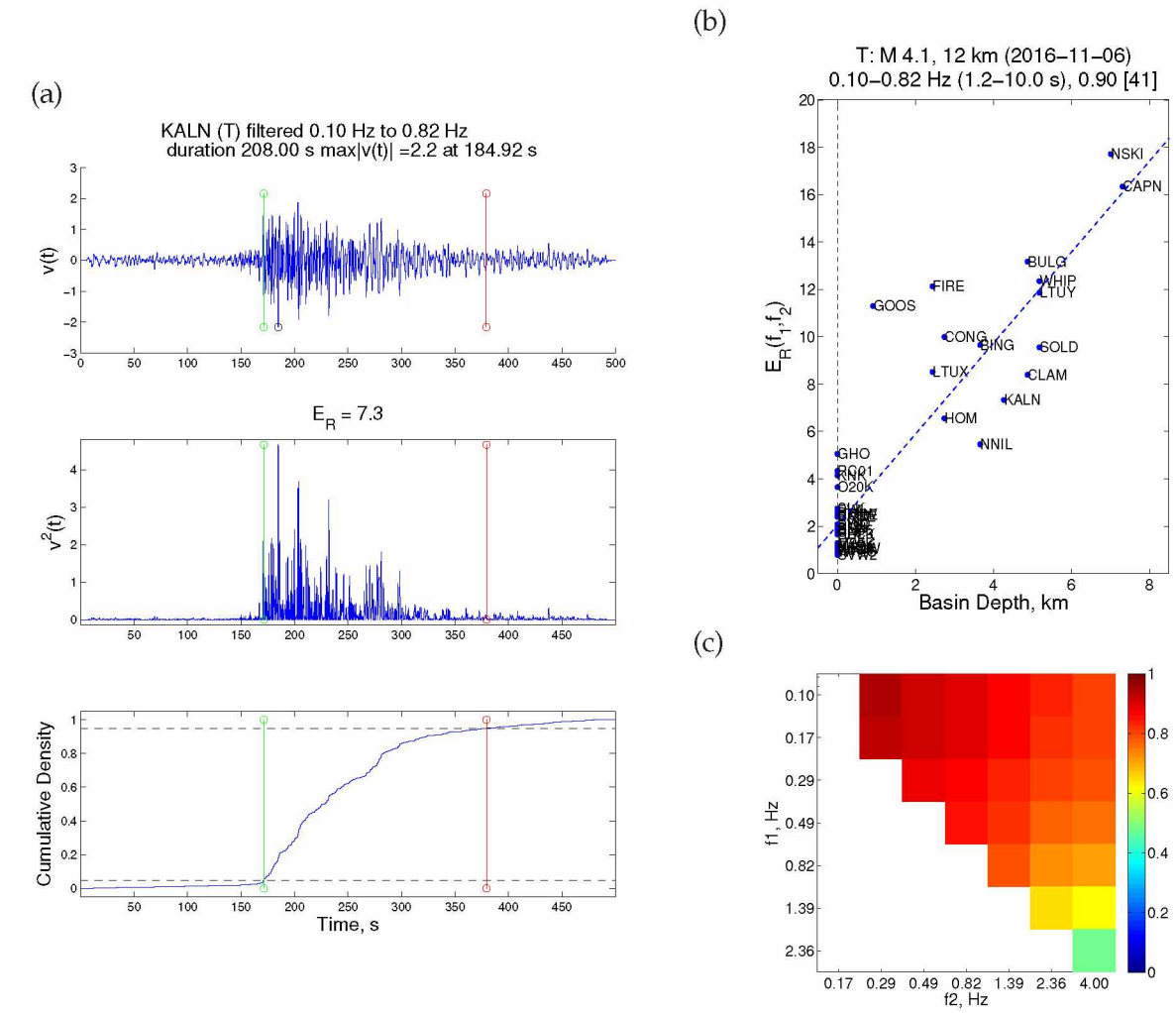

Figure 3.7: Construction of a matrix plot (c) from filtered seismograms. (a) Example calculation of metrics (dur, E_R) for a seismogram (KALN, T component, 0.10–0.82 Hz) from Figure 3.6b. Vertical lines denote the estimated start (t_1) and end (t_2) times for the duration, which are determined from the bottom plot. *Top:* Velocity seismogram. *Middle:* Squared waveform. The value of $E_R = 7.3$ is the integration of $v^2(t)$ between t_1 and t_2. *Bottom:* Cumulative squared waveform, normalized by E_R. The horizontal dashed lines are values of 0.05 and 0.95, used to determine the seismogram duration. (b) Scatterplot between a seismogram metric (E_R) and basin depth. Station KALN, from (a), is plotted at 4.3 km and $E_R = 7.3$. The correlation coefficient is 0.90, and the number in square brackets is the number of stations used. (c) Matrix plot, which displays a colored correlation coefficient for each bandpass $[f_1, f_2]$ applied to a set of seismograms. The correlation coefficient of 0.90, from (b), is represented by the box on the top row and fourth column. This matrix plot appears in row 2, column 3 of Figure 3.8.

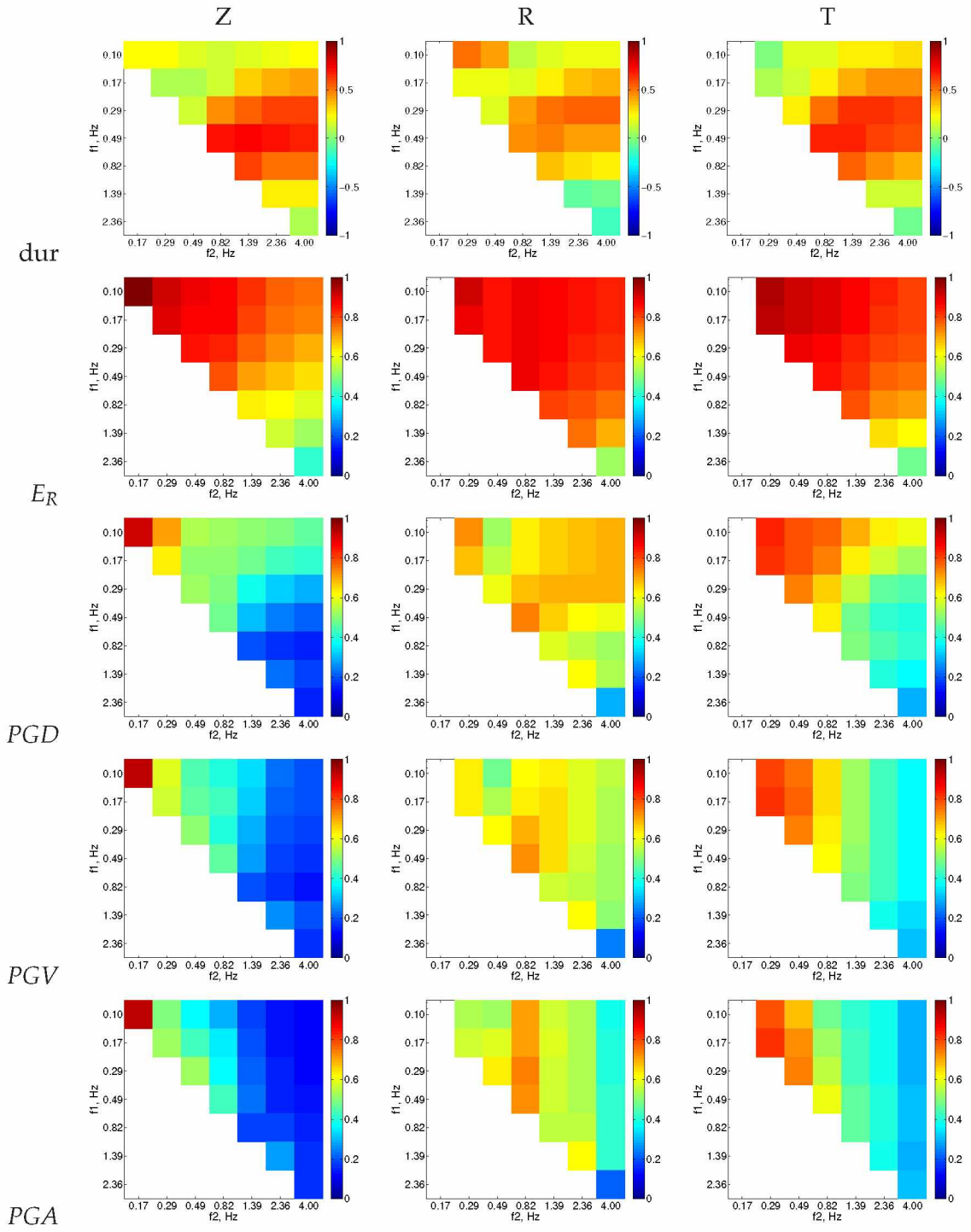

Figure 3.8: Matrix plots for earthquake metrics (dur, E_R, *PGD*, *PGV*, *PGA*) for thee components (Z vertical, R radial, T transverse). The earthquake is M_l 4.1 on 2016-11-06 with depth 12 km event in the Cook Inlet region. A full set of explanatory figures for earthquake metrics is shown in Figures 3.6–3.8.

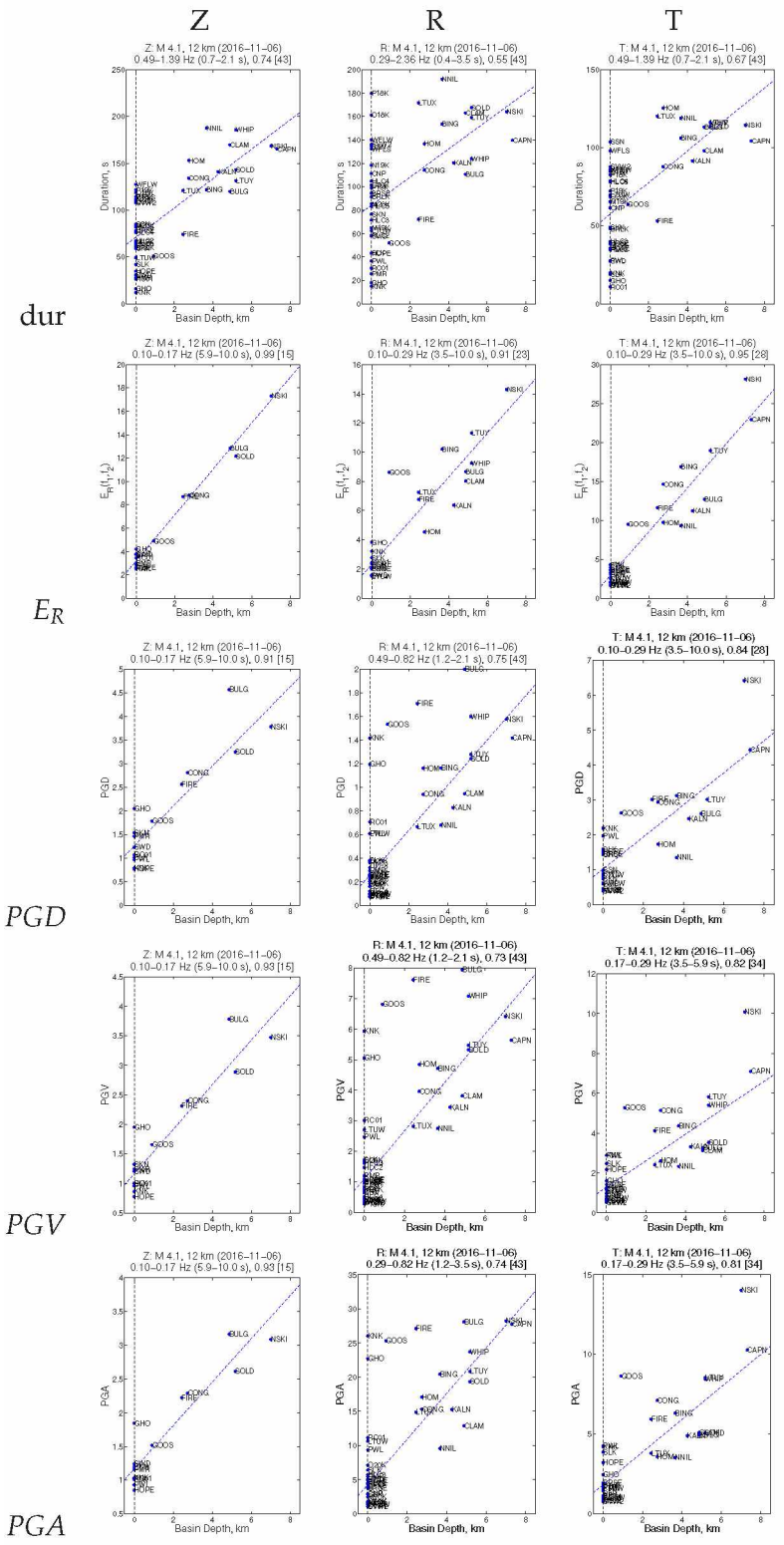

Figure 3.9: Scatterplots corresponding to the highest correlation coefficients in each of the 15 matrix plots in Figure 3.8. The bandpass filter may be different for each subplot. This may also affect the number of data points used, which is determined by the number of filtered seismic waveforms that exceed our signal-to-noise threshold.

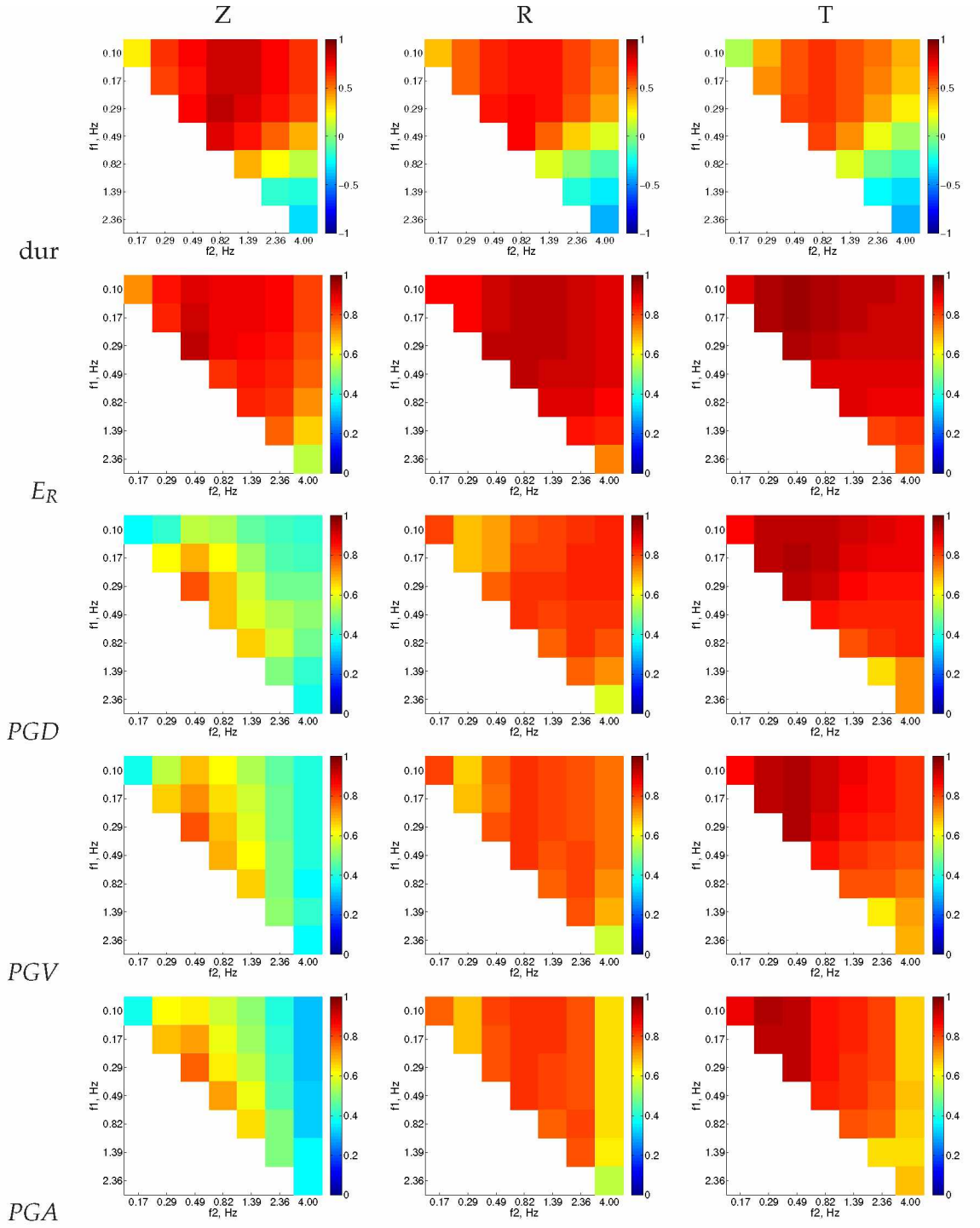

Figure 3.10: Matrix plots for earthquake metrics (dur, E_R, PGD, PGV, PGA) for thee components (Z vertical, R radial, T transverse). The earthquake is M_l 5.2 on 2015-07-25 with depth 126 km event in the Cook Inlet region.

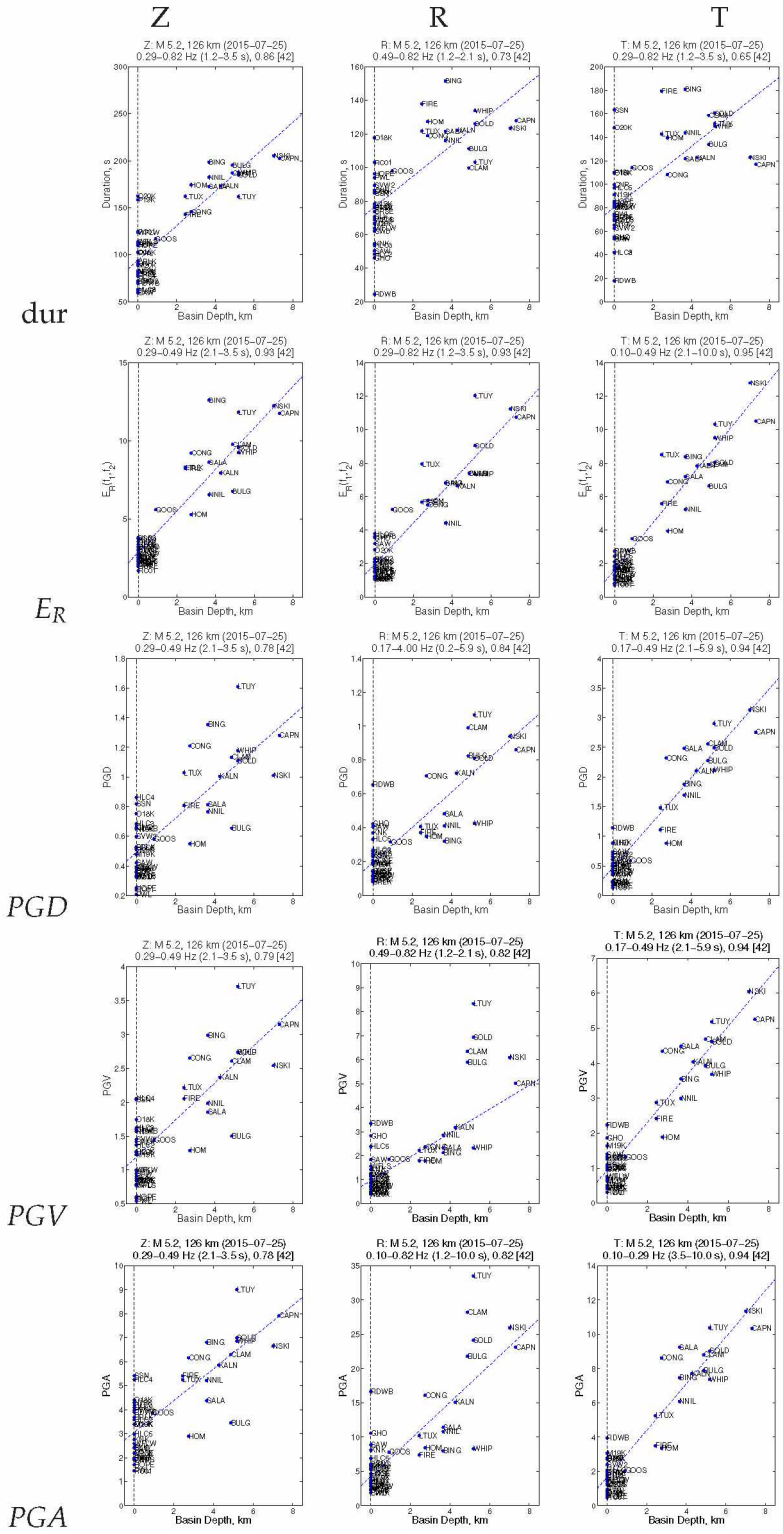

Figure 3.11: Scatterplots corresponding to the highest correlation coefficients in each of the 15 matrix plots in Figure 3.10.

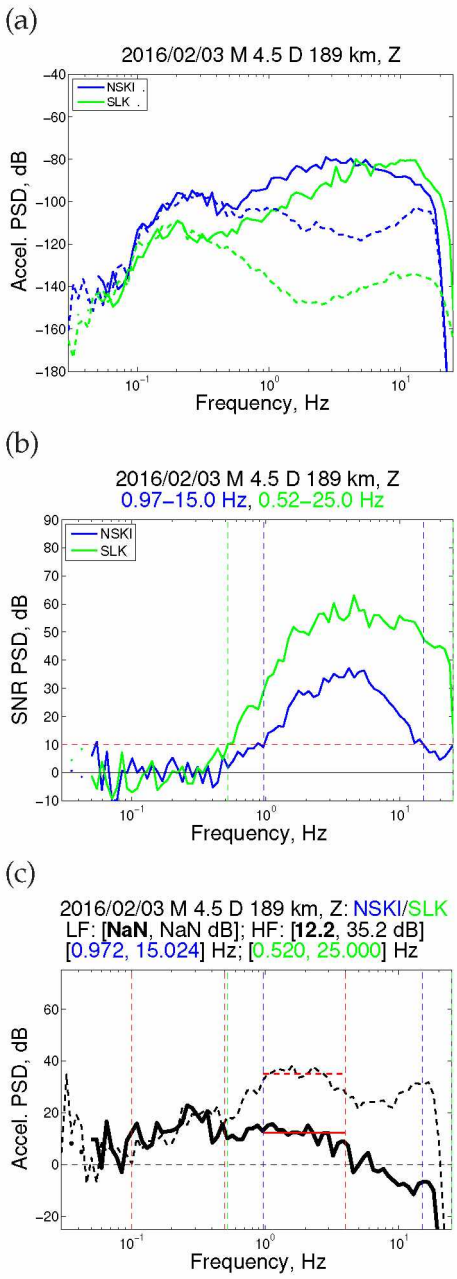

Figure 3.12: Example calculation of a spectral ratio for station NSKI, with respect to SLK, for a M_l 4.5 earthquake on 2016-02-03 at a depth of 189 km. The frequency range shown is between 0.03 Hz and 25 Hz. (a) Acceleration power spectra calculated using the method of McNamara & Buland (2004). Solid-line earthquake spectra are calculated from the 500 s following the origin time of the earthquake for target station NSKI and for reference station SLK. Dashed-line noise spectra are calculated from the 500 s prior to the origin time. (b) Signal-to-noise ratios (SNR) calculated by subtraction (in log space) of the dashed-line spectra in (a) from the solid-line spectra. The vertical dashed lines mark the frequency boundaries where the spectra exceed 10 dB (red horizontal dashed line); in this case, these are $[0.97, 15.0]$ Hz for NSKI and $[0.52, 25]$ Hz for SLK. (c) Spectral ratios (SR) between two stations, shown for an earthquake (solid) and for pre-earthquake noise (dashed). The vertical red dashed lines denote two intervals (0.1–0.5 Hz and 0.5–4.0 Hz) over which median measurements of the SR are made; the measurements are listed in the middle row of the title. The frequency intervals for the SR measurements may be reduced according to the SNR levels at the target station (blue) and the reference station (green). The SR measurements are denoted by horizontal red segments (solid and dashed) and are bounded by the vertical dashed red lines.

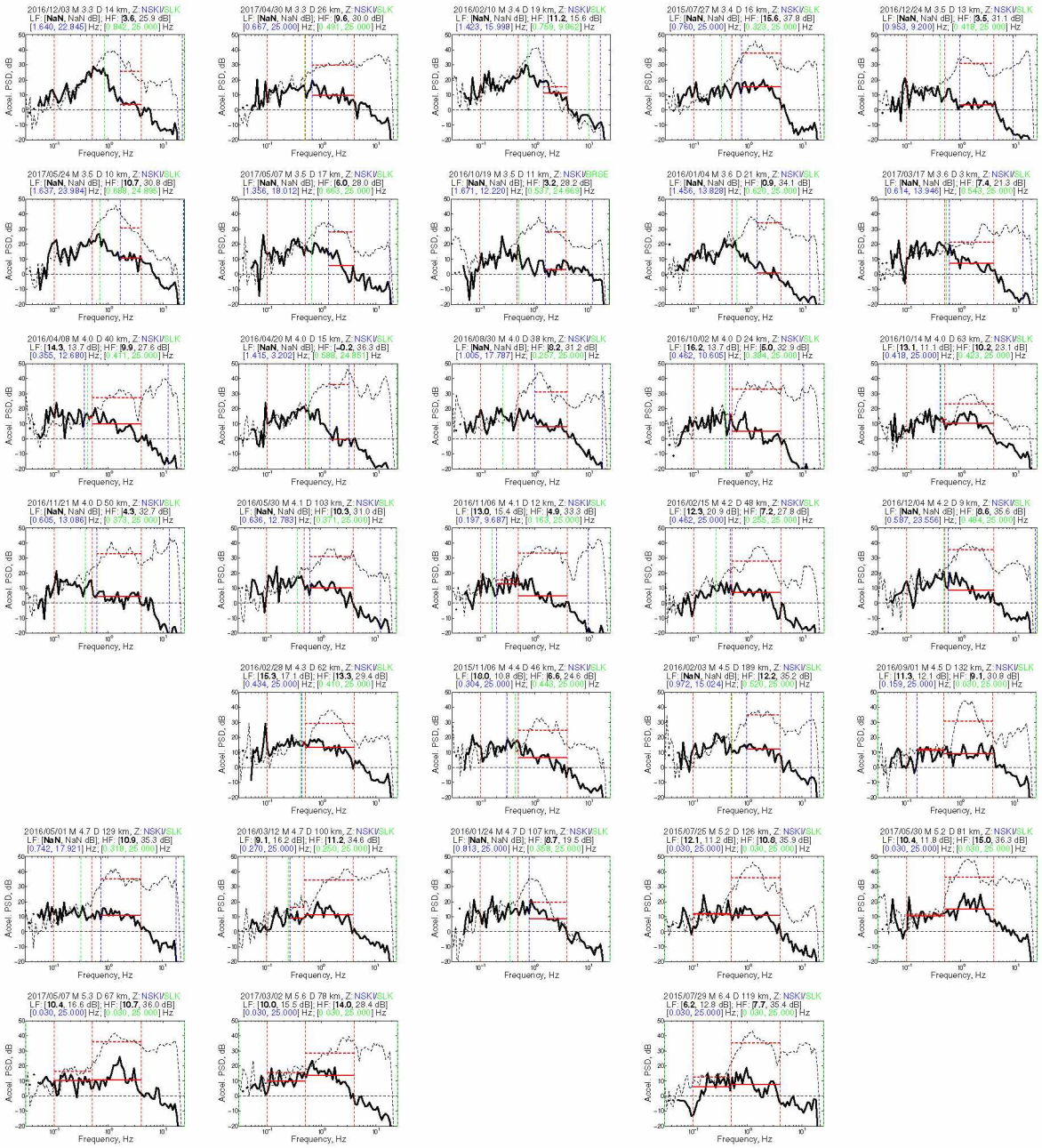

Figure 3.13: Spectral ratios (SR) between station NSKI (basin depth 7.0 km) and non-basin reference station SLK for a subset of 32/34 earthquakes sorted by increasing magnitude. The solid-line SR spectrum is for the earthquake; the dashed-line SR spectrum is for pre-earthquake noise. See Figure 3.12c for details.

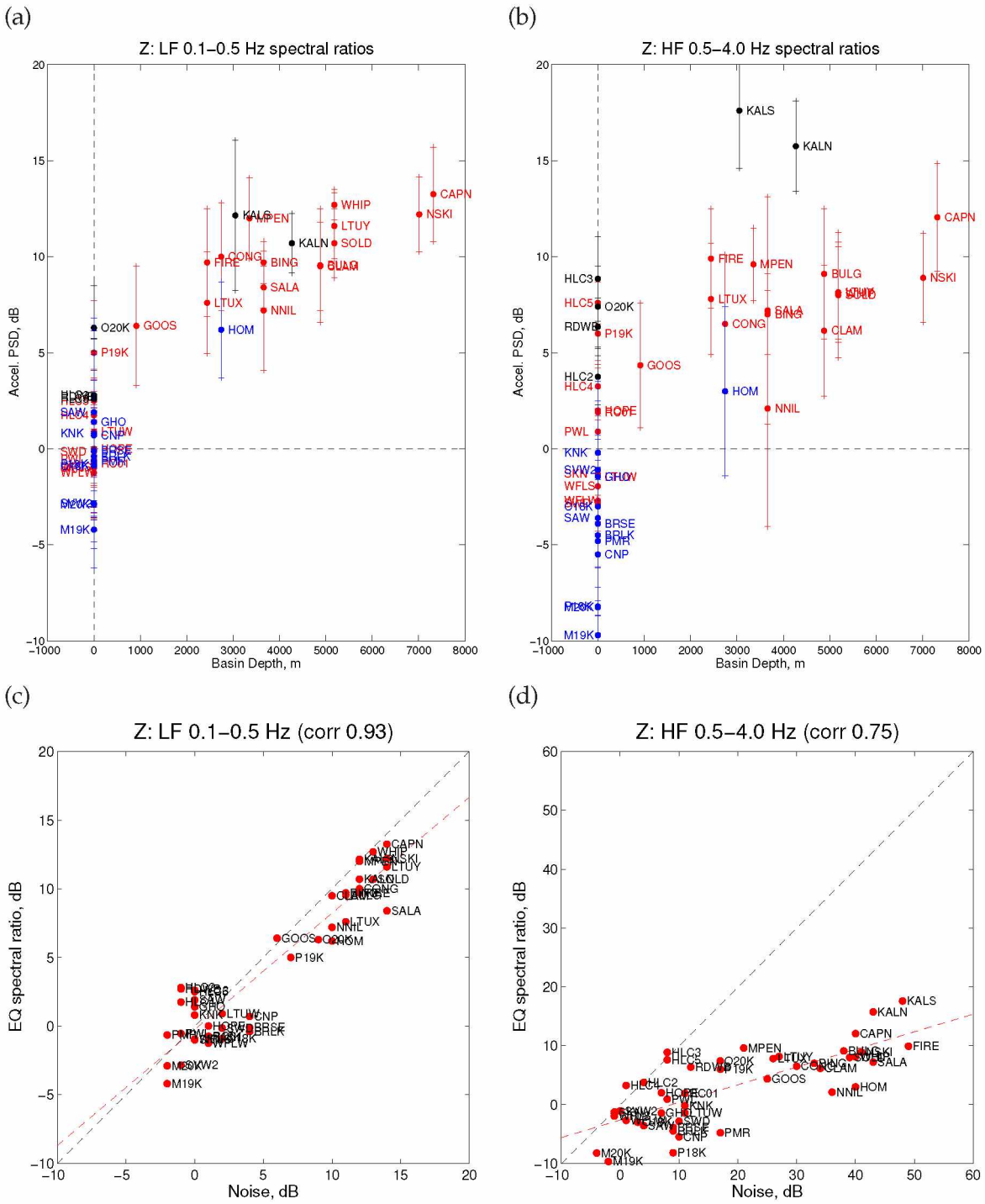

Figure 3.14: Summary of spectral ratio results for 45 seismic stations in the Cook Inlet region. (a) Spectral ratios for vertical component, 0.1–0.5 Hz. Each data point and error bar is derived from spectral ratios at one station for up to 34 earthquakes (see Table B.2); an example for one station is shown in Figure 3.13. The points are colored to highlight the influence of different distances from stations to events (see Results). See Figure B.10 for results for the radial and transverse components. (b) Same as (a) but for the high-frequency bandpass (0.5–4.0 Hz). (c) Comparison between vertical-component seismic power from earthquakes and from noise, calculated for the vertical component for 0.1–0.5 Hz. The noise values, on the x-axis, are from Figure 3.4b. The earthquake spectral ratios, on the y-axis, are from (a) (d) Same as (c) but for the high-frequency bandpass (0.5–4.0 Hz). The noise and earthquake data are in general agreement for 0.1–0.5 Hz but not for 0.5–4.0 Hz.

3.13 References

Anderson, J. G., Bodin, P., Brune, J. N., Prince, J., Singh, S. K., Quaas, R., & Onate, M., 1986. Strong ground motion from the Michoacan, Mexico, earthquake, *Science*, **233**, 1043–1049.

Bard, P.-Y. & Bouchon, M., 1980. The seismic response of sediment-filled valleys. Part 1. The case of incident *SH* waves, *Bull. Seismol. Soc. Am.*, **70**(4), 1263–1286.

Bard, P.-Y. & Bouchon, M., 1985. The two-dimensional resonance of sediment-filled valleys, *Bull. Seismol. Soc. Am.*, **75**(2), 519–541.

Bard, P.-Y., Campillo, M., Chávez-Garcia, F. J., & Sánchez-Sesma, F., 1988. The Mexico earthquake of September 19, 1985—A theoretical investigation of large- and small-scale amplification effects in the Mexico City valley, *Earthquake Spectra*, **4**(3), 609–633.

Beyreuther, M., Barsch, R., Krischer, L., Megies, T., Behr, Y., & Wassermann, J., 2010. ObsPy: A Python toolbox for seismology, *Seismol. Res. Lett.*, **81**(3), 530–533, doi: 10.1785/gssrl.81.3.530.

Bindi, D., Parolai, S., Cara, D., Di Giulio, G., Ferretti, G., Luzi, L., Monachesi, G., Pacor, F., & Rovelli, A., 2009. Site amplifications observed in the Gubbio basin, central Italy: Hints for lateral propagation effects, *Bull. Seismol. Soc. Am.*, **99**(2A), 741–760, doi: 10.1785/0120080238.

Borcherdt, R. D., 1970. Effects of local geology on ground motion near San Francisco Bay, *Bull. Seismol. Soc. Am.*, **60**(1), 29–61.

Bowden, D. C. & Tsai, V. C., 2017. Earthquake ground motion amplification for surface waves, *Geophys. Res. Lett.*, **44**, 121–127, doi: 10.1002/2016GL071885.

Carder, D. S., 1963. The Requirements of a High-Sensitivity Seismograph Stations, VESIAC State-of-the-Art Report 4410-63-X, Acoustics and Seismic Laboratory, Institute of Science and Technology, University of Michigan, Ann Arbor, Michigan, 72 pp.

Casey, R., Templeton, M. E., Sharer, G., Keyson, L., Weertman, B. R., & Ahern, T., 2018. Assuring the quality of IRIS data with MUSTANG, *Seismol. Res. Lett.*, **89**(2A), 630–639, doi: 10.1785/0220170191.

Choi, Y., Stewart, J. P., & r. W. Graves, 2005. Empirical model for basin effects accounts for basin depth and source location, *Bull. Seismol. Soc. Am.*, **95**(4), 1412–1427, doi: 10.1785/0120040208.

Clift, P. & Vannucchi, P., 2004. Controls on tectonic accretion versus erosion in subduction zones: Implications for the origin and recycling of the continental crust, *Rev. Geophys.*, **42**, 1–31, 2003RG000127.

Cruz-Atienza, V. M., Tago, J., Sanabria-Gómez, J. D., Chaljub, E., Etienna, V., Virieux, J., & Quintanar, L., 2016. Long duration of ground motion in the paradigmatic Valley of Mexico, *Sci. Rep.*, **6**, 38807, doi: 10.1038/srep38807.

Dahlen, F. A., 2005. Finite-frequency sensitivity kernels for boundary topography perturbations, *Geophys. J. Int.*, **162**, 525–540, doi: 10.1111/j.1365-246X.2005.02682.x.

Day, S. M., Graves, R., Bielak, J., Dreger, D., Larsen, S., Olsen, K. B., Pitarka, A., & Ramirez-Guzman, L., 2008. Model for basin effects on long-period response spectra in southern California, *Earthquake Spectra*, **24**(1), 257–277.

Doser, D. I. & Brown, W. A., 2001. A study of historic earthquakes of the Prince William Sound, Alaska, Region, *Bull. Seismol. Soc. Am.*, **91**(4), 842–857.

Eberhart-Phillips, D., Christensen, D. H., Brocher, T. M., Hansen, R., Ruppert, N. A., Haeussler, P. J., & Abers, G. A., 2006. Imaging the transition from Aleutian subduction to Yakutat collision in central Alaska, with local earthquakes and active source data, *J. Geophys. Res.*, **111**, B11303, doi: 10.1029/2005JB004240.

Feng, L. & Ritzwoller, M. H., 2017. The effect of sedimentary basins on surface waves that pass through them, *Geophys. J. Int.*, **211**, 572–592, doi: 10.1093/gji/ggx313.

Field, E. & Jacob, K., 1993. The theoretical response of sedimentary layers to ambient seismic noise, *Geophys. Res. Lett.*, **20**(24), 2925–2928.

Fisher, M. A. & Magoon, L. B., 1978. Geologic framework of lower Cook Inlet, *Am. Assoc. Petroleum Geol. Bull.*, **62**(3), 373–402.

Fletcher, J. B. & Wen, K.-L., 2005. Strong ground motion in the Taipei basin from the 1999 Chi-Chi, Taiwan, earthquake, *Bull. Seismol. Soc. Am.*, **95**(4), 1428–1446, doi: 10.1785/0120040022.

Frankel, A., 1993. Three-dimensional simulations of ground motions in the San Bernadino Valley, California, for hypothetical earthquakes on the San Andreas fault, *Bull. Seismol. Soc. Am.*, **83**(4), 1020–1041.

Frankel, A., Stephenson, W., & Carver, D., 2009. Sedimentary basin effects in Seattle, Washington: Ground-motion observations and 3D simulations, *Bull. Seismol. Soc. Am.*, **99**(3), 1579–1611, doi: 10.1785/0120080203.

Grapenthin, R., West, M., Tape, C., Gardine, M., & Freymueller, J., 2018. Single-frequency instantaneous GNSS velocities resolve dynamic ground motion of the 2016 M_w 7.1 Iniskin, Alaska, earthquake, *Seismol. Res. Lett.*, **89**(3), 1040–1048, doi: 10.1785/0220170235.

Graves, R. W., Pitarka, A., & Somerville, P. G., 1998. Ground-motion amplification in Santa Monica area: Effects of shallow basin-edge structure, *Bull. Seismol. Soc. Am.*, **88**(5), 1224–1242.

Gregersen, L. S. & Shellenbaum, D. P., 2016. Top Mesozoic unconformity subcrop map, Cook Inlet basin, Alaska, Alaska Div. Geol. Geophys. Surv. Report of Investigation 2016-4, 1 sheet, scale 1:500,000, available at http://www.dggs.alaska.gov/pubs/id/29658 (last accessed 2016-10-30).

Gutenberg, B., 1957. Effects of ground on earthquake motion, *Bull. Seismol. Soc. Am.*, **47**(3), 221–250.

Haeussler, P. J., Bruhn, R. L., & Pratt, T. L., 2000. Potential seismic hazards and tectonics of the upper Cook Inlet basin, Alaska, based on analysis of Pliocene and younger deformation, *Geol. Soc. Am. Bull.*, **112**(9), 1414–1429.

Hayes, G. P., Moore, G. L., Portner, D. E., Hearne, M., Flamme, H., Furtney, M., & Smoczyk, G. M., 2018. Slab2, a comprehensive subduction zone geomety model, *Science*, doi: 10.1126/science.aat4723.

Hisada, Y. & Yamamoto, S., 1996. One-, two-, and three-dimensional site effects in sediment-filled basins, in *Proceedings of the Eleventh World Conference on Earthquake Engineering*, Acapulco, Mexico, June 23–28, 1996, Paper No. 2040.

Joyner, W., 2000. Strong motion from surface waves in deep sedimentary basins, *Bull. Seismol. Soc. Am.*, **90**(6B), S95–S112.

Kawase, H., 1996. The cause of the damage belt in Kobe: "The basin-edge effect," constructive interference of the direct S-wave with the basin-induced diffracted/Rayleigh waves, *Seismol. Res. Lett.*, **67**(5), 25–34.

Koehler, R. D., Farrell, R.-E., Burns, P. A. C., & Combellick, R. A., 2012. Quaternary faults and folds in Alaska: A digital database, Alaska Div. Geol. Geophys. Surv. Miscellaneous Publication 141, 31 p., 1 sheet, scale 1:3,700,000.

Krischer, L., Mengies, T., Barsch, R., Beyreuther, M., Lecocq, T., Caudron, C., & Wassermann, J., 2015. ObsPy: a bridge for seismology into the scientific Python ecosystem, *Computational Science & Discovery*, **8**(1), 014003, doi: 10.1088/1749-4699/8/1/014003.

Lawson, A. C., 1908. *The California Earthquake of April 18, 1906: Report of the State Earthquake Investigation Commission in two volumes and atlas*, vol. 1, Carnegie Institution, Washington, D.C.

Li, J., Abers, G. A., Kim, Y., & Christensen, D., 2013. Alaska megathrust 1: Seismicity 43 years after the great 1964 Alaska megathrust earthquake, *J. Geophys. Res.*, **118**, 4861–4871, doi: 10.1002/jgrb.50358.

Liu, C., Lay, T., Xie, Z., & Xiong, X., 2019. Intraslab deformation in thr 30 November 2018 Anchorage, Alaska, M_w 7.1 earthquake, *Geophys. Res. Lett.*, **46**, 2449–2457, doi: 10.1029/2019GL082041.

Lomnitz, C., 1988. The 1985 Mexico earthquake, in *Natural and Man-Made Hazards: Proceedings of the International Symposium held at Rimouski, Quebec, Canada, 3–9 August, 1986*, pp. 63–79, eds El-Sabh, M. I. & Murty, T. S., D. Riedel.

McNamara, D. E. & Buland, R. P., 2004. Ambient noise levels in the continental United States, *Bull. Seismol. Soc. Am.*, **94**(4), 1517–1527, doi: 10.1785/012003001.

Moschetti, M. P., Hartzell, S., Ramírez-Guzmán, L., Frankel, A. D., Angster, S. J., & Stephenson, W. J., 2017. 3D ground-motion simulations of M_w 7 earthquakes on the Salt Lake City segment of the Wasatch fault zone: Variability of long-period ($T \geq 1$ s) ground motions and sensitivity to kinematic rupture parameters, *Bull. Seismol. Soc. Am.*, **107**(4), 1704–1723, doi: 10.1785/0120160307.

Moschetti, M. P., Thompson, E. M., Rekoske, J., Hearne, M. G., Powers, P. M., McNamara, D., & Tape, C., 2019. Ground-motion amplification in Cook Inlet Region, Alaska from intermediate-depth earthquakes, including the 2018 M_w 7.1 Anchorage earthquake, *Seismol. Res. Lett.*, **91**(1), 142–152, doi: 10.1785/0220190179.

Olsen, K. B., 2000. Site amplification in the Los Angeles basin from three-dimensional modelling of ground motion, *Bull. Seismol. Soc. Am.*, **60**(6B), S77–S94, doi: 10.1785/0120000506.

Peterson, J., 1993. Observations and Modeling of Seismic Background Noise, Open-File Report 93-322.

Pratt, T. L., Brocher, T. M., Weaver, C. S., Creager, K. C., Snelson, C. M., Crosson, R. S., Miller, K. C., & Trehu, A. M., 2003. Amplification of seismic waves by the Seattle basin, Washington state, *Bull. Seismol. Soc. Am.*, **93**(2), 533–545.

Rial, J. A., Saltzman, N. G., & Ling, H., 1992. Earthquake-induced resonance in sedimentary basins, *American Scientist*, **80**, 566–578.

Saltus, R. W., Stanley, R. G., Haeussler, P. J., Jones III, J. V., Potter, C. J., & Lewis, K. A., 2016. Late Oligocene to present contractional structure in and around the Susitna basin, Alaska—Geophysical evidence and geological implications, *Geosphere*, **12**(5), 1–13, doi: 10.1130/GES01279.1.

Sánchez-Sesma, F. & Luzón, F., 1995. Seismic response of three-dimensional alluvial valleys for incident *P*, *S*, and Rayleigh waves, *Bull. Seismol. Soc. Am.*, **85**(1), 269–284.

Shellenbaum, D. P., Gregersen, L. S., & Delaney, P. R., 2010. Top Mesozoic unconformity depth map of the Cook Inlet Basin, Alaska, Alaska Div. Geol. Geophys. Surv. Report of Investigation 2010-2, 1 sheet, scale 1:500,000, available at http://www.dggs.alaska.gov/pubs/id/21961 (last accessed 2016-10-30).

Silwal, V. & Tape, C., 2016. Seismic moment tensors and estimated uncertainties in southern Alaska, *J. Geophys. Res. Solid Earth*, **121**, 2772–2797, doi: 10.1002/2015JB012588.

Silwal, V., Tape, C., & Lomax, A., 2018. Crustal earthquakes in the Cook Inlet and Susitna region of southern Alaska, *Tectonophysics*, **745**, 245–263, doi: 10.1016/j.tecto.2018.08.013.

Smith, K., 2019. Supplement to "Seismic response of Cook Inlet sedimentary basin, southern Alaska", ScholarWorks@UA at http://hdl.handle.net/11122/10568 (last accessed July 2019): descriptor file, figures of seismic noise spectra, ground motion metrics, and spectral ratios.

Sorrells, G. G., McDonald, J. A., Der, Z. A., & Herrin, E., 1971. Earth motion caused by local atmospheric pressure changes, *Geophys. J. R. Astron. Soc.*, **26**, 83–98.

Stanley, R. G., Haeussler, P. J., Benowitz, J. A., Goodman, D. K., Ravn, R. L., Shellenbaum, D. P., Saltus, R. W., Lewis, K. A., & Potter, C. J., 2013. New stratigraphic revelations in the subsurface Susitna basin, south-central Alaska, from geochronology and biostratigraphy [poster]: GSA Cordilleran Section Meeting, Fresno, CA, May 22, 2013: Alaska Division of Geological & Geophysical Surveys, 1 sheet. http://doi.org/10.14509/26887.

Stein, S. & Wysession, M., 2003. *An Introduction to Seismology, Earthquakes, and Earth Structure*, Blackwell, Malden, Mass., USA.

Tape, C., Christensen, D., Moore-Driskell, M. M., Sweet, J., & Smith, K., 2017. Southern Alaska Lithosphere and Mantle Observation Network (SALMON): a seismic experiment covering the active arc by road, boat, plane, and helicopter, *Seismol. Res. Lett.*, **88**(4), 1185–1202, doi: 10.1785/0220160229.

Tape, C., Heath, D. C., Baker, M. G., Dalton, S., Aderhold, K., & West, M. E., 2019. Bear encounters with seismic stations in Alaska and northwestern Canada, *Seismol. Res. Lett.*, **90**(5), 1950–1970, doi: 10.1785/0220190081.

Tong, P., Komatitsch, D., Tseng, T.-L., Hung, S.-H., Chen, C.-W., Basini, P., & Liu, Q., 2014. A 3-D spectral-element and frequency-wave number hybrid method for high-resolution seismic array imaging, *Geophys. Res. Lett.*, **41**, 7025–7034, doi: 10.1002/2014GL061644.

Tsai, V. C., Bowden, D. C., & Kanamori, H., 2017. Explaining extreme ground motion in Osaka basin during the 2011 Tohoku earthquake, *Geophys. Res. Lett.*, **44**, 7239–7244, doi: 10.1002/2017GL074120.

Wald, D. J. & Graves, R. W., 1998. The seismic response of the Los Angeles basin, California, *Bull. Seismol. Soc. Am.*, **88**(2), 337–356.

Wang, Y. & Tape, C., 2014. Seismic velocity structure and anisotropy of the Alaska subduction zone derived from surface wave tomography, *J. Geophys. Res. Solid Earth*, **119**, 8845–8865, doi: 10.1002/2014JB011438.

Ward, K. M. & Lin, F.-C., 2018. Lithospheric structure across the Alaskan cordillera from the joint inversion of surface waves and receiver functions, *J. Geophys. Res. Solid Earth*, **123**, 8780–8797, doi: 10.1029/2018JB015967.

West, M. E., Bender, A., Gardine, M., Gardine, L., Gately, K., Haeussler, P., Hassan, W., Meyer, F., Richards, C., Ruppert, N. A., Tape, C., Thornley, J., & Witter, R., 2019. The 30 November 2018 M_w7.1 Anchorage earthquake, *Seismol. Res. Lett.*, **91**(1), 66–84, doi: 10.1785/0220190176.

Wirth, E. A., Vidale, J. E., Frankel, A. D., Pratt, T. L., Marafi, N. A., Thompson, M., & Stephenson, W. J., 2019. Source-dependent amplification of earthquake ground motions in deep sedimentary basins, *Geophys. Res. Lett.*, **46**, 6443–6450, doi: 10.1029/2019GL082474.

Yoshimoto, K. & Takemura, S., 2014. A study on the predominant period of long-period ground motions in the Kanto Basin, Japan, *Earth Planets Space*, **66**, 100, doi: 10.1186/1880-5981-66-100.

Zweck, C., Freymueller, J. T., & Cohen, S. C., 2002. Three-dimensional elastic dislocation modeling of the postseismic response to the 1964 Alaska earthquake, *J. Geophys. Res.*, **107**(B4), 2064, doi: 10.1029/2001JB000409.

Chapter 4

Seismic response of Nenana sedimentary basin, central Alaska[1]

4.1 Abstract

Nenana basin in central Alaska is a long (90 km), narrow (12 km), deep (7 km) sedimentary basin aligned with an active fault zone producing $M_w \geq 6$ earthquakes. From 2015–2019, 16 broadband seismic stations were deployed in the region as part of the FLATS (Fault Locations and Alaska Tectonics from Seismicity) project. These stations recorded a wide range of earthquakes, including M_w 3–4 directly below the basin, as well as several regional earthquakes $M_w > 6$. These 43 local and regional earthquakes, in addition to 5 teleseismic events and also continuously recorded ambient noise, provide a data set which we use to quantify the response of Nenana basin to the seismic wavefield. We calculate spectral ratios between each station and a bedrock reference station (XV.F8KN) for 48 earthquakes. We find amplification of 11–14 dB (amplification ratio 3.5–5.0) for low frequencies (0.1–0.5 Hz), and 8–15 dB (amplification ratio 2.5–5.6) for high frequencies (0.5–4.0 Hz) on the vertical component. At low frequencies, amplification of the earthquake wavefield agrees well with amplification of seismic noise, with both data sets exhibiting stronger amplification on the horizontal components, in comparison with the vertical component. Furthermore, stations overlying the deeper part of the basin exhibit stronger amplification, while stations at the margin of the basin exhibit minimal amplification. At higher frequencies, amplification occurs at both deeper basin stations and also marginal basin stations. Our study establishes a catalog of diverse events for future theoretical and numerical studies that can use Nenana basin to better understand the complex influence of sedimentary basins on the seismic wavefield. At a regional scale, we hope to better understand the expected ground motion of a M_w 7 scenario earthquake on the Minto Flats fault zone beneath the basin.

4.2 Introduction

Nenana basin is a major sedimentary basin in central Alaska and associated with an active fault zone producing $M_w \geq 6$ earthquakes (Figure 4.1). Prior to 2014, no seismic station had been installed in Nenana basin. In August 2014 the first of 13 broadband seismic stations was installed

[1]To be published as: Smith, K., C. Tape, and V. Tsai (2020), Seismic response of Nenana sedimentary basin, central Alaska, *Bull. Seismol. Soc. Am.* (in prep.)

in the Minto Flats region as part of an experiment entitled Fault Locations and Alaska Tectonics from Seismicity (FLATS) (Figure 4.1).

This study builds upon two recent publications. In Smith & Tape (2019a) we documented the influences of environment (wind, river) and structure (basin or not) on ambient seismic noise in the Minto Flats region of central Alaska. Here, following the approach of Smith & Tape (2019b), we examine basin amplification due to local, regional, and teleseismic earthquakes. The combined data set of earthquake recordings and ambient noise allows us to characterize the influence of Nenana basin on the seismic wavefield across a wide range of frequencies.

Our main objective is to use a set of high-quality stations installed in a large sedimentary basin to better understand the complex influence of basins on the seismic wavefield. Examples of data-based studies of specific basins include Pratt et al. (2003), Bindi et al. (2009), and Yoshimoto & Takemura (2014). These studies provide measurements and catalogs of earthquakes for testing theoretical and numerical models for basin effects (Bard et al., 1988; Sánchez-Sesma & Luzón, 1995; Day et al., 2008; Cruz-Atienza et al., 2016; Bowden & Tsai, 2017; Tsai et al., 2017; Wirth et al., 2019). A second objective is to better understand events within the tectonically active setting of the Minto Flats, a region that has produced exotic events, such as very-low-frequency earthquakes and also earthquakes preceded by a nucleation signal (Tape et al., 2018). Our final motivation is to better understand how local larger earthquakes, such as M_w 6-7, might be influenced by the structure of Nenana basin. Data from smaller, local earthquakes can help establish the basin response, while future numerical studies can extrapolate the observations to larger earthquakes, similar to efforts in southern California (Olsen et al., 2006; Graves et al., 2011). With the FLATS deployment of 13 stations from 2015–2019, we quantify the amplification in Nenana basin from 48 earthquakes and from ambient noise.

4.3 Minto Flats Fault Zone and Nenana Basin

Several sub-parallel, northeast-striking seismic zones are visible in the greater Fairbanks area of central Alaska. These have been categorized into three seismic zones (Biswas & Tytgat, 1988; Page et al., 1995): from east to west, these are the Salcha seismic zone (Biswas & Tytgat, 1988), the Fairbanks seismic zone (Gedney et al., 1980), and the Minto Flats seismic zone (Gedney et al., 1972; Pulpan, 1986). The largest known earthquakes on these faults occurred on 1937-07-22 M_s 7.3

(Abe & Noguchi, 1983), 1967-06-21 M_w 5.9 (Page et al., 1991), and 1995-10-06 M_w 6.0 (Dziewonski et al., 1981; Ekström et al., 2012). Another notable earthquake that strongly shook the Minto Flats region occurred to the south on 1947-10-16 M_s 7.2 (Abe & Noguchi, 1983). Analyzing earthquake focal mechanisms, including for the 1995 earthquake and its aftershocks, Ratchkovski & Hansen (2002) characterized the Minto Flats seismic zone as left-lateral strike slip faulting, consistent with the tectonic model proposed by Page et al. (1995).

Within the Fairbanks and Minto Flats seismic zones, Page et al. (1995) noted that "activity is not confined to a single linear feature; thus, it intimates the possible presence of overlapping parallel faults, splays, and cross faults" (p. 631). Tape et al. (2013) examined log-scaled seismicity rates and digitized two seismic lineaments within the Minto Flats seismic zone (Figure 4.1). Tape et al. (2015) examined the highest-quality, largest-magnitude earthquakes in the fault zone and found an overall consistent pattern of strike-slip faulting, suggestive of left-lateral faulting on the northeast-striking faults. Although there is seismic evidence for two primary faults in the fault zone, there is no geological expression of the faults at the surface (Koehler et al., 2015).

A geophysical map of the variations in gravity in central Alaska reveals a conspicuous low anomaly northwest of the town of Nenana (Barnes, 1961; Saltus et al., 2008). This gravity-low coincides with Minto Flats, where the Tanana River flows from Nenana to Manley Hot Springs and eventually into the Yukon River. Two-dimensional active-source seismic data revealed the basin, and the map of Ehm (1983) included detailed depth contours up to 6 km for the basin (labeled "Middle Tanana basin"). Kirschner (1988) labeled the basin as Nenana and reported: "Gravity data, outcrop data, and the data from one exploratory test well are interpreted to indicate 1 to 3 km of less dense, nonmarine, coal-bearing Cenozoic fill in northwestern part of basin." In the 2000s Doyon Limited began a large-scale geophysical exploration effort of Nenana basin, including airborne magnetic and gravity surveys, 3D active source data, and four exploratory wells (2009 Nunivak #1, 2013 Nunivak #2, 2016 Toghotthele #1, 2018 Toghotthele #2). Van Kooten et al. (2012) documented the subsurface geometry and structure of Nenana basin derived from some of these data. Tape et al. (2015) identified the basin's relationship with respect to the two northeast-trending seismic lineaments that comprise the Minto Flats fault zone. They invoked a transtensional setting to account for the active faulting and basin development over the past few

million years. Dixit et al. (2017) provided a tectonic reconstruction of the basin, including its origin as a graben system in the Late Paleocene.

Basement surface maps of Nenana basin exhibit significant variations, especially for the deepest parts of the basin, for which only gravity data (combined with measured rock and sediment densities) have been used. The basement map of Doyon Limited (2012), used in Van Kooten et al. (2012) and Tape et al. (2015), has a maximal depth of 8.2 km. The map of Dixit (2017) has a maximal depth of 6.6 km, and the map by PRA (2017), used here and shown in Figure 4.1, has a maximal depth of 6.7 km. Based on these maps, we characterize Nenana basin as having approximate dimensions of 90 km long, 12 km wide, and 7 km deep. The Minto Flats fault zone, as defined by the two main seismic lineaments, is 180 km long, including a 67 km overlapping section with a separation of 10 km (Figure 4.2b) (Tape et al., 2015).

4.4 Methods

4.4.1 Station Selection

Our analysis of Nenana basin focuses on the same 16 stations in Smith & Tape (2019a), including 13 stations from the FLATS deployment and three additional bedrock stations (AK.NEA2, TA.I23K, AK.MLY) (Figure 4.1, Table C.1). Two FLATS stations (F3TN and FPAP) were installed in September 2014, while the remaining stations were installed in September 2015. All FLATS stations were removed in September 2019. For some of the analyses of high-frequency noise, we excluded stations FPAP and FAPT—both of which are near the town of Nenana—because we assume these stations are influenced by cultural noise (e.g., Smith & Tape, 2019a, Figure 3).

For some analyses, we use the sedimentary thickness—or basin depth—beneath each station. We use these depths to categorize the 13 stations into 2 non-basin stations (FTGH, F8KN), 4 marginal basins (FPAP, FAPT, F6TP, F7TV) and 7 basin stations (F1TN, F2TN, F3TN, F4TN, F5TN, FNN1, FNN2). We assign basin depths of 1 km to the four marginal basin stations that are outside the coverage of PRA (2017).

4.4.2 Earthquake Selection

Events for analysis were selected from the Alaska Earthquake Center (AEC) catalog. The date range for event selection was 2015-09-01 to 2019-10-01, spanning the deployment of all 13 FLATS stations. Our goal was to obtain a set of events having maximal signal-to-noise levels across the widest range of frequencies. We also wanted a set of events spanning the widest range of azimuthal incidence and vertical incidence. To achieve these objectives, we focus on three subsets of events.

The first subset includes all 11 $M_l \geq 3.0$ earthquakes within the Minto Flats fault zone (see W-E-N-S regions in Tape et al. (2015), Fig. 4b). The largest events in this subset were 2019-04-11 M_w 4.15, directly beneath Nenana basin, and 2016-12-08 M_w 4.35 and 2016-11-06 M_w 4.00, which were south of Nenana basin, near the town of Anderson.

The second subset includes local and regional Alaska earthquakes, which we select by following a reproducible, *ad hoc* procedure. Centered at station F3TN, we draw four small circles with arc-distance radii of 30, 120, 500, and 1200 km. We partition each annulus into 12 azimuthal sections of 30° each. This gives 48 regions, each of which is divided into two subvolumes at a depth boundary of 30 km. By only selecting the largest events from each of the 96 subvolumes, we obtain a reasonable number of distinct events. For each subvolume with $\Delta < 30$ km, we keep the largest 2 events with $M_l \geq 3.0$. For $\Delta = 30$–120 km, we keep the largest 2 events with $M_l \geq 3.5$. For $\Delta = 120$–500 km, we keep the largest 3 events with $M_l \geq 4.5$. For $\Delta = 500$–1200 km, we keep the largest 2 events with $M_l \geq 6.0$. This procedure starts with 5144 events $M_l \geq 3.0$ within 1200 km of F3TN and finishes with 39 events.

The third subset includes all four $M_w \geq 8$ earthquakes in the GCMT catalog (Dziewonski et al., 1981; Ekström et al., 2012) from our time window, in addition to the 2017-09-03 North Korea nuclear explosion (Wang et al., 2018), which generated unusual (relative to earthquakes) body waves and was well-recorded in Alaska. We also note that for one event (2015-09-16), our study region of Nenana basin is in the shadow zone for the P wave, meaning that the arriving P wave is diffracted along the core-mantle-boundary, which decreases its amplitude.

The three subsets of events are then merged to obtain the final set of 48 events. (Some events are common to subsets 1 and 2.) For convenience we classify these events as local ($\Delta < 120$ km),

regional (Δ = 120–1200 km), and teleseismic ($\Delta > 1200$ km). These events are listed in order of local (L), regional (R), and teleseismic (T) in Table 4.1, and ordered by increasing magnitude within each group. The events are plotted in Figure 4.2, and comparisons among depth, magnitude, and distance-to-basin are shown in Figure C.3. Incident angles, tabulated in Table 4.1, were calculated for station F3TN using tau-p (Crotwell et al., 1999) with the 1D model used by AEC for locating earthquake (tactmod) (Beaudoin et al., 1992; Ratchkovski & Hansen, 2002). (The 1D model is merged with the global model AK135f for depths 210 km and below.) A low incident angle indicates a ray path arriving from directly below the station.

4.4.3 Earthquake Source Mechanisms

The declustering selection of Alaska earthquakes depends on the depths and magnitudes of the initial set of events. The source parameters (origin time, hypocenter, M_l) were obtained from the AEC catalog. We revised the depths and magnitudes in Table 4.1 based on our own moment tensor inversions for $M_l < 6$ events and based on the GCMT catalog for $M_l \geq 6$ events. (If we performed the declustering with our revised magnitudes and depths, we might end up with a different set of events.) The resulting list of magnitudes is therefore M_w, not M_l.

Seismic moment tensors provide the radiation pattern of seismic waves. These source mechanisms could be valuable when determining the amplification of seismic waves for two stations having different azimuths (or distances) from an earthquake. For all earthquakes $M_l < 6$ we estimate double couple moment tensors by fitting waveforms for body waves and surface waves (Zhu & Helmberger, 1996; Silwal & Tape, 2016). We perform a grid search over the full range of orientations (strike, dip, rake) and use a magnitude increment of 0.05 and a depth increment of 1 km. Full details, including waveform fits, are provided in Smith (2020a). In general, the station coverage is exceptional, owing to the EarthScope Transportable Array (2014–present) for regional events and the FLATS stations for local events. The depth estimates from moment tensor estimation are in agreement with AEC catalog estimates derived from P and S arrival times. For earthquakes $M_l \geq 6$ we rely on the source parameters estimated in the GCMT catalog: centroid time, hypocenter, deviatoric moment tensor.

4.4.4 Earthquake Spectral Ratios

Earthquake spectra are calculated as in Smith & Tape (2019b), but here we also apply a distance correction. Amplitudes of surface waves decrease as they spread out over the Earth's surface. The geometrical spreading correction for surface waves can be expressed as $K_i = \sqrt{\sin\Delta_i}/\sqrt{\sin\Delta_0}$, where Δ is the epicentral distance in radians, and the subscripts are for the target station (i) and the reference station (0). If station i is farther from an earthquake than a reference station, then the amplitude at i needs to be increased $K_i > 1$ to account for the decreased amplitude between Δ_0 and Δ_i. For each pair of target and reference station, we calculate K_i and multiply the target seismogram by this value.

For local and regional events, the spectra are calculated from time windows that extend from 200 s before the origin time to 300 s and 800 s after, respectively. The pre-event noise time windows have the same duration and finish at 200 s before origin time.

An example spectral ratio is shown in Figure 4.3 for station F3TN relative to F8KN for a M_w 3.70 earthquake recorded on the vertical component. For each station pair, two measurements are attempted within two bandpasses (0.1–0.5 Hz and 0.5–4.0 Hz). These bandpasses will be shortened if there is insufficient signal for the target or reference station; in Figure 4.3 the low-frequency interval is shortened to 0.27–0.50 Hz due to insufficient low-frequency signals. In this example, the amplification values of 13.4 dB and 16.2 dB correspond to amplification ratios of 4.7 and 6.5.

Examples of teleseismic body waves are shown in Figure 4.4. The P wave trains—a collection of P waves arriving from a finite-duration source—are filtered 0.1–0.5 Hz (a) and 0.5–4.0 Hz (b) and last $>$ 200 s due to a combination of the M_w 8.0 source duration and scattering near the station. The P wave trains are much larger at basin station F3TN than at marginal station F7TV and bedrock station F8KN. As shown in Figures C.5 and C.6, this pattern is revealed for the P and S wave trains on vertical and transverse components.

For each earthquake, the time window for the P and S waves are based on the predicted arrival times calculated for a 1D Earth model (Crotwell et al., 1999; Montagner & Kennett, 1996). For teleseismic P waves, the time window used for calculating the spectra starts 150 s before the P wave arrival time and ends 100 s before the S arrival time. The S wave time window starts from 100 s before the S arrival time and has a duration of 300 s. The noise spectra use time windows

that end at 150 s before the P wave arrival time and have the same duration as the signal time windows.

4.4.5 Earthquake Metrics

We follow the procedures in Smith & Tape (2019b) to calculate the correlation coefficients between seismogram-derived metrics and basin depth for 43 local and regional earthquakes. The procedure involves filtering each seismogram over a set of 28 different bandpass filters, with limits defined from the following set of frequencies: 0.10, 0.17, 0.29, 0.49, 0.82, 1.39, 2.36, 4.00. Then for each set of filtered seismograms, some are excluded based on signal-to-noise criteria. A geometrical spreading correction is then applied to the remaining non-basin seismograms. Five metrics are calculated from each distance-corrected seismogram: duration (dur), radiated energy (E_R), peak ground displacement (PGD), peak ground velocity (PGV), and peak ground acceleration (PGA).

The duration of time used to calculate each seismogram metric depends on the event distance. In both local and regional cases, the noise is calculated using 150 s before the origin time. For local events, the signal is calculated from 150 s before the origin time to 300 s after the origin time; for regional events, 800 s after the origin time is used. For teleseismic events the noise is calculated using 150 s before the P arrival time. The P extends to 50 s before the S arrival. The S wave extends extends from 50 s before the S arrival and has a duration of 200 s.

As discussed previously, we obtain basin depths from PRA (2017). There are considerable uncertainties in the estimates of basin depths, especially considering that the deepest parts of the basin appear to be constrained by gravity data, not active-source seismic data. When calculating a correlation coefficient between basin depth and a seismogram metric, it is important to recognize that the basin depths have uncertainties.

4.4.6 Ambient Noise

We previously discovered that wind-free hourly periods during winter provided the best times for characterizing the effects of Nenana basin Smith & Tape (2019a). Here we use the same ambient noise spectra to quantify basin amplification levels for two frequency intervals: 0.1–0.5 Hz and

0.5–4 Hz, which allows for direct comparison with the results obtained for Cook Inlet basin (Smith & Tape, 2019b).

4.5 Results

Figure 4.5 summarizes all the spectral ratio measurements in our study. We examine 13 target stations on the y-axis and 6 reference stations on the x-axis. Each colored box is a median over all available spectral ratio measurements. For example the upper left box of the upper left subplot represents the median of F3TN/F8KN spectral ratios for 0.1–0.5 Hz, vertical component, for 43 earthquakes. The value is 13.65 ± 2.35 dB and is tabulated in Table 4.2; this corresponds to an amplification factor of 4.81(Table 4.3).

The overall pattern in Figure 4.5 confirms our expectation that the seismic wavefield is amplified at basin stations. The strongest amplification occurs at FNN1, FNN2, F1TN–F5MN (Figure 4.2c). Weaker amplification occurs at marginal stations F6TP, FAPT, FPAP, and F7TV. No amplification occurs at non-basin stations NEA2, FTGH, MLY and I23K. At low frequencies (0.1–0.5 Hz), amplification is stronger on the horizontal components than the vertical components.

Spectral ratios for higher frequencies (0.5–4.0 Hz) differ significantly from those at low frequencies (Figure 4.5). Three stations with the strongest vertical LF amplification (F3TN, F4TN, F5MN) also have strong HF amplification. Marginal stations F6TP and F7TV both have moderate LF and HF amplification. Other stations have relative differences (FNN2, F2TN, F1TN, FAPT, FPAP). Figure 4.6 highlights some of these differences for two stations, FNN1 and FNN2, separated by 10.93 km (Figure 4.2c). The results for the two earthquakes are consistent with the results for all earthquakes, which show that FNN1 and FNN2 have similar LF amplification (12.70 dB, 15.10 dB: Table 4.2) but different HF amplification (16.20 dB, 5.80 dB: Table 4.2). We attribute these differences to the two stations seeing different excitation of the basin; substantial modeling is needed to understand the observations.

Figure 4.7 displays spectral ratios for P and S waves from a M_w 8.0 teleseismic earthquake. Seismograms displayed in Figure C.5 and Figure C.6 show clear amplification of the body waves at basin station F3TN relative to marginal station F7TV and bedrock station F8KN. The spectral ratios have characteristics exhibited by other teleseismic earthquakes. We generalize these as follows:

1. The elevated spectral ratios at higher frequencies ($\geq$ 4 Hz) arise because at these large distances the high frequencies have been attenuated. The elevated ratios indicate that the noise at the basin station (F3TN) and marginal basin station (F7TV) are both greater than the noise at the reference bedrock station.

2. At basin stations, P and S waves are amplified on the vertical, radial, and transverse components. Amplification is larger at F3TN than at F7TV for P and S on all three components.

3. P and S amplification is larger on horizontal components for high frequencies (0.5–4.0 Hz).

4. At F3TN, amplification of P extends down to 0.1 Hz on the horizontal component, yet down to 0.2 Hz on the vertical component.

A complete analysis of ground motion metrics is presented in Smith (2020b). Similar to the study of Smith & Tape (2019b), we find good correlations between basin depth and radiated seismic energy (E_R), especially on the vertical component. In Figure C.19 we present matrix plots for all 43 local and regional earthquakes. The predominance of red indicates that for most events and for many different bandpasses between 0.1–4 Hz, the correlation coefficient between basin depth and E_R exceeds 0.8. Figure C.20 shows the scatterplot data corresponding with the bandpass the produces the highest CC in the corresponding matrix plot in Figure C.19.

Our results from ambient noise, after Smith & Tape (2019a), are displayed in Figure 4.8. Here we quantify the noise amplification in two frequency bands, as shown in Figures C.21–C.22 and displayed as a function of basin depth in Figure 4.9.

4.6 Discussion

4.6.1 Comparison between Cook Inlet and Nenana Basins

Cook Inlet basin and Nenana basin are very different, in terms of size, shape, sedimentary strata, and creation. Nevertheless, both basins have a similar response to incoming seismic waves from earthquakes. For Nenana basin, the summary plots in Figure 4.10 can be compared with Figure 14 of Smith & Tape (2019b). At low frequencies (0.1–0.5 Hz), marginal basin stations appear similar to non-basin stations, and basin amplification on the vertical component is larger in Nenana (11–

14 dB; 3.5–5.0) than in Cook Inlet (6–14 dB; 2.0–5.0). At high frequencies (0.5–4 Hz), amplification is similar to low frequencies, though there is more variance in the measurements.

Amplification of the ambient noise wavefield is also similar at both basins, as shown in Figures 4.9 and 4.10 for Nenana basin and Figures 5 and 14 of Smith & Tape (2019b) for Cook Inlet basin. Scatterplots between earthquake amplification versus noise amplification (e.g., Figure 4.10) show a linear trend, with a one-to-one slope for low frequencies and a skewed line for high frequencies, due to noise amplification values exceeding earthquake amplification values.

Our measurements for both basins show that the high-frequency (0.5–4 Hz) ambient noise seismic wavefield exhibits higher amplitudes inside the basin than outside the basin. One possible explanation is that there could be a persistent, unknown source of high-frequency noise within the basins. While it is tempting to invoke oceanographic effects for Cook Inlet (e.g., strong tidal currents), such an explanation would not be valid for Nenana basin, far from the ocean. (Recall that the noise calculations are during zero-wind winter conditions, to minimize the influence of wind, river and anthroprogenic sources.) A second possible explanation is that the high-frequency ambient noise wavefield is sampling a different part of the Earth than the earthquake wavefield. A third possible explanation is that the basin response could be nonlinear with respect to the amplitude of the incoming waves. The observations would suggest that higher-amplitude earthquake waves are amplified less than lower amplitude seismic noise.

To understand these possibilities, we need to better understand ground motion in basins, both from the earthquake wavefield and from ambient noise. A frequency-dependent polarization analysis and frequency-wavenumber analysis could provide insights into the types of waves manifest within the complex seismograms. Earthquake simulations with realistic sources, basin geometries, and seismic velocity models would likely provide key results.

4.6.2 Consideration of Source Mechanism and Attenuation

A relative amplitude measurement between two stations is used to represent structural differences at one station relative to the other station. We apply a distance correction in order to account for the fact that the distance from our target station differs from the distance to our reference station. (In choosing an exponent for the distance correction, we assume that the wavefield is dominantly

comprised of surface waves.) Two other corrections, which we did not apply, should be considered. The first is a correction for attenuation, since high-frequency waves will attenuate more rapidly (i.e., over shorter paths) than low-frequency waves. The second is a correction for source mechanism. We have taken an important step toward this option by estimating high-quality moment tensors and depths for 34 earthquakes, providing a set of 48 events with waveform-estimated moment tensors. With these moment tensors, one could calculate synthetic seismograms as a function of frequency, and this would provide an amplitude estimate for each station. By generating synthetic seismograms, the influence of both attenuation and source mechanisms could be addressed.

Many of our sources are shallow (< 40 km) which indicates larger amplitudes at higher frequencies (0.04–0.06 Hz). However, a few of our events are deeper which means they will have greater influence at lower frequencies (0.01–0.04 Hz) (Rösler & van der Lee, 2020). At higher freqencies (>1 Hz), one of the challenges is discerning the radiation pattern which is complicated by the rupture process (Graves & Pitarka, 2016). The radiation pattern at high frequencies is complicated by heterogenous velocity models, burial depth, and hypocentral distance and can become indistinguishable (Takemura et al., 2009).

4.6.3 Apparent Amplification

Reducing the velocity of a shallow slow layer will result in a higher-amplitude surface wave (e.g., Tsai & Atiganyanun, 2014). Strong velocity contrasts, such as those that define a basin boundary (laterally and at depth), can trap the seismic waves, resulting extended shaking and enhanced amplitudes. These are the effects we are hoping to quantify by making spectral ratio measurements between in-basin and out-of-basin stations.

We acknowledge other factors that could result in apparent amplification. Consider a vertically incident P wave at the base of the crust. Under the target station, assuming a layered Earth model, the P wave is isolated to the vertical component. Under a basin station, the deep sedimentary basin could affect the true incident angle, such that the wavefield appears on the horizontal components. This would be measured as amplification, even though it is an effect of 3D structure and the P amplitude could possibly be the same in both cases. A second scenario is that basin includes small-

scale stochastic heterogeneity, so although the P wave could be vertically incident, it is strongly scattered and is recorded on horizontal components.

4.7 Summary points

1. A five-year deployment of stations in Nenana basin allows us to document the amplification of seismic waves from earthquakes and from ambient noise. We establish a catalog of 48 events: 22 local, 21 regional, and 5 teleseismic.

2. Spectral ratios (Table 4.2 and Figure 4.5) reveal a striking pattern of basin amplification for a diverse set of 43 earthquakes. Amplification for 0.1–0.5 Hz is strongest on the horizontal components, with values of 18–20 dB, corresponding to amplification factors of 8–10 at basin stations, relative to a bedrock station outside the basin.

3. Spectral ratios at higher frequencies (0.5–4 Hz) reveal amplification at basin stations of 5–18 dB (1.8–7.9). Marginal basin stations (F7TV, FPAP, FAPT) have enhanced amplification at higher frequencies relative to lower frequencies (Figure 4.5). We hypothesize that shallower intra-basin structures and the basin edge geometry are more influential at higher frequencies.

4. Ambient noise provides similar basin amplification results to earthquakes data for the low-frequency range (0.1–0.5 Hz) (Figure 4.10c). It is likely that the ambient noise wavefield is comparable to the earthquake wavefield at these frequencies, with both being dominated by surface waves.

   At high frequencies (0.5–4 Hz), the apparent amplification of seismic waves by basins is stronger for ambient noise than for earthquake waves (Figure 4.10d).

5. Teleseismic P and S waves from $M_w \geq 8$ earthquakes exhibit comparable basin amplification to waves from local and regional earthquakes.

It is widely known that sedimentary basins amplify and prolong earthquake ground motion, yet most major sedimentary basins lack a physical model (such as a complex 3D velocity model) to explain a wide range of recorded earthquakes. In this study we quantify basin amplification by

examining continuous ambient noise and 48 earthquakes over a four-year period. The observations provide constraints for future 3D seismic wavefield simulations that include Nenana basin. The frequency range of 0.1–4 Hz is computationally formidable yet feasible at simulation domains of a few hundred kilometers. Accurate modeling of the seismic wavefield in sedimentary basins is a societally relevant scientific challenge. Our data set of stations and events establishes an opportunity to improve our understanding of seismic wave propagation in sedimentary basins.

4.8 Tables

Table 4.1: Source metrics for 48 earthquakes grouped as local, regional, and teleseismic. Within each group they are ordered by origin time. Magnitude and depths are from MT catalog when available. Earthquakes are sorted by origin time with teleseismic events listed at the end. Local is for events <120 km and regional is for events <1200 km.

index	origin time	longitude	latitude	magnitude	depth (km)	distance to basin (km)	type	P incident angle (°)
1	2017-05-27 16:33:05.640	-149.2261	64.6896	3.20	17	10	L	26
2	2018-08-25 18:15:51.481	-149.2033	64.6164	3.20	17	17	L	40
3	2017-06-28 12:58:51.897	-148.9082	64.7566	3.30	19	11	L	29
4	2019-06-24 09:04:23.195	-149.8657	64.2797	3.35	19	65	L	58
5	2015-10-31 02:56:35.572	-149.6969	64.4285	3.40	25	46	L	49
6	2017-11-08 06:49:11.318	-148.6552	64.8620	3.55	16	25	L	48
7	2019-01-17 12:13:55.493	-149.0340	64.2410	3.55	17	59	L	57
8	2019-03-09 23:39:58.332	-147.7368	64.5498	3.60	26	71	L	49
9	2018-09-16 19:11:54.565	-151.3493	65.1562	3.70	12	112	L	43
10	2016-01-14 19:04:10.727	-149.2479	64.6827	3.70	17	11	L	29
11	2019-09-25 13:45:13.442	-149.2576	63.7657	3.85	16	112	L	60
12	2017-12-30 11:43:16.278	-149.0240	63.8011	3.90	6	108	L	60
13	2018-11-13 15:26:41.907	-150.9466	64.7938	3.95	16	85	L	59
14	2017-06-13 07:39:36.181	-148.2574	63.8685	3.95	106	109	L	31
15	2018-10-03 03:29:37.544	-148.9191	64.8979	4.00	19	18	L	39
16	2016-11-06 09:29:10.579	-150.0626	64.1639	4.00	21	81	L	49
17	2016-05-18 03:25:48.320	-151.0651	65.2466	4.10	12	104	L	60
18	2018-01-19 23:55:05.310	-148.9897	63.9765	4.15	137	89	L	23
19	2019-04-11 10:42:45.609	-149.1761	64.7370	4.15	17	4	L	12
20	2016-07-11 20:05:57.702	-149.2282	63.8056	4.20	120	107	L	27
21	2018-08-28 15:18:43.464	-150.5718	65.1780	4.30	16	81	L	59
22	2016-12-08 10:18:13.868	-150.0376	64.1937	4.35	21	77	L	49
23	2015-12-02 10:05:25.798	-147.2622	61.6966	3.75	39	355	R	43
24	2019-09-06 23:32:28.461	-152.3552	64.6032	4.25	8	154	R	43
25	2016-05-21 11:34:09.789	-152.4627	62.3598	4.50	135	314	R	37
26	2016-01-18 04:05:56.098	-150.6400	62.1032	4.55	18	306	R	43
27	2017-04-29 11:15:48.898	-151.1656	63.1225	4.80	16	208	R	43
28	2018-10-14 23:53:14.769	-156.3956	67.7739	4.85	16	465	R	43
29	2019-03-26 21:27:18.519	-157.2445	66.2996	4.90	6	409	R	43
30	2018-10-27 16:57:28.350	-151.5744	65.2283	4.90	15	125	R	43
31	2019-01-13 16:45:55.437	-150.0647	61.2993	4.90	48	389	R	43
32	2019-03-06 21:33:13.991	-157.2186	66.3108	5.05	2	409	R	43
33	2017-11-27 22:18:30.467	-147.4303	60.5552	5.20	30	477	R	43
34	2017-02-13 07:17:12.642	-142.7477	62.5120	5.20	12	403	R	43
35	2016-05-15 05:51:00.219	-150.9465	63.0765	5.25	135	208	R	34
36	2018-08-12 21:15:00.999	-144.3388	69.5227	6.02	15	567	R	43
37	2017-05-01 12:31:53.025	-136.6772	59.8523	6.20	15	843	R	40
38	2016-04-02 05:50:00.932	-157.9322	57.0080	6.22	12	983	R	40
39	2017-05-01 14:18:14.672	-136.7105	59.7899	6.25	14	846	R	40
40	2018-08-12 14:58:53.503	-145.2910	69.5762	6.43	12	559	R	43
41	2018-11-30 17:29:29.330	-149.9552	61.3464	7.05	48	383	R	43
42	2016-01-24 10:30:29.557	-153.3392	59.6204	7.11	111	612	R	40
43	2018-01-23 09:31:40.994	-149.0431	55.7747	7.93	34	1000	R	40
44	2017-09-03 03:30:01.760	129.0297	41.3324	5.18	1	5560	T	22
45	2019-05-26 07:41:52.800	-75.3600	-5.2500	7.99	127	9780	T	13
46	2018-08-19 00:19:59.000	-177.8500	-17.8600	8.20	555	9510	T	14
47	2017-09-08 04:49:46.700	-94.6600	15.3800	8.23	45	6830	T	19
48	2015-09-16 22:55:22.900	-72.0900	-31.1300	8.27	17	12530	T	12

Table 4.2: Summary of spectral ratios for 15 stations for 43 earthquakes. Spectral ratios are calculated for two frequency ranges: 0.1–0.5 Hz (lf) and 0.5–4.0 Hz (hf). SR values (dB) correspond to Figure C.18 with reference station F8KN. Converted amplitude factors are in Table 4.3.

station	recorded events	Zlf ± MAD	Rlf ± MAD	Tlf ± MAD	Zhf ± MAD	Rhf ± MAD	Thf ± MAD
F3TN	40	13.65 ± 2.35	20.00 ± 1.85	19.30 ± 2.30	14.80 ± 1.45	18.10 ± 2.60	18.05 ± 1.80
F4TN	43	14.20 ± 2.00	20.40 ± 1.90	17.90 ± 2.20	13.10 ± 1.10	16.30 ± 2.10	16.10 ± 1.80
FNN2	41	12.10 ± 1.30	15.90 ± 1.70	15.10 ± 1.40	9.50 ± 1.45	6.55 ± 2.35	5.80 ± 1.80
F2TN	42	13.65 ± 2.00	15.50 ± 1.30	14.95 ± 2.25	10.50 ± 1.00	7.65 ± 2.85	7.10 ± 3.00
F5MN	43	14.40 ± 2.10	16.00 ± 1.40	14.90 ± 2.70	13.70 ± 1.50	14.10 ± 2.20	14.90 ± 2.60
F1TN	43	11.40 ± 1.90	15.30 ± 1.80	14.60 ± 2.05	8.90 ± 1.90	6.00 ± 2.70	5.20 ± 2.00
FNN1	41	11.00 ± 2.40	13.80 ± 1.80	12.70 ± 1.50	14.20 ± 1.50	16.60 ± 1.30	16.20 ± 2.00
F6TP	42	5.85 ± 2.60	12.50 ± 2.20	11.55 ± 2.15	9.15 ± 1.85	5.40 ± 1.40	5.60 ± 2.45
FAPT	43	0.50 ± 2.40	5.10 ± 2.70	5.40 ± 2.80	8.60 ± 2.10	13.50 ± 2.80	12.90 ± 1.80
FPAP	39	1.60 ± 1.80	4.30 ± 2.10	4.70 ± 2.30	11.00 ± 2.10	16.00 ± 2.10	14.40 ± 3.00
F7TV	43	0.50 ± 0.80	3.80 ± 1.40	3.20 ± 1.05	7.00 ± 1.20	10.40 ± 1.00	9.90 ± 1.70
I23K	43	1.30 ± 1.90	1.70 ± 1.80	1.90 ± 2.40	0.00 ± 1.50	0.70 ± 1.90	0.20 ± 2.00
NEA2	43	-1.20 ± 2.10	-0.00 ± 2.30	0.30 ± 2.00	-1.60 ± 1.80	-1.70 ± 2.60	-2.10 ± 2.50
FTGH	41	0.00 ± 1.60	-0.30 ± 2.10	0.10 ± 1.65	0.80 ± 1.90	-0.55 ± 1.95	-0.10 ± 1.60
MLY	31	0.00 ± 1.50	-1.00 ± 1.80	-0.30 ± 3.00	-2.90 ± 1.50	-3.50 ± 1.60	-3.90 ± 2.60

Table 4.3: Spectral ratios in Table 4.2, expressed in terms of amplification ratios. A conversion table is shown in Table B.1.

station	recorded events	Zlf	Rlf	Tlf	Zhf	Rhf	Thf
F3TN	40	4.81	10.00	9.23	5.50	8.04	7.99
F4TN	43	5.13	10.47	7.85	4.52	6.53	6.38
FNN2	41	4.03	6.24	5.69	2.99	2.13	1.95
F2TN	42	4.81	5.96	5.59	3.35	2.41	2.26
F5MN	43	5.25	6.31	5.56	4.84	5.07	5.56
F1TN	43	3.72	5.82	5.37	2.79	2.00	1.82
FNN1	41	3.55	4.90	4.32	5.13	6.76	6.46
F6TP	42	1.96	4.22	3.78	2.87	1.86	1.91
FAPT	43	1.06	1.80	1.86	2.69	4.73	4.42
FPAP	39	1.20	1.64	1.72	3.55	6.31	5.25
F7TV	43	1.06	1.55	1.45	2.24	3.31	3.13
I23K	43	1.16	1.22	1.24	1.00	1.08	1.02
NEA2	43	0.87	1.00	1.04	0.83	0.82	0.79
FTGH	41	1.00	0.97	1.01	1.10	0.94	0.99
MLY	31	1.00	0.89	0.97	0.72	0.67	0.64

Table 4.4: Summary of noise spectral ratios for 15 stations. Noise spectral ratios are calculated for two frequency ranges: 0.1–0.5 Hz (lf) and 0.5–4.0 Hz (hf). Noise SR values (dB) correspond to Figure 4.9 with reference station F8KN.

station	Zlf ± MAD	Hlf ± MAD	Zhf ± MAD	Hhf ± MAD	Zlf Amp	Hlf Amp	Zhf Amp	Hhf Amp
F3TN	12.8 ± 2.5	20.0 ± 0.4	21.1 ± 2.6	21.6 ± 1.2	4.4	10.0	16.4	15.5
F4TN	12.3 ± 3.9	20.1 ± 0.1	20.8 ± 3.8	20.8 ± 1.3	4.1	10.1	20.9	14.3
FNN2	12.6 ± 1.9	16.3 ± 0.5	8.3 ± 3.8	4.6 ± 6.9	4.3	6.5	4.6	6.9
F2TN	13.0 ± 2.0	15.9 ± 0.6	14.2 ± 1.3	10.0 ± 4.1	4.5	6.2	6.4	5.9
F5MN	12.2 ± 2.9	16.8 ± 0.8	17.1 ± 3.2	15.2 ± 1.0	4.1	6.9	11.2	7.2
F1TN	12.7 ± 0.9	15.0 ± 0.5	13.2 ± 1.5	10.4 ± 5.1	4.3	5.6	6.9	6.5
FNN1	9.9 ± 2.2	13.9 ± 0.2	17.8 ± 1.6	15.4 ± 0.6	3.1	5.0	9.3	7.0
F6TP	0.6 ± 1.5	12.2 ± 2.9	12.8 ± 1.4	6.7 ± 4.4	1.1	4.1	5.6	4.5
FAPT	0.3 ± 0.3	2.0 ± 1.0	30.6 ± 7.4	27.0 ± 1.5	1.0	1.3	80.4	26.9
FPAP	0.9 ± 0.1	3.2 ± 0.7	18.4 ± 10.9	22.8 ± 2.6	1.1	1.4	53.1	19.3
F7TV	-0.1 ± 0.2	2.1 ± 0.6	14.5 ± 5.1	12.5 ± 3.1	1.0	1.3	10.0	7.7
I23K	0.3 ± 0.1	1.4 ± 0.1	0.7 ± 0.6	-0.1 ± 2.5	1.0	1.2	1.2	1.5
NEA2	0.2 ± 0.2	0.7 ± 0.2	1.0 ± 1.6	0.2 ± 0.7	1.0	1.1	1.8	1.3
FTGH	0.2 ± 0.2	-0.8 ± 0.1	0.6 ± 0.3	-0.3 ± 1.5	1.0	0.9	1.8	1.2
MLY	-0.4 ± 0.1	-0.6 ± 0.6	-3.8 ± 2.2	-6.2 ± 3.8	1.0	0.9	1.0	1.1

4.9 Figures

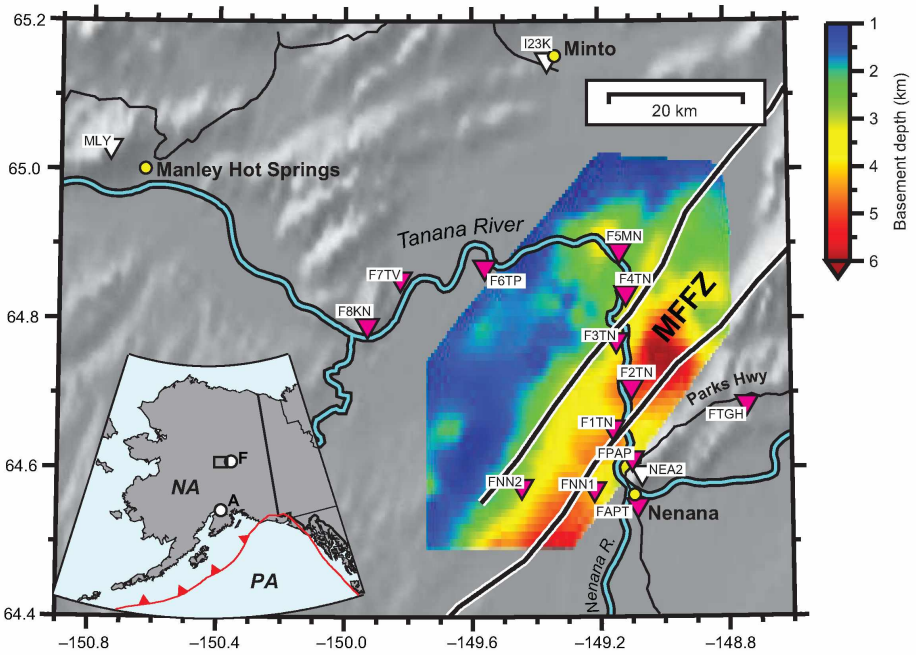

Figure 4.1: Setting for Nenana basin and Minto Flats fault zone (MFFZ), central Alaska. The color denotes the depth to the basement surface of Nenana basin PRA (2017). Triangles denote seismic stations, with magenta representing FLATS stations (2015–2019). Inset shows the study region as a small box west of Fairbanks (F) in central Alaska. The Pacific plate (PA) subducts beneath the North American plate (NA).

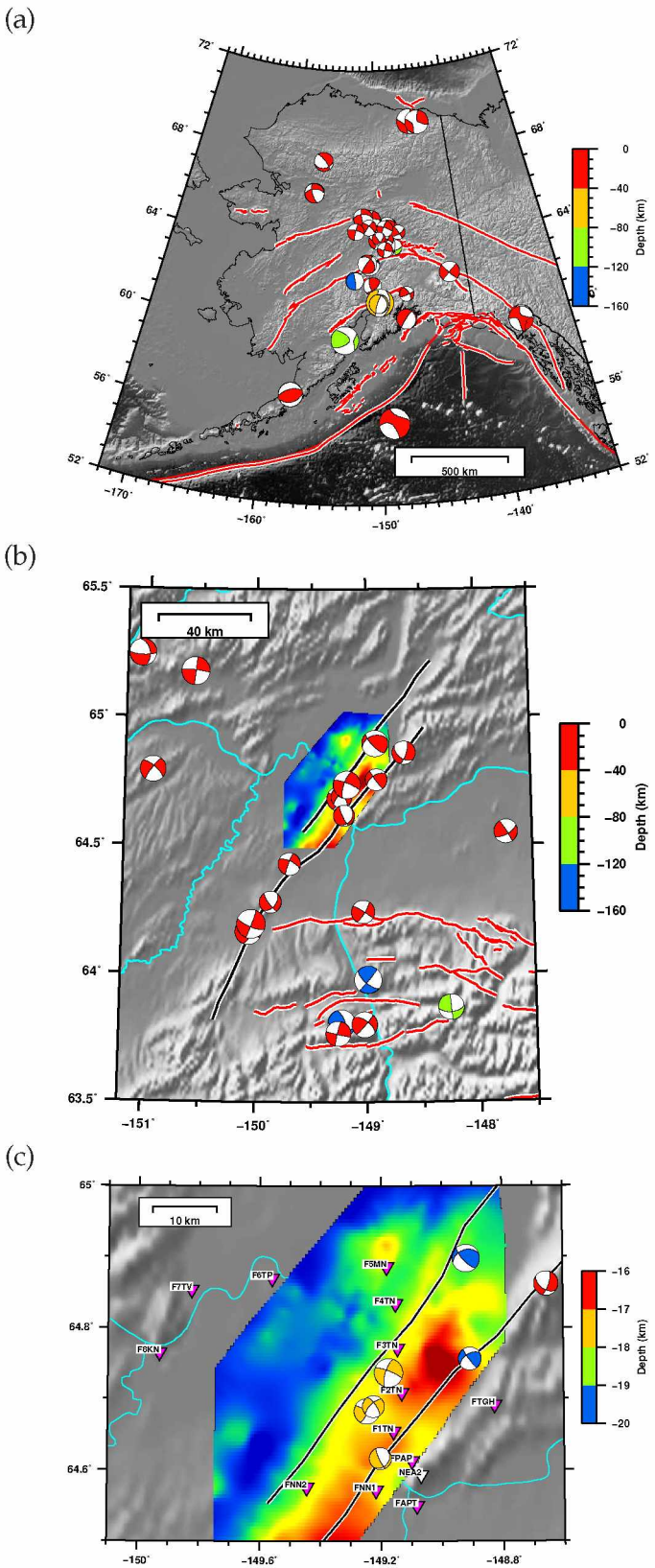

Figure 4.2: Regional and local earthquakes analyzed in this study (Table 4.1). The 43 earthquakes are displayed at three different scales (a, b, c). Within each map, earthquakes are sized by magnitude and colored by depth.

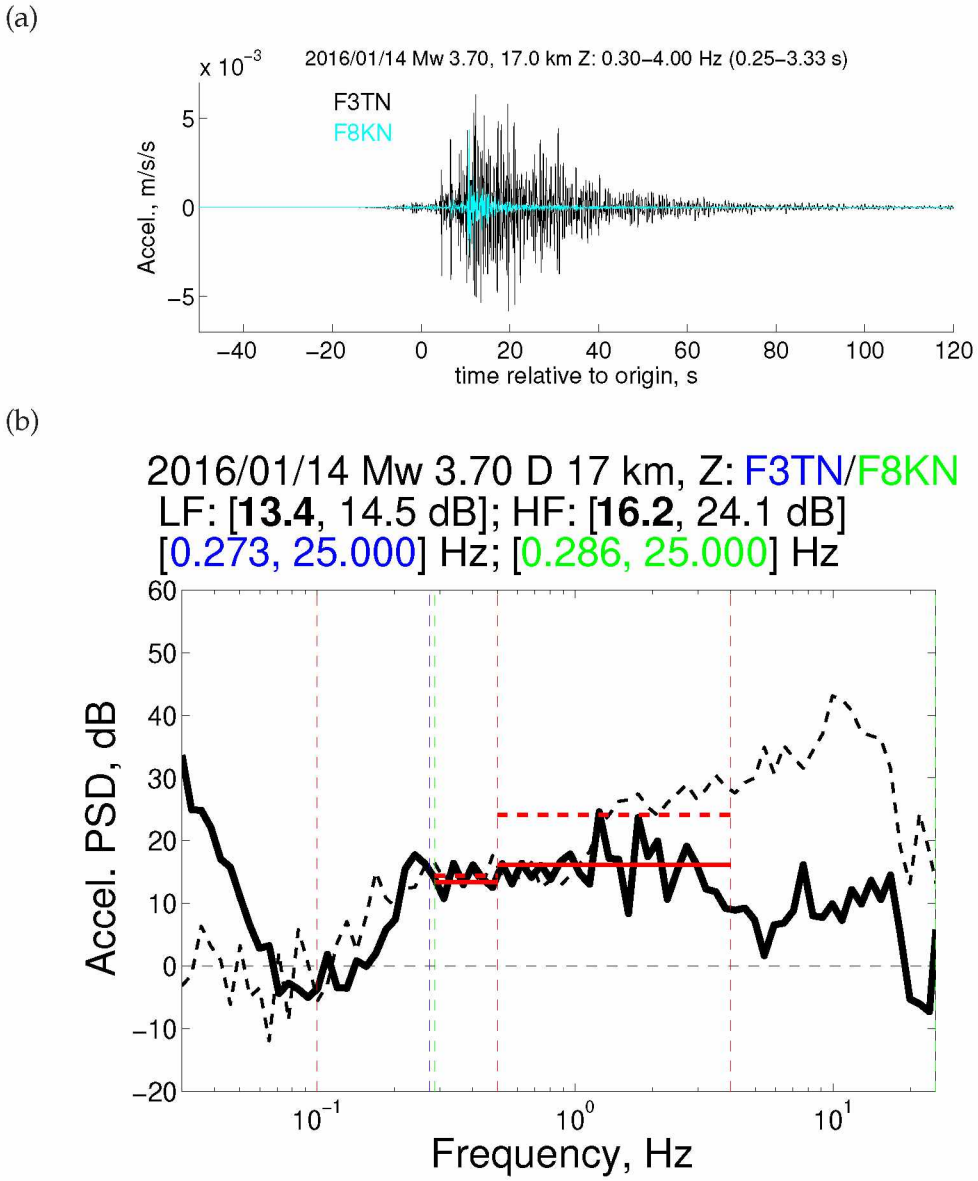

Figure 4.3: Example of amplification of seismic waves at basin station F3TN in comparison to bedrock station F8KN, for a M_w 3.70 earthquake on 2016-01-14 at a depth of 17 km and directly beneath the basin. The amplitude of the F8KN seismograms have been adjusted for geometrical spreading, such that the amplitudes are those expected at the epicentral distance of F8KN. (a) Vertical-component acceleration seismograms filtered 0.3–4 Hz. (b) Spectral ratio between F3TN and F8KN. The frequency range shown is between 0.03 Hz and 25 Hz. Solid-line earthquake differential spectrum is calculated from 200 s before the earthquake to 300 s following the origin time of the earthquake for target station F3TN and for reference station F8KN. Dashed-line noise differential spectrum is calculated from the 200 s prior to the origin time with the same duration. Here the amplification of the earthquake waves is 13.4 dB for 0.1–0.5 Hz and 16.2 dB for 0.5–4 Hz; amplification of the pre-earthquake noise is 14.5 dB and 24.1 dB for the two frequency ranges. The vertical dashed lines mark the frequency boundaries where the each station's signal-to-noise spectrum exceeds 10 dB; in this case, these are [0.273, 25.000] Hz for F3TN and [0.286, 25.000] Hz for F8KN.

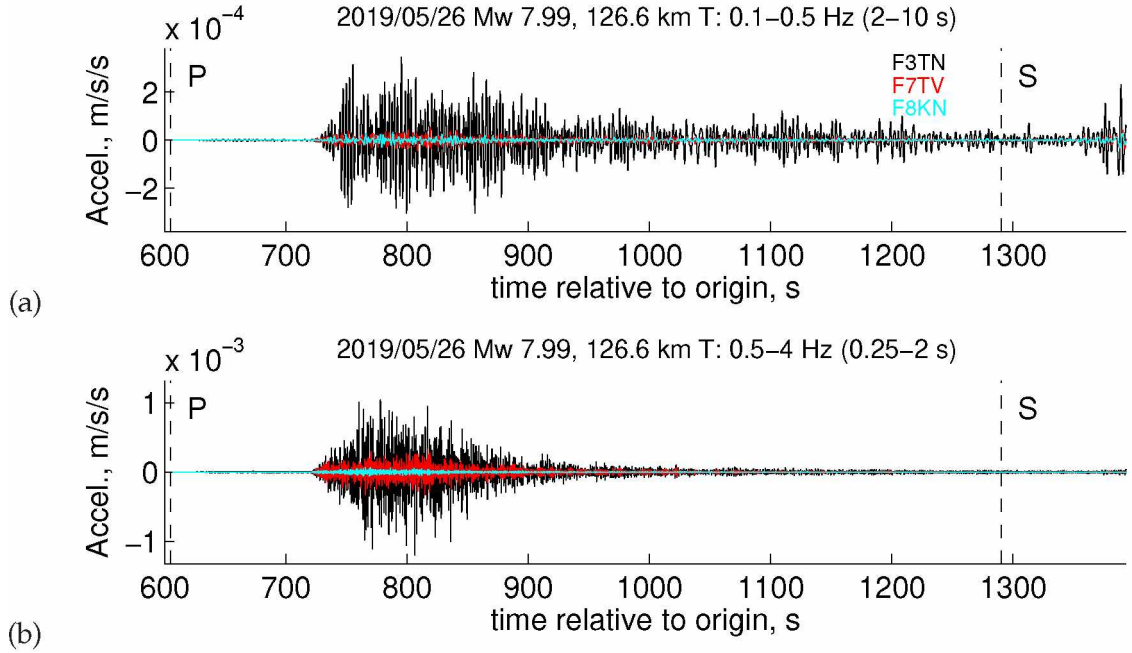

Figure 4.4: Example of amplification of P wave from a teleseismic earthquake (2019-05-26,M_w7.99, depth 127 km) recorded on the transverse component. See Figures C.5 and C.6 for P and S on vertical and transverse components. (a) Seismograms filtered 0.1–0.5 Hz at F8KN, F7TV, and F3TN. (b) Same as (a) but filtered 0.5–4.0 Hz.

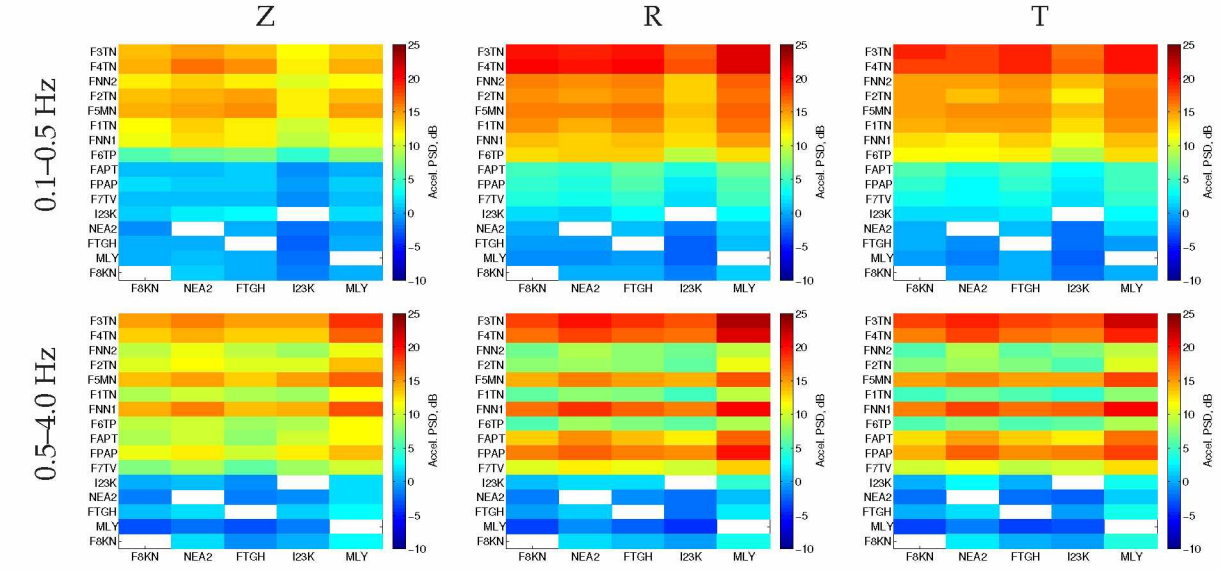

Figure 4.5: Median spectral ratios for each station for all 43 local and regional earthquakes. The calculations are performed for the low-frequency band (0.1–0.5 Hz: top) and the high-frequency band (0.5–4 Hz: bottom) for the vertical (left), radial (center), and transverse (right) component seismograms. Five different reference stations are used for the spectral ratios: F8KN, NEA2, FTGH, I23K, and MLY . Stations are ordered from top to bottom in decreasing order of low-frequency amplification on the transverse component with respect to F8KN (left column of top right subplot).

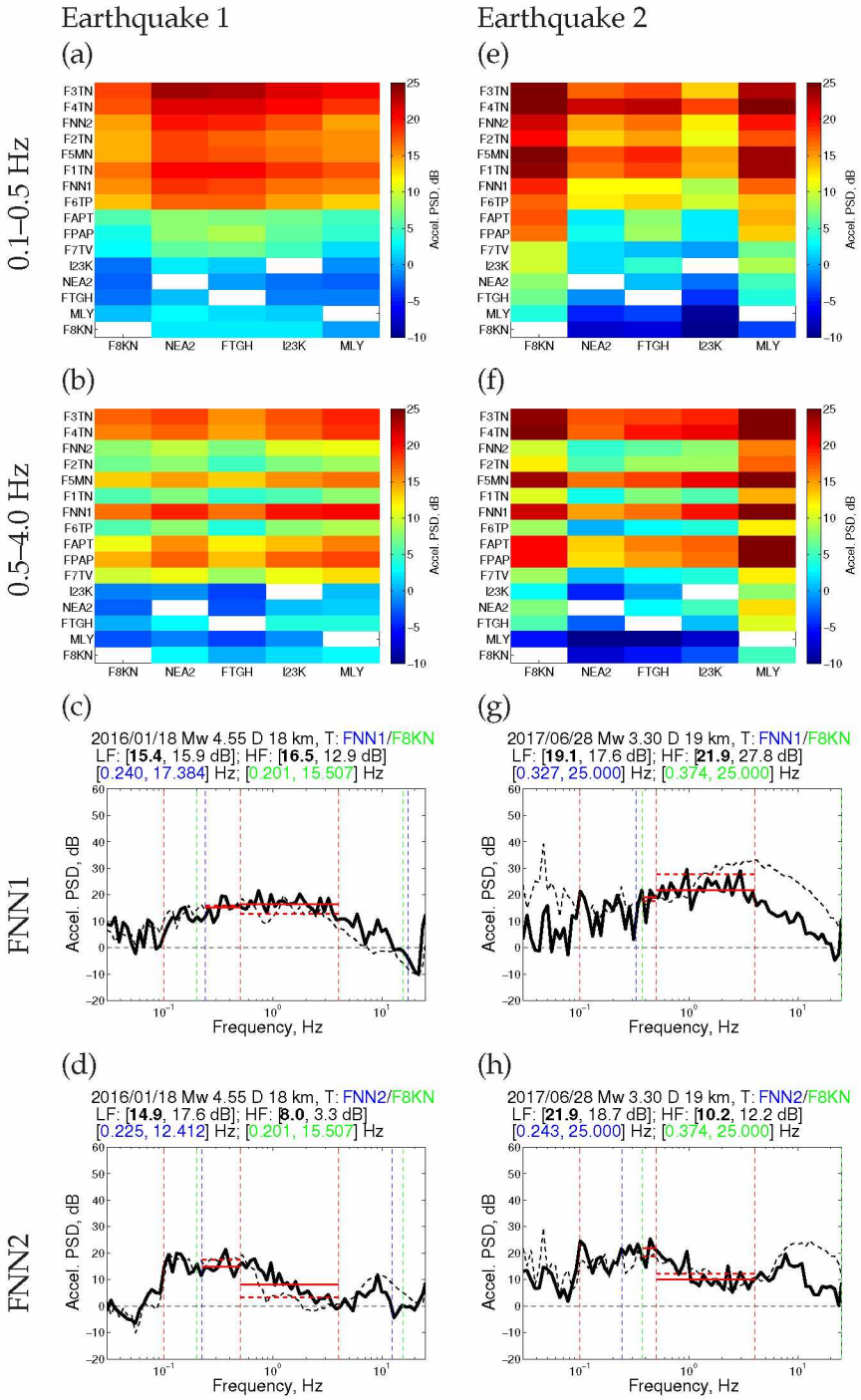

Figure 4.6: Spectral ratios for stations FNN1 and FNN2 for two earthquakes. The basin stations are separated by 11 km (Figure 4.1) and display significant differences for high-frequency (0.5–4.0 Hz) amplification. The solid spectrum is for the earthquake spectral ratios; the dashed spectrum is for the noise spectral ratios. The examples here are for the transverse component. (a) Earthquake 1: Event 20160118040556098 (2016-01-18, M_w 4.55, depth 18 km), bandpass 0.1–0.5 Hz. (b) Event 20160118040556098, bandpass 0.5–4.0 Hz. (c) Spectral ratio FNN1/F8KN. Amplification values are 16.5 dB (0.5–4.0 Hz) and 15.4 dB (0.1–0.5 Hz). (d) Spectral ratio FNN2/F8KN. Amplification values are 8.0 dB (0.5–4.0 Hz) and 14.9 dB (0.1–0.5 Hz). (e)-(h) Same as (a)-(d) but for Earthquake 2: event 20170628125851897 (2017-06-28, M_w 3.30, depth 19 km).

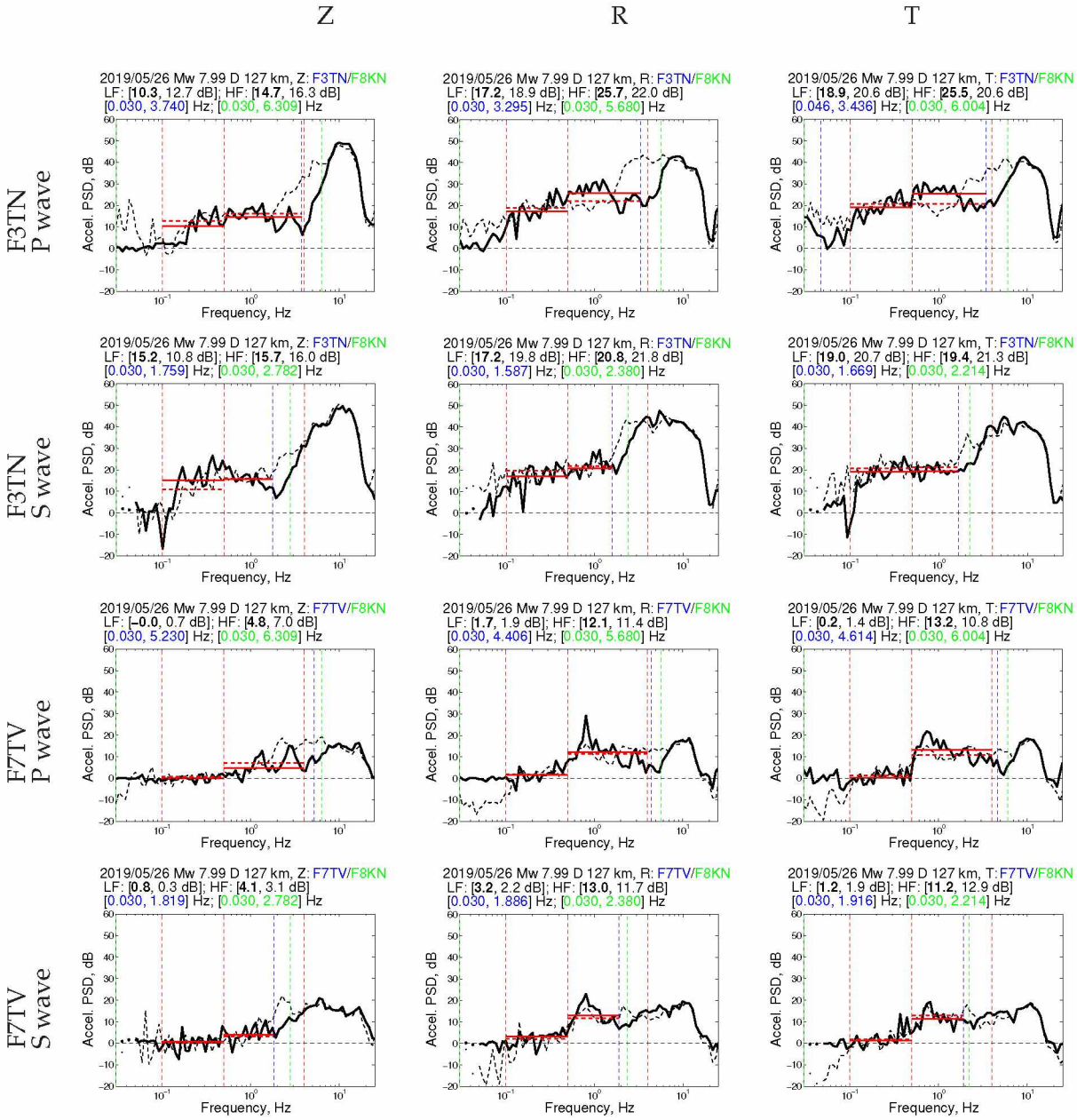

Figure 4.7: Spectral ratios for a basin station (F3TN) and a marginal basin station (F7TV) for P and S waves from a M_l 7.99 teleseismic earthquake (2019-05-26, depth 127 km). This figure is explained in the Results section. The horizontal red lines denote the amplification measurement (see Figure 4.3). See results for other teleseismic events in Figures C.13–C.17.

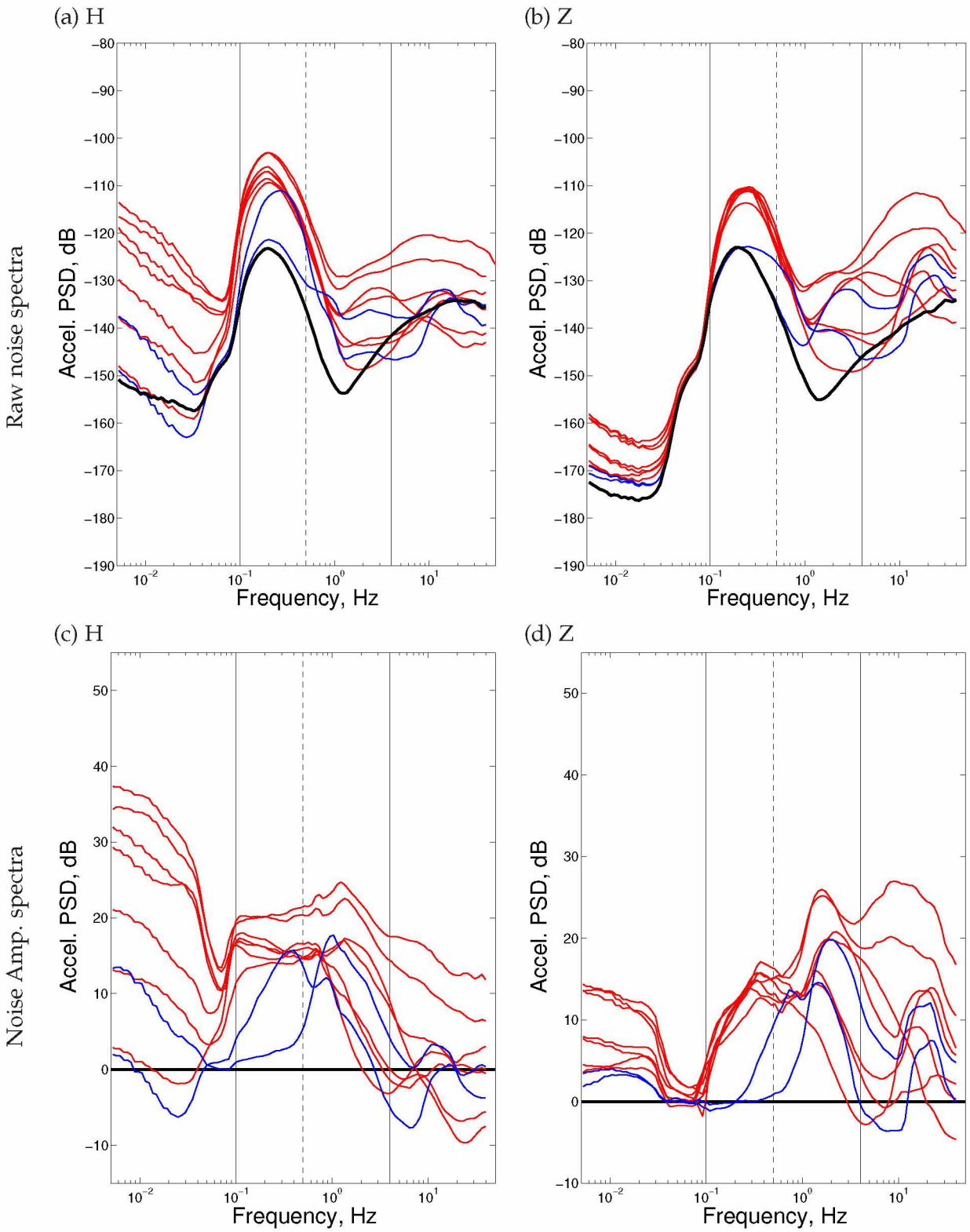

Figure 4.8: Seismic noise spectra and their differences from a non-basin reference station (F8KN). (a) Horizontal-component annual ambient noise for 10 stations in the Minto Flats region; FAPT and FPAP are excluded due to their suspected influences from cultural noise. Red spectra are for 7 basin stations. Blue spectra are for 2 marginal basin stations that exhibit non-basin characteristics. The thick black line is the non-basin reference spectrum F8KN. The solid lines denote the frequency range of basin influence on seismic waves: 0.1–4 Hz (separated at 0.5 Hz). (b) Same as (a), but for the vertical component. (c) Spectra in (a), minus the non-basin reference spectrum in (a). (d) Spectra in (b), minus the non-basin reference spectrum in (b).

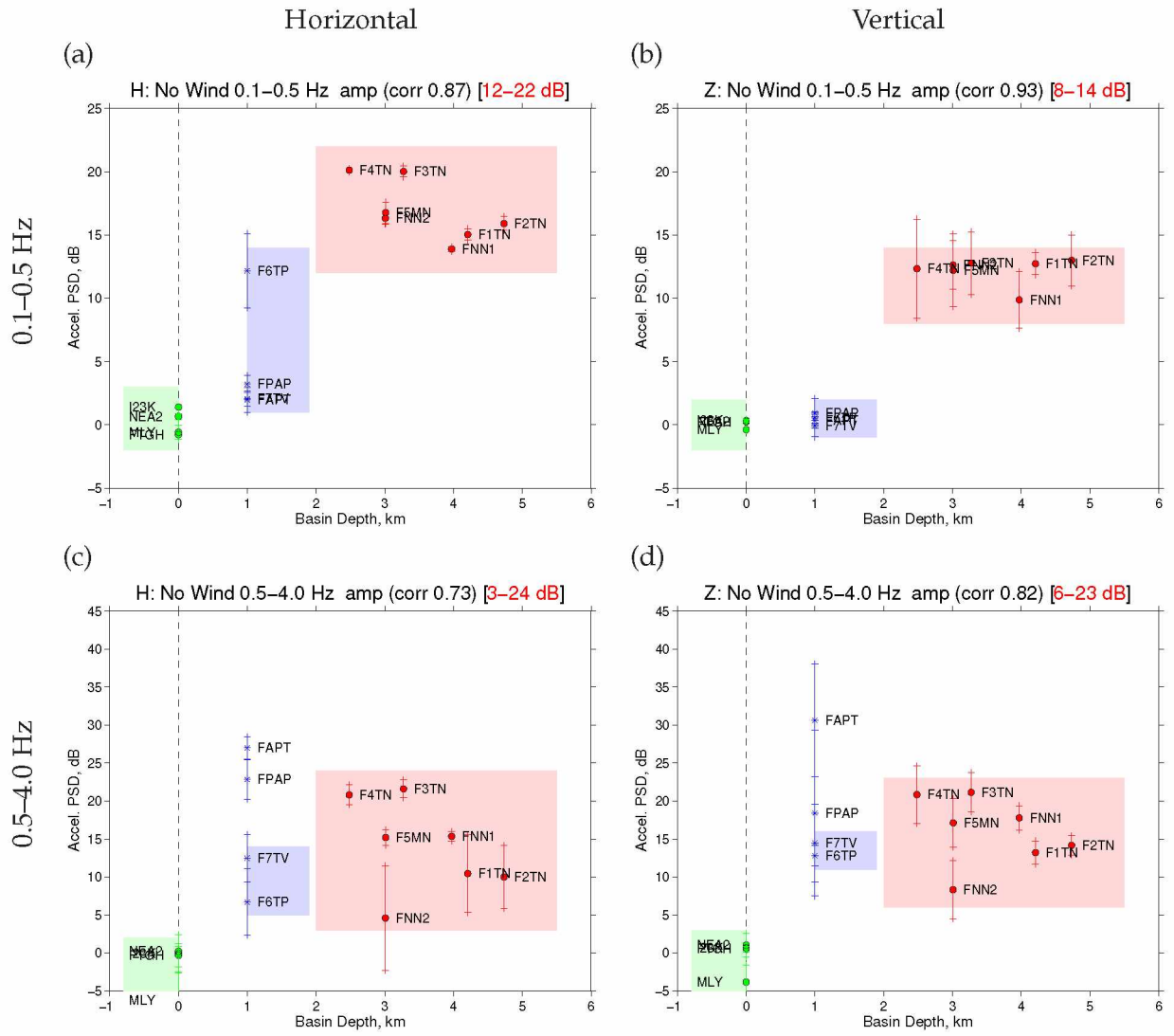

Figure 4.9: Seismic noise amplitudes compared with basin depth, shown for 15 stations in the Minto Flats region. Red circles, highlighted by the red shaded region, denote 7 basin stations. Blue circles (and stars), highlighted by the blue shaded region, denote 4 marginal basin stations. Green circles, highlighted by the green shaded region, are 4 non-basin stations. Figure C.22 shows the ambient noise spectra used to calculate the values displayed here. (a) Horizontal-component seismic noise amplitudes for the frequency range 0.1–0.5 Hz. Note the y-axis limits from $[-5, 25]$ dB. (b) Vertical component for 0.1–0.5 Hz. (c) Horizontal component for 0.5–4 Hz. Note the y-axis limits from $[-5, 45]$ dB. (d) Vertical component for 0.5–4 Hz.

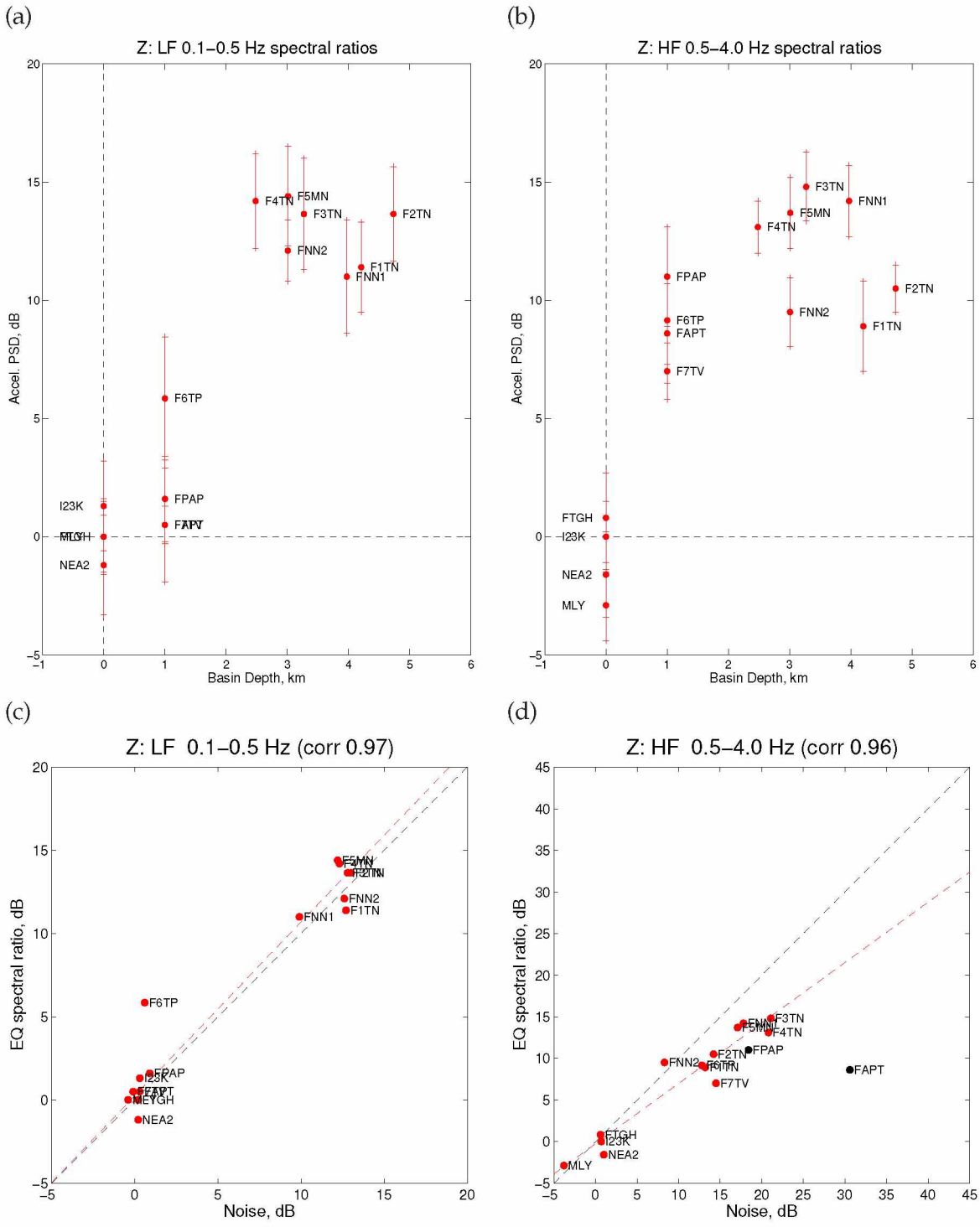

Figure 4.10: Summary of spectral ratio results for 12 seismic stations within or near Nenana basin. (a) Spectral ratios for vertical component, 0.1–0.5 Hz. Each data point and error bar is derived from spectral ratios at one station for up to 43 earthquakes. See Figure C.18 for results for the radial and transverse components. (b) Same as (a) but for the high-frequency bandpass (0.5–4.0 Hz). (c) Amplification from earthquakes (y) versus amplification from ambient noise (x), calculated for the vertical component for 0.1–0.5 Hz. The noise values are from Figure 4.9; the earthquake values are from (a). (d) Same as (c) but for the high-frequency bandpass (0.5–4.0 Hz). Stations FPAP and FAPT are excluded from the line-fitting due to suspected influence of cultural noise. The noise and earthquake data are in general agreement for 0.1–0.5 Hz but not for 0.5–4 Hz.

4.10 References

Abe, K. & Noguchi, S., 1983. Revision of magnitudes of large shallow earthquakes, 1897–1912, *Phys. Earth Planet. Inter.*, **33**, 1–11.

Bard, P.-Y., Campillo, M., Chávez-Garcia, F. J., & Sánchez-Sesma, F., 1988. The Mexico earthquake of September 19, 1985—A theoretical investigation of large- and small-scale amplification effects in the Mexico City valley, *Earthquake Spectra*, **4**(3), 609–633.

Barnes, D. F., 1961. Gravity low at Minto flats, in *Short Papers in the Geologic and Hydrologic Sciences, Articles 293–435: Geological Survey Research 1961*, pp. D254–D257, U.S. Geol. Survey, Washington, D.C., Professional Paper 424-D.

Beaudoin, B. C., Fuis, G. S., Mooney, W. D., Nokleberg, W. J., & Christensen, N. I., 1992. Thin, low-velocity crust beneath the southern Yukon-Tanana terrane, east central Alaska: Results from Trans-Alaska Crustal Transect refraction/wide-angle reflection data, *J. Geophys. Res.*, **97**(B2), 1921–1942.

Bindi, D., Parolai, S., Cara, D., Di Giulio, G., Ferretti, G., Luzi, L., Monachesi, G., Pacor, F., & Rovelli, A., 2009. Site amplifications observed in the Gubbio basin, central Italy: Hints for lateral propagation effects, *Bull. Seismol. Soc. Am.*, **99**(2A), 741–760, doi: 10.1785/0120080238.

Biswas, N. N. & Tytgat, G., 1988. Intraplate seismicity in Alaska, *Seismol. Res. Lett.*, **59**(4), 227–233.

Bowden, D. C. & Tsai, V. C., 2017. Earthquake ground motion amplification for surface waves, *Geophys. Res. Lett.*, **44**, 121–127, doi: 10.1002/2016GL071885.

Crotwell, H. P., Owens, T. J., & Ritsema, J., 1999. The TauP Toolkit: Flexible Seismic travel-time and ray-path utilities, *Seismol. Res. Lett.*, **70**(2), 154–160.

Cruz-Atienza, V. M., Tago, J., Sanabria-Gómez, J. D., Chaljub, E., Etienna, V., Virieux, J., & Quintanar, L., 2016. Long duration of ground motion in the paradigmatic Valley of Mexico, *Sci. Rep.*, **6**, 38807, doi: 10.1038/srep38807.

Day, S. M., Graves, R., Bielak, J., Dreger, D., Larsen, S., Olsen, K. B., Pitarka, A., & Ramirez-Guzman, L., 2008. Model for basin effects on long-period response spectra in southern California, *Earthquake Spectra*, **24**(1), 257–277.

Dixit, N., Hanks, C., Rizzo, A., McCarthy, P., & Coakley, B., 2017. Cenozoic tectonic and thermal history of the Nenana basin, central interior Alaska: new constraints from seismic reflection data, fracture history, and apatite fission-track analyses, *Can. J. Earth Sci.*, **54**, 766–784, doi: 10.1139/cjes-2016-0197.

Dixit, N. C., 2017. *Tectono-thermal history modeling and reservoir simulation stud of the Nenana basin, central Alaska: Implications for regional tectonics and geologic carbon sequestration*, Ph.D. thesis, University of Alaska Fairbanks, Fairbanks, Alaska, USA.

Doyon Limited, 2012. Nenana Basin Depth Map, Available as an interactive website at http://doyonoil.com/HiResImage/NenDepthMap-ForWeb, last accessed 2015-04-12, depth data and contours from Gary Thompson.

Dziewonski, A., Chou, T.-A., & Woodhouse, J. H., 1981. Determination of earthquake source parameters from waveform data for studies of global and regional seismicity, *J. Geophys. Res.*, **86**(B4), 2825–2852, doi: 10.1029/JB086iB04p02825.

Ehm, A., 1983. Oil and gas basins map of Alaska, Alaska Div. Geol. Geophys. Surv. Special Report 32.

Ekström, G., Nettles, M., & Dziewoński, A. M., 2012. The global GCMT project 2004–2010: Centroid-moment tensors for 13,017 earthquakes, *Phys. Earth Planet. Inter.*, **200-201**, 1–9, doi: 10.1016/j.pepi.2012.04.002.

Gedney, L., Shapiro, L., & VanWormer, D., 1972. Correlation of Epicenters with Mapped Faults, East-Central Alaska, 1968–1971, U.S. Geol. Survey Open-File Report 72-128, 7 p., 1 map.

Gedney, L., Estes, S., & Biswas, N., 1980. Earthquake migration in the Fairbanks, Alaska seismic zone, *Bull. Seismol. Soc. Am.*, **70**(1), 223–241.

Graves, R. & Pitarka, A., 2016. Kinematic ground-motion simulations on rough faults including effects of 3D stochastic velocity perturbations, *Bull. Seismol. Soc. Am.*, **106**(5), 2136–2153, doi: 10.1785/0120160088.

Graves, R., Jordan, T. H., Callaghan, S., Deelman, E., Field, E., Juve, G., Kesselman, C., Maechling, P., Mehta, G., Milner, K., Okaya, D., Small, P., & Vahi, K., 2011. CyberShake: A physics-based seismic hazard model for southern California, *Pure App. Geophys.*, **168**, 367–381.

Kirschner, C. E., 1988. Map Showing Sedimentary Basins of Onshore and Continental Shelf Areas, Alaska, U.S. Geol. Survey Miscellaneous Investigation Series I-1873.

Koehler, R. D., Reger, R. D., Spangler, E. R., & Gould, A. I., 2015. Investigation of potentially active tectonic faults along the route of the proposed Alaska Stand Alone Pipeline, Livengood to Cook Inlet, Alaska, Alaska Div. Geol. Geophys. Surv., Report of Investigation 2015-4, 71 p.

Montagner, J.-P. & Kennett, B. L. N., 1996. How to reconcile body-wave and normal-mode reference earth models, *Geophys. J. Int.*, **125**, 229–248.

Olsen, K. B., Day, S. M., Minster, J. B., Cui, Y., Chourasia, A., Faerman, M., Moore, R., Maechling, P., & Jordan, T., 2006. Strong shaking in Los Angeles expected from southern San Andreas earthquake, *Geophys. Res. Lett.*, **33**, L07305, doi: 10.1029/2005GL0254720.

Page, R. A., Biswas, N. N., Lahr, J. C., & Pulpan, H., 1991. Seismicity of continental Alaska, in *Neotectonics of North America*, The Geology of North America, chap. 4, pp. 47–68, eds Slemmons, D. B., Engdahl, E. R., Zoback, M. D., & Blackwell, D. D., Geol. Soc. Am., Boulder, Colo., USA, Decade Map Volume 1.

Page, R. A., Plafker, G., & Pulpan, H., 1995. Block rotation in east-central Alaska: A framework for evaluating earthquake potential?, *Geology*, **23**(7), 629–632.

PRA, 2017. Depth to Basement Map of Nenana Basin, Alaska, Proprietary map provided by Petrotechnical Resources of Alaska, April 2017.

Pratt, T. L., Brocher, T. M., Weaver, C. S., Creager, K. C., Snelson, C. M., Crosson, R. S., Miller, K. C., & Trehu, A. M., 2003. Amplification of seismic waves by the Seattle basin, Washington state, *Bull. Seismol. Soc. Am.*, **93**(2), 533–545.

Pulpan, H., 1986. Seismic-Hazard Analysis of the Nenana Agricultural Development Area, Central Alaska, Alaska Div. Geol. Geophys. Surv. Public-data File 86–78.

Ratchkovski, N. A. & Hansen, R. A., 2002. New constraints on tectonics of interior Alaska: Earthquake locations, source mechanisms, and stress regime, *Bull. Seismol. Soc. Am.*, **92**(3), 998–1014, doi: 10.1785/0120010182.

Rösler, B. & van der Lee, S., 2020. Using seismic source parameters to model frequency-dependent surface-wave radiation patterns, *Seismol. Res. Lett.*, **91**(2A), 992–1002, doi: 10.1785/0220190128.

Saltus, R. W., Brown II, P. J., Morin, R. L., & Hill, P. L., 2008. 2006 Compilation of Alaska Gravity Data and Historical Reports, U.S. Geol. Survey Digital Series 264, CD-ROM.

Sánchez-Sesma, F. & Luzón, F., 1995. Seismic response of three-dimensional alluvial valleys for incident *P*, *S*, and Rayleigh waves, *Bull. Seismol. Soc. Am.*, **85**(1), 269–284.

Silwal, V. & Tape, C., 2016. Seismic moment tensors and estimated uncertainties in southern Alaska, *J. Geophys. Res. Solid Earth*, **121**, 2772–2797, doi: 10.1002/2015JB012588.

Smith, K., 2020a. Seismic moment tensor catalog for local and regional earthquakes recorded in Nenana basin, central Alaska, ScholarWorks@UA at http://hdl.handle.net/11122/10984 (last accessed April 2020): descriptor file, text file of catalog, figures with waveform fits, and input weight files.

Smith, K., 2020b. Supplement to "Seismic response of Nenana sedimentary basin, central Alaska", ScholarWorks@UA at http://hdl.handle.net/11122/11005 (last accessed April 2020): descriptor file, figures of seismic noise spectra, ground motion metrics, and spectral ratios.

Smith, K. & Tape, C., 2019a. Seismic noise in central Alaska and influences from rivers, wind, and sedimentary basins, *J. Geophys. Res. Solid Earth*, **124**, 11,678–11,704, doi: 10.1029/2019JB017695.

Smith, K. & Tape, C., 2019b. Seismic response of Cook Inlet sedimentary basin, southern Alaska, *Seismol. Res. Lett.*, **91**(1), 33–55, doi: 10.1785/0220190205.

Takemura, S., Furumura, T., & Saito, T., 2009. Distortion of the apparent S-wave radiation pattern in the high-frequency wavefield: Tottori-Ken Seibu, Japan, earthquake of 2000, *Geophys. J. Int.*, **178**, 950–961, doi: 10.1111/j.1365-246X.2009.04210.x.

Tape, C., West, M., Silwal, V., & Ruppert, N., 2013. Earthquake nucleation and triggering on an optimally oriented fault, *Earth Planet. Sci. Lett.*, **363**, 231–241, doi: 10.1016/j.epsl.2012.11.060.

Tape, C., Silwal, V., Ji, C., Keyson, L., West, M. E., & Ruppert, N., 2015. Transtensional tectonics of the Minto Flats fault zone and Nenana basin, central Alaska, *Bull. Seismol. Soc. Am.*, **105**(4), 2081–2100, doi: 10.1785/0120150055.

Tape, C., Holtkamp, S., Silwal, V., Hawthorne, J., Kaneko, Y., Ampuero, J. P., Ji, C., Ruppert, N., Smith, K., & West, M. E., 2018. Earthquake nucleation and fault slip complexity in the lower crust of central Alaska, *Nature Geoscience*, **11**, 536–541, doi: 10.1038/s41561-018-0144-2.

Tsai, V. C. & Atiganyanun, S., 2014. Green's functions for surface waves in a generic velocity structure, *Bull. Seismol. Soc. Am.*, **104**(5), 2573–2578, doi: 10.1785/0120140121.

Tsai, V. C., Bowden, D. C., & Kanamori, H., 2017. Explaining extreme ground motion in Osaka basin during the 2011 Tohoku earthquake, *Geophys. Res. Lett.*, **44**, 7239–7244, doi: 10.1002/2017GL074120.

Van Kooten, G. K., Richter, M., & Zippi, P. A., 2012. Alaska's Interior rift basins: a new frontier for discovery, *Oil & Gas J.*, **110**(1a), 48–57.

Wang, T., Shi, Q., Nikkhoo, M., Wei, S., Barbot, S., Dreger, D., Bürgmann, R., Motagh, M., & Chen, Q.-F., 2018. The rise, collapse, and compaction of Mt. Mantap from the 3 September 2017 North Korean nuclear test, *Science*, doi: 10.1126/science.aar7230.

Wirth, E. A., Vidale, J. E., Frankel, A. D., Pratt, T. L., Marafi, N. A., Thompson, M., & Stephenson, W. J., 2019. Source-dependent amplification of earthquake ground motions in deep sedimentary basins, *Geophys. Res. Lett.*, **46**, 6443–6450, doi: 10.1029/2019GL082474.

Yoshimoto, K. & Takemura, S., 2014. A study on the predominant period of long-period ground motions in the Kanto Basin, Japan, *Earth Planets Space*, **66**, 100, doi: 10.1186/1880-5981-66-100.

Zhu, L. & Helmberger, D., 1996. Advancement in source estimation techniques using broadband regional seismograms, *Bull. Seismol. Soc. Am.*, **86**(5), 1634–1641.

Chapter 5

Conclusion

This thesis provides empirical evidence for the effects of ground motion from environmental sources and from basins. Ambient noise is affected by various sources and we use it to monitor the environment. Our study suggests that the Tanana river is affecting frequencies 4–30 Hz, wind is affecting frequencies $>$ 2.0 Hz (as well as previously documented tilt effects for $<$0.05 Hz), and basins are affecting frequencies 0.1–4.0 Hz. Due to the proximity of our seismometers to the river, we were able to learn about activity on the river as well as discharge. The study of wind on ambient noise allowed us to quantify the spatial extent of wind and to separate the effects of wind from the effects of the basin. Both basin studies demonstrate amplification of ground motion for earthquakes and ambient noise sources, and we found that horizontal motion is more amplified than vertical motion. Amplification is also correlated with basin depth at lower frequencies (0.1–0.5 Hz). Each study shows ambient noise can be used to study amplification from earthquakes. The Nenana basin has larger amplification than Cook Inlet basin. The study shows that more seismic stations are needed on basins to study amplification since millions of people world-wide live on basins. Future work with 3D simulations will give a better understanding of shaking.

5.1 Ground Motion Prediction Equations

Ground motion prediction equations (GMPEs) or ground motion models (GMMs) are often used to predict PGV, and peak ground acceleration (PGA) from earthquake sources. They prove to be useful for predicting ground motion in California. Many GMPEs are used throughout the US to produce seismic hazard maps (Petersen et al., 2020) but they sometimes fail to account for basin and regional effects in other areas. Current GMPEs use data from the Next Generation Attenuation 2 project which consists of a rich data set from stations and events in California. The stations have data of the average shear velocity to 30 m depth and the earthquakes are usually 20 km deep (Ancheta et al., 2014) which points to a bias in the dataset. Further examination of some GMPEs such as from Campbell & Bozorgnia (2014) shows a large dependence on regression models and a dependence on critical values for which ground motion prediction changes. The model from Campbell & Bozorgnia (2014) does account for basin depth but only does so for certain basins

such as Los Angeles basin, Salt Lake City basin, and San Francisco. Another GMPE from Abrahamson et al. (2014) shows that the most important factor for sediment amplification is the depth to the 1 km/s shear wave velocity layer. This neglects other factors important to amplification that include geometry and structural heterogeneity. Currently there are no GMPEs specific to Alaska and that can lead to the failure of GMPE models for significant events like the M_w 7.1 Anchorage earthquake (McNamara et al., 2019). Similar GMPEs fail for certain events observed in New Zealand and Japan (Mak et al., 2018). Douglas (2007) discusses the importance of regional differences that are due to the distribution of data from sites and earthquakes which bias the GMPE model.

5.2 Future Work

From Chapter 1, there are still some puzzling signals to investigate, fine tuning to do, and future modelling to do. One of the puzzling signals occurs on Figure 2.14 (In Chapter 2) at 20 Hz at stations within the basin or margins. The signal could be due to a changing water table depth or permafrost effects. Another source of high frequency at 10 Hz is the signal at FTGH. We expected a correlation with highway activity but found none. Many of the spectra have been smoothed but rougher spectra can give greater detail about the specific frequencies affected. Rougher ambient noise spectra will also be useful for giving more details about other sources of motion such as nearby towers. Now that a data analysis has been carried out for river and wind sources, the next step would be to model the ambient noise of these sources. The model can explain important features of wind and river that give rise to ground motion and extrapolate hypothetical events. One model of river turbulence from Gimbert et al. (2014) already exists but its implementation proves to be challenging due to the complex nature of the Tanana River.

The basin amplification studies raised a lot of regional specific questions to basin response. One issue with the Cook Inlet basin study that still needs to be addressed is accounting for site-to-source distance of the non-basin reference station and basin station for spectral ratios. In the Nenana basin study, we implemented this distance correction but did not observe notable differences that could affect the main points. I expect this to be the case with Cook Inlet basin but it is best to rerun calculations to be sure. The Cook Inlet basin study also did not account for the effects of wind or other environmental sources when basin amplification was computed for ambi-

ent noise. Accounting for wind in Cook inlet will be a more formidable task since a wider area is covered and more weather stations are available.

Since many of the events in our study did not have moment tensor solutions, it would be advantageous for us to obtain them to get a more complete picture of the earthquake characteristics and its effect on basin amplification. In Nenana basin, moment tensors are available but the frequency-dependent role of source mechanism on basin amplification is still unclear, especially at higher frequencies. A deeper analysis on azimuthal variations with respect to the geometry of the focal plane and azimuth of the event to the basin will need to be explored. For all of our events we have computed PGV, E_R, etc. but have only done our analysis for specific components however an analysis of total PGV, total E_R, etc will be useful for assessing seismic hazard. Since our study includes only a limited amount of teleseismic events, it would be beneficial to explore other teleseismic events to test the robustness of our current results and possibly extend our analysis to include other phases and the isolation of surface waves.

Three-dimensional seismic wavefield simulations provide an opportunity to model the large number of earthquake seismograms recorded from the FLATS, SALMON, TA and AK networks. Many earthquake simulations have already been carried out across the world including areas like Taipei (Lee et al., 2008), Los Angeles (Olsen, 2000), and Kobe (Pitarka et al., 1998), and the results show detailed views of the wavefield and its interaction with faults and sedimentary basins. In Nenana basin, we would like to do computer simulation of the wavefield to assess amplification and that would involve building a structural earth model, solving the wave equation, verifying simulations with known earthquakes, and simulating scenario earthquakes for characterizing hazard, similar to the approach of Graves et al. (2011). We would use unstructured meshes since they better fit the complex geometry of the basin (Pelties et al., 2010) and solve the wave equation using the spectral element method from Komatitsch & Tromp (2002a,b). The model and solver can then be applied, evaluated and refined for point source earthquakes in our study.

A refined earth model can be used to test and improve our data analysis methods. This includes the response from teleseismic waves. Teleseismic waves are simple to examine because the propagation direction is primarily on the vertical component. Some simulations of vertically incident P and S waves have been done by Olsen & Schuster (1995) and Luzon et al. (2004). Olsen & Schuster (1995) concluded that the impedance contrast and resonance from deep basin structure

control amplification of P waves. Luzon et al. (2004) simulated SH waves and found the depth dependence of shear wave velocities in basins to be important for characterizing basin resonance. To characterize seismic hazard, it would be beneficial to produce some scenario earthquakes that include a M_w 7 earthquake like in Olsen et al. (1995), Olsen & Archuleta (1996) and Harmsen et al. (2008). A M_w 7 earthquake at close proximity would realistically need to be described with a finite fault. Since no such earthquakes have been recorded, a scenario finite fault can be produced from a spatial random field model (Mai & Beroza, 2002). A suite of earthquake simulations will allow the seismic hazard to be evaluated by identifying areas prone to intense shaking which can be the result of generated surface waves on the basin edges, focusing, and trapping. As a whole the basin will also have normal modes which can amplify shaking at specific frequencies. Simulations will be able to investigate the differences we see in the data such as FNN1 and FNN2.

In summary, this thesis offers empirical evidence of basin amplification of seismic noise and earthquakes waves in Nenana basin and Cook Inlet basin. The catalogs of documented earthquakes, as well as the database archive of continuously recorded seismic noise, provide a solid foundation for future studies of these basins, as well as for studying the effects of basin amplification, in general. During the time period of the FLATS and SALMON deployments, the stations in the basin recorded a wide range of local, regional, crustal, intraslab, and of course teleseismic earthquakes. Future work on numerical simulations will be needed to fully understand the complex empirical evidence of basin amplification.

5.3 References

Abrahamson, N. A., Silva, W. J., & Kamai, R., 2014. Summary of the ASK14 ground motion relation

for active crustal regions, *Earthquake Spectra*, **30**(3), 1025–1055, doi: 10.1193/070913EQS198M.

Ancheta, T. D., Darragh, R. B., Stewart, J. P., Seyhan, E., Silva, W. J., Chiou, B. S.-J., Wooddell, K. E., Graves, R. W., Kottke, A. R., Boore, D. M., et al., 2014. NGA-West2 database, *Earthquake Spectra*, **30**(3), 989–1005, doi: 10.1193/070913EQS197M.

Campbell, K. W. & Bozorgnia, Y., 2014. NGA-West2 ground motion model for the average horizontal components of PGA, PGV, and 5% damped linear acceleration response spectra, *Earthquake Spectra*, **30**(3), 1087–1115, doi: 10.1193/062913EQS175M.

Douglas, J., 2007. On the regional dependence of earthquake response spectra.

Gimbert, F., Tsai, V. C., & Lamb, M. P., 2014. A physical model for seismic noise generation by turbulent flow in rivers, *J. Geophys. Res. Earth Surface*, **119**, 2209–2238, doi: 10.1002/2014JF003201.

Graves, R., Jordan, T. H., Callaghan, S., Deelman, E., Field, E., Juve, G., Kesselman, C., Maechling, P., Mehta, G., Milner, K., Okaya, D., Small, P., & Vahi, K., 2011. CyberShake: A physics-based seismic hazard model for southern California, *Pure App. Geophys.*, **168**, 367–381.

Harmsen, S., Hartzell, S., & Liu, P., 2008. Simulated ground motion in Santa Clara Valley, California, and vicinity from M$\geq$ 6.7 scenario earthquakes, *Bull. Seismol. Soc. Am.*, **98**(3), 1243–1271, doi: 10.1785/0120060230.

Komatitsch, D. & Tromp, J., 2002a. Spectral-element simulations of global seismic wave propagation—I. Validation, *Geophys. J. Int.*, **149**, 390–412.

Komatitsch, D. & Tromp, J., 2002b. Spectral-element simulations of global seismic wave propagation—II. Three-dimensional models, oceans, rotation and self-gravitation, *Geophys. J. Int.*, **150**, 308–318.

Lee, S.-J., Chen, H.-W., & Huang, B.-S., 2008. Simulations of strong ground motion and 3D amplification effect in the Taipei Basin by using a composite grid finite-difference method, *Bull. Seismol. Soc. Am.*, **98**(3), 1229–1242, doi: 10.1785/0120060098.

Luzon, F., Ramirez, L., Sánchez-Sesma, F., & Posadas, A., 2004. Simulation of the seismic response of sedimentary basins with vertical constant-gradient velocity for incident SH waves, in *Geodetic and Geophysical Effects Associated with Seismic and Volcanic Hazards*, pp. 1533–1547, Springer.

Mai, P. M. & Beroza, G. C., 2002. A spatial random field model to characterize complexity in earthquake slip, *J. Geophys. Res.*, **107**(B11), 2308, doi: 10.1029/2001JB000588.

Mak, S., Cotton, F., Gerstenberger, M., & Schorlemmer, D., 2018. An Evaluation of the Applicability of NGA-West2 Ground-Motion Models for Japan and New Zealand, *Bull. Seismol. Soc. Am.*, **108**(2), 836–856, doi: 10.1785/0120170146.

McNamara, D. E., Wolin, E., Powers, P. M., Shumway, A. M., Moschetti, M. P., Rekoske, J., Thompson, E. M., Mueller, C. S., & Petersen, M. D., 2019. Evaluation of Ground-Motion Models for US Geological Survey Seismic Hazard Models: 2018 Anchorage, Alaska, Mw 7.1 Subduction Zone Earthquake Sequence, *Seismol. Res. Lett.*, **91**(1), 183–194, doi: 10.1785/0220190188.

Olsen, K. & Schuster, G., 1995. Causes of low-frequency ground motion amplification in the Salt Lake Basin: the case of the vertically incident P wave, *Geophys. J. Int.*, **122**, 1045–1061.

Olsen, K. B., 2000. Site amplification in the Los Angeles basin from three-dimensional modelling of ground motion, *Bull. Seismol. Soc. Am.*, **60**(6B), S77–S94, doi: 10.1785/0120000506.

Olsen, K. B. & Archuleta, R. J., 1996. Three-dimensional simulation of earthquakes on the Los Angeles fault system, *Bull. Seismol. Soc. Am.*, **86**(3), 575–596.

Olsen, K. B., Archulete, R. J., & Matarese, J. R., 1995. Three-dimensional simulation of a magnitude 7.75 earthquake on the San Andreas fault, *Science*, **270**, 1628–1632.

Pelties, C., Käser, M., Hermann, V., & Castro, C. E., 2010. Regular versus irregular meshing for complicated models and their effect on synthetic seismograms, *Geophys. J. Int.*, **183**, 1031–1051, doi: 10.1111/j.1365-246X.2010.04777.x.

Petersen, M. D., Shumway, A. M., Powers, P. M., Mueller, C. S., Moschetti, M. P., Frankel, A. D., Rezaeian, S., McNamara, D. E., Luco, N., Boyd, O. S., Rukstales, K. S., Jaiswal, K. S., Thompson, E. M., Hoover, S. M., Clayton, B. S., Field, E. H., & Zeng, Y., 2020. The 2018 update of the US National Seismic Hazard Model: Overview of model and implications, *Earthquake Spectra*, **36**(1), 5–41, doi: 10.1177/8755293019878199.

Pitarka, A., Irikura, K., Iwata, T., & Sekiguchi, H., 1998. Three-dimensional simulation of the near-fault ground motion for the 1995 Hyogo-Ken Nanbu (Kobe), Japan earthquake, *Bull. Seismol. Soc. Am.*, **88**(2), 428–440.

Appendix A

Supporting Information for Chapter 2 (Seismic noise in central Alaska and influences from rivers, wind, and sedimentary basins)

A.1 Tree measurements

Our compilation of measurements of nearby trees at each seismic station site is shown in Table A.2. The information in Table A.2 provides information on one tree at each site; it does not fully characterize the setting of vegetation in the region of each seismic station.

As discussed in Section 2.5.4.2, the resonant frequency of trees depends on the dimension (circumference, height, branches) and the elastic properties. For each site, we measured the distance to the closest tree with trunks larger than 50 cm in circumference (i.e., 16 cm in diameter). We estimated the height of each tree using a clinometer. We noted the type of tree (spruce, birch, aspen), which has bearing on the elastic properties and also the branching structure, both of which will affect the resonant frequency.

For sites whose closest large trees were >30 m away, we used Google Earth imagery dated from 2017-06-01. All other measurements in Table A.2 were made on 2019-06-09. Next we provide some details on some of the sites, notably ones for which no data are listed in Table A.2.

1. No tree measurements are listed for F2TN due to having multiple reinstallations on account of a rapidly eroding riverbank.

2. F6TP is within a large forest fire burn area, with large spruce logs having toppled all over. There are no standing trees within 100 m of F6TP, but there are many fallen trees within 10 m of the site.

3. FNN1 is in the middle of a former exploratory well pad and is at least 50 m from any tree.

4. FNN2 is within a forest fire burn area, >50 m from large trees.

5. FAPT is near a lattice tower (Section 2.5.4.1), a shed, and an area of small aspens. The tree data for NEA2 are based on the nearest tree; there is also a lattice tower nearby that has a clear imprint on the seismic noise (Section 2.5.4.1).

6. I23K is on the outskirts of the village of Minto. It is not near any tree, but it is within 50 m of telephone poles and buildings.

7. MLY is on the top of a treeless rock-covered dome.

A.2 Wind vs seismic noise for EarthScope TA stations

The EarthScope Transportable Array (TA) includes several stations with co-located meteorological sensors that record air pressure, wind speed and direction, and temperature. Taking into account the operating times and data availability from TA seismic and meteorological sensors, we selected the closest four stations to our study area: J19K, I20K, H22K, and J25K (Figure A.52).

Wind speeds from TA stations are available every second, as opposed to every hour, as is the case for Nenana meteorological station PANN. Therefore we take the mean of the TA wind speeds every hour, and from the hourly time series we stack the hourly ambient noise spectra according to the wind speed interval (Section 2.5.4.1). The results are shown in Figures A.53–A.56 and reveal a systematic increase in seismic noise with increasing wind—similar to what we identified when comparing seismic noise from stations that were tens of km from a weather station (Section 2.5.4.1). The influence of wind on high-frequency seismic noise is extreme at I20K, strong at J19K, and minimal at J25K and H22K. Knowledge of the sensor installation and site conditions could help in understanding these differences. For some cases (e.g., H22K), the noise stack for 0 m/s exhibits higher noise than for 0–2 m/s; we speculate that the 0 m/s wind speeds may also reflect time periods of when the sensor is returning a null value during windy conditions.

A.3 Analysis of P picks in relation to seismic noise seasonality

We examine events within the Alaska Earthquake Center earthquake catalog that occurred within the Minto Flats fault zone during 2016 and 2017. (The catalog for 2018 was not finalized at the time of writing.) In both 2016 and 2017, there were 3D active-source seismic surveys in Minto Flats that included hundreds of explosion shots, many of which were picked up in the catalog. For simplicity, we excluded the months of March and April, 2016 and 2017, from the analysis.

To test the influence of seismic noise levels on the numbers of events detected in the earthquake catalog, we focus on a subset of events and a subset of stations. The starting set of events

for each year is shown in Figures A.79 and A.80. From this set of events we collect P picks in the Alaska Earthquake Center catalog from FLATS river stations F2TN, F3TN, F4TN, F5MN, and F7TV, shown in Figure A.81a for 2016 and Figure A.83a for 2017. In Figure A.81b and Figure A.83b we show the subset of events for which there is at least one P pick for a FLATS river station. A summary of the event numbers and P pick numbers is listed in Table A.3.

The time variations of P picks and events within Minto Flats fault zone show a seasonality (Figures A.81 and A.83), with fewer picks and events during summer and more during winter. During these same two years, the 10 Hz seismic noise is lowest in winter and highest in summer (Figures A.82 and A.84). The results suggest that changing noise levels due to the river cause changing detection levels for P waveforms and, in turn, for earthquakes in the Minto Flats fault zone.

A.4 Tables

Table A.1: Types of microseisms. This table is retyped from Gutenberg (1958, Table 1), which is based on Gutenberg (1951, Table 1). We have added frequency ranges for convenience of comparison with our study.

Period (sec)			Frequency (Hz)	Type of movement	Hypothetical cause	Distance of cause
0.001	–	0.5	2–1000	Regular	Traffic, industry, wind	Nearby
0.2	–	2	0.5–5	Irregular	Surf	Nearby
1	–	4	0.25–1	Regular	Fronts, turbulent wind	Nearby
1	–	4	0.25–1	Irregular	Effects of wind on trees, buildings	Local
2	–	6	0.17–0.5	Regular	Ocean waves in hurricanes, typhoons	Distant
4	–	10	0.10–0.25	Regular	Ocean waves in extratropical disturbances	Distant
4	–	10	0.10–0.25	Regular	Surf driven by wind against steep coasts	Distant
4	–	10	0.10–0.25	Regular	Air-pressure pulsations?	Medium?
4	–	10	0.10–0.25	Regular	Monsoon and similar types of wind	Medium?
10	–	20	0.05–0.10	Regular	Water waves striking the coast	Medium?
20	–	100	0.01–0.05	Irregular	Wind? Air currents in instrument vault?	Nearby
40	–	200	0.005–0.025	Irregular	Freezing of ground? "Icing" of instruments?	Medium

Table A.2: Classification of 16 stations (Table 2.1) based on the presence trees as a possible noise source. See Section A.1 for details, including explanations for the NA entries. The coloring is a qualitative indicator of how present trees are expected to be as a source of noise: red present, blue somewhat present, green not present.

network	station	distance to tree (m)	tree height (m)	tree circumference (cm)	tree type
XV	F1TN	1.8	17.1	97	spruce
XV	F2TN	N/A	N/A	N/A	spruce
XV	F3TN	7.2	33.8	178	spruce
XV	F4TN	3.0	27.4	135	spruce
XV	F5MN	3.7	15.2	74	birch
XV	F6TP	N/A	N/A	N/A	
XV	F7TV	6.4	14.9	66	aspen
XV	FNN1	N/A	N/A	N/A	
XV	FNN2	N/A	N/A	N/A	
XV	FAPT	N/A	N/A	N/A	
XV	FPAP	10.8	17.1	58	aspen
XV	FTGH	40	> 10	> 50	spruce
AK	NEA2	5.5	15.8	69	birch
TA	I23K	N/A	N/A	N/A	
AK	MLY	N/A	N/A	N/A	
XV	F8KN	13	> 10	> 50	spruce

Table A.3: Events in Minto Flats fault zone, 2016 and 2017. See Section A.3 for details.

year	MFFZ events	number of events	number of P picks
2016	total	1316	17578
2016	w/o Mar & Apr	907	15410
2016	w/o Mar & Apr AND w/ $\geq$1 river FLATS station pick	822	2483
2017	total	1582	24588
2017	w/o Mar & Apr	1034	17262
2017	w/o Mar & Apr AND w/ $\geq$1 river FLATS station pick	887	2685

A.5 Figures

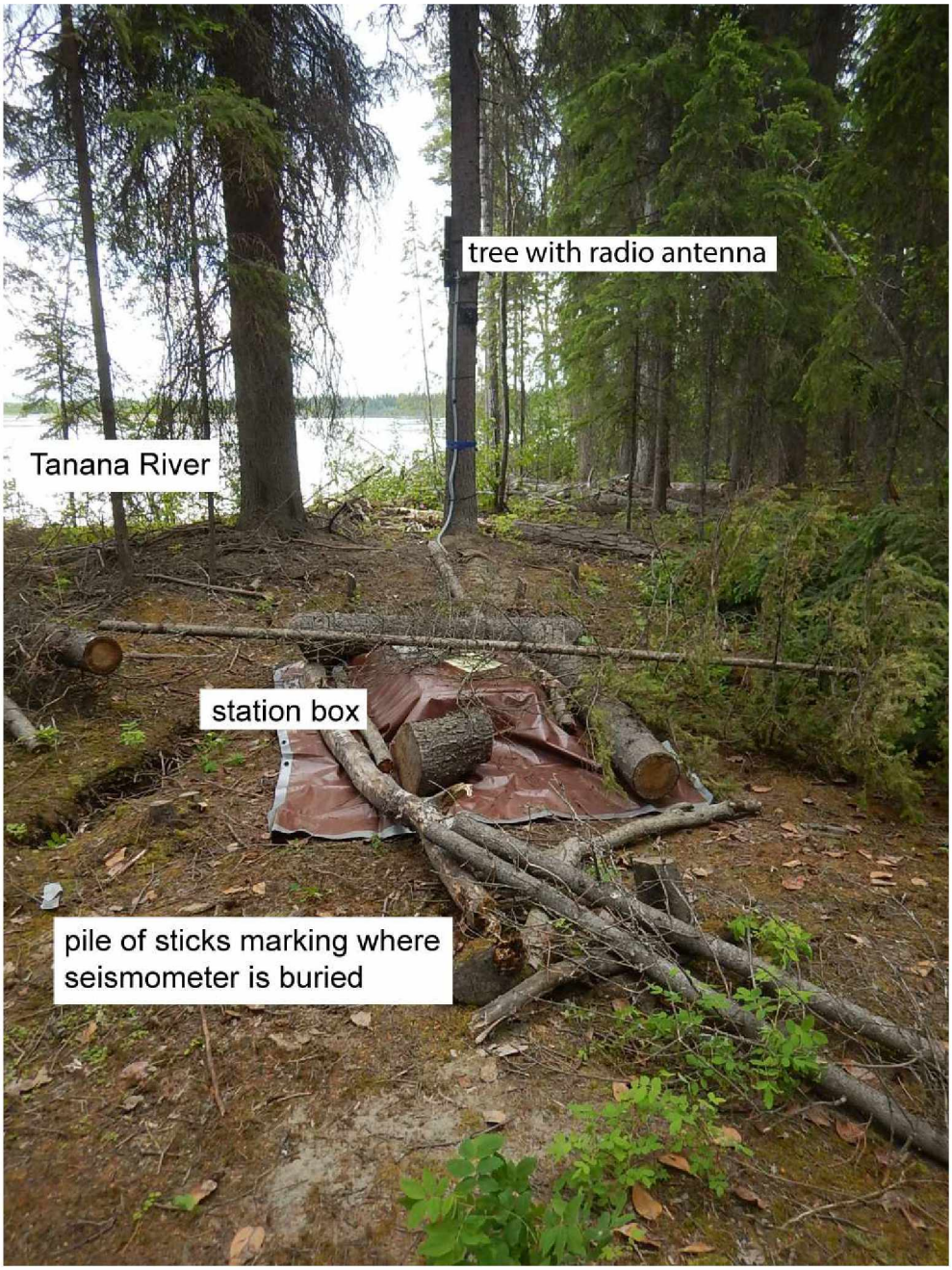

Figure A.1: Example of FLATS stations, shown for F3TN on the Tanana River (Figure 2.1). The direct-burial T120PH sensor is powered by air-alkaline batteries inside the station box. At this site, the Tanana River is 14 m from the sensor, and a significantly tall tree (34 m) is 7 m from the sensor. Note that snow covers the ground between October and April.

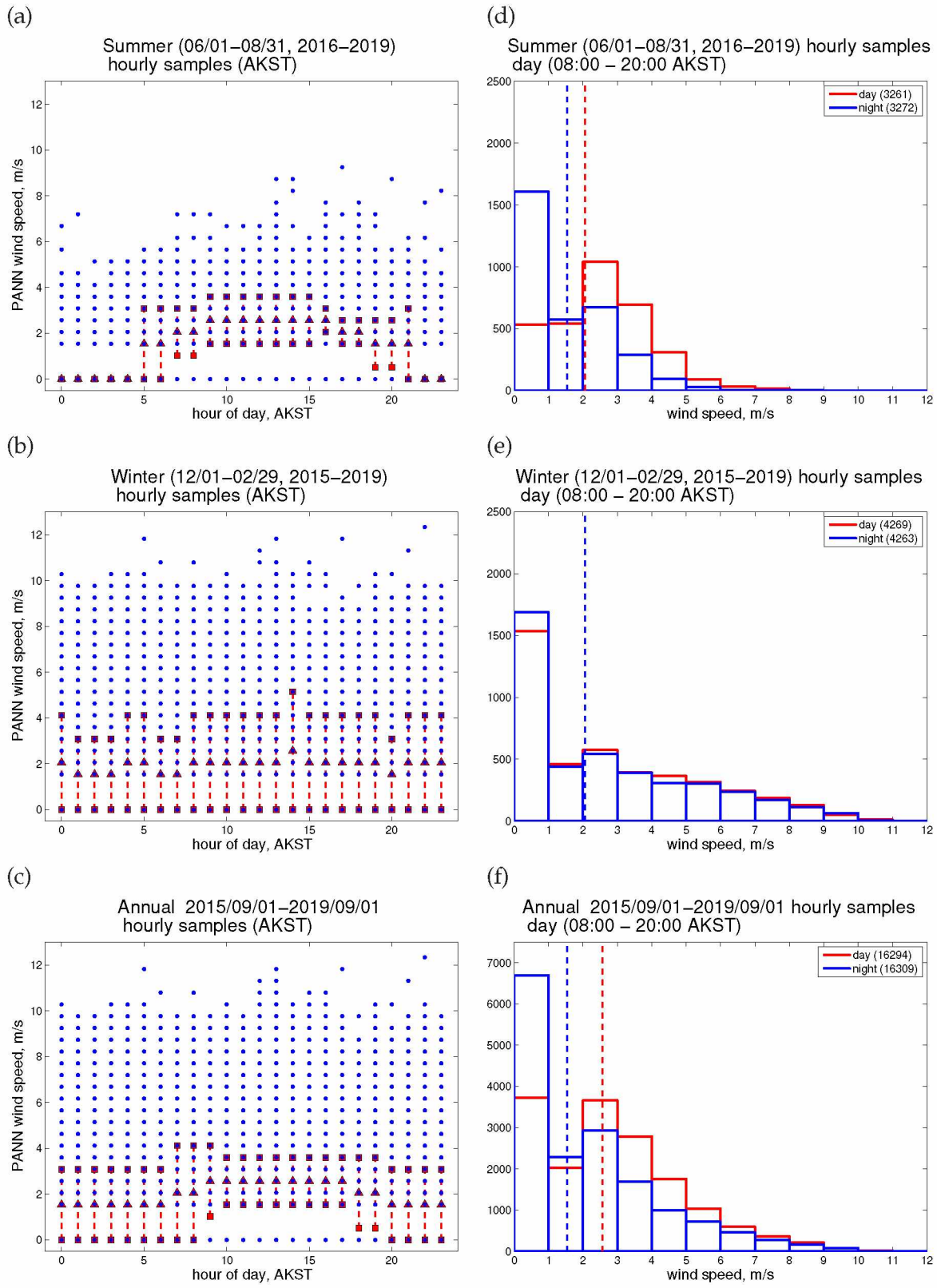

Figure A.2: Seasonal and diurnal variations in wind speed at Nenana, Alaska, between 2015-09-01 and 2019-09-01, at station PANN. (a)-(c) Median hourly wind speed as a function of hour-of-day (Alaska Standard Time) for summer (a), winter (b), and all year (c). The red triangles are the median value; the red squares denote 1 median absolute deviation. (d)-(f) Distribution of hourly wind speeds for summer (d), winter (e), and all year (f). The red histogram is for daytime measurements (08:00–20:00), the blue is for nighttime.

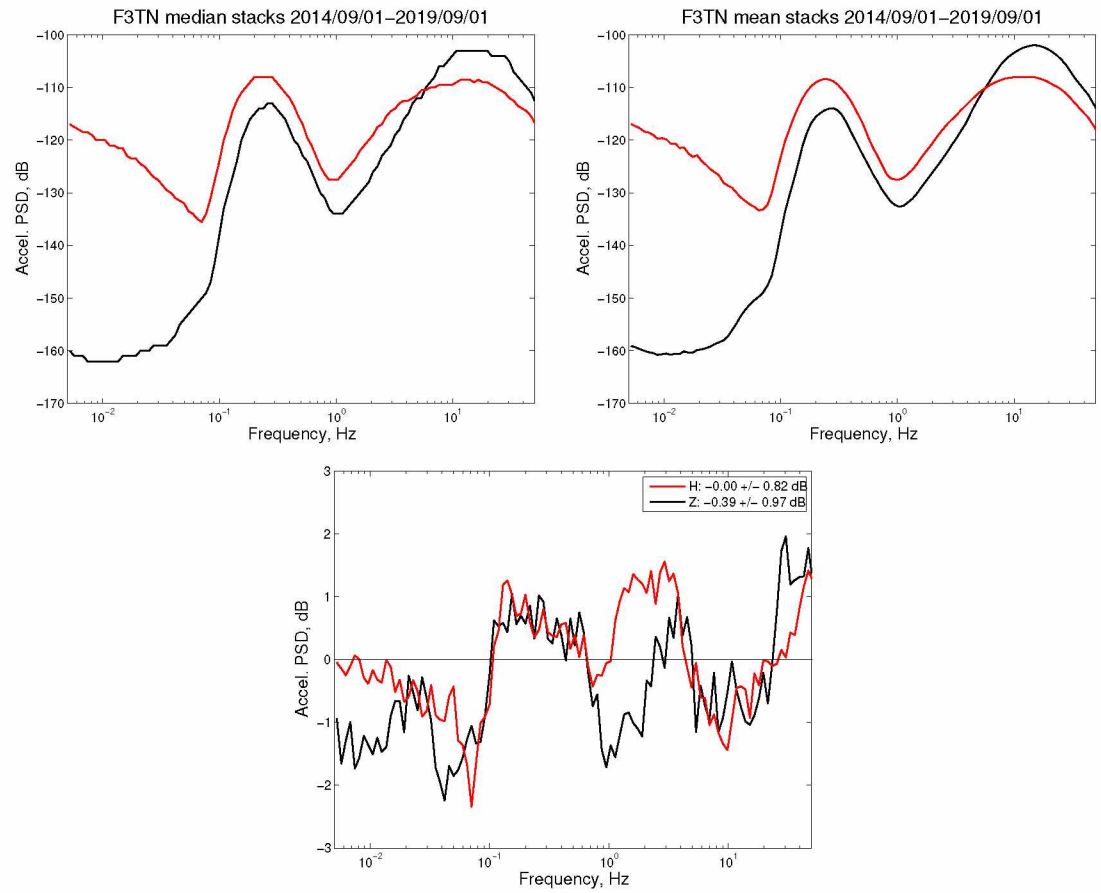

Figure A.3: Stacks of seismic spectra calculated using median (top left) and mean (top right) for horizontal (red) and vertical (black) components. The example is for a set of daily spectra at F3TN between 2014-09-01 and 2019-09-01. The differences between the median and mean are shown in the bottom and vary between ± 2 dB. The median operation leads to a spectral stack that is more jagged than when using the mean operation.

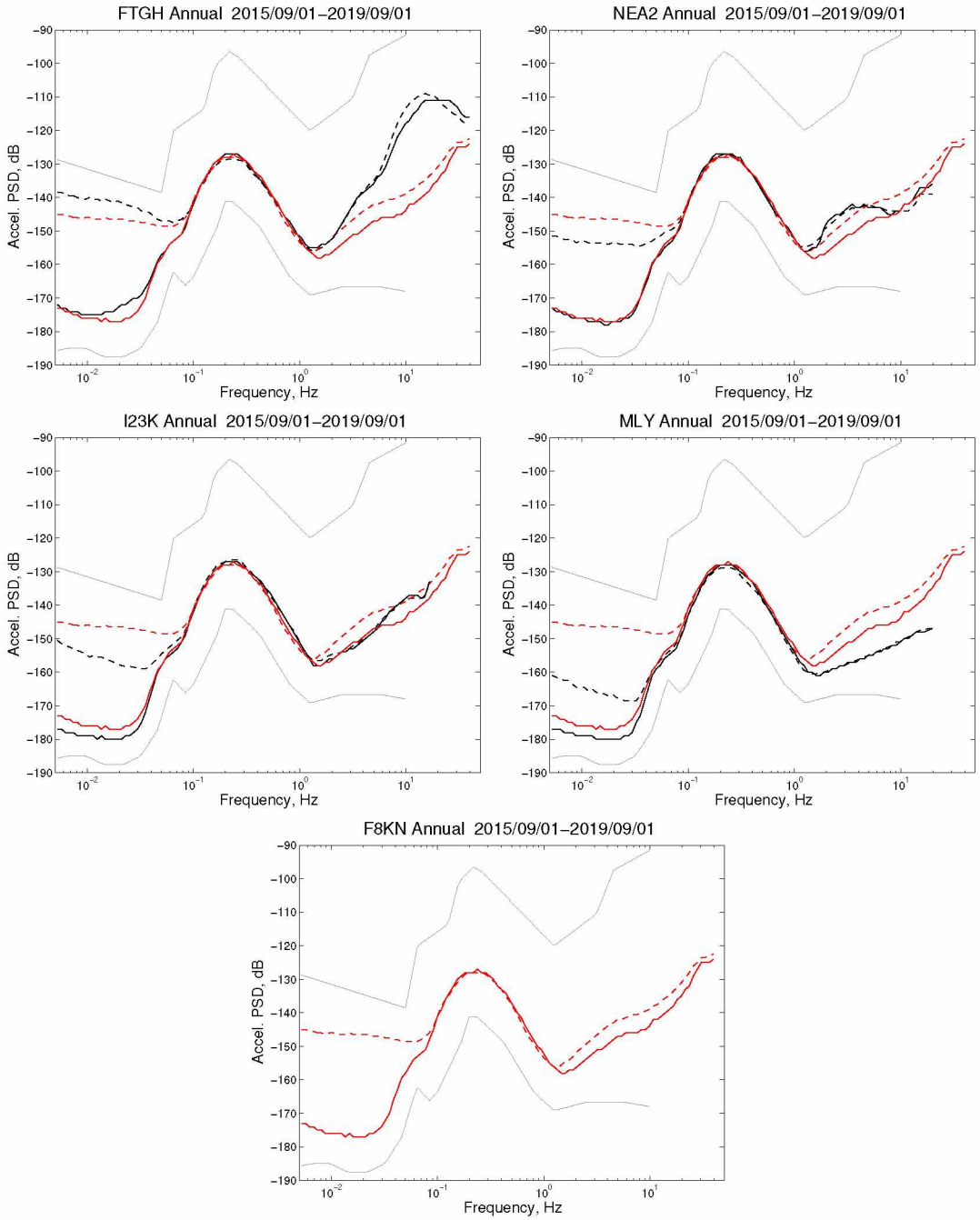

Figure A.4: Final four subplots from Figure 2.3 (XV.FTGH, AK.NEA2, TA.I23K, AK.MLY), plus the reference station XV.F8KN, whose spectra are plotted in red for each subplot. The black bold lines are the NHNM and NLNM reference spectra (Peterson, 1993).

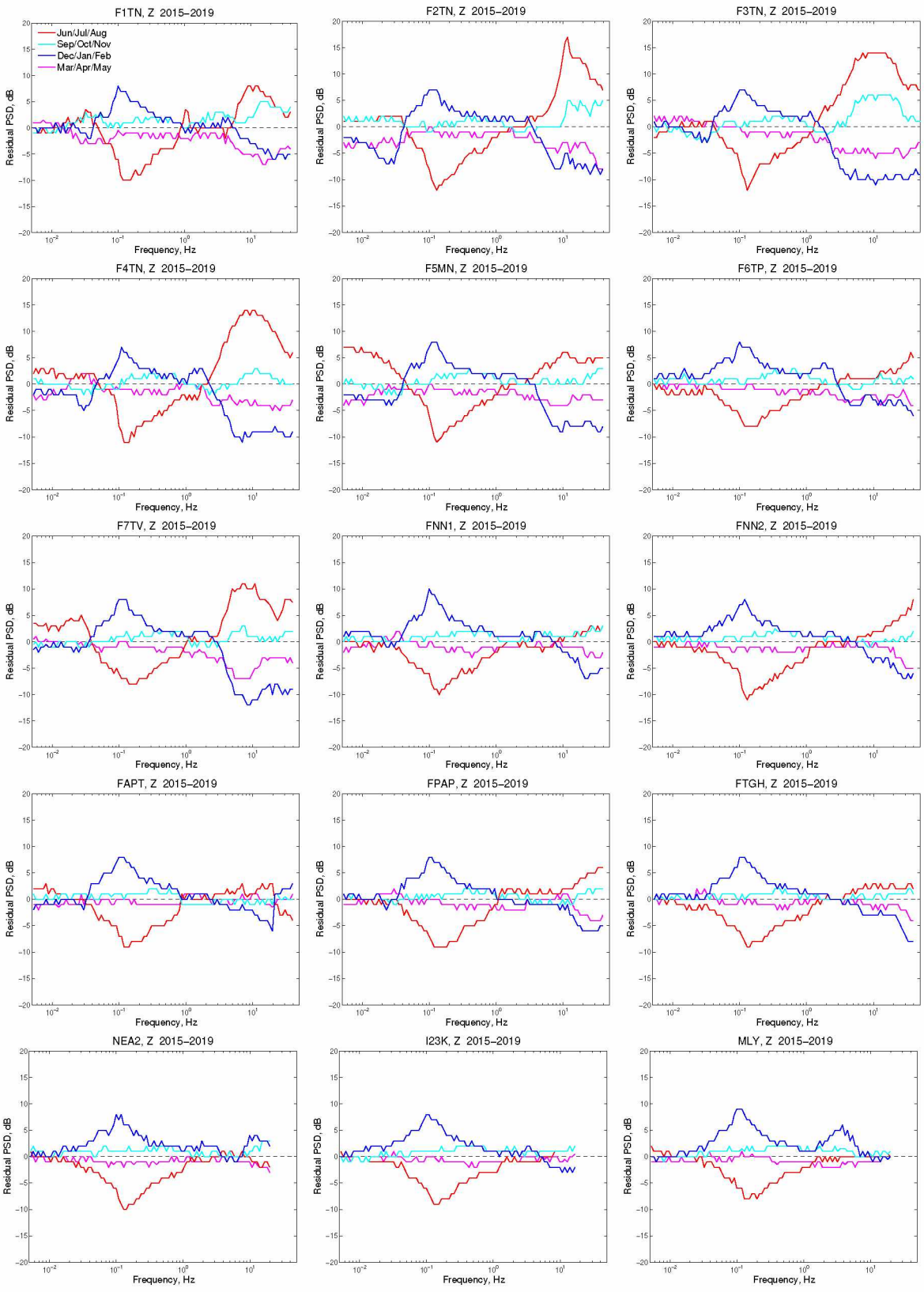

Figure A.5: Seasonal variations of the annual noise spectra from Figure 2.3. Same as Figure 2.4 but for the vertical component. Variations for F8KN are shown in Figure A.6b.

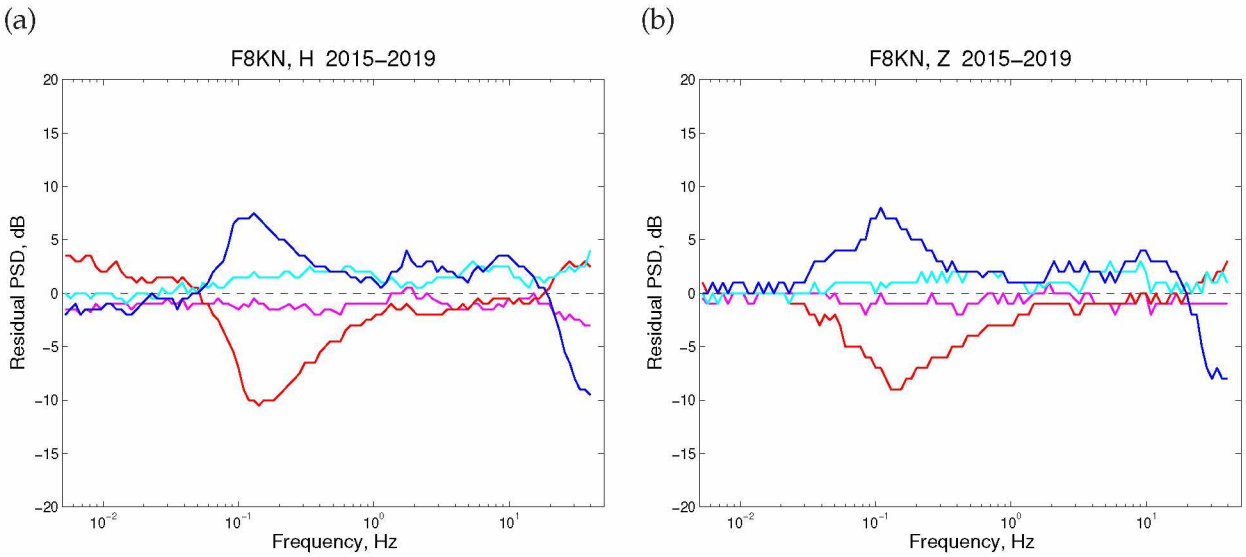

Figure A.6: Seasonal variations of ambient noise at F8KN. The annual noise stack for F8KN are the red spectra in each subplot of Figure 2.3. Note the slightly elevated high-frequency (1–10 Hz) noise during fall and winter; we attribute this to wind (see also Figure A.49). See Figures 2.4 and A.5 for comparison with other stations.

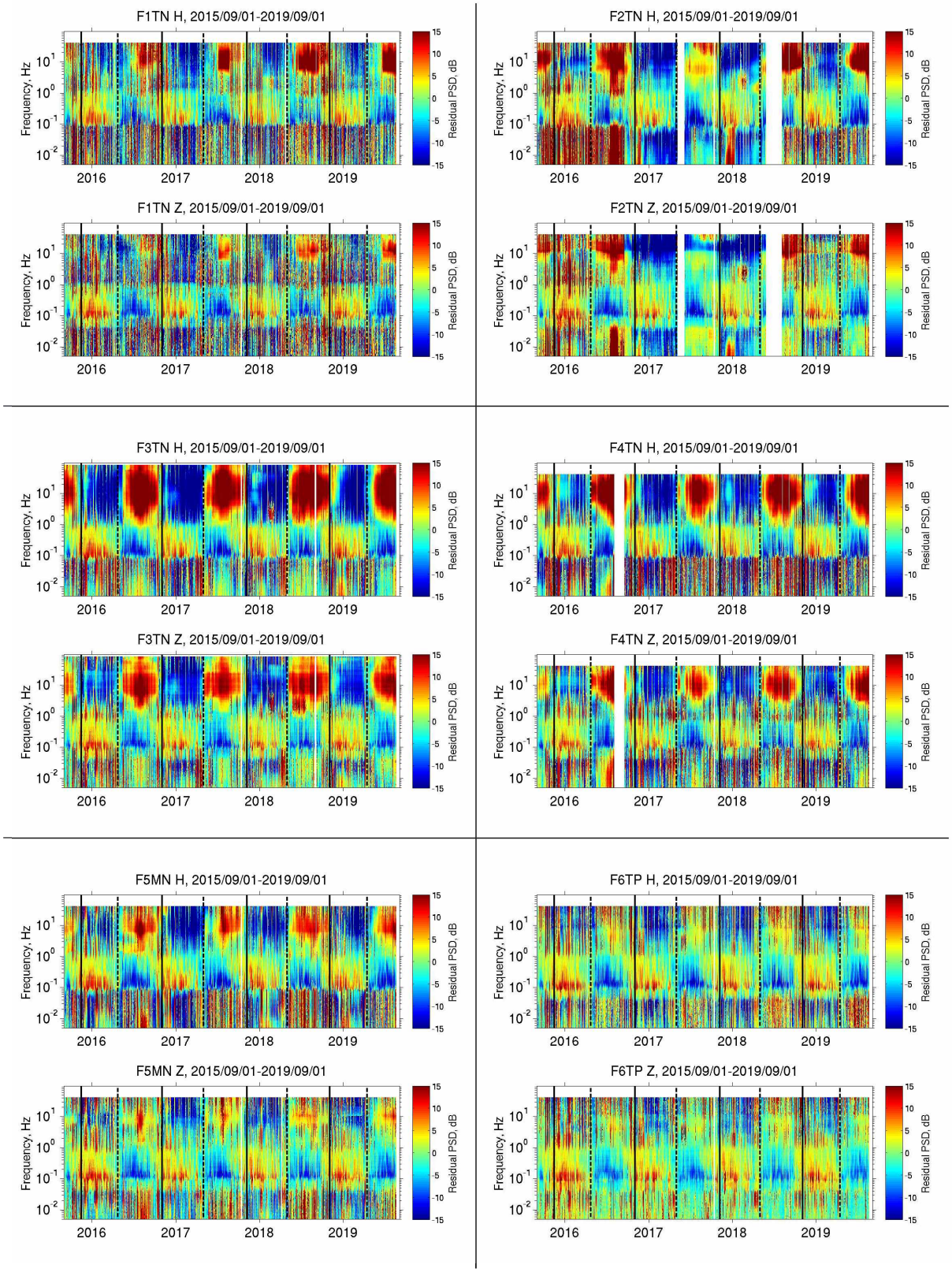

Figure A.7: Residual spectrograms for FLATS stations (F1TN, F2TN, F3TN, F4TN, F5MN, F6TP); see Figure 2.6 caption for details.

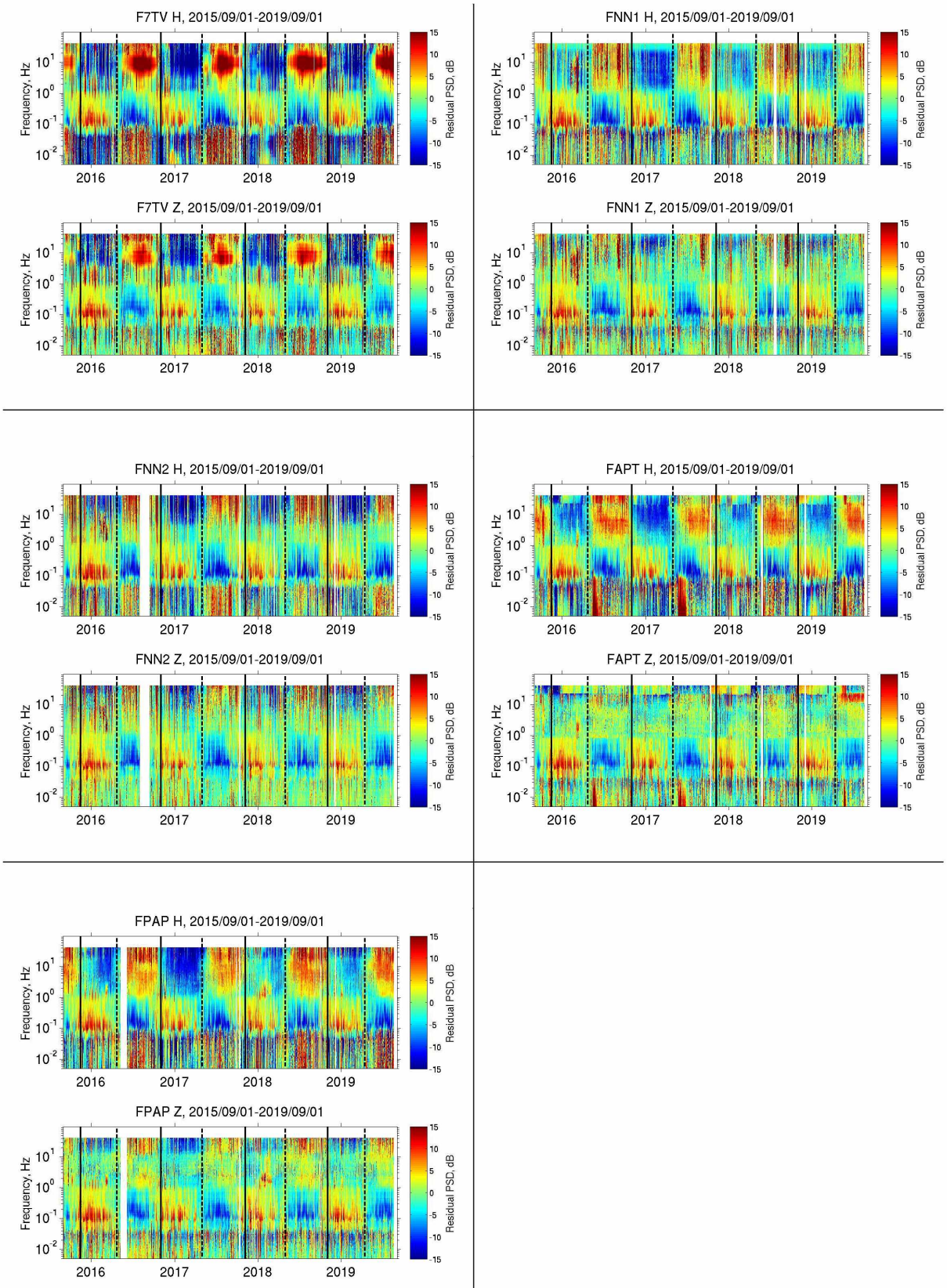

Figure A.7 continued: F7TV, FNN1, FNN2, FAPT, FPAP

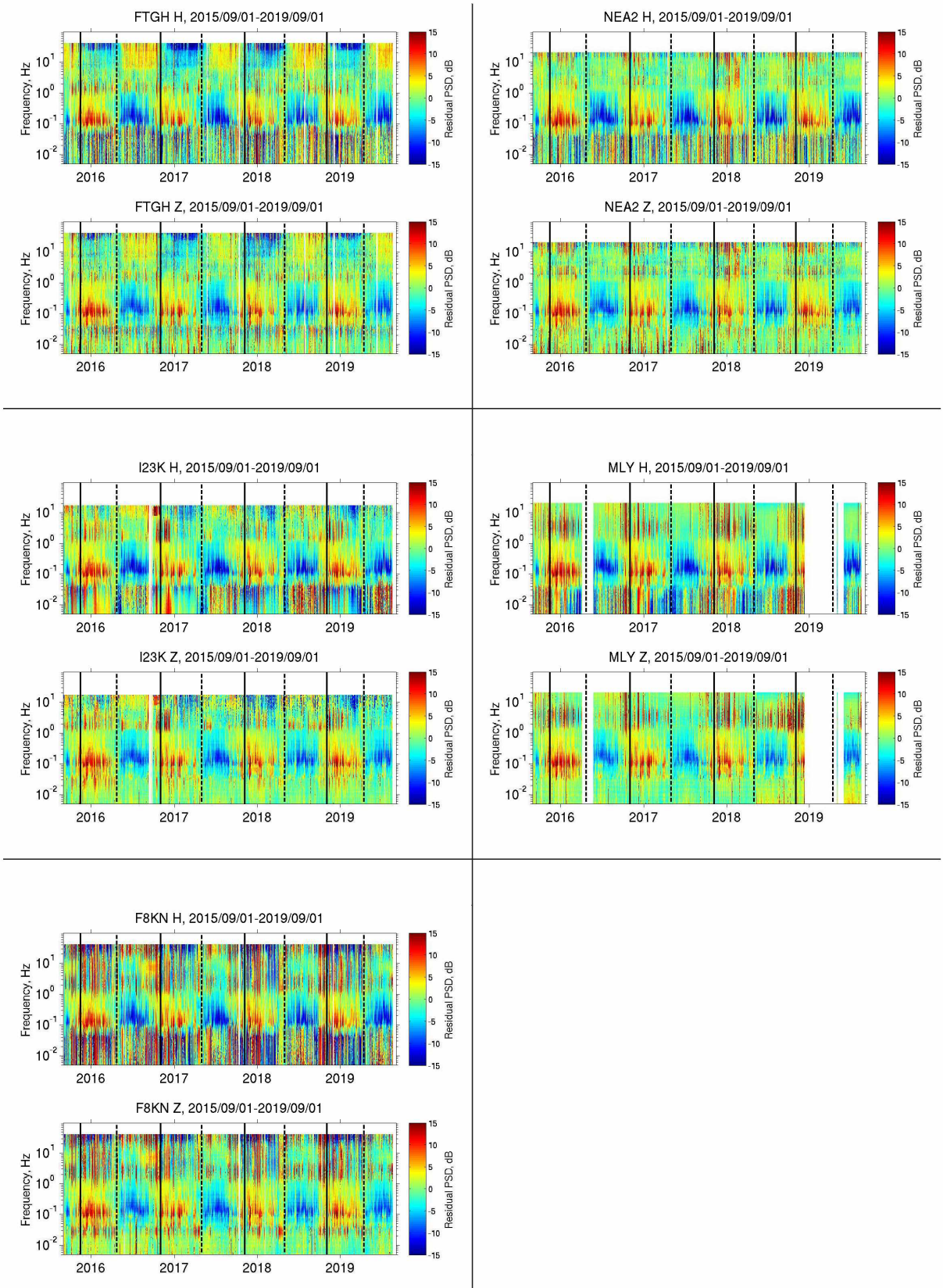

Figure A.7 continued: FTGH, NEA2, I23K, MLY, F8KN

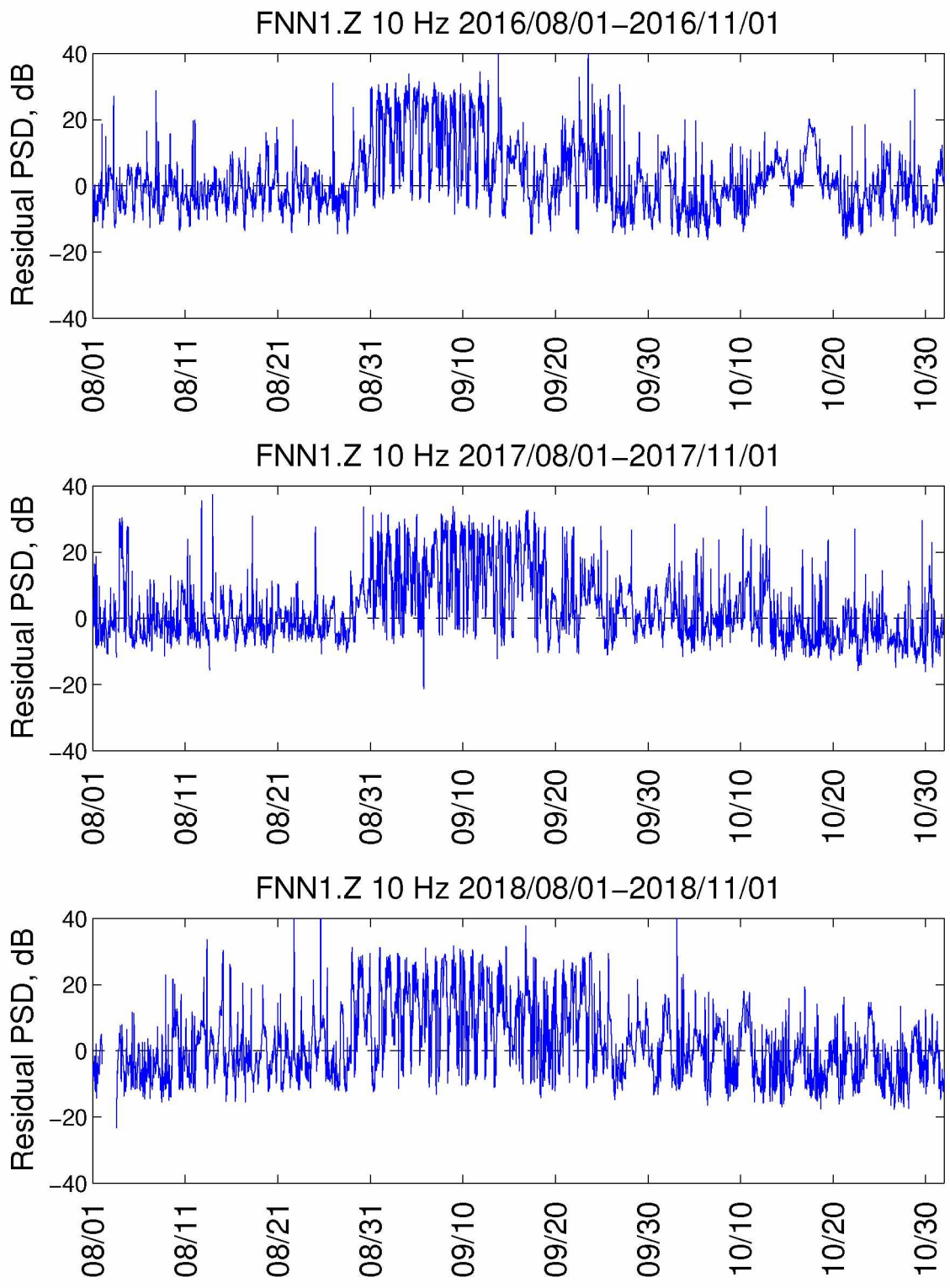

Figure A.8: Time-dependent variations in 10 Hz seismic noise at FNN1 between August 1st and November 1st in 2015, 2016, and 2017. The noise power is based on hourly time periods of the Z component; the median value has been subtracted and corresponds to the 0 dB values. The elevated, diurnal noise that starts near September 1st is from a hunting camp that sets up within 50 m of the station.

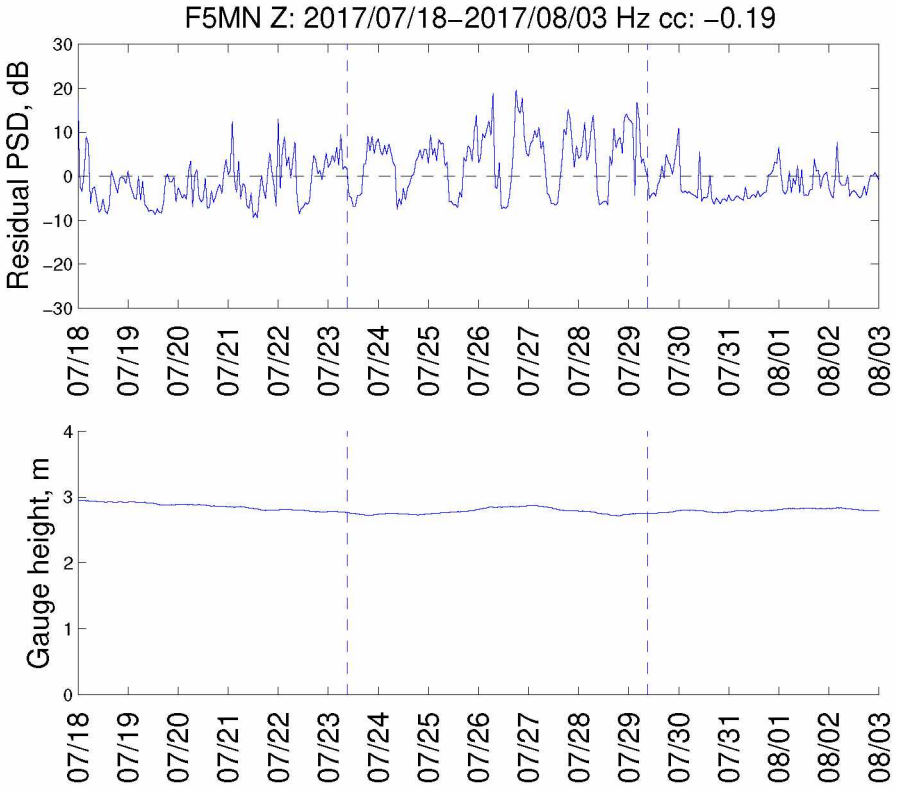

Figure A.9: Example of cultural noise: event at Old Minto Cultural Heritage Camp, July 2017. The vertical lines indicate the approximate start and end times of camp at Old Minto. (*Top*) Residual seismic noise at 10 Hz at F5MN, which is within 50 m of the Camp. (*Bottom*) Tanana River gauge height, measured at Nenana.

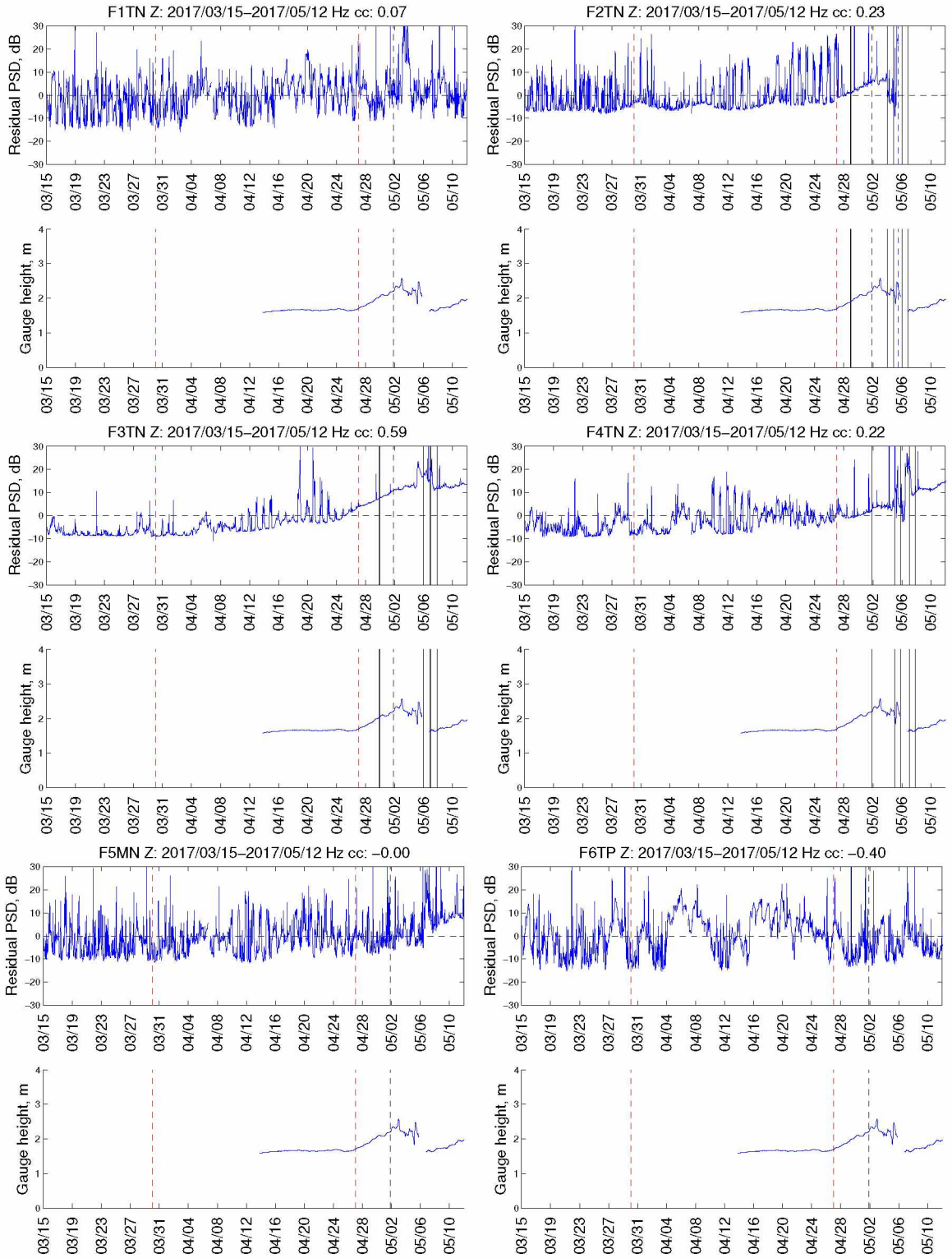

Figure A.10: Anthropogenic noise. Seismic noise power at 10 Hz (*Top*) and Tanana river gauge height at Nenana (*Bottom*). Thin dashed black line is the tripod fall over date. Solid black line are the observed breakup and freezeup times. Red dashed lines are the start and end time of active source seismic experiments. The active sources were detonated from north to south and are manifested by the southward propagating diurnal signal that is visible at F4TN (April 10–16), F3TN (April 18–23), and F2TN (April 20–28).

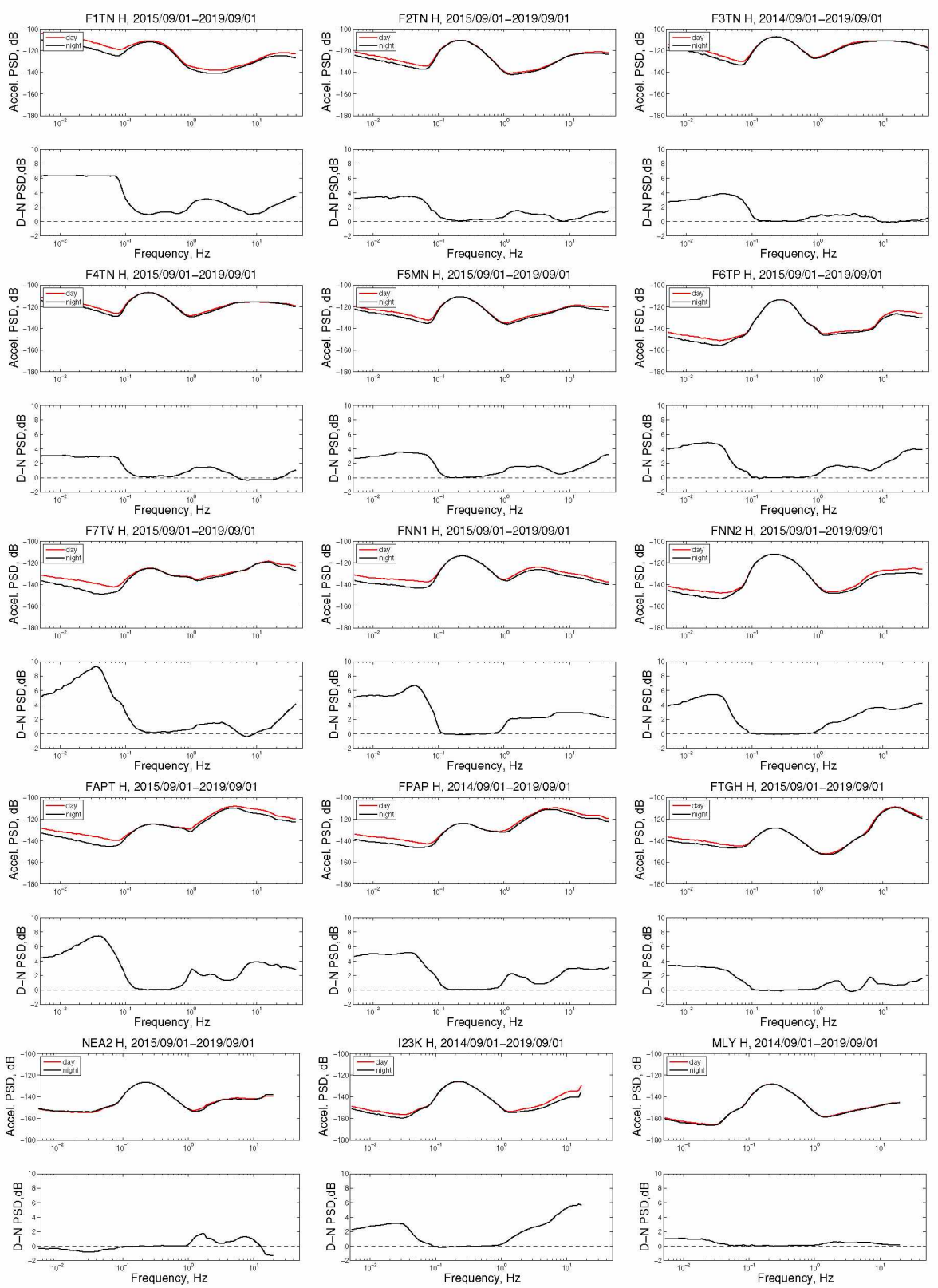

Figure A.11: H: (*Top*) Median PSD of night and day. (*Bottom*) Difference between day and night stacks. Daily noise power almost always exceeds night power.

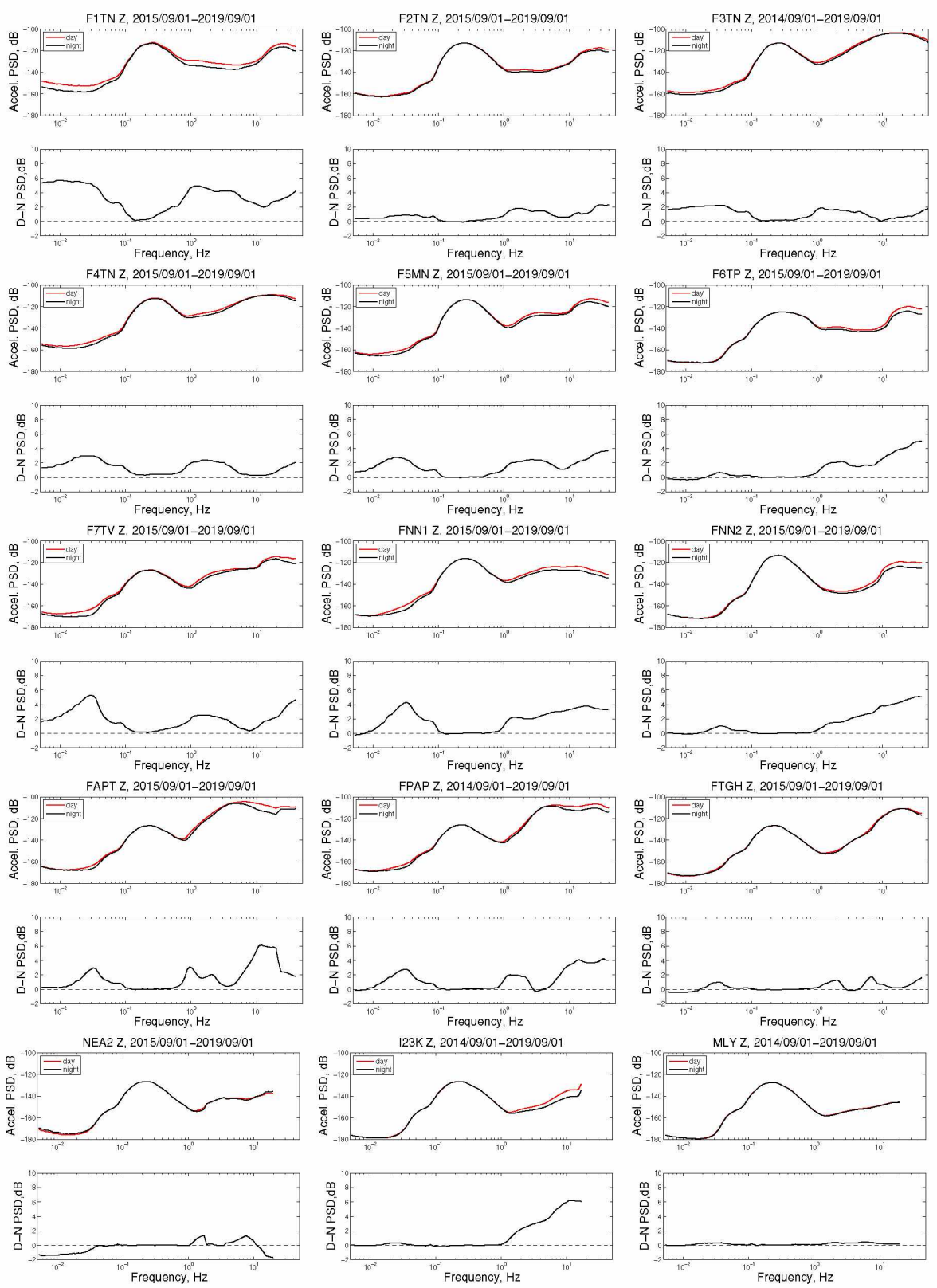

Figure A.12: Z: (*Top*) Median PSD of night and day. (*Bottom*) Difference between day and night stacks. Daily noise power almost always exceeds night power.

(a)

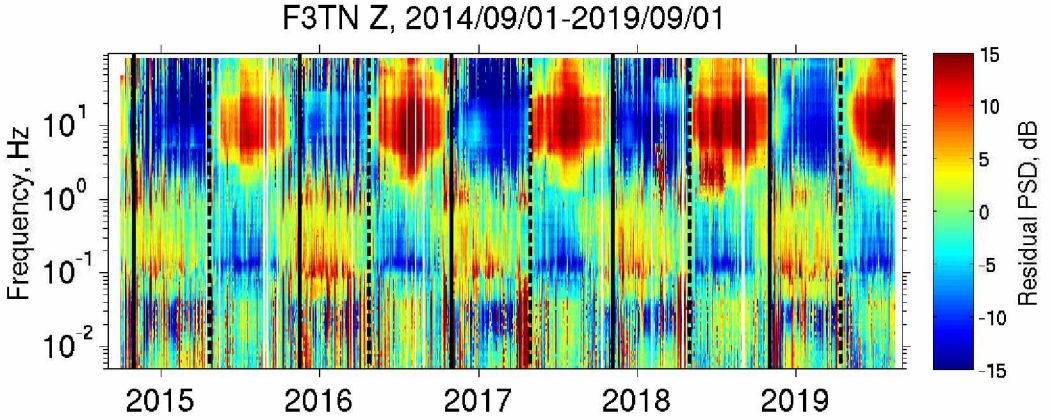

(b)

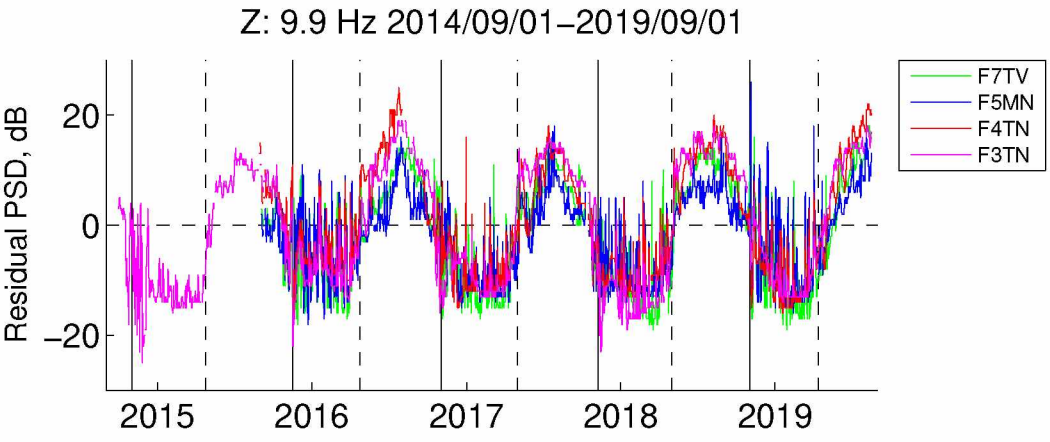

Figure A.13: Same as Figure 2.7ab but for the vertical component of seismic noise.

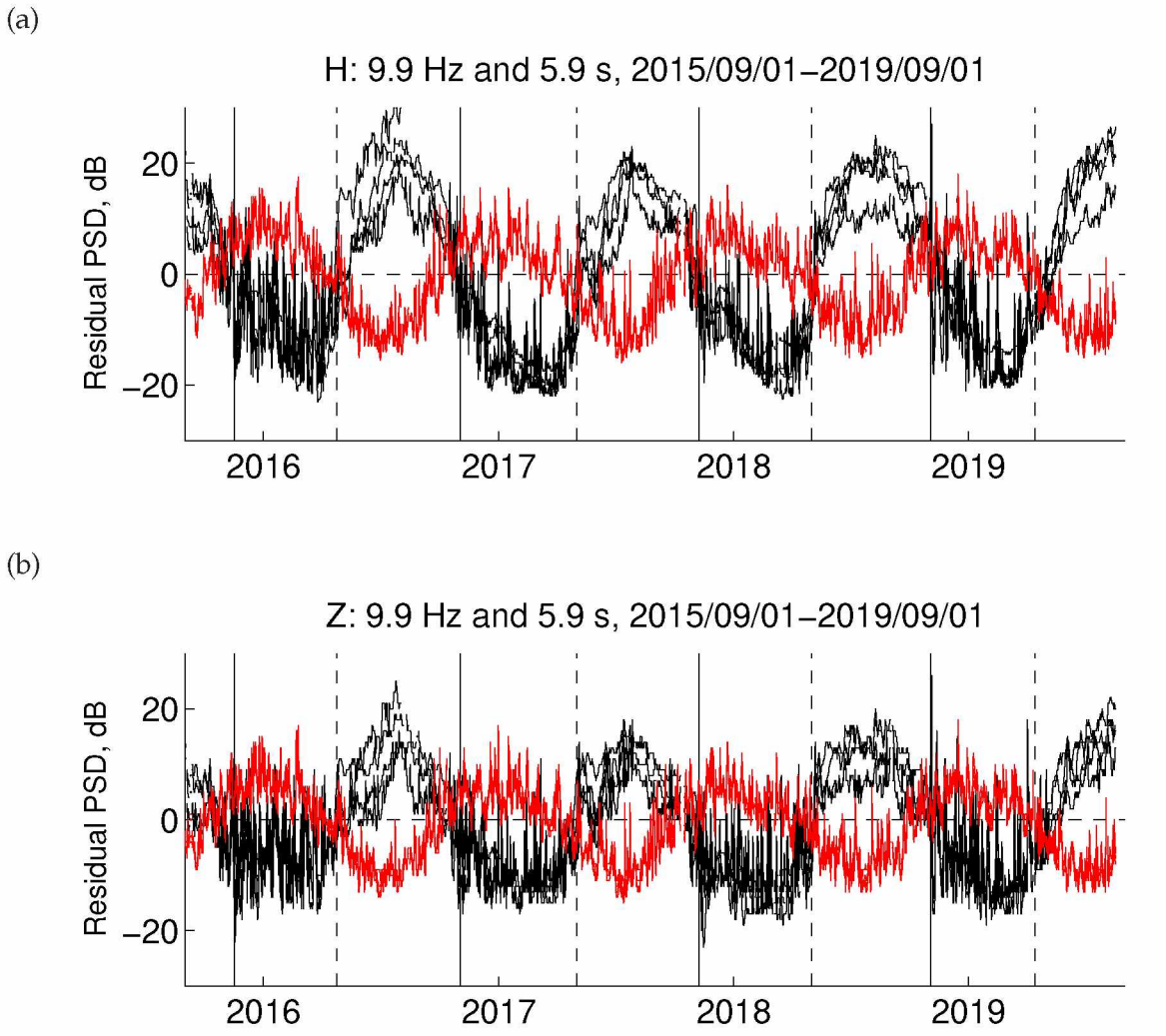

Figure A.14: Time series of residual seismic noise at four FLATS river stations (F3TN, F4TN, F5MN, F7TV) for two frequencies: 10 Hz (black; see also Figure 2.7b) and 0.16 Hz (6 s; red), for the horizontal (a) and vertical (b) components. The vertical dashed lines denote river ice breakup; the vertical solid lines denote river freezeup (Section 2.5.3). Both frequencies have clear annual cycles that are anticorrelated, with summer exhibiting a maximum for 10 Hz and a minimum for 6 s.

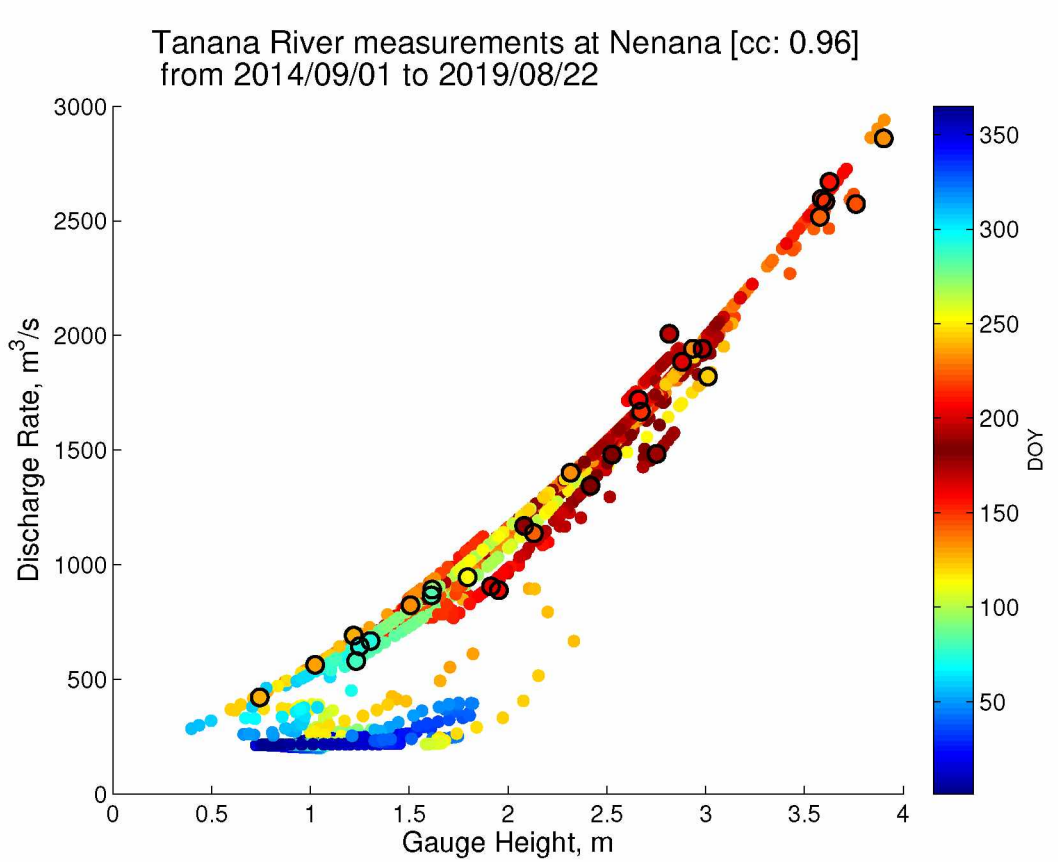

Figure A.15: Comparison of the discharge rates and gauge height at the Tanana river measured in Nenana (USGS, 2016) between 2014-09-01 and 2019-09-01. Measurements of discharge rate are made every few months and are plotted as larger circles. Measurements of gauge height are made continuously; the corresponding discharge rates are calibrated (i.e., extrapolated) from the measured discharge rates.

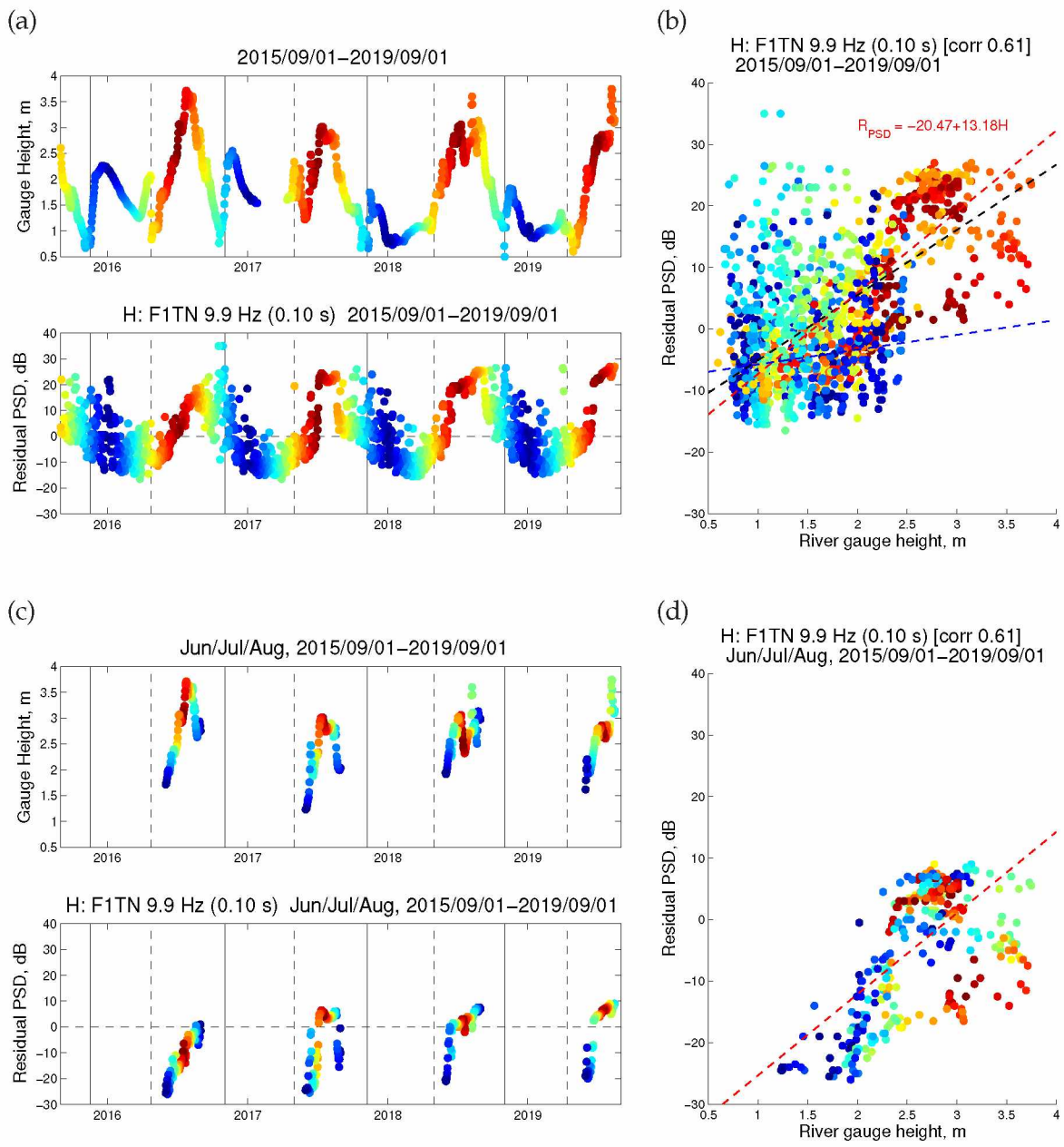

Figure A.16: Comparison between Tanana river gauge height and the 10 Hz seismic noise at station F1TN. (a) Time series of the river gauge height (top) and the residual seismic noise power at 10 Hz, H component (bottom). Each dot is for one day and is colored with red for summertime and blue for wintertime. (b) Scatter plot of seismic power versus river gauge height. The best-fit lines for the whole year, summer, and winter are indicated in black, red, and blue respectively. See Figures A.16–A.24 for other seismic stations. (c) and (d) are the same as (a) and (b) but for the summer with peak summer (mid-July) colored red.

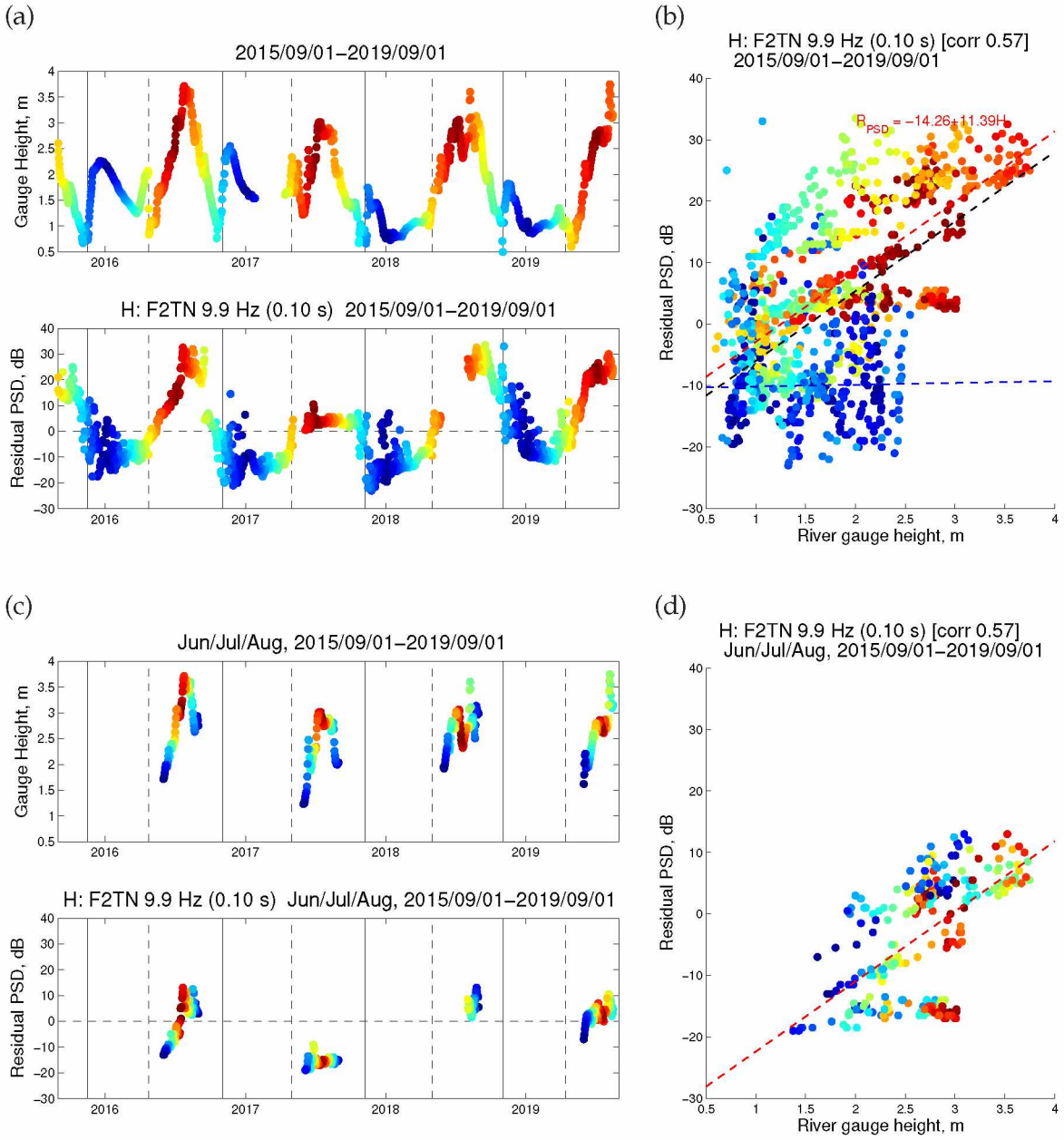

Figure A.17: Comparison between Tanana river gauge height and the 10 Hz seismic noise at station F2TN. (a) Time series of the river gauge height (top) and the residual seismic noise power at 10 Hz, H component (bottom). Each dot is for one day and is colored with red for summertime and blue for wintertime. (b) Scatter plot of seismic power versus river gauge height. The best-fit lines for the whole year, summer, and winter are indicated in black, red, and blue respectively. See Figures A.16–A.24 for other seismic stations. (c) and (d) are the same as (a) and (b) but for the summer with peak summer (mid-July) colored red.

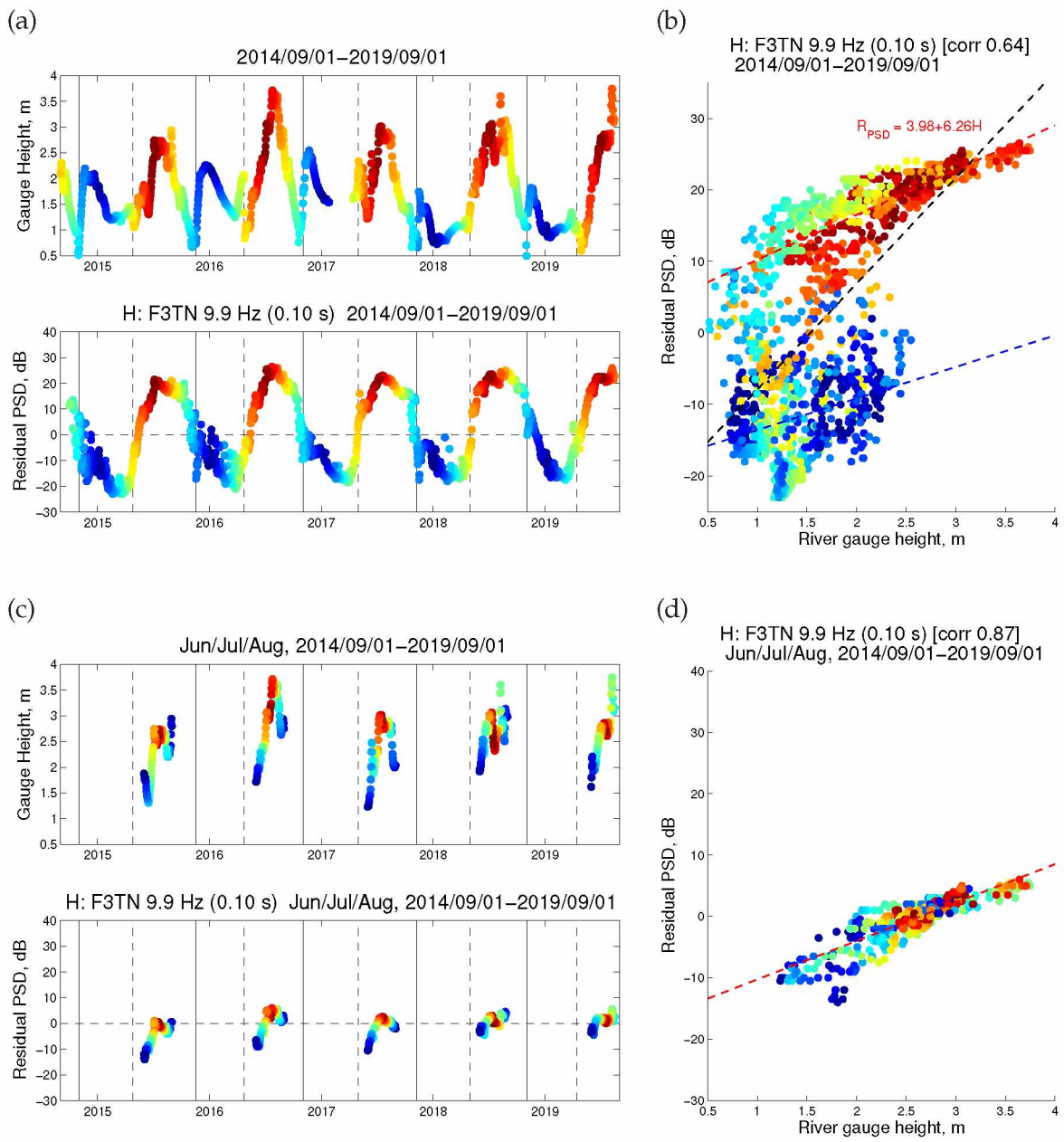

Figure A.18: Comparison between Tanana river gauge height and the 10 Hz seismic noise at station F3TN. (a) Time series of the river gauge height (top) and the residual seismic noise power at 10 Hz, H component (bottom). Each dot is for one day and is colored with red for summertime and blue for wintertime. (b) Scatter plot of seismic power versus river gauge height. The best-fit lines for the whole year, summer, and winter are indicated in black, red, and blue respectively. See Figures A.16–A.24 for other seismic stations. (c) and (d) are the same as (a) and (b) but for the summer with peak summer (mid-July) colored red.

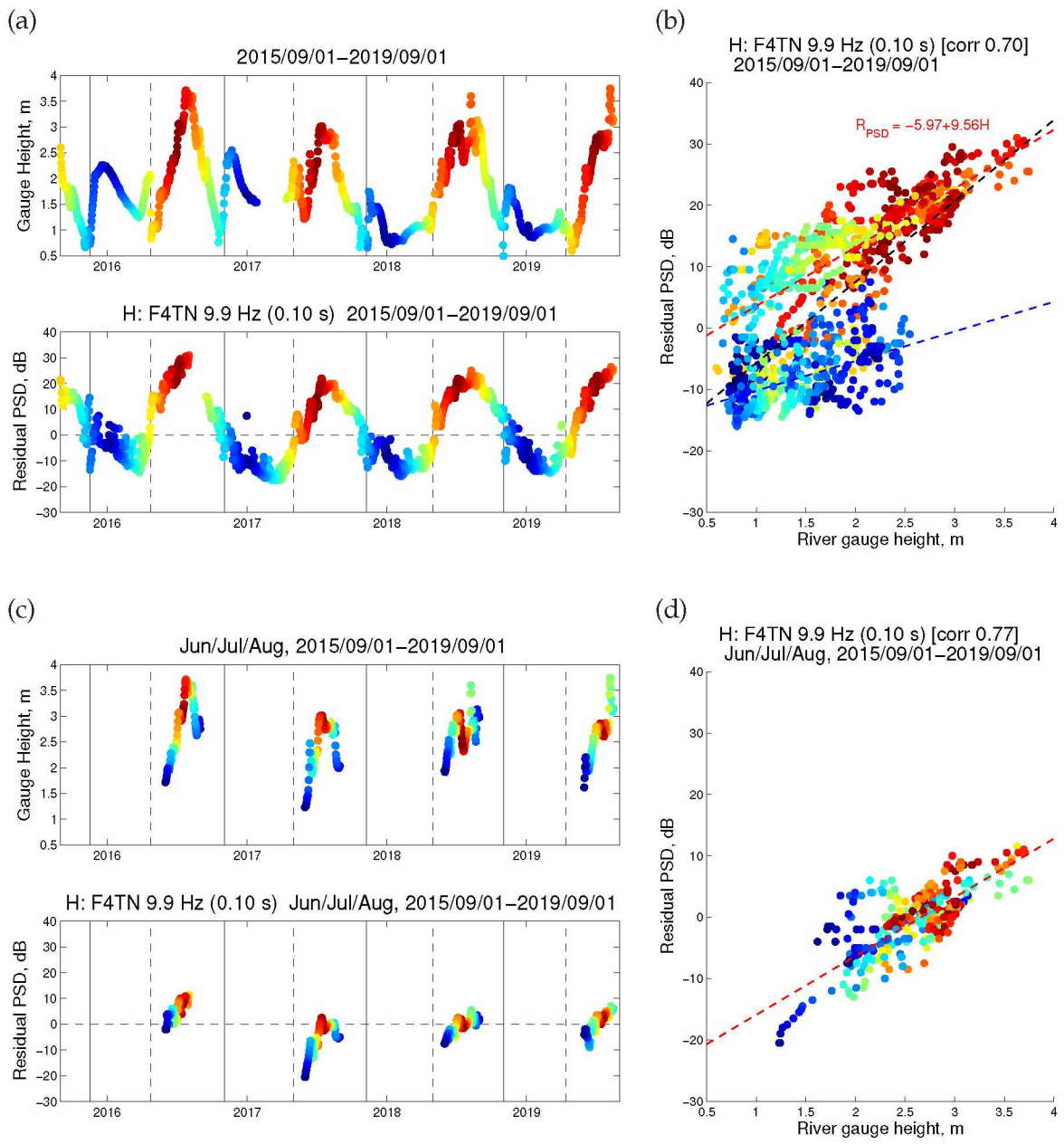

Figure A.19: Comparison between Tanana river gauge height and the 10 Hz seismic noise at station F4TN. (a) Time series of the river gauge height (top) and the residual seismic noise power at 10 Hz, H component (bottom). Each dot is for one day and is colored with red for summertime and blue for wintertime. (b) Scatter plot of seismic power versus river gauge height. The best-fit lines for the whole year, summer, and winter are indicated in black, red, and blue respectively. See Figures A.16–A.24 for other seismic stations. (c) and (d) are the same as (a) and (b) but for the summer with peak summer (mid-July) colored red.

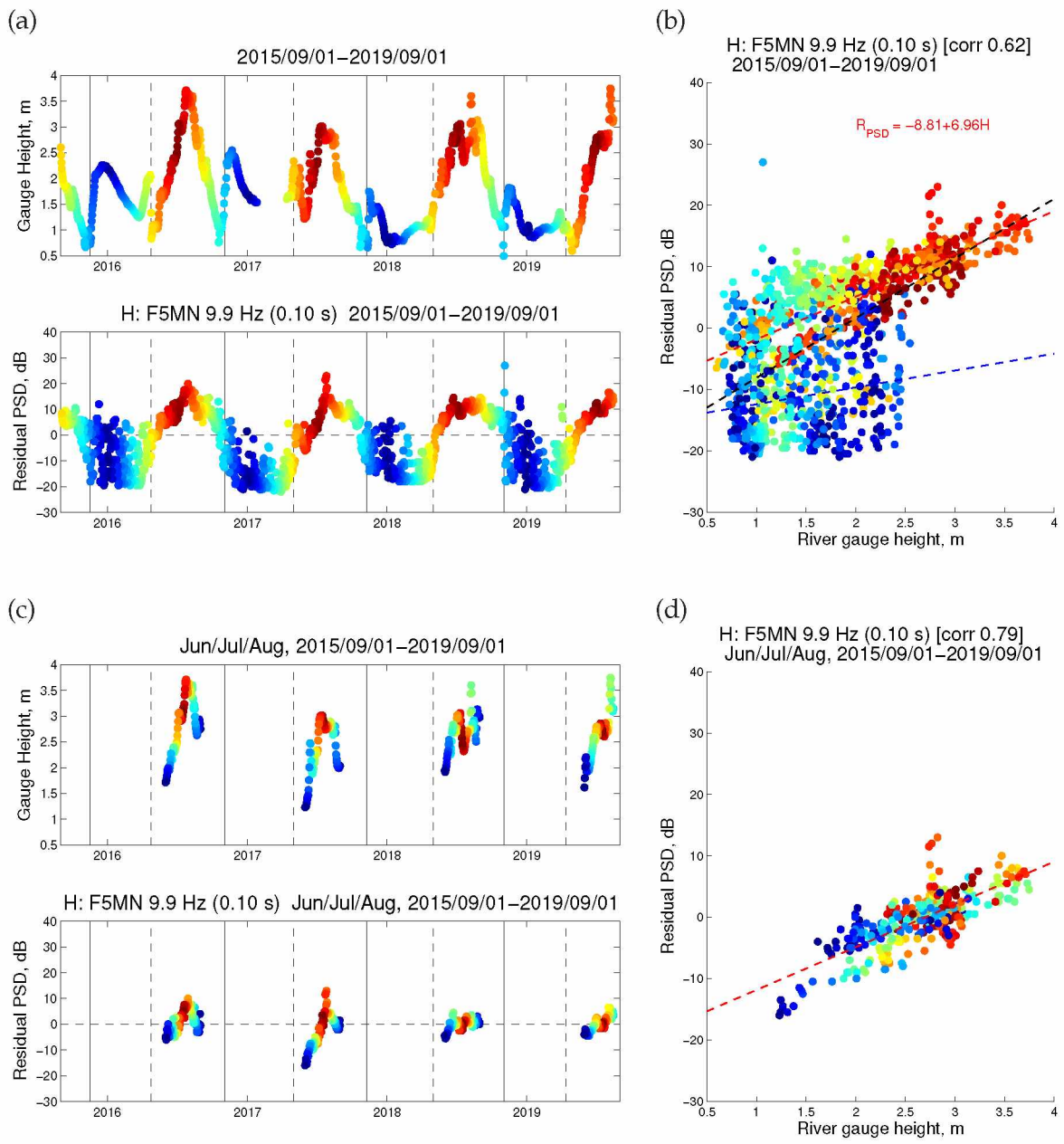

Figure A.20: Comparison between Tanana river gauge height and the 10 Hz seismic noise at station F5MN. (a) Time series of the river gauge height (top) and the residual seismic noise power at 10 Hz, H component (bottom). Each dot is for one day and is colored with red for summertime and blue for wintertime. (b) Scatter plot of seismic power versus river gauge height. The best-fit lines for the whole year, summer, and winter are indicated in black, red, and blue respectively. See Figures A.16–A.24 for other seismic stations. (c) and (d) are the same as (a) and (b) but for the summer with peak summer (mid-July) colored red.

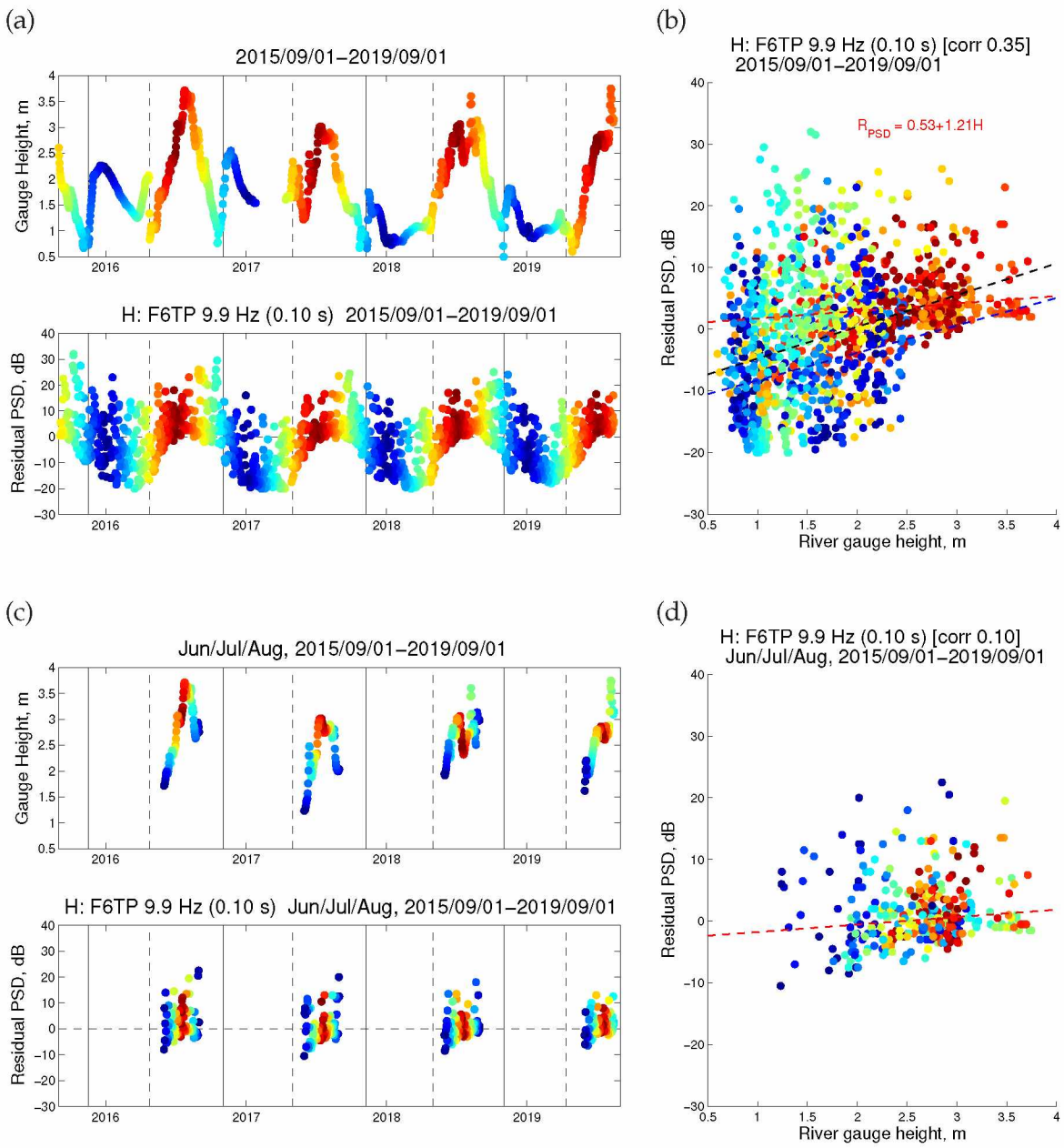

Figure A.21: Comparison between Tanana river gauge height and the 10 Hz seismic noise at station F6TP. (a) Time series of the river gauge height (top) and the residual seismic noise power at 10 Hz, H component (bottom). Each dot is for one day and is colored with red for summertime and blue for wintertime. (b) Scatter plot of seismic power versus river gauge height. The best-fit lines for the whole year, summer, and winter are indicated in black, red, and blue respectively. See Figures A.16–A.24 for other seismic stations. (c) and (d) are the same as (a) and (b) but for the summer with peak summer (mid-July) colored red.

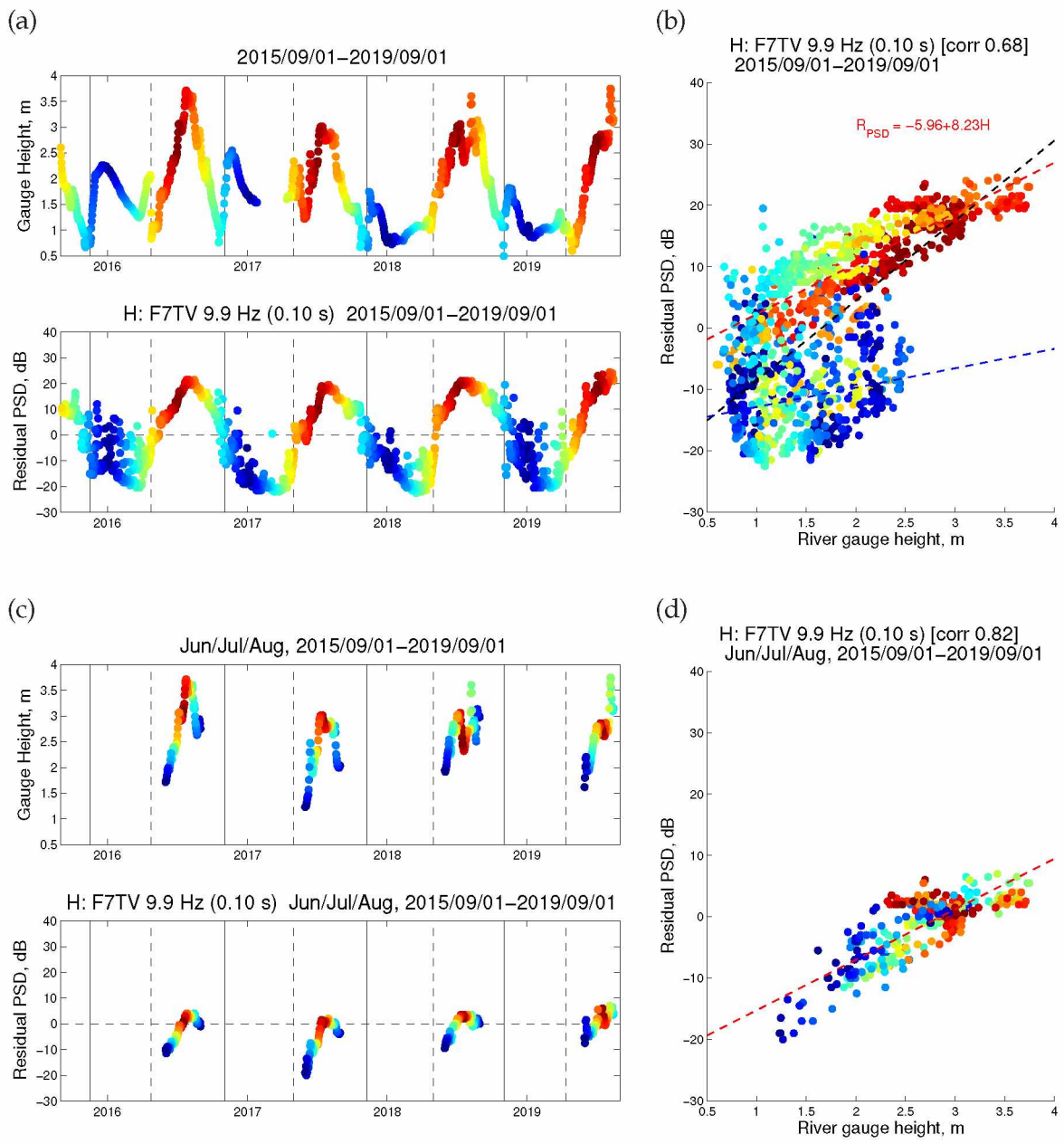

Figure A.22: Comparison between Tanana river gauge height and the 10 Hz seismic noise at station F7TV. (a) Time series of the river gauge height (top) and the residual seismic noise power at 10 Hz, H component (bottom). Each dot is for one day and is colored with red for summertime and blue for wintertime. (b) Scatter plot of seismic power versus river gauge height. The best-fit lines for the whole year, summer, and winter are indicated in black, red, and blue respectively. See Figures A.16–A.24 for other seismic stations. (c) and (d) are the same as (a) and (b) but for the summer with peak summer (mid-July) colored red.

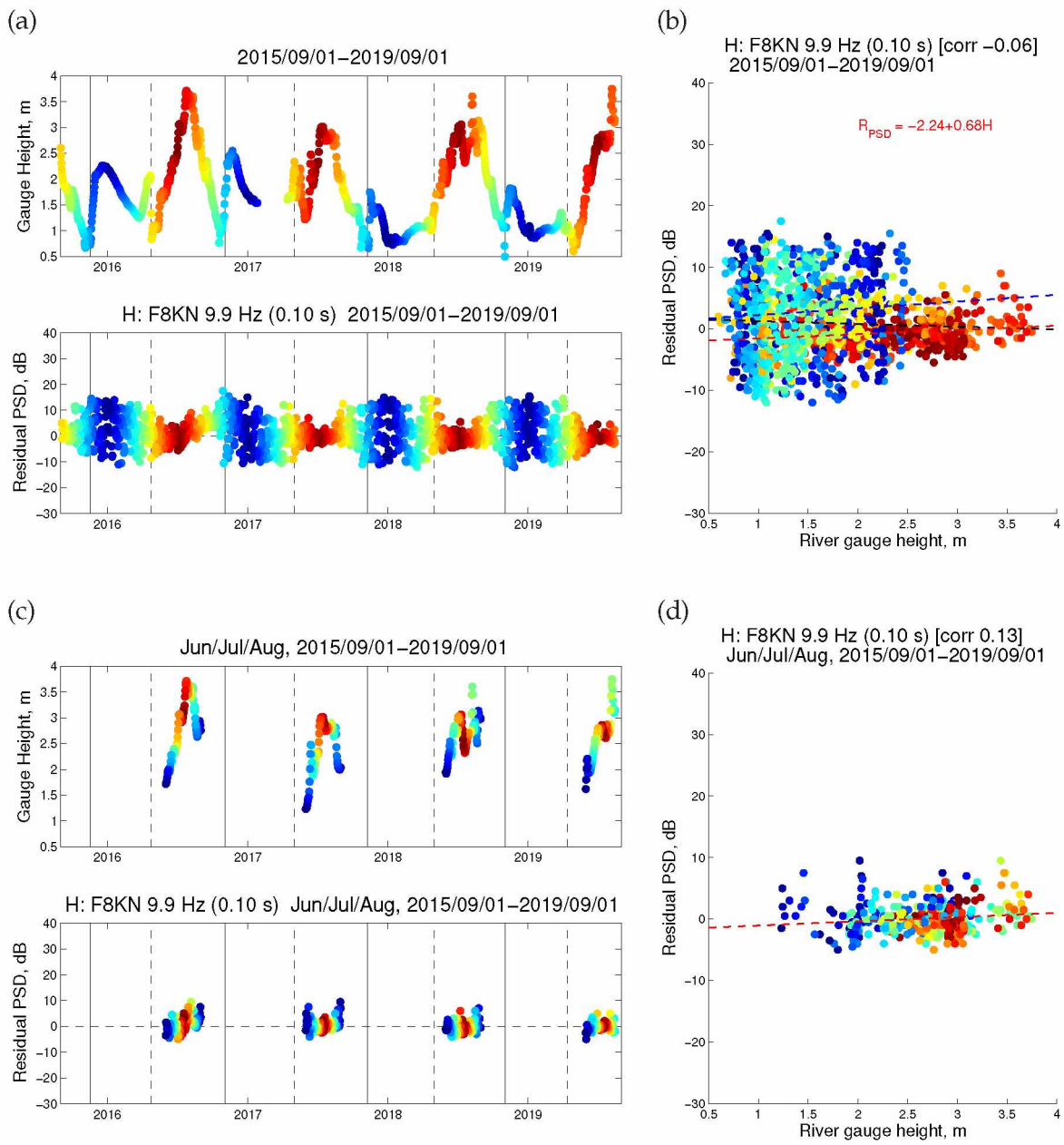

Figure A.23: Comparison between Tanana river gauge height and the 10 Hz seismic noise at station F8KN. (a) Time series of the river gauge height (top) and the residual seismic noise power at 10 Hz, H component (bottom). Each dot is for one day and is colored with red for summertime and blue for wintertime. (b) Scatter plot of seismic power versus river gauge height. The best-fit lines for the whole year, summer, and winter are indicated in black, red, and blue respectively. See Figures A.16–A.24 for other seismic stations. (c) and (d) are the same as (a) and (b) but for the summer with peak summer (mid-July) colored red.

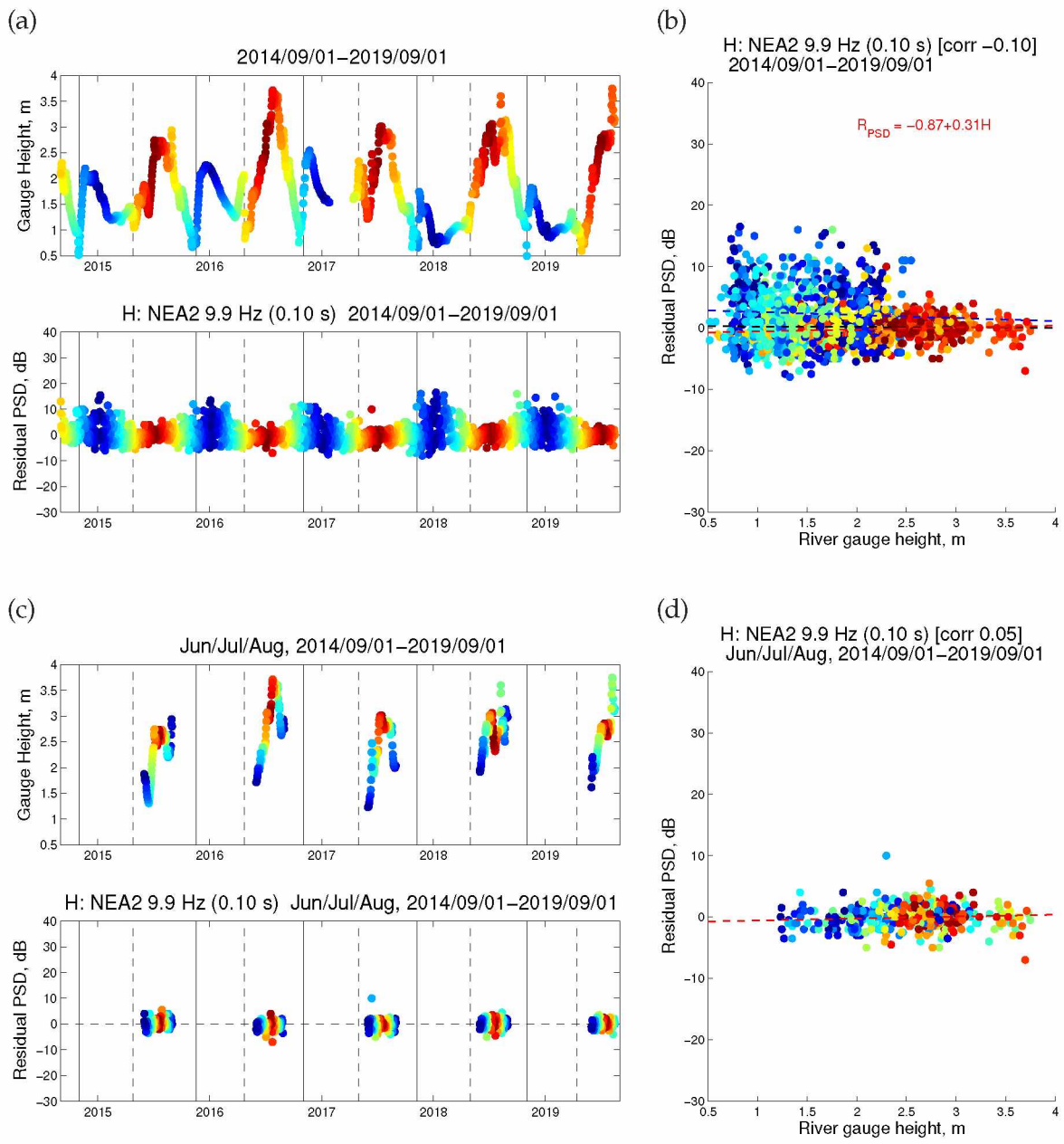

Figure A.24: Comparison between Tanana river gauge height and the 10 Hz seismic noise at station NEA2. (a) Time series of the river gauge height (top) and the residual seismic noise power at 10 Hz, H component (bottom). Each dot is for one day and is colored with red for summertime and blue for wintertime. (b) Scatter plot of seismic power versus river gauge height. The best-fit lines for the whole year, summer, and winter are indicated in black, red, and blue respectively. See Figures A.16–A.24 for other seismic stations. (c) and (d) are the same as (a) and (b) but for the summer with peak summer (mid-July) colored red.

(a)

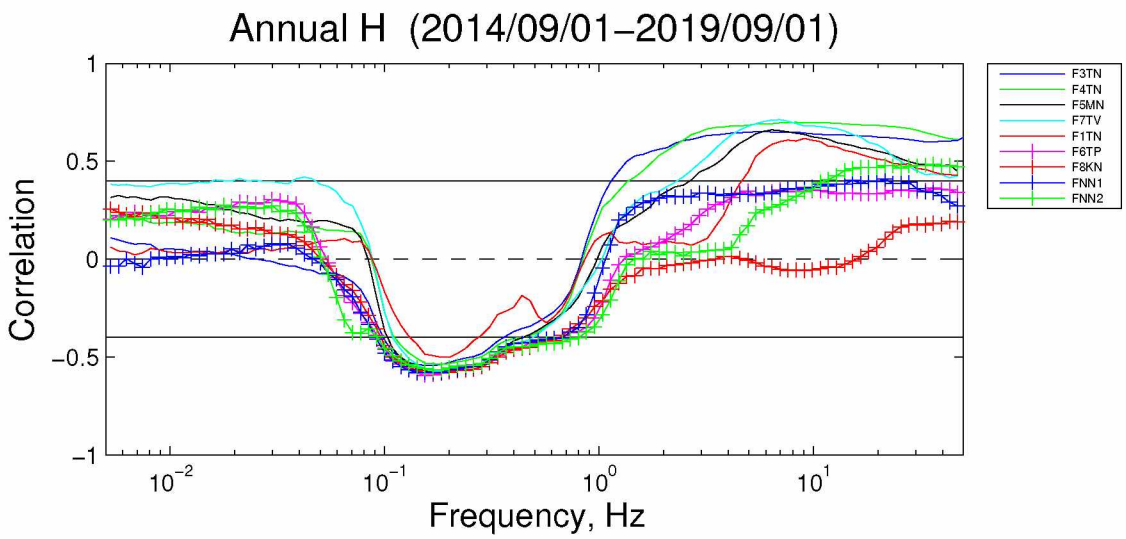

(b)

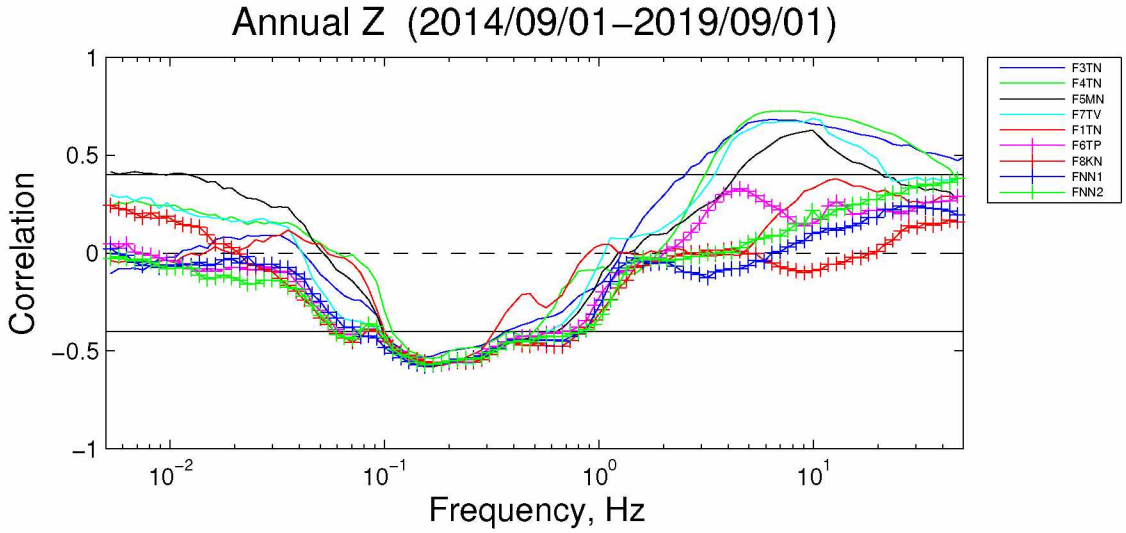

Figure A.25: Same as Figure 2.9, but for annual period of time and for both the horizontal (a) and vertical (b) components of seismic noise.

(a)

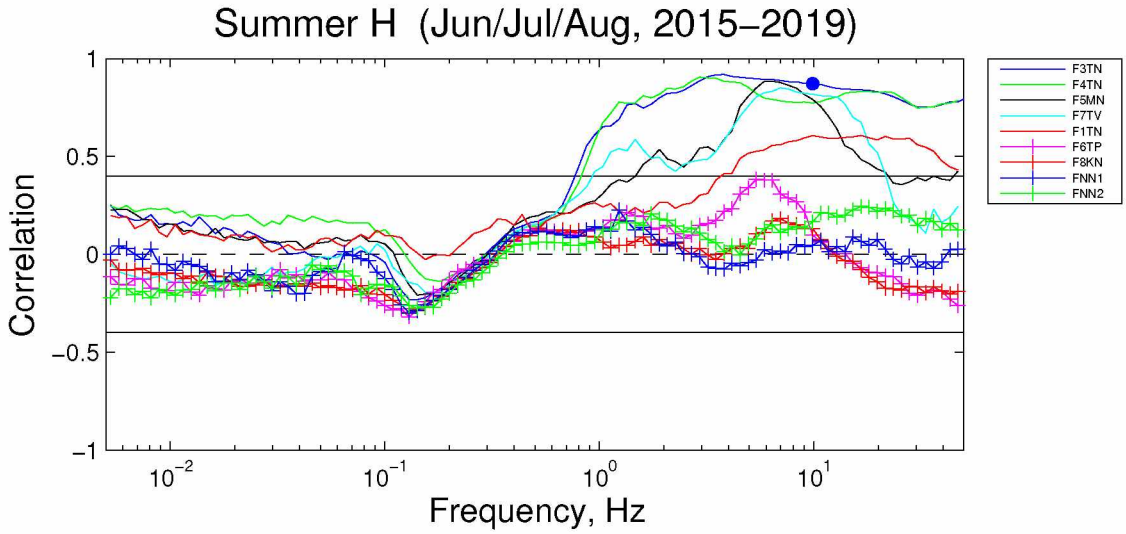

(b)

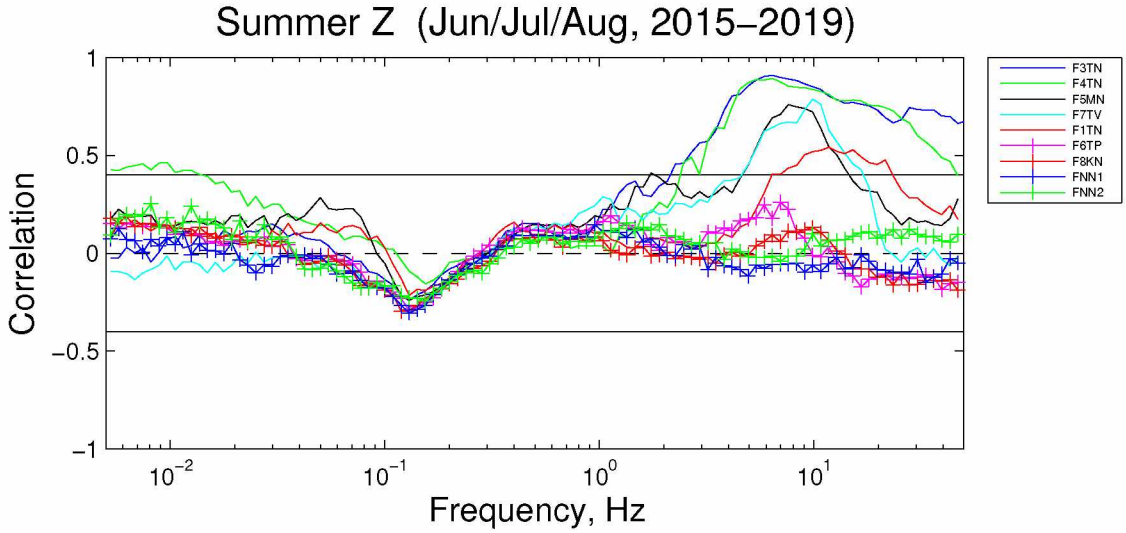

Figure A.26: Same as Figure 2.9, but for summer period of time and for both the horizontal (a) and vertical (b) components of seismic noise.

(a)

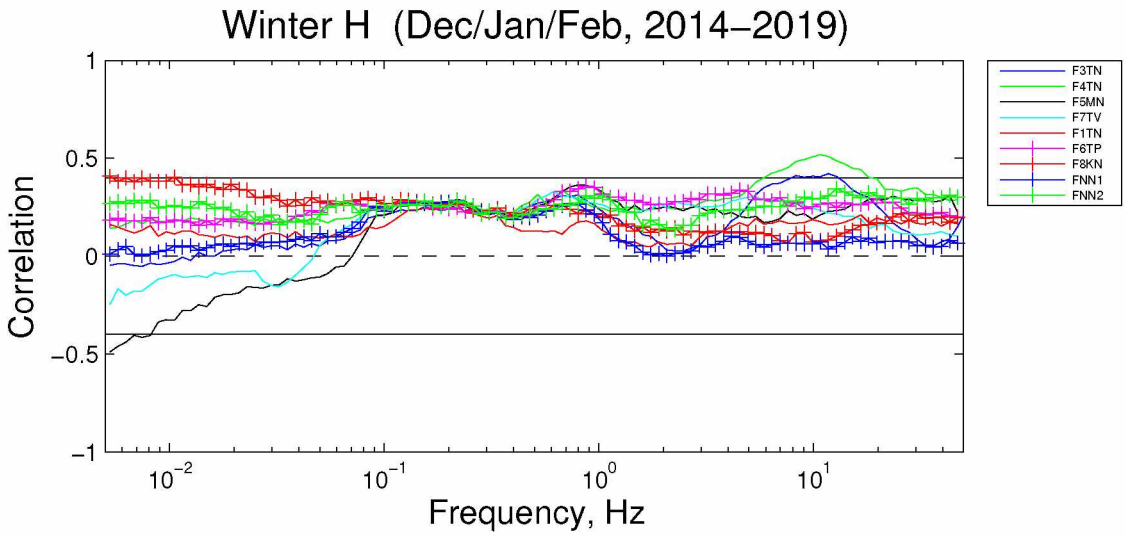

(b)

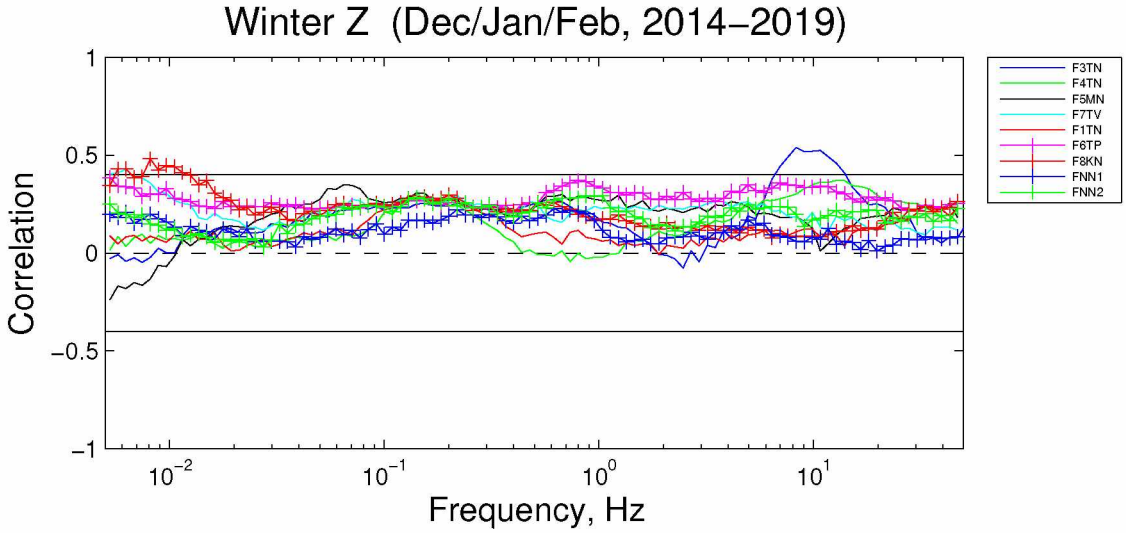

Figure A.27: Same as Figure 2.9, but for winter period of time and for both the horizontal (a) and vertical (b) components of seismic noise.

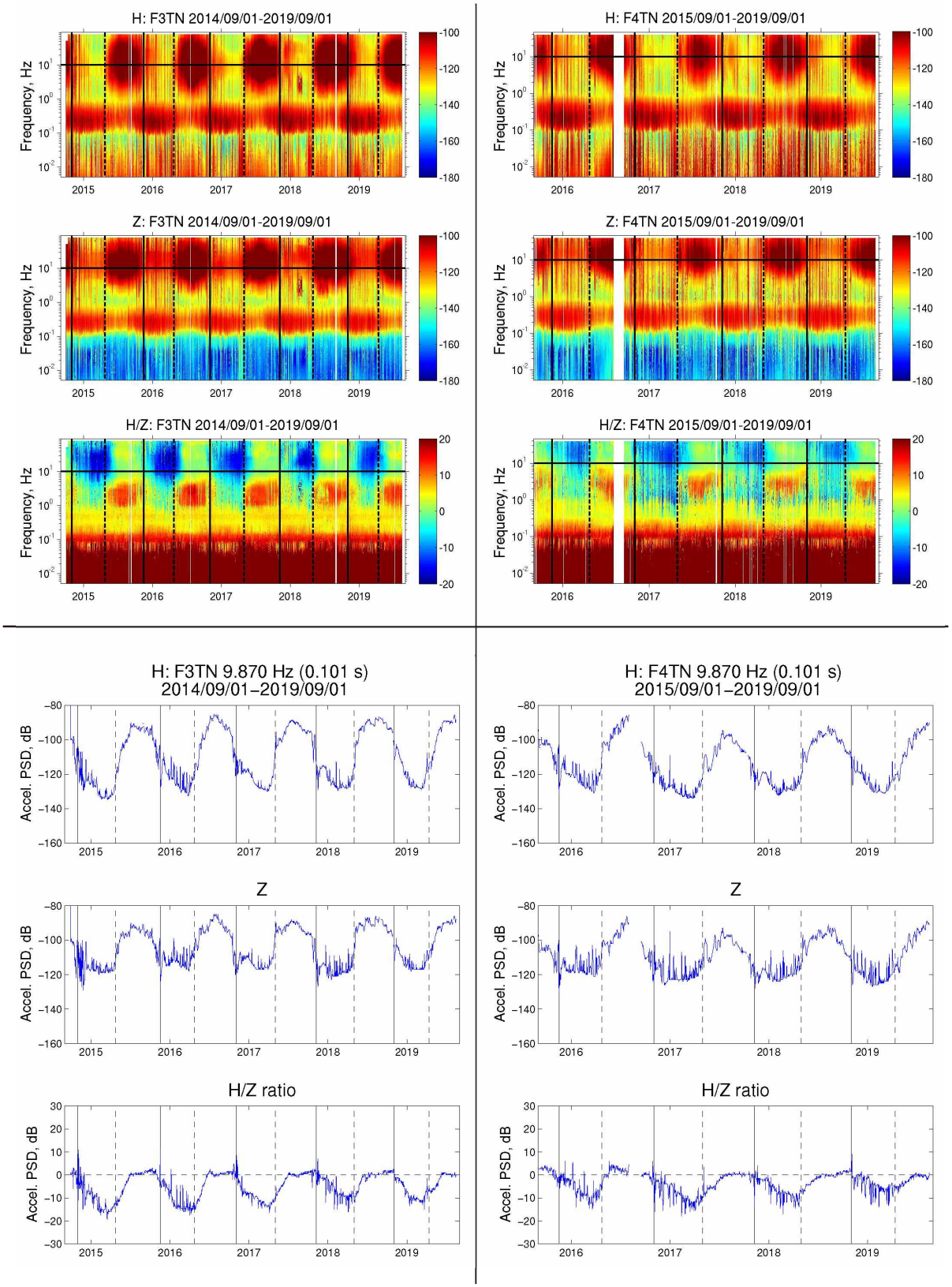

Figure A.28: Time series of daily seismic noise at F3TN and F4TN. Top plots show spectrograms and bottom plots show a 10 Hz cross section. Within each subplot: horizontal H (top), vertical Z (middle), and the H/Z ratio (bottom).

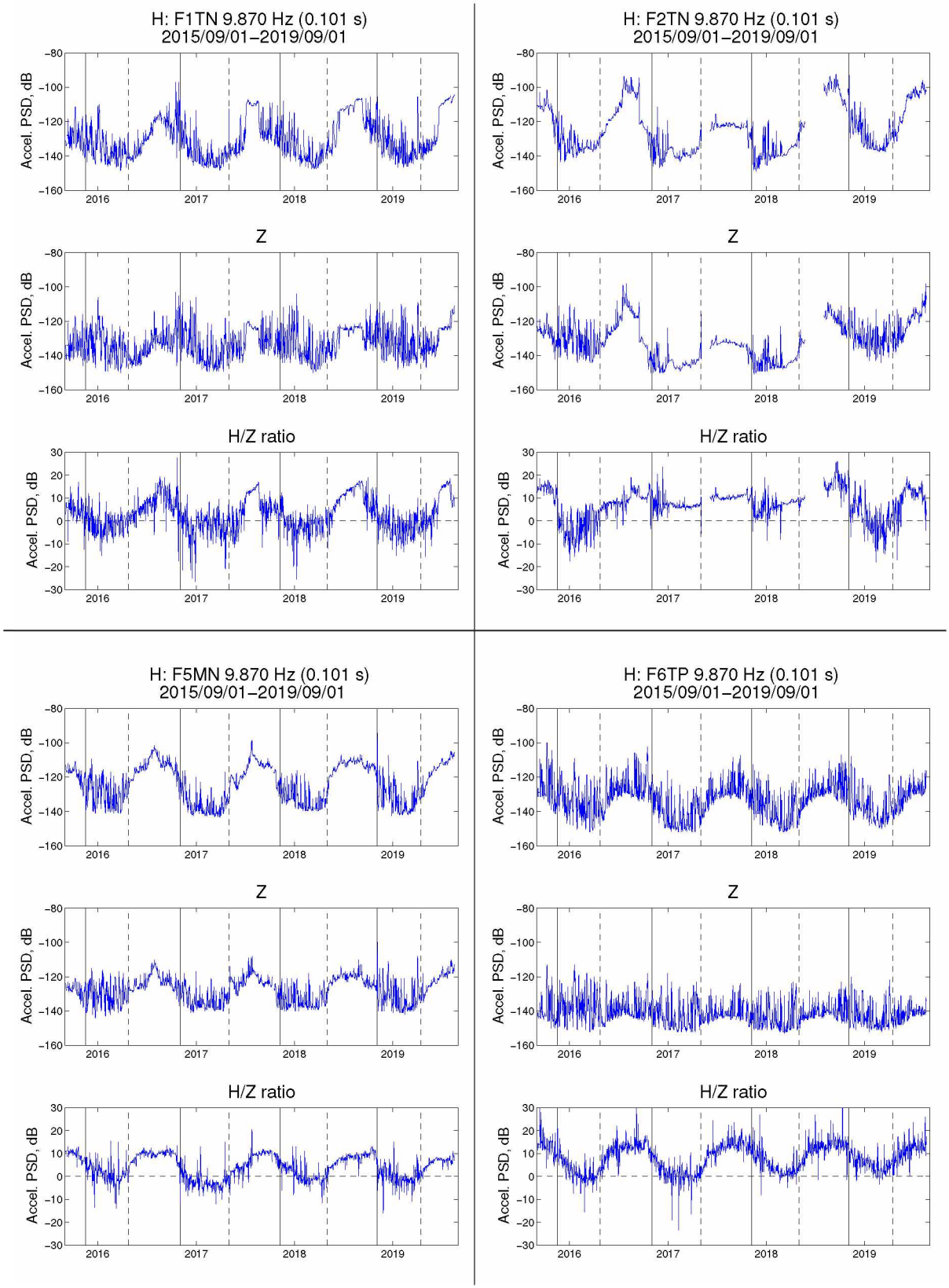

Figure A.29: Time series of daily seismic noise at 10 Hz at four stations: horizontal H (top), vertical Z (middle), and the H/Z ratio (bottom).

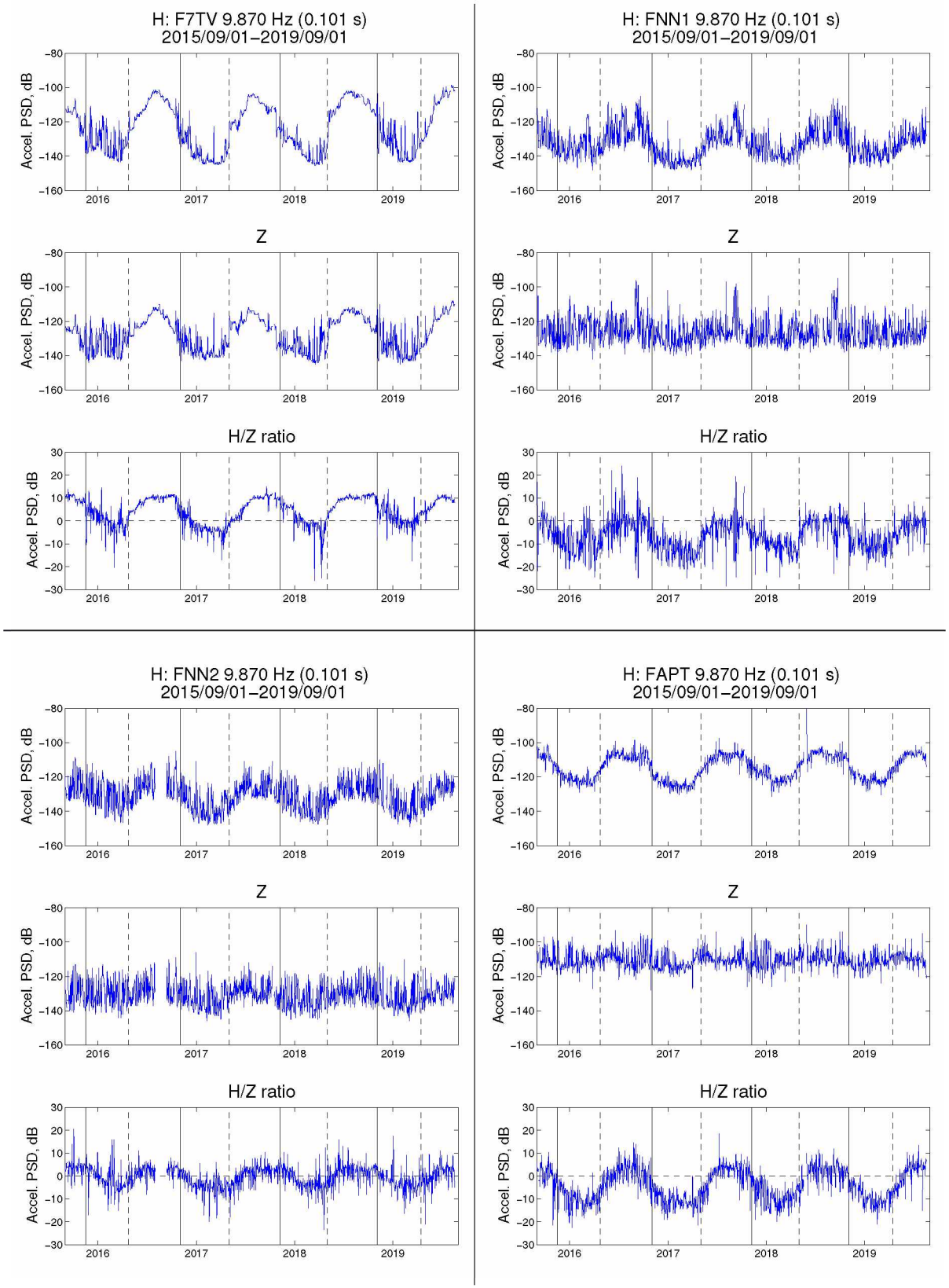

Figure A.30: Time series of daily seismic noise at 10 Hz at four stations: horizontal H (top), vertical Z (middle), and the H/Z ratio (bottom).

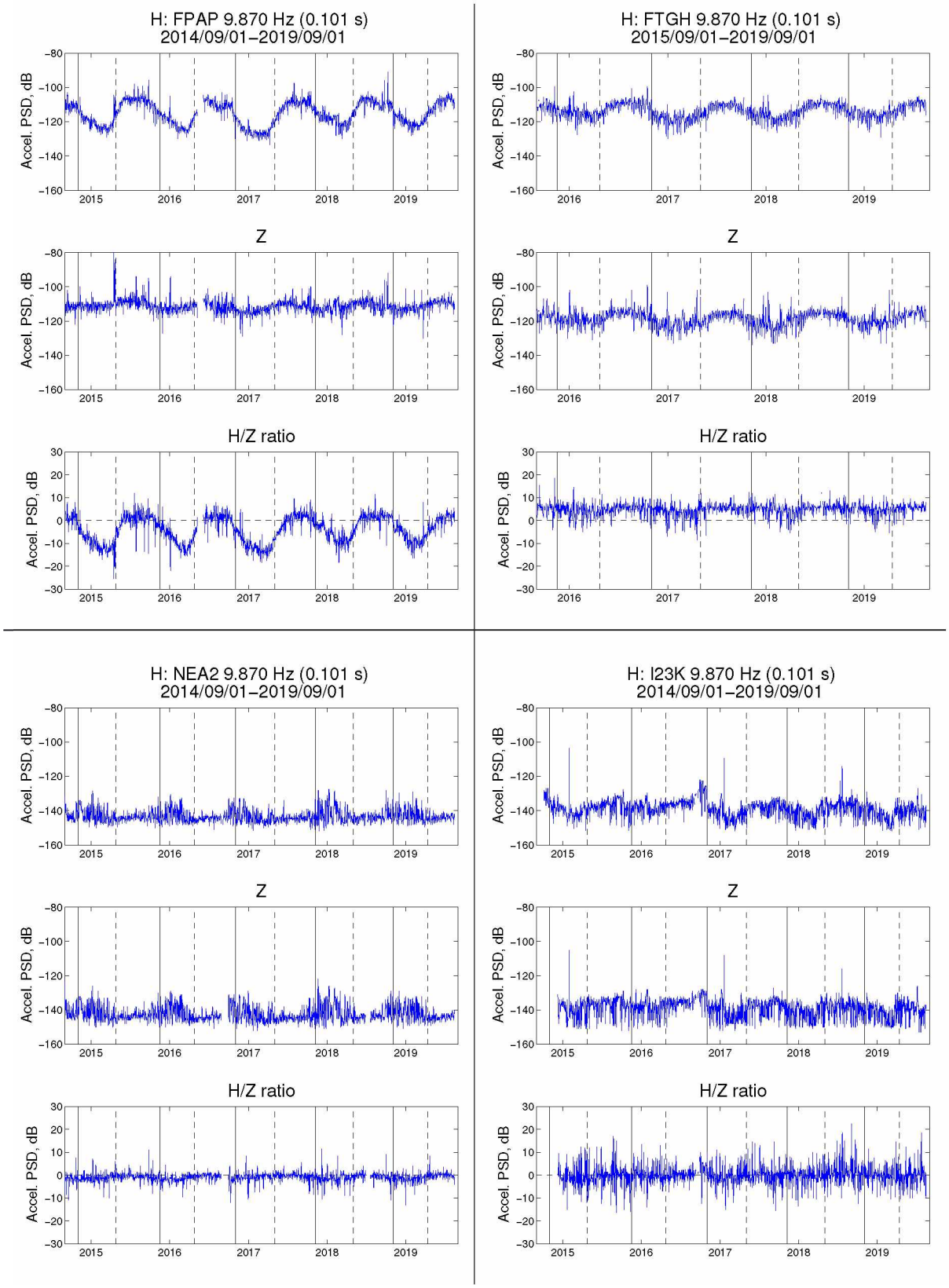

Figure A.31: Time series of daily seismic noise at 10 Hz at four stations: horizontal H (top), vertical Z (middle), and the H/Z ratio (bottom).

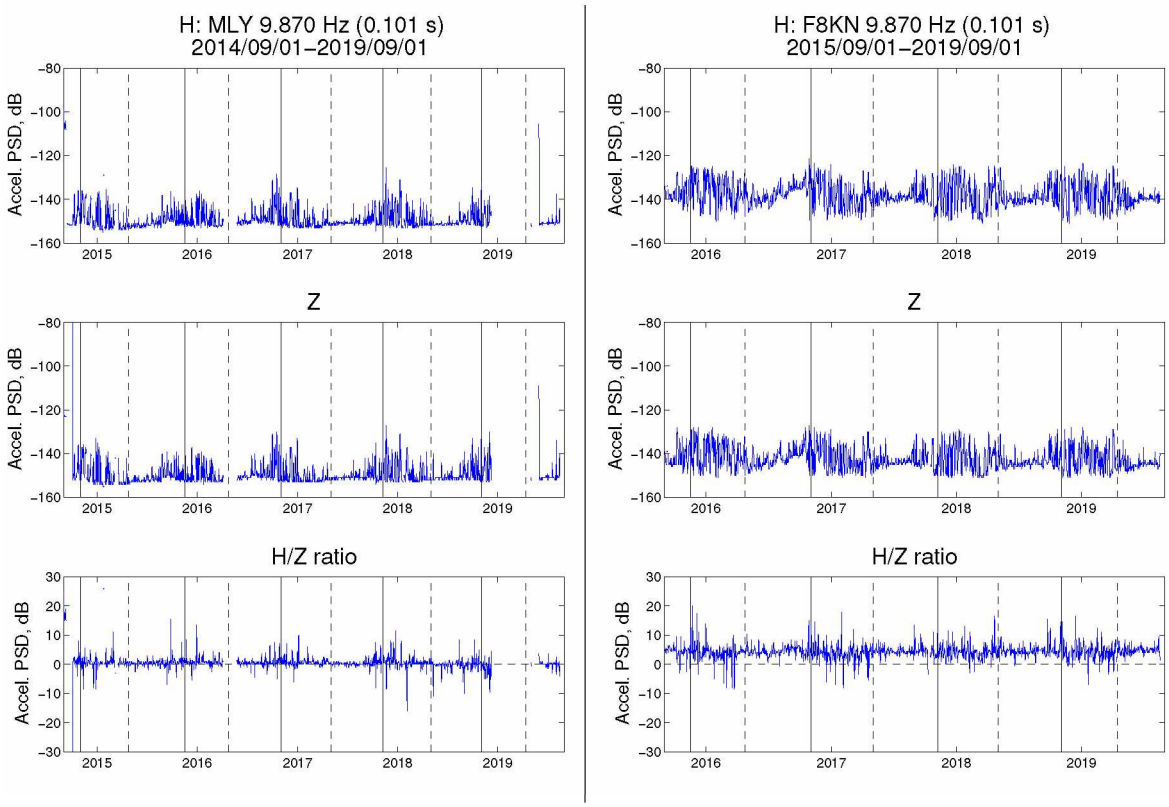

Figure A.32: Time series of daily seismic noise at 10 Hz at two stations: horizontal H (top), vertical Z (middle), and the H/Z ratio (bottom).

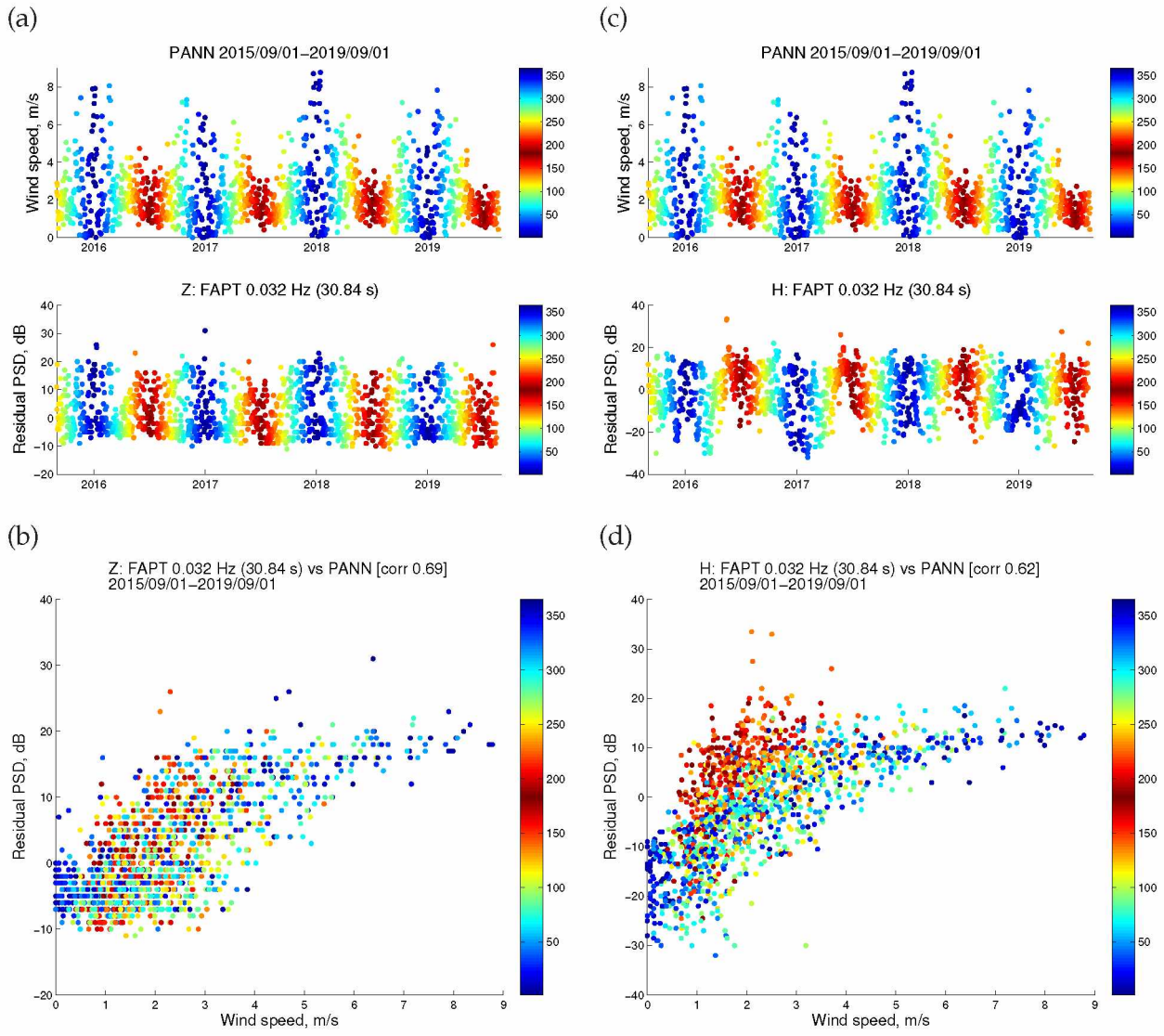

Figure A.33: Comparison between wind speed and seismic noise at a period of 30 s. (a) Time series of daily wind speed at PANN (top) and residual seismic noise (vertical component) at FAPT at a period of 30 s (0.032 Hz) (bottom). The seismic station (FAPT) and weather station (PANN) are near the Nenana runway and separated by 513 m (Figure 2.1b, Table 2.1). Daily data points are colored by time of year: cool colors are wintertime and warm colors are summertime. (b) Scatter plot comparing the two time series in (a). (c)-(d) Same as (a)-(b), but for the horizontal component of seismic noise.

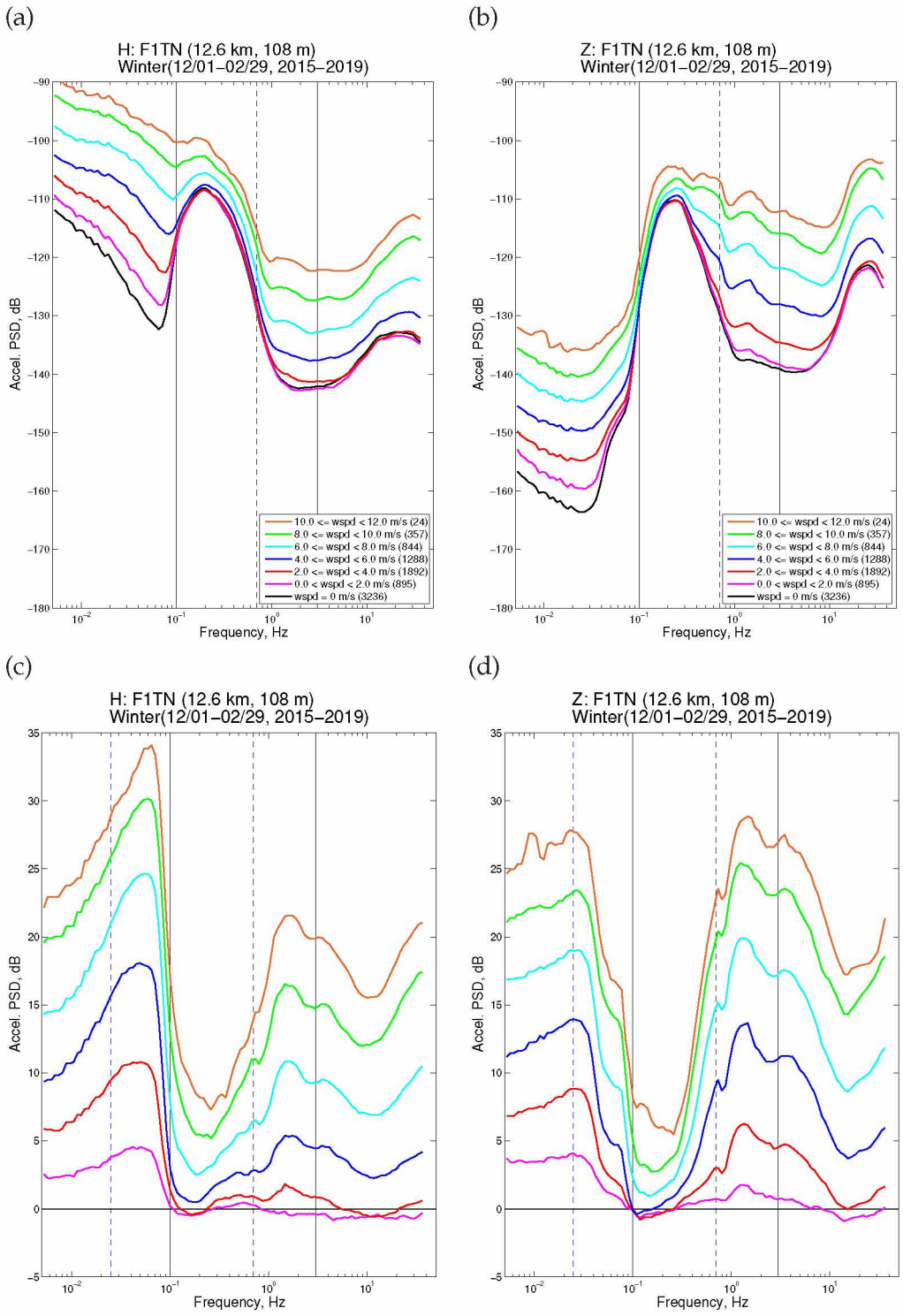

Figure A.34: The influence of wind on seismic noise during winter (Dec/Jan/Feb) at station F1TN; other stations shown in Figures A.34–A.49. The plot title includes the distance from the station to the meteorological sensor, followed by the station elevation (Table 2.1). (a) Horizontal-component seismic noise spectra made during time periods of different wind speeds. The number of hours used for each stack is listed in the legend. (b) Same as (a), but for the vertical component of seismic noise. (c) Spectra in (a) minus the spectrum made from the times of the lowest wind speed for winter (black). The dashed blue line at 0.025 Hz highlights a visible peak in the spectra shown for most stations (e.g. F6TP). (d) Spectra in (b) minus the spectrum made from the times of the lowest wind speed for winter (black).

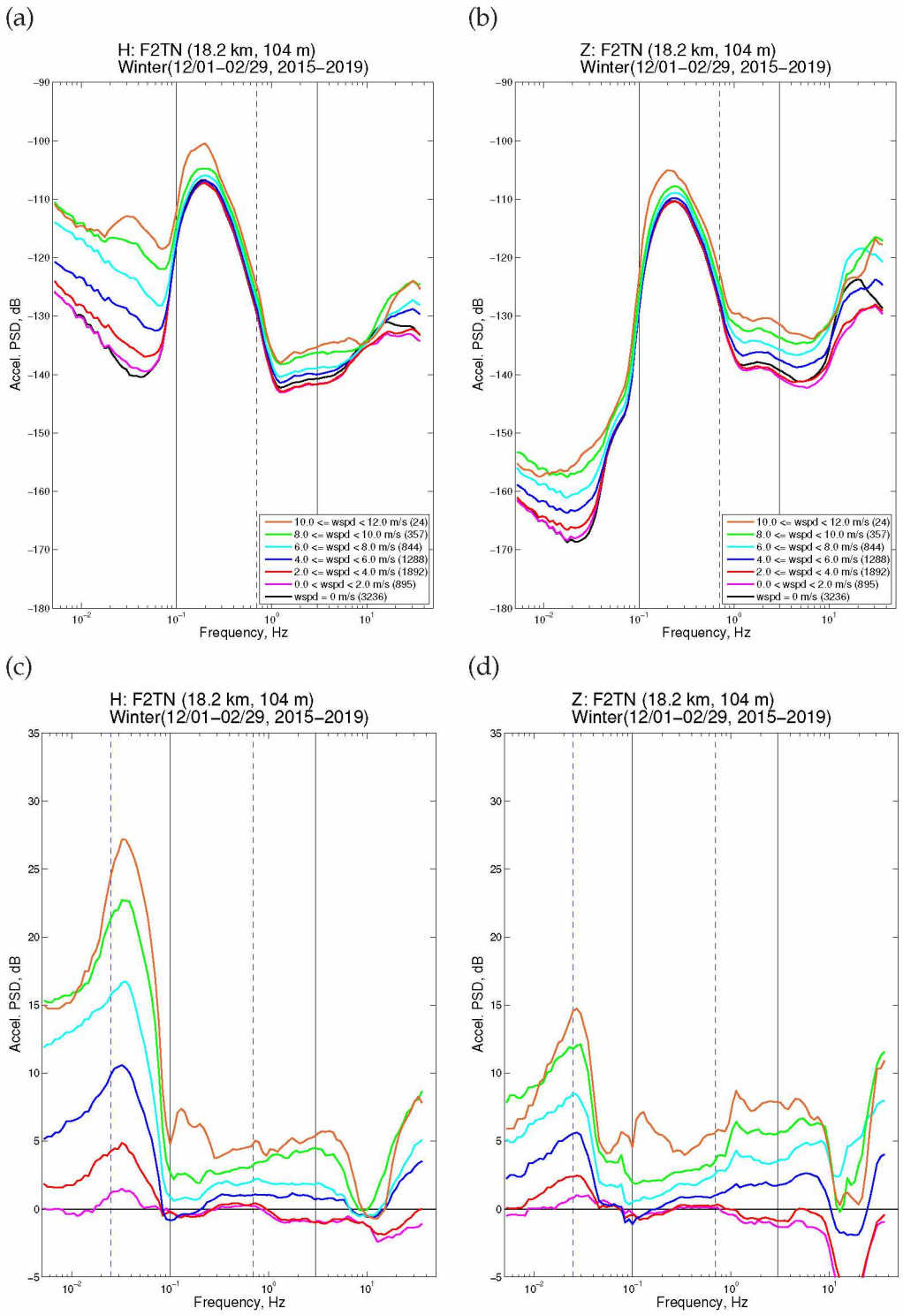

Figure A.35: The influence of wind on seismic noise during winter (Dec/Jan/Feb) at station F2TN; other stations shown in Figures A.34–A.49. The plot title includes the distance from the station to the meteorological sensor, followed by the station elevation (Table 2.1). (a) Horizontal-component seismic noise spectra made during time periods of different wind speeds. The number of hours used for each stack is listed in the legend. (b) Same as (a), but for the vertical component of seismic noise. (c) Spectra in (a) minus the spectrum made from the times of the lowest wind speed for winter (black). The dashed blue line at 0.025 Hz highlights a visible peak in the spectra shown for most stations (e.g. F6TP). (d) Spectra in (b) minus the spectrum made from the times of the lowest wind speed for winter (black).

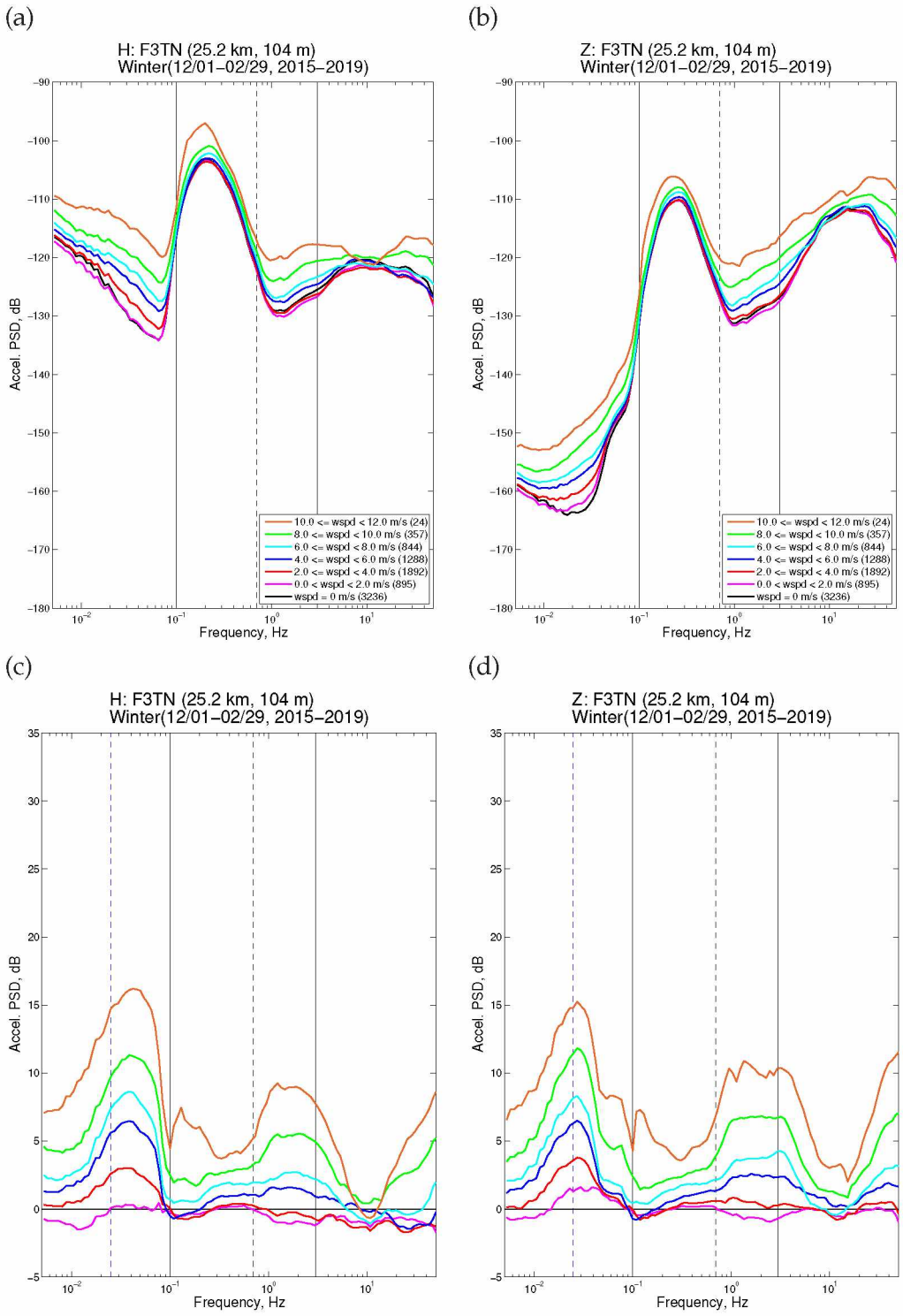

Figure A.36: The influence of wind on seismic noise during winter (Dec/Jan/Feb) at station F3TN; other stations shown in Figures A.34–A.49. The plot title includes the distance from the station to the meteorological sensor, followed by the station elevation (Table 2.1). (a) Horizontal-component seismic noise spectra made during time periods of different wind speeds. The number of hours used for each stack is listed in the legend. (b) Same as (a), but for the vertical component of seismic noise. (c) Spectra in (a) minus the spectrum made from the times of the lowest wind speed for winter (black). The dashed blue line at 0.025 Hz highlights a visible peak in the spectra shown for most stations (e.g. F6TP). (d) Spectra in (b) minus the spectrum made from the times of the lowest wind speed for winter (black).

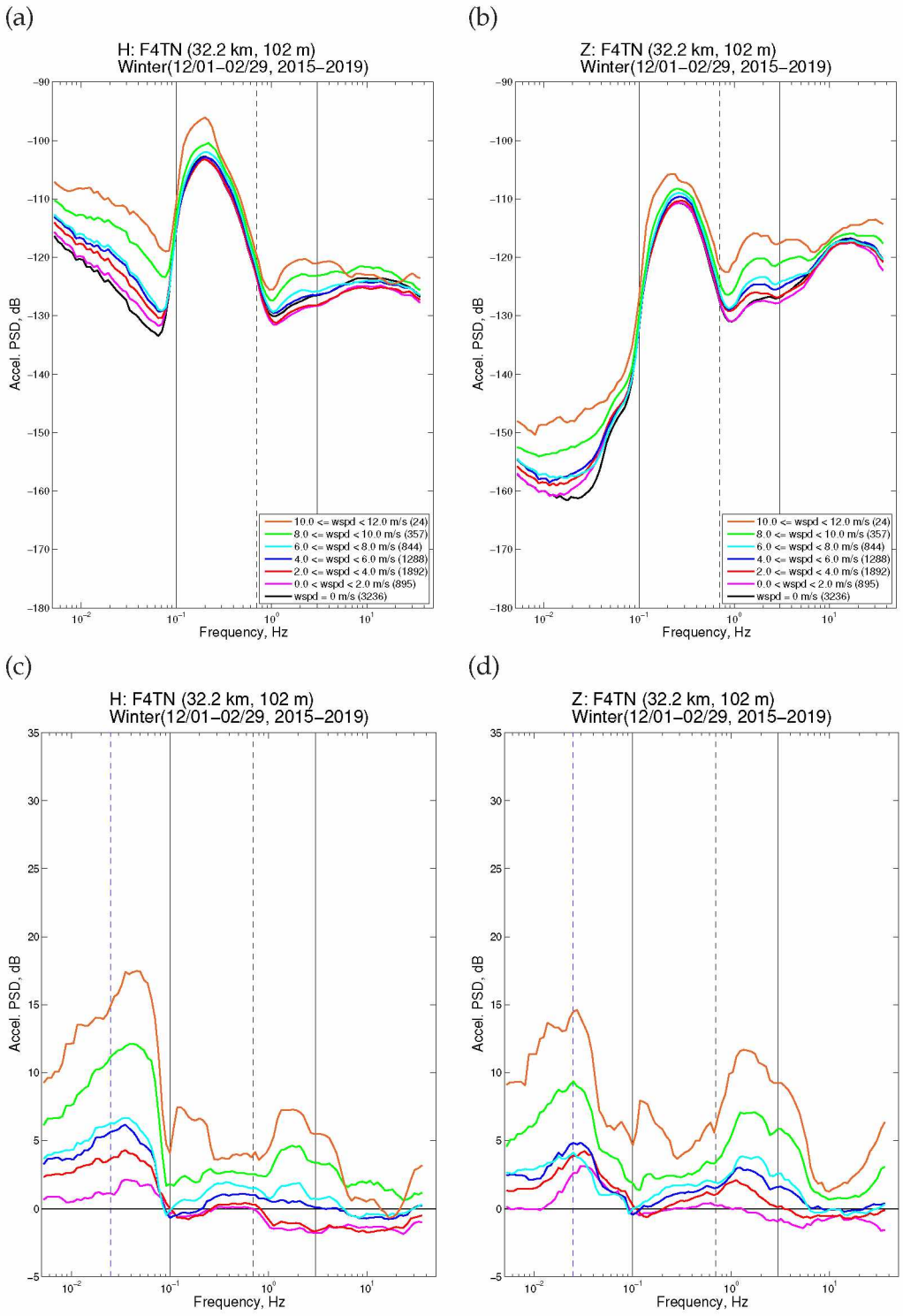

Figure A.37: The influence of wind on seismic noise during winter (Dec/Jan/Feb) at station F4TN; other stations shown in Figures A.34–A.49. The plot title includes the distance from the station to the meteorological sensor, followed by the station elevation (Table 2.1). (a) Horizontal-component seismic noise spectra made during time periods of different wind speeds. The number of hours used for each stack is listed in the legend. (b) Same as (a), but for the vertical component of seismic noise. (c) Spectra in (a) minus the spectrum made from the times of the lowest wind speed for winter (black). The dashed blue line at 0.025 Hz highlights a visible peak in the spectra shown for most stations (e.g. F6TP). (d) Spectra in (b) minus the spectrum made from the times of the lowest wind speed for winter (black).

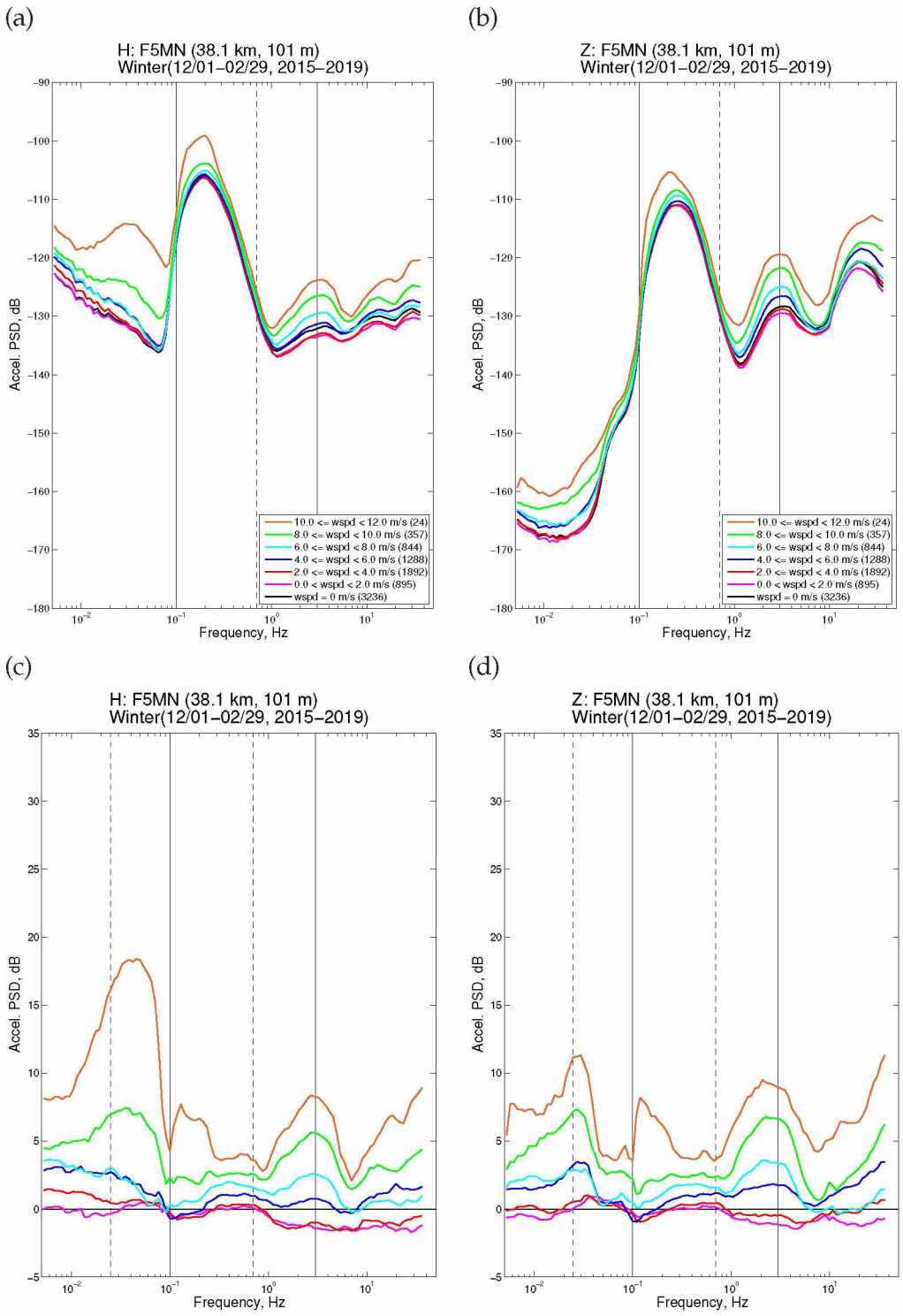

Figure A.38: The influence of wind on seismic noise during winter (Dec/Jan/Feb) at station F5MN; other stations shown in Figures A.34–A.49. The plot title includes the distance from the station to the meteorological sensor, followed by the station elevation (Table 2.1). (a) Horizontal-component seismic noise spectra made during time periods of different wind speeds. The number of hours used for each stack is listed in the legend. (b) Same as (a), but for the vertical component of seismic noise. (c) Spectra in (a) minus the spectrum made from the times of the lowest wind speed for winter (black). The dashed blue line at 0.025 Hz highlights a visible peak in the spectra shown for most stations (e.g. F6TP). (d) Spectra in (b) minus the spectrum made from the times of the lowest wind speed for winter (black).

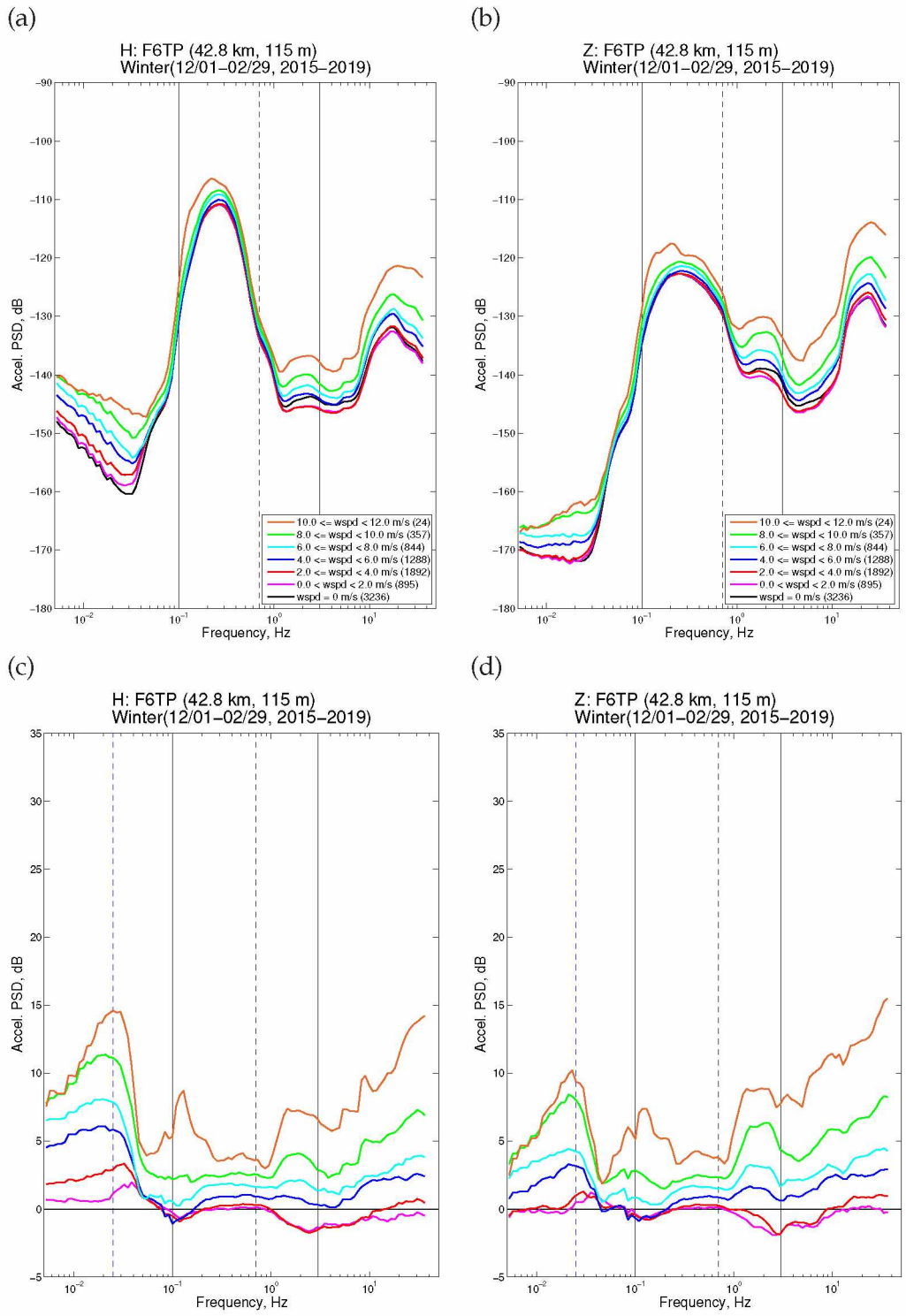

Figure A.39: The influence of wind on seismic noise during winter (Dec/Jan/Feb) at station F6TP; other stations shown in Figures A.34–A.49. The plot title includes the distance from the station to the meteorological sensor, followed by the station elevation (Table 2.1). (a) Horizontal-component seismic noise spectra made during time periods of different wind speeds. The number of hours used for each stack is listed in the legend. (b) Same as (a), but for the vertical component of seismic noise. (c) Spectra in (a) minus the spectrum made from the times of the lowest wind speed for winter (black). The dashed blue line at 0.025 Hz highlights a visible peak in the spectra shown for most stations (e.g. F6TP). (d) Spectra in (b) minus the spectrum made from the times of the lowest wind speed for winter (black).

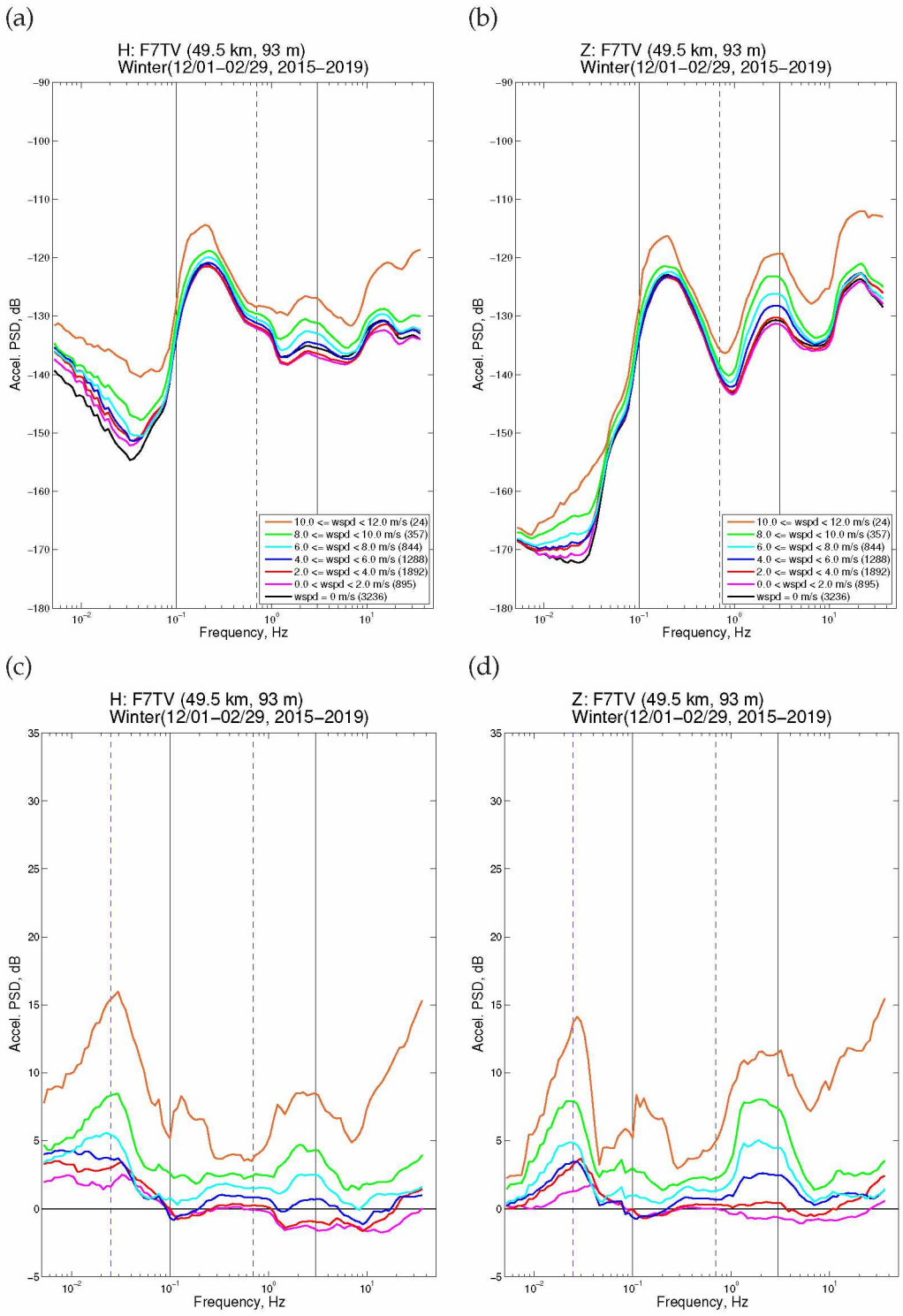

Figure A.40: The influence of wind on seismic noise during winter (Dec/Jan/Feb) at station F7TV; other stations shown in Figures A.34–A.49. The plot title includes the distance from the station to the meteorological sensor, followed by the station elevation (Table 2.1). (a) Horizontal-component seismic noise spectra made during time periods of different wind speeds. The number of hours used for each stack is listed in the legend. (b) Same as (a), but for the vertical component of seismic noise. (c) Spectra in (a) minus the spectrum made from the times of the lowest wind speed for winter (black). The dashed blue line at 0.025 Hz highlights a visible peak in the spectra shown for most stations (e.g. F6TP). (d) Spectra in (b) minus the spectrum made from the times of the lowest wind speed for winter (black).

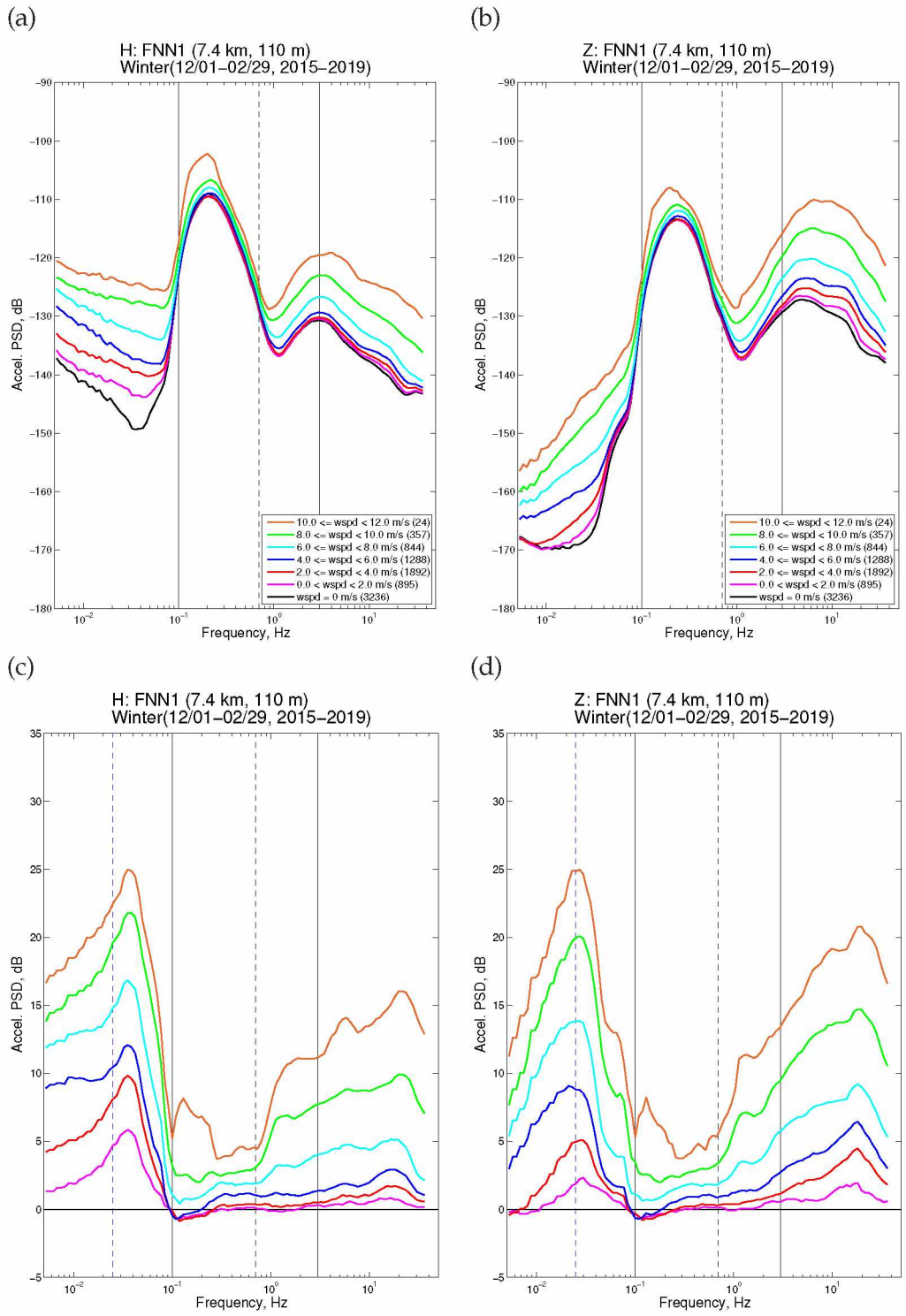

Figure A.41: The influence of wind on seismic noise during winter (Dec/Jan/Feb) at station FNN1; other stations shown in Figures A.34–A.49. The plot title includes the distance from the station to the meteorological sensor, followed by the station elevation (Table 2.1). (a) Horizontal-component seismic noise spectra made during time periods of different wind speeds. The number of hours used for each stack is listed in the legend. (b) Same as (a), but for the vertical component of seismic noise. (c) Spectra in (a) minus the spectrum made from the times of the lowest wind speed for winter (black). The dashed blue line at 0.025 Hz highlights a visible peak in the spectra shown for most stations (e.g. F6TP). (d) Spectra in (b) minus the spectrum made from the times of the lowest wind speed for winter (black).

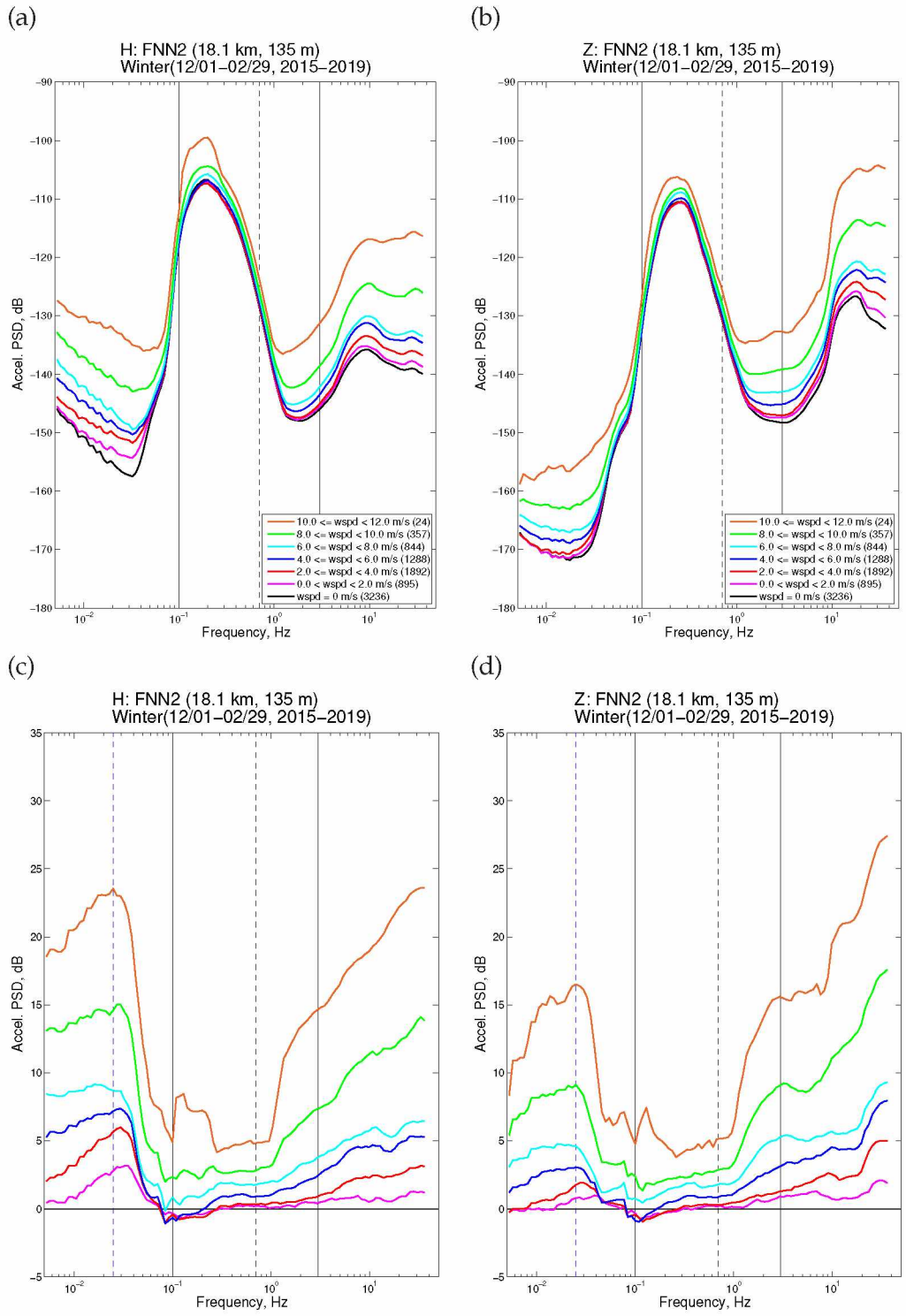

Figure A.42: The influence of wind on seismic noise during winter (Dec/Jan/Feb) at station FNN2; other stations shown in Figures A.34–A.49. The plot title includes the distance from the station to the meteorological sensor, followed by the station elevation (Table 2.1). (a) Horizontal-component seismic noise spectra made during time periods of different wind speeds. The number of hours used for each stack is listed in the legend. (b) Same as (a), but for the vertical component of seismic noise. (c) Spectra in (a) minus the spectrum made from the times of the lowest wind speed for winter (black). The dashed blue line at 0.025 Hz highlights a visible peak in the spectra shown for most stations (e.g. F6TP). (d) Spectra in (b) minus the spectrum made from the times of the lowest wind speed for winter (black).

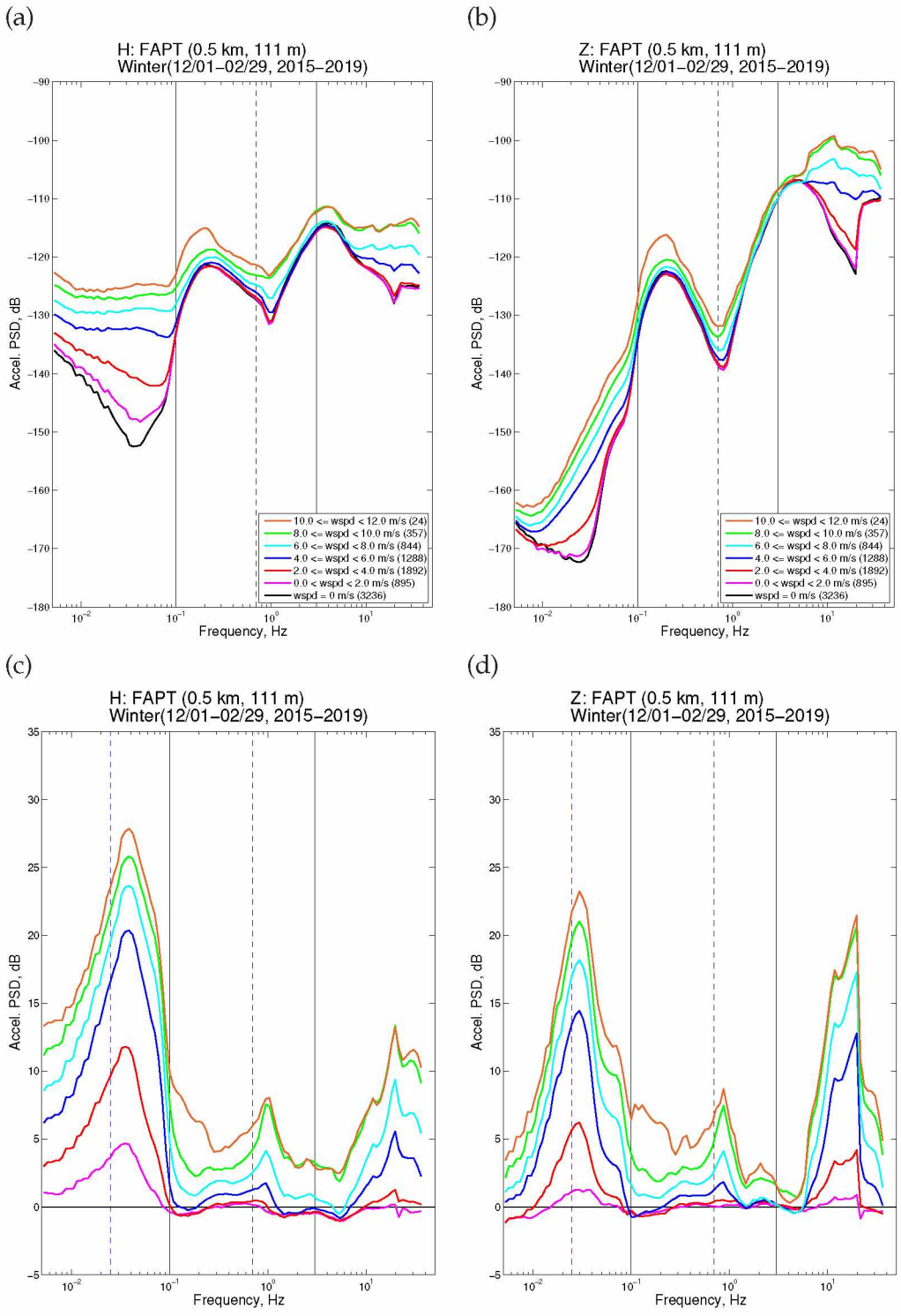

Figure A.43: The influence of wind on seismic noise during winter (Dec/Jan/Feb) at station FAPT; other stations shown in Figures A.34–A.49. The plot title includes the distance from the station to the meteorological sensor, followed by the station elevation (Table 2.1). (a) Horizontal-component seismic noise spectra made during time periods of different wind speeds. The number of hours used for each stack is listed in the legend. (b) Same as (a), but for the vertical component of seismic noise. (c) Spectra in (a) minus the spectrum made from the times of the lowest wind speed for winter (black). The dashed blue line at 0.025 Hz highlights a visible peak in the spectra shown for most stations (e.g. F6TP). (d) Spectra in (b) minus the spectrum made from the times of the lowest wind speed for winter (black).

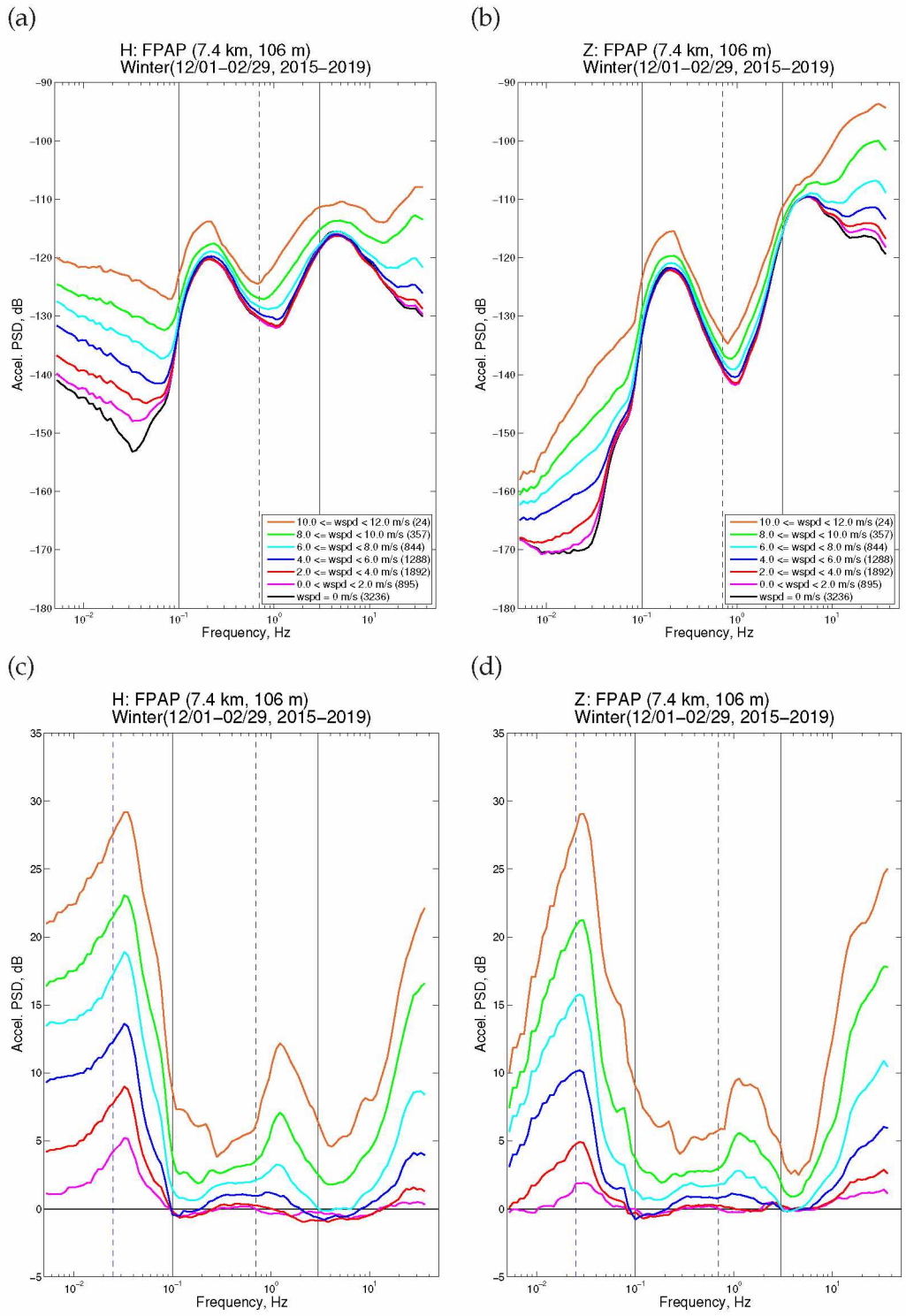

Figure A.44: The influence of wind on seismic noise during winter (Dec/Jan/Feb) at station FPAP; other stations shown in Figures A.34–A.49. The plot title includes the distance from the station to the meteorological sensor, followed by the station elevation (Table 2.1). (a) Horizontal-component seismic noise spectra made during time periods of different wind speeds. The number of hours used for each stack is listed in the legend. (b) Same as (a), but for the vertical component of seismic noise. (c) Spectra in (a) minus the spectrum made from the times of the lowest wind speed for winter (black). The dashed blue line at 0.025 Hz highlights a visible peak in the spectra shown for most stations (e.g. F6TP). (d) Spectra in (b) minus the spectrum made from the times of the lowest wind speed for winter (black).

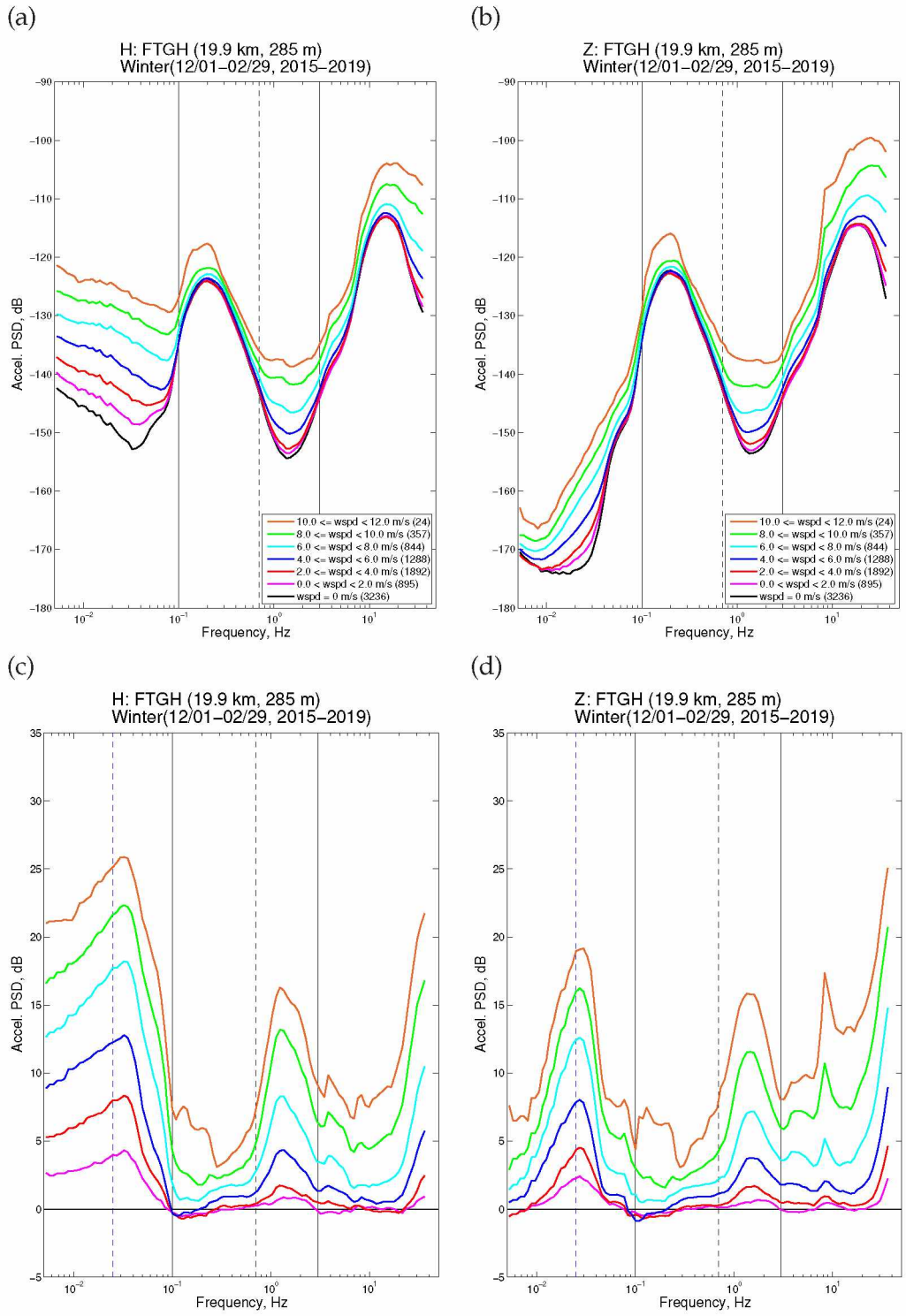

Figure A.45: The influence of wind on seismic noise during winter (Dec/Jan/Feb) at station FTGH; other stations shown in Figures A.34–A.49. The plot title includes the distance from the station to the meteorological sensor, followed by the station elevation (Table 2.1). (a) Horizontal-component seismic noise spectra made during time periods of different wind speeds. The number of hours used for each stack is listed in the legend. (b) Same as (a), but for the vertical component of seismic noise. (c) Spectra in (a) minus the spectrum made from the times of the lowest wind speed for winter (black). The dashed blue line at 0.025 Hz highlights a visible peak in the spectra shown for most stations (e.g. F6TP). (d) Spectra in (b) minus the spectrum made from the times of the lowest wind speed for winter (black).

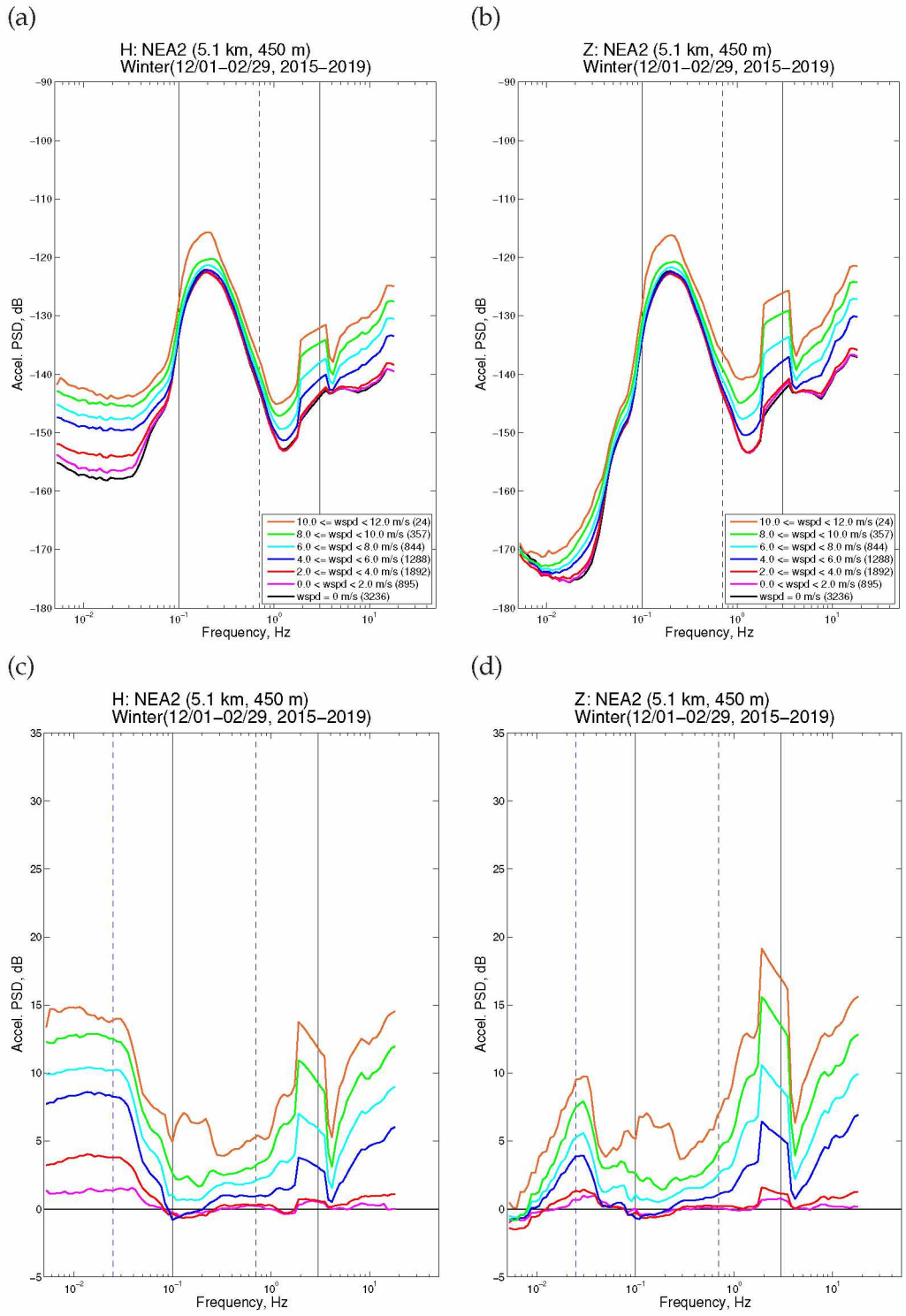

Figure A.46: The influence of wind on seismic noise during winter (Dec/Jan/Feb) at station NEA2; other stations shown in Figures A.34–A.49. The plot title includes the distance from the station to the meteorological sensor, followed by the station elevation (Table 2.1). (a) Horizontal-component seismic noise spectra made during time periods of different wind speeds. The number of hours used for each stack is listed in the legend. (b) Same as (a), but for the vertical component of seismic noise. (c) Spectra in (a) minus the spectrum made from the times of the lowest wind speed for winter (black). The dashed blue line at 0.025 Hz highlights a visible peak in the spectra shown for most stations (e.g. F6TP). (d) Spectra in (b) minus the spectrum made from the times of the lowest wind speed for winter (black).

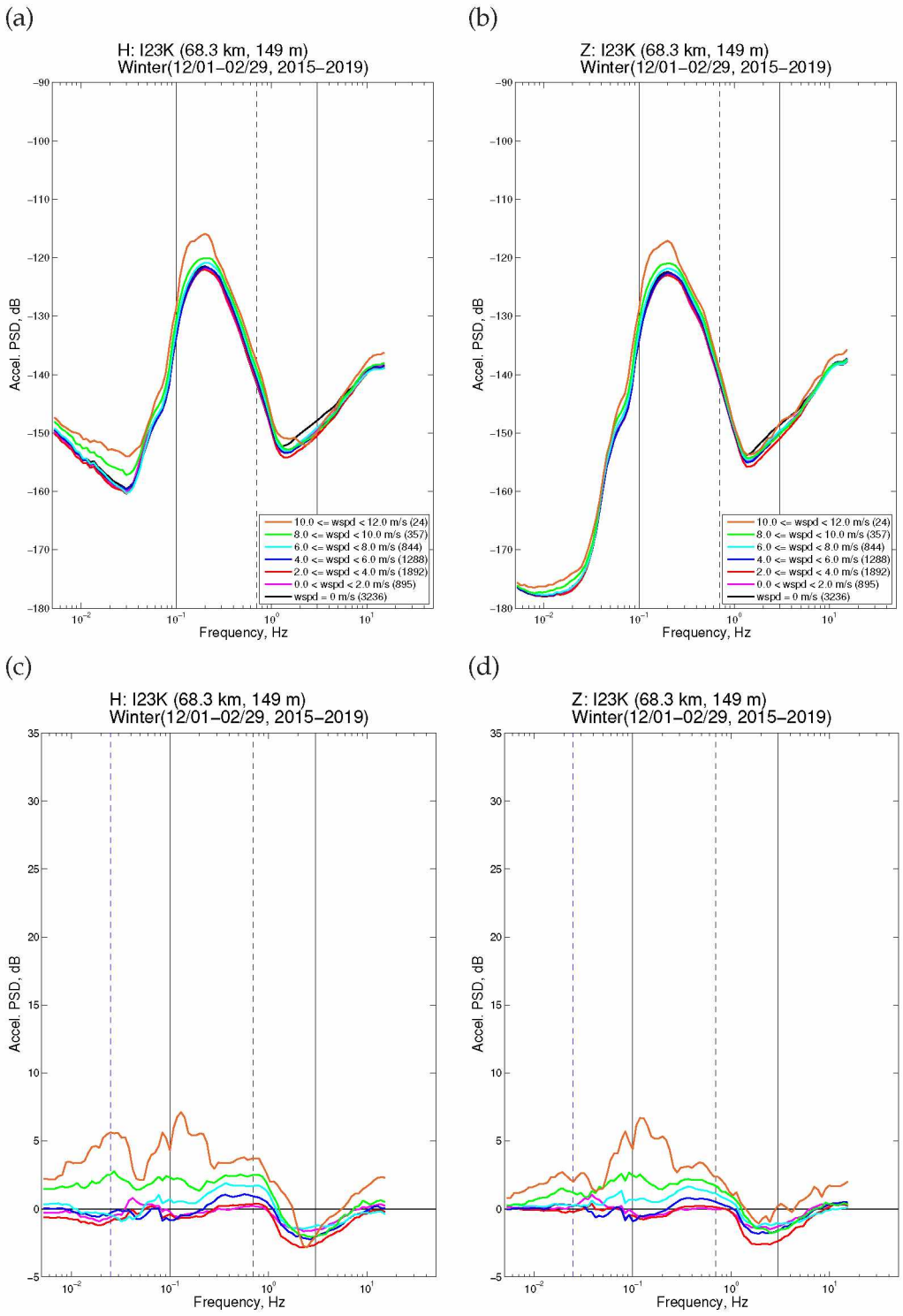

Figure A.47: The influence of wind on seismic noise during winter (Dec/Jan/Feb) at station I23K; other stations shown in Figures A.34–A.49. The plot title includes the distance from the station to the meteorological sensor, followed by the station elevation (Table 2.1). (a) Horizontal-component seismic noise spectra made during time periods of different wind speeds. The number of hours used for each stack is listed in the legend. (b) Same as (a), but for the vertical component of seismic noise. (c) Spectra in (a) minus the spectrum made from the times of the lowest wind speed for winter (black). The dashed blue line at 0.025 Hz highlights a visible peak in the spectra shown for most stations (e.g. F6TP). (d) Spectra in (b) minus the spectrum made from the times of the lowest wind speed for winter (black).

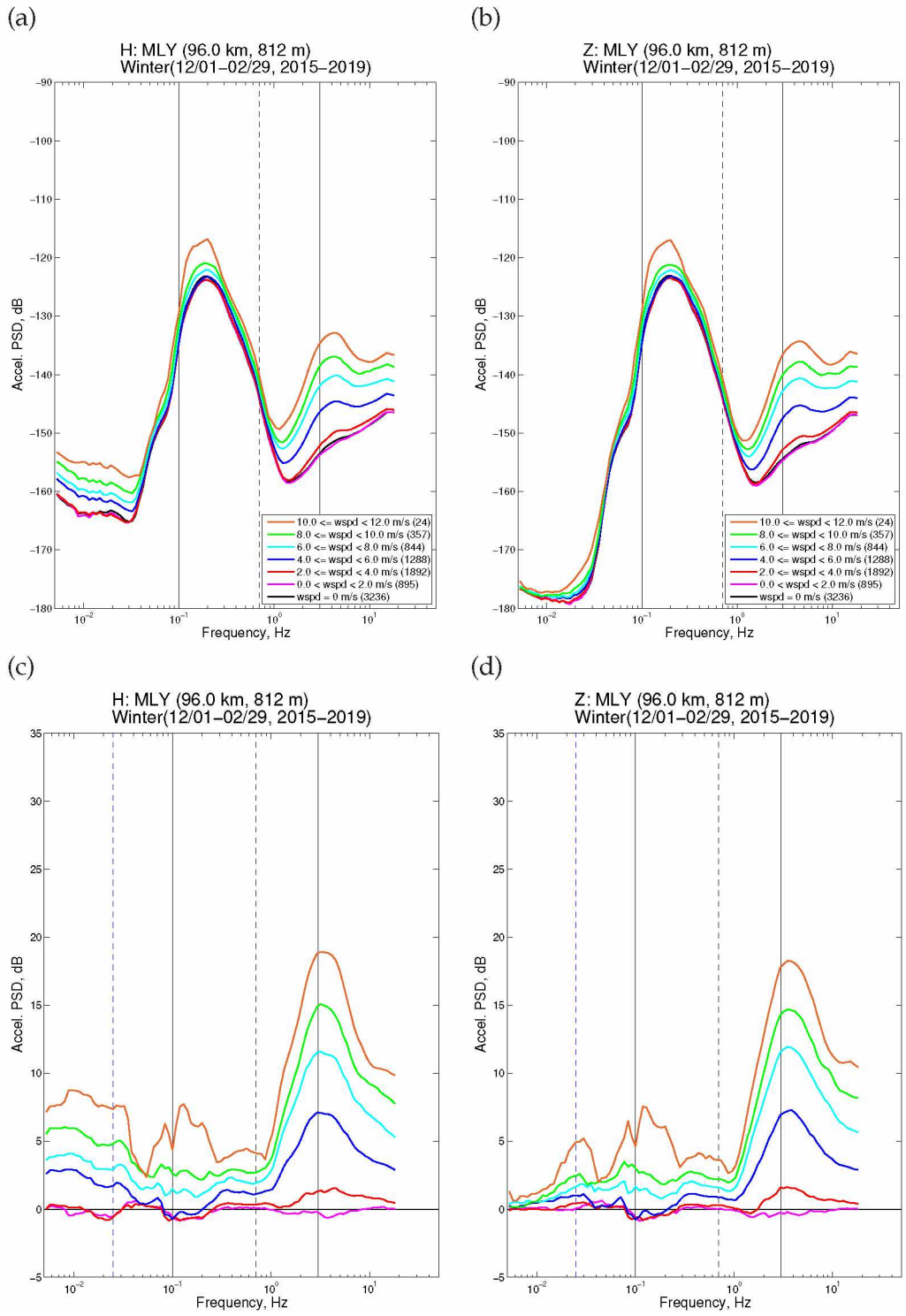

Figure A.48: The influence of wind on seismic noise during winter (Dec/Jan/Feb) at station MLY; other stations shown in Figures A.34–A.49. The plot title includes the distance from the station to the meteorological sensor, followed by the station elevation (Table 2.1). (a) Horizontal-component seismic noise spectra made during time periods of different wind speeds. The number of hours used for each stack is listed in the legend. (b) Same as (a), but for the vertical component of seismic noise. (c) Spectra in (a) minus the spectrum made from the times of the lowest wind speed for winter (black). The dashed blue line at 0.025 Hz highlights a visible peak in the spectra shown for most stations (e.g. F6TP). (d) Spectra in (b) minus the spectrum made from the times of the lowest wind speed for winter (black).

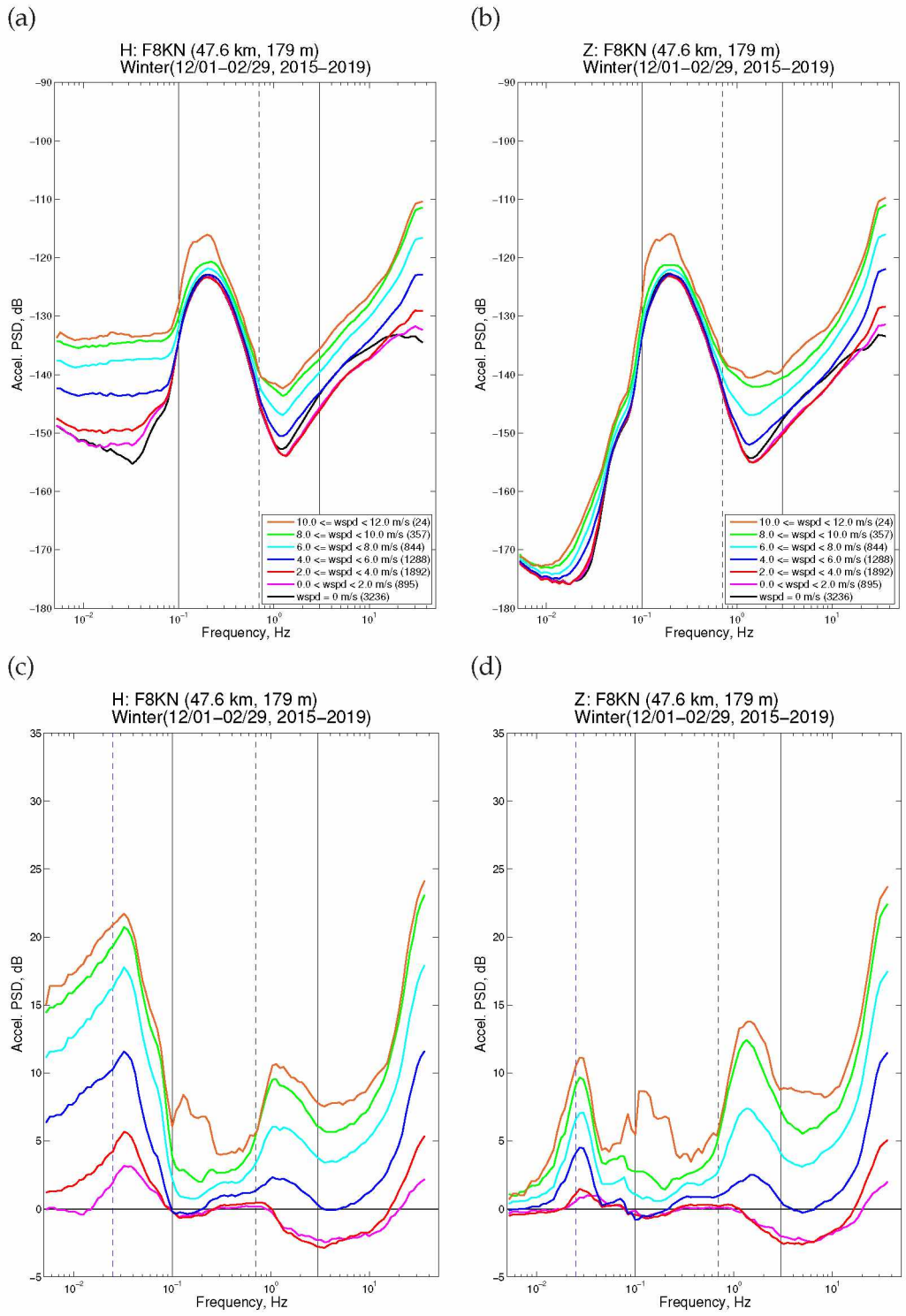

Figure A.49: The influence of wind on seismic noise during winter (Dec/Jan/Feb) at station F8KN; other stations shown in Figures A.34–A.49. The plot title includes the distance from the station to the meteorological sensor, followed by the station elevation (Table 2.1). (a) Horizontal-component seismic noise spectra made during time periods of different wind speeds. The number of hours used for each stack is listed in the legend. (b) Same as (a), but for the vertical component of seismic noise. (c) Spectra in (a) minus the spectrum made from the times of the lowest wind speed for winter (black). The dashed blue line at 0.025 Hz highlights a visible peak in the spectra shown for most stations (e.g. F6TP). (d) Spectra in (b) minus the spectrum made from the times of the lowest wind speed for winter (black).

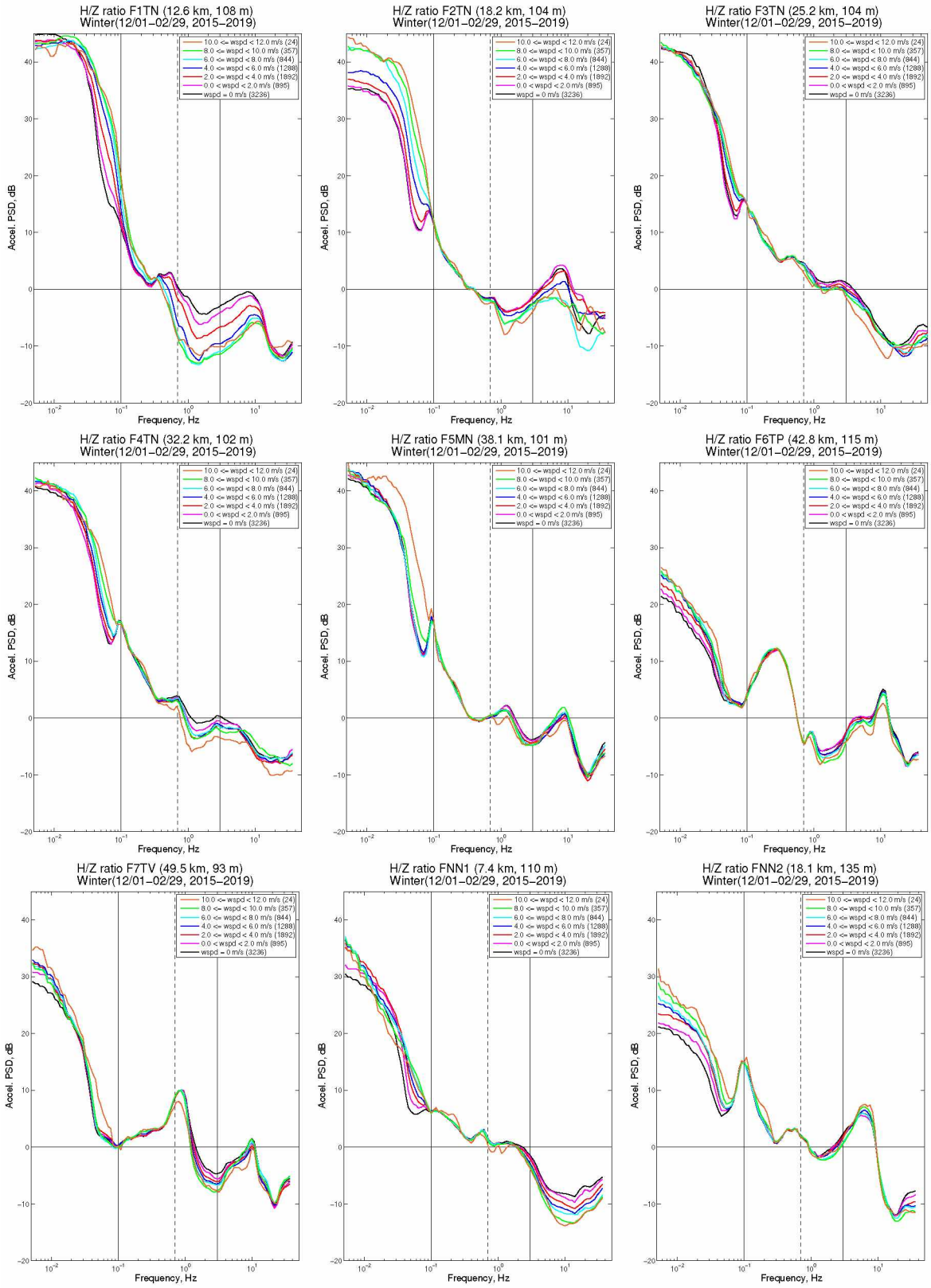

Figure A.50: The influence of wind on the H/Z ratio during winter (Dec/Jan/Feb). Each set of spectra is obtained by subtracting (b) from (a) in Figures A.34–A.42. See also Figure A.51.

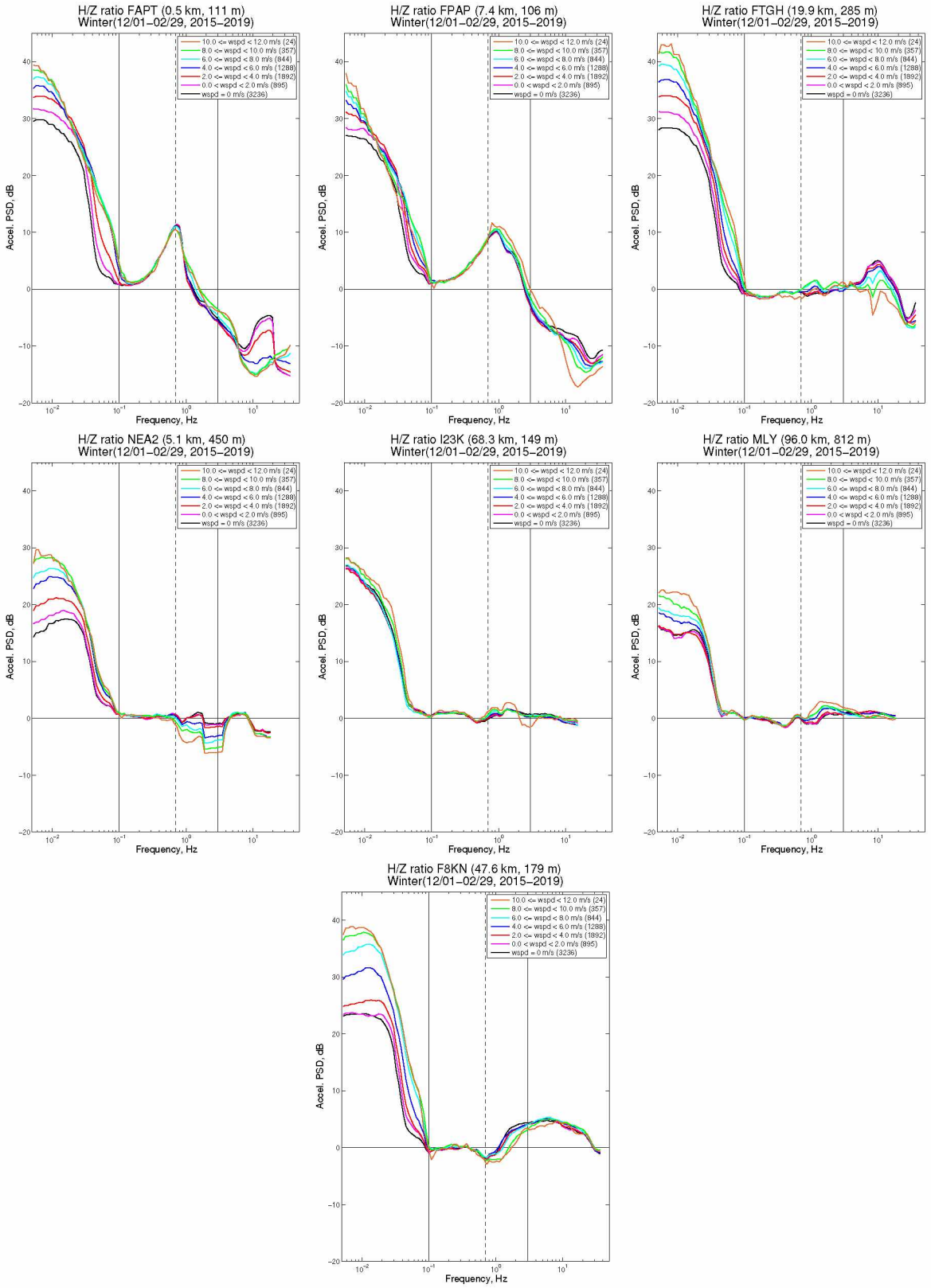

Figure A.51: The influence of wind on the H/Z ratio during winter (Dec/Jan/Feb). Each set of spectra is obtained by subtracting (b) from (a) in Figures A.43–A.49. See also Figure A.50.

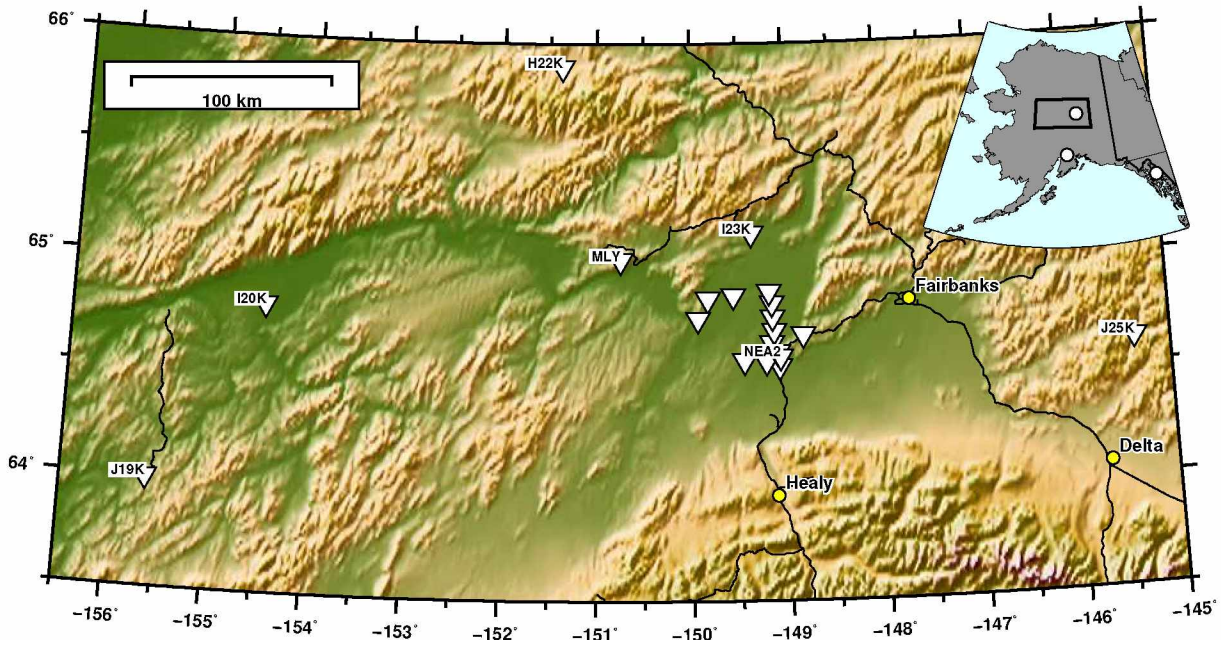

Figure A.52: Study area of the Minto Flats region, central Alaska (Figure 2.1), surrounded by the four closest TA stations with co-located meteorological sensors: J19K, I20K, H22K, and J25K.

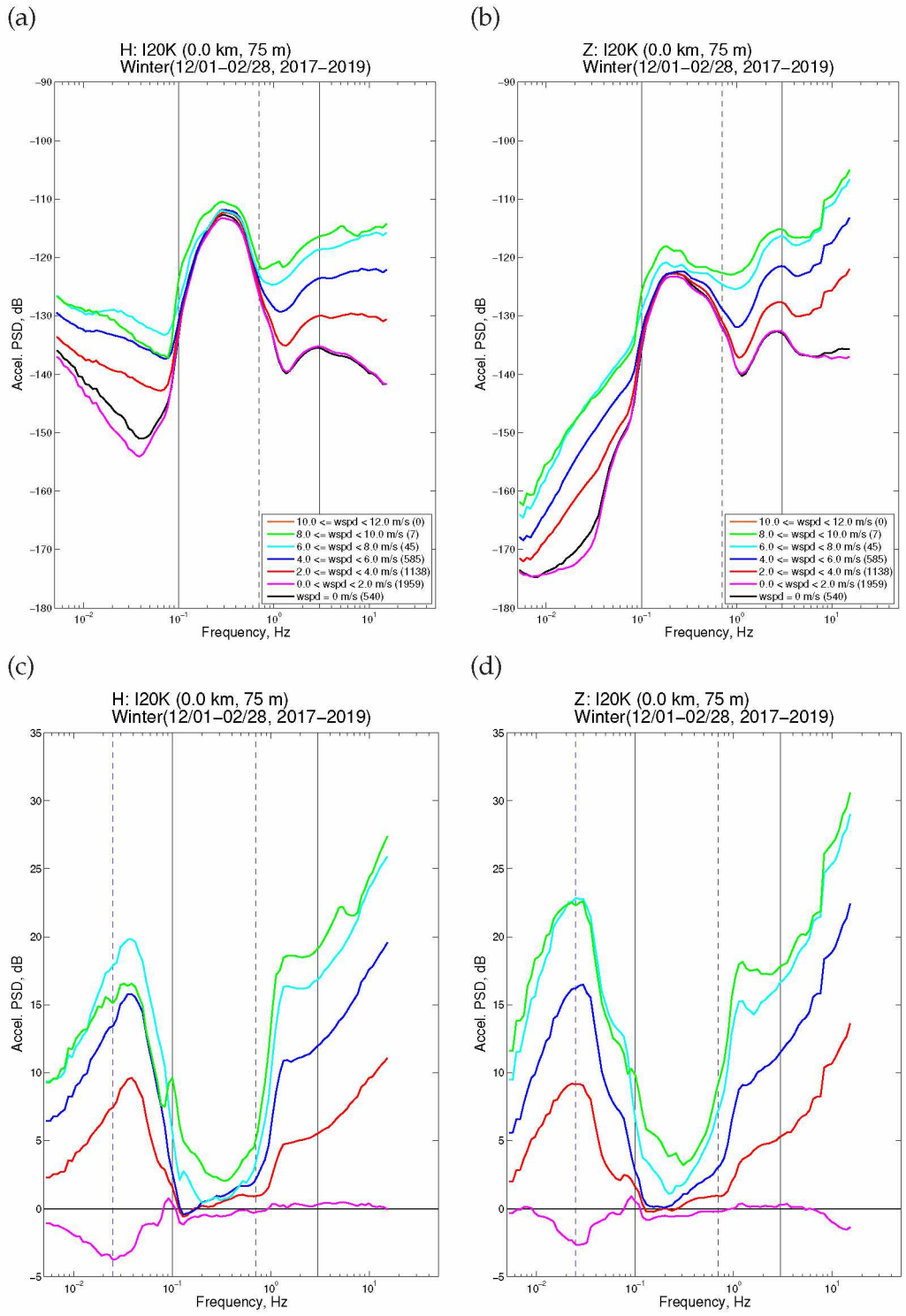

Figure A.53: The influence of wind on seismic noise during winter (Dec/Jan/Feb) at station I20K. Other stations shown in Figures A.34–A.49. (a) Horizontal-component seismic noise spectra made during time periods of different wind speeds. The number of hours used for each stack is listed in the legend. (b) Same as (a), but for the vertical component of seismic noise. (c) Spectra in (a) minus the spectrum made from the times of the lowest wind speed for winter (black). The dashed blue line at 0.025 Hz highlights a visible peak in the spectra shown for most stations (e.g. F6TP). (d) Spectra in (b) minus the spectrum made from the times of the lowest wind speed for winter (black).

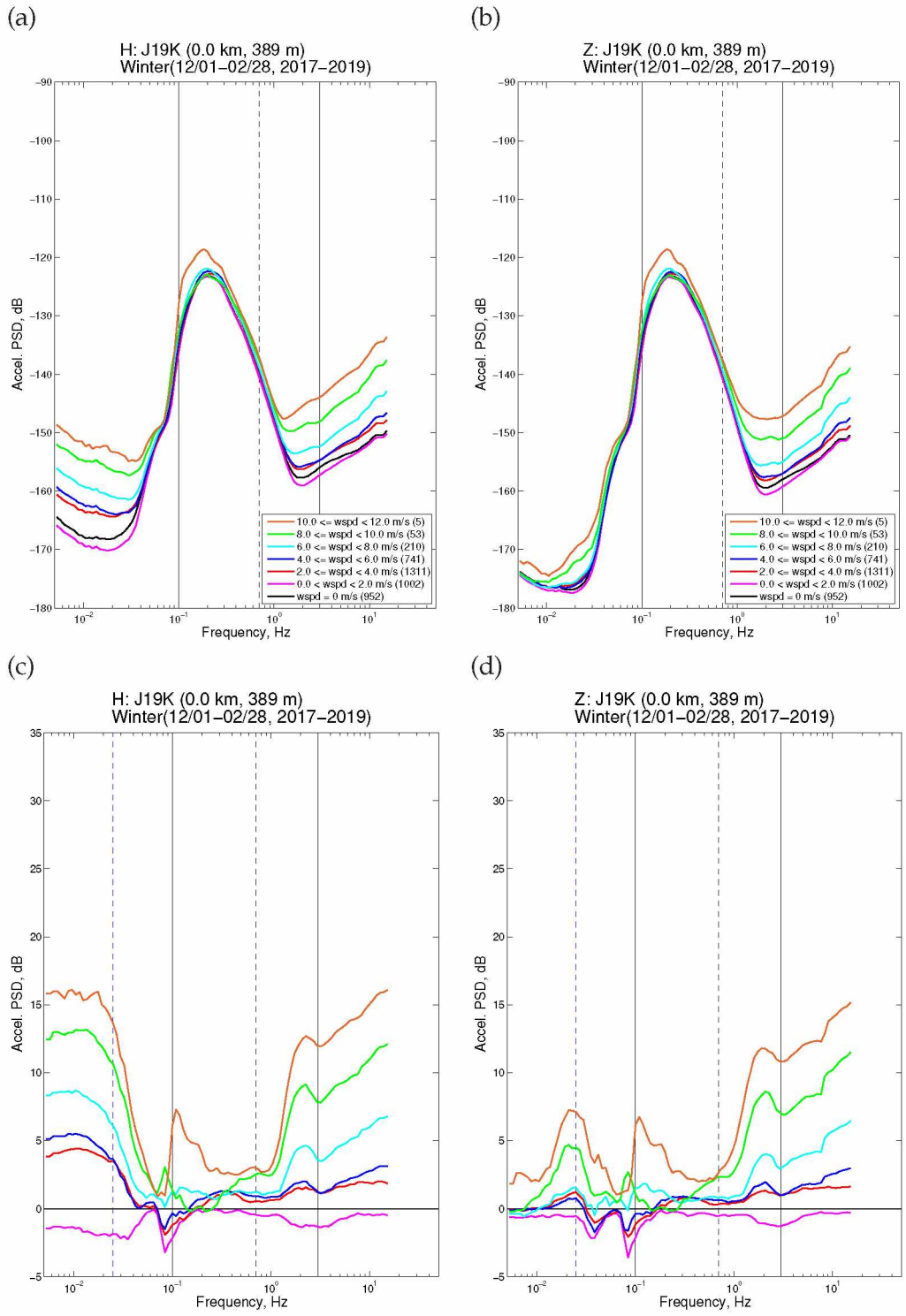

Figure A.54: The influence of wind on seismic noise during winter (Dec/Jan/Feb) at station J19K. Other stations shown in Figures A.34–A.49. (a) Horizontal-component seismic noise spectra made during time periods of different wind speeds. The number of hours used for each stack is listed in the legend. (b) Same as (a), but for the vertical component of seismic noise. (c) Spectra in (a) minus the spectrum made from the times of the lowest wind speed for winter (black). The dashed blue line at 0.025 Hz highlights a visible peak in the spectra shown for most stations (e.g. F6TP). (d) Spectra in (b) minus the spectrum made from the times of the lowest wind speed for winter (black).

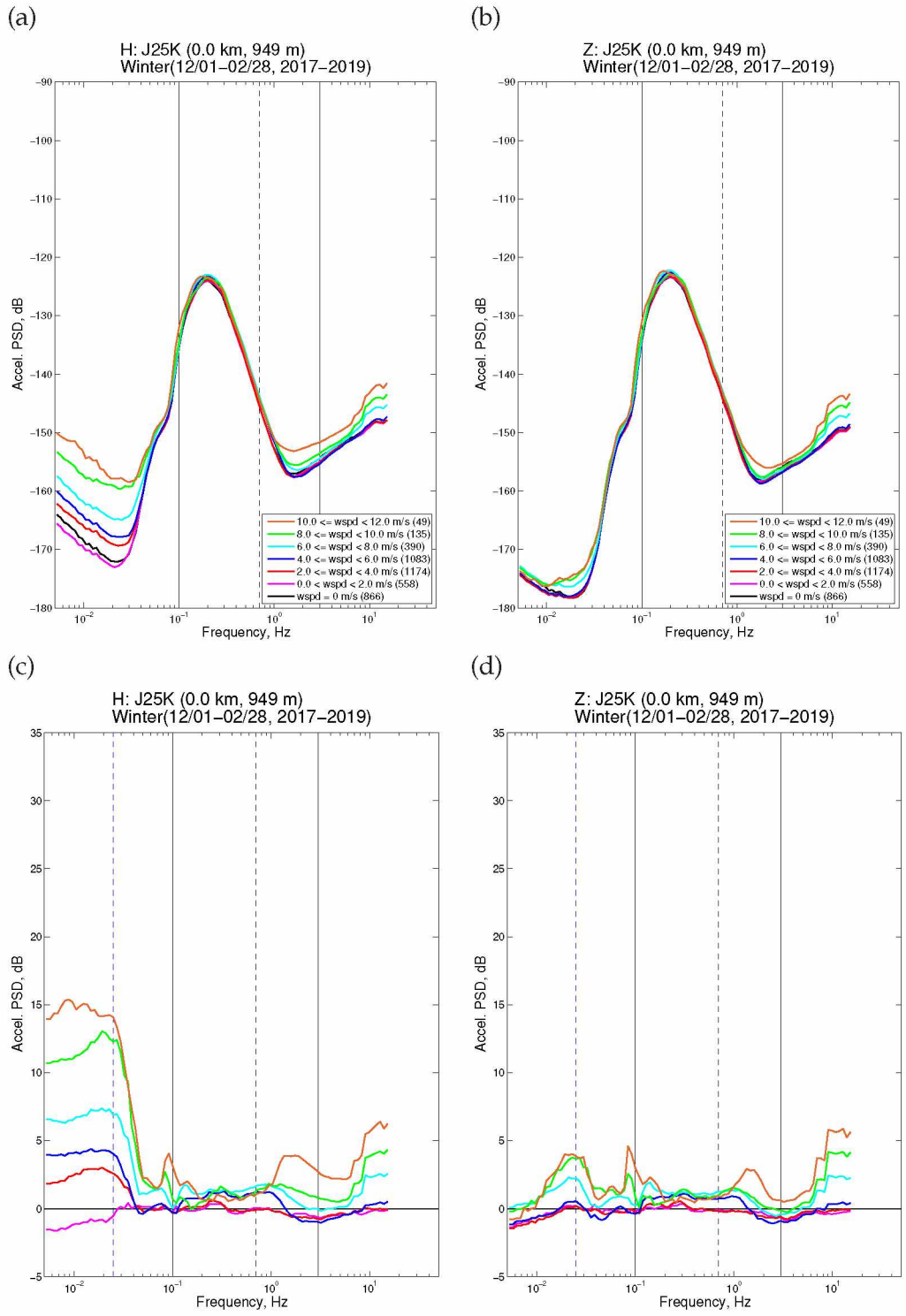

Figure A.55: The influence of wind on seismic noise during winter (Dec/Jan/Feb) at station J25K. Other stations shown in Figures A.34–A.49. (a) Horizontal-component seismic noise spectra made during time periods of different wind speeds. The number of hours used for each stack is listed in the legend. (b) Same as (a), but for the vertical component of seismic noise. (c) Spectra in (a) minus the spectrum made from the times of the lowest wind speed for winter (black). The dashed blue line at 0.025 Hz highlights a visible peak in the spectra shown for most stations (e.g. F6TP). (d) Spectra in (b) minus the spectrum made from the times of the lowest wind speed for winter (black).

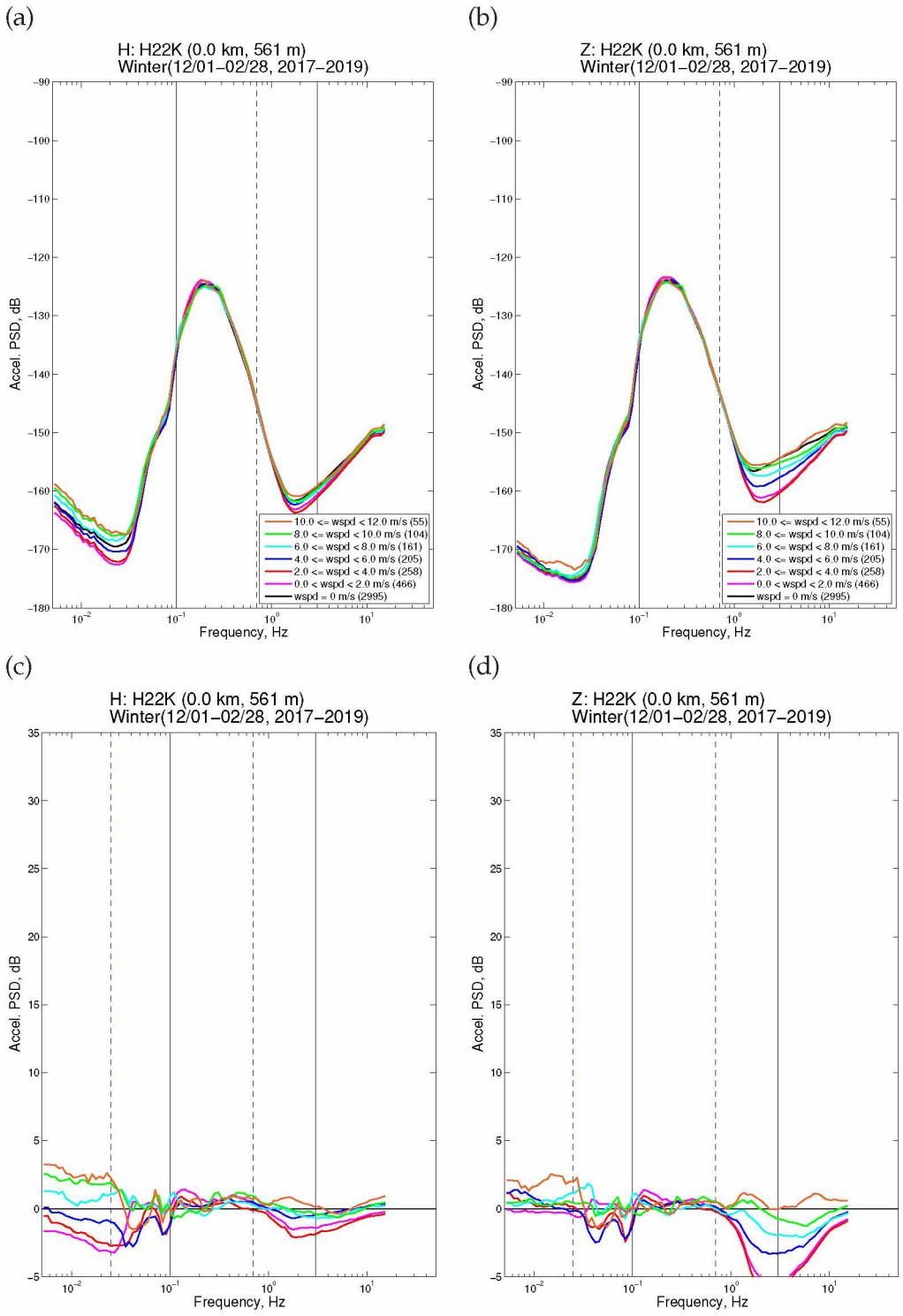

Figure A.56: The influence of wind on seismic noise during winter (Dec/Jan/Feb) at station H22K. Other stations shown in Figures A.34–A.49. (a) Horizontal-component seismic noise spectra made during time periods of different wind speeds. The number of hours used for each stack is listed in the legend. (b) Same as (a), but for the vertical component of seismic noise. (c) Spectra in (a) minus the spectrum made from the times of the lowest wind speed for winter (black). The dashed blue line at 0.025 Hz highlights a visible peak in the spectra shown for most stations (e.g. F6TP). (d) Spectra in (b) minus the spectrum made from the times of the lowest wind speed for winter (black).

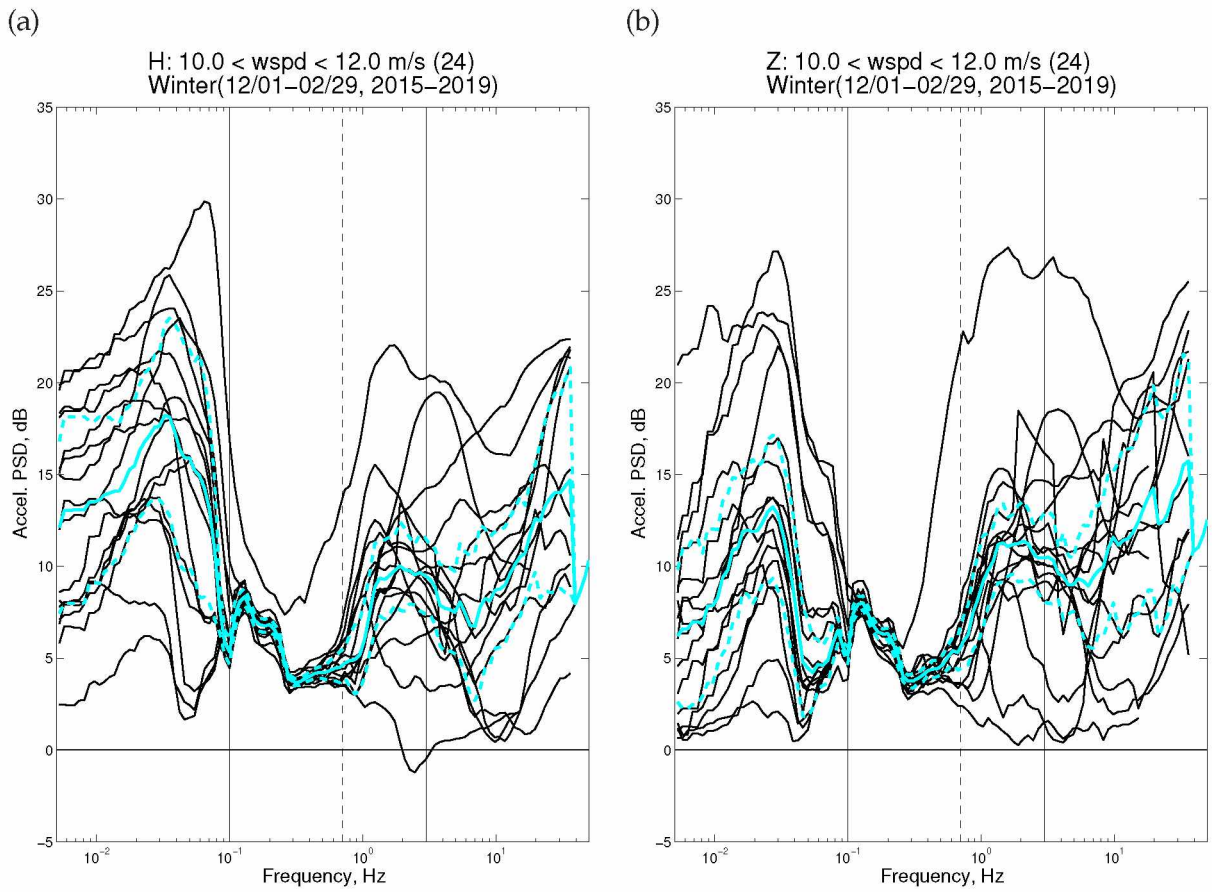

Figure A.57: The influence of wind on seismic noise during winter (Dec/Jan/Feb) for all 16 stations in Table 2.1. (a) Horizontal component spectra for 16 stations. Each spectrum is constructed by taking the median of all spectra recorded during hours of 10–12 m/s wind speeds, then subtracting the median spectrum made from all spectra recorded during hours of no wind. The bold cyan spectrum is the median of all 16 stacks and the dashed lines represent uncertainties ($\pm$ 1 median absolute deviation). (b) Same as (a), but for the vertical component.

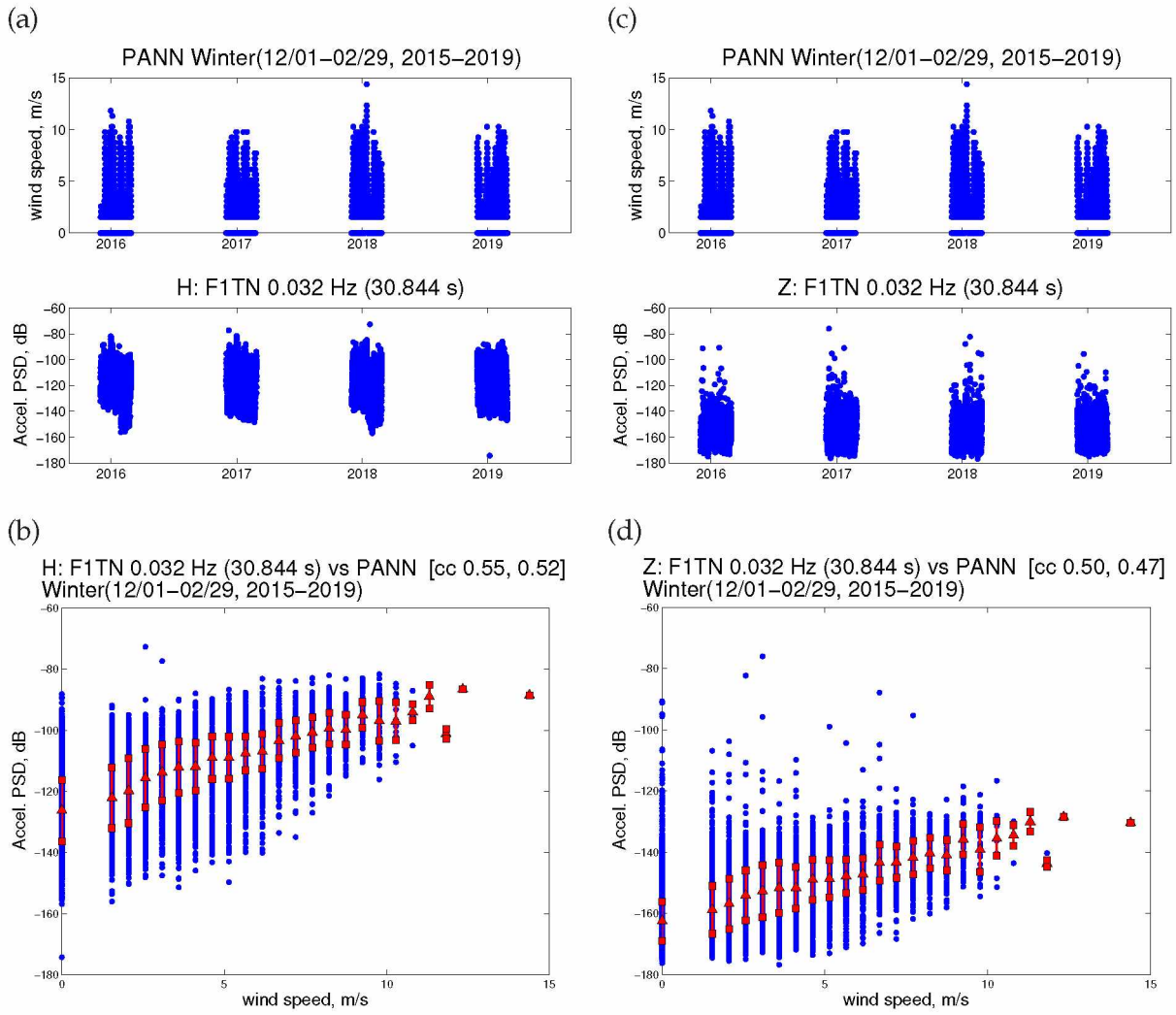

Figure A.58: Scatter plot and time series of wind speed at PANN and 30 s ambient noise of F1TN during the winter. The sample rate for both data sets is hourly. (a) Time series comparison of wind speed and horizontal-component seismic noise at 30 s. (b) Scatter plot of the two time series in (a). The red triangles are the median power for each wind speed and the squares are variation at 1 MAD. The first correlation is for all available data. The second correlation excludes all wind speed measurements at 0 m/s. (c)-(d) Same as (a)-(b), but for the vertical component of seismic noise.

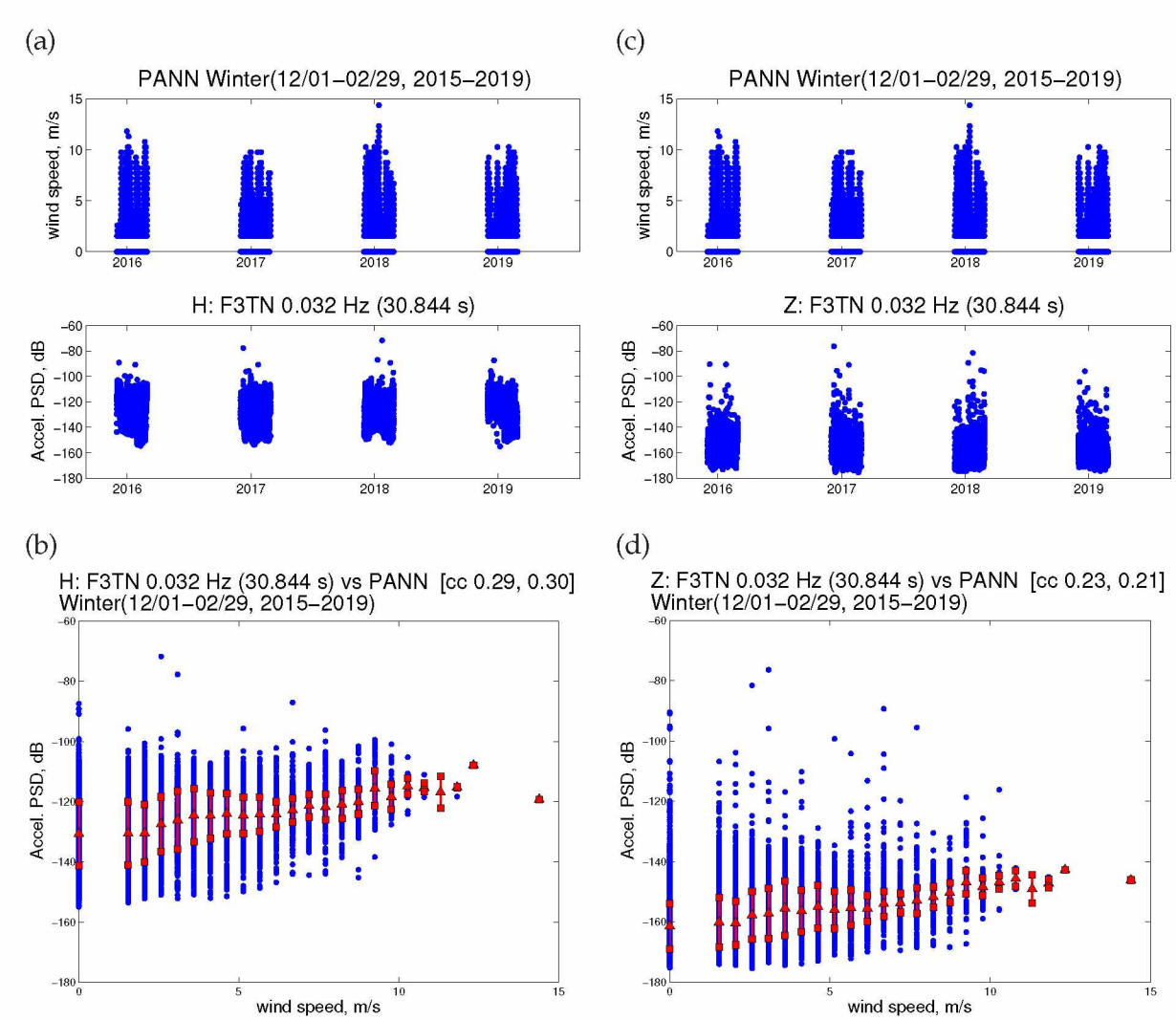

Figure A.59: Scatter plot and time series of wind speed at PANN and 30 s ambient noise of F3TN during the winter. The sample rate for both data sets is hourly. (a) Time series comparison of wind speed and horizontal-component seismic noise at 30 s. (b) Scatter plot of the two time series in (a). The red triangles are the median power for each wind speed and the squares are variation at 1 MAD. The first correlation is for all available data. The second correlation excludes all wind speed measurements at 0 m/s. (c)-(d) Same as (a)-(b), but for the vertical component of seismic noise.

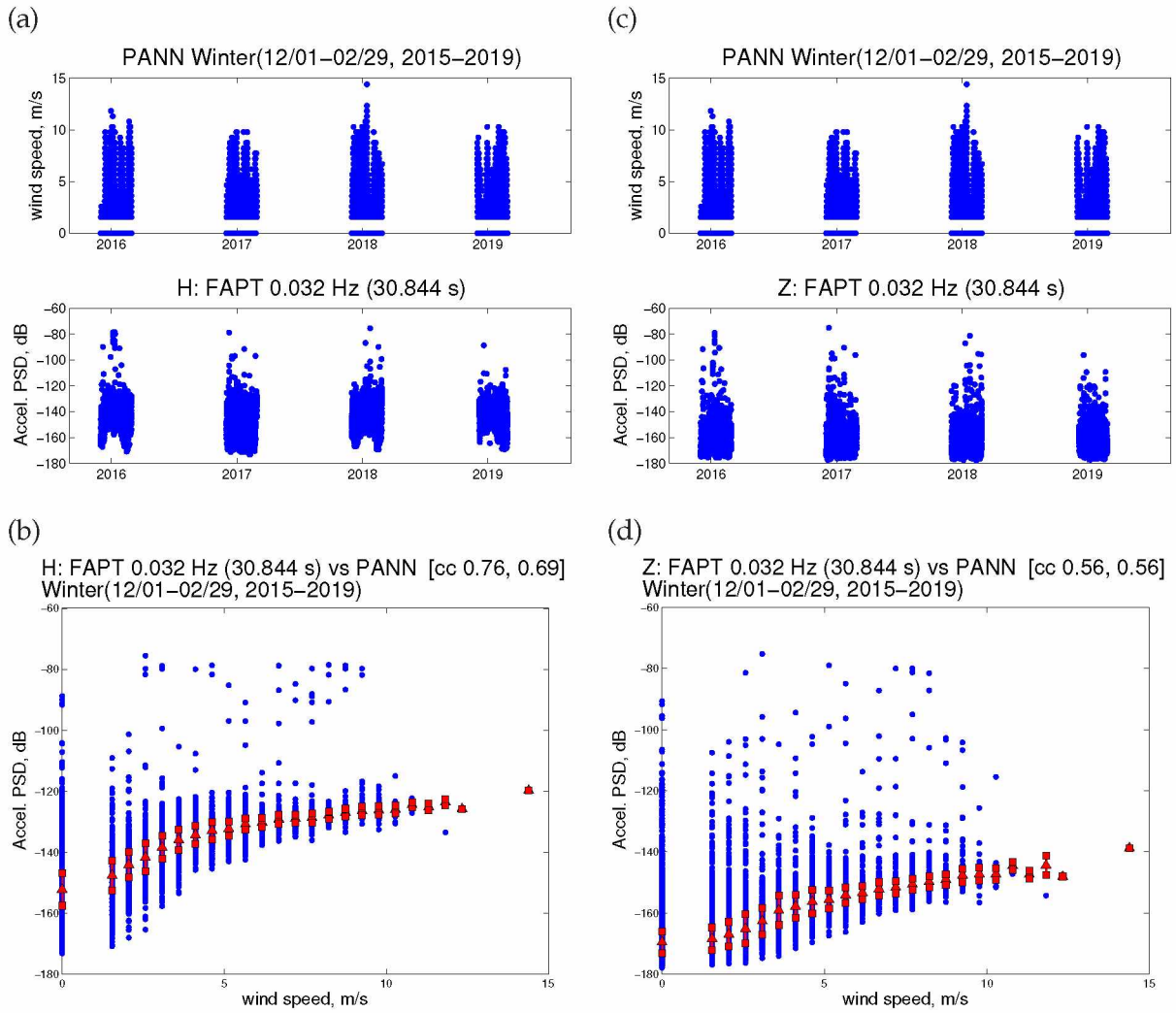

Figure A.60: Scatter plot and time series of wind speed at PANN and 30 s ambient noise of FAPT during the winter. The sample rate for both data sets is hourly. (a) Time series comparison of wind speed and horizontal-component seismic noise at 30 s. (b) Scatter plot of the two time series in (a). The red triangles are the median power for each wind speed and the squares are variation at 1 MAD. The first correlation is for all available data. The second correlation excludes all wind speed measurements at 0 m/s. (c)-(d) Same as (a)-(b), but for the vertical component of seismic noise.

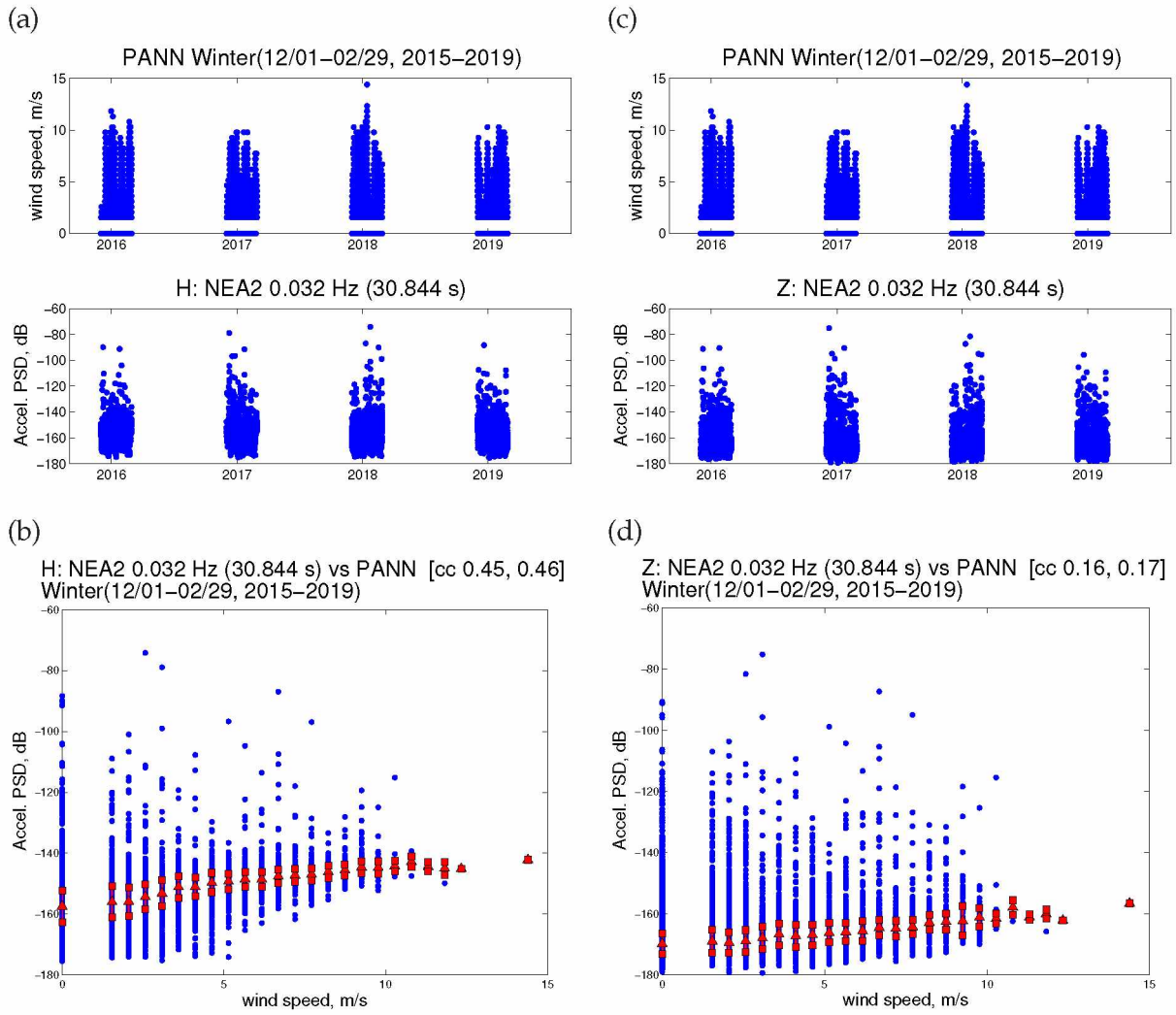

Figure A.61: Scatter plot and time series of wind speed at PANN and 30 s ambient noise of NEA2 during the winter. The sample rate for both data sets is hourly. (a) Time series comparison of wind speed and horizontal-component seismic noise at 30 s. (b) Scatter plot of the two time series in (a). The red triangles are the median power for each wind speed and the squares are variation at 1 MAD. The first correlation is for all available data. The second correlation excludes all wind speed measurements at 0 m/s. (c)-(d) Same as (a)-(b), but for the vertical component of seismic noise.

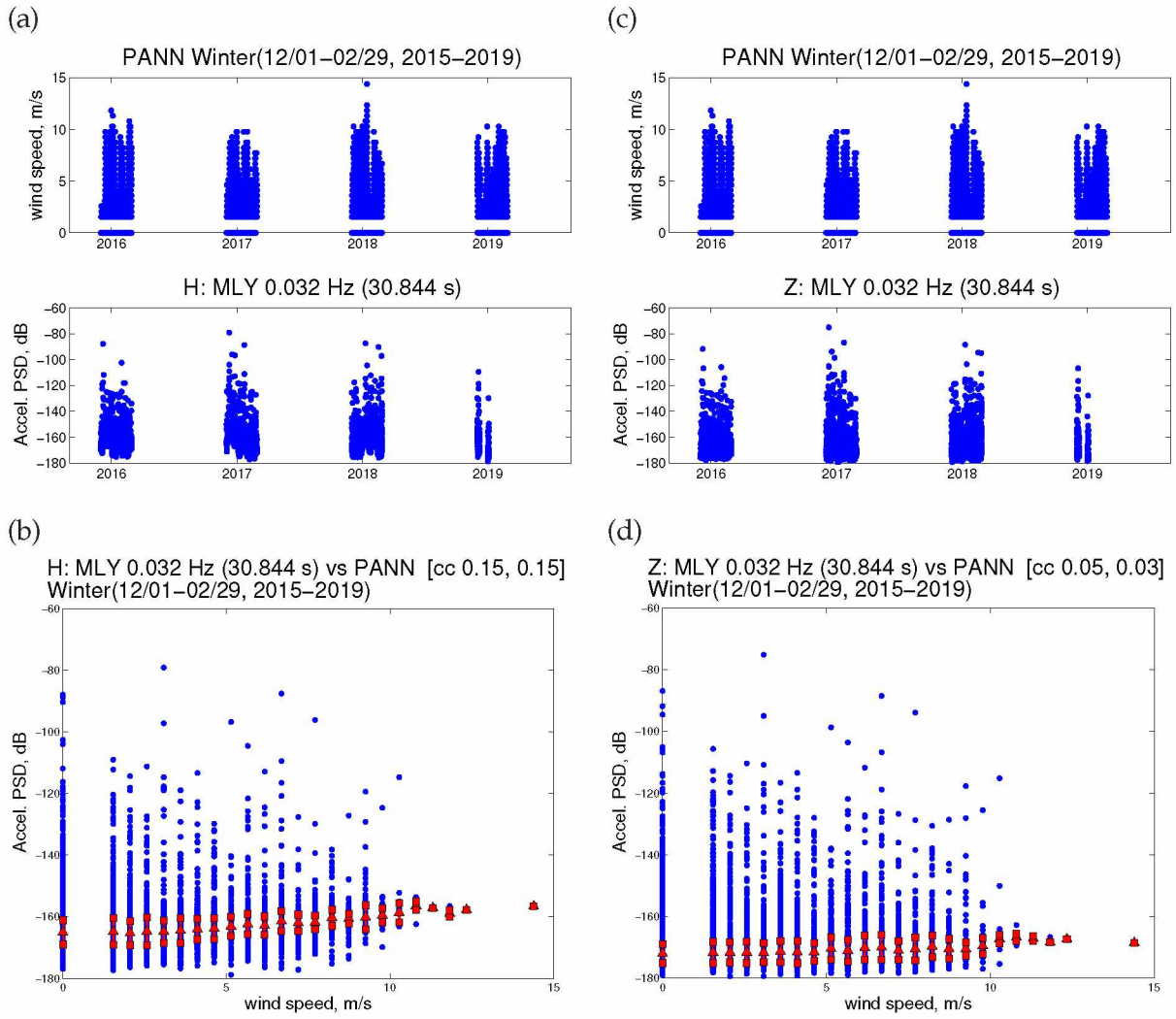

Figure A.62: Scatter plot and time series of wind speed at PANN and 30 s ambient noise of MLY during the winter. The sample rate for both data sets is hourly. (a) Time series comparison of wind speed and horizontal-component seismic noise at 30 s. (b) Scatter plot of the two time series in (a). The red triangles are the median power for each wind speed and the squares are variation at 1 MAD. The first correlation is for all available data. The second correlation excludes all wind speed measurements at 0 m/s. (c)-(d) Same as (a)-(b), but for the vertical component of seismic noise.

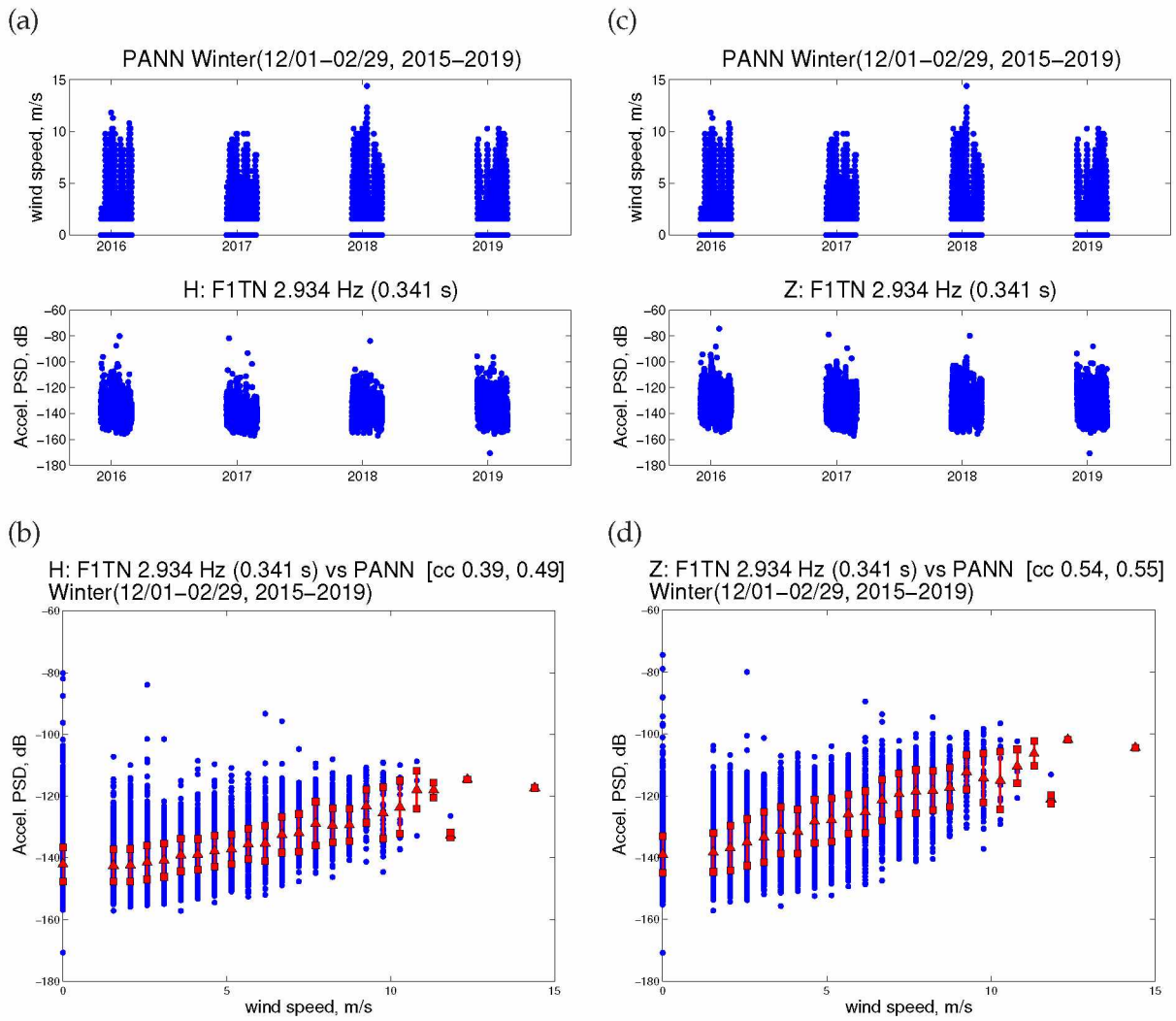

Figure A.63: Scatter plot and time series of wind speed at PANN and 3 Hz ambient noise of F1TN during the winter. The sample rate for both data sets is hourly. (a) Time series comparison of wind speed and horizontal-component seismic noise at 3 Hz. (b) Scatter plot of the two time series in (a). The red triangles are the median power for each wind speed and the squares are variation at 1 MAD. The first correlation is for all available data. The second correlation excludes all wind speed measurements at 0 m/s. (c)-(d) Same as (a)-(b), but for the vertical component of seismic noise.

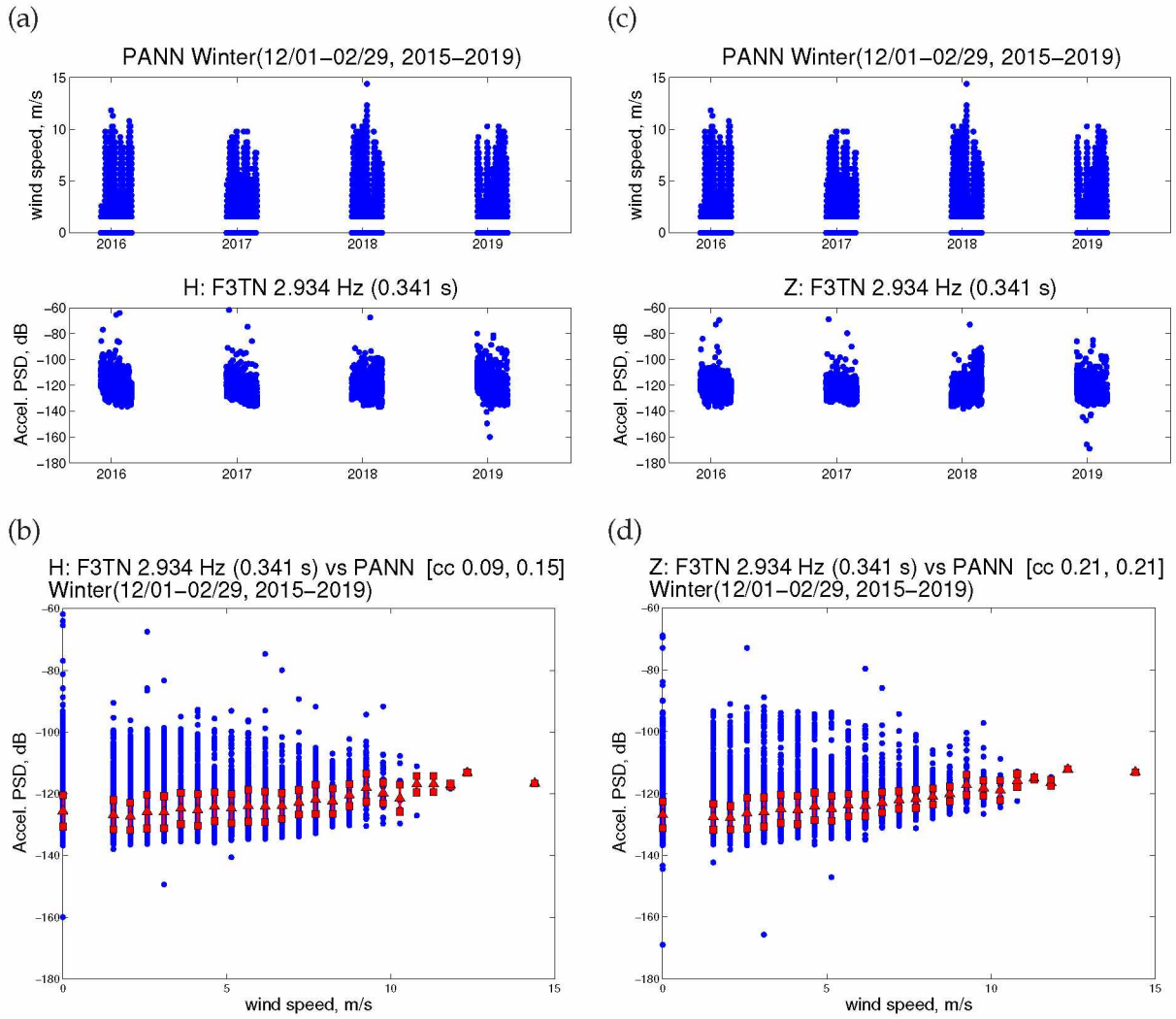

Figure A.64: Scatter plot and time series of wind speed at PANN and 3 Hz ambient noise of F3TN during the winter. The sample rate for both data sets is hourly. (a) Time series comparison of wind speed and horizontal-component seismic noise at 3 Hz. (b) Scatter plot of the two time series in (a). The red triangles are the median power for each wind speed and the squares are variation at 1 MAD. The first correlation is for all available data. The second correlation excludes all wind speed measurements at 0 m/s. (c)-(d) Same as (a)-(b), but for the vertical component of seismic noise.

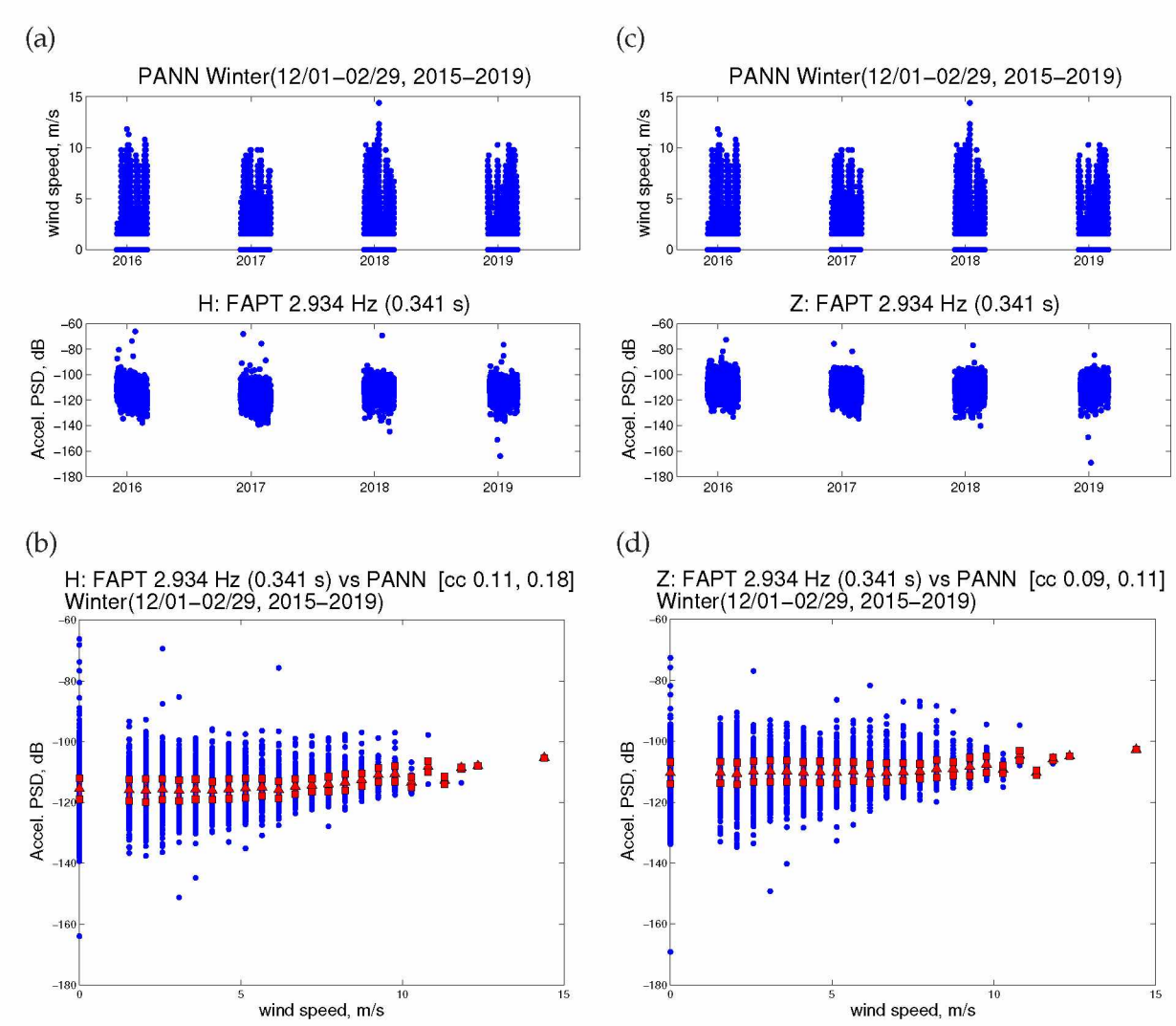

Figure A.65: Scatter plot and time series of wind speed at PANN and 3 Hz ambient noise of FAPT during the winter. The sample rate for both data sets is hourly. (a) Time series comparison of wind speed and horizontal-component seismic noise at 3 Hz. (b) Scatter plot of the two time series in (a). The red triangles are the median power for each wind speed and the squares are variation at 1 MAD. The first correlation is for all available data. The second correlation excludes all wind speed measurements at 0 m/s. (c)-(d) Same as (a)-(b), but for the vertical component of seismic noise.

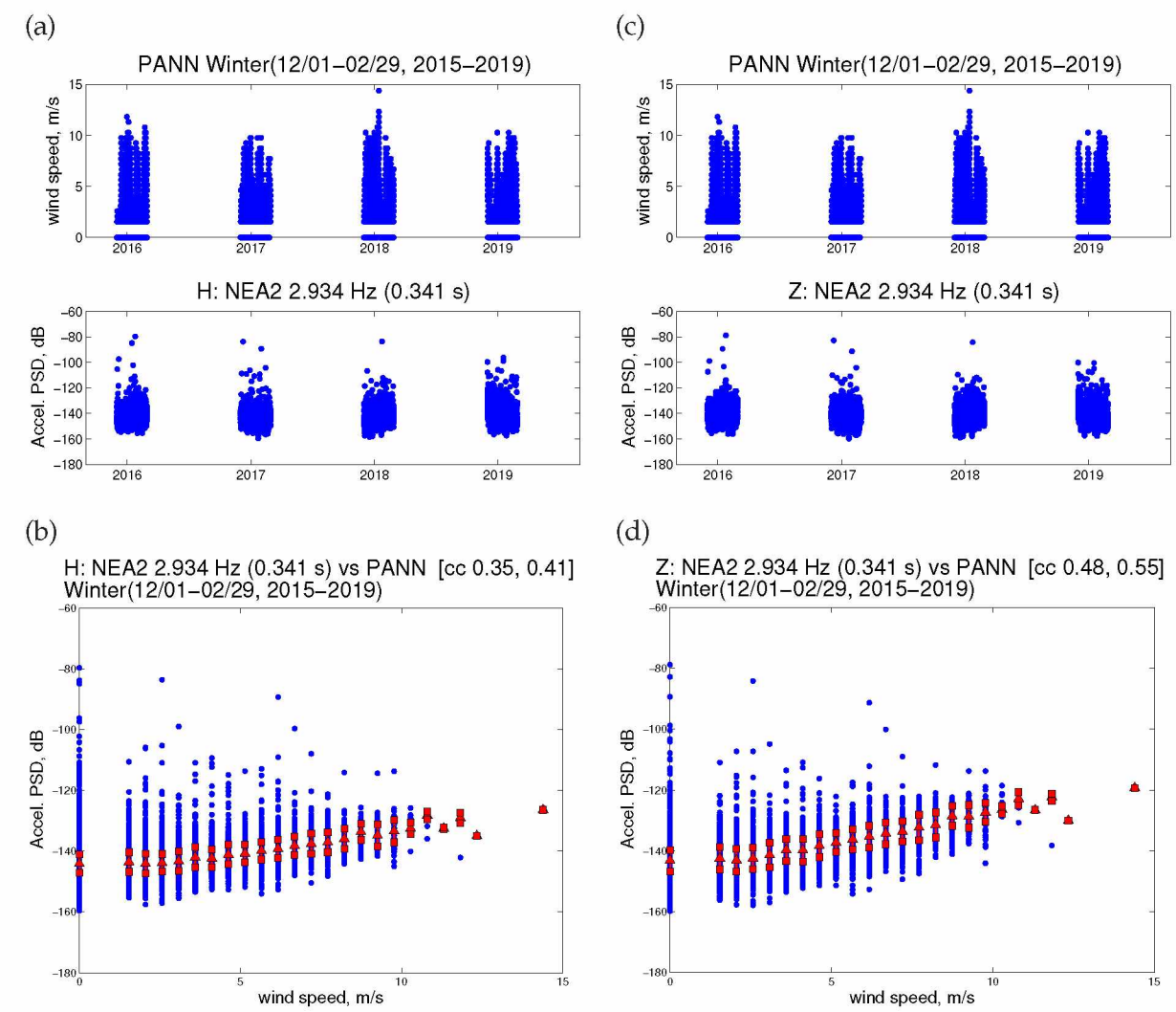

Figure A.66: Scatter plot and time series of wind speed at PANN and 3 Hz ambient noise of NEA2 during the winter. The sample rate for both data sets is hourly. (a) Time series comparison of wind speed and horizontal-component seismic noise at 3 Hz. (b) Scatter plot of the two time series in (a). The red triangles are the median power for each wind speed and the squares are variation at 1 MAD. The first correlation is for all available data. The second correlation excludes all wind speed measurements at 0 m/s. (c)-(d) Same as (a)-(b), but for the vertical component of seismic noise.

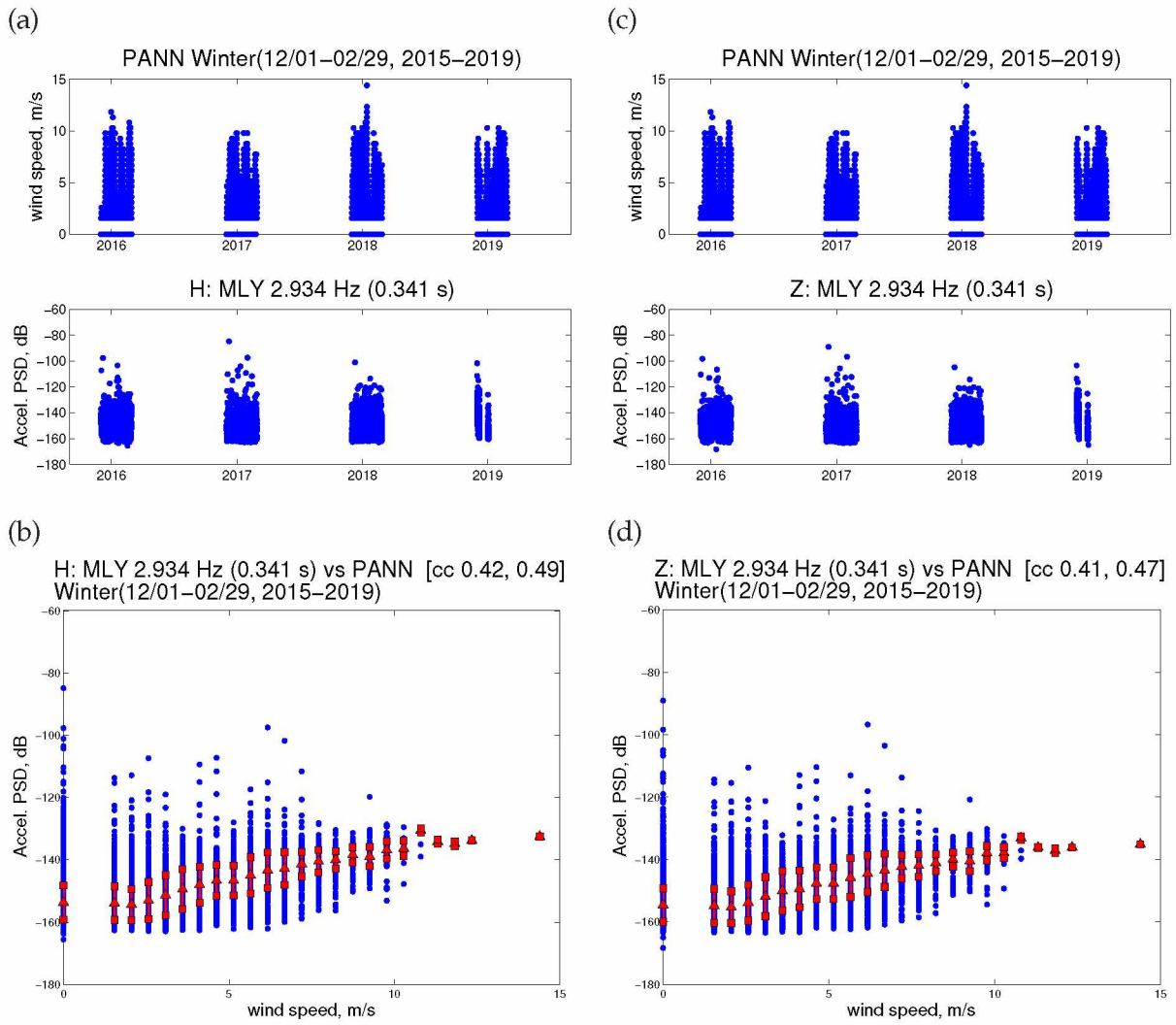

Figure A.67: Scatter plot and time series of wind speed at PANN and 3 Hz ambient noise of MLY during the winter. The sample rate for both data sets is hourly. (a) Time series comparison of wind speed and horizontal-component seismic noise at 3 Hz. (b) Scatter plot of the two time series in (a). The red triangles are the median power for each wind speed and the squares are variation at 1 MAD. The first correlation is for all available data. The second correlation excludes all wind speed measurements at 0 m/s. (c)-(d) Same as (a)-(b), but for the vertical component of seismic noise.

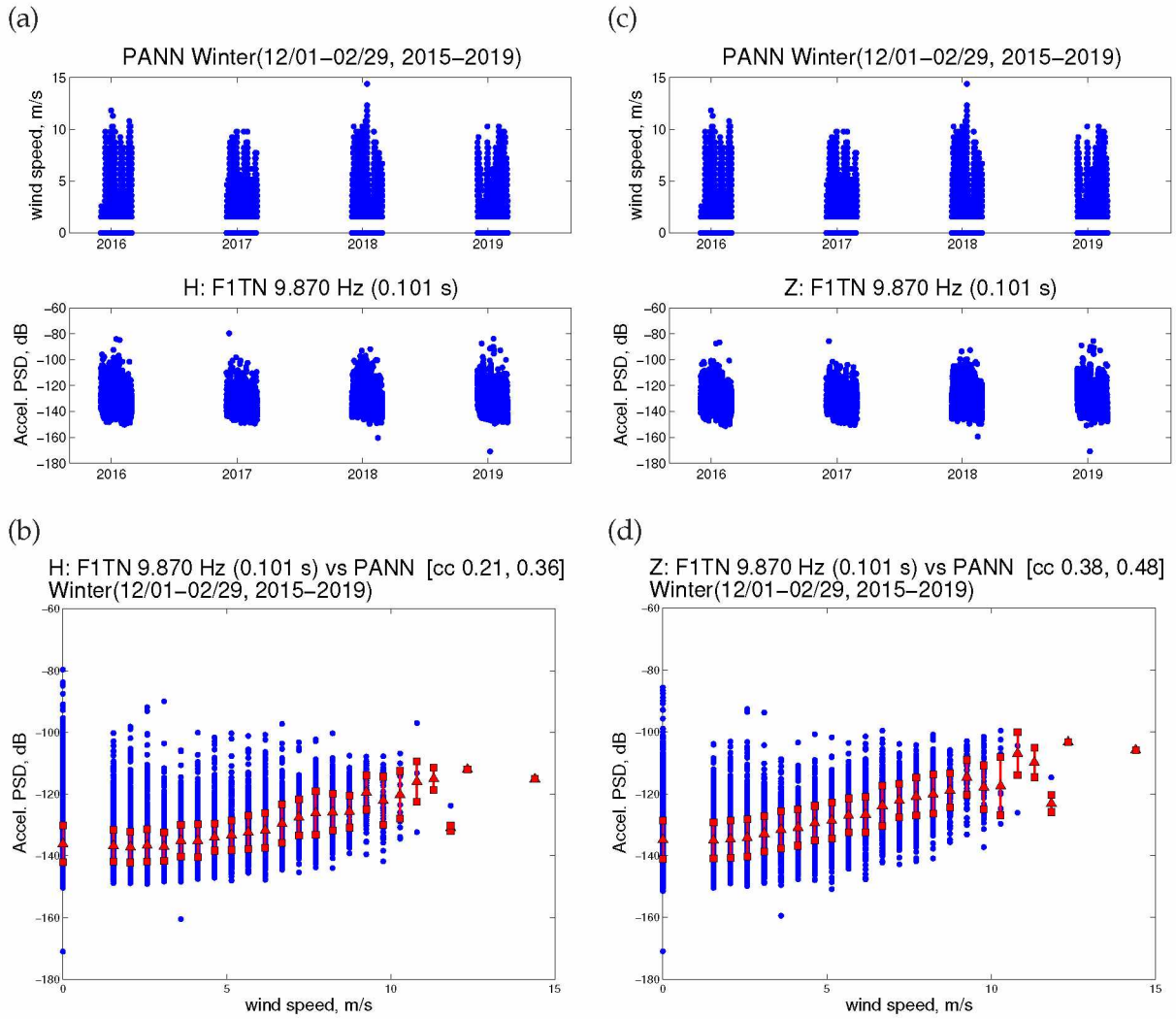

Figure A.68: Scatter plot and time series of wind speed at PANN and 10 Hz ambient noise of F1TN during the winter. The sample rate for both data sets is hourly. (a) Time series comparison of wind speed and horizontal-component seismic noise at 10 Hz. (b) Scatter plot of the two time series in (a). The red triangles are the median power for each wind speed and the squares are variation at 1 MAD. The first correlation is for all available data. The second correlation excludes all wind speed measurements at 0 m/s. (c)-(d) Same as (a)-(b), but for the vertical component of seismic noise.

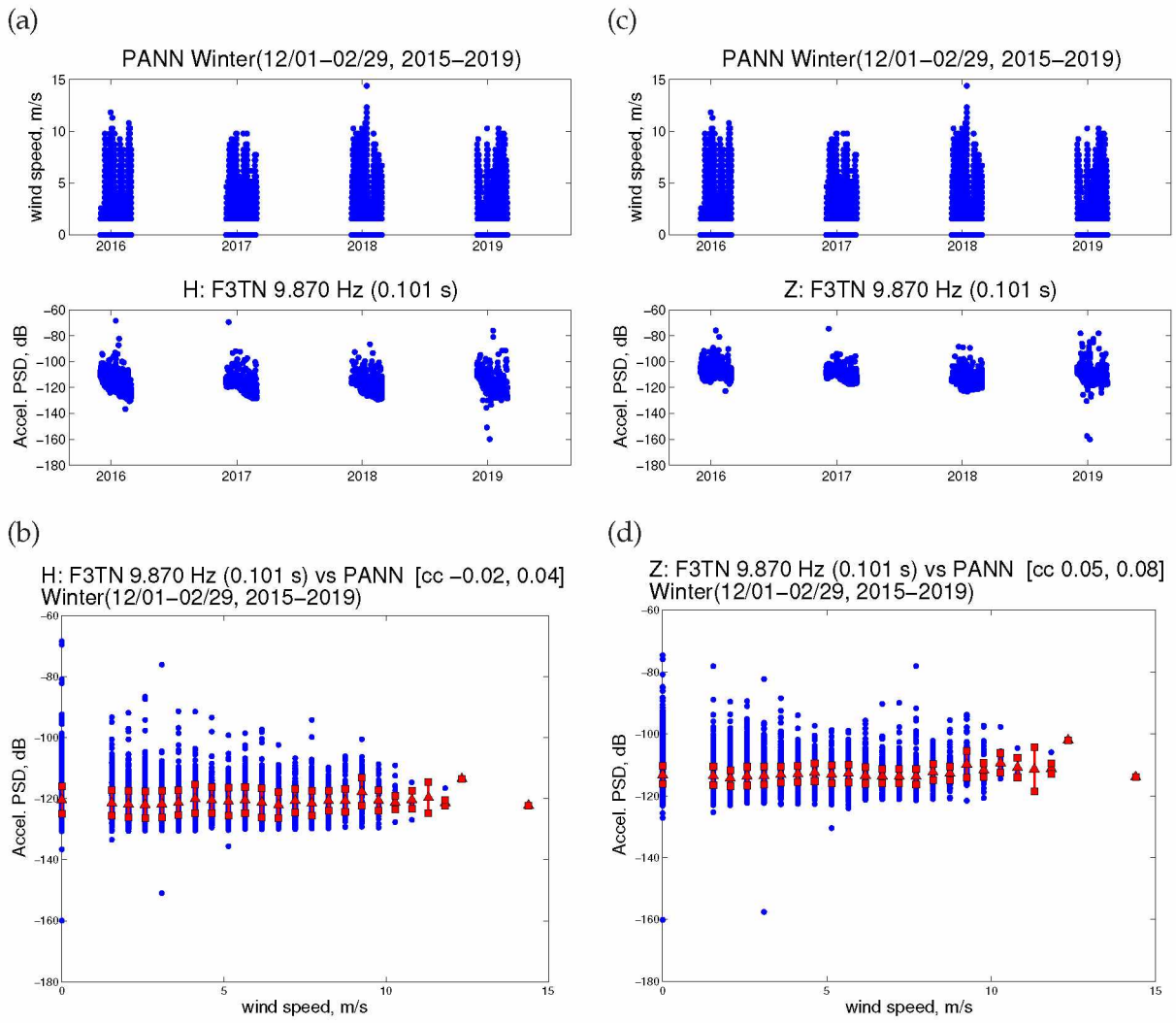

Figure A.69: Scatter plot and time series of wind speed at PANN and 10 Hz ambient noise of F3TN during the winter. The sample rate for both data sets is hourly. (a) Time series comparison of wind speed and horizontal-component seismic noise at 10 Hz. (b) Scatter plot of the two time series in (a). The red triangles are the median power for each wind speed and the squares are variation at 1 MAD. The first correlation is for all available data. The second correlation excludes all wind speed measurements at 0 m/s. (c)-(d) Same as (a)-(b), but for the vertical component of seismic noise.

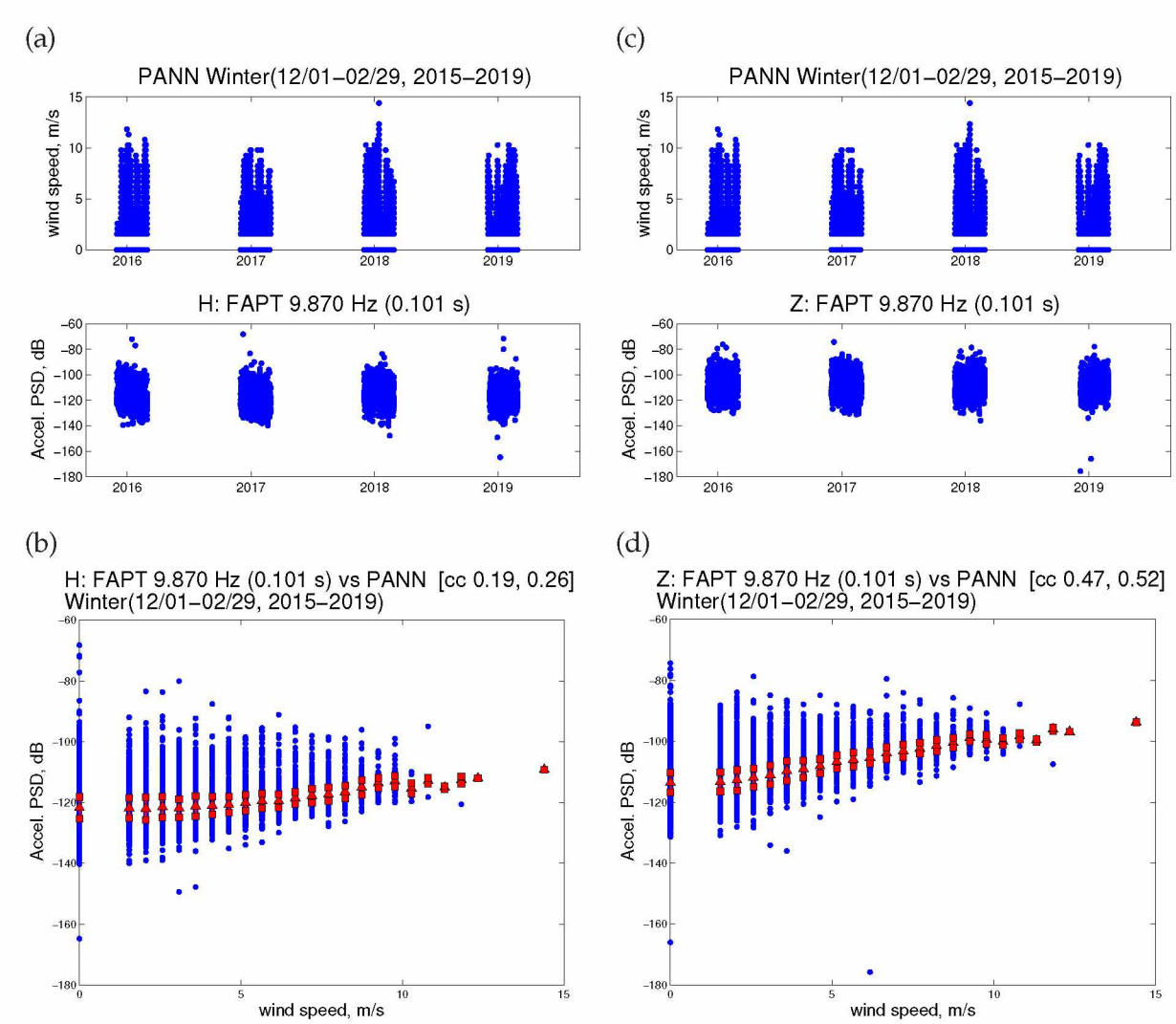

Figure A.70: Scatter plot and time series of wind speed at PANN and 10 Hz ambient noise of FAPT during the winter. The sample rate for both data sets is hourly. (a) Time series comparison of wind speed and horizontal-component seismic noise at 10 Hz. (b) Scatter plot of the two time series in (a). The red triangles are the median power for each wind speed and the squares are variation at 1 MAD. The first correlation is for all available data. The second correlation excludes all wind speed measurements at 0 m/s. (c)-(d) Same as (a)-(b), but for the vertical component of seismic noise.

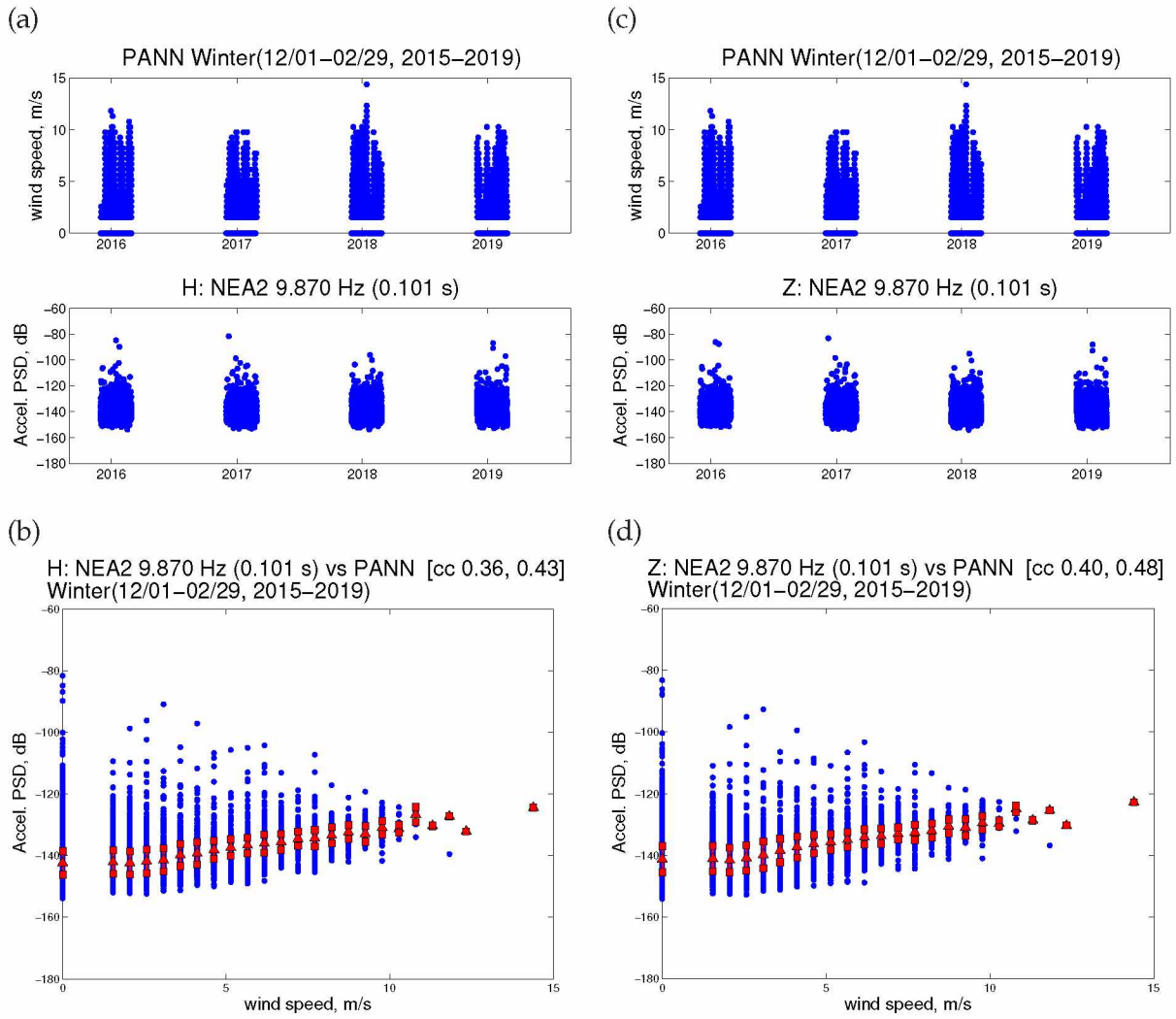

Figure A.71: Scatter plot and time series of wind speed at PANN and 10 Hz ambient noise of NEA2 during the winter. The sample rate for both data sets is hourly. (a) Time series comparison of wind speed and horizontal-component seismic noise at 10 Hz. (b) Scatter plot of the two time series in (a). The red triangles are the median power for each wind speed and the squares are variation at 1 MAD. The first correlation is for all available data. The second correlation excludes all wind speed measurements at 0 m/s. (c)-(d) Same as (a)-(b), but for the vertical component of seismic noise.

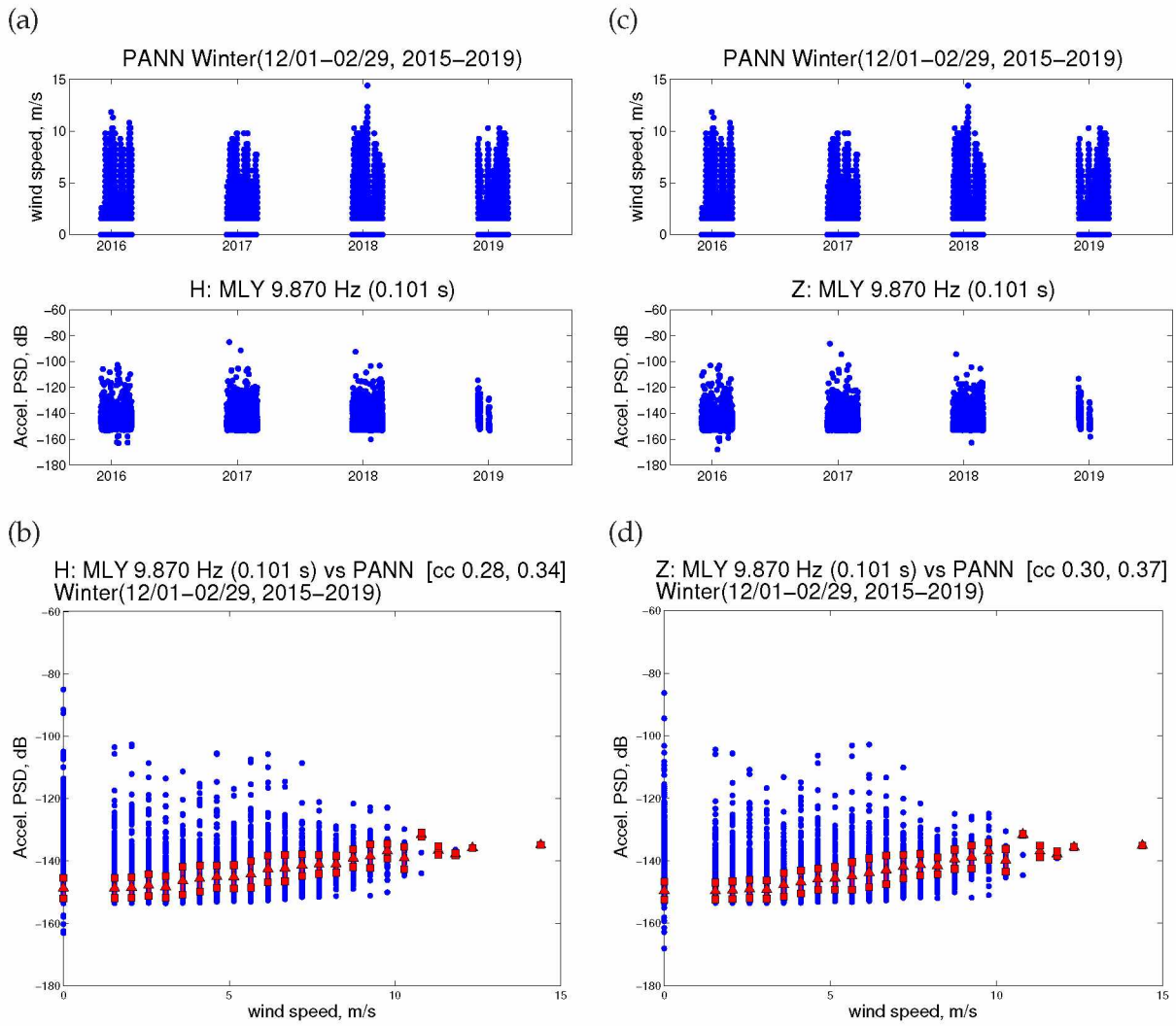

Figure A.72: Scatter plot and time series of wind speed at PANN and 10 Hz ambient noise of MLY during the winter. The sample rate for both data sets is hourly. (a) Time series comparison of wind speed and horizontal-component seismic noise at 10 Hz. (b) Scatter plot of the two time series in (a). The red triangles are the median power for each wind speed and the squares are variation at 1 MAD. The first correlation is for all available data. The second correlation excludes all wind speed measurements at 0 m/s. (c)-(d) Same as (a)-(b), but for the vertical component of seismic noise.

(a)

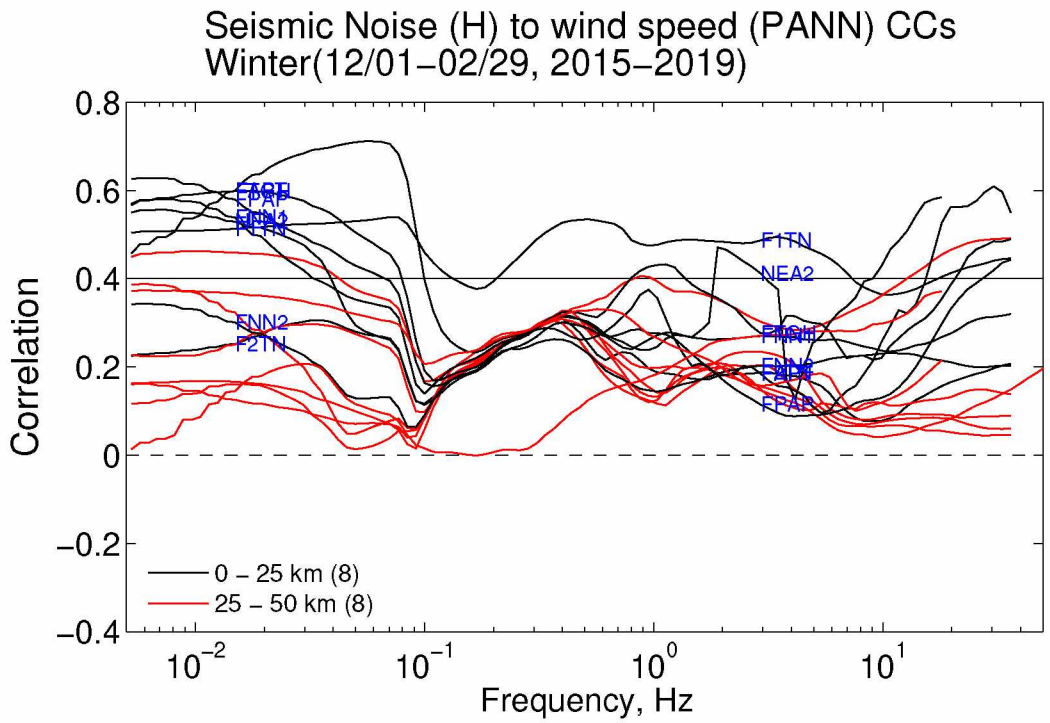

(b)

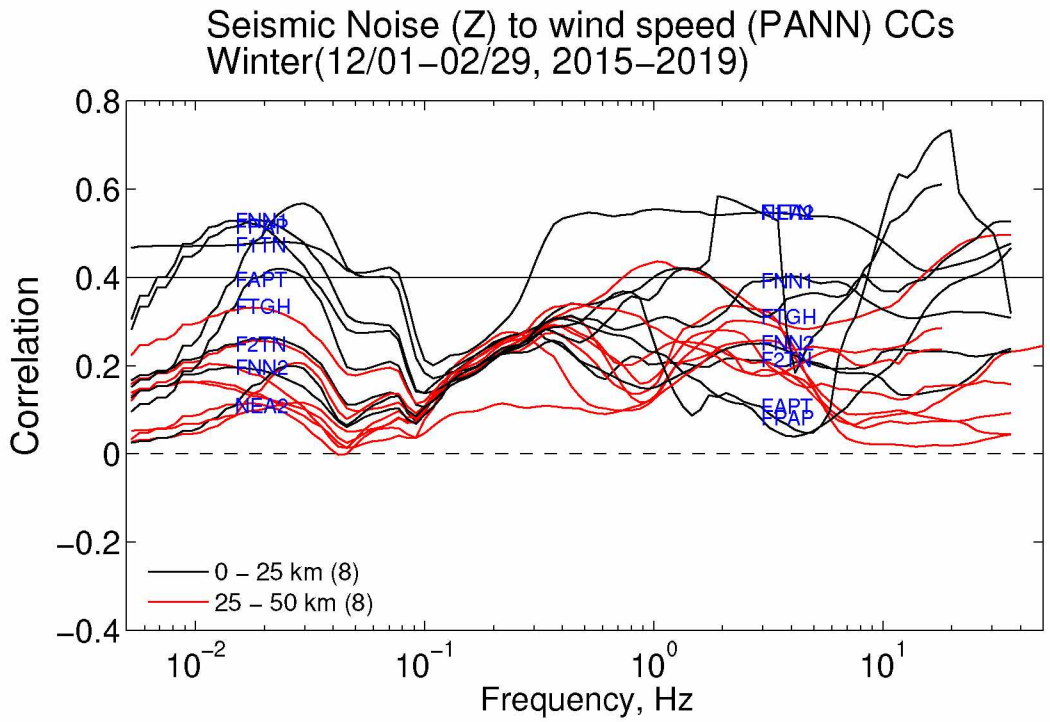

Figure A.73: Correlations of hourly non-zero winter wind speed to seismic noise across all frequencies. Curves for 16 seismic stations are colored black (0–25 km) or red (25–50 km), according to the station's distance from weather station PANN, in Nenana. Higher correlations at frequencies 0.01–0.03 Hz are evident at stations closer to PANN. The horizontal line is shown as a reference correlation of 0.4.

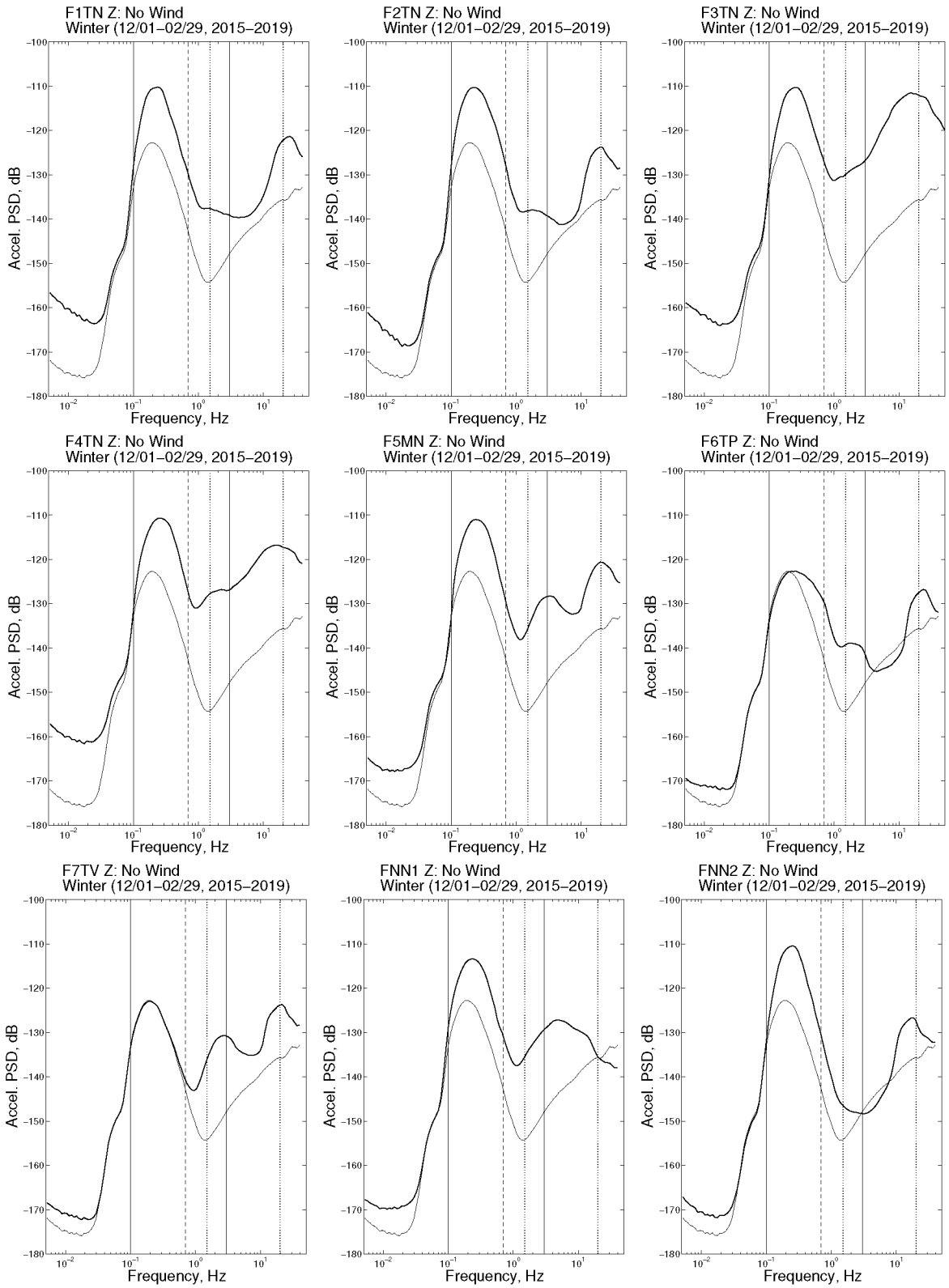

Figure A.74: Ambient noise spectra for winter (Dec/Jan/Feb) and without wind. The unbolded line is F8KN (for the same time period), which is used as a non-basin reference spectrum.

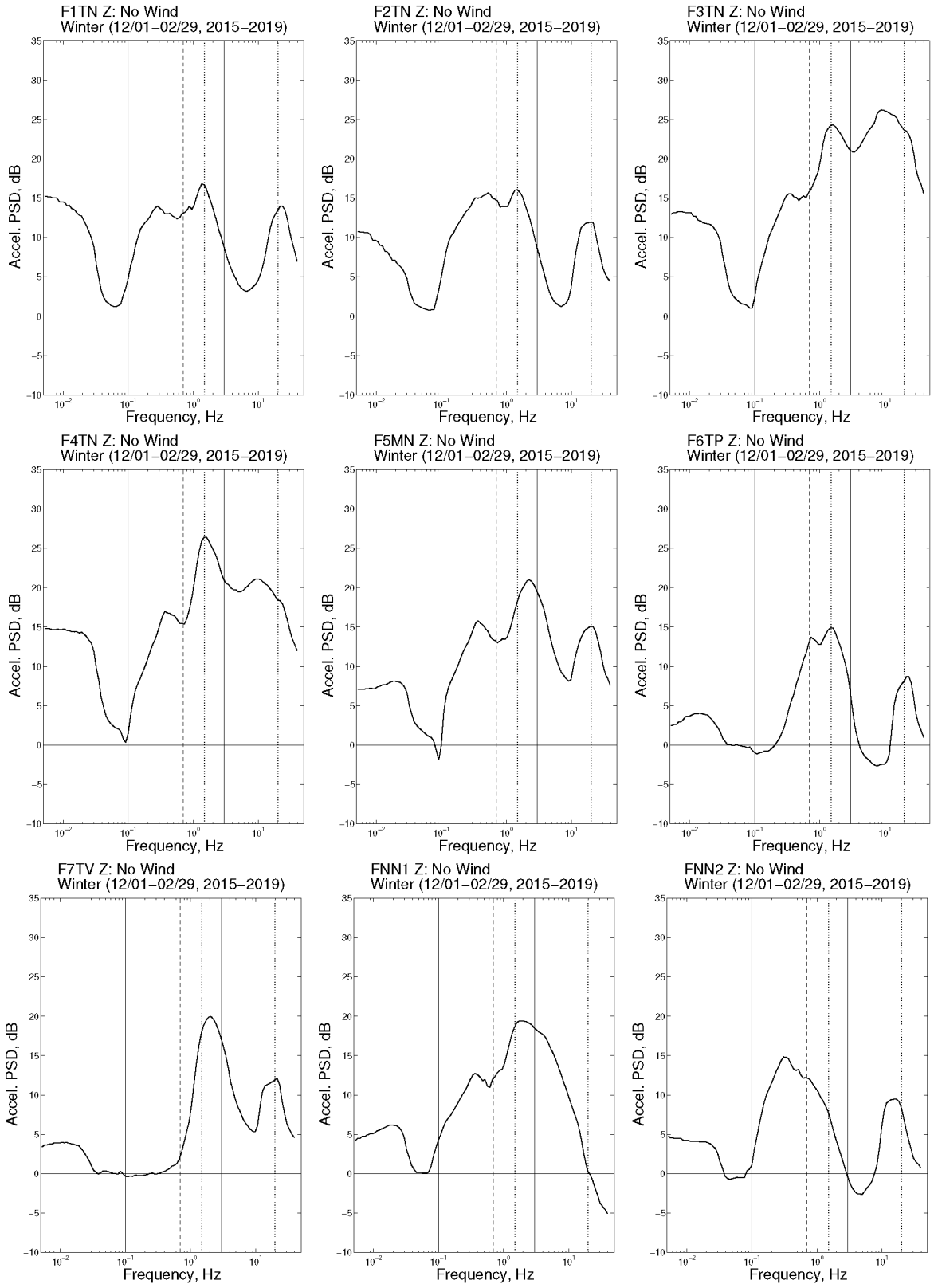

Figure A.75: Spectra in Figure A.74 minus the F8KN reference spectrum.

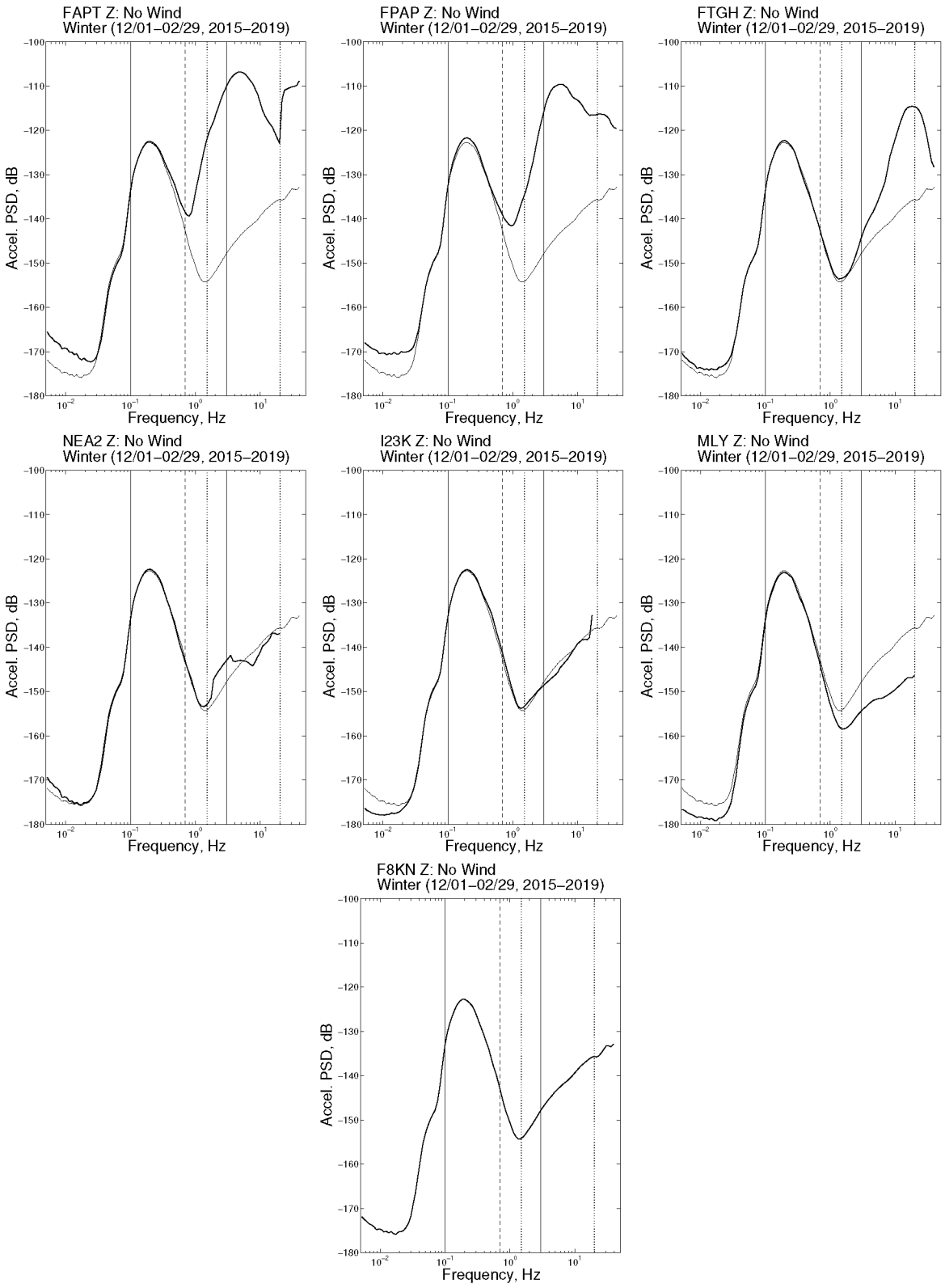

Figure A.76: Ambient noise spectra for winter (Dec/Jan/Feb) and without wind. The unbolded line is F8KN.

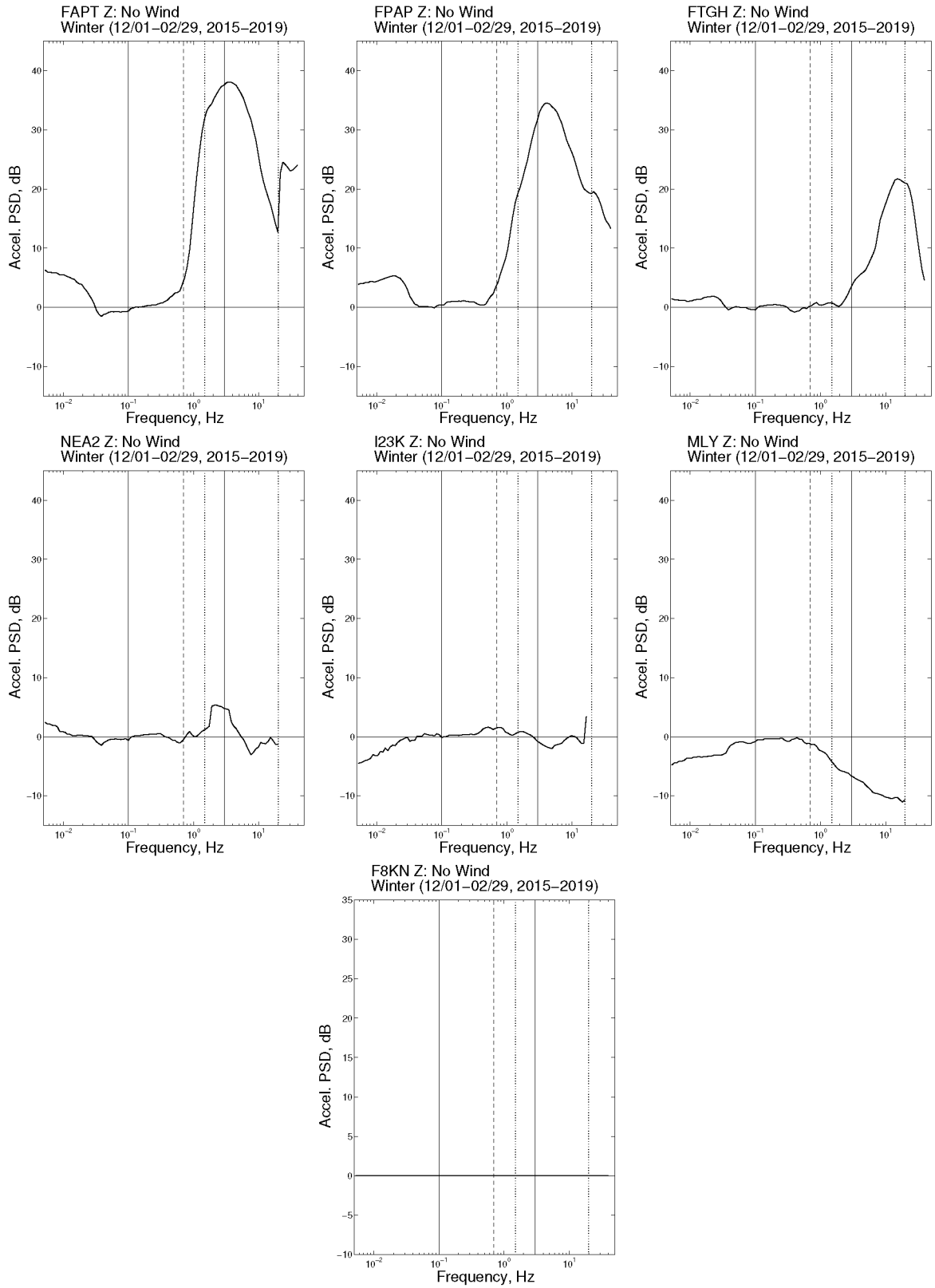

Figure A.77: Spectra in Figure A.76 minus the F8KN reference spectrum. The patterns shown are attributed to cultural noise (FAPT, FPAP, FTGH) and a lattice tower at NEA2. The negative values at MLY show that it has overall lower noise levels than at F8KN.

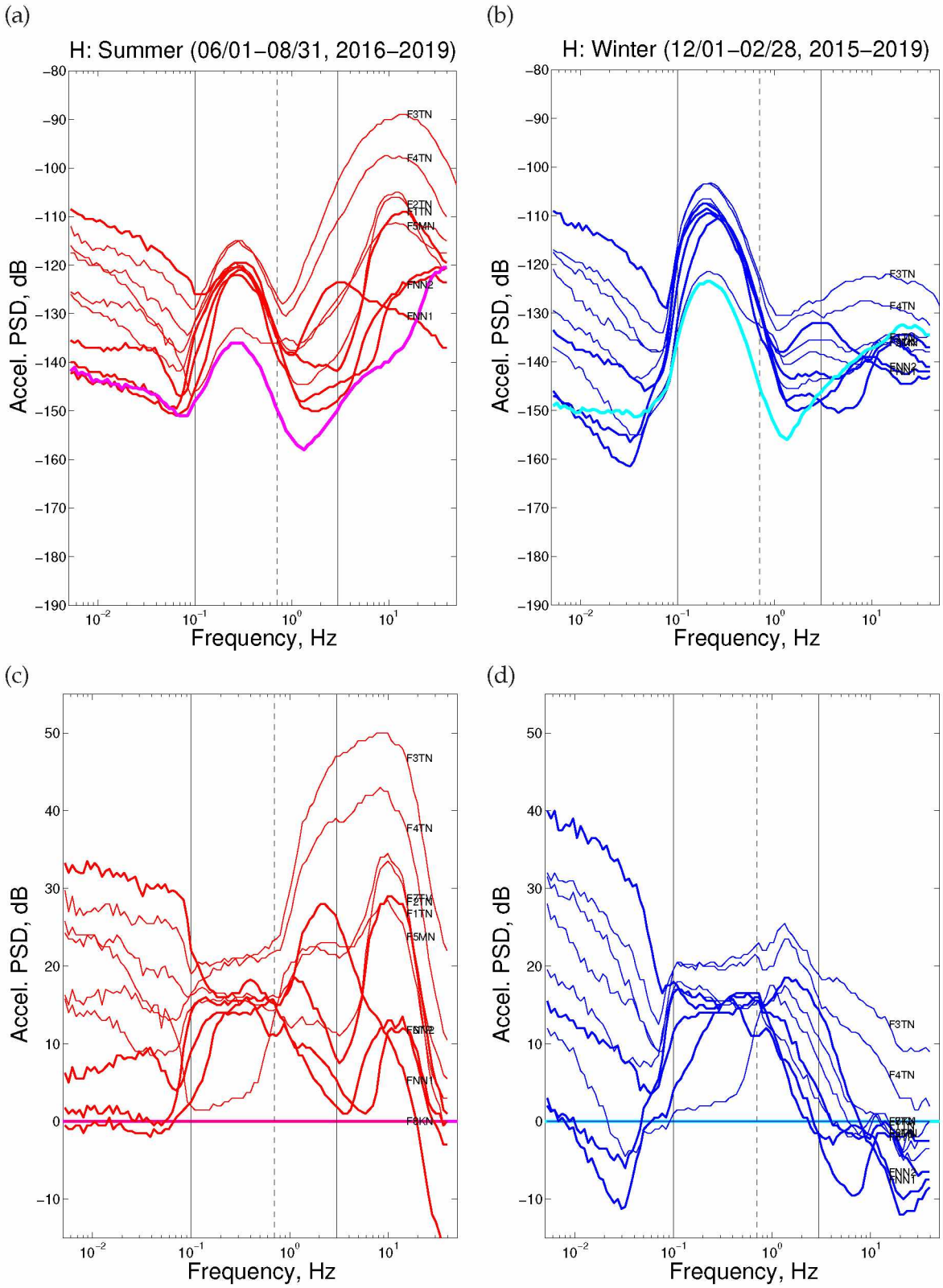

Figure A.78: Same as Figure 2.14 but for the horizontal component.

Event detection in MFFZ (and relationship to noise levels)

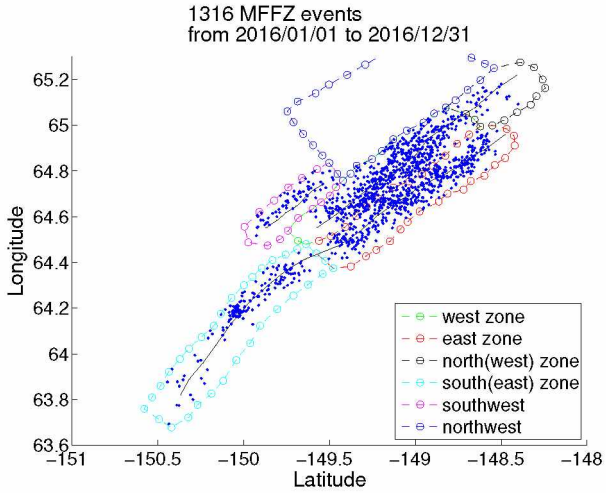

Figure A.79: Seismicity in subregions of the Minto Flats fault zone near Nenana, Alaska (e.g., Tape et al., 2015). The seismicity from 2016 and includes all events from the Alaska Earthquake Center Catalog.

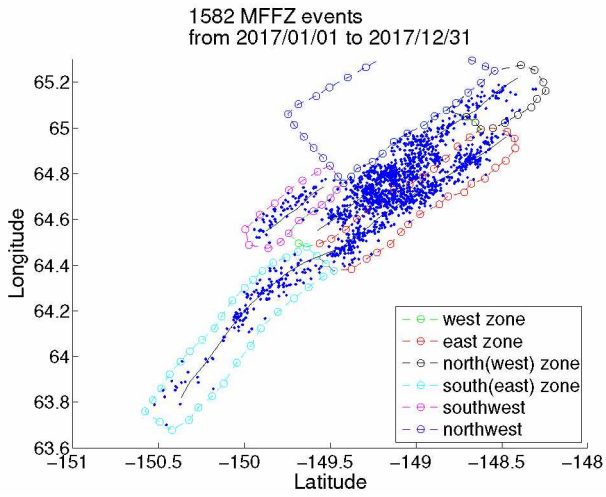

Figure A.80: Seismicity in subregions of the Minto Flats fault zone near Nenana, Alaska (e.g., Tape et al., 2015). The seismicity from 2017 and includes all events from the Alaska Earthquake Center Catalog.

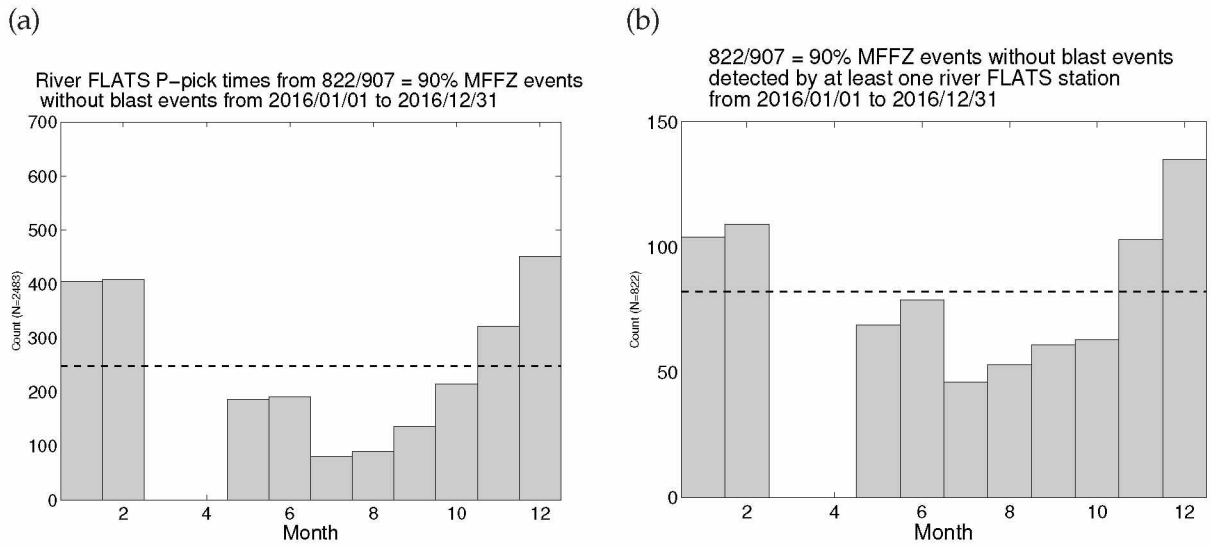

Figure A.81: (a) Histogram of all P-picks from FLATS seismometers <100 m from the main channel of the Tanana River (F2TN, F3TN, F4TN, F5MN, F7TV). The P-picks were selected from events in Figure A.79. Events in March and April are excluded for 2016. Collectively, the FLATS stations detect do not detected all events in MFFZ and there exists a seasonal bias of P-picks that propagate into the catalog. The horizontal dashed line is the mean. (b) Histogram of all events in MFFZ detected by at least one FLATS seismometer close to the main river channel (F2TN, F3TN, F4TN, F5MN, F7TV) in 2016. The horizontal dashed line is the mean.

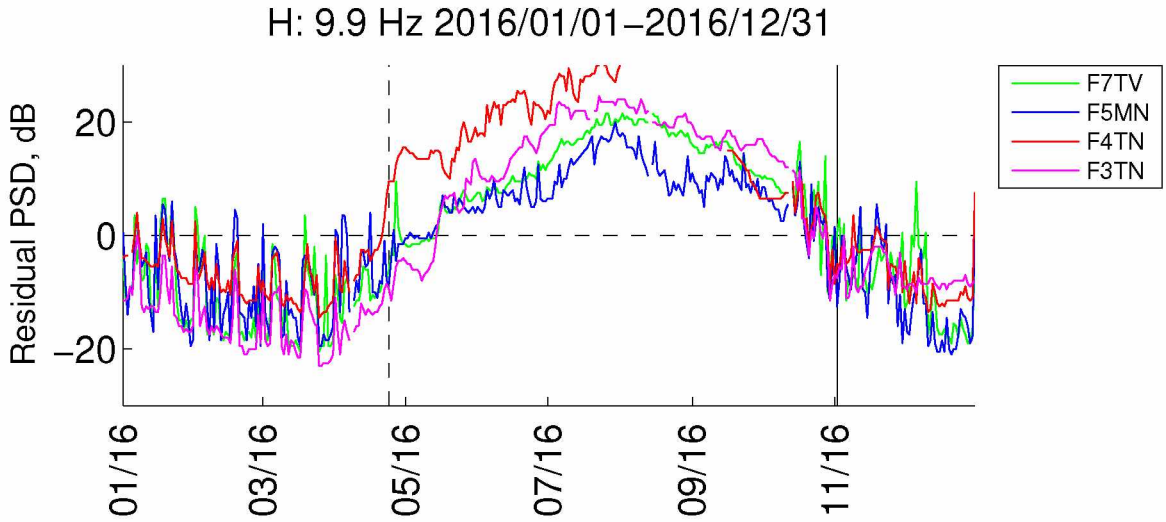

Figure A.82: Time series of 10 Hz noise at all stations near the main river channel (Table 2.1) except F2TN. F2TN was excluded because it has frequently moved its location but it is still considered for P-picks. The vertical solid lines are dates of river freezeup observed at F3TN. The vertical dashed lines are ice breakup in Nenana marked by the tipping of the Nenana Ice Classic tripod.

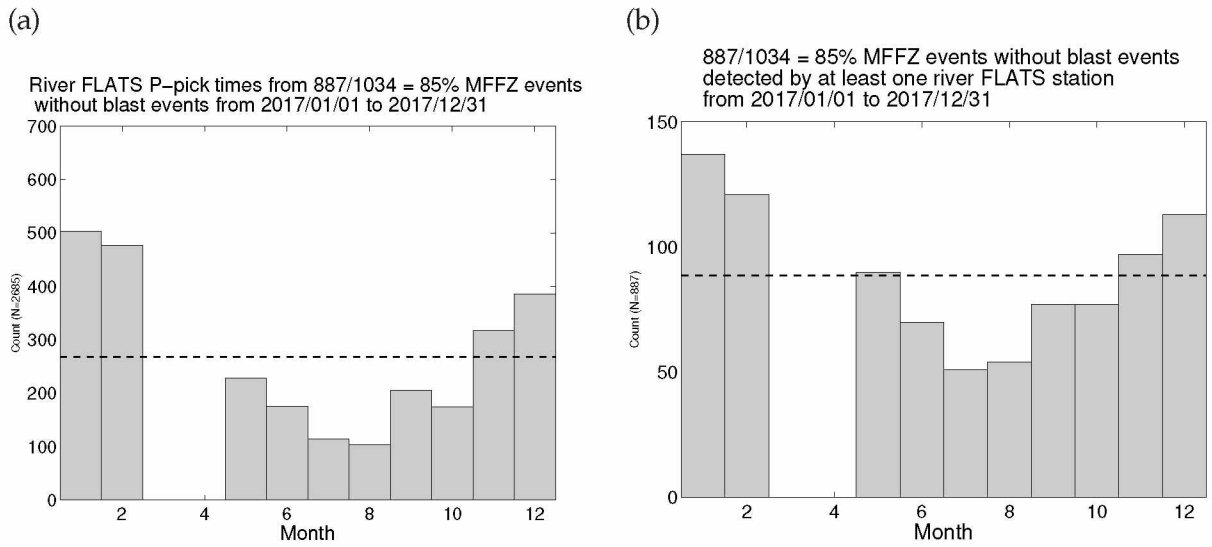

Figure A.83: (a) Histogram of all P-picks from FLATS seismometers <100 m from the main channel of the Tanana River (F2TN, F3TN, F4TN, F5MN, F7TV). The P-picks were selected from events in Figure A.80. Events in March and April are excluded for 2017. Collectively, the FLATS stations detect do not detected all events in MFFZ and there exists a seasonal bias of P-picks that propagate into the catalog. The horizontal dashed line is the mean. (b) Histogram of all events in MFFZ detected by at least one FLATS seismometer close to the main river channel (F2TN, F3TN, F4TN, F5MN, F7TV) in 2017. The horizontal dashed line is the mean.

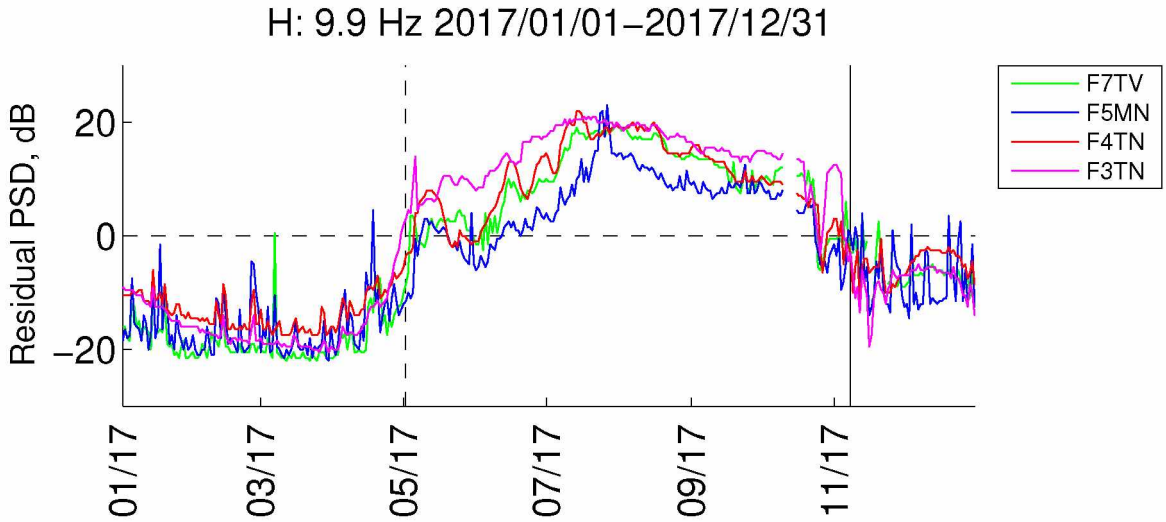

Figure A.84: Time series of 10 Hz noise at all stations near the main river channel (Table 2.1) except F2TN. F2TN was excluded because it has frequently moved its location but it is still considered for P-picks. The vertical solid lines are dates of river freezeup observed at F3TN. The vertical dashed lines are ice breakup in Nenana marked by the tipping of the Nenana Ice Classic tripod.

A.6 References

Gutenberg, B., 1951. Observations and theory of microseisms, in *Compendium of Meterology*, pp.

1303–1311, ed. Malone, T. S., American Meteorological Society, Boston, Mass.

Gutenberg, B., 1958. Microseisms, *Advances in Geophysics*, **5**, 53–92.

Peterson, J., 1993. Observations and Modeling of Seismic Background Noise, Open-File Report 93-322.

Tape, C., Silwal, V., Ji, C., Keyson, L., West, M. E., & Ruppert, N., 2015. Transtensional tectonics of the Minto Flats fault zone and Nenana basin, central Alaska, *Bull. Seismol. Soc. Am.*, **105**(4), 2081–2100, doi: 10.1785/0120150055.

USGS, 2016. National Water Information System data available on the World Wide Web (USGS Water Data for the Nation), accessed [June 1, 2019], at https://waterdata.usgs.gov/ak/nwis/uv?site_no=15515500.

Appendix B

Supporting Information for Chapter 3 (Seismic response of Cook Inlet sedimentary basin, southern Alaska)

B.1 Tables

Table B.1: Comparison of three different quantities representing amplitude ratios of seismograms: power ratio x in dB, power ratio P, amplitude ratio A, and log-scaled amplitude ratio $\ln A$. Let $A_1(f)$ and $A_2(f)$ be the spectral amplitudes at a target and reference station, respectively. If $A_2 = 1$ m/s^2, then $P_2 = 1$ (m/s^2)^2, and the dB value can be thought of in the traditional usage (e.g., McNamara & Buland, 2004), in absolute terms. In our case, A_2 is the acceleration for a particular reference station, and the dB value can be thought of as a relative measure between two stations. The relationship between x and P are $x = 10\log_{10} P$ and $P = 10^{x/10}$.

x, dB	$P = P_1(f)/P_2(f)$	$A = A_1(f)/A_2(f)$	$\ln A$
50	100000.00000	316.22777	5.76
45	31622.77660	177.82794	5.18
40	10000.00000	100.00000	4.61
35	3162.27766	56.23413	4.03
30	1000.00000	31.62278	3.45
25	316.22777	17.78279	2.88
20	100.00000	10.00000	2.30
15	31.62278	5.62341	1.73
10	10.00000	3.16228	1.15
5	3.16228	1.77828	0.58
0	1.00000	1.00000	0.00
-5	0.31623	0.56234	-0.58
-10	0.10000	0.31623	-1.15
-15	0.03162	0.17783	-1.73
-20	0.01000	0.10000	-2.30
-25	0.00316	0.05623	-2.88
-30	0.00100	0.03162	-3.45
-35	0.00032	0.01778	-4.03
-40	0.00010	0.01000	-4.61
-45	0.00003	0.00562	-5.18
-50	0.00001	0.00316	-5.76
0.00	1	1	0.00
6.02	4	2	0.69
9.54	9	3	1.10
12.04	16	4	1.39
13.98	25	5	1.61
15.56	36	6	1.79
16.90	49	7	1.95
18.06	64	8	2.08
19.08	81	9	2.20
20.00	100	10	2.30

Table B.2: Summary of spectral ratios for 45 stations for 34 earthquakes. Spectral ratios are graphically displayed with respect to basin depth values in Figure 3.14 and Figure B.10. Spectral ratios are calculated for two frequency ranges: 0.1–0.5 Hz (lf) and 0.5–4.0 Hz (hf). If N19K is unavailable as a reference station, then we use WFLW or SLK. If SSN is unavailable as a reference station, then we use SKN or SLK. If SLK is unavailable as a reference station, then we use BRSE. Stations are ordered according to Figure 3.2. The horizontal double bars separates basin stations from other stations.

station	reference station	recorded events	Zlf ± MAD	Rlf ± MAD	Tlf ± MAD	Zhf ± MAD	Rhf ± MAD	Thf ± MAD
CAPN	SLK	34	13.25 ± 2.45	17.60 ± 2.00	15.10 ± 1.80	12.05 ± 2.80	17.05 ± 2.80	14.85 ± 3.15
NSKI	SLK	32	12.20 ± 1.95	16.80 ± 1.90	13.40 ± 3.10	8.90 ± 2.30	13.20 ± 3.10	10.75 ± 3.30
LTUY	SLK	30	11.60 ± 1.70	14.95 ± 2.00	11.10 ± 2.90	8.15 ± 2.60	10.15 ± 4.10	7.65 ± 3.30
SOLD	SLK	32	10.70 ± 1.80	13.10 ± 2.90	12.55 ± 2.40	8.00 ± 3.25	12.40 ± 2.75	9.85 ± 4.55
WHIP	SLK	31	12.70 ± 0.80	15.60 ± 2.30	14.10 ± 2.40	8.10 ± 2.40	11.20 ± 3.20	9.40 ± 2.70
BULG	SSN	21	9.55 ± 2.95	12.30 ± 3.00	9.20 ± 3.05	9.10 ± 3.40	12.00 ± 3.50	11.90 ± 3.20
CLAM	SLK	32	9.50 ± 2.30	11.05 ± 3.05	8.45 ± 2.65	6.15 ± 3.40	10.85 ± 2.80	7.75 ± 3.40
KALN	N19K	32	10.70 ± 1.55	15.80 ± 2.65	13.85 ± 3.15	15.75 ± 2.35	21.20 ± 2.85	20.90 ± 3.25
BING	SLK	34	9.70 ± 1.10	14.00 ± 1.40	11.20 ± 1.30	7.00 ± 2.10	10.35 ± 2.40	7.55 ± 2.50
NNIL	SLK	32	7.20 ± 3.10	9.60 ± 4.15	7.30 ± 3.00	2.10 ± 6.15	5.40 ± 5.55	2.85 ± 6.45
SALA	SSN	15	8.40 ± 1.10	12.30 ± 2.60	8.50 ± 3.30	7.20 ± 5.90	13.20 ± 6.10	10.70 ± 5.30
MPEN	SLK	31	12.00 ± 2.10	14.75 ± 1.80	11.65 ± 2.55	9.60 ± 1.90	11.60 ± 2.70	10.30 ± 1.40
KALS	N19K	30	12.15 ± 3.90	14.55 ± 4.05	13.10 ± 4.50	17.60 ± 3.00	17.20 ± 2.90	17.00 ± 4.00
CONG	SSN	32	10.00 ± 2.80	11.45 ± 2.75	9.85 ± 3.00	6.50 ± 3.60	9.40 ± 3.85	8.95 ± 4.45
HOM	SLK	33	6.20 ± 2.50	10.05 ± 4.95	8.55 ± 5.65	3.00 ± 4.40	6.80 ± 7.60	5.80 ± 7.20
FIRE	SSN	34	9.70 ± 2.80	12.60 ± 2.35	11.90 ± 3.20	9.90 ± 2.60	9.20 ± 2.80	8.75 ± 4.10
LTUX	SLK	21	7.60 ± 2.65	13.45 ± 2.10	9.70 ± 1.50	7.80 ± 2.90	10.80 ± 3.20	8.70 ± 2.90
GOOS	SSN	32	6.40 ± 3.10	9.20 ± 3.80	10.80 ± 5.80	4.35 ± 3.25	7.15 ± 3.50	6.25 ± 2.70
O20K	N19K	32	6.30 ± 2.20	8.70 ± 3.60	9.00 ± 3.25	7.40 ± 2.10	12.35 ± 3.00	11.30 ± 3.25
P19K	N19K	25	5.00 ± 2.70	8.25 ± 3.10	4.40 ± 2.50	6.00 ± 2.70	12.10 ± 3.40	6.50 ± 2.80
PMR	SSN	32	-0.65 ± 4.20	-4.75 ± 2.85	-3.40 ± 4.20	-4.80 ± 3.85	-5.50 ± 4.30	-6.15 ± 3.95
RC01	SSN	34	-0.75 ± 2.90	-2.05 ± 4.65	-1.00 ± 4.60	1.90 ± 4.60	-0.30 ± 4.50	-0.15 ± 3.50
LTUW	SLK	16	0.90 ± 2.70	2.50 ± 1.90	0.40 ± 1.20	-1.45 ± 2.95	0.40 ± 2.25	-1.95 ± 3.65
BRLK	SLK	34	-0.40 ± 2.30	-1.20 ± 3.90	-2.45 ± 2.50	-4.50 ± 4.20	-5.10 ± 4.10	-7.00 ± 4.50
GHO	SSN	32	1.40 ± 4.75	-2.25 ± 3.55	-2.90 ± 5.60	-1.45 ± 3.95	1.00 ± 4.50	-0.30 ± 3.40
CNP	SLK	34	0.70 ± 4.20	0.30 ± 5.40	-0.80 ± 4.95	-5.50 ± 4.10	-5.60 ± 5.15	-5.50 ± 5.55
BRSE	SLK	34	-0.10 ± 2.10	0.70 ± 3.70	-1.85 ± 2.55	-3.90 ± 3.30	-4.40 ± 4.60	-4.90 ± 2.50
HOPE	SLK	32	-0.00 ± 1.50	1.40 ± 2.60	-2.10 ± 4.40	2.00 ± 2.60	2.70 ± 3.70	1.60 ± 2.40
SAW	SSN	34	1.90 ± 4.90	-2.20 ± 3.90	-2.90 ± 3.45	-3.60 ± 4.30	-2.30 ± 3.45	-2.80 ± 3.75
RDWB	N19K	16	2.70 ± 3.00	1.80 ± 2.30	4.35 ± 3.50	6.35 ± 1.50	9.80 ± 1.35	9.25 ± 1.25
KNK	SSN	33	0.80 ± 6.00	-2.55 ± 5.10	-0.80 ± 5.60	-0.20 ± 3.70	0.10 ± 3.90	2.20 ± 3.80
HLC2	N19K	20	2.80 ± 2.95	1.40 ± 4.50	-0.80 ± 1.40	3.75 ± 1.45	3.60 ± 0.80	2.70 ± 0.95
HLC3	N19K	30	2.60 ± 2.50	2.40 ± 1.90	0.20 ± 3.15	8.85 ± 2.20	11.40 ± 2.15	10.45 ± 2.50
SWD	SLK	34	-0.15 ± 3.15	-1.00 ± 1.80	-5.10 ± 3.75	-2.85 ± 1.55	-4.40 ± 1.90	-6.15 ± 1.95
HLC4	N19K	18	1.75 ± 2.40	1.25 ± 4.65	-0.20 ± 2.40	3.25 ± 1.15	4.25 ± 1.50	3.05 ± 1.10
SKN	SSN	20	-1.00 ± 2.05	-2.10 ± 2.55	-2.80 ± 3.90	-1.30 ± 3.00	-3.30 ± 3.40	-0.55 ± 2.65
PWL	SLK	33	-0.55 ± 3.00	-0.60 ± 1.90	-3.00 ± 4.40	0.90 ± 3.30	1.20 ± 3.80	-0.10 ± 4.10
HLC5	N19K	32	2.50 ± 1.20	5.35 ± 1.15	5.30 ± 2.35	7.60 ± 1.10	9.60 ± 1.20	9.05 ± 1.10
M20K	SSN	20	-2.90 ± 2.30	-3.80 ± 3.70	-6.45 ± 2.10	-8.25 ± 2.10	-9.55 ± 2.20	-9.70 ± 1.95
P18K	N19K	28	-0.80 ± 2.90	-3.90 ± 3.50	-0.45 ± 3.35	-8.20 ± 2.00	-9.95 ± 3.25	-9.65 ± 2.00
O18K	N19K	29	-0.90 ± 2.70	-2.90 ± 3.50	-2.15 ± 1.95	-3.00 ± 1.40	-3.90 ± 2.30	-2.90 ± 1.80
WFLS	N19K	32	-0.95 ± 1.05	-0.85 ± 1.45	-0.65 ± 1.20	-1.95 ± 1.00	-1.05 ± 0.90	-1.40 ± 1.00
M19K	SSN	29	-4.20 ± 2.00	-8.60 ± 2.25	-7.95 ± 2.80	-9.70 ± 1.80	-12.10 ± 3.20	-11.60 ± 3.50
WFLW	N19K	32	-1.25 ± 0.65	-2.35 ± 1.70	-1.60 ± 1.90	-2.70 ± 1.10	-3.30 ± 0.85	-3.70 ± 1.50
SVW2	N19K	33	-2.85 ± 1.45	-3.45 ± 1.20	-2.80 ± 2.05	-1.10 ± 1.60	-2.80 ± 0.80	-2.30 ± 1.30

B.2 Figures

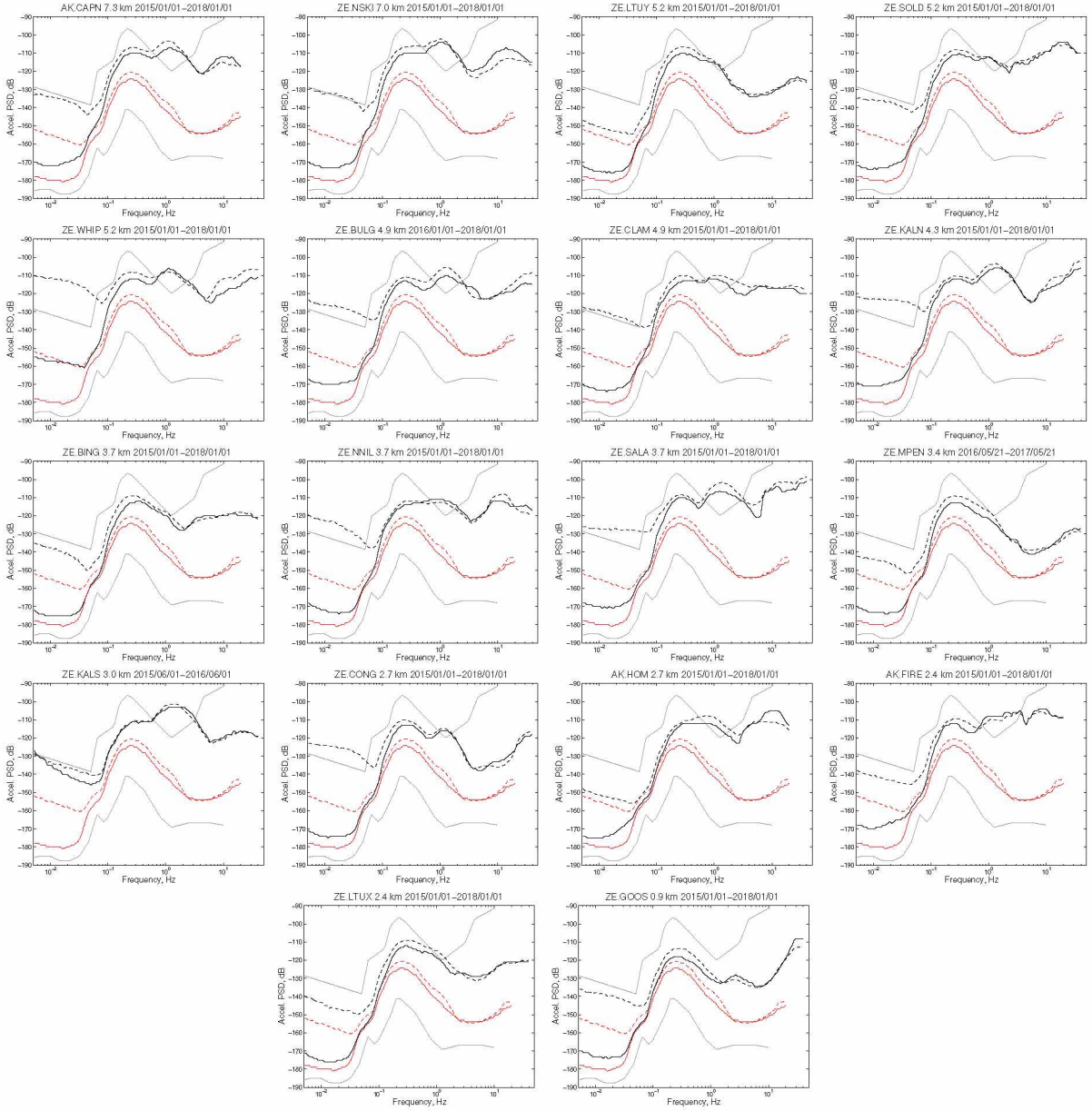

Figure B.1: Spectra for 18 basin stations in the Cook Inlet region, sorted by Figure 3.2. The depth-to-basement is listed in the header of each subplot. Solid and dashed black spectra are vertical and horizontal components, respectively. The spectra for each station are compared with those of nonbasin station SSN (red). The grey lines are the NHNM and NLNM reference spectra (Peterson, 1993).

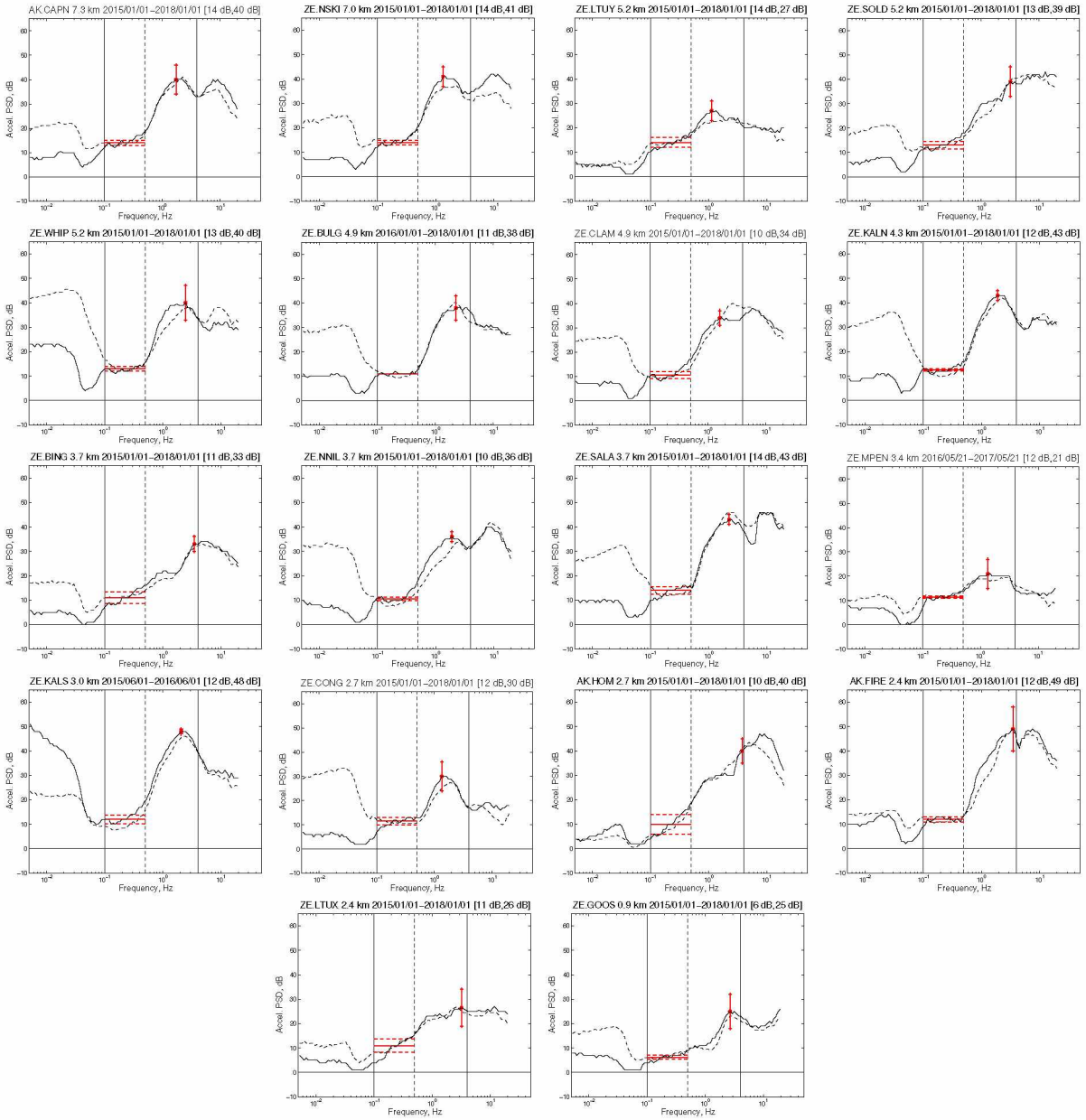

Figure B.2: Differential spectra for the vertical component (solid) and horizontal component (dashed) shown in Figure B.1. The 0 dB horizontal line represents the reference station SSN.

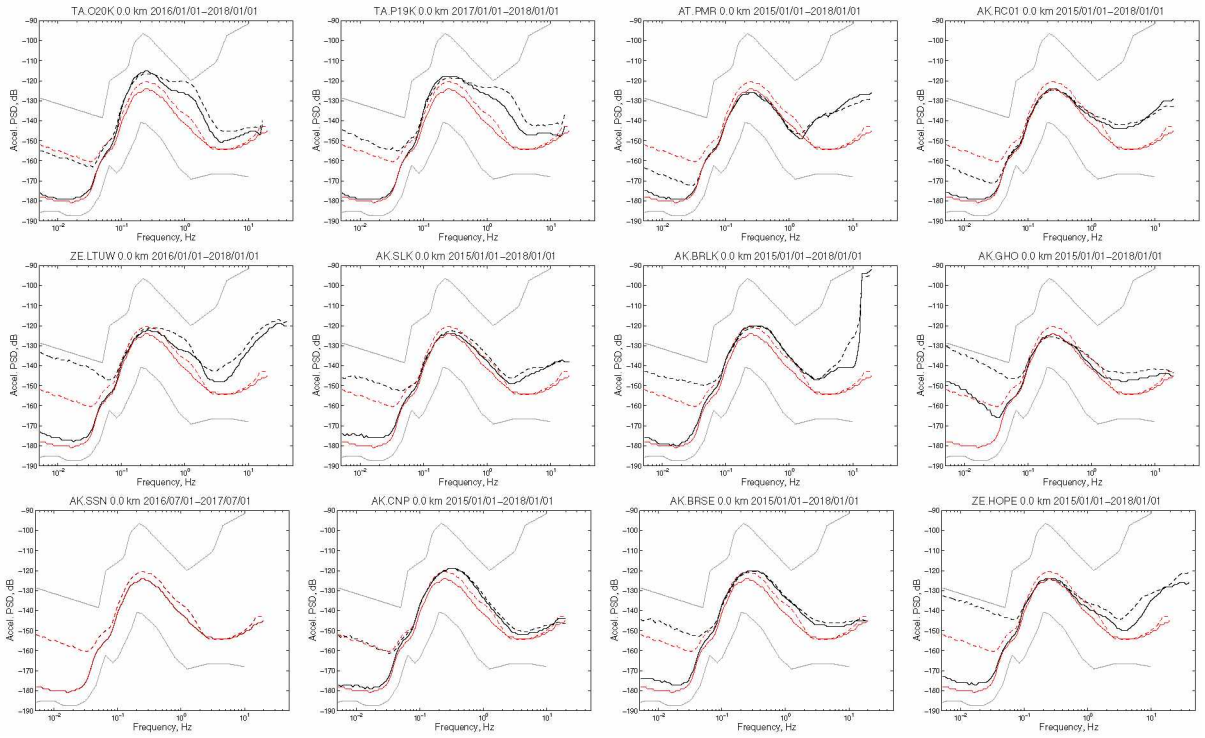

Figure B.3: Spectra for 12 marginal basin stations in the Cook Inlet region, sorted by Figure 3.2.

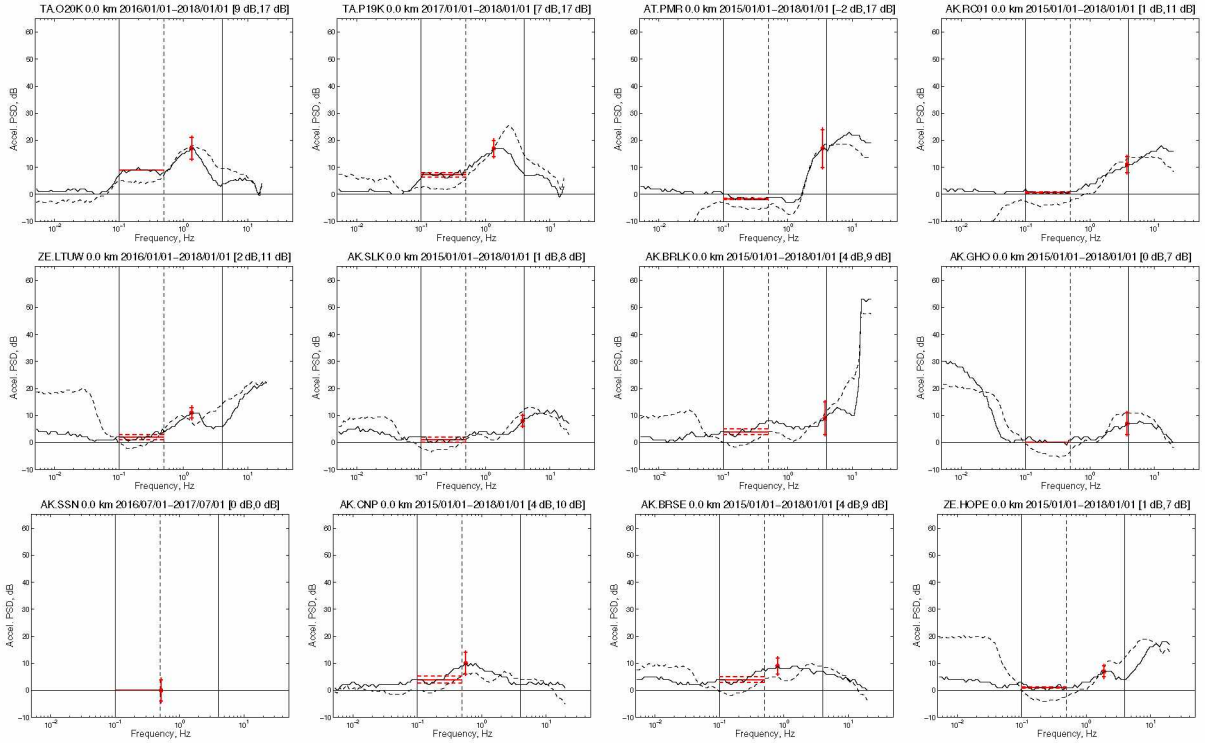

Figure B.4: Differential spectra for the vertical component (solid) and horizontal component (dashed) shown in Figure B.3. The 0 dB horizontal line represents the reference station SSN.

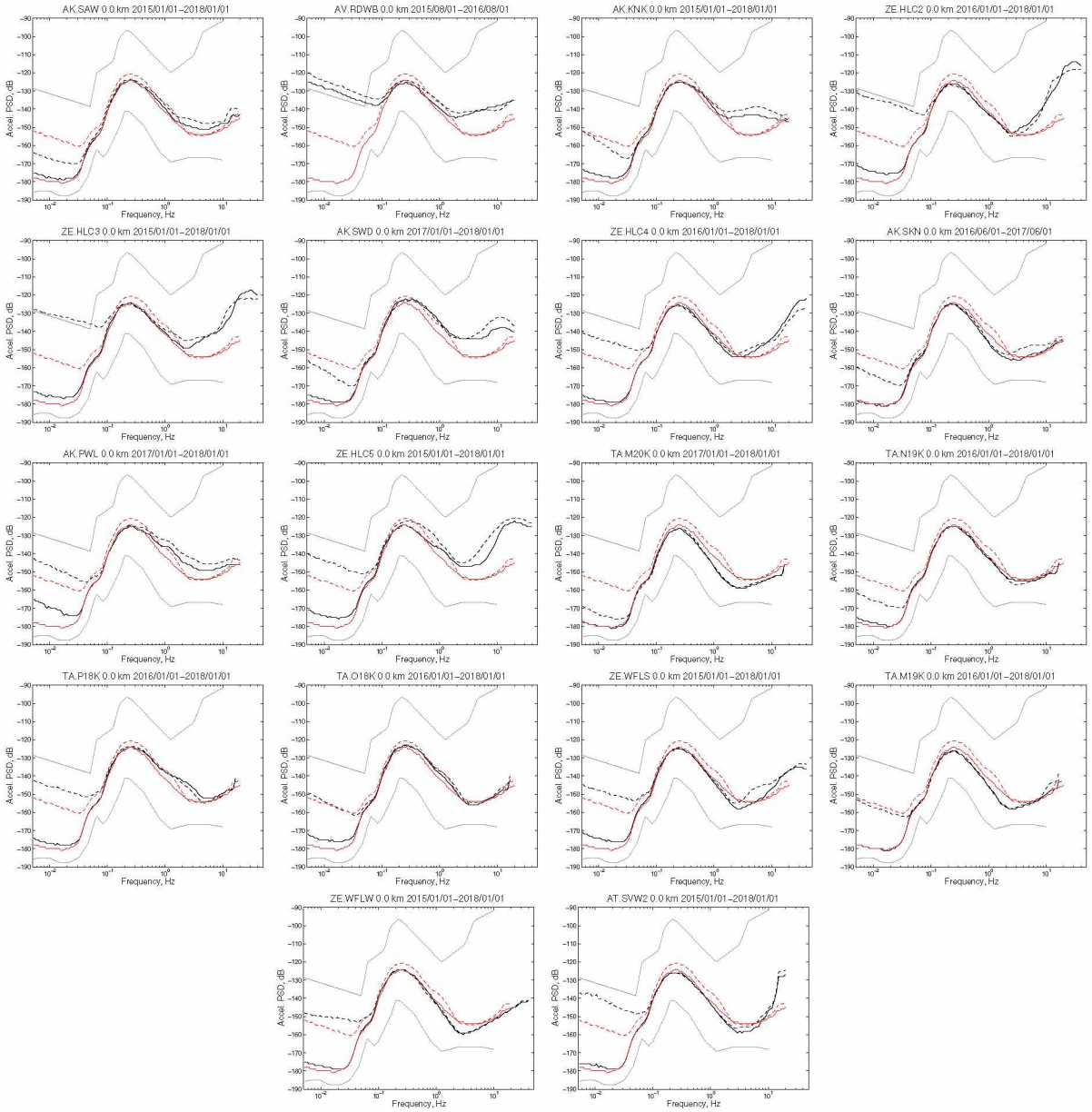

Figure B.5: Spectra for 18 nonbasin stations in the Cook Inlet region, sorted by Figure 3.2.

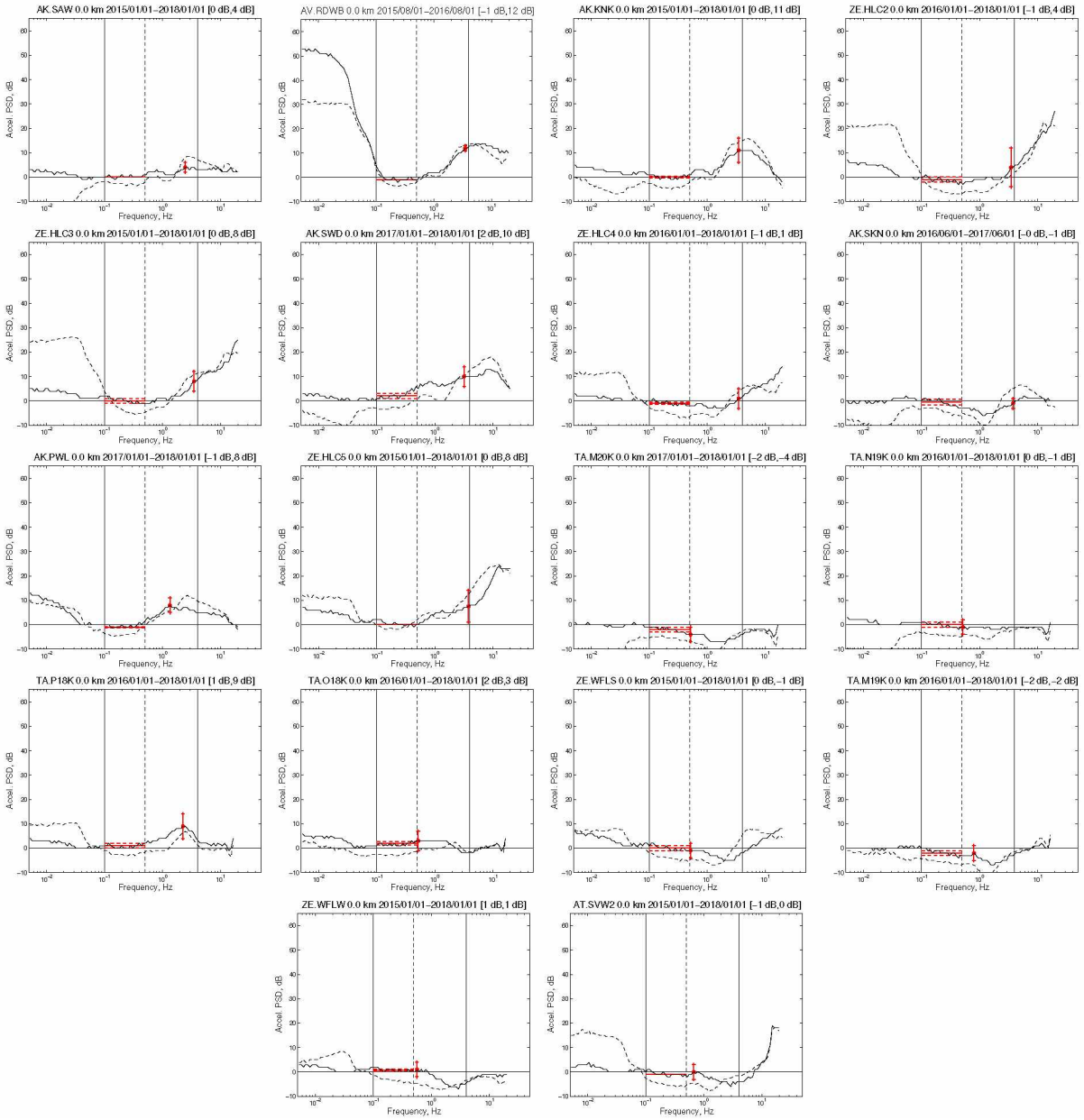

Figure B.6: Differential spectra for the vertical component (solid) and horizontal component (dashed) shown in Figure B.5. The 0 dB horizontal line represents the reference station SSN.

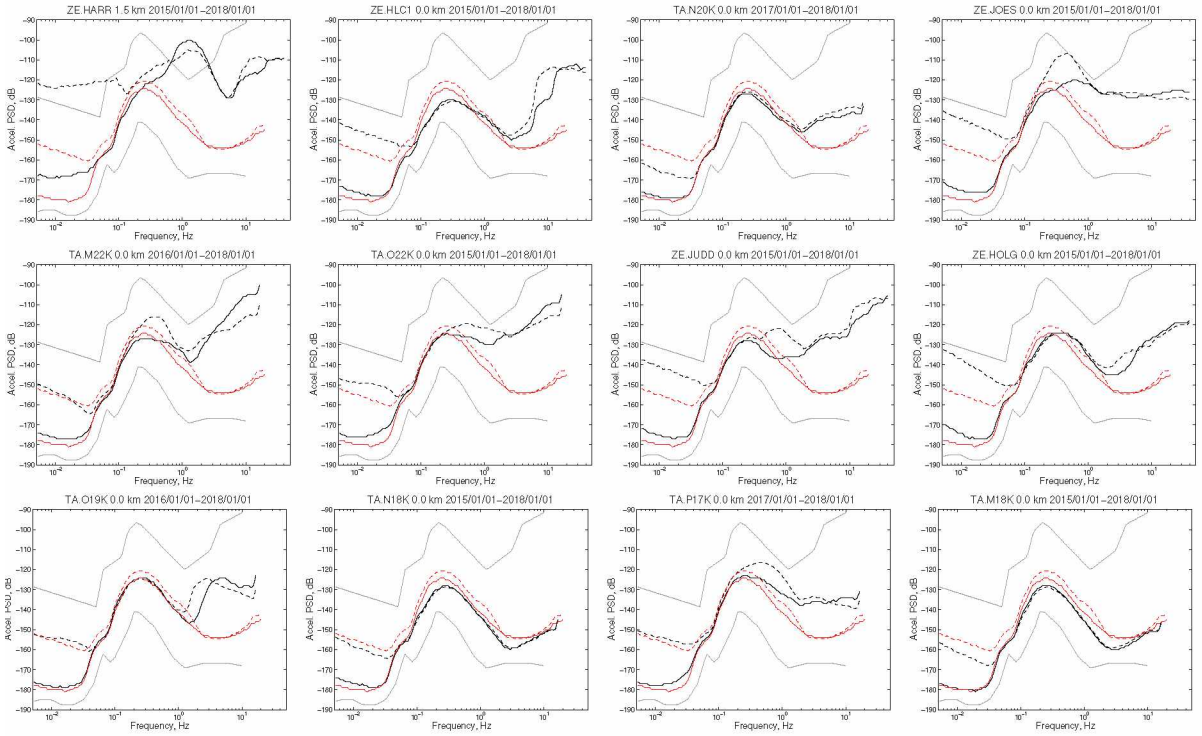

Figure B.7: Spectra for 12 unused stations in the Cook Inlet region, sorted by Figure 3.2. These stations were not used in our analysis.

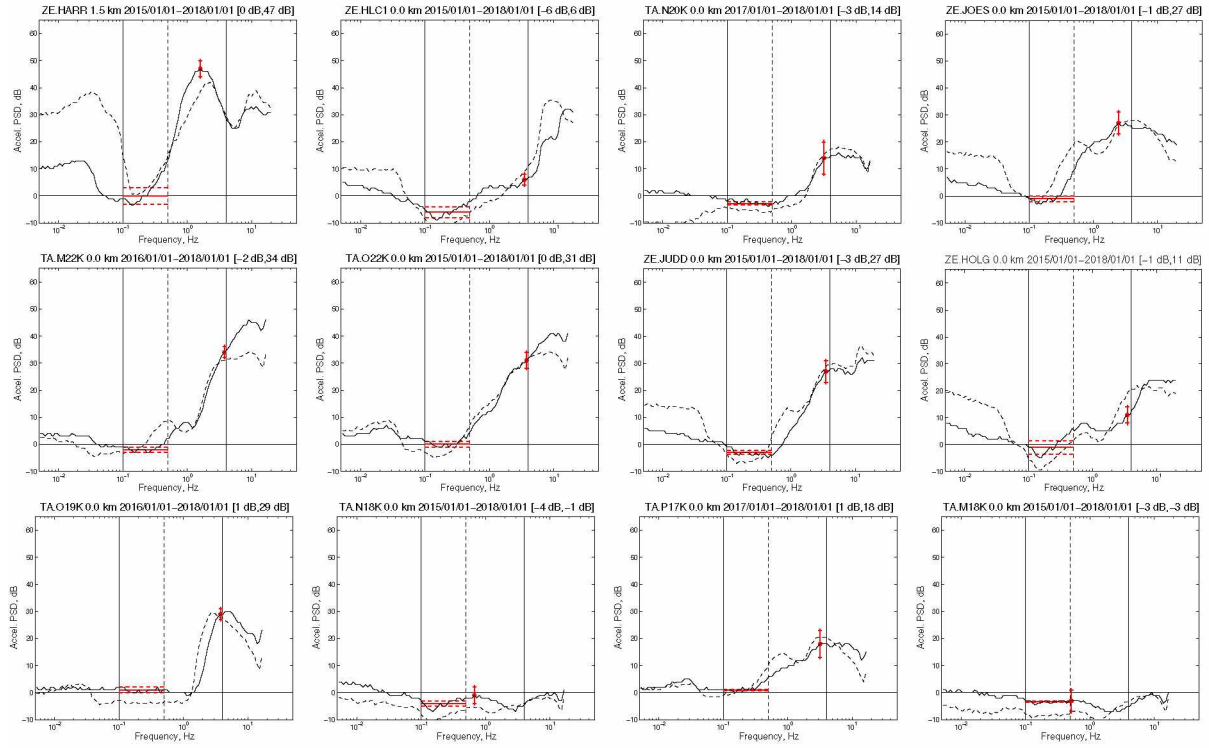

Figure B.8: Differential spectra for the vertical component (solid) and horizontal component (dashed) shown in Figure B.7. The 0 dB horizontal line represents the reference station SSN.

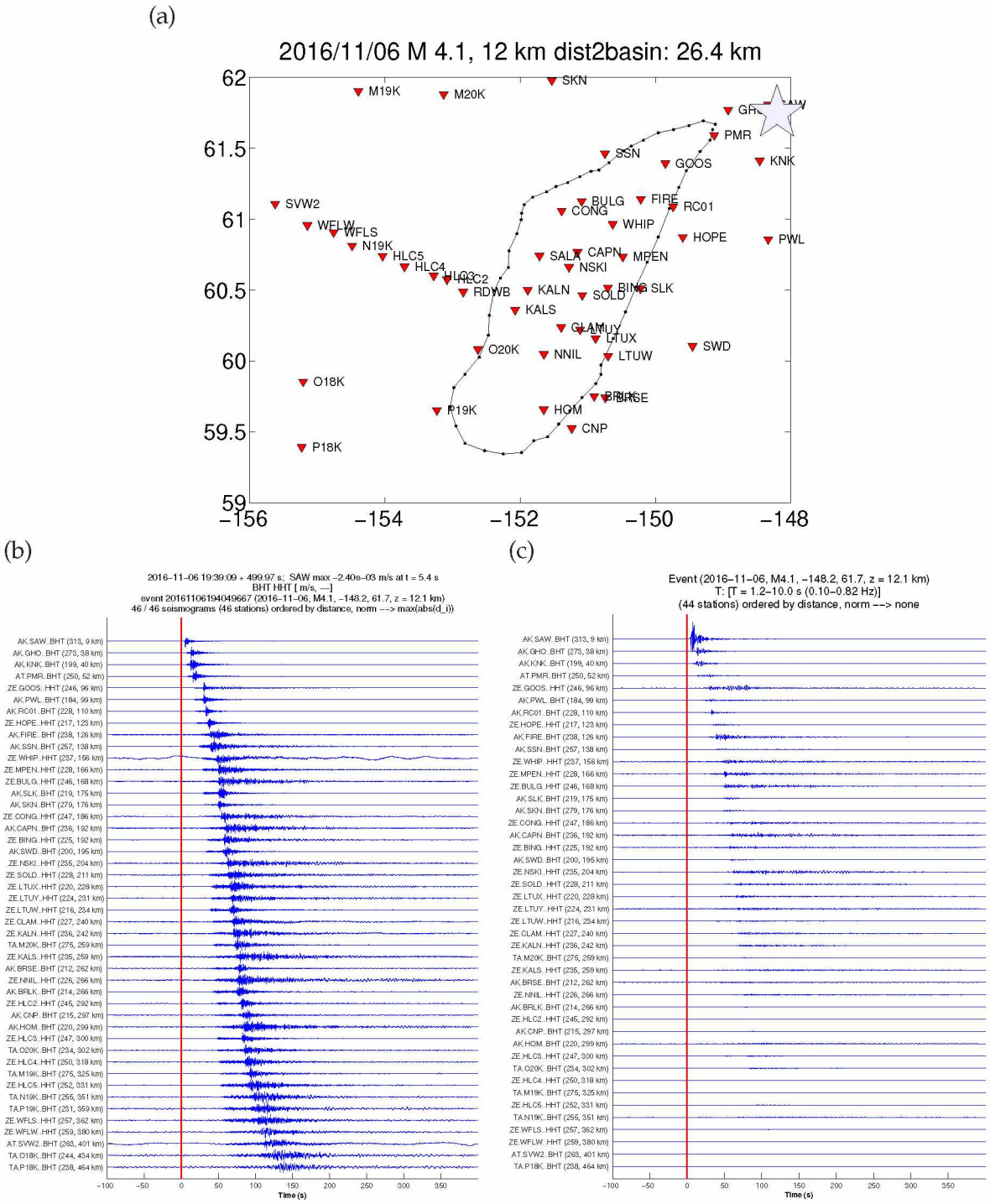

Figure B.9: Starting point for calculation of ground motion metrics. A full set of explanatory figures for earthquake metrics is shown in Figures 3.6–3.8. The example earthquake here occurreed on 2016-11-06 with M_l 4.1 and depth 12 km. (a) Map of epicenter (star), recording stations (triangles), and the boundary of Cook Inlet basin. (b) Record section of transverse-component velocity seismograms with instrument response removed. Each seismogram is normalized to its maximal amplitude. Next to the station labels are the distance and azimuth from the epicenter. (c) Filtered record section (0.10–0.82 Hz) unnormalized amplitudes, showing the expected decrease in amplitude with increasing epicentral distance. TA.O18K, TA.P19K were rejected due to low signal-to-noise.

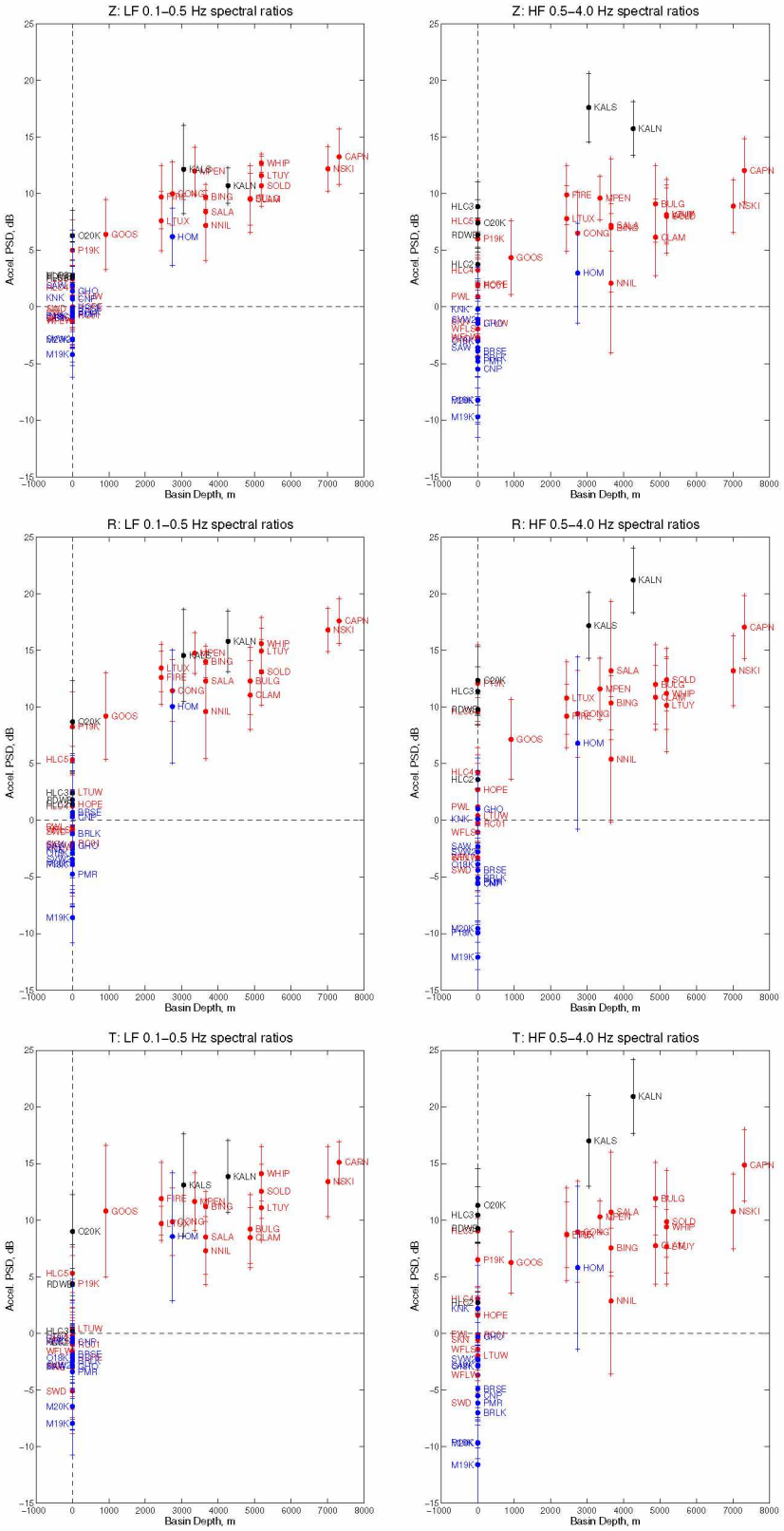

Figure B.10: Same as Figure 3.14ab, but shown here for the radial (middle row) and transverse (bottom row) components as well.

B.3 References

McNamara, D. E. & Buland, R. P., 2004. Ambient noise levels in the continental United States,

Bull. Seismol. Soc. Am., **94**(4), 1517–1527, doi: 10.1785/012003001.

Peterson, J., 1993. Observations and Modeling of Seismic Background Noise, Open-File Report 93-322.

Appendix C

Supporting Information for Chapter 4 (Seismic response of Nenana sedimentary basin, central Alaska)

C.1 Tables

Table C.1: Seismic stations in this study.

network	station	longitude	latitude	basin depth (km)	description
XV	F1TN	-149.1595	64.6544	4.2	adjacent to Tanana River
XV	F2TN	-149.1327	64.7090	4.7	adjacent to Tanana River
XV	F3TN	-149.1465	64.7716	3.3	adjacent to Tanana River
XV	F4TN	-149.1529	64.8338	2.5	adjacent to Tanana River
XV	F5MN	-149.1814	64.8857	3.0	Old Minto, adjacent to Tanana River
XV	F6TP	-149.5598	64.8700	1.0	small hill, 600 m from Tanana River
XV	F7TV	-149.8256	64.8537	1.0	Tolovana Lodge, adjacent to Tanana River
XV	FNN1	-149.2178	64.5716	4.0	Nunivak 1 well site
XV	FNN2	-149.4456	64.5756	3.0	near Nunivak 2 well site
XV	FAPT	-149.0831	64.5498	1.0	adjacent to Nenana airport shed and tower
XV	FPAP	-149.0992	64.6130	1.0	adjacent to home outside Nenana
XV	FTGH	-148.8279	64.6917	0.0	on ridge and 228 m from the Parks Highway
AK	NEA2	-149.0694	64.5928	0.0	on ridge and adjacent to microwave tower
TA	I23K	-149.3603	65.1479	0.0	outer road of Minto, at airport
AK	MLY	-150.7442	65.0304	0.0	bedrock hill near Manley
XV	F8KN	-149.9307	64.7653	0.0	bedrock bluff above Tanana River

C.2 Figures

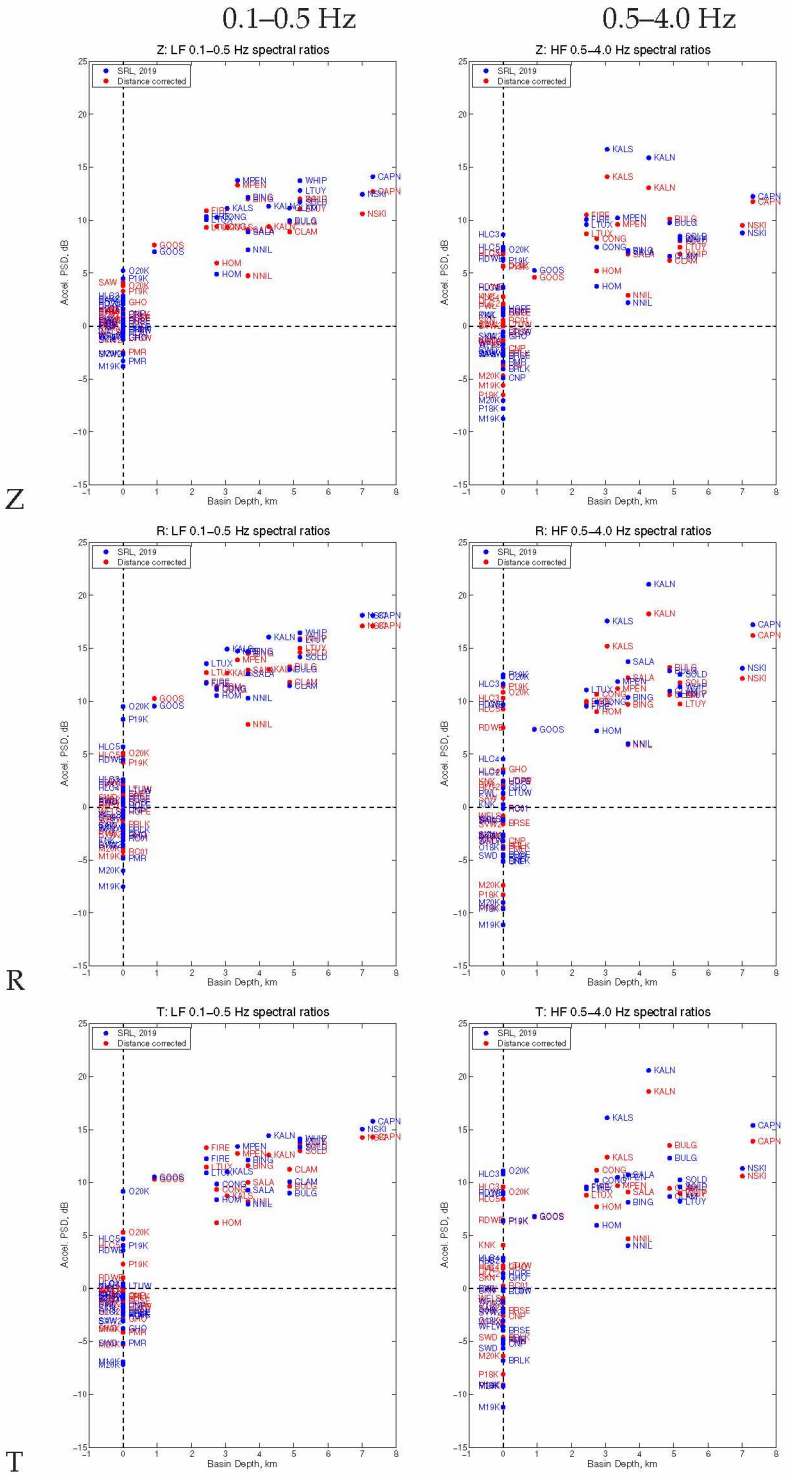

Figure C.1: Comparison of earthquake SR amplification values of Smith & Tape (2019b) and correcting for distance and using a time window of 500 s.

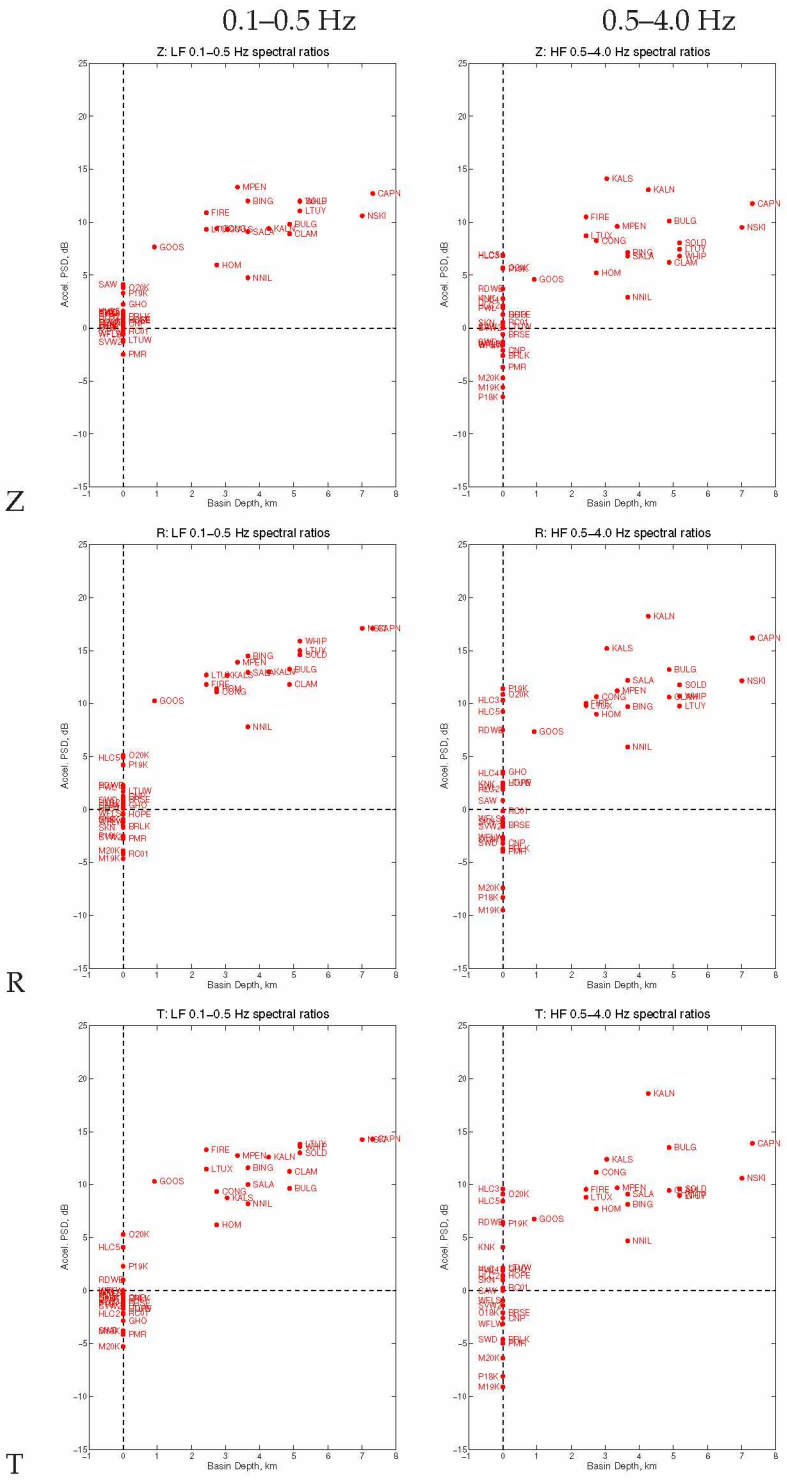

Figure C.2: Earthquake SR amplification values of Smith & Tape (2019b) after correcting for distance and using a time window of 500 s.

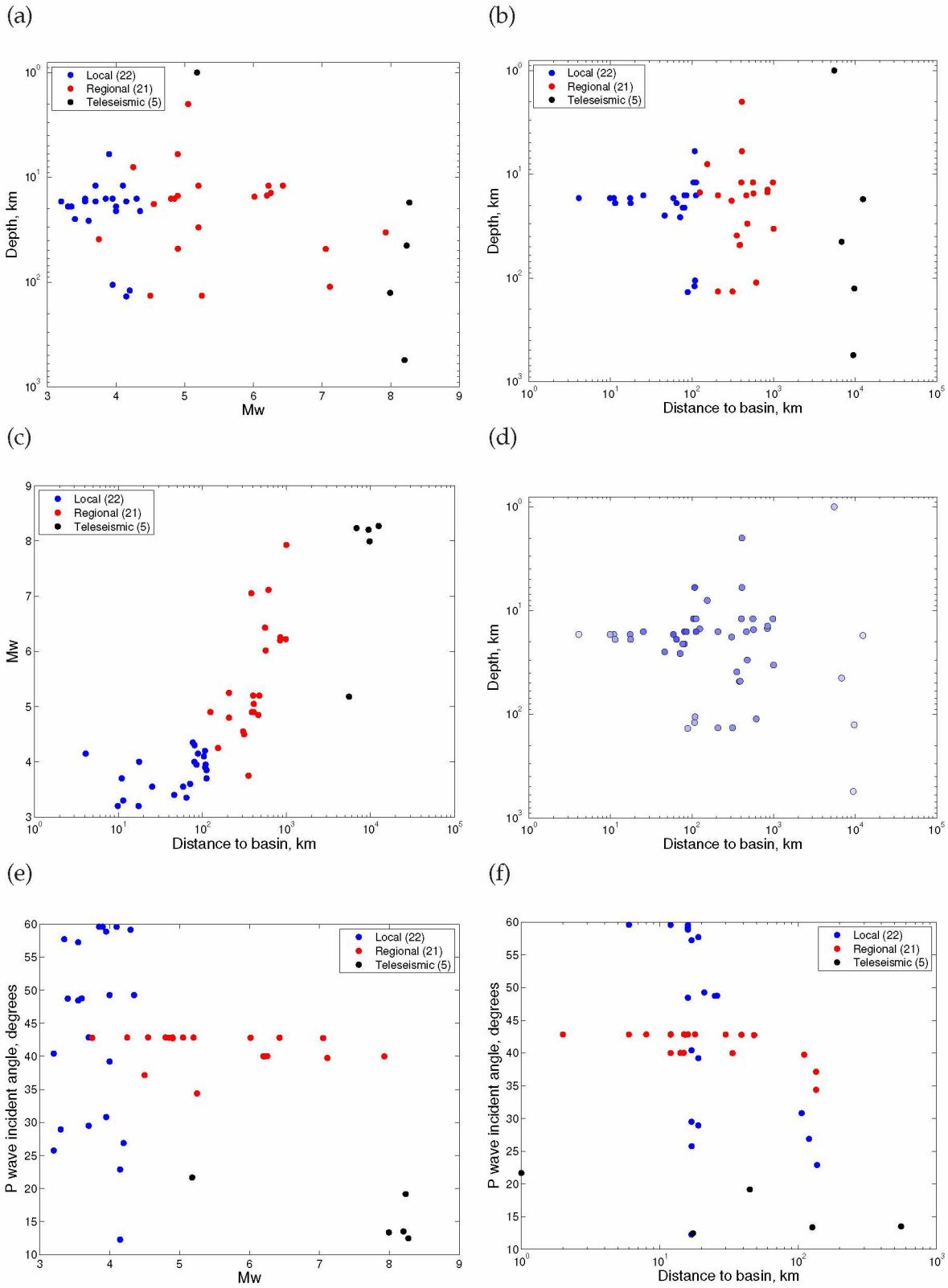

Figure C.3: Relationships among M_w, depth, incident angle and distance-to-basin for the 48 earthquakes in this study (Table 4.1). Our earthquake selection criteria results in a catalog having larger events at greater distances. Colors in (d) indicate P wave incident angle from 0 to 90 degrees.

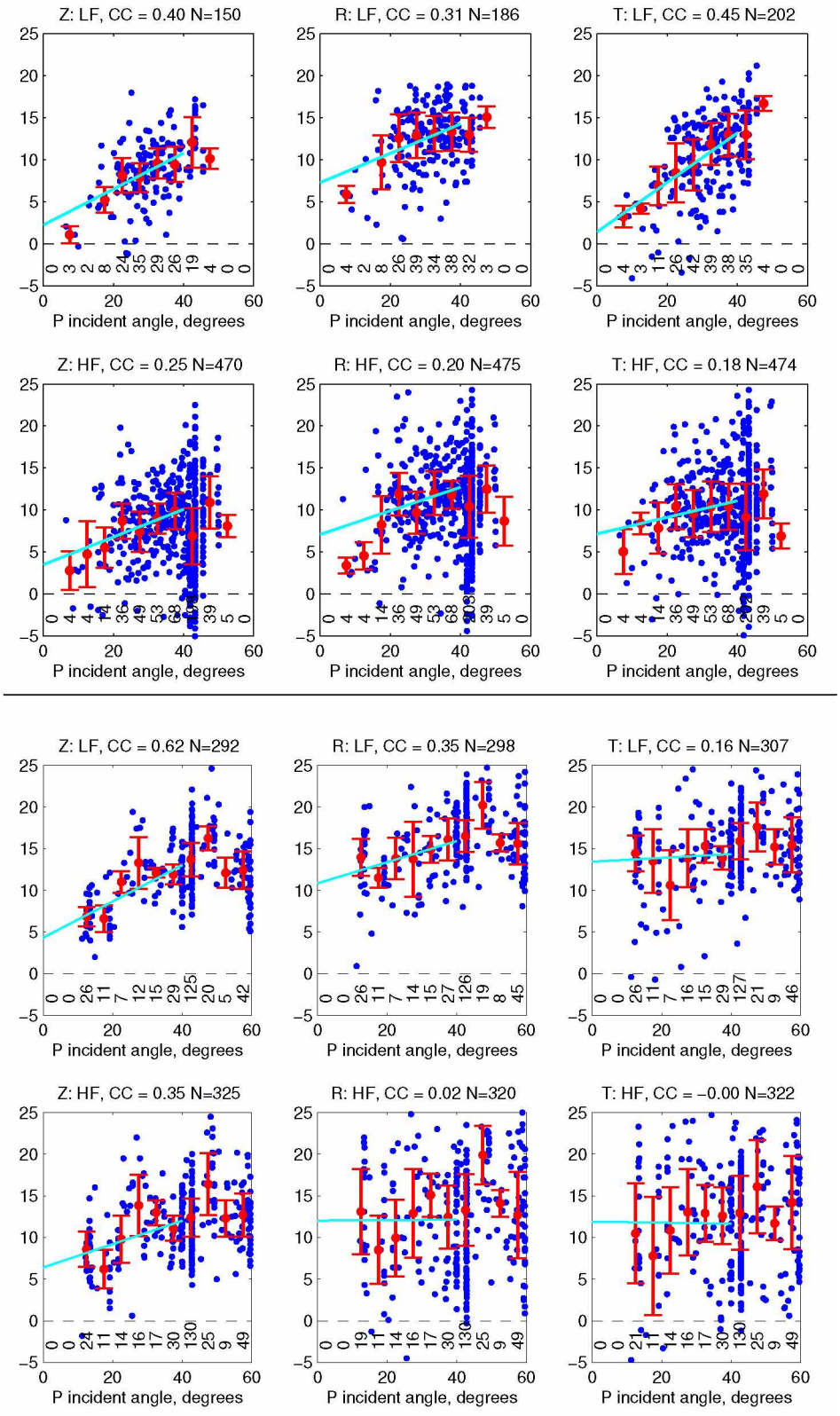

Figure C.4: Cook Inlet basin *(Top)* and Nenana basin *(Bottom)* SR amplification for all stations and each earthquake in previous figures. Also shown are the median and MAD of each bin. The color bar indicates the magnitude. The Cook Inlet basin amplifications are from BING, BULG, CAPN, CLAM, CONG, FIRE, GOOS, HOM, KALN, KALS, LTUX, LTUY, NNIL, NSKI, SALA, and SOLD. The Nenana basin amplifications are from F1TN, F2TN, F3TN, F4TN, F5MN, FNN1, and FNN2.

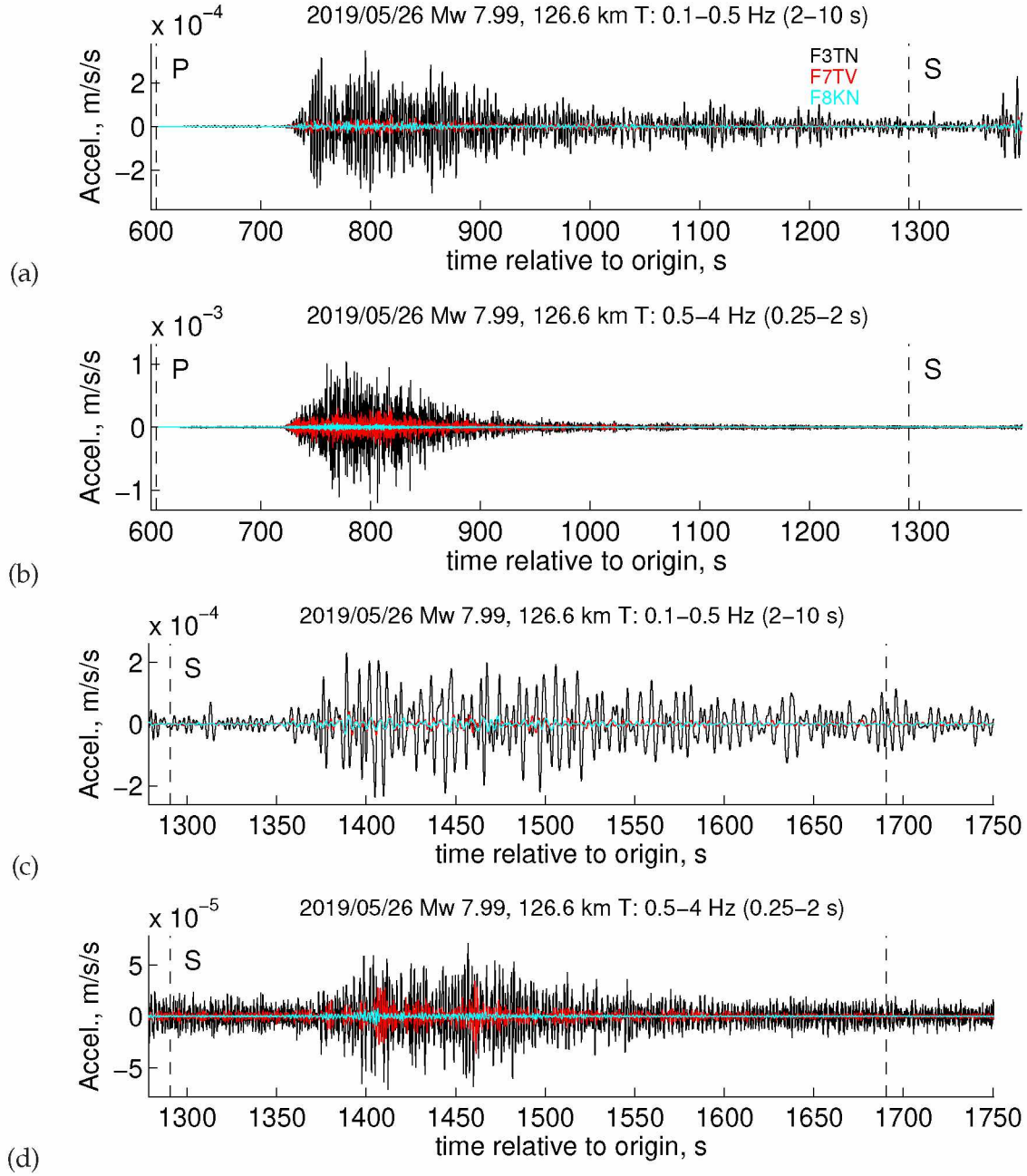

Figure C.5: Example of amplification of P and S waves from a teleseismic earthquake (2019-05-26,M_w7.99, depth 127 km) recorded on the transverse component. See Figure C.5 for the vertical component. (a) Transverse component recording of P wavetrain, filtered 0.1–0.5 Hz, at F8KN, F7TV, and F3TN. (b) Same as (a) but filtered 0.5–4.0 Hz. (c) Transverse component recording of S wavetrain, filtered 0.1–0.5 Hz, at F8KN, F7TV, and F3TN. (d) Same as (c) but filtered 0.5–4.0 Hz.

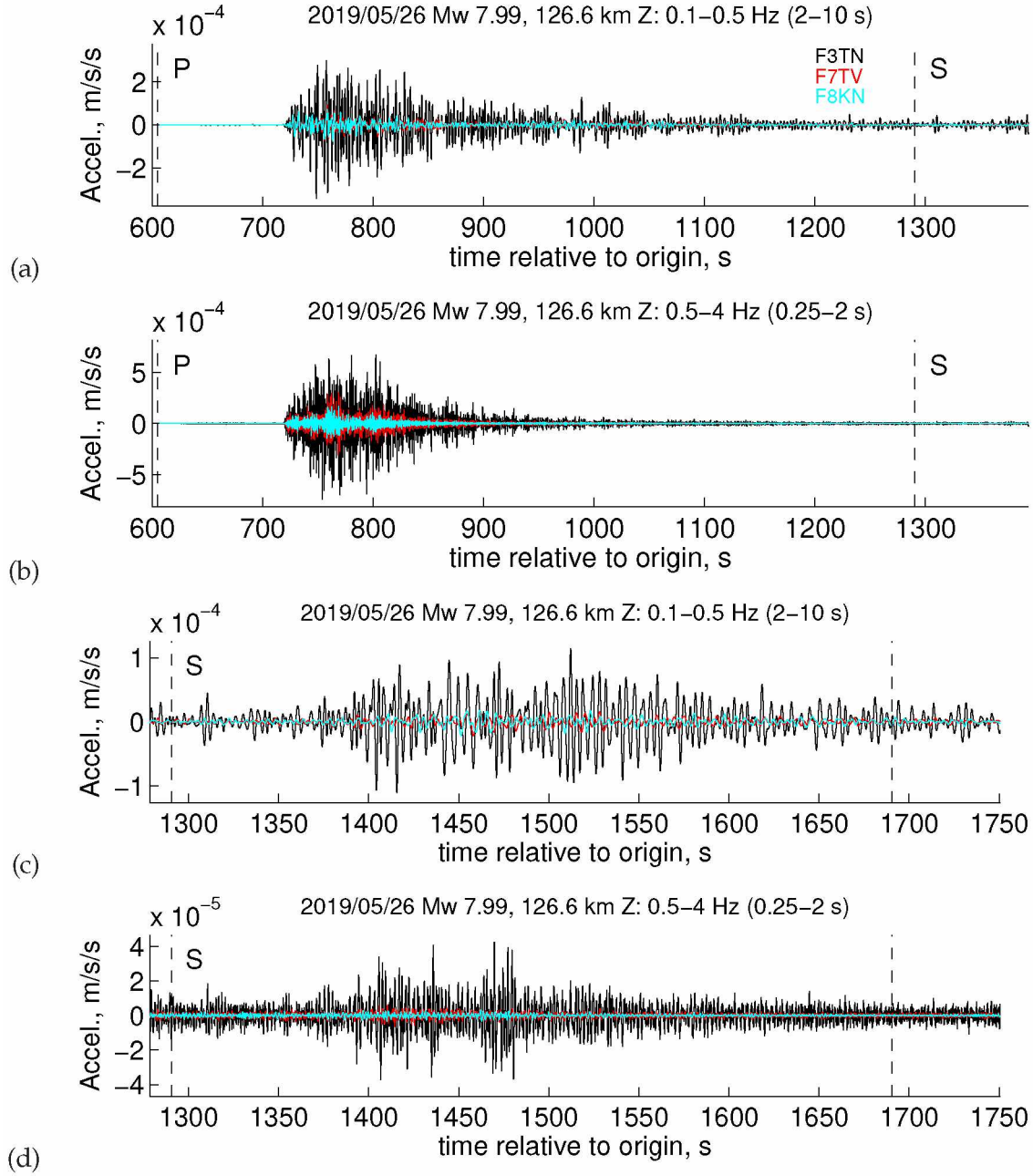

Figure C.6: Example of amplification of P and S waves from a teleseismic earthquake (2019-05-26,M_w7.99, depth 127 km) recorded on the transverse component. See Figure C.5 for the vertical component. (a) Transverse component recording of P wavetrain, filtered 0.1–0.5 Hz, at F8KN, F7TV, and F3TN. (b) Same as (a) but filtered 0.5–4.0 Hz. (c) Transverse component recording of S wavetrain, filtered 0.1–0.5 Hz, at F8KN, F7TV, and F3TN. (d) Same as (c) but filtered 0.5–4.0 Hz.

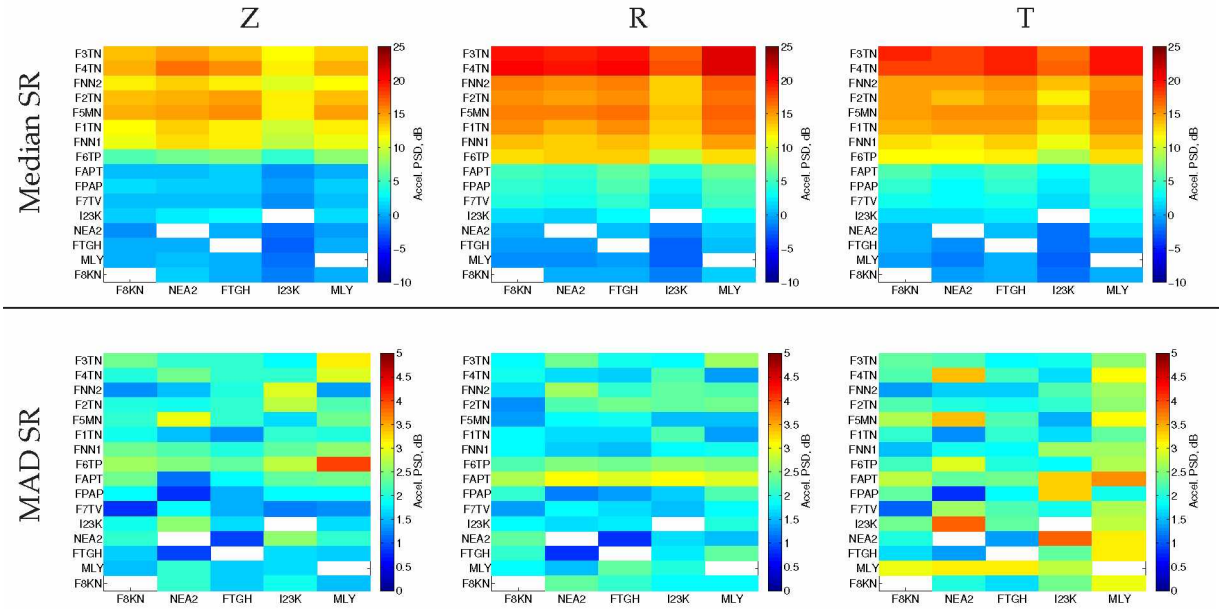

Figure C.7: *Top*: Median spectral ratio of all local and regional events in **LFband**. *Bottom*: MAD of spectral ratios of local and regional events in LFband. Vertical axis is sorted by SR values with reference station F8KN from the transverse component in Figure 4.5. Horizontal axis is sorted by median distance to all local events.

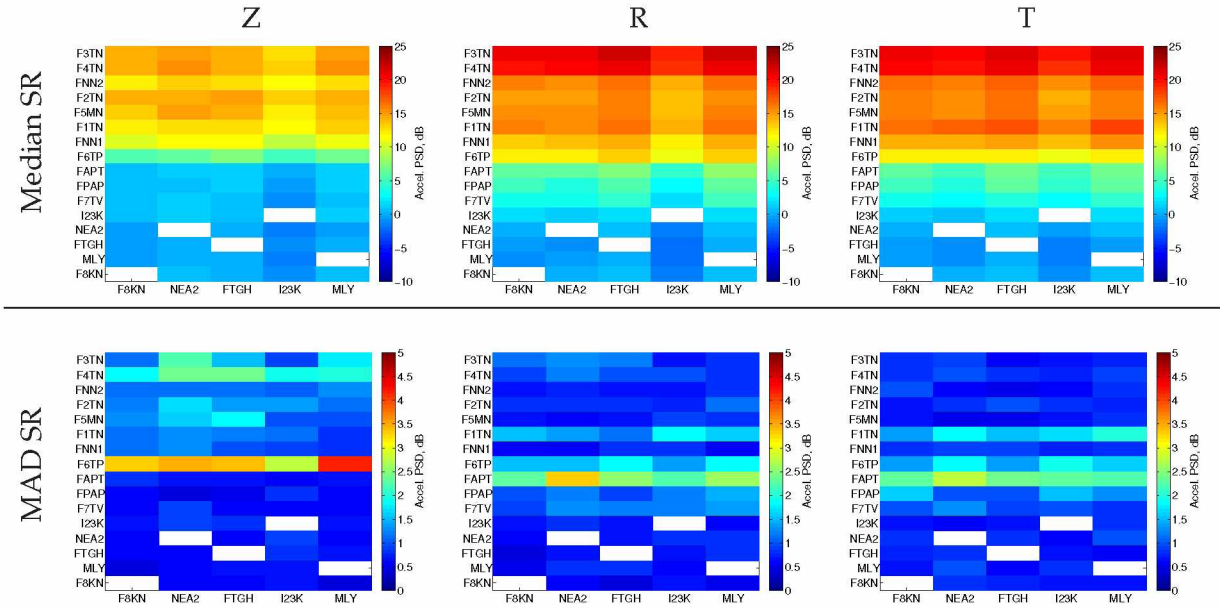

Figure C.8: *Top*: Median spectral ratio of all local and regional events in **Pre-EQ Noise LFband**. *Bottom*: MAD of spectral ratios of local and regional events in Pre-EQ Noise LFband. Vertical axis is sorted by SR values with reference station F8KN from the transverse component in Figure 4.5. Horizontal axis is sorted by median distance to all local events.

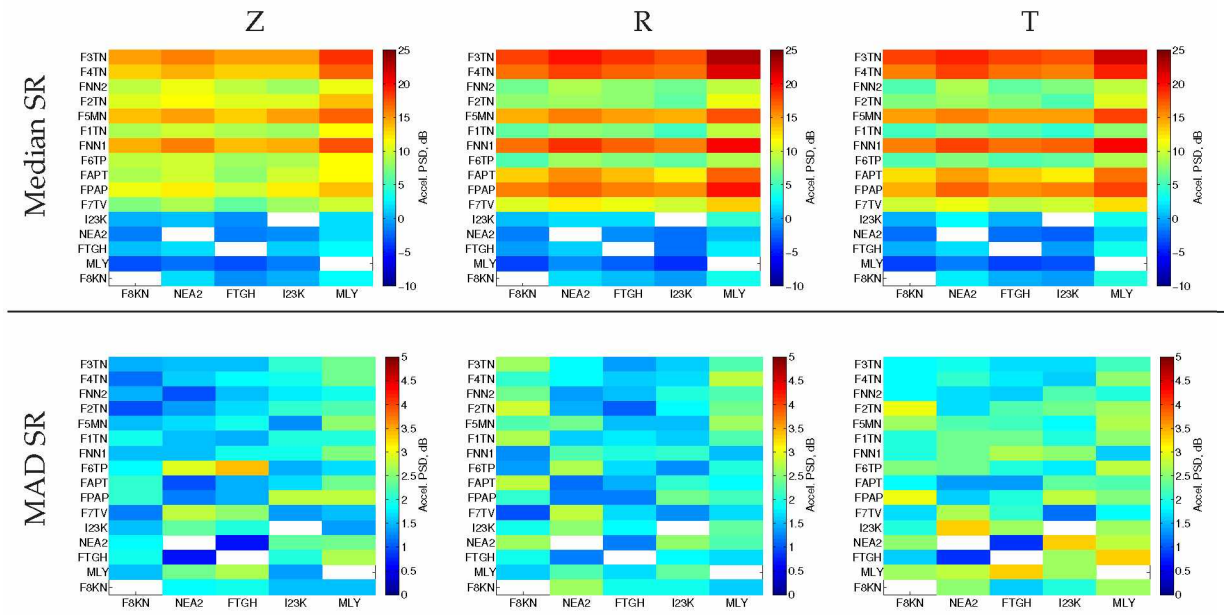

Figure C.9: *Top*: Median spectral ratio of all local and regional events in **HFband**. *Bottom*: MAD of spectral ratios of local and regional events in HFband. Vertical axis is sorted by SR values with reference station F8KN from the transverse component in Figure 4.5. Horizontal axis is sorted by median distance to all local events.

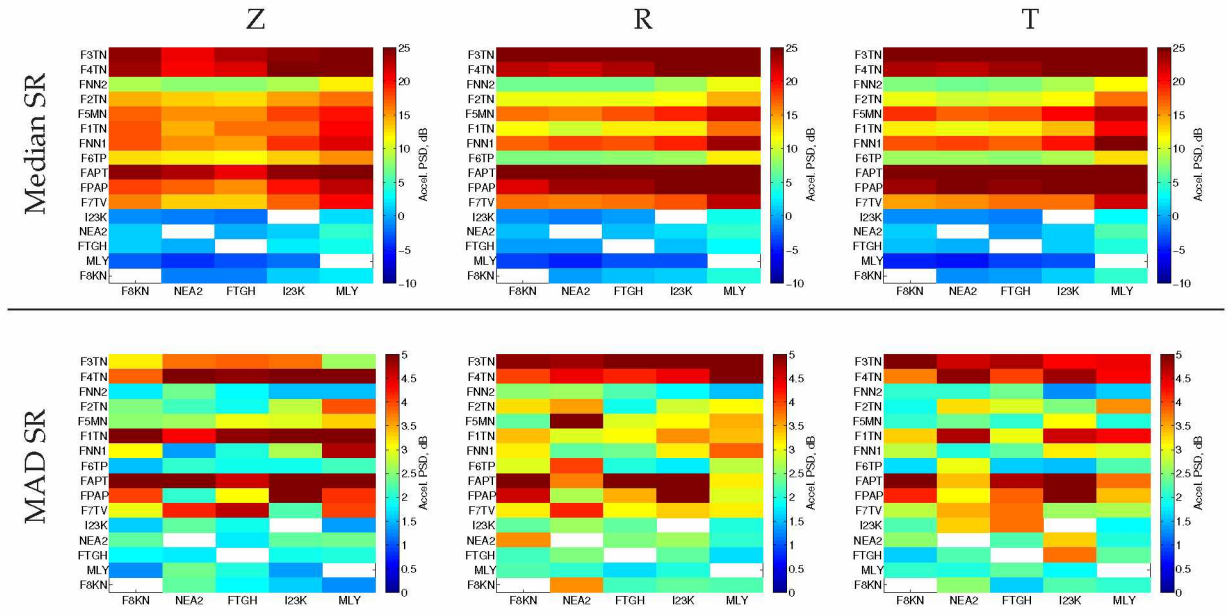

Figure C.10: *Top*: Median spectral ratio of all local and regional events in **Noise HFband**. *Bottom*: MAD of spectral ratios of local and regional events in Noise HFband. Vertical axis is sorted by SR values with reference station F8KN from the transverse component in Figure 4.5. Horizontal axis is sorted by median distance to all local events.

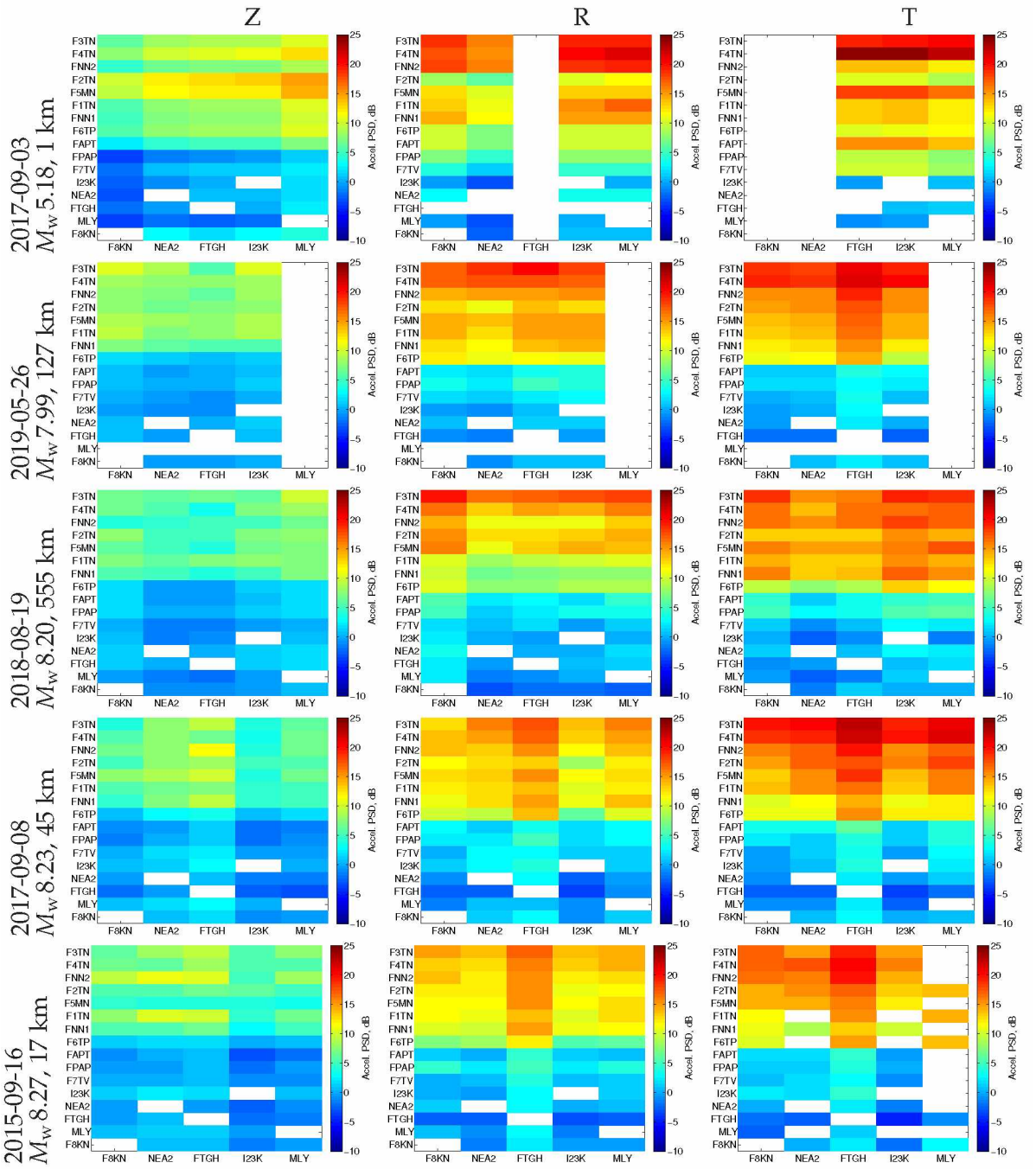

Figure C.11: **LFband**: **Teleseismic P** wave spectral ratios sorted by increasing **magnitude**. The vertical axis is sorted by descending SR's reference station F8KN in the transverse component in Figure 4.5. The horizontal axis is sorted by median distance to all local events. Event 2017-09-08 is a nuclear explosion test from North Korea and did not produce significant S waveforms so it is excluded.

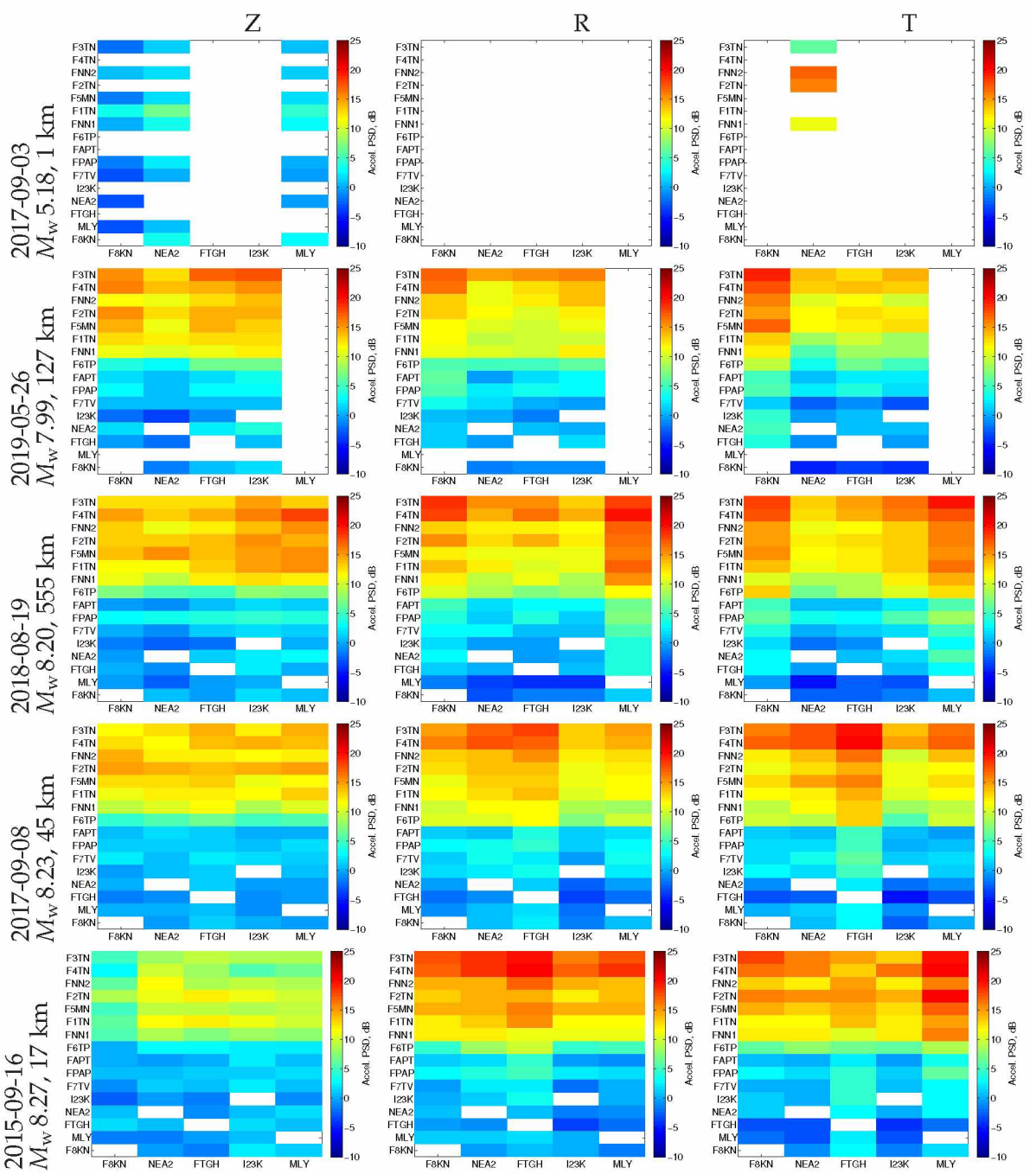

Figure C.12: **LFband**: **Teleseismic S** wave spectral ratios sorted by increasing **magnitude**. The vertical axis is sorted by descending SR's reference station F8KN in the transverse component in Figure 4.5. The horizontal axis is sorted by median distance to all local events. Event 2017-09-08 is a nuclear explosion test from North Korea and did not produce significant S waveforms so it is excluded.

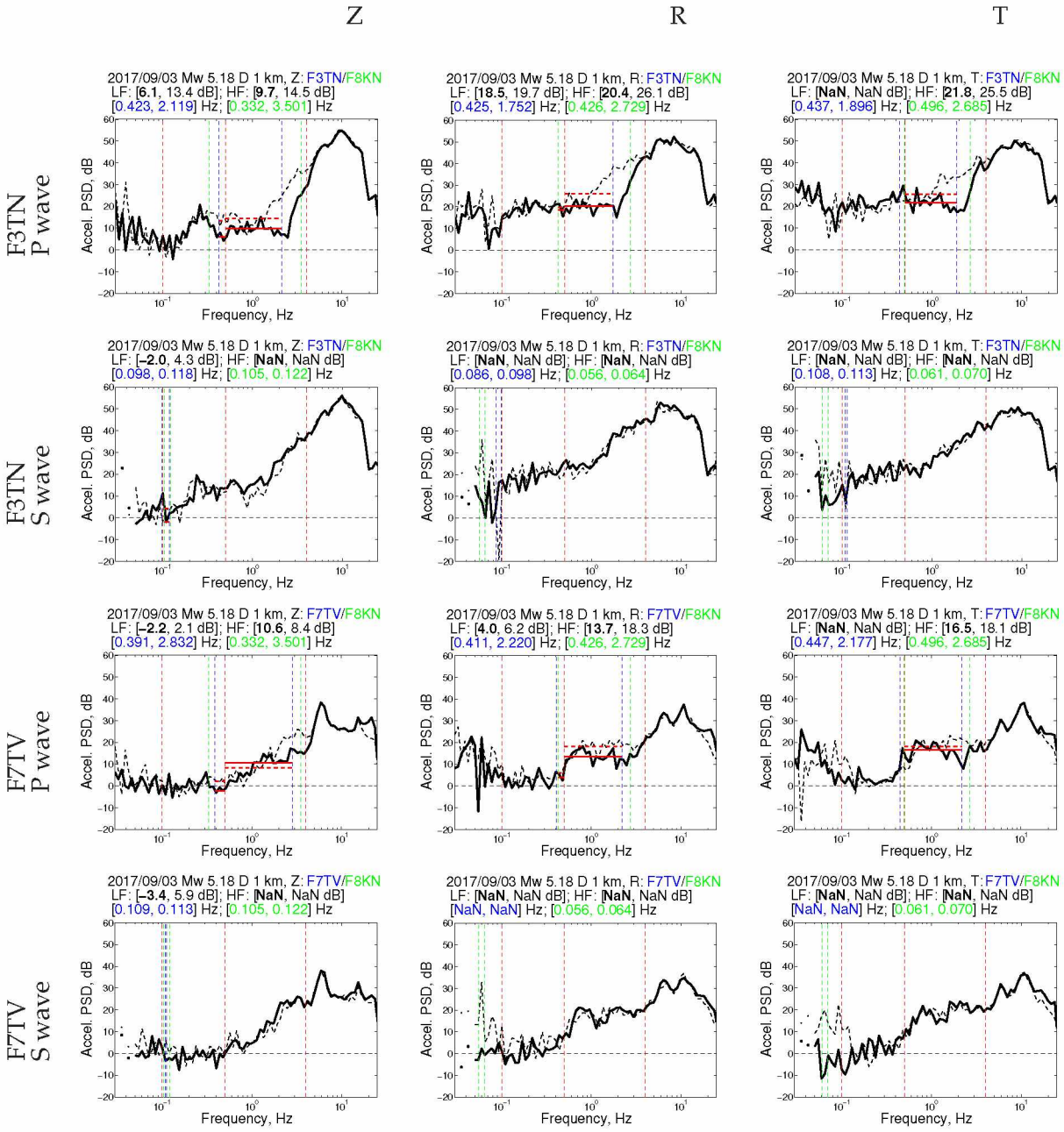

Figure C.13: Spectral ratio of teleseismic earthquake (solid) and pre-earthquake noise (dashed) for M_l **5.18** on **2017-09-03** with depth **1 km** and **5560 km** from the basin. Events are sorted by **magnitude**. D is the event depth. See Figures C.11 and C.12 for complete view of other stations of P and S wave amplifications for LFband.

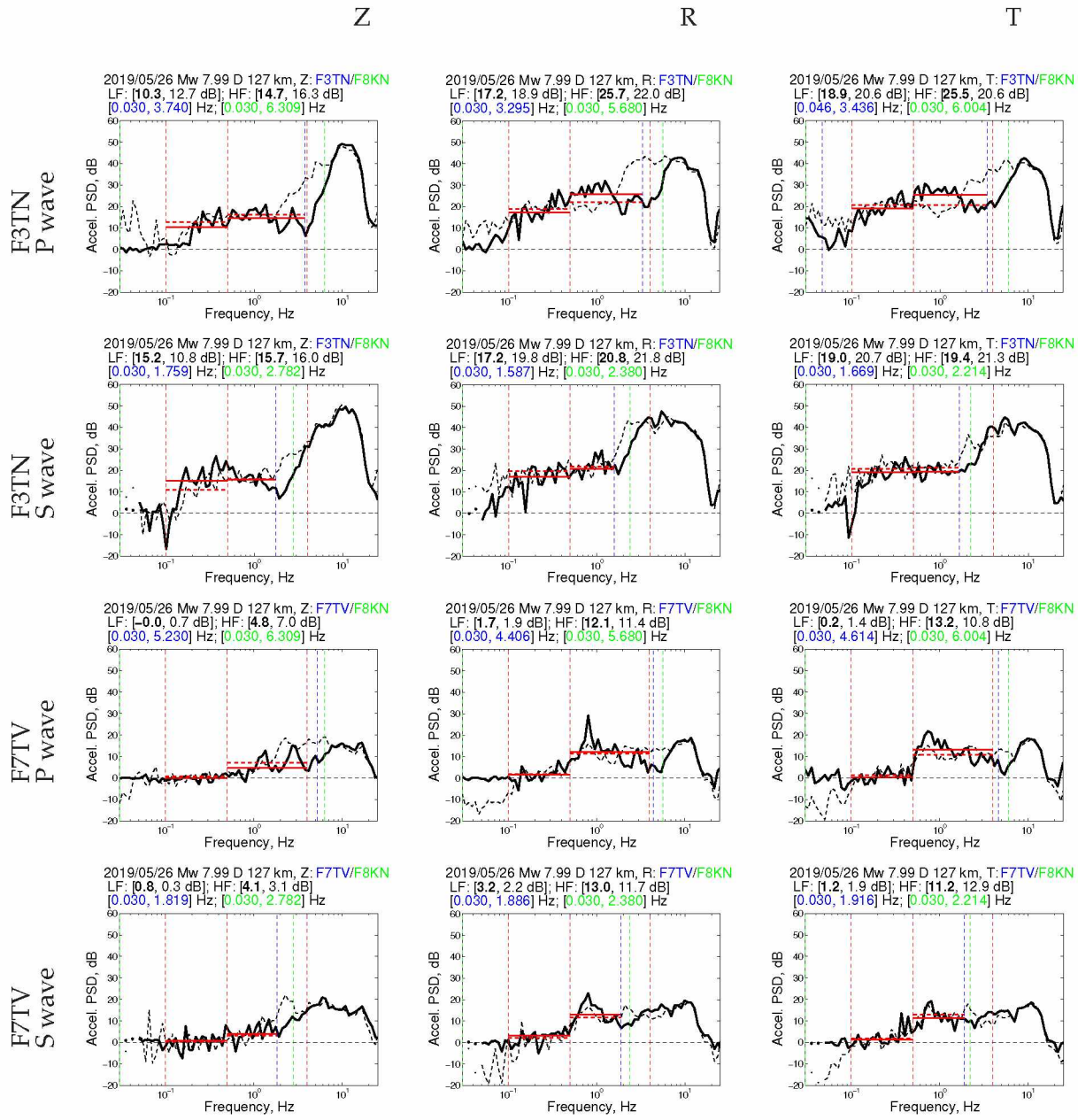

Figure C.14: Spectral ratio of teleseismic earthquake (solid) and pre-earthquake noise (dashed) for M_l **7.99** on **2019-05-26** with depth **127 km** and **9780 km** from the basin. Events are sorted by **magnitude**. D is the event depth. See Figures C.11 and C.12 for complete view of other stations of P and S wave amplifications for LFband.

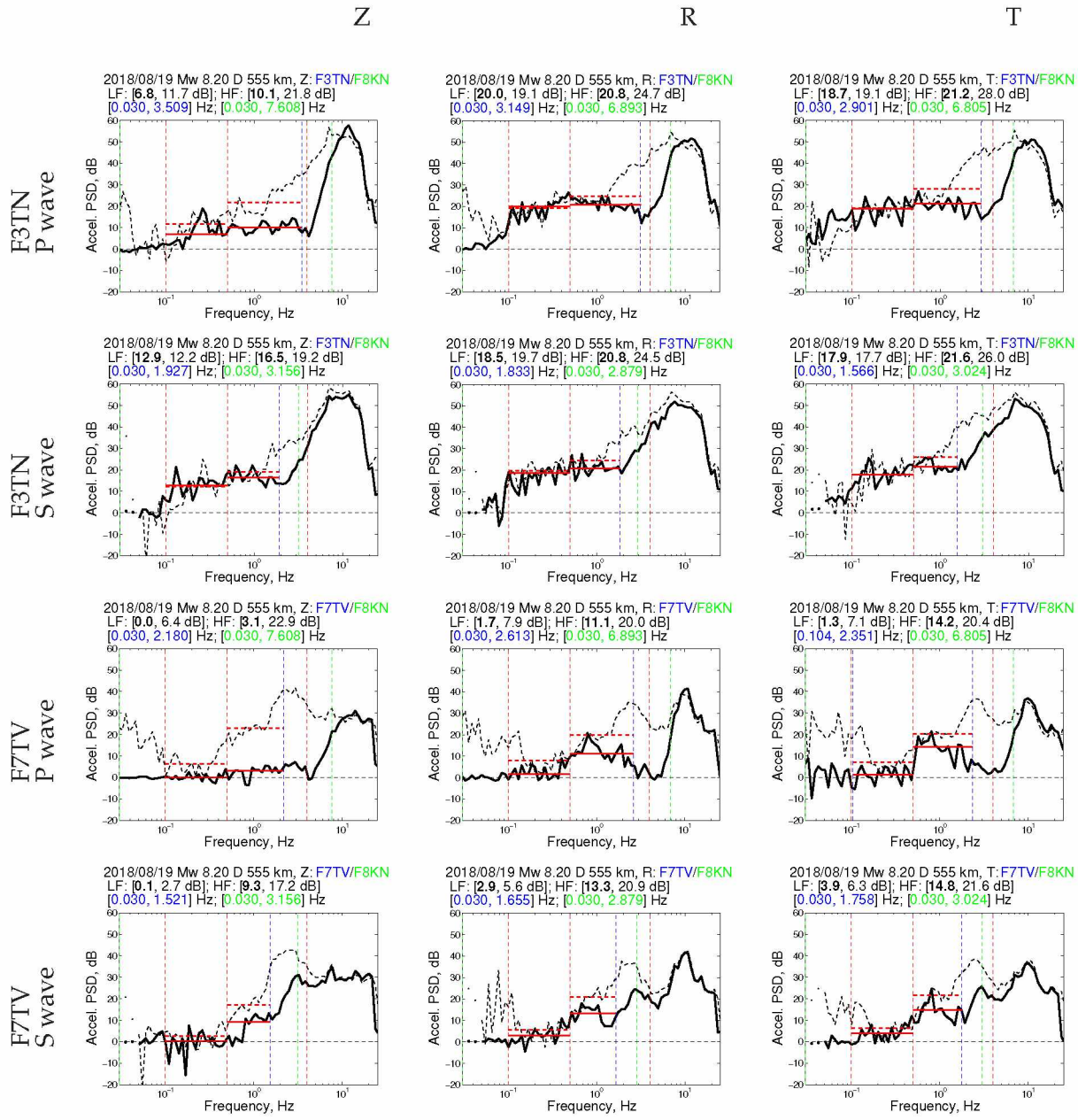

Figure C.15: Spectral ratio of teleseismic earthquake (solid) and pre-earthquake noise (dashed) for M_l **8.20** on **2018-08-19** with depth **555 km** and **9510 km** from the basin. Events are sorted by **magnitude**. D is the event depth. See Figures C.11 and C.12 for complete view of other stations of P and S wave amplifications for LFband.

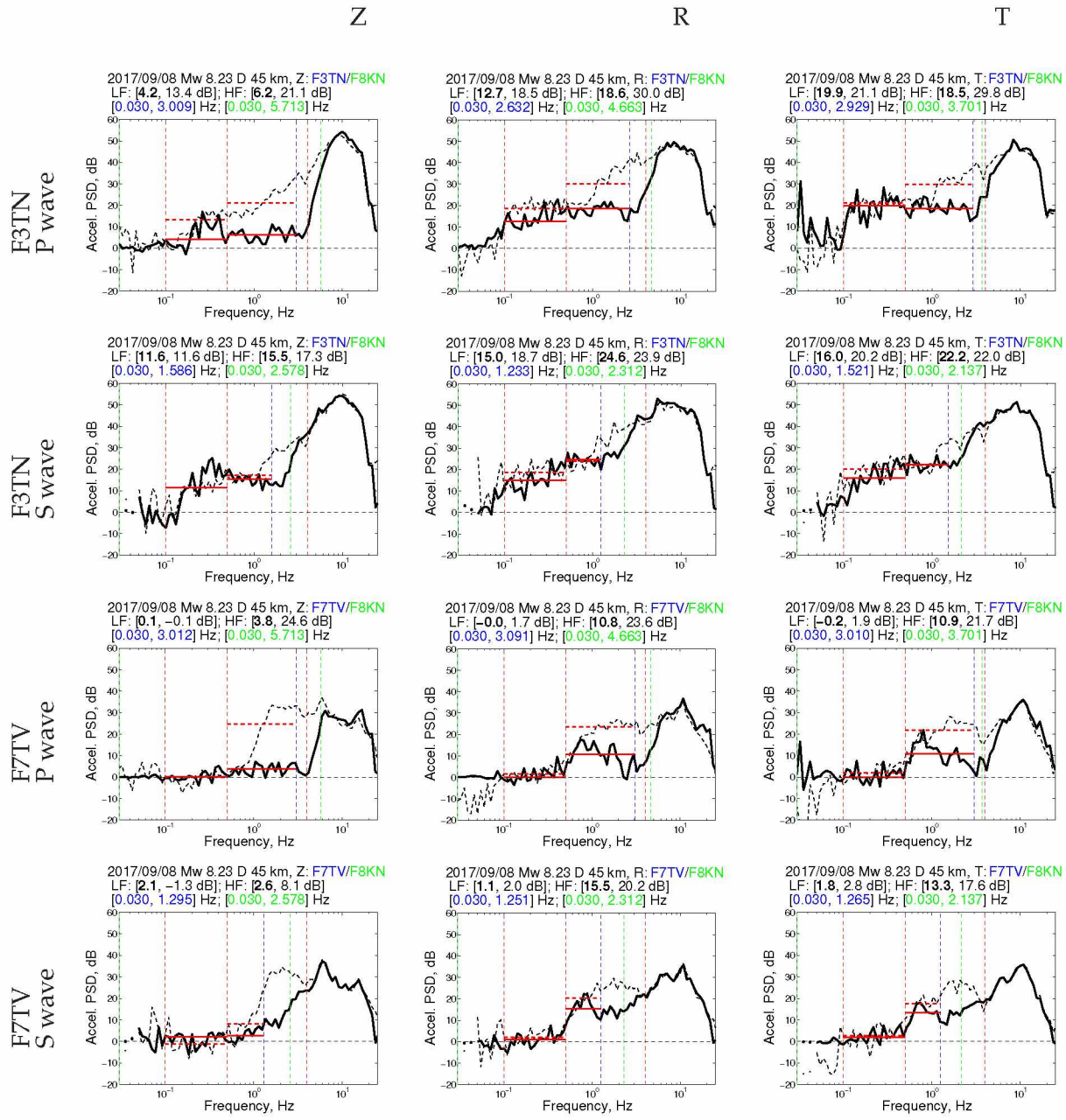

Figure C.16: Spectral ratio of teleseismic earthquake (solid) and pre-earthquake noise (dashed) for M_{l} **8.23** on **2017-09-08** with depth **45 km** and **6830 km** from the basin. Events are sorted by **magnitude**. D is the event depth. See Figures C.11 and C.12 for complete view of other stations of P and S wave amplifications for LFband.

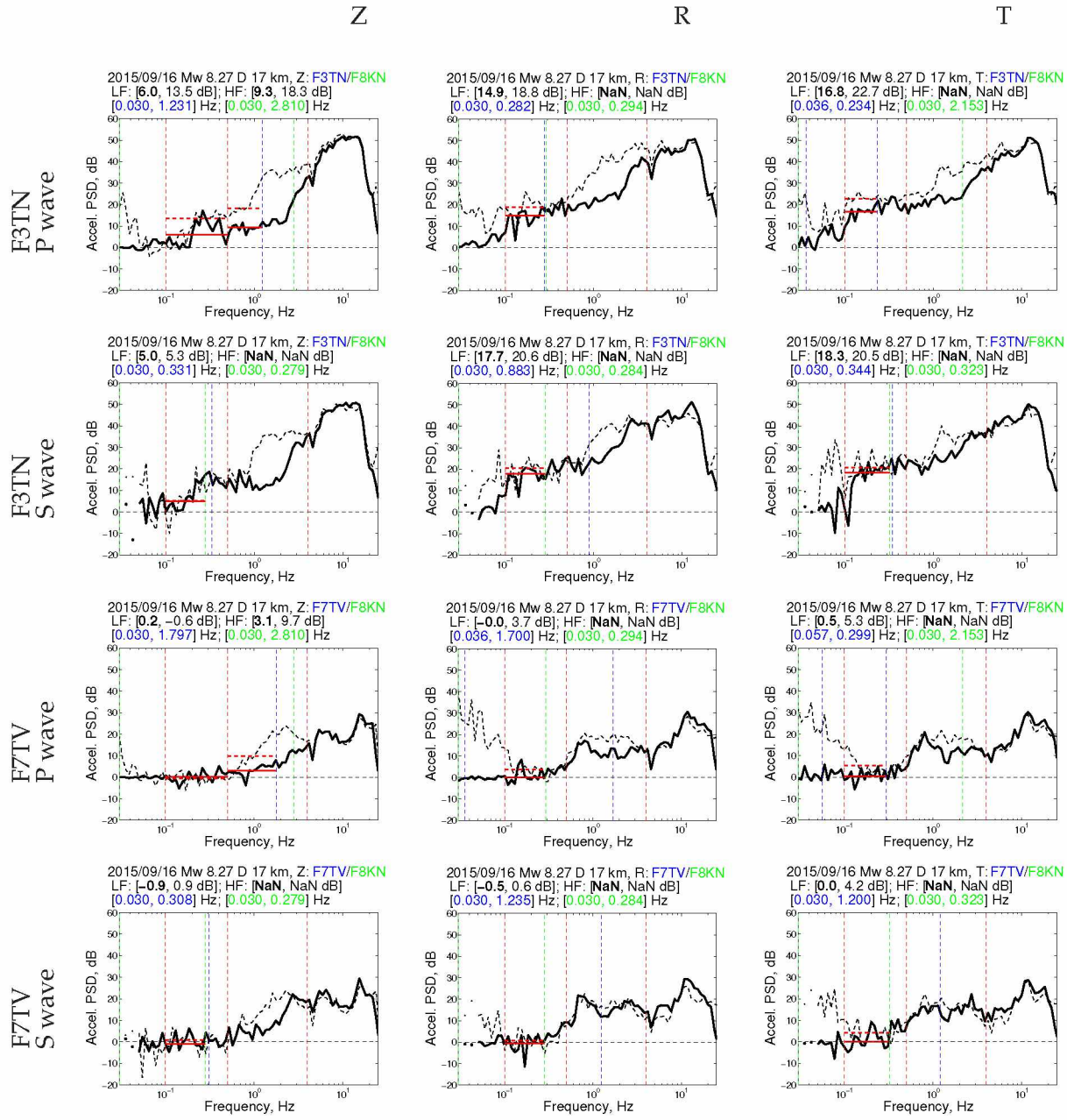

Figure C.17: Spectral ratio of teleseismic earthquake (solid) and pre-earthquake noise (dashed) for M_l **8.27** on **2015-09-16** with depth **17 km** and **12530 km** from the basin. Events are sorted by **magnitude**. D is the event depth. See Figures C.11 and C.12 for complete view of other stations of P and S wave amplifications for LFband.

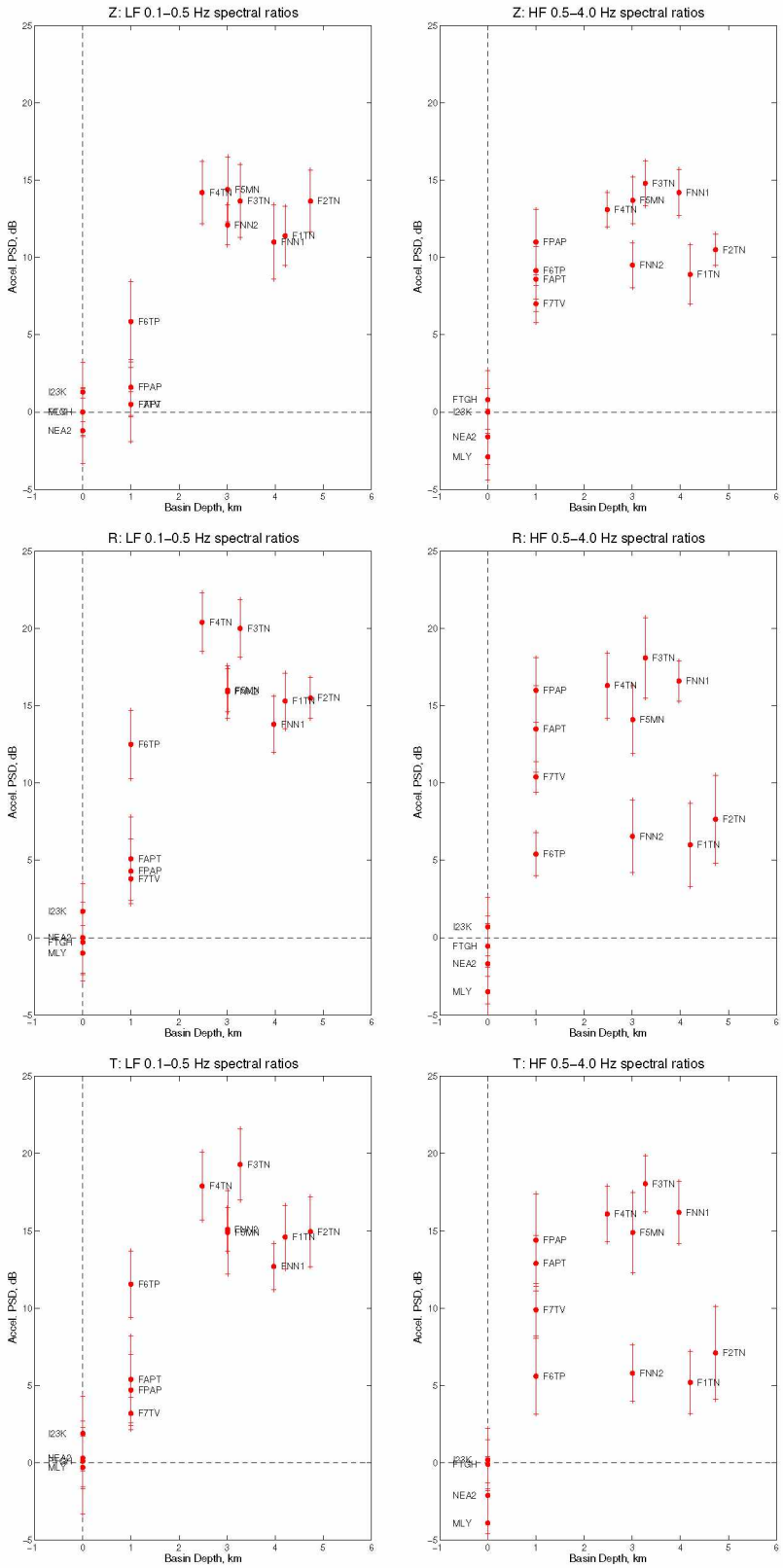

Figure C.18: Same as Figure 4.10ab, but shown here for the radial (middle row) and transverse (bottom row) components as well.

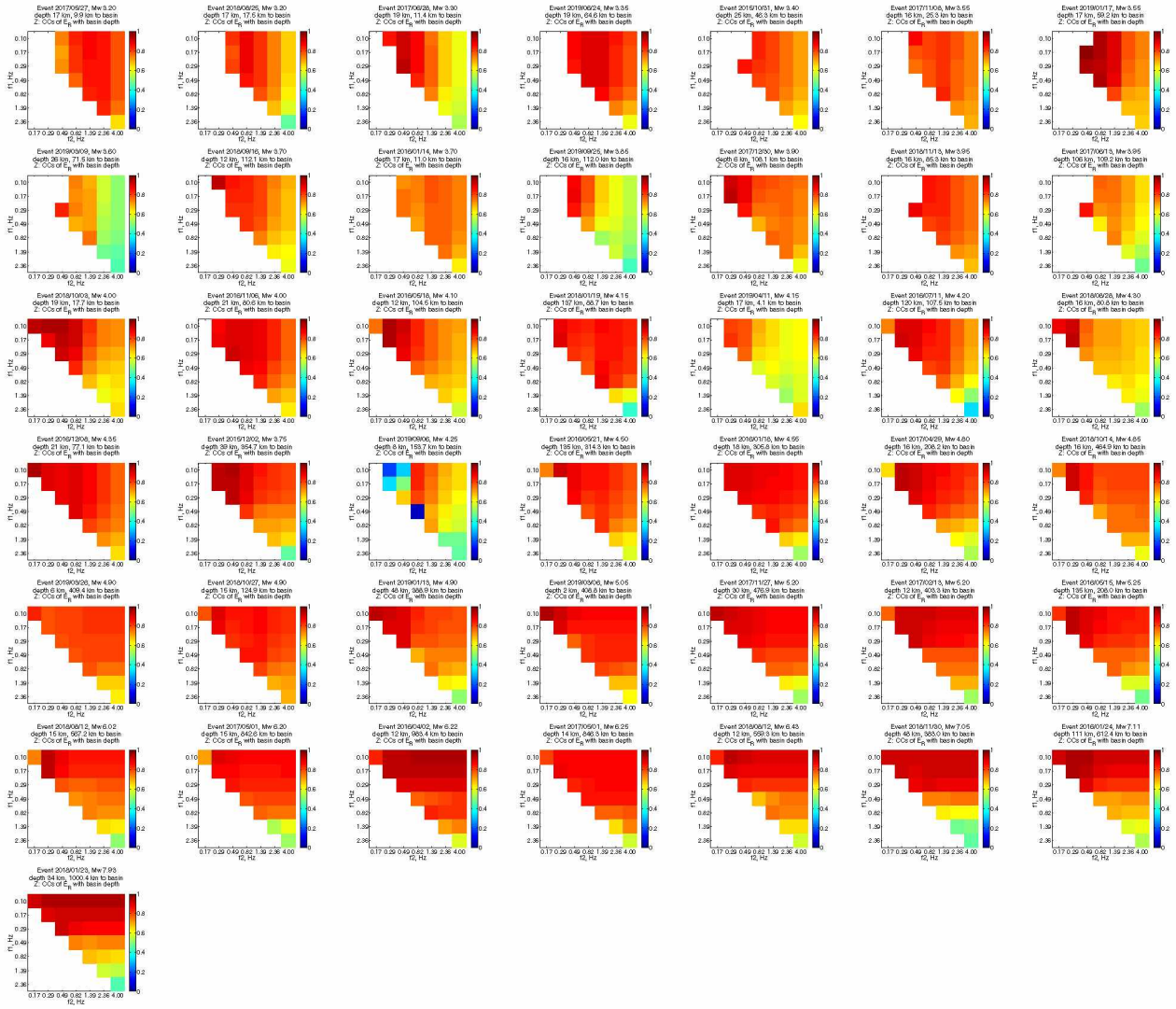

Figure C.19: Matrix plots for 43 local and regional earthquakes, ordered according to Table 4.1. Each colored box in a matrix plot indicates the correlation coefficient (CC) between a scatterplot between basin depth and a ground motion metric (here, E_R) calculated from a filtered set of seismograms (Smith & Tape, 2019b). The abundance of red here indicate that E_R correlates with basin depth across a wide range of frequencies and especially for 0.1–0.5 Hz. The highest-CC scatterplot for each matrix plot is shown in Figure C.20.

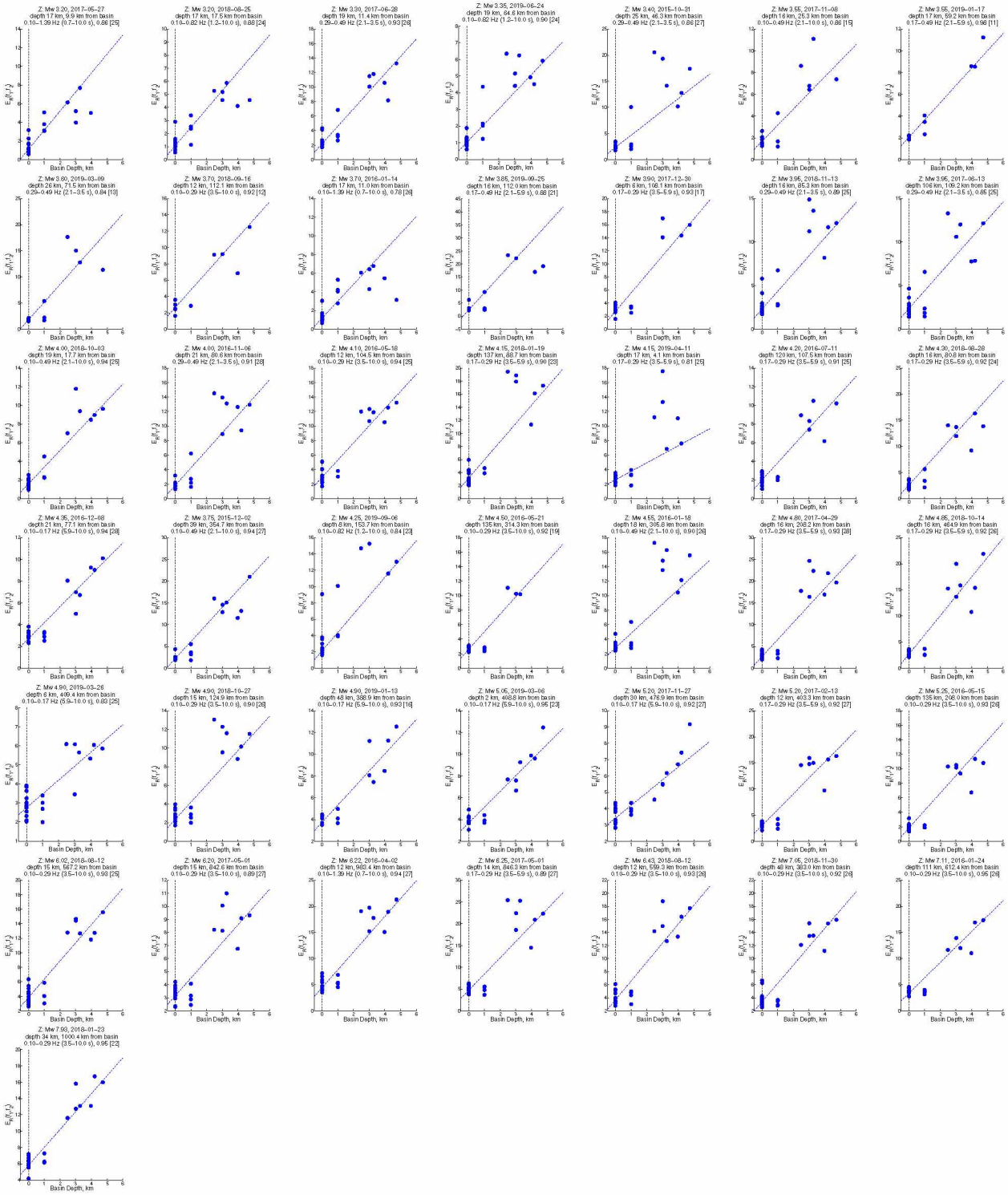

Figure C.20: Correlation between basin depth and E_R on the vertical component. Each scatterplot shown corresponds to the frequency bandpass $[f_1, f_2]$ associated with the highest-CC value in the corresponding matrix plot. Most bandpasses fall within the low-frequency range of 0.1–0.5 Hz. Note that the y-limits vary for each subplot.

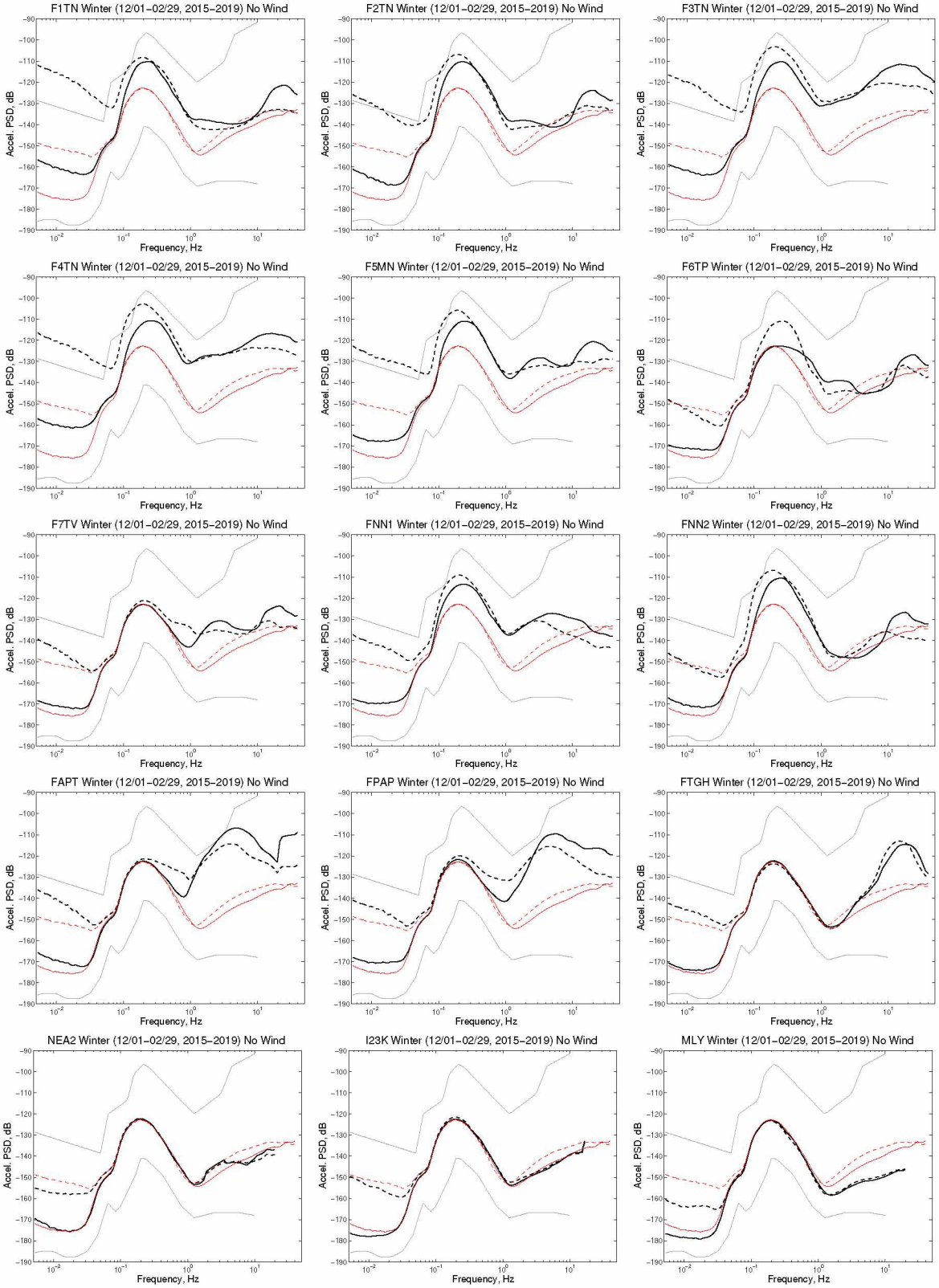

Figure C.21: Ambient noise stacks for no wind in winter for seismometers around Minto Flats: 13 FLATS stations plus AK.NEA2 (Nenana), AK.MLY (Manley Hot Springs) and TA.I23K (Minto). Solid and dashed lines are vertical and horizontal components, respectively. The spectra for each station are compared with those of bedrock station XV.F8KN (red). The FLATS stations exhibit higher noise levels than F8KN due to a combination of structural and environmental influences. The black bold lines are the NHNM and NLNM reference spectra (Peterson, 1993).

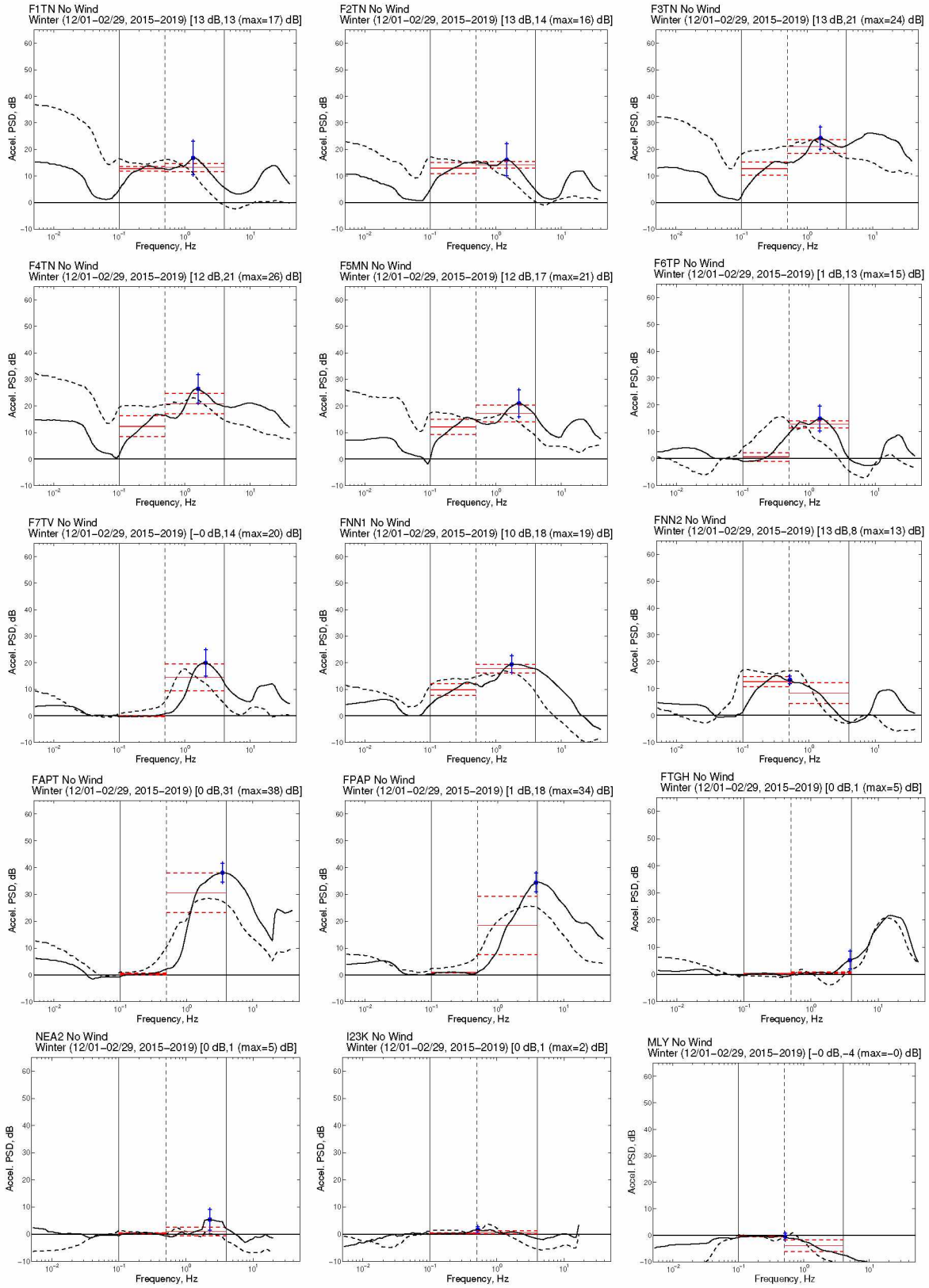

Figure C.22: Stack differences for the spectra in Figure C.21. The solid line shows the median power of all frequencies in the frequency interval 0.1–0.5 Hz and the dashed line shows one median absolute deviation (MAD). The red dot shows the maximum in the interval 0.5–4 Hz, and the uncertainty lines correspond to 1 MAD of the spectrogram at the station.

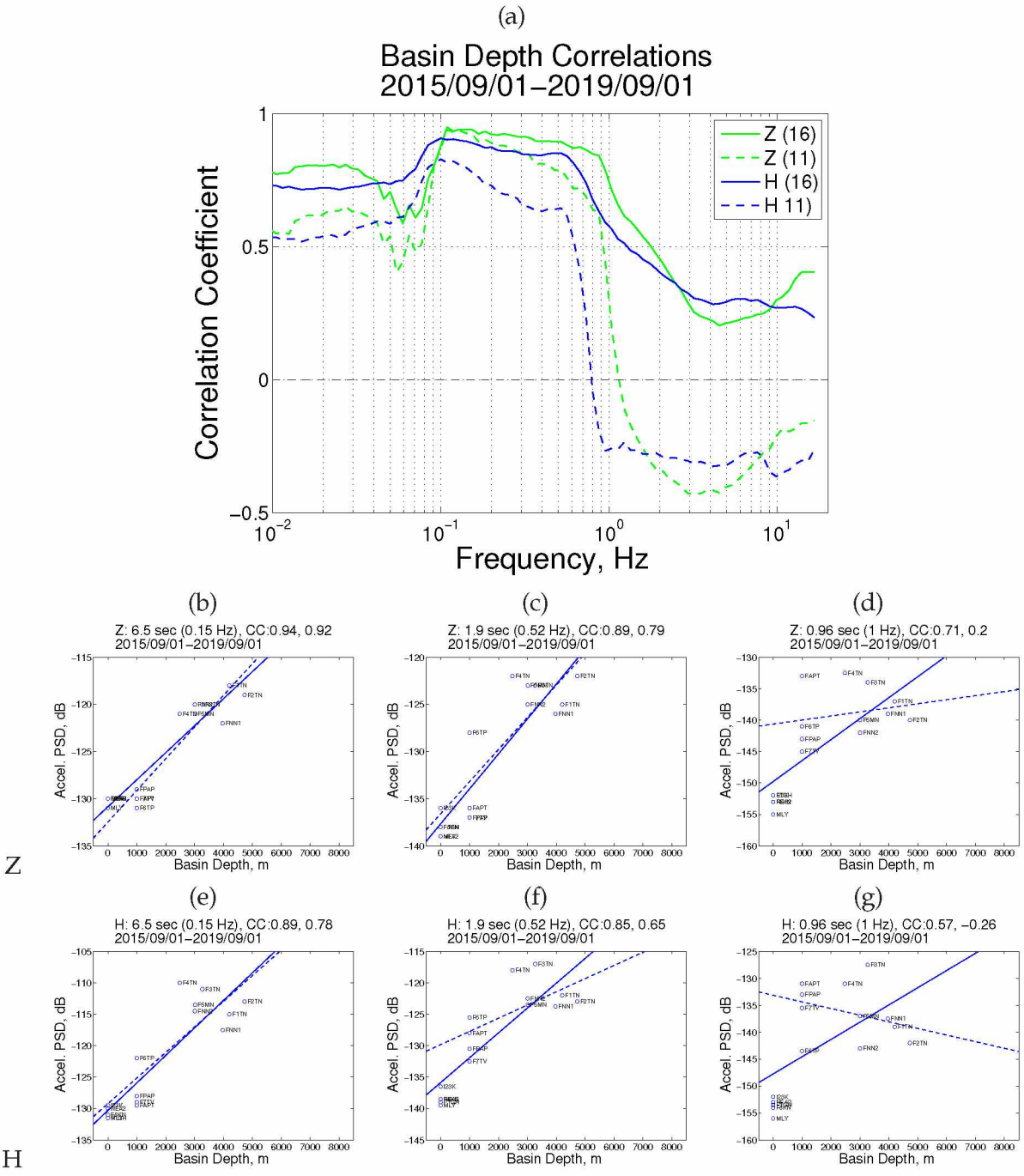

Figure C.23: (a) Frequency-dependent correlation between basin depth and noise amplitude from Smith & Tape (2019a, Figure 13) over the time period 2015-09-01 to 2019-09-01. Using basin depth map from PRA (2017). The curves are for the vertical (green) and horizontal (blue) components. The correlation is highest at periods 0.1–10 Hz and is high for longer periods. The solid lines are all stations in Smith & Tape (2019a, Table 1). Dashed lines are all FLATS stations excluding bedrock sites. Negative correlations at high frequencies are partly from cultural noise at stations FAPT and FPAP. (b)-(g) Scatterplots of ambient noise at 0.15, 0.5, and 1 Hz from (a) with basin depth. Basin depth source is from PRA (2017). Correlation coefficients for other frequencies are shown in (a). The solid lines are all Smith & Tape (2019a, Table 1). Dashed lines are all FLATS stations except bedrock sites. The first correlations coefficient (CC) is for all stations. The second CC is for all stations with non-zero depth.

C.3 References

Peterson, J., 1993. Observations and Modeling of Seismic Background Noise, Open-File Report 93-322.

PRA, 2017. Depth to Basement Map of Nenana Basin, Alaska, Proprietary map provided by Petrotechnical Resources of Alaska, April 2017.

Smith, K. & Tape, C., 2019a. Seismic noise in central Alaska and influences from rivers, wind, and sedimentary basins, *J. Geophys. Res. Solid Earth*, **124**, 11,678–11,704, doi: 10.1029/2019JB017695.

Smith, K. & Tape, C., 2019b. Seismic response of Cook Inlet sedimentary basin, southern Alaska, *Seismol. Res. Lett.*, **91**(1), 33–55, doi: 10.1785/0220190205.